Henk A. Dijkstra

Dynamical Oceanography

Springer

Dynamical Oceanography

Henk A. Dijkstra

Dynamical Oceanography

Springer

Henk A. Dijkstra
Univ. Utrecht
Inst. Marine and Atmospheric
Research
Princetonplein 5
3584 CC Utrecht
Netherlands
dijkstra@phys.uu.nl

ISBN: 978-3-540-76375-8 e-ISBN: 978-3-540-76376-5

Library of Congress Control Number: 2007941789

Cover design: deblik, Berlin

Printed on acid-free paper

9 8 7 6 5 4 3 2 1

springer.com

Preface

This text provides an introduction to the theory of the large-scale ocean circulation. There are excellent textbooks on physical oceanography (Pond and Pickard, 1983; OU-staff, 1989; Pickard and Emery, 1990; Tomczak and Godfrey, 1994; Pedlosky, 1996; Knaus, 1997), and geophysical fluid dynamics (Pedlosky, 1987; Cushman-Roisin, 1994; Salmon, 1998; Pedlosky, 2003; Mc Williams, 2006; Vallis, 2006). However, for a typical course where one wants to focus on the ocean circulation only at a challenging level for physics and mathematics students, a combination of material from these books is needed. This text is an attempt into this direction which has resulted in a book on a level between Pond and Pickard (1983) and Pedlosky (1996) with much basic material from Pedlosky (1987).

The book consists of four parts. In part I (chapters 1 - 4) a brief introduction is given into the ocean circulation and the governing equations of ocean flows. In addition, concepts are introduced that are necessary to describe and understand the behavior of large-scale ocean currents. In part II (chapters 5 - 10), the theory of the midlatitude wind-driven ocean circulation is presented. Considering model development, there is a top-down approach and reduced equations are derived using asymptotic methods and scaling. Part III (chapters 11 - 12) focusses on the understanding of equatorial currents and El Niño. In the last part IV, chapters 13 - 16, basic theory of planetary scale flows is presented, covering topics as the thermocline problem, the Antarctic Circumpolar Current, the Arctic Ocean circulation and the stability of the thermohaline circulation.

Additional material both in broadening (indicated by a **B**) and deepening (indicated by a **D**) of the topics discussed is indicated in separated blocks. At the end of each chapter several exercises are formulated and pointers to these exercises appear in the left margin of the main text. Many of these exercises are aimed to further develop methodological skills and to become familiar with the physical concepts. New material is introduced in only a few of these exercises. Solutions to the exercises are available at the website of the book at

http://www.phys.uu.nl/∼dijkstra/DO

It should be possible to go through this text with an elementary knowledge of mathematics and physics. Mathematical techniques such as Green's functions and the method of inner and outer expansions are presented using elementary examples. The use of proper asymptotic methods requires dimensionless equations while for understanding of physical concepts dimensional quantities are best suited. Throughout the text I therefore have used a strict *-subscript notation to indicate dimensional dependent quantities except in chapters where only dimensional quantities are used. In this way reduced model equations, such as the quasi-geostrophic model in chapter 5, are derived using dimensionless quantities and the dimensional result is stated afterwards. Results and models which are frequently used in the literature are presented in separate boxes for easy reference. Important issues can also be found in the Summary boxes at the end of each chapter.

I hope that students and interested researchers will like the way I have chosen to present the material and find this book a useful addition.

SEPTEMBER 2007, UTRECHT

To my parents, Klaas
and Sjoukje Dijkstra

Acknowledgments

The book is based on the (mandatory) course on Dynamical Oceanography which I gave for several years at the Institute for Marine and Atmospheric research Utrecht (IMAU) which is within the Department of Physics and Astronomy of Utrecht University, the Netherlands. I want to thank Will de Ruijter for his support of all my activities at the IMAU and for his efforts to make the IMAU such a pleasant and interesting place to work. His comments on the chapters 1 to 6 have been very valuable and for the material in the chapters 1 to 3, I have benefitted from notes of his course 'Introduction to Physical Oceanography'.

My former Ph.D. student Lianke te Raa is thanked for the efficient collaboration during the courses on Dynamical Oceanography at IMAU. Her comments on the chapters 13 and 14 are gratefully acknowledged as well as her input on the exercises. Leela Frankcombe read the entire manuscript and corrected much of the text and many equations. Ole Anders Nøst (Norsk Polar Institute, Norway) kindly provided files of figures for chapter 15.

My publishers at Springer (first Geert Jan Geraeds and later Chris Bendall) are thanked for their stimulus to complete this book. Laurence Mysak is thanked for his useful comments on parts of an early version of the text and for suggesting to include a chapter on the Arctic Ocean circulation.

The many students who have been actively involved in the IMAU courses on Dynamical Oceanography over the years are thanked for their patience, enthusiasm and input. Finally, my wife Julia contributed to the writing of this book in her own special way. I thank her for her patience and understanding.

Contents

I

INTRODUCTION

Chapter 1

A FIRST IMPRESSION

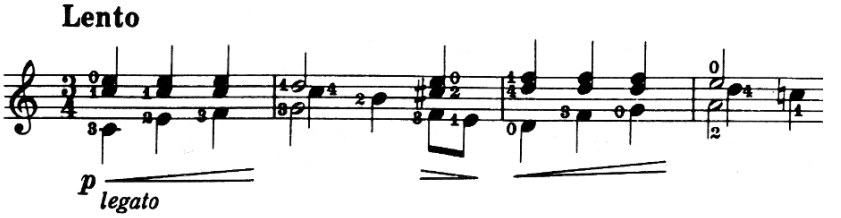

Estudio No 1., F. Sor

Physical oceanography is the study of the physics of the oceans and seas and is thus part of geophysics. Other oceanographic disciplines are biological oceanography and chemical oceanography. Over the last decades, physical oceanography has developed from a descriptive to an explanatory and predictive science and has matured within the field of environmental physics. In section 1.1, a brief description is given of the bathymetry of the ocean basins. Some historical notes on the exploration of the oceans are provided in section 1.2. In section 1.3, an introduction is given into the properties of seawater with focus on the concepts of static stability, potential temperature and the T-S diagram. Furthermore, a first peak of the global sea surface temperature and sea surface salinity distributions is given.

1.1. The ocean basins

The Earth is a spheroid, i.e., a sphere that is flattened somewhat near the poles compared to the equator, due to the action of the centrifugal force. Some characteristics of the Earth which are relevant for physical oceanography are provided in Table 1.1. At the moment there are accurate data sets of the surface relief of the Earth. An important data set is the ETOPO bathymetry, which is available now at $2'$ resolution (see http://www.gfdl.noaa.gov/products/vis/data/datasets/etopo2_topography.html). In Fig. 1.1, a plot of the $5'$ data set (ETOPO5) is provided using plotting software from http://iridl.ldeo.columbia.edu/. The global ocean consists of three interconnected basins: the Pacific Ocean, the Atlantic Ocean and the Indian Ocean. The largest connection between the basins is in the Southern Hemisphere; part of this connection is unblocked by continents. A much smaller connection between the Pacific and the Indian Ocean exists through the Indonesian Straits. A connection also exists in the Northern Hemisphere between the Pacific and the Atlantic through the shallow Bering Strait.

A typical ocean basin starts from the coast, with the continental margin extending to a depth of about 200 m. In width, this margin can vary between several tens to hundreds of kilometers. Further from the coast there is usually an abrupt transition from the continental margin to the continental slope, the latter with a slope of about 5 to 10%. The continental slope connects to the deep basin which has a typical slope of 0.01 to 0.1%. The deep sea plains are sometimes intersected by undersea mountain ridges, such as the Mid-Atlantic ridge, and deep trenches, such as the Marianas trench near the Philippines.

The majority of the surface of the Earth (70.8%) is covered by ocean water (361×10^6 km^2) The volume of land that extends above sea level is about 10^8 km^3

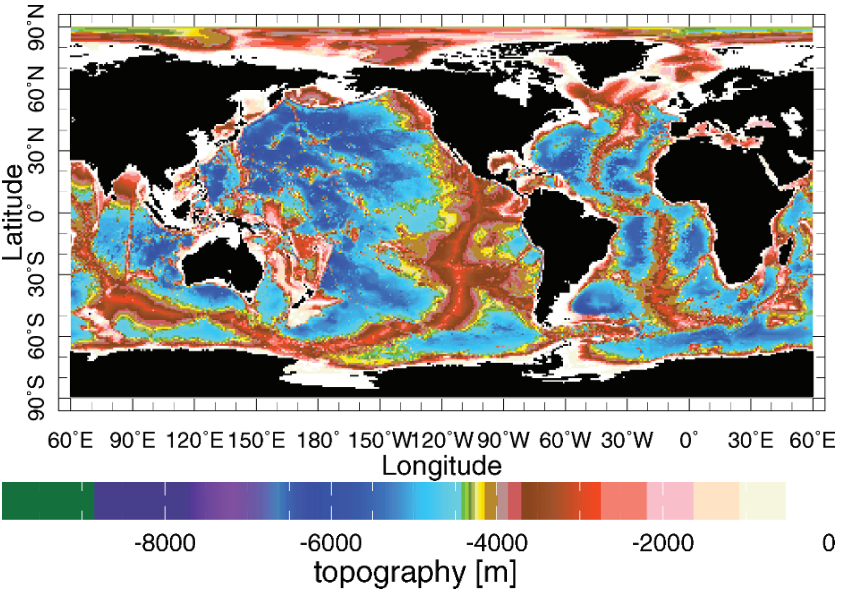

Figure 1.1. Ocean bathymetry as plotted from the ETOPO5 global bathymetry dataset; the color scale below indicates the depth below sea level.

Characteristic	Value
Average radius	6.37×10^6 m
Angular velocity	7.5×10^{-5} s^{-1}
Total volume	1.37×10^9 km^3
Total mass	5.97×10^{24} kg
Total surface area	5.10×10^{14} m^2
Ocean surface area	3.61×10^{14} m^2
Mean ocean depth	3.8×10^3 m
Mean land elevation	8.4×10^2 m

Table 1.1. Some characteristic properties of the Earth relevant for physical oceanography.

and the volume of seawater is about 14×10^8 km^3. In the Northern Hemisphere about 60% of the surface is ocean and 40% is land. In the Southern Hemisphere

the ocean surface is much more dominant with about 80% being ocean (Fig. 1.2). As we will see later in this book, this equatorial asymmetry in land-sea contrast is important to understanding the differences in the ocean circulation and its effect on climate in both hemispheres. The average depth of the ocean (about 3800 m)

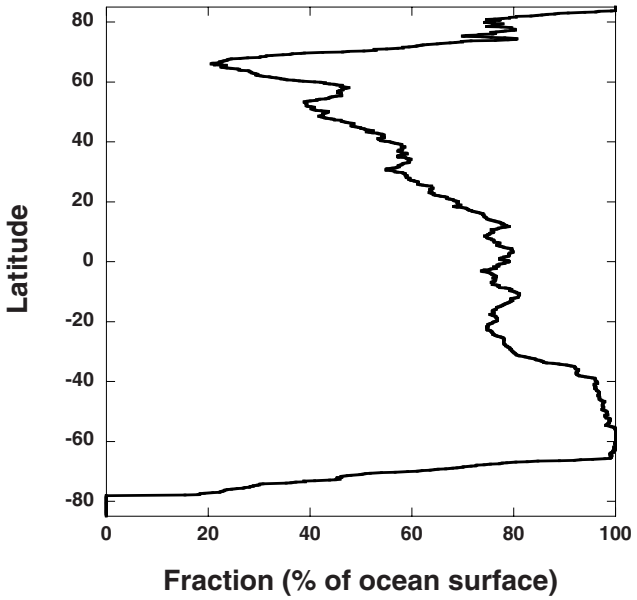

Figure 1.2. Fraction (in % of the total surface) covered by the ocean as a function of latitude.

is more than a factor of 1000 times smaller than the width of the ocean basins. In plots of measured or modeled quantities in physical oceanography the vertical scale is usually greatly exaggerated with respect to the horizontal scale.

Additional Material

B: Chapter 3 on the 'Sea Floor and its Sediments' (in particular the sections 3.1-3.2) of Duxbury et al. (2000) provides a broader view on the ocean basin bathymetry and its connection to geodynamical processes with many color figures. An elementary introduction can also be found in chapter 2 of OU-staff (2004b).

1.2. Exploration of the oceans

In section 1.2.1 we mention some of the important facts of oceanographic history. The availability of data in the modern era and the relatively easy processing of all these data today is discussed in section 1.2.2.

1.2.1. A tiny bit of history

Both the Vikings and the Polynesians made use of their experience with ocean currents in their exploration of new areas in the Atlantic and Pacific, respectively. The Normans for example had settlements near New Foundland around the year 1000 AD and travelled back and forth to their home country using Atlantic currents.

First documented knowledge on the ocean currents was gathered during the expeditions of Christopher Columbus (1492–1494), Vasco da Gama (1497–1499) and Ferdinand Magellan (1519–1522). Columbus pioneered the measurements of currents in the Atlantic. These measurements were continued by James Cook (1728–1779) on the ships the Endeavour, the Resolution and the Adventure, and by Charles Darwin (1809–1882) on the Beagle. It was James Clark Ross and John Ross who crossed the Arctic and Antarctic with the Victory, the Isabella and the Erebus.

The first map of the Gulf Stream was made in 1769 by Benjamin Franklin and Timothy Folger (Fig. 1.3) and was motivated by the problem to reduce the time to cross the Atlantic. Each ship captain was advised to follow the Gulf Stream to Britain and to avoid it when going back to the United States. It is quite likely that the existence of the Gulf Stream contributed to the discovery of America. In Columbus' time, wood and other objects frequently appeared on the coast of Norway, Scotland and Ireland. For someone like Columbus this may have lead to the idea that there had to be land westward of Europe.

An important discovery was made in 1751 near 24°N in the Atlantic by Henry Ellis, captain of a British slave transport vessel. Using a new instrument, that had been developed by British preacher Stephen Hales, he measured the temperature of the deep ocean and found that the deep water was unexpectedly cold. Although the impact of these measurements would become clear only two centuries later, Ellis had discovered a characteristic of the global ocean circulation: deep water is relatively cold everywhere. Until that time, it was believed that the heat would have diffused from the surface to deep layers. This riddle was solved by Count Rumford in the early 1800s: the cold water sinks in polar seas and moves equatorward through deep currents.

In the 19th century, many incidental measurements on ships followed which were collected and analyzed by the American scientist Maury (1806-1873). Maury was the first to make detailed maps of winds and currents and wrote the

Figure 1.3. The Franklin-Folger map of the Gulf Stream made in 1769.

first book on Physical Oceanography entitled: *The Physical Geography of the Sea*; he is usually called the first physical oceanographer.

The famous Challenger expedition (December 1872 - May 1876) was mainly motivated by biological scientific questions. One of the hypotheses was the so-called 'Azoic' hypothesis stating that there would be no ocean life in the deep ocean because of the high pressure and the lack of light. Under leadership of Wyville Thomson, a 'consortium' of scientists performed measurements including 492 profiles of temperature along the route. During the expedition 4717 new species were discovered and the 'Azoic' hypothesis was falsified. The Challenger expedition concluded with a 50-volume report containing a wealth of oceanographical information.

It took until 1925 for a dedicated physical oceanographic expedition was organized. From 1925-1927, the German Meteor expedition collected many measurements of temperature and salinity over a large area in the Atlantic. The CTD (Conductivity, Temperature, Depth), the instrument to accurately and simultaneously measure conductivity of seawater (and hence salinity) and temperature, was not invented until 1955 by Bruce Hamon and Neil Brown.

During the International Geophysical Year in 1957-1958 international cooperation between different countries grew and measurements were done over a relatively large ocean domain. Many details of the sea surface temperature during the 1957 El Niño, for example, were measured and it appeared that the sea surface

temperature was anomalously high over a much larger area of the Pacific than previously thought. This lead Jacob Bjerknes to the discovery of the connection between changes in the equatorial trade winds and those in the sea surface temperature in the eastern Pacific. It also provided the first clear example of the important role of the ocean circulation in the climate system.

1.2.2. The modern era

The World Ocean Circulation Experiment (WOCE) was operational from 1985-1995 and aimed to measure, describe, model and understand the global ocean circulation. Along many sections hydrographic measurements (temperature, salinity) have been collected and several of these sections have been repeated two or three times to determine long term variations in temperature and salinity. The data are freely available through the website http://whpo.ucsd.edu/ and can be viewed and analyzed relatively easily by using, for example, the Ocean Data View software (http://odv.awi-bremerhaven.de/) or the Java Ocean Atlas (http://odf.ucsd.edu/joa/). The WOCE program also contained a large component dedicated to ocean modeling and there are now a dozen or so ocean models available to the community. Other large-scale international programs in which the study of the oceans was central were the Tropical Ocean Atmosphere Program (TOGA) and the (still ongoing) Climate Variability (CLIVAR) project.

The first satellite for oceanographic research, the SEASAT, was launched in 1978. Although the satellite was only operational for one month, important measurements of the sea surface topography were performed through radar altimetry. With instruments on a satellite there is the possibility for global coverage of the ocean surface (remote sensing). Measurements of the sea surface height (TOPEX, ERS), surface chlorophyll concentration (SeaWiFs) and sea surface temperature (AVHRR) are now routinely performed and can be downloaded from the internet (see http://topex-www.jpl.nasa.gov/).

First steps have been taken now towards an ocean global observing system. For example, ARGO is a global array of 3,000 free-drifting profiling floats that measures the temperature and salinity of the upper 2000 m of the ocean. This allows, for the first time, continuous monitoring of the temperature, salinity, and velocity of the upper ocean, with all data being relayed and made publicly available within hours after collection (see http://www.argo.ucsd.edu/).

An overview of all data available is provided by the NOAA National Oceanographic Data Center (http://www.nodc.noaa.gov/index.html) where all links are provided to the locations of the different data sets.

Additional Material

B: A brief but interesting overview of the history of oceanography can be read in the Prologue of Duxbury et al. (2000). Chapter 1.3 of WOCE (2001) provides a good impression on the origin, development and conduct of WOCE. A historical overview of the developments in physical oceanography since 1950 can be found in (Jochum and Murtugudde, 2006).

1.3. Characteristics of seawater

Many of the unique features of the oceans can be attributed to the special properties of water itself. The water molecule (H_2O) is composed of two hydrogen atoms which are connected through an oxygen atom. The water molecule has a clear asymmetric structure because the axes between the H atoms and O atom intersect at an angle of 105°. As a consequence, the electric charge in the H_2O is anisotropic providing the water molecule with an electric dipole moment. Water can dissolve more substances than any other liquid on Earth which explains the presence of many ions in the ocean and the high salinity of ocean water.

Because of its large electric dipole moment, water molecules form chains through hydrogen bonds. This means that water has an extremely high surface tension compared to other liquids. One of the effects of this high surface tension is the occurrence of capillary waves on the ocean surface. These waves play an important role in transferring momentum between the atmosphere and the ocean. Another consequence of the chain formation is the high specific heat and large latent heat of evaporation of water. The heat absorbing capacity is increased by the transparency of water to sunlight; only a small part of the solar radiation is reflected at the sea surface. The oceans therefore have a large thermal inertia and play an important role in the storage and transport of heat in the climate system.

1.3.1. Salinity

Sea water consists of a dilute solution of ions, such as Cl^- and Mg^{2+}. In a certain volume element, let there be $n-1$ of these ion types with masses $m_i, i = 1, \cdots, n-1$ and indicate the mass of the water by m_n. The total mass m and the mass fractions $c_i, i = 1, \cdots, n-1$ are then given by

$$\sum_{k=1}^{n} m_k = m \; ; \; c_k = \frac{m_k}{m} \rightarrow \sum_{k=1}^{n} c_k = 1. \tag{1.1}$$

It is an experimental fact that the relative composition of the different ions is constant in seawater far from continental boundaries. Actually, this was one of the discoveries of the Challenger expedition (cf. section 1.2). It indicates that the

ocean water is well mixed over geological time scales. This motivates to define the salinity S and the water fraction W as

$$S = \frac{1}{m}\sum_{k=1}^{n-1} m_k \; ; \; W = \frac{m_n}{m}, \tag{1.2}$$

such that all mass fractions can be expressed as $c_k = \lambda_k S$, $k = 1, \cdots, n-1$ with

$$\lambda_k = \frac{m_k}{\sum_{l=1}^{n-1} m_l} \rightarrow \sum_{k=1}^{n-1} \lambda_k = 1 \; ; \; S + W = 1. \tag{1.3}$$

In this way, seawater can be considered as a two-component liquid (water and salt) in which there is only one independent variable, the salinity S.

In early times, the salinity was determined from samples of seawater through titration of chloride ions (Cl^-) and the use of the constant relationship between chloride content Cl and salinity S, given by

$$S = 1.806\, Cl. \tag{1.4}$$

Nowadays one determines the salinity through the electrical conductivity of a particular seawater sample which is much more accurate than the titration method. For the open ocean, a typical value of the salinity is 35 gram of salt per kg of seawater, also indicated as $S = 35$ ppt (parts per thousand). Often the Practical Salinity Unit (psu), defined as the ratio of the conductivity of the sample and a standard $NaCl$ solution, is used as a measure of the salinity; values in psu hardly differ from those in ppt ($S_{ppt} = 1.004867 S_{psu}$).

1.3.2. The surface distribution of temperature and salinity

A still often used climatology of temperature and salinity data is the Levitus and Boyer multivolume ocean atlas (Levitus and Boyer, 1994; Levitus et al., 1994). This multivolume atlas presents global, objectively analyzed fields of major ocean parameters on a one-degree latitude-longitude grid for selected standard depth levels from the sea surface to 5500 m depth. Work to date includes quality control of historical in-situ temperature, salinity, oxygen, phosphate, nitrate, and silicate data and the preparation of one-degree latitude-longitude mean fields for each of these parameters. A more modern data set is from Gouretski and Koltermann (2004) and these data can be conveniently inspected and plotted using the Ocean Data View software (http://odv.awi-bremerhaven.de/).

From the Gouretski and Koltermann (2004) data, the mean sea surface temperature of the ocean is plotted in Fig. 1.4a. At mid-latitudes, the temperature at the western part of each basin is substantially warmer than that at the eastern side. At high latitudes in the Atlantic Ocean, the water in the Norwegian Sea is

relatively warm compared to water at the same latitude in the northern Pacific. There is a marked temperature gradient in the equatorial Pacific with a relatively cold tongue in the east and a relatively warm pool in the west. In Fig. 1.4b, the

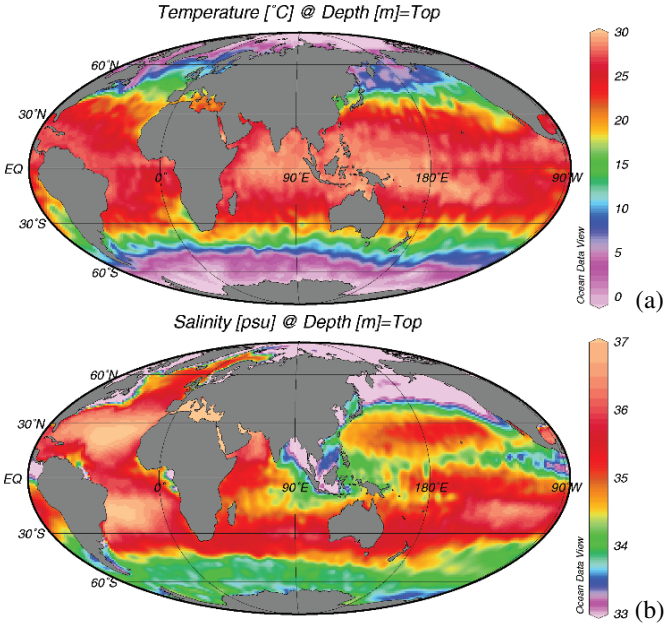

Figure 1.4. Pattern of the mean (a) sea surface temperature and (b) sea surface salinity of the ocean as plotted using the ODV software and the Gouretski and Koltermann (2004) gridded ocean data atlas.

mean sea surface salinity is plotted. The spatial structure of the sea surface salinity is strongly coupled to the pattern of evaporation, precipitation and inflow of freshwater through rivers and the melting of ice. As we will see in chapter 2, the subtropical Atlantic is an area where evaporation is larger than precipitation giving a relatively high sea surface salinity. The average salinity is larger in the Atlantic than in the Pacific. In the Southern Ocean the salinity is zonally very uniform. Extreme values of sea surface salinity occur in the Red Sea (values larger than 40 ppt) due to large evaporation and the East Sea between Sweden and Finland (values of about 7 ppt), the latter due to the large inflow of freshwater from rivers and the small exchange with the Atlantic.

1.3.3. T - S diagrams and water masses

Salinity is a very important controlling agent of the density of ocean water which increases with increasing salinity. Apart from the salinity, the temperature T also exerts an influence on the density of ocean water. When pure water is heated, the velocities of the water molecules increase which leads to thermal expansion. The supplied energy is also used for the formation of hydrogen bridges which leads to thermal compression. The combination of both effects causes the maximum density of pure water at 4°C, instead of at the freezing point.

Increasing salinity values decrease the freezing temperature of seawater (Fig. 1.5). Also the temperature at which a maximum density occurs decreases with increasing salinity and at $S = 24.695$ ppt both temperatures are equal to T = -1.332 °C. A lake therefore freezes more easily than an ocean surface. In the motionless freshwater of the lake the upper water column can be cooled from 4°C to 0°C with no resulting mixing. In the salty ocean, mixing would result immediately and the whole water column needs to be cooled to induce ice formation.

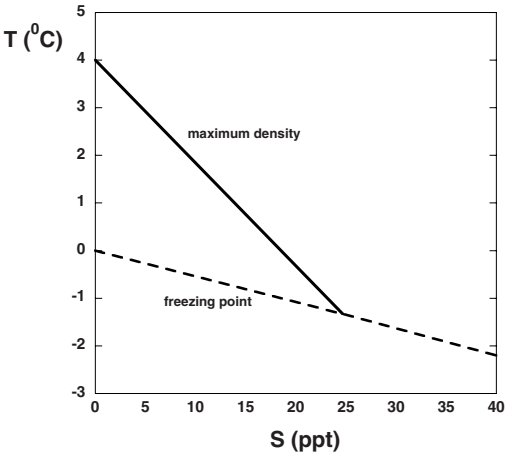

Figure 1.5. Plot of the freezing temperature and the temperature at maximum density versus the salinity.

During a hydrographic CTD measurement both temperature and salinity (through conductivity) are recorded as a function of depth, while depth is recorded indirectly through a pressure sensor. Salinity can be determined with an accuracy of 0.005 ppt and temperature with an accuracy of 0.005°C. The vertical salinity differences in the deep ocean are usually very small and hence accurate

measurement is important because of the large effect on the density distribution in the water column.

A typical result of hydrographic measurements is shown in Fig. 1.6, where the temperature (Fig. 1.6a) and salinity (Fig. 1.6b) are plotted along the WOCE A16 section in the Atlantic (Fig. 1.6c). From these plots, one can observe that the

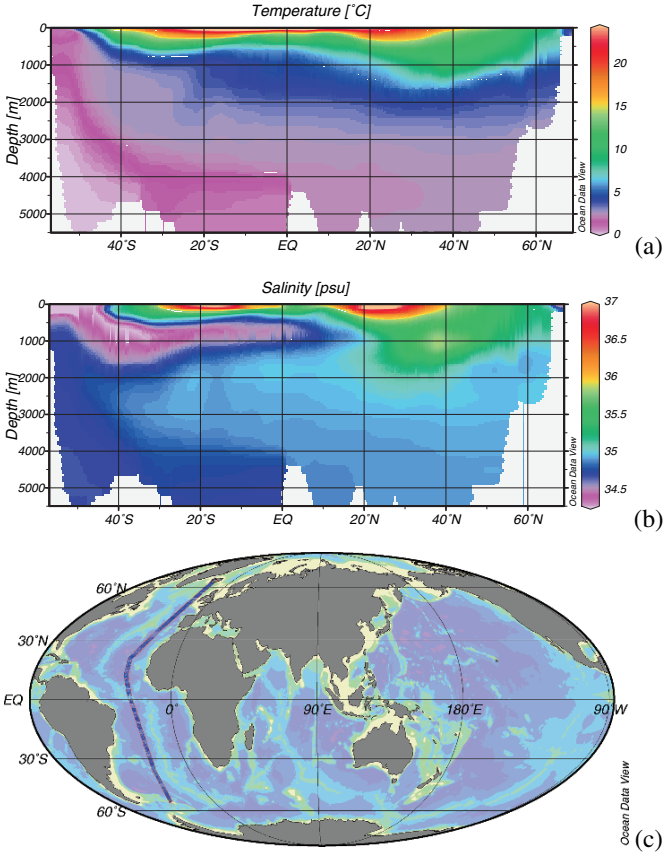

Figure 1.6. (a)Temperature and (b) Salinity along the A16 section (c) of the WOCE program as plotted using the ODV software and the Gouretski and Koltermann (2004) gridded ocean data atlas.

vertical distribution of ocean water properties seems to be organized into different layers. For example, the water from the south (pink in Fig. 1.6a) having a

temperature near 0°C seems to sink downward from Antarctica and then extends northward along the bottom of the Atlantic (this is the so-called Antarctic Bottom Water or AABW).

For one station along a specific section, an important result of hydrographic measurements is a so-called T-S curve; an example of such a curve measured along the WOCE A16 section (which is at 12°N in Fig. 1.6) is shown in Fig. 1.7. At this station, the temperature decreases monotonically with depth (Fig. 1.7a)

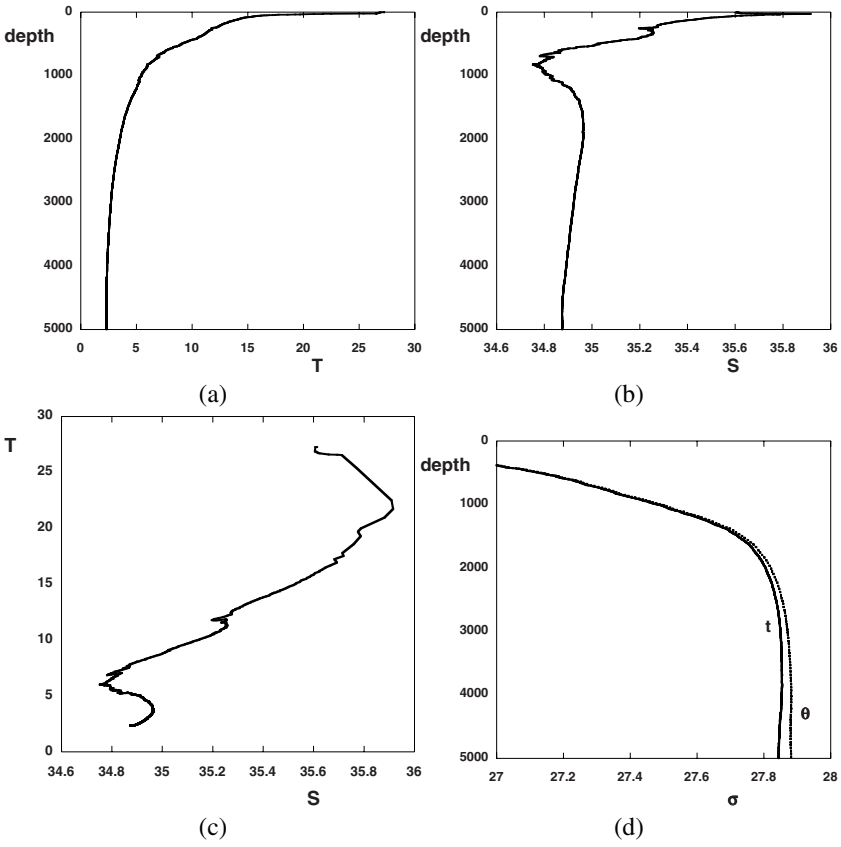

Figure 1.7. Data from station 129 (12°N, 21°W) along the A16 section of the WOCE program. (a) Temperature versus depth; (b) Salinity versus depth. (c) T-S diagram. (d) Densities σ_t (solid) and σ_θ (dashed) versus depth.

and the salinity has a minimum at about 800 m depth (Fig. 1.7b).

Water Mass	T (°C)	S (ppt)
North Atlantic Deep Water (NADW)	2-4	34.9-35.0
Antarctic Bottom Water (AABW)	-0.5 - 0	34.6 - 34.7
Antarctic Intermediate Water (AAIW)	3-4	34.2 - 34.3

Table 1.2. Range of characteristic properties from several water masses in the Atlantic.

Ex. 1.1

It appears that certain volumes of water with particular T-S characteristics can be found in the hydrographic measurements. The characteristics of these so-called water masses can be traced great distances from the locations at which they were formed. This is because the water is advected through the ocean basins without much mixing. For example, part of the North Atlantic Deep Water (NADW) is formed in the Greenland-Iceland-Norwegian seas through cooling of the upper layers of the ocean and subsequent vigorous vertical mixing. The NADW has a temperature range of 2 - 4 °C and its salinity is in the range of 34.9 - 35.0 ppt. In the T-S diagram at 12°N in the Atlantic (Fig. 1.7c) the NADW is found at a depth of 1500 m. In this way, the NADW can be identified even in the South Atlantic, which indicates the existence of a large-scale ocean circulation system. The T-S characteristics of some important water masses are given in Table 1.7.

Ex. 1.2

1.3.4. Static stability

As soon as the in-situ temperature T, salinity S and the pressure p of a water parcel are known, its density can be determined through the equation of state $\rho = \rho(T, S, p)$. This equation of state is determined accurately in the laboratory and a standard UNESCO formula exists (Fofonoff and Millard, 1983) with modern modifications of it (McDougall et al., 2003; Jackett et al., 2006).

Instead of the actual density, many relative density differences are used in the literature. Often a relative density σ_t (kgm^{-3}) is used defined by

$$\sigma_t = \rho(T, S, 0) - 1000. \tag{1.5}$$

This is the value of the density with respect to pure water at the mean atmospheric pressure at sea level. A plot of σ_t over a range of T-S values is shown in Fig. 1.8 where the standard UNESCO formula was used in (1.5). As can be seen the sensitivity of the density versus temperature decreases in colder water. Hence in polar areas the influence of salinity on the density is larger than in tropical areas.

A complication is that seawater is slightly compressible. With each meter depth in the ocean, the pressure increases by 0.1 Pa and hence the temperature of a water parcel will increase with depth just by adiabatic (without the addition of

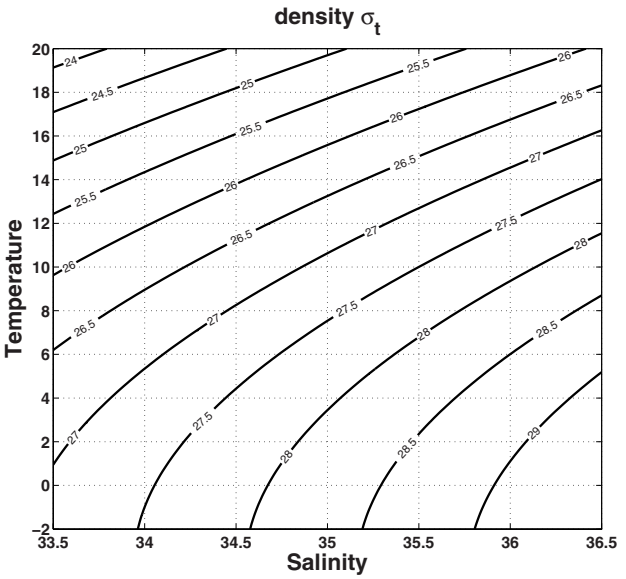

Figure 1.8. Contour plot of the density σ_t versus temperature T and salinity S using the UNESCO formula (Fofonoff and Millard, 1983).

heat) compression since work is imposed on the parcel. On the other hand, the temperature of a water parcel will decrease when it is raised adiabatically in the ocean. In the deep ocean, in particular where vertical temperature variations are very small, it is important to correct for compressibility effects to obtain the right picture of the vertical density profile. To account for compressibility effects, the concept of potential temperature ϑ is introduced. It is defined as that temperature a sample of sea water would obtain when adiabatically raised to the surface.

Ex. 1.3

The relation between potential temperature and in-situ temperature follows from considering the vertical movement of water parcels in a background stratification determined by a density profile $\rho(z)$. At a vertical level $z = -z_i$ the in situ properties (Fig. 1.9) of the water are (ρ_i, S_i, T_i) and the pressure is p_i. Assume that a water parcel with volume ΔV moves downwards from $z = -z_1$ to $z = -z_2$ adiabatically and without changes in salinity. The temperature in the water parcel, say T_2^W, is only changed through adiabatic compression ($T_2^W > T_1$). Hence,

$$T_2^W = T_1 + \Delta T \ , \ \Delta T = \frac{\partial T}{\partial p} \Delta p, \tag{1.6}$$

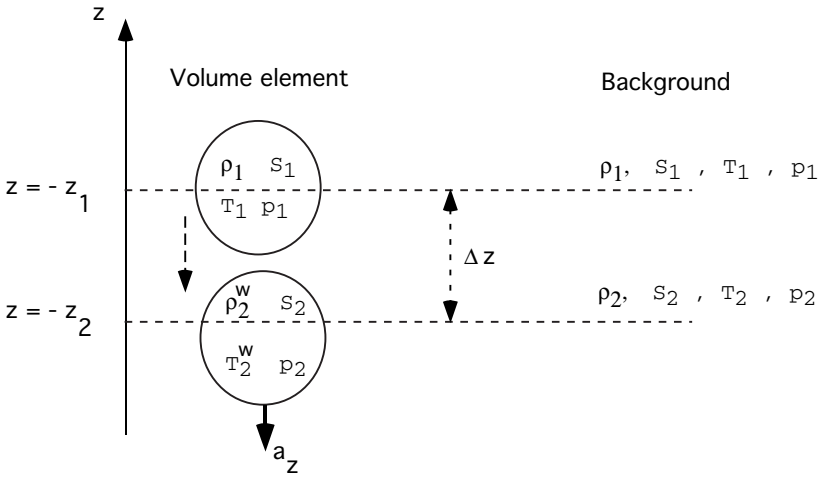

Figure 1.9. Sketch to clarify the concept of static stability. The in-situ temperature and salinity of the water parcel are indicated by the superscript W. The water parcel moves vertically only adiabatically and without change in salinity from $z = -z_1$ to $z = -z_2$. It experiences an acceleration a_z due to the density difference between the parcel and the background density field.

where $\partial T/\partial p > 0$ indicates the adiabatic compression and $\Delta p = p_2 - p_1 > 0$ the vertical pressure difference. Because of near hydrostatic equilibrium we have (with $\Delta z = -z_2 + z_1 < 0$):

$$\Delta p = -\rho_1 g \Delta z, \tag{1.7}$$

such that

$$\Delta T = -\frac{\partial T}{\partial p}\, \rho_1\, g\, \Delta z \equiv -\Gamma \Delta z. \tag{1.8}$$

In the equation above, Γ (°C m^{-1}) is the adiabatic temperature gradient. Down to a depth of 1 km, the value of Γ is negligibly small. At a depth of 5 km, the value of $\Gamma \approx 0.14$ °C/km and at a depth of 9 km the value of $\Gamma \approx 0.19$ °C/km.

By Newton's second law, the vertical acceleration a_z on the parcel with volume ΔV is

$$a_z = \frac{\Delta V g(\rho_2 - \rho_2^W)}{\Delta V \rho_2^W}. \tag{1.9}$$

In the limit $\Delta z \to 0$, we use

$$\rho_2 = \rho_1 + \frac{\partial \rho}{\partial z}_{|_{z=-z_1}} \Delta z + \ldots = \rho_1 + \left[\frac{\partial \rho}{\partial S}\frac{\partial S}{\partial z} + \frac{\partial \rho}{\partial T}\frac{\partial T}{\partial z} + \frac{\partial \rho}{\partial p}\frac{\partial p}{\partial z}\right]_{z=-z_1} \Delta z + \ldots, \tag{1.10}$$

and

$$\rho_2^W = \rho_1 + \frac{\partial \rho}{\partial z}^W{}_{|_{z=-z_1}} \Delta z + \ldots = \rho_1 + \left[-\Gamma \frac{\partial \rho^W}{\partial T} + \frac{\partial \rho^W}{\partial p} \frac{\partial p}{\partial z} \right]_{z=-z_1} \Delta z + \ldots . \tag{1.11}$$

As the variations in T and S are small, $\partial \rho^W / \partial p \approx \partial \rho / \partial p$ and we find that as $\Delta z \to 0$

$$a_z = \frac{g}{\rho_1} \left[\frac{\partial \rho}{\partial S} \frac{\partial S}{\partial z} + \frac{\partial \rho}{\partial T} \left(\frac{\partial T}{\partial z} + \Gamma \right) \right] \Delta z. \tag{1.12}$$

The quantity $E = -a_z/(g\ \Delta z)$ is defined as the static stability of the water column and with (1.12) it follows (with $\rho = \rho_1$) that

$$E = -\frac{1}{\rho} \left[\frac{\partial \rho}{\partial S} \frac{\partial S}{\partial z} + \frac{\partial \rho}{\partial T} \left(\frac{\partial T}{\partial z} + \Gamma \right) \right]. \tag{1.13}$$

When $E > 0$ (and hence $a_z < 0$), then the water column is statically stable since the force on the water parcel is in the opposite direction to the initial movement. The water parcel will return towards its initial position and in fact, oscillatory motion can result, with the Brunt-Väisälä (or buoyancy) frequency N defined by

Ex. 1.4

$$N^2 = gE. \tag{1.14}$$

Values of E in the upper 1000 m of the open ocean are in the range 10^{-6} – 10^{-5} m^{-1}. Below this depth, values of E can decrease to 10^{-7} m^{-1} in trenches; here $\partial S/\partial z$ is small and hence $E \to 0$ implies that $\partial T/\partial z = -\Gamma$. Thus the in-situ temperature changes at great depth are mainly due to pressure changes.

The potential temperature is the in-situ temperature corrected for the adiabatic temperature gradient Γ and by good approximation given by $\vartheta = T + \Gamma z$. Hence,

$$E = -\frac{1}{\rho} \frac{\partial \sigma_\vartheta}{\partial z}, \tag{1.15}$$

where the potential density σ_ϑ (kgm^{-3}) is defined as

$$\sigma_\vartheta = \rho(\vartheta, S, 0) - 1000. \tag{1.16}$$

The concept of potential temperature is important to determine whether the water column is stably stratified or not. When the relative density σ_t as in (1.5) is used, compressibility effects are completely neglected. The difference between σ_t and σ_ϑ is illustrated with the data of the WOCE A16 section in Fig. 1.7d. The profile of σ_t would indicate that the water column is statically unstable at depth, but σ_ϑ correctly indicates that it is indeed statically stable: the in situ temperature increase at depth is only due compressibility effects.

Characteristic	Notation	Value
Reference density	ρ_0	1.0×10^3 kgm^{-3}
Heat Capacity	C_p	4.2×10^3 Jkg^{-1}K^{-1}
Thermal expansion coefficient	α_T	1.0×10^{-4} K^{-1}
Haline expansion coefficient	α_S	7.6×10^{-4} –
Kinematic viscosity	ν	1.0×10^{-6} m^{2}s^{-1}.

Table 1.3. Typical values of characteristic parameters of seawater.

Additional Material

B: There is plenty of material on static stability and about T-S diagrams and their interpretation, An elementary introduction can be found the chapters 2 to 4 of OU-staff (2004a) and section 6.4 of OU-staff (1989). To become more familiar with temperature and salinity distributions in the ocean basins, download the Ocean Data View software from http://odv.awi-bremerhaven.de/ and view the Gouretski and Koltermann (2004) ocean atlas. Alternatively, you can explore the Levitus data sets by making plots of the temperature and salinity fields at http://iridl.ldeo.columbia.edu/SOURCES/.LEVITUS94/.

D: Chapter 1 in Emery and Thomson (2004) provides an overview of the type of measurements performed in physical oceanography and the analysis methods of these data. Appendix 3 of Gill (1982) lists formula's for the full UNESCO equation of state, for the potential temperature, for the specific heat and for the freezing point of seawater. You can practice with the concepts of potential temperature, static stability and water masses by making the exercises at http://gyre.umeoce.maine.edu/physicalocean/Tomczak/index2.html where also the textbook of R. Steward can be downloaded (see also http://oceanworld.tamu.edu/ocean410/ocng410_text_book.html).

An accurate evaluation of the equation of state is also important to compute the speed of sound c_s, defined by

$$c_s = (\frac{\partial \rho}{\partial p})_{S,\vartheta} \tag{1.17}$$

evaluated at constant potential temperature and constant salinity. A thorough discussion is given in Wright (1997) where also a comparison is made of the different equations of state. Often approximations of the equation of state $\rho = \rho(T, S, p)$ such as a linear equation of state, i.e.,

$$\rho = \rho_0(1 - \alpha_T(T - T_0) + \beta_S(S - S_0)), \tag{1.18}$$

are adequate. In the equation above, ρ_0, T_0 and S_0 are a reference density, a reference salinity and a reference temperature. The two expansion coefficients α_T and α_S are both positive as the density increases with both decreasing temperature and increasing salinity. Several typical properties of seawater are summarized in Table 1.9. Nonlinearities in the equation of state can, however, lead to interesting phenomena such as cabelling (where the two water masses mix and the resulting water mass is heavier that each of them) and thermobaricity (the thermal expansion coefficient increases with depth).

Ex. 1.5

Summary

- Salinity is defined as the mass fraction of all ions in seawater and its units are ppt (parts for thousand) or psu (practical salinity unit).
- The potential temperature ϑ of a water parcel is that temperature that would be obtained when the parcel is adiabatically raised to the surface. It is always lower than the in-situ temperature because water is compressed at depth. A rough approximation is $\vartheta = T - \Gamma\, d$ where d is depth (in meter) and $\Gamma \approx 0.15°$C/m is the adiabatic temperature gradient.
- The static stability of seawater is measured through its local buoyancy frequency

$$N^2 = -\frac{g}{\rho}\frac{\partial \sigma_\vartheta}{\partial z} \approx -\frac{g}{\rho}\left[\frac{\partial \rho}{\partial S}\frac{\partial S}{\partial z} + \frac{\partial \rho}{\partial T}\left(\frac{\partial T}{\partial z} + \Gamma\right)\right]$$

  where σ_ϑ is the potential density. If $N^2 < 0$ the water column is statically unstable.
- A T-S diagram is a parameter curve in the $T - S$ space with depth (or pressure) as the parameter. In these diagrams, typical extrema can be associated with particular water masses.

1.4. Exercises on chapter 1

(1.1) *Mixing*

A water mass A, with a temperature $T_A = 5°$C and a salinity $S_A = 35.5$ ppt, is mixed with a water mass B, with a temperature $T_B = 2°$C and a salinity $S_B = 34.5$ ppt. The resulting water has a temperature of 3°C and a salinity of 34.85 ppt.

a. Calculate the volume ratio of the water masses A and B in the mixture.

b. How can one determine this ratio graphically using a T-S diagram?

(1.2) *Potential temperature*

Consider in the table below some in-situ measurements of the temperature and salinity at a certain location in the Atlantic.

Depth(m)	Temperature (°C)	Salinity (ppt)
0	18.909	32.574
1000	2.697	34.410
2000	1.868	34.600
3000	1.528	34.661
4000	1.456	34.679
5000	1.503	34.686
5460	1.547	34.688

a. Investigate whether the water column is statically stable when a linear equation of state is assumed (with $\alpha_T = 10^{-4}K^{-1}$ and $\alpha_S = 7.6 \times 10^{-4}$).

b. Why is the pressure dependence in the equation of state here important?

c. Determine the potential temperature as a function of depth for these measurements.

d. Is the water column statically stable?

A water parcel with an in-situ temperature of $T = 10°$C and a salinity of $S = 35$ ppt moves adiabatically and without salinity changes from a depth of

2 km to a depth of 5 km.

e. What is the in-situ temperature and the potential temperature of the parcel at the final depth?

(1.3) *Buoyancy frequency*

Consider a stratified water column with a density profile $\rho(z)$.

a. Derive the equation of motion for a water parcel that, without any exchange of heat and salt with its environment, is subjected to a small initial vertical displacement.

b. At $t = 0$, the position of the parcel is $z = z_0$ and the velocity of the parcel is zero. Show that the buoyancy frequency N can be seen as the characteristic oscillation frequency of the water parcel in a stably stratified water column.

c. Consider now the same situation but in the presence of friction that is linearly related to the velocity of the water parcel. Derive in this case also the equation of motion for the water parcel. When is the water column unstably stratified?

(1.4) *Neutral surface and neutral density*

The concept of a neutral surface is important when we consider the (small scale) mixing processes between water masses.

a. Argue that the local mixing in the ocean is much larger along a surface of constant density than perpendicular to this surface.

Neutral directions are the directions in which a parcel can move in an adiabatic and isohaline manner without altering its buoyancy, i.e., neutral directions are parallel to lines of constant buoyancy.

b. For a linear equation of state, show that neutral directions are orthogonal to the vector $\nabla\rho$ where ρ is the local density. How can one identify these directions in a typical T-S diagram such as Fig. 1.8?

c. With a nonlinear equation of state, it is necessary to perform the gradient operation that removes pressure effects, just as is done for static stability. Show

that neutral directions are orthogonal to the vector $\mathbf{n}$ with

$$\mathbf{n} = \nabla\vartheta\,(\frac{\partial\rho}{\partial\vartheta})_{S,p} + \nabla S\,(\frac{\partial\rho}{\partial S})_{\vartheta,p}$$

where ϑ is the potential temperature. Argue that $\mathbf{n}$ is the normal of the local potential density surface.

d. Determine the vertical component of the vector $\mathbf{n}$ expressed in terms of N^2.

Neutral surfaces represent an accumulation of tangents to locally referenced potential density surfaces. These neutral density surfaces, defined by a value of the neutral density γ^n, are essentially a continuous analog of the discrete potential density surfaces referred to at various pressures.

e. Argue why γ^n is not only a function of T, S and p but also of latitude and longitude.

(1.5) *Nonlinear equation of state*

A water mass A with potential temperature $\vartheta_A = 2°\text{C}$ and a salinity $S_A = 34.04$ ppt, is mixed with a water mass B, having a potential temperature $\vartheta_B = 8.5°\text{C}$ and a salinity $S_B = 36.0$ ppt.

a. If these water masses are mixed in about equal proportions, what is so special about the resulting mixture? This phenomenon is called cabelling.

b. Illustrate this effect, called cabelling, graphically in a T-S (or ϑ-S) diagram.

In general, the thermal expansion coefficient depends on pressure. Consider an equation of state of the form

$$\rho = \rho_0(1 - \alpha_T(z)(T - T_0) + \beta_S(S - S_0))$$

with $\alpha_T(z) = \alpha_0 - \alpha_1 z$ (z is negative) and α_0 and α_1 are positive constants. Consider now two water parcels with temperature T_1, salinity S_1 and T_2, salinity S_2, respectively. At the sea surface the densities of both parcels are the same (i.e., $\rho_1 = \rho(T_1, S_1, 0) = \rho(T_2, S_2, 0) = \rho_2$).

c. Determine the density difference of both parcels at a depth h.

d. How can this effect, called thermobaricity, be illustrated graphically using T-S diagrams?

Chapter 2

PRESENT OCEAN CIRCULATION

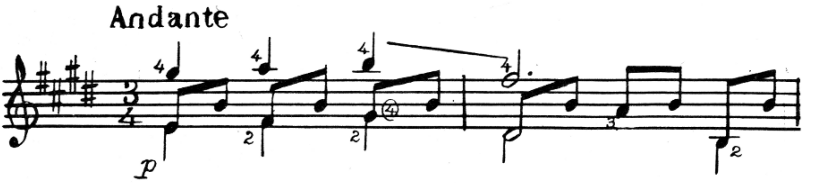

Preludio (Lagrima), F. Tarrega

The main characteristics of the surface forcing of the ocean circulation, the annual mean patterns of wind stress, heat flux and freshwater flux are presented section 2.1. In section 2.2, the patterns of the ocean currents in the different basins are described with a focus on major surface currents, the thermohaline circulation and the associated heat- and freshwater transport. Section 2.3 provides an overview of the role of the ocean circulation in climate and naturally leads to the formulation of a few central problems in dynamical oceanography (section 2.4) which help to organize the structure of this book.

2.1. Forcing fields

The large-scale ocean circulation is driven by a surface wind stress and affected by surface fluxes of heat and fresh water.

2.1.1. Wind stress

The magnitude and direction of the shear stress which is exerted by the atmospheric winds on the ocean surface depends on the wind velocities. If $\mathbf{U} = (U, V)$ indicates the wind velocity at 10 m height, then a semi-empirical bulk relation provides the wind stress $\boldsymbol{\tau}$ (in Pa = Nm^{-2}) as

Ex. 2.1

$$\boldsymbol{\tau} = C_D \rho_a |\mathbf{U}| \mathbf{U}, \tag{2.1}$$

where $\rho_a = 1.2$ kgm^3 is the density of air and $C_D \approx 10^{-3}$ is a friction coefficient that depends on $|\mathbf{U}|$.

The annual average zonal wind stress on the ocean-atmosphere surface from observations (Trenberth et al., 1989) is plotted in Fig. 2.1a and the meridional wind stress in Fig. 2.1b. Maximum values of the zonal wind stress are about 0.3 Pa and occur at the Southern Hemisphere. Typical values are about 0.1 Pa and the general pattern is the same during the whole year: strong easterly winds near the equator, strong westerly winds at midlatitudes and weaker easterly winds at polar latitudes. The meridional wind stress is somewhat weaker than the zonal wind stress and largest values occur over the Southern Ocean.

2.1.2. Heat flux

The total net heat flux Q_{oa} in Wm^{-2} which is positive when heat is transported from the atmosphere into the ocean) is the sum of several components, i.e.,

$$Q_{oa} = Q_H + Q_E + Q_{LW} + Q_{SW}. \tag{2.2}$$

In this expression, Q_H is the sensible heat flux, Q_E is the latent heat flux, Q_{LW} is the longwave heat flux and Q_{SW} is the shortwave heat flux. The magnitudes

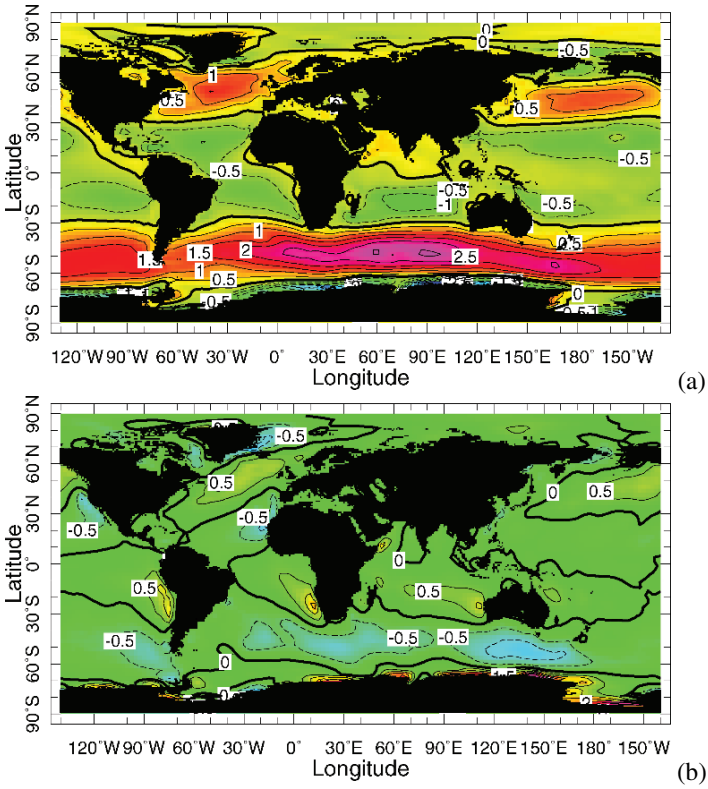

Figure 2.1. Annual average of the zonal wind stress (a) and the meridional wind stress (b) on the ocean-atmosphere surface. Contour values are in units of 0.1 Pa (in dyn/cm^2). This plot was made using the data and software at http://ingrid.ldeo.columbia.edu/.

of these fluxes can also be estimated by bulk formulae that have the same form as (2.1).

For example, the sensible heat flux Q_H is the flux of heat arising through random motion near the ocean-atmosphere interface (a 'diffusive flux') and it is proportional to the difference between the sea-surface temperature (T_s) and the atmospheric temperature (T_a) at a height (z_a) just above this interface. The bulk formula estimating this flux is given by

Ex. 2.2

$$Q_H = \rho_a C_{pa} C_H |\mathbf{U}|(T_s - (T_a + \gamma_a z_a)) \tag{2.3}$$

where ρ_a (kgm^{-3}) and C_{pa} (Jkg^{-1}K^{-1}) are the density and heat capacity of air, $|\mathbf{U}|$ (ms^{-1}) is the wind speed, γ_a (Km^{-1}) the (dry or moist) atmospheric 'lapse rate' and C_H is a dimensionless semi-empirical transfer coefficient.

In Fig. 2.2, the long term monthly average values of Q_{oa} are plotted for January, April, July and October (Oberhuber, 1988). In the annual average, there is a net positive heat flux in the equatorial region and a net negative flux at high latitudes. In the Southern (Northern) Hemisphere summer, there is a net input of heat in the Southern (Northern) Hemisphere. Maximum values of Q_{oa} are about 200 Wm^{-2} and these occur in January over areas near the Gulf Stream (Atlantic) (Fig. 2.2) and Kuroshio (Pacific), providing a strong zonal asymmetry of the heat flux in both basins. There are other sources of heat into the oceans, such as geothermal activity, but these are of minor importance for the ocean circulation and we will not consider them.

2.1.3. Freshwater flux

The evaporation E (ms^{-1}) over the ocean can be estimated by a bulk formula of the form

$$E = C_E|\mathbf{U}|(q_s - q_a), \tag{2.4}$$

where C_E is a semi-empirical exchange coefficient, q_a the relative humidity in the atmosphere and q_s the saturation relative humidity at the ocean-atmosphere boundary. The latent heat flux Q_E in (2.2) is related to the evaporation E through

Ex. 2.3

$$Q_L = \rho_a L_f E, \tag{2.5}$$

where $L_f = 2.5 \times 10^6$ Jkg^{-1} is the latent heat of evaporation. It is hard to determine the precipitation, P, from direct observations and in most cases an empirical relation between precipitation and temperature/pressure is used.

The long term monthly mean values of $P - E$ in mm/month are plotted for January, April, July and October (Oberhuber, 1988) in Fig. 2.3. There is quite a zonally uniform pattern in the Atlantic as well as in the Pacific. The zones of high precipitation near the equator are related to the Intertropical Convergence Zone (ITCZ) and can be seen as maxima of the freshwater flux with amplitudes of 200 mm/month (Fig. 2.3b). The central midlatitude regions are zones of net evaporation and there is less seasonal variation than in the heat flux. At very high latitudes precipitation again dominates over evaporation. There are other sources of freshwater into the oceans, such as river outflow, but these are again of minor importance for the large-scale ocean circulation and we will not consider them.

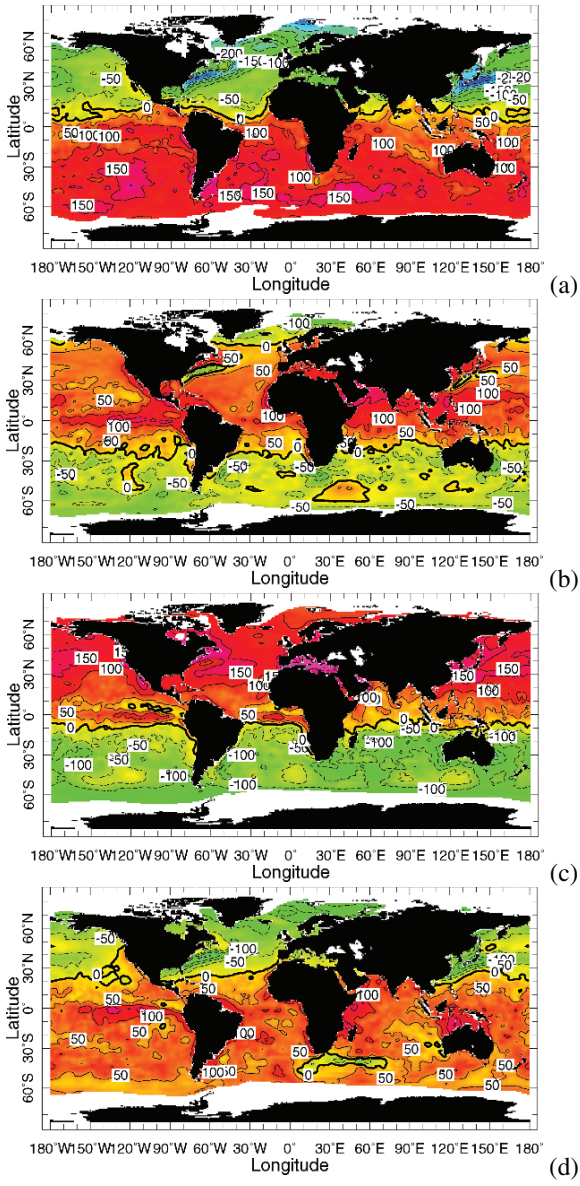

Figure 2.2. Seasonal mean net downward heat flux in Wm^{-2} *(positive when heat is transferred into the ocean) in (a) January, (b) April, (c) July, and (d) October.*

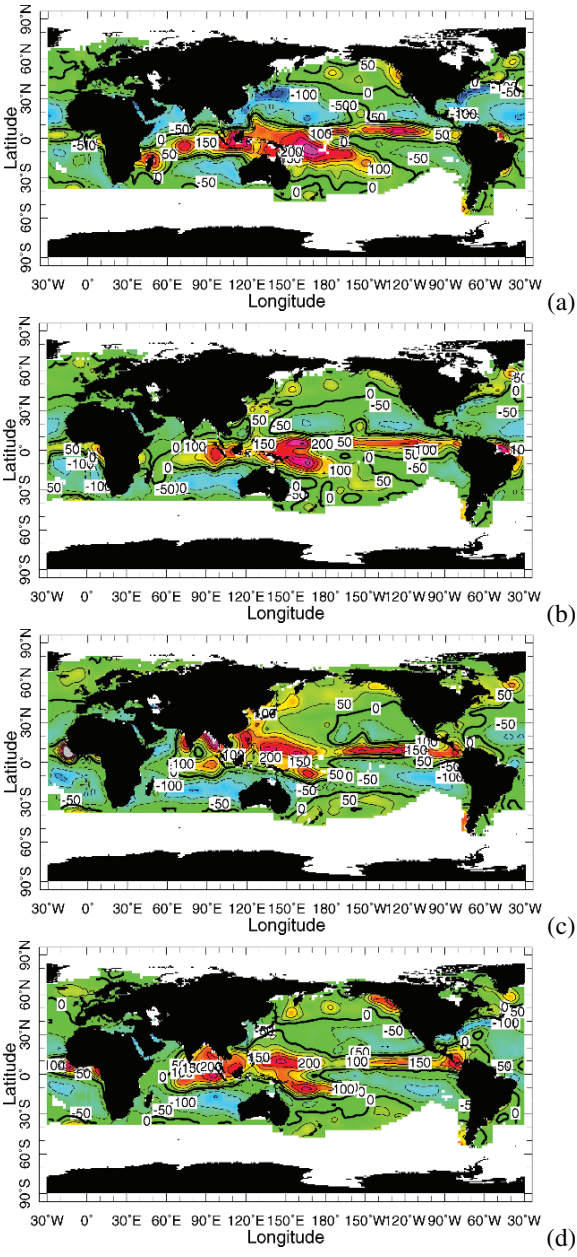

Figure 2.3. Seasonal mean net climatological monthly mean freshwater flux in mm/month for (a) January, (b) April, (c) July, and (d) October.

Additional Material

D: To become more familiar with the forcing fields and their variability it is recommended to explore several data sets available at http://iridl.ldeo.columbia.edu/SOURCES/. Elementary statistical analysis can be performed on many of these data sets at Geert Jan van Oldenborgh's Climate Explorer, available at http://climexp.knmi.nl/.

2.2. Ocean circulation

Apart from hydrographic measurements from which current information can be extracted (we will see later how this is done), there are two methods to measure currents directly. One of these methods is measurement of the Eulerian velocity, for example with a current meter along a rope in the water column. The other is the measurement of the velocity of an object that moves with the currents using, for example, a satellite tracking system. Examples of these Lagrangian instruments are the ARGO floats which were briefly mentioned at the end of section 1.2. These floats can also be positioned at a certain density level.

2.2.1. Surface circulation

A textbook picture (Peixoto and Oort, 1992) of the surface ocean circulation is plotted in Fig. 2.4a together with a snapshot of a surface speed plot (Fig. 2.4b) computed with the high-resolution NLOM model (see http://www7320.nrlssc.navy.mil/global_nlom32/skill.html). As could be expected, the surface currents follow the patterns of the annual mean winds (Fig. 2.1a), with westward currents near the equator and eastward currents at midlatitudes. This gives the characteristic 'gyre' flows in the Atlantic and the Pacific, consisting of a subpolar gyre and a subtropical gyre. Strong poleward currents appear at the western side of each ocean basin with the Gulf Stream, the Kuroshio, the Brazil Current and the Agulhas Current being pronounced examples.

A short overview of volume transports of some major currents in the ocean is provided in Table 2.1. These transports are measured in Sverdrup (SV) where 1 Sv = 10^6 m^3s^{-1}, or about one million 'bathtubs' per second. The zonal width of these currents is relative small compared to the zonal basin scale (Fig. 2.4b). At the eastern side of each basin are less strong equatorward currents with the California Current, the Canary Current and the Benguela Current as clear examples. In the equatorial region there are strong currents both in the Pacific and Atlantic: the South Equatorial Currents and North Equatorial Currents (Fig. 2.4). North of the equator (at about 4°N), there is the Equatorial Countercurrent that is directed in the opposite direction to the wind.

Ex. 2.4

Finally, the Antarctic Circumpolar Current (ACC) is the dominant current in the Southern Hemisphere and a comparable current does not exist in the Northern

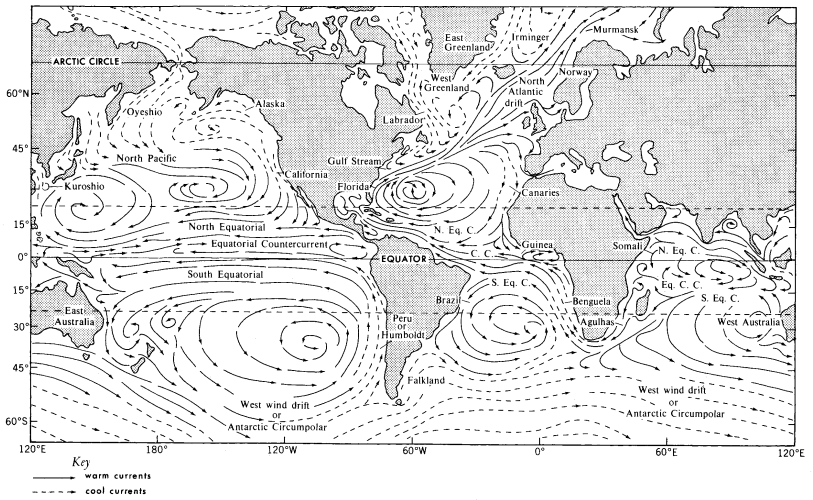

(a)

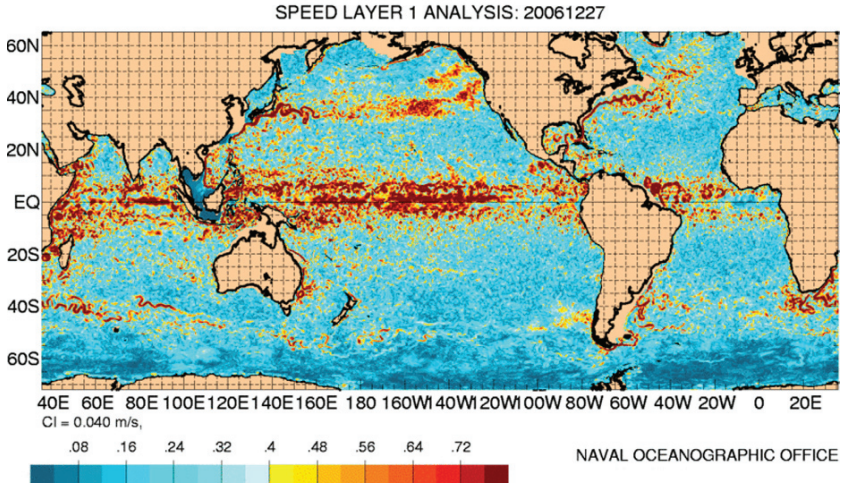

(b)

Figure 2.4. (a) Sketch of surface circulation pattern of the ocean (Peixoto and Oort, 1992). (b) Snapshot of a 'nowcast' of the surface current speed in the NLOM model (see http://www7320.nrlssc.navy.mil/global_nlom32/skill.html) at 1/32° resolution for December 27, 2006.

Some typical transports of the prominent ocean currents		
Current	Location	Value
Agulhas	31°S, Indian	70 Sv
Gulf Stream	26°N, Atlantic	32 Sv
Gulf Stream	38°N, Atlantic	88 Sv
Brazil Current	28°S, Atlantic	22 Sv
Kuroshio	25°N, Pacific	22 Sv
Kuroshio	33°N, Pacific	57 Sv
East Australian	30°S, Pacific	22 Sv
ACC	150°E, Southern	147 Sv
ACC	60°E, Southern	137 Sv

Table 2.1. Some typical transports of the ocean currents as determined during WOCE.

Hemisphere. This is mainly caused by the positioning of the continents: near the location of the Drake Passage (55-70°S) the ocean is zonally unblocked. This leads to very large transports and peculiar phenomena which will be discussed in chapter 14.

2.2.2. Thermohaline circulation

The circulation of heat and salt through the ocean basins is called the thermohaline circulation (Wunsch, 2002), usually abbreviated with THC. In the North Atlantic, the relatively warm and saline water transported by the Gulf Stream is cooled on its way northward. In certain regions, i.e., the Greenland Sea and the Labrador Sea, the water column becomes unstably stratified and vigorous convection occurs. The net effect is the formation the North Atlantic Deep Water (NADW), see section 1.3.2. This water is transported southwards at mid-depth as a deep (western boundary) current, it crosses the equator and connects to the water masses of the Southern Ocean.

In the North-Pacific, no deep water is formed because the surface waters are too fresh and hence there is no equivalent of NADW. Deep water formation also occurs near the Antarctic continent. In the Pacific, this inflow of heavy deep water is compensated by a surface return flow which again connects with water masses in the Southern Ocean. The water mass entering the Atlantic from the south is the Antarctic Bottom Water (AABW). The outflow of NADW in the Atlantic is, apart from AABW, also compensated by surface inflow of water coming from the Indian Ocean and water coming through Drake Passage (Schmitz, 1995).

The three-dimensional flow of different water masses through the ocean basins has been termed (Gordon, 1986; Broecker, 1991) the ‘Ocean Conveyor’. Analysis

of the section data of the World Ocean Circulation Experiment (WOCE, see http://oceanic.cms.udel.edu/woce/), combined with inversion studies have lead to a more detailed estimates over the volume transports through the world oceans (Ganachaud and Wunsch, 2000). In Fig. 2.5, the zonally integrated mass transports over several sections are presented. The boundaries between water masses are taken as certain neutral density surfaces (defined by a value of the quantity γ^n as introduced in exercise 1.5). In this way, the red arrows represent the surface transport, the blue arrows show the transport at intermediate depths and the green arrows indicate the transport in the deep ocean. Upwelling and downwelling are indicated by arrows and dots, respectively, and their color indicates from which level the water is originating.

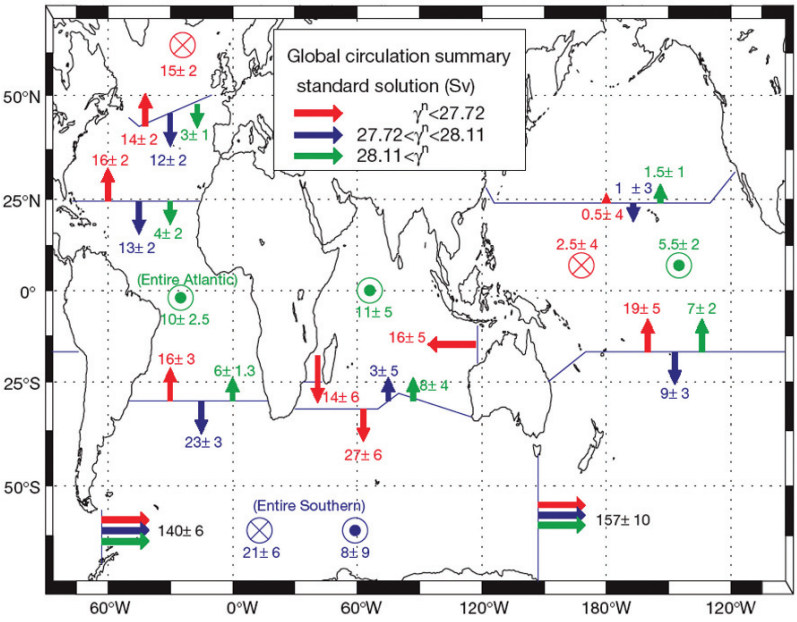

Figure 2.5. Estimated section integrated mass transports as determined in Ganachaud and Wunsch (2000) from the WOCE data. See text for an explanation of the colors and symbols.

2.2.3. Heat and freshwater transport

The oceans take care of about one third to a half of the total meridional heat transport of the combined ocean-atmosphere system. The total meridional heat transport due to the ocean circulation is difficult to measure directly and only a

few estimates at certain locations have been obtained. Recent inversion studies of the WOCE-section data have lead to section estimates (Ganachaud and Wunsch, 2000) and a summary result is presented in Fig. 2.6. The meridional heat transport

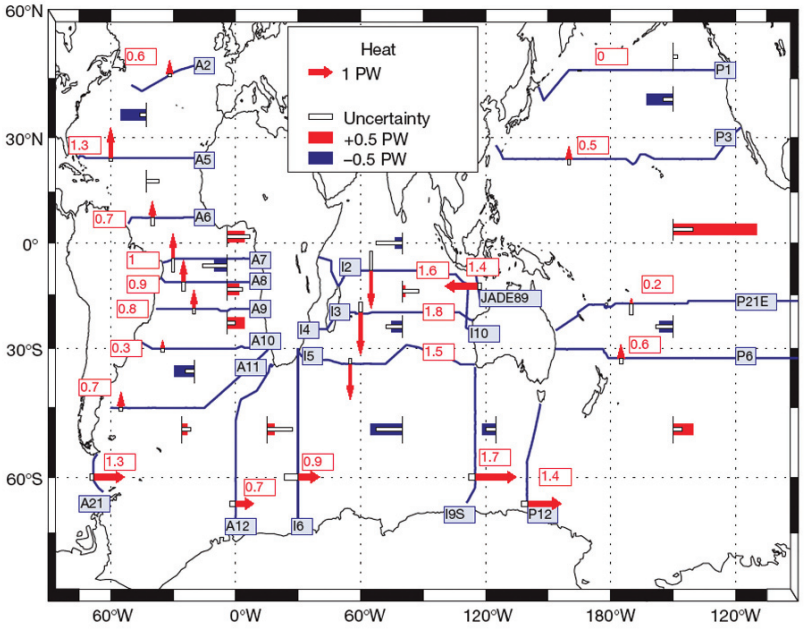

Figure 2.6. Estimated section averaged heat transport over WOCE sections (Ganachaud and Wunsch, 2000); the WOCE sections are indicated by their number (such as P12, A8, etc.), and 1 PW = 10^{15} W.

in the Atlantic is positive over the whole basin with a maximum of about 1.3 PW at about 30°N. In the Pacific, the heat transport is at least a factor two smaller than in the Atlantic. The meridional heat transport in the Indian Ocean is mainly southward with a maximum of 1.8 PW near 20°S. Best estimates of the total zonally averaged meridional heat transport are also presented in Ganachaud and Wunsch (2000) with a maximal northward heat transport of about 1.8 PW at 30°N.

Ex. 2.5

Estimates of the freshwater transport through the oceans are also hard to obtain from direct observations. As can be seen from the surface freshwater flux in Fig. 2.3, there is net precipitation in the tropical and high-latitude regions, and there is net evaporation in the subtropics. The ocean circulation must transport water into the evaporative zones and away from precipitation regions for

compensation. Wijffels et al. (1992) present estimates of this freshwater transport (Fig. 2.7) and demonstrate the importance of the Bering Strait throughflow. The Pacific is a net precipitative basin with much of the gain occurring between 0-15 °N (the location of the Intertropical Convergence Zone), while the Atlantic and Indian Ocean are evaporative basins. Over the whole North Atlantic Ocean, there is southward transport of freshwater with a maximum of about 0.95×10^9 kgs^{-1} at 60°N.

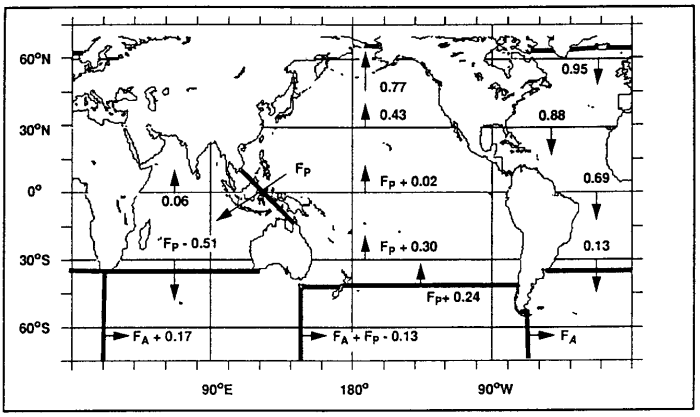

Figure 2.7. Meridional freshwater transport (in 10^9 kg/s) in the ocean, with the quantities F_P and F_A referring to the freshwater transport of the Pacific-Indian through flow and that of the Antarctic Circumpolar Current at Drake Passage, respectively (Wijffels et al., 1992).

Additional Material

B: Chapter 7 of Knaus (1997) provides many pictures of property (temperature, salinity, velocity) sections of western boundary currents and equatorial currents. Descriptions of western boundary currents and water masses can also be found in introductory textbooks on physical oceanography (Pickard and Emery, 1990; Tomczak and Godfrey, 1994).

D: For a better understanding of the thermohaline circulation it is useful to read the short paper Wunsch (2002). In-depth descriptions on heat- and freshwater transports are presented in section 6.1 (Ocean Heat Transport by H. Bryden) and section 6.2 (Ocean Transport of Fresh Water (by. S. Wijffels) of WOCE (2001).

2.3. Oceans and climate

Over the last decades, many techniques have become available to construct climatic records from geological, biological and physical data. These proxy records show that climate variations on different time scales have been very common in the past. The enormous amount of instrumental data that has been collected over the last 150 years contributes in turn to a more and more complete picture of the climate system's variability.

An 'artist's rendering' of climate variability on all time scales is provided in Fig. 2.8. This power spectrum is not computed directly by spectral analysis from a time series of a given climatic quantity, such as (local or global) temperature; indeed, there is no single time series that is 10^7 years long and has a sampling interval of hours, as the figure would suggest. Fig. 2.8, however, includes information obtained by analyzing the spectral content of many different time series, for example the 335 year long record of Central England temperatures. Figure

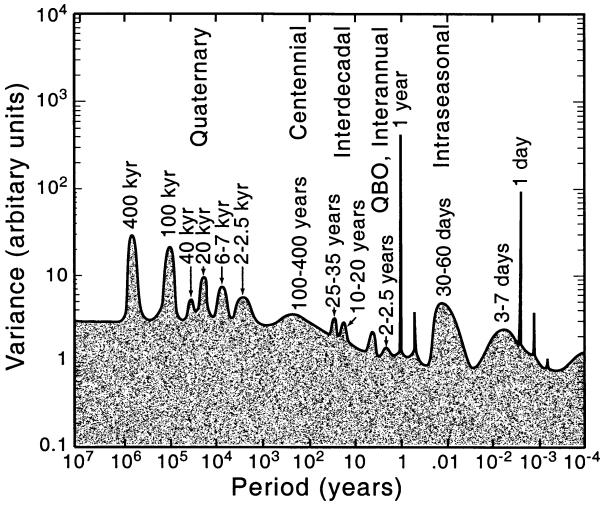

Figure 2.8. An 'artist's rendering' of the composite power spectrum of climate variability showing the amount of variance in each frequency range (from Dijkstra and Ghil (2005)).

2.8 reflects three types of variability: (i) sharp lines that correspond to periodically forced variations, at one day and one year; (ii) broader peaks that arise from internal modes of variability; and (iii) a continuous portion of the spectrum that reflects stochastically forced variations, as well as deterministic chaos.

Between the two sharp lines at 1 day and 1 year lies the synoptic variability of midlatitude weather systems, concentrated at 3–7 days, as well as intraseasonal variability, i.e. variability that occurs on the time scale of 1–3 months. The latter is also called low-frequency atmospheric variability, a name that refers to the fact that this variability has longer periods than the life cycle of weather systems. Immediately to the left of the seasonal cycle in Fig. 2.8 lies interannual, i.e. year-to-year, variability. An important component of this variability is the El Niño variability in the Tropical Pacific. About every four years, over a period of about one year, the sea-surface temperature (SST) in the Eastern Tropical Pacific increases by a few degrees. This is associated with variations (the Southern Oscillation) in the tropical Pacific surface winds, the trade winds. The ENSO (El Niño/Southern Oscillation) phenomenon arises through large-scale interaction between the equatorial Pacific and the global atmosphere. The last strong El Niño was in 1997 and the pattern of the sea surface temperature anomalies is plotted in Fig. 2.9. The temperature of the eastern Pacific was in December 1997 about 6°C higher than normal.

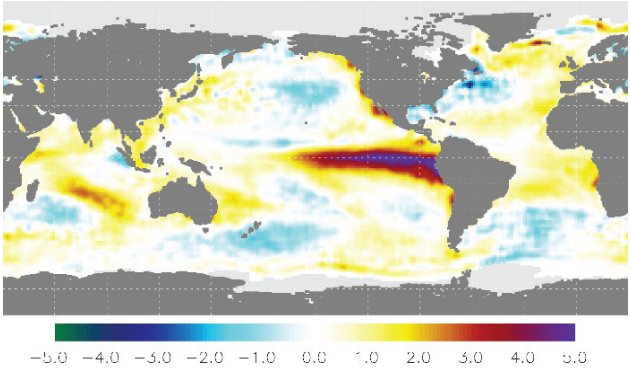

Figure 2.9. Sea surface temperature anomaly with respect to a long term mean for December 1997, at the maximum of the 1997-1998 El Nino (from Dijkstra and Burgers (2002)).

The energy in the spectrum at interdecadal time scales is likely due to the climate system's internal processes: each spectral component can be associated, at least tentatively, with a mode of interannual or interdecadal variability. Interdecadal variability is present in global records, instrumental as well as paleoclimatic. The leftmost part of Fig. 2.8 represents paleoclimatic variability. The information summarized there comes exclusively from proxy indicators of climate. These include coral records and tree rings for the historic past, as well as marine-sediment and ice-core records for the last two million years of Earth history, the

Quaternary. During this period an alternation of warmer and colder episodes, called glaciation cycles, is prominent. The cyclicity is manifest in the broad peaks present in Fig. 2.8 between roughly 1 kyr and 1 Myr. The three peaks at about 20 kyr, 40 kyr and 400 kyr reflect variations in Earth's orbit. These orbital variations represent, respectively, variations in precession, obliquity and eccentricity, three parameters that are used to describe Earth's orbit.

Within these glaciation cycles there are higher frequency oscillations prominent in the North Atlantic paleoclimatic records. These are the Bond cycle, with a near-periodicity of 6–7 kyr, and the Dansgaard-Oeschger cycles providing the peak at around 1–2.5 kyr in Fig. 2.8. Rapid changes in temperature, of up one half of the amplitude of a typical glacial-interglacial temperature difference, occur in a Dansgaard-Oeschger cycle. Progressive cooling through several of these cycles followed by an abrupt warming defines the Bond cycle. In North Atlantic sediment cores, the coldest part of each Bond cycle is marked by a so-called Heinrich layer that is rich in ice-rafted debris.

In summary, climate variations range from the large-amplitude climatic transitions of the past millennia to small-amplitude fluctuations on shorter time scales. Several frequencies of variability are clearly related to forcing mechanisms. However, variability can also arise through processes internal in the climate system giving rise to frequencies that are not directly related to the temporal variability of the forcing. Examples are the 3–7 day synoptic variability of midlatitude weather which arises through instability of the zonal mean circulation of atmosphere, and the El Niño variability whose frequency is set by the coupled interaction and intrinsic processes in the equatorial Pacific and atmosphere. Internal variability on longer time scales can occur through instabilities of states in the slower components of the climate system, such as the ocean and the ice caps. Hence, even if the external, i.e., solar, forcing was steady, the climate system would display variability on many time scales. It is the response of this highly complex climate system to relatively small time-dependent variations in the forcing, which is recorded in the sediment cores, ice cores and instrumental data.

Changes in the ocean circulation can influence climate substantially through the impact on the meridional heat transport. This can affect mean global temperature and precipitation, as well as their distribution in space and time. Subtle changes in the North Atlantic surface circulation and interactions with the overlying atmosphere are thought to be involved in the interannual and interdecadal climate variability as observed in the instrumental record of the last century. Changes in the circulation may also occur on a global scale, involving a transition to different large-scale patterns. Such changes may have been involved in the large-amplitude climate variations of the past, like the Dansgaard-Oeschger cycles.

This is enough motivation to try to understand the ocean circulation in more detail! In the following chapters of part I we make a first step by (i) identification of the characteristic time scales of the different processes and (ii) presenting the

governing equations of ocean flows. First, however, we conclude this chapter by specifying the problems which motivate the structure of the text in parts II, III and IV of this book.

Additional Material

B: We here touched upon the role of the ocean circulation in climate and the processes of climate variability in general. For the interested reader, the beautifully illustrated book of Ruddiman (2001) is a must. For bedtime reading on the subject I recommend the books by Imbrie and Imbrie (1986) and Bigg (2003).

2.4. Motivating problems and approach

There are several fundamental problems in dynamical oceanography and a few will be discussed in this book. In this section, we sketch the different problems and also the approach followed in later chapters to formulate theories for the particular phenomena.

2.4.1. Western boundary currents

Looking at the surface currents as in Fig. 2.4b, we see relatively strong currents at the western side of ocean basins and relatively weak ones at the eastern side of these basins. This is illustrated in Fig. 2.10, where a snapshot of the observed sea surface temperature in part of the North Atlantic Ocean is plotted. As the wind-stress field is fairly zonally homogeneous (Fig. 2.1) there is no immediate cause of the zonal asymmetry in the currents. If we restrict to the Atlantic Ocean, this leads to the following specific questions:

- Why does a Gulf Stream exist, i.e., why is the flow western intensified?
- Which physical processes control the volume transport of the Gulf Stream?

In the chapters 5 and 6, these issues will be discussed and answers based on the principles of geophysical fluid dynamics will be formulated. The special case of a steady wind-driven ocean flow of constant density water is considered in chapter 5. Using asymptotic methods, the pure wind-driven flow field can be divided into several regions where different equations (balances) apply. The solutions in each of these regions can be determined analytically and the resulting flow field is analyzed in chapter 6.

2.4.2. Internal variability of ocean flows

Flows in the ocean are far from stationary and vary on many time scales. A direct cause of this temporal variability are variations in external forcing, such

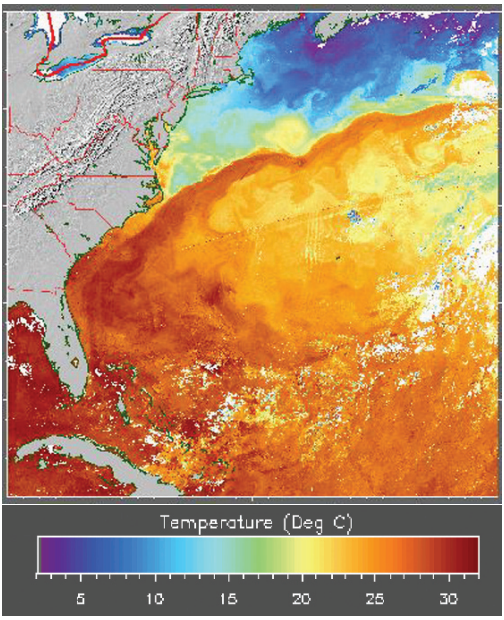

Figure 2.10. 'Multipass image' (from a satellite) of the sea surface temperature in the Gulf Stream region in May 1996 (image from http://fermi.jhuapl.edu/avhrr/).

as that in the wind-stress forcing. Such wind-stress changes cause waves that propagate through the flow field inducing an adjustment of the flow to the new forcing conditions. Temporal variations can also occur because mean flows are sensitive to disturbances which leads to instabilities. These instabilities are at the origin of the formation of meanders and eddies in currents such as the Gulf Stream (Fig. 2.10). These considerations lead to the following specific questions:

- How is the adjustment of an ocean flow when the wind stress is changing?
- What type of instabilities of ocean currents exist and what are the physical mechanisms of destabilization?

In the chapters 7 to 10, these questions are addressed and again an attempt is made to answer them from principles of geophysical fluid dynamics. To formulate the problems, basic material on the propagation of free waves in a rotating liquid is needed and this is introduced in chapter 7. This theory on free waves is then generalized in chapter 8 to a stratified flow in a midlatitude ocean basin. To study

the adjustment process, the special problem of an initially motionless flow that is suddenly accelerated by a time-independent wind stress is studied in chapter 9. The results provide an answer to the first question above. In chapter 10, the linear stability of a zonal current is studied with focus on two instability mechanisms: barotropic and baroclinic instability.

2.4.3. Special equatorial phenomena

Fig. 2.4 indicates that there are peculiar equatorial currents both in the Pacific and Atlantic. Although the wind stress is directed westward, eastward currents are observed north of the equator. Another special phenomenon is the occurrence, about once every four years, of El Niño in the Pacific (and not in the Atlantic) with a sea-surface temperature anomaly pattern as in Fig. 2.9. This leads to the following specific questions:

- Why are there equatorial countercurrents in the Atlantic and Pacific?
- Which physical processes are responsible for the occurrence of El Niño?

Theory for the steady equatorial ocean circulation, the equatorial free waves and the equatorial adjustment, is presented in chapter 11. It appears that the answer to the first question is directly related to the meridional gradients of the zonal wind stress. The material in chapter 11 is necessary to understand the dynamics of El Niño as a phenomenon arising through coupled processes between the equatorial Pacific and the global atmosphere. The coupled processes will be presented in chapter 12 and a basic explanation of the anomaly patterns and time scale of El Niño is given.

2.4.4. Phenomena on the planetary scale

In the last chapters, we consider ocean flow phenomena on a planetary scale. The Antarctic Circumpolar Current (ACC) is special in that there are no lateral boundaries over a substantial part of the flow domain. This leads to interesting dynamics controlling the volume transport of the current. The Arctic Ocean circulation is special because of the strong coupling between the spatial pattern of the ocean currents and the bottom topography. On this planetary scale, there is an intricate coupling between the large-scale flow and the density gradients in the ocean water. The flow transports heat and salt and thus causes density differences. The density gradients in turn cause pressure gradients and hence influence the large-scale flow. One of the phenomena that is caused by this large-scale nonlinear interaction is the thermocline, the region with a relatively large vertical temperature (and density) gradient in the ocean (cf. Fig. f:A16). The sharp transitions in the temperature during the Dansgaard-Oeschger cycles (section 2.3) may have been caused by changes in

the meridional heat transport caused by changes in the global ocean circulation. The thermohaline circulation is indeed sensitive to perturbations, in particular to those in the surface freshwater flux, because the atmosphere reacts differently to salt perturbations than to heat perturbations. This leads to the following questions:

- Why is there a thermocline and what processes control its shape?
- What controls the volume transport of the ACC near Drake Passage?
- Why are the surface currents in the Arctic Ocean closely following topographic features?
- Is the global ocean circulation sensitive to perturbations and if yes, what are the physical processes responsible?

All these questions can only be partially answered by current theory on the planetary circulation. The basis for the theory is presented in chapter 13 where two theories for the existence of the thermocline are studied. In both theories, the different effect that temperature and salt on the flow can be neglected and only the density field is important. The theory is used in chapter 14 to study the effect of bottom topography on the ACC and slightly extended in chapter 15 to address the dynamical processes controlling the Arctic Ocean circulation. The stability of the large-scale circulation is subject of chapter 16 and theory on the stability of the thermohaline circulation is presented with the help of conceptual models.

Summary

- The large-scale annual mean wind-stress pattern, forcing the ocean circulation, consists of easterlies in the Tropics, westerlies in the mid-latitudes and again easterlies at high latitudes. The maximum zonal wind stress is about 0.1 Pa in the tropics and 0.2 Pa at midlatitudes.
- The large-scale net annual mean heat flux pattern, affecting the ocean circulation, shows maximum positive values of about 100 Wm^{-2} in the tropics and minimum values of -150 Wm^{-2} at high latitudes in particular in regions of western boundary currents.
- The large-scale annual mean net freshwater flux pattern, affecting the ocean circulation, shows maximum positive values of about 150 mm/month in the tropics (related to the ITCZ) and minimum values of about -100 mm/month at midlatitudes. At high latitudes, the freshwater is again positive with maximum values of about 50 mm/month
- Major surface currents in the ocean basins are western intensified, i.e., they are all located at the western part of each ocean basin. Typical current velocities in the western boundary currents are 1 ms^{-1} and a typical transport is 50 Sv.
- The ocean circulation transports heat poleward with a maximum of about 1.5 PW at 25°N in the North Atlantic. Heat transport is northward over the whole Atlantic while over the Pacific and Indian Ocean it is poleward in each hemisphere.
- Ocean processes play a role in the climate system on time scales from months to thousands of years.

2.5. Exercises on chapter 2

(2.1) *Wind stress*

The average windspeed over the region of the Antarctic Circumpolar Current is about 10 ms^{-1}.

a. Give an estimate of the mean wind-stress at the ocean-atmosphere interface in this region.

b. If a unidirectional wind blows over an initially motionless water column of 10 m thickness, then calculate the flow velocity in this layer after 3 hours.

(2.2) *Heat flux*

Consider a layer of seawater (heat capacity $C_p = 4.2 \times 10^3$ $\mathrm{Jkg}^{-1}\mathrm{K}^{-1}$, density $\rho = 1.027 \times 10^3$ kgm^{-3}) with a thickness of 1 m and an area of 10^4 m^2.

a. Determine how much energy is needed to raise the temperature of the water by 1 °C.

Assume that a constant heat flux $Q = 400$ Wm^{-2} is applied over the area, for example due to a warmer atmosphere.

b. How long does it take before the temperature of the water layer has increased by 1 °C?

During a seasonal cycle, there is heat uptake in an ocean region whereas during the winter the opposite occurs.

c. Assume that the upper 100 m of ocean water is in contact with the atmosphere and that the seasonal temperature change in the water is about 10°C. Calculate the amount of energy which is stored (released) by the water layer.

d. Determine the same quantity for a land surface and a seasonal temperature change of about 20°C.

(2.3) *Freshwater balance*

Consider the freshwater balance for a thin layer of seawater. The salinity of the water changes through evaporation (E) and precipitation (P). The dimension of E and P is $\mathrm{m^3 s^{-1}}$ per $\mathrm{m^2}$ and hence $\mathrm{ms^{-1}}$. Let F_w be the vertical flux of salt at the bottom of the layer, which has a salinity S and let F_S be the freshwater flux through the ocean-atmosphere surface.

a. Show that the balance of freshwater can be written as

$$E - P + F_w(1 - S) = 0$$

b. Show that the salt balance can be written as

$$F_w S = F_S$$

c. Derive that, to a good approximation, the flux F_S can be written as

$$F_S = (E - P)S$$

(2.4) *Gulf Stream*

Warm western boundary currents such as the Gulf Stream play an important role in the climate system because they contribute to the meridional heat transport. The Gulf Stream is about 100 km wide, has a depth of 500 m and has a mean speed of 1 $\mathrm{ms^{-1}}$.

a. Provide an estimate of the volume transport of the Gulf Stream (in Sv).

The meridional heat transport due to the Gulf Stream depends on the temperature difference between the warm water flowing northward and the cooler water flowing southward.

b. Provide an estimate of this temperature difference and of the meridional heat transport associated with the Gulf Stream.

(2.5) *Mediterranean Outflow*

Consider a flow over a sill such as that in the Gibraltar Strait. West of the sill, the water has a salinity $S_a = 36.2$ ppt and east of the sill (in the Mediterranean basin), the salinity is $S_b = 38.4$ ppt. The volume flux of the surface transport of the Atlantic to Mediterranean is Q_a, and the reverse transport at depth has

a volume flux of Q_b (both in Sv).

a. Derive that

$$\begin{aligned} Q_a + Q_b &= 0 \\ Q_a S_a + Q_b S_b &= (E - P) A S_0 \end{aligned}$$

where S_0 is a mean salinity in the Mediterranean basin.

Assume that the difference between evaporation E and precipitation P is about 1 m/year over the Mediterranean basin. This basin has an area of about $A = 2.5 \times 10^{12}$ m^2.

b. Determine Q_a and Q_b for the Mediterranean outflow and compare the result to values in the literature.

Chapter 3

MATHEMATICAL DESCRIPTION

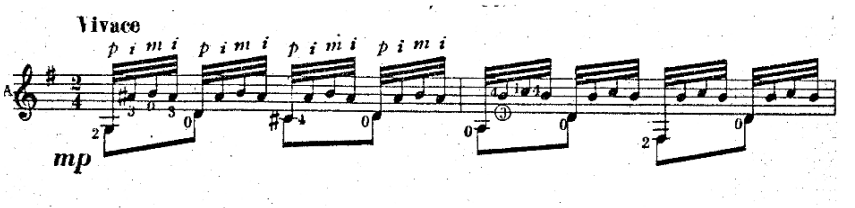

El Abejorro, E. Pujol

In this chapter the basis for a quantitative description of ocean currents will be provided. After an introduction into the relevant temporal and spatial scales in section 3.1, the governing equations of ocean flows, representing the momentum, mass, heat and salt balances are given in section 3.2. These are the equations of 'classical physics', describing the flow of a rotating stratified layer of ocean water on a sphere. It comes as no surprise that the general equations are much too complicated to solve analytically and even with numerical solution techniques all the relevant scales of motion cannot be resolved on current supercomputers. Fortunately there are many flow phenomena in the ocean that can be described by less complicated balances in the flow field. These phenomena can be understood using simplified forms of the equations. As explained in section 3.3, with help of the specific time scales of processes one can a priori identify some dominant balances.

3.1. A priori scales

From the description of the ocean basins and the surface forcing in the previous chapters we know that the ocean flows occur in a relatively thin layer of rotating liquid, that the liquid is stratified, that the flows are forced at the surface by wind stress and buoyancy flux, and that the domain is bounded by continental geometry and bottom topography.

It is important to consider characteristic time scales of each of the processes involved in the circulation. As we will see later, processes with comparable characteristic time scales are able to balance. The characteristic time scale of a particular process is also directly related to the contribution of that process to the vorticity balance of the flow. Note that if the velocity vector of the flow is indicated by $\mathbf{v}$, the vorticity vector is given by $\boldsymbol{\omega} = \nabla \wedge \mathbf{v}$ (where $\wedge$ indicates the vector cross product) and has therefore a dimension of s^{-1}. A process with a relatively small characteristic time scale hence provides a larger contribution to the vorticity balance in the flow than a process with a larger characteristic time scale.

3.1.1. Geometry

Let L and U be characteristic horizontal length and velocity scales of a particular ocean flow. For example, L could be the width of an ocean basin (L = $\mathcal{O}(10^6)$ m) and U a maximum depth-averaged horizontal velocity in the basin (U = $\mathcal{O}(10^{-2}$ ms$^{-1})$). The advective time scale τ_a associated with the flow is then given by

$$\tau_a = \frac{L}{U}. \tag{3.1}$$

This indicates the time scale on which the ocean flow with velocity U changes on the length scale L. Typical values for the basin scale flow above would be $\tau_a = 10^8$ s ≈ 3 years.

The advective time scale also has an interpretation in terms of vorticity, which is related to velocity gradients. Consider a flow with a gradient in the horizontal velocity U over a length scale L. This gradient provides a contribution to the vertical component of the vorticity vector of magnitude $U/L = 1/\tau_a$ (Fig. 3.1a). Ex. 3.1

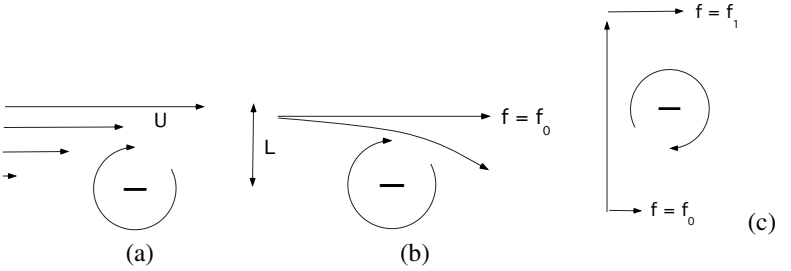

Figure 3.1. Illustration of (a) the advective time scale τ_a, (b) the inertial time scale τ_f and (c) the time scale τ_β where $f_1 = f_0 + \beta_0 L$.

The average depth of the ocean, say D, is much smaller than the horizontal scale of a typical ocean flow. This introduces a small parameter $\delta = D/L$, the so-called aspect ratio; for basin scale flows with $L = 10^6$ m and $D = 10^3$ m the value of $\delta \approx 10^{-3}$.

3.1.2. Coriolis acceleration

For an observer who moves along with the rotating Earth (with rotation vector $\mathbf{\Omega}$ and angular velocity $\Omega = |\mathbf{\Omega}|$) ocean flows with a velocity field $\mathbf{v}$ are influenced through an apparent acceleration $\mathbf{a}^c$, the Coriolis acceleration, given by $\mathbf{a}^c = -2\mathbf{\Omega} \wedge \mathbf{v}$.

To briefly illustrate the appearance of the Coriolis acceleration consider (Fig. 3.2a) an orthogonal basis $(\mathbf{e}_1, \mathbf{e}_2, \mathbf{e}_3)$ at a point P (with latitude θ) at the surface of the Earth. The vector $\boldsymbol{OP}$ connecting the point P and the origin O of an inertial coordinate system, the latter located at the center of the Earth, rotates with an angular velocity $\Omega = |\mathbf{\Omega}|$. Hence a fluid parcel that does not have any velocity with respect to the rotating basis moves with an angular velocity Ω with respect to the inertial coordinate system. Ex. 3.2

The coordinate system, with $\mathbf{e}_3$ locally vertical (i.e., opposite to the direction of the effective gravity, the resultant of the gravity force and the centrifugal force) rotates with respect to O (Fig. 3.2b) as follows (in the northern hemisphere),

- The horizontal plane spanned by $\mathbf{e}_1$ and $\mathbf{e}_2$ rotates counterclockwise with angular velocity $\Omega \sin\theta$.

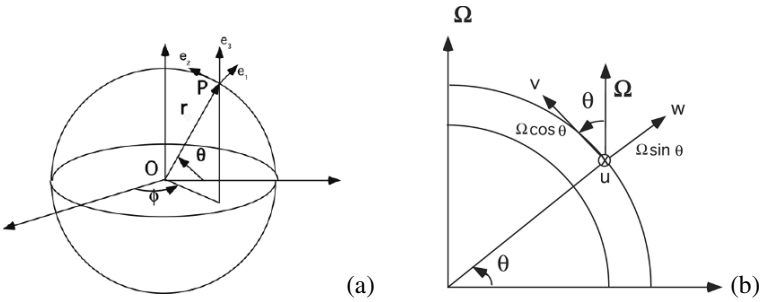

Figure 3.2. (a) Situation of a coordinate system ($\mathbf{e}_1, \mathbf{e}_2, \mathbf{e}_3$) on a rotating sphere, with ϕ indicating longitude, θ latitude and r the distance of a point to the center of the Earth. (b) Sketch to determine the Coriolis acceleration in spherical coordinates.

- The vertical plane spanned by $\mathbf{e}_1$ and $\mathbf{e}_3$ rotates clockwise with angular velocity $\Omega \cos\theta$.

Consider first the movement of fluid parcels in the horizontal plane (Fig. 3.3). Within a time Δt the coordinate system $(\mathbf{e}_1, \mathbf{e}_2)$ rotates over an angle

$$\alpha = \Delta t \, \Omega \sin\theta. \tag{3.2}$$

Hence, a parcel which moves at t = 0 uniformly along $\mathbf{e}_2$ with velocity v arrives after a time Δt in point A, with $\mid \boldsymbol{OA} \mid = v\Delta t$. With respect to the rotating coordinate system (it becomes $(\mathbf{e}_1', \mathbf{e}_2')$ after a time Δt) the parcel appears to have undergone an acceleration to the right (in the positive $\mathbf{e}_1$ direction). In a time Δt, the result is the displacement (for small α)

$$\mid \boldsymbol{AA'} \mid = \mid \boldsymbol{OA} \mid \sin\alpha \approx \mid \boldsymbol{OA} \mid \alpha = v(\Delta t)^2 \Omega \sin\theta. \tag{3.3}$$

The acceleration is uniform in the direction of $\mathbf{e}_1$, and when denoted by a_1^c, given by

$$\mid \boldsymbol{AA'} \mid = \frac{1}{2} a_1^c (\Delta t)^2. \tag{3.4}$$

From (3.3) and (3.4) it follows that

$$a_1^c = 2\Omega v \sin\theta. \tag{3.5}$$

In the same way, an expression can be derived for the component of the apparent acceleration in the direction of $\mathbf{e}_2$ (Fig. 3.3). A fluid parcel which moves uniformly in the $\mathbf{e}_1$ direction with velocity u is displaced (with respect to the rotating coordinate system) over $\boldsymbol{BB'}$ in a time Δt en hence in the negative $\mathbf{e}_2$ direction. In the same way as in the determination of a_1^c, it follows that

$$\mid \boldsymbol{BB'} \mid = \frac{1}{2} a_2^c (\Delta t)^2 = - \mid \boldsymbol{OB} \mid \sin\alpha = -u(\Delta t)^2 \Omega \sin\theta, \tag{3.6}$$

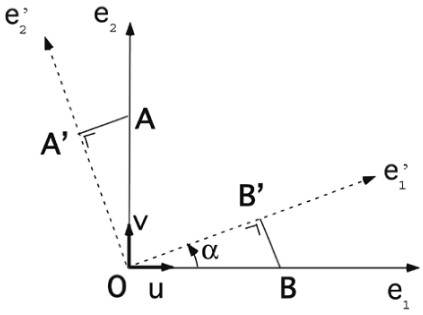

Figure 3.3. Sketch to help to determine the components a_1^c en a_2^c of the Coriolis acceleration.

and finally

$$a_2^c = -2\Omega u \sin\theta. \tag{3.7}$$

It can be shown in the same way that the rotation of the $(\mathbf{e}_1, \mathbf{e}_3)$ plane induces an acceleration of magnitude $-2\Omega w \cos\theta$ in the $\mathbf{e}_1$-direction and an acceleration of magnitude $2\Omega u \cos\theta$ in the $\mathbf{e}_3$ direction. The complete expression of the Coriolis acceleration hence becomes

$$\mathbf{a}^c = -2\boldsymbol{\Omega} \wedge \mathbf{v} = \begin{pmatrix} 2\Omega(v\sin\theta - w\cos\theta) \\ -2\Omega u \sin\theta \\ 2\Omega u \cos\theta \end{pmatrix}. \tag{3.8}$$

The horizontal component $f = 2\Omega \sin\theta$ of the Coriolis acceleration is the most important term affecting the ocean circulation. Its characteristic time scale is the inertial timescale

$$\tau_f = \frac{1}{f}. \tag{3.9}$$

Near the equator this time scale increases rapidly and τ_f reaches a minimum at the poles. To determine its interpretation in terms of vorticity, consider a fluid parcel moving on the sphere in the northern hemisphere at a latitude θ_0; the Coriolis acceleration deflects its path to the right which gives a contribution (Fig. 3.1b) to the vertical component of the vorticity with a magnitude $f_0 = 2\Omega \sin\theta_0$. The inertial time scale is about 10^4 s at 45°N .

If the horizontal scale of the motion is so small that we can take a constant $f_0 = 2\Omega \sin\theta$, we say we use the f-plane approximation. Introduction of a local coordinate $y = (\theta - \theta_0) r_0$ and then a Taylor series near θ_0 gives

$$f = f_0 + \beta_0 y + \mathcal{O}(\theta - \theta_0)^2) \; ; \; \beta_0 = \frac{2\Omega}{r_0} \cos\theta_0. \tag{3.10}$$

This linear meridional variation of f is part of the β-plane approximation. The characteristic time scale associated with the meridional variation of the Coriolis acceleration is

$$\tau_\beta = \frac{1}{\beta_0 L}. \tag{3.11}$$

An interpretation in terms in vorticity is again possible (Fig. 3.1c). A water parcel that moves northward in the northern hemisphere is deflected more strongly at a more northerly position. This gives a contribution to the vertical component of the vorticity with a magnitude of $\beta_0 L$. At 45°N, a value of τ_β is 10^4 s for a flow with a length scale $L = 5000$ km.

3.1.3. Stratification

Because the density of ocean water depends on temperature, salinity and pressure, ocean water is stratified. A characteristic quantity of the stratification is the buoyancy (or Brunt-Väisälä) frequency N, given by

$$N^2 = -\frac{g}{\rho}\frac{\partial \rho}{\partial z}, \tag{3.12}$$

In a stably stratified water column ($N > 0$), a fluid parcel can locally depart from its equilibrium due to a perturbation, but because the restoring force always counteracts its motion, the parcel will eventually return towards its equilibrium position. It can, however, overshoot and this behavior will lead to a damped oscillation with an oscillation frequency N.

A stable stratification of the water column introduces a characteristic time scale

$$\tau_s \; = \; N^{-1}. \tag{3.13}$$

The profile of N^2 along the WOCE A16 section is plotted in Fig. 3.4 (in cycle/hour). In the upper layers the profile follows that of salinity (see Fig. 1.6). The time scale τ_s increases from a minimum of 1/10 hr just below the ocean surface to about 1/2 hr at a depth of 2 km.

The ocean-atmosphere interface is deformable and it can be considered as a special case of a stratified liquid in which there is a layer of air with thickness D and constant density ρ_a situated above a liquid layer also with depth D and density ρ. The buoyancy frequency N^2 can for this case be approximated by

$$N^2 \approx g(\rho - \rho_a)/(D\rho), \tag{3.14}$$

and because $\rho_a/\rho \ll 1$ it follows that $N^2 \cong g/D$. This introduces the timescale

$$\tau_g = \sqrt{D/g}, \tag{3.15}$$

which is associated with oscillations in the ocean-atmosphere surface, i.e., long gravity waves with phase speed $c = D/\tau_g = \sqrt{gD}$. Deformations of the air-sea interface provide also a contribution to the vorticity balance, as we will see later.

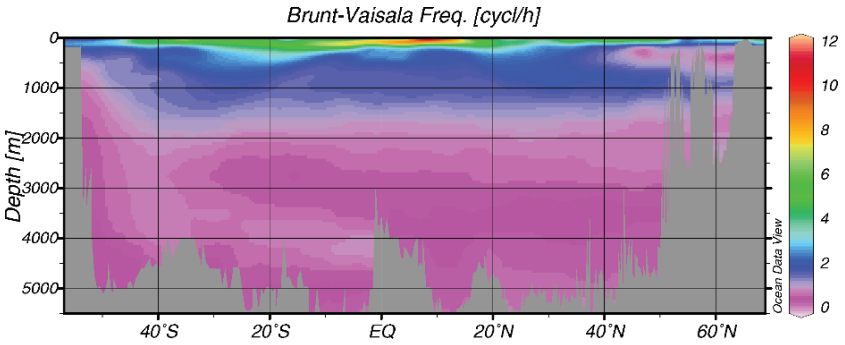

Figure 3.4. Buoyancy frequency (N) along the WOCE A16 section as plotted using the ODV software and the Gouretski and Koltermann (2004) gridded ocean data atlas.

3.1.4. Mixing of momentum, heat and salt

.

With $\nu = 10^{-6}$ m^{2}s^{-1} (Table 1.3) being the kinematic viscosity of water and U, L characteristic velocity and length scales of the flow, the Reynolds number $Re = UL/\nu$ is the ratio of inertial and viscous accelerations in a liquid. For basin scale flows in the ocean, with $U = 10^{-1}$ ms^{-1} and $L = 10^6$ m, a typical value of the Reynolds number is $Re = 10^{11}$. This is far above typical critical values of Re marking transitions from laminar to turbulent flow and hence the ocean flow is highly turbulent. Molecular viscous effects can be neglected on those scales with respect to inertial effects.

In turbulent flows there are rapid fluctuations that result in a fast redistribution of momentum, heat and salt. Because of their apparent random nature these fluctuations have the character of diffusion, but one that is much larger than diffusion due to molecular processes. In one of the simplest representations of these mixing processes, called first-order closure, the mixing is represented as being down gradient diffusion with turbulent mixing coefficients (also called 'eddy viscosities' and 'eddy diffusivities'). Contrary to the molecular coefficients, these coefficients are not a material property but are flow dependent.

In this first-order closure theory, the turbulent flux $\mathbf{\Psi}$ of a scalar quantity (for example, heat) ψ is proportional to the gradient $\nabla\psi$, with mixing coefficient K, i.e.,

$$\mathbf{\Psi} = -K \nabla \psi. \tag{3.16}$$

Below, we will indicate the mixing coefficients for momentum with A, and take those of heat and salt the same and indicate them with K. It should be stressed that the first-order closure theory is certainly incorrect over large parts of the ocean.

However, many aspects of the ocean circulation theory developed in later chapters are eventually independent of the representation of mixing processes and hence using the simplest one is useful. It may therefore not come as a surprise that values of the mixing coefficients are not well-known. A rough estimate of the momentum mixing coefficient is given by the product of the relevant length scale and velocity scale in the flow. However, in realistic flows these are usually hard to determine. Because horizontal and vertical length scales differ considerably in the ocean and the ocean is strongly stratified (inhibiting vertical mixing) horizontal mixing coefficients are usually orders of magnitude larger than vertical ones. We use the subscripts H and V to indicate the different coefficients, i.e., A_V and A_H for the vertical and horizontal mixing coefficients of momentum.

In this first-order closure theory, the mixing of momentum is represented by

$$\mathcal{F}_I = \nabla \cdot \mathcal{T}, \tag{3.17}$$

with $\mathcal{T}$ the part of the stress tensor representing shear. The general form of $\mathcal{T}$ is

$$\mathcal{T} = A_H(\nabla_H \otimes \mathbf{v} + (\nabla_H \otimes \mathbf{v})^T) + A_V(\nabla_z \otimes \mathbf{v} + (\nabla_z \otimes \mathbf{v})^T), \tag{3.18}$$

where the superscript T indicates the transpose, ∇_H is the horizontal gradient operator and $\nabla_z = (0, 0, \partial/\partial z)$. The notation $\otimes$ is the dyadic product

$$\mathbf{a} \otimes \mathbf{b} = \begin{pmatrix} a_1 b_1 & a_1 b_2 & a_1 b_3 \\ a_2 b_1 & a_2 b_2 & a_2 b_3 \\ a_3 b_1 & a_3 b_2 & a_3 b_3 \end{pmatrix}. \tag{3.19}$$

Estimates of A_H are within the range $10 - 10^5$ m^{2}s^{-1} and A_V varies from values of 10^{-5} m^{2}s^{-1} in the deep ocean to values of 10^{-1} m^{2}s^{-1} in the upper layer. In the same way the mixing of heat and salt is represented as

$$\mathcal{F}_T = \rho_0 C_p(\nabla_H \cdot (K_H \nabla_H T) + \frac{\partial}{\partial z}(K_V \frac{\partial T}{\partial z})), \tag{3.20a}$$

$$\mathcal{F}_S = \rho_0(\nabla_H \cdot (K_H \nabla_H S) + \frac{\partial}{\partial z}(K_V \frac{\partial S}{\partial z})), \tag{3.20b}$$

with estimates $K_V = 10^{-5} - 10^{-4}$ m^{2}s^{-1} and $K_H = 10 - 10^3$ m^{2}s^{-1}.

Some form of friction is needed to be able to satisfy boundary conditions, for example no-slip (zero tangential and normal velocity) conditions on the continental boundaries and on the bottom topography. In many cases, this leads to boundary layers (e.g., the Ekman layers) whose thickness depends on the mixing coefficients. Friction introduces characteristic time scales

$$\tau_w^H = \frac{L^2}{A_H} \; ; \; \tau_w^V = \frac{D^2}{A_V}. \tag{3.21}$$

In vorticity terms: random transport of momentum leads to diffusion of vorticity, with a magnitude proportional to the mixing coefficients.

3.1.5. Ratio of scales

Ratios of time scales provide a priori insight into the importance of dynamical processes in the flow. In a stationary flow, this ratio provides information as to whether the dynamical processes represented in both time scales are able to balance. In time-dependent flows, the ratio provides information on which process contributes most to the tendency of certain quantities in the flow.

Dimensionless parameters can always be written as the ratio of length scales or the ratio of time scales. For example, the (local) Rossby number ϵ is the ratio of τ_f and τ_a, according to

$$\epsilon = \frac{\tau_f}{\tau_a} = \frac{U}{f_0 L}. \tag{3.22}$$

If $\epsilon \ll 1$, then the inertial acceleration is much smaller than the Coriolis acceleration, i.e., $\tau_a \gg \tau_f$. In the vorticity view the relative vorticity is much smaller than the planetary vorticity. For motions on a length scale much larger than $L = U/f_0$ the effect of inertia is not important with respect to Coriolis effects.

Another parameter that is important for the large-scale ocean flows in the dimensionless quantity β defined by

$$\beta = \frac{\tau_a}{\tau_\beta} = \frac{\beta_0 L^2}{U}. \tag{3.23}$$

If $\beta \gg 1$, then the effect of the inertial acceleration on the motion is much smaller than that due to the gradient in the Coriolis acceleration. In other words, the relative vorticity is much smaller than the gradient of planetary vorticity; for motions on a length scale larger than $\sqrt{U/\beta_0}$, effects of inertia can be neglected with respect to effects due to variations in the Coriolis acceleration.

The Ekman numbers E_H and E_V, defined by

$$E_H = \frac{A_H}{fL^2} = \frac{\tau_f}{\tau_w^H}\ ;\ E_V = \frac{A_V}{fD^2} = \frac{\tau_f}{\tau_w^D}, \tag{3.24}$$

measure the ratio of the acceleration due to friction and the Coriolis acceleration. If $E_V \ll 1$, then the vorticity input due to 'diffusive' vertical momentum transport is not important compared to that due to the Coriolis acceleration. As an example, E_H can also be written as $E_H = (L_w/L)^2$, where $L_w = \sqrt{A_H/f}$ is a frictional length scale. For motions on a much larger length scale than L_w, the effects of friction can be neglected.

Stratification introduces a dimensionless parameter, the Burger number S, that can be represented as ratio of length and time scales as,

$$S = (L_D/L)^2 = \frac{N^2 D^2}{f^2 L^2} = \frac{\tau_f^2 \delta^2}{\tau_s^2}. \tag{3.25}$$

The length scale L_D is the internal Rossby deformation radius, given by

$$L_D = \frac{ND}{f}, \tag{3.26}$$

and with $N = 10^{-3}$ s^{-1} as a typical value in the midlatitude surface ocean and $D = 4$ km, the scale $L_D = 50$ km. For motions on this length scale, the deformations of isopycnal (constant density) surfaces provide accelerations that are comparable to the Coriolis acceleration.

Ex. 3.3

For deformations of the ocean-atmosphere interface with the approximation (3.14), the Burger number S transforms into the rotational Froude number F with

$$F^{-1} = \frac{gD}{f^2 L^2} = \frac{R_D^2}{L^2}. \tag{3.27}$$

Here R_D is referred to as the external Rossby deformation radius given by

$$R_D^2 = \frac{gD}{f_0^2}, \tag{3.28}$$

with typical midlatitude values of $R = 1000$ km. Deformations of the ocean-atmosphere interface on this scale cause accelerations comparable to the Coriolis acceleration.

Additional Material

B: On the Coriolis acceleration and its counter-intuitive effects, see Stommel and Moore (1989) and chapter 2 of Cushman-Roisin (1994). All the other processes here are also part of many textbooks such as Cushman-Roisin (1994). An overview of all processes in which turbulence is involved is provided in Thorpe (2005).

D: In the sections 10.1-10.5 of Vallis (2006), a thorough discussion is given on turbulent transport. The modern formulation of mixing processes of momentum and heat/salt in ocean models is discussed systematically in Griffies (2004). At this point, his chapter 7 would be useful to read.

3.2. Large-scale balances

In the chapters 1 and 2, we obtained a first impression of the large-scale ocean circulation and the distribution of ocean temperature and salinity. To understand these flows our starting point are the local conservation laws on a typical ocean domain such as a sector of the sphere (Fig. 3.5) which rotates with angular velocity $\Omega = |\mathbf{\Omega}|$.

3.2.1. Equations of motion

The equations of motion for a flow of fluid with density ρ and velocity $\mathbf{v}$ (for an observer moving with the rotating sphere) are

$$\rho\left[\frac{D\mathbf{v}}{dt}+2\boldsymbol{\Omega}\wedge\mathbf{v}\right] = -\nabla p+\rho\nabla\Phi+\rho\mathcal{F}_I, \tag{3.29a}$$

$$\frac{D\rho}{dt}+\rho\nabla\cdot\mathbf{v} = 0, \tag{3.29b}$$

where I will use D/dt to indicate the material derivative given by $D/dt=\partial/\partial t+\mathbf{v}\cdot\nabla$, with t the time coordinate. In the equations above, p is the pressure and Φ the geopotential ($\nabla\Phi=-g\mathbf{e}_3$), with g the gravitational acceleration and $\mathbf{e}_3$ the unit vector in the radial direction. The vector $\mathcal{F}_I$ represents the effect of mixing due to random (turbulent) small-scale motions as formulated in (3.17).

The left hand side of (3.29a) represents the change in momentum of a fluid parcel. It is caused by velocity changes of the fluid parcel with time ($D\mathbf{v}/dt$) consisting of local velocity changes ($\partial\mathbf{v}/\partial t$) and the changes due to advection of the fluid parcel ($\mathbf{v}\cdot\nabla\mathbf{v}$), and effects induced by the frame of reference, taking into account the Coriolis acceleration. Terms on the right hand side of (3.29a) represent the causes of these changes and are given by pressure forces, shear stresses and volume forces. Equation (3.29b) is the conservation of mass of a particular fluid parcel when moving with the flow.

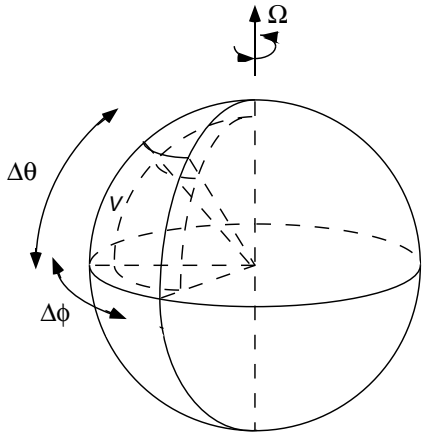

Figure 3.5. Example of a typical subdomain of ocean flow on the sphere.

Conservation of heat and salt is formulated as

$$\rho C_p \frac{DT}{dt} = \mathcal{F}_T + Q_T, \tag{3.30a}$$

$$\rho \frac{DS}{dt} = \mathcal{F}_S + Q_S, \tag{3.30b}$$

where $\mathcal{F}_T$ (Wm^{-3}) and $\mathcal{F}_S$ (kg m^{-3}s^{-1}) represent the mixing due to turbulent motions as in (3.20). The terms Q_T (Wm^{-3}) and Q_S (kg m^{-3} s^{-1}) represent the internal sources/sinks of heat and salt.

The unknown quantities in the equations are the velocity field $\mathbf{v}$, the pressure p, the density ρ, the temperature T and the salinity S, a total of 7. The last equation needed to close the system of equations is the equation of state

$$\rho = \rho(T, S, p), \tag{3.31}$$

which was discussed at length in chapter 1 (section 1.3).

3.2.2. Spherical coordinates

In traditional fluid mechanics on the sphere, the equations of motion are usually given in spherical coordinates (r, ϑ, φ). In oceanography we work with longitude $\phi = -\varphi$, latitude $\theta = \pi/2 - \vartheta$ and the velocity components in zonal, meridional and vertical direction are represented as $\mathbf{v} = (u, v, w)$. The equations of motion (3.29) can be written in coordinates (ϕ, θ, r), using (3.8)), as

$$\frac{Du}{dt} + \frac{uw}{r} - \frac{uv}{r}\tan\theta - 2\Omega\,(v\sin\theta - w\cos\theta) = -\frac{1}{\rho r\cos\theta}\frac{\partial p}{\partial \phi} + \mathcal{F}_I^{\phi}, \tag{3.32a}$$

$$\frac{Dv}{dt} + \frac{wv}{r} + \frac{u^2}{r}\tan\theta + 2\Omega u\sin\theta = -\frac{1}{\rho r}\frac{\partial p}{\partial \theta} + \mathcal{F}_I^{\theta}, \tag{3.32b}$$

$$\frac{Dw}{dt} - \frac{u^2+v^2}{r} - 2\Omega u\cos\theta = -\frac{1}{\rho}\frac{\partial p}{\partial r} - g + \mathcal{F}_I^{r}, \tag{3.32c}$$

$$\frac{D\rho}{dt} + \rho\left(\frac{\partial w}{\partial r} + \frac{2w}{r} + \frac{1}{r\cos\theta}\left(\frac{\partial (v\cos\theta)}{\partial \theta} + \frac{\partial u}{\partial \phi}\right)\right) = 0, \tag{3.32d}$$

$$\rho C_p \frac{DT}{dt} = \mathcal{F}_T + Q_T, \tag{3.32e}$$

$$\rho \frac{DS}{dt} = \mathcal{F}_S + Q_S, \tag{3.32f}$$

$$\rho = \rho(T, S, p), \tag{3.32g}$$

with

$$\frac{D}{dt} = \frac{\partial}{\partial t} + \frac{u}{r\cos\theta}\frac{\partial}{\partial \phi} + \frac{v}{r}\frac{\partial}{\partial \theta} + w\frac{\partial}{\partial r}. \tag{3.33}$$

Ex. 3.4

Below we will use the vertical coordinate $z = r - r_0$ instead of r, where r_0 is the distance of the mean sea level from the center of the Earth. To close the set of equations we will use the first-order closure formulation relating the terms $\mathcal{F}$ in the equations above to the gradients of properties, i.e. the relations (3.18) and (3.20).

3.2.3. Boundary conditions

To obtain a well-defined mathematical problem, boundary conditions have to be specified. An ocean basin is bounded zonally by continents, and vertically by bottom topography and the ocean-atmosphere interface (Fig. 3.6). The bottom

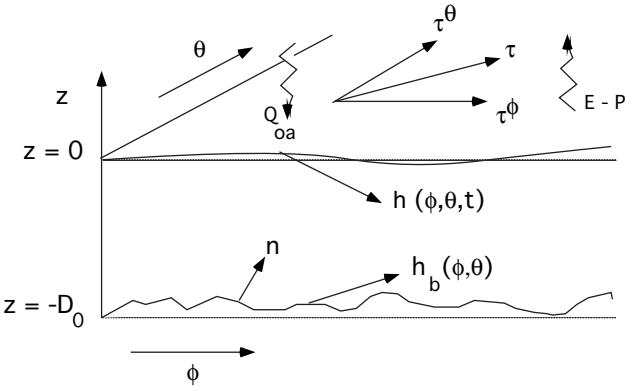

Figure 3.6. Sketch to help define the general boundary conditions at ocean boundaries.

topography is specified as a function

$$z = -D_0 + h_b(\phi, \theta), \tag{3.34}$$

where D_0 is a reference depth. At the bottom both tangential and normal velocities are zero (no-slip) and there is no large-scale transport of heat and salt. Hence the boundary conditions at $z = -D_0 + h_b(\phi, \theta)$ become

$$\mathbf{t}_i.\mathbf{v}. = 0\ ;\ \frac{D(z + D_0 - h_b)}{dt} = 0, \tag{3.35a}$$

$$\mathbf{n}.\nabla T = 0\ ;\ \mathbf{n}\cdot\nabla S = 0, \tag{3.35b}$$

where $\mathbf{n}$ is the outward normal and $\mathbf{t}_i$, $i = 1, 2$ the tangent vectors at the bottom. The eastern and western boundaries can, in most cases, be described by functions

$\phi_e = \phi_e(\theta)$ and $\phi_w = \phi_w(\theta)$. On these lateral boundaries, we also assume that there is no-slip and no transport of heat and salt. This gives the same conditions as (3.35), where $\mathbf{n}$ is now the outward normal on the eastern or western boundary.

The ocean-atmosphere interface is described by

$$z = h(\phi, \theta, t), \tag{3.36}$$

where the average interface position is at $z = 0$. The tangential stress and the normal stress are continuous over this interface and the interface is a material surface. If we denote the atmospheric pressure at the interface by $p_a(\phi, \theta, t)$, the boundary conditions at $z = h(\phi, \theta, t)$ become

$$\begin{aligned}
\frac{D}{dt}(z - h(\phi, \theta, t)) &= 0, && \text{(3.37a)}\\
\rho_0 A_V r \frac{\partial}{\partial r}(\frac{u}{r}) + \frac{\rho_0 A_H}{r \cos\theta}\frac{\partial w}{\partial \phi} &= \tau^{\phi}, && \text{(3.37b)}\\
\rho_0 A_V r \frac{\partial}{\partial r}(\frac{v}{r}) - \frac{\rho_0 A_H}{r}\frac{\partial w}{\partial \theta} &= \tau^{\theta}, && \text{(3.37c)}\\
p - p_a(\phi, \theta, t) &= 0, && \text{(3.37d)}
\end{aligned}$$

where τ^{ϕ} and τ^{θ} (N m^{-2}) are the zonal and meridional component of the wind stress. In the equations (3.37) already the approximation is made that the curvature of the surface is very small.

With Q_{oa} (Wm^{-2}) as the net downward heat flux into the ocean, the heat balance at the interface can be written as

$$\rho C_p K_V \frac{\partial T}{\partial z} = Q_{oa}, \tag{3.38}$$

with C_p in J kg^{-1}K^{-1} and K_V in m^{2}s^{-1}. As discussed in chapter 2, changes in salt can be induced by net changes in evaporation E and precipitation P (both in ms^{-1}). Therefore, the fresh water balance can be written as

$$\rho K_V \frac{\partial S}{\partial z} = (E - P) S_0, \tag{3.39}$$

where S_0 is a reference salinity, usually taken as $S_0 = 35$ ppt.

Additional Material

B: A discussion of the governing equations can be found in any textbook on geophysical fluid dynamics, (Pedlosky, 1987; Cushman-Roisin, 1994; Salmon, 1998; Mc Williams, 2006; Vallis, 2006). An elementary derivation can be found in chapter 4 of Gill (1982) and in Batchelor (2000).

B: For those interested in the derivation of the equations from Hamilton's principle in mechanics, see chapter I (sections 1-10) in Salmon (1998).

3.3. Dominant balances

We return to the general equations (3.32) and ask the question whether we can determine *a priori* dominant balances of terms in the these equations. Therefore it is useful to consider the stationary solution of these equations when the water is motionless. After substitution of $\mathbf{v} = 0$ into (3.32), we find that this solution (indicated by $\bar{p}, \bar{T}, \bar{S}, \bar{\rho}$) must satisfy (with $z = r - r_0$)

$$\frac{\partial \bar{p}}{\partial \phi} = \frac{\partial \bar{p}}{\partial \theta} = 0, \tag{3.40a}$$

$$\frac{\partial \bar{p}}{\partial z} = -\bar{\rho} g, \tag{3.40b}$$

$$\mathcal{F}_T + \frac{Q_T}{\bar{\rho} C_p} = 0, \tag{3.40c}$$

$$\mathcal{F}_S + \frac{Q_S}{\bar{\rho}} = 0, \tag{3.40d}$$

$$\bar{\rho} - \rho(\bar{p}, \bar{T}, \bar{S}) = 0, \tag{3.40e}$$

where the fact that there is no mixing of momentum when $\mathbf{v} = 0$ has been used. If $Q_S = Q_T = 0$, then $\bar{T}$ and $\bar{S}$ are only functions of z which are determined by the boundary conditions. The density $\bar{\rho}(z)$ is calculated from (3.40e) and (3.40b) and determines the hydrostatic pressure $\bar{p}(z)$.

Next we consider deviations from this hydrostatic steady state and introduce the dynamic pressure $\tilde{p}$ and density $\tilde{\rho}$ such that $p = \bar{p} + \tilde{p}$ and $\rho = \bar{\rho} + \tilde{\rho}$. To estimate the magnitude of these dynamic quantities, we use the time scales τ_a, τ_f and τ_w. For flows with a horizontal length scale L and a horizontal velocity scale U, we first consider the horizontal momentum balances. The magnitude of the inertial accelerations $\rho \mathbf{v}.\nabla \mathbf{v}$ can be estimated as $\rho_0 U^2/L = \rho_0 U/\tau_a$ and that of the Coriolis accelerations as $2\Omega\rho_0 U \sin\theta = \rho_0 U/\tau_f$. As the time scale τ_w is much larger than both τ_a and τ_f and $\tau_f \ll \tau_a$, the dominant balance must be between Coriolis acceleration and pressure gradient. But because the Coriolis acceleration depends on the latitude θ, we have to consider three different cases:

Ex. 3.5

(i) Midlatitude ocean circulation

The flow can be considered near a latitude $\theta_0 \neq 0$ and it is local so that L/r_0 is small. The scales for dynamic pressure and density are determined in chapters 5 (homogeneous case) and 7 (stratified case) and the governing equations are reduced according to these scales.

(ii) Equatorial ocean circulation

The flow can be considered locally near the latitude $\theta_0 \approx 0$ and L/r_0 is small. In this case, the Coriolis acceleration at the equator is zero, but it is nonzero

just north and south of the equator. The scales for dynamic pressure and density are determined in chapter 11 and the governing equations are reduced according to these scales.

(iii) Planetary circulation

The flow is on such a large scale that L/r_0 is not small. In this case, the magnitude of the Coriolis acceleration is scaled by its maximum value 2Ω at $\theta = \pi/2$. The scales for dynamic pressure and density are determined in chapter 13 and the governing equations are (unfortunately not much) reduced according to these scales.

Through the dependence of the Coriolis acceleration on latitude, and the a priori dominant balance between this acceleration and the pressure gradient, the mathematical description of ocean flows is divided naturally into three different problems. In the remaining chapters this logical division is followed with focus first on stationary and then on time-dependent flows. Before we turn to the first type of these flows (at mid-latitude) however, we first consider the concept of vorticity in more detail, since it will play an important role in the interpretation of the dynamical processes causing a particular type of ocean flow.

Summary

- Processes with the smallest time scales are expected to be most dominant in steady balances. Ratio's of time scales lead to dimensional parameters and indicate whether balances in a flow can occur between different processes. A process with a small time scale is expected to lead to a large contribution to the vorticity balance in a flow.
- For flows with a characteristic horizontal length scale L and a vertical length scale D, near a certain latitude θ_0 (with $f_0 = 2\Omega \sin\theta_0$) in water with a vertical density gradient set by the buoyancy frequency N, important scales are the inertial time scale τ_f, the inverse buoyancy frequency τ_s and the internal and external radii of deformation (L_D and R_D, respectively), defined by

$$\tau_f = \frac{1}{f_0} \; ; \; \tau_s = \frac{1}{N} \; ; \; L_D = \frac{ND}{f_0} \; ; \; R_D = \frac{\sqrt{gD}}{f_0}$$

- In a stratified, rotating flow with a characteristic horizontal velocity U the most important dimensionless parameters are the Rossby number ϵ, the Burger number S and the rotational Froude number F defined by

$$\epsilon = \frac{U}{f_0 L} \; ; \; S = \frac{N^2 D^2}{f_0^2 L^2} \; ; \; F = \frac{f_0^2 L^2}{gD}$$

3.4. Exercises on chapter 3

(3.1) *Vorticity*

Consider a flow having a width of 200 km directed northward with a maximum velocity of 2 ms^{-1} near the latitude 27°N.

a. Calculate the value of the Coriolis parameter f_0 of this flow.

b. Determine a typical value of the relative vorticity of the flow.

c. Provide estimates of the time scales τ_f, τ_a and the Rossby number ϵ.

(3.2) *Properties of the Coriolis acceleration*

a. Show, in the same way as in section 3.1.2, that the rotation of the $(\mathbf{e}_1, \mathbf{e}_3)$ plane induces an acceleration $-2\Omega w \cos\theta$ in the $\mathbf{e}_1$ direction and an acceleration $2\Omega u \cos\theta$ in the $\mathbf{e}_3$ direction.

In section 3.1.2 we derived the expression for the Coriolis acceleration $\boldsymbol{a}^c$.

b. Show that $\boldsymbol{a}^c \perp \boldsymbol{\Omega}$ and $\boldsymbol{a}^c \perp \boldsymbol{v}$.

(3.3) *Rossby deformation radius*

Both the external (R_D) and internal (L_D) Rossby deformation radii are important length scales in the ocean.

a. Use typical values of ocean depth (Fig. 1.1) and buoyancy frequency (Fig. 3.4) to estimate L_D and R_D in the Atlantic Ocean at a latitude of 5°N, 30°N and 55°N.

b. Provide a priori arguments whether effects of stratification are important in (i) the 'gyre' circulation, (ii) the mean Gulf Stream, and (iii) rings which develop from the Gulf Stream (see Fig. 2.10).

c. Same as b. but now for the effects of ocean-atmosphere deformation.

(3.4) *Equations of motion*

It is a useful exercise to derive the equations of motion (3.32a-c) from the specification of the Navier-Stokes equations in spherical coordinates (r, ϑ, φ) such as provided, for example in appendix 2 of Batchelor (2000).

First consider the isotropic case for which $A_H = A_V$.

a. Give an explicit expression for the inertial terms in (3.32a).

b. Give an explicit expression for the term $\mathcal{F}_I^\phi$ in (3.32a).

Next consider the nonisotropic case, but now in Cartesian coordinates.

c. Give an explicit expression for the term $\mathcal{F}_I^\phi$ in (3.32a) using (3.18).

(3.5) *Damped inertial motion*

We consider the situation where a particular wind stress has driven a flow in an ocean basin (containing water of constant density) for a while and then suddenly ceases. At this point there are no external forces acting on the water. There is a linear friction damping the motion with a friction coefficient r. The horizontal momentum equations are

$$\begin{aligned} \frac{Du}{dt} &= 2\Omega v \sin\phi - ru \\ \frac{Dv}{dt} &= -2\Omega u \sin\phi - rv \end{aligned}$$

where D/dt is the material derivative. Assume that a water parcel has a horizontal velocity $(u, v) = (0, v_0)$ at $t = 0$.

a. Show that

$$\frac{D}{dt}(u^2 + v^2) = -2r(u^2 + v^2)$$

We now search for solutions of the form

$$(u(t), v(t)) = e^{-rt}(c_1 \sin(\alpha t + \Psi_1), c_2 \cos(\alpha t + \Psi_2)).$$

with constants α, c_1, c_2 and Ψ_2.

b. Determine $(u(t), v(t))$ and explain what kind of motion of the water parcel results.

Chapter 4

VORTICITY

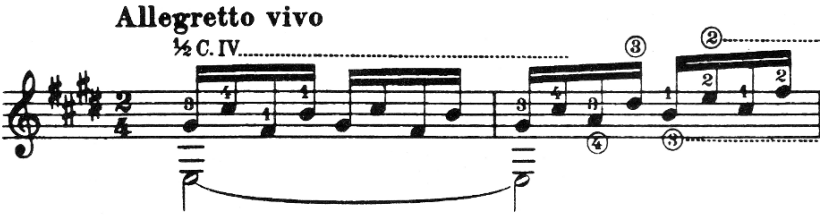

Prelude IX, M. Ponce

Because the concept of vorticity plays an important role in the interpretation of the results of ocean models, a special section is devoted to the vorticity equation (section 4.1), the different mechanisms of vorticity transport (section 4.2) and the concept of potential vorticity (section 4.3). The shallow-water equations are presented in section 4.4 to nicely illustrate vorticity concepts for flows in thin liquid layers. Here we also see a first example of scaling and the use of dimensionless equations.

4.1. The vorticity equation

As we have seen in chapter 3, the relative vorticity is the local spin of a fluid parcel and defined mathematically as $\boldsymbol{\omega} = \nabla \wedge \mathbf{v}$. In a rotating frame of reference, it is useful to define the planetary vorticity as $2\boldsymbol{\Omega}$ and the absolute vorticity $\boldsymbol{\omega}_a = \boldsymbol{\omega} + 2\boldsymbol{\Omega}$. Streamlines are the integral curves of the instantaneous velocity field

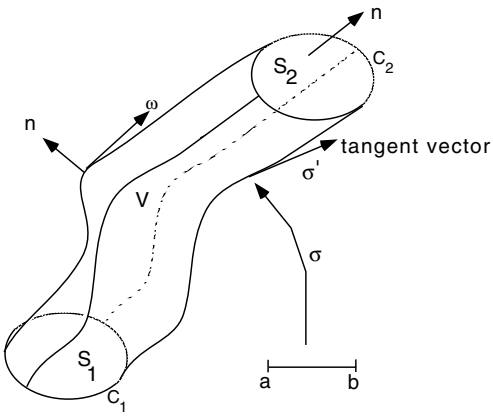

Figure 4.1. A vortex tube consisting of vortex lines through a closed curve C_1. The mapping $\boldsymbol{\sigma} : [a, b] \subset \mathbb{R} \to \mathbb{R}^3$ is a curve which can parameterize a particular vortex line.

Ex. 4.1

and similarly vortex lines are the integral curves of the instantaneous absolute vorticity field (or more generally, as integral curves of the vector field $\boldsymbol{\omega}_a/\rho$). Hence, for fixed t_0, the range of a curve $\boldsymbol{\sigma} : \mathbb{R} \to \mathbb{R}^3$ is a vortex line if

$$\boldsymbol{\sigma}'(s) = \frac{\boldsymbol{\omega}_a}{\rho}(t_0, \boldsymbol{\sigma}(s)). \tag{4.1}$$

Ex. 4.2

A vortex tube consists of vortex lines which pass through a closed curve (Fig. 4.1).

Because the vorticity field is divergence free, Helmholtz' theorem states that if C_1 and C_2 are two closed curves on a vortex tube (Fig. 4.1) then

$$\Gamma_1 = \int_{C_1} \mathbf{v} \cdot \mathbf{ds} = \int_{C_2} \mathbf{v} \cdot \mathbf{ds} = \Gamma_2, \tag{4.2}$$

where Γ is the circulation of the velocity field with respect to a closed curve C.

The balance of vorticity follows from the momentum balance (3.29a) by taking the curl of both sides of the equation. With help of

$$\mathbf{v} \cdot \nabla \mathbf{v} \; - \frac{\nabla v^2}{2} + \boldsymbol{\omega} \wedge \mathbf{v} \;\; = \;\; 0, \tag{4.3a}$$

$$\nabla \wedge (\frac{\nabla p}{\rho}) + \frac{\nabla \rho \wedge \nabla p}{\rho^2} \;\; = \;\; 0, \tag{4.3b}$$

where $v^2 = \mathbf{v} \cdot \mathbf{v}$, the vorticity equation is written as

$$\frac{\partial \boldsymbol{\omega}}{\partial t} + \nabla \wedge ((2\boldsymbol{\Omega} + \boldsymbol{\omega}) \wedge \mathbf{v}) = \rho^{-2} \nabla \rho \wedge \nabla p + \nabla \wedge \mathcal{F}_I. \tag{4.4}$$

Using $\nabla \cdot \boldsymbol{\omega} = 0$ and $\nabla \wedge (\mathbf{v} \wedge \boldsymbol{\omega}) = \boldsymbol{\omega} \cdot \nabla \mathbf{v} - \boldsymbol{\omega} \nabla \cdot \mathbf{v} - \mathbf{v} \cdot \nabla \boldsymbol{\omega}$, it follows that (4.4) can be written as

$$\frac{\partial \boldsymbol{\omega}_a}{\partial t} = -\mathbf{v} \cdot \nabla \boldsymbol{\omega}_a + \boldsymbol{\omega}_a \cdot \nabla \mathbf{v} - \boldsymbol{\omega}_a \nabla \cdot \mathbf{v} + \frac{\nabla \rho \wedge \nabla p}{\rho^2} + \nabla \wedge \mathcal{F}_I. \tag{4.5}$$

Ex. 4.3

This equation shows that the local vorticity can change through advection, changes in orientation of vortex lines, changes in thickness of vortex tubes, density (or baroclinic) effects and random mixing (diffusion) of vorticity. Of these, advection needs no further explanation: the other vorticity changing mechanisms are considered in the next section.

4.2. Vorticity transport

Using elementary examples, we will present the mechanisms of vortex stretching, vortex tilting, baroclinic vorticity production and diffusion of vorticity.

4.2.1. Vortex stretching and tilting

Consider in Fig. 4.2 a situation where in a local Cartesian coordinate system, the vector $\boldsymbol{\omega}_a$ is initially parallel to the z-axis, i.e., $\boldsymbol{\omega}_a = (\omega_1, \omega_2, \omega_3)^T = \bar{\omega}\,(0, 0, 1)^T$, where the superscript T indicates transpose and $\bar{\omega} > 0$. If the components of the velocity vector are defined as $\mathbf{v} = (u, v, w)$ then the sum of the second and third terms of the right hand side of (4.5) becomes

$$\boldsymbol{\omega}_a \cdot \nabla \mathbf{v} - \boldsymbol{\omega}_a \nabla \cdot \mathbf{v} = \begin{pmatrix} \bar{\omega} \frac{\partial u}{\partial z} \\ \bar{\omega} \frac{\partial v}{\partial z} \\ -\bar{\omega} (\frac{\partial u}{\partial x} + \frac{\partial v}{\partial y}) \end{pmatrix}. \tag{4.6}$$

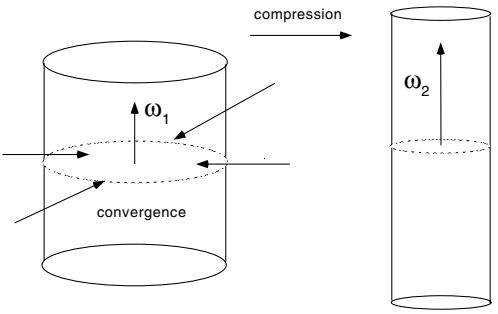

Figure 4.2. Illustration of vortex stretching. Convergencies in a flow lead to compression of a vortex tube and hence to larger vorticity component in direction of the stretching ($\omega_2 > \omega_1$).

When no other effects of vorticity production are present, then the third component of (4.5) with (4.6) gives

$$\frac{\partial \omega_3}{\partial t} = -\bar{\omega}(\frac{\partial u}{\partial x} + \frac{\partial v}{\partial y}). \tag{4.7}$$

The time change of the z-component of $\boldsymbol{\omega}_a$ is thus proportional to the horizontal divergence of the velocity field orthogonal to the z-axis. When $\partial u/\partial x + \partial v/\partial y < 0$, there is a local convergence of liquid in this horizontal plane. Consider the local vortex tube parallel to the z-axis (Fig. 4.2a). This vortex tube is being compressed and hence the vorticity in the z-direction must increase (Fig. 4.2b) according to (4.6); this is the mechanism of *vortex stretching*.

From the first component of (4.6), it follows that the change in the vorticity component in the x-direction is proportional to $\bar{\omega}\partial u/\partial z$. Consider a vortex line that is initially parallel to the z-axis (Fig. 4.3) in a flow for which $\partial u/\partial z > 0$. Because of the vertical shear in this flow the vortex line tilts and hence provides a contribution to the x-component of the vorticity (Fig. 4.3). The same mechanism of *vortex tilting* can change the vorticity component in the y-direction when $\partial v/\partial z \neq 0$.

4.2.2. Baroclinic vorticity production

The vector $\nabla\rho \wedge \nabla p$ in (4.5) is called the baroclinic vector. According to (4.5) there is vorticity production when this vector is not equal to the zero vector. To illustrate how vorticity is produced when $\nabla\rho \wedge \nabla p \neq 0$, we look at the following example. Assume that for $z \in [-1, 0]$ the pressure field is given by $p(z) = -z$ and in addition, for $x \in [0, 1]$, the density is given by $\rho = \rho_0 - \delta z - \gamma x$, with $\delta > 0$ and $\gamma > 0$. The surfaces (planes) of constant pressure (isobars) and constant density (isopycnals) are sketched in Fig. 4.4. Consider two fluid parcels on the same level

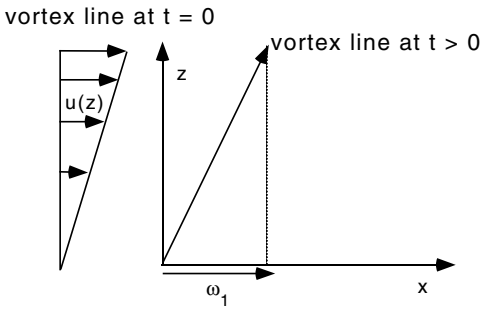

Figure 4.3. Illustration of vortex tilting. The vortex line is aligned with the $z-$axis at t = 0 and is tilted by the vertical shear in the flow. This induces a nonzero x-component of the vorticity (ω_1).

z but at different horizontal positions x, say at x_1 and x_2 (with $x_2 > x_1$).

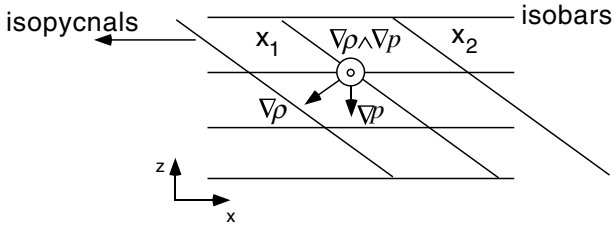

Figure 4.4. Sketch to illustrate the production of vorticity through baroclinic effects.

The parcel at x_1 has a larger density than the one at x_2, while the same pressure gradient acts on both parcels. The parcel at x_1 will therefore move downwards with respect to that at x_2, which induces a vorticity component in the y-direction. Direct calculation also confirms this since

$$\nabla\rho \wedge \nabla p = \begin{pmatrix} 0 \\ -\gamma \\ 0 \end{pmatrix}. \tag{4.8}$$

There is a particular case when the baroclinic vector is zero, i.e., when surfaces of constant density are also surfaces of constant pressure. In this case, the pressure is a unique function of density, $p = p(\rho)$. Such a flow, where baroclinic vorticity production is absent, is called a barotropic flow.

4.2.3. Diffusion of vorticity

Consider a flow of a viscous liquid with (in Cartesian coordinates) $\mathcal{F}_I = \nu \nabla^2 \mathbf{v}$, where ν is the kinematic viscosity. If we take the rotation of this term (as it appears in the vorticity equation (4.5)), it follows that $\nabla \wedge \mathcal{F}_I = \nu \nabla^2 \boldsymbol{\omega}$. Imagine a circular flow around the y-axis (Fig. 4.5) where $r^2 = x^2 + z^2$, for which $\boldsymbol{\omega} = (0, \omega(t, r), 0)^T$. The equation for the y-component of the relative vorticity (assuming that all other effects are absent and that $\Omega = 0$) from (4.5) is

$$\frac{\partial \omega}{\partial t} = \nu \nabla^2 \omega. \tag{4.9}$$

If we assume that a concentrated vortex with magnitude Γ is present at the origin at $t = 0$ then $\omega(0, r) = \Gamma \delta(r)$, with $\delta(r)$ being the delta distribution. The solution to the problem (4.9) is then given by

$$\omega(t, r) = \frac{\Gamma}{4\pi\nu t} e^{-\frac{r^2}{4\nu t}}. \tag{4.10}$$

For $\nu = \Gamma = 1$, ω component is plotted for three different times in Fig. 4.5b and we see that through the presence of viscosity the vorticity is diffused in time over the flow field.

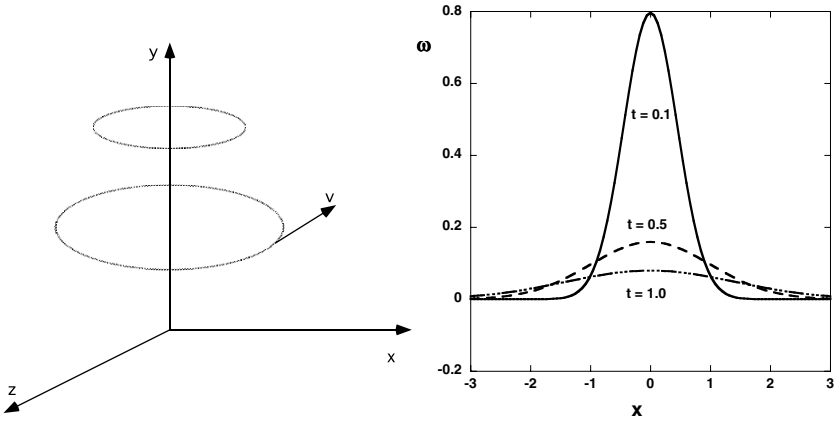

(a) (b)

Figure 4.5. Illustration of the mechanism of vorticity diffusion. (a) Flow situation where only the azimuthal velocity component v is nonzero. (b) For $\nu = \Gamma = 1$, the vorticity component (4.10) at $y = 0$ (i.e., r = x) for three values of t.

4.3. Potential vorticity

It is now time to introduce the important concept of potential vorticity. In many flows there are constraints of the motion of fluid parcels set by particular invariants. In non-rotating flows Kelvin's theorem is one of these constraints. These constraints become more powerful when they hold for scalar quantities instead of for vector quantities. Potential vorticity is one of these scalar quantities and we will introduce the concept below in its most general form.

Consider a general scalar quantity λ that satisfies

$$\frac{D\lambda}{dt} = \mathcal{F}_\lambda \tag{4.11}$$

where $\mathcal{F}_\lambda$ represent the sources and sinks of λ. For each such λ a potential vorticity Π_λ is defined as

$$\Pi_\lambda = \frac{\boldsymbol{\omega} + 2\boldsymbol{\Omega}}{\rho} \cdot \nabla\lambda. \tag{4.12}$$

The i^{th} component of $D(\nabla\lambda)/dt$ can be written as

$$(\frac{D}{dt}\nabla\lambda)_i = \left[\frac{\partial}{\partial t} + \sum_j v_j \frac{\partial}{\partial x_j}\right] \frac{\partial\lambda}{\partial x_i}.$$

If we take the inner product of this vector with $\boldsymbol{\omega}_a/\rho$, then it follows (denoting $\omega_i = (\boldsymbol{\omega}_a)_i$) that

$$\frac{\boldsymbol{\omega}_a}{\rho} \cdot \frac{D(\nabla\lambda)}{dt} = \sum_i \frac{\omega_i}{\rho} \left[\frac{\partial}{\partial t} + \sum_j v_j \frac{\partial}{\partial x_j}\right] \frac{\partial\lambda}{\partial x_i} =$$

$$= \sum_i \frac{\omega_i}{\rho} \frac{\partial}{\partial x_i} \left[\frac{\partial}{\partial t} + \sum_j v_j \frac{\partial}{\partial x_j}\right] \lambda - \sum_i \frac{\omega_i}{\rho} \sum_j \frac{\partial\lambda}{\partial x_j} \frac{\partial v_j}{\partial x_i} =$$

$$= \sum_i \frac{\omega_i}{\rho} \frac{\partial}{\partial x_i} \left[\frac{\partial}{\partial t} + \sum_j v_j \frac{\partial}{\partial x_j}\right] \lambda - \sum_j \frac{\partial\lambda}{\partial x_j} \sum_i \frac{\omega_i}{\rho} \frac{\partial v_j}{\partial x_i} =$$

$$= \frac{\boldsymbol{\omega}_a}{\rho} \cdot \nabla \frac{D\lambda}{dt} - \nabla\lambda \cdot \frac{\boldsymbol{\omega}_a}{\rho} \cdot \nabla\mathbf{v}. \tag{4.13}$$

Next, the vorticity equation (4.5) is written as

$$\frac{D\boldsymbol{\omega}_a}{dt} = \boldsymbol{\omega}_a \cdot \nabla\mathbf{v} - \boldsymbol{\omega}_a \nabla \cdot \mathbf{v} + \frac{\nabla\rho \wedge \nabla p}{\rho^2} + \nabla \wedge \mathcal{F}_I.$$

From the continuity equation (3.29) we derive $\nabla \cdot \mathbf{v} = -\rho^{-1} D\rho/dt$, we then divide both sides by ρ, then substitute the result in (4.3) and take the inner product of the result with $\nabla\lambda$. This gives

$$\nabla\lambda \cdot (\rho^{-1}\frac{D}{dt}\boldsymbol{\omega}_a - \frac{\boldsymbol{\omega}_a}{\rho^2}\frac{D\rho}{dt}) = \nabla\lambda \cdot \frac{D}{dt}\frac{\boldsymbol{\omega}_a}{\rho} =$$

$$\nabla\lambda \cdot (\frac{\boldsymbol{\omega}_a}{\rho} \cdot \nabla\mathbf{v} + \frac{\nabla\rho \wedge \nabla p}{\rho^3} + \frac{\nabla \wedge \mathcal{F}_I}{\rho}), \tag{4.14}$$

Summing (4.13) and (4.14) and using (4.11) we eventually derive

$$\frac{D\Pi_\lambda}{dt} = \frac{\boldsymbol{\omega}_a \cdot \nabla\mathcal{F}_\lambda}{\rho} + \nabla\lambda \cdot (\frac{\nabla\rho \wedge \nabla p}{\rho^3} + \frac{\nabla \wedge \mathcal{F}_I}{\rho}). \tag{4.15}$$

When

(i) λ is a conserved quantity, i.e., $\mathcal{F}_\lambda = 0$,

(ii) $\mathcal{F}_I = 0$, and

(iii) $\lambda = \lambda(\rho, p)$

then it follows from (4.15) that

$$\frac{D\Pi_\lambda}{dt} = 0. \tag{4.16}$$

This is the famous *Ertel's theorem*. Conservation of potential vorticity provides a strong constraint on the flow. In subsequent chapters, the importance of these type of constraints will become clear and several examples will be given.

Additional Material

B: You are now ready to read the more comprehensive discussion on the vorticity concepts in chapter 2 (sections 2.1 to 2.5) of Pedlosky (1987) chapter 4 of Vallis (2006) and chapter 3 of Mc Williams (2006).

D: In the review paper "Ertel's potential vorticity theorem in physical oceanography" (Müller, 1995) there is an overview of the different potential vorticities used, their interpretation and their origin (derived from a Lagrangian description of the fluid motion).

4.4. Shallow-water equations

In this section several concepts of vorticity are studied in more detail along with the introduction of the shallow-water equations. As we will both use dimensional and dimensionless quantities, we use a star subscript to indicate dimensional quantities.

Consider the flow in a shallow liquid layer having a constant density ρ on a plane that is rotating with angular velocity Ω. We choose a Cartesian coordinate system with the gravity vector parallel to the z_*-axis. Let the bottom be described by $z_* = -D_0 + h_{b*}(x_*, y_*)$ and the liquid-gas interface by $z_* = h_*(x_*, y_*, t_*)$. The equations (3.32), with $f = 2\Omega$, then become

$$\rho(\frac{Du_*}{dt_*} - fv_*) = -\frac{\partial p_*}{\partial x_*} + \rho A_H \left[\frac{\partial^2 u_*}{\partial x_*^2} + \frac{\partial^2 u_*}{\partial y_*^2}\right] + \rho A_V \frac{\partial^2 u_*}{\partial z_*^2}, \quad (4.17a)$$

$$\rho(\frac{Dv_*}{dt_*} + fu_*) = -\frac{\partial p_*}{\partial y_*} + \rho A_H \left[\frac{\partial^2 v_*}{\partial x_*^2} + \frac{\partial^2 v_*}{\partial y_*^2}\right] + \rho A_V \frac{\partial^2 v_*}{\partial z_*^2}, \quad (4.17b)$$

$$\rho\frac{Dw_*}{dt_*} = -g\rho - \frac{\partial p_*}{\partial z_*} + \rho A_H \left[\frac{\partial^2 w_*}{\partial x_*^2} + \frac{\partial^2 w_*}{\partial y_*^2}\right] + \rho A_V \frac{\partial^2 w_*}{\partial z_*^2}, \quad (4.17c)$$

$$\frac{\partial u_*}{\partial x_*} + \frac{\partial v_*}{\partial y_*} + \frac{\partial w_*}{\partial z_*} = 0, \quad (4.17d)$$

with

$$\frac{D}{dt_*} = \frac{\partial}{\partial t_*} + u_*\frac{\partial}{\partial x_*} + v_*\frac{\partial}{\partial y_*} + w_*\frac{\partial}{\partial z_*}. \quad (4.18)$$

4.4.1. Hydrostatic equilibrium

A characteristic vertical length scale of the problem is the average liquid layer depth D, L is a characteristic horizontal length scale, U is a horizontal velocity scale and τ is a characteristic time scale. Let W and P be a priori unknown scales of vertical velocity and dynamic pressure, then we define dimensionless quantities

$$x = \frac{x_*}{L}, y = \frac{y_*}{L}, z = \frac{z_*}{D}, t = \frac{t_*}{\tau} \quad (4.19a)$$

$$u = \frac{u_*}{U}, v = \frac{v_*}{U}, w = \frac{w_*}{W}, \quad (4.19b)$$

$$p_* = -g\rho z_* + p\,P. \quad (4.19c)$$

Because $\partial u_*/\partial x_* = \mathcal{O}(U/L)$ and $\partial v_*/\partial y_* = \mathcal{O}(U/L)$, it follows from (4.17d) that W cannot be larger than

$$W = \frac{D}{L}U. \quad (4.20)$$

The estimate (4.20) is an upper boundary; W can be smaller than (4.20) if the terms $\partial u_*/\partial x_*$ and $\partial v_*/\partial y_*$ partially cancel.

With the choice of (4.20) for W and the advective time scale $\tau_a = U/L$ for τ, the equations (4.17) become

$$\epsilon\frac{Du}{dt} - v = -\frac{P}{\rho f L U}\frac{\partial p}{\partial x} + E_H\left[\frac{\partial^2 u}{\partial x^2} + \frac{\partial^2 u}{\partial y^2}\right] + E_V\frac{\partial^2 u}{\partial z^2}, \tag{4.21a}$$

$$\epsilon\frac{Dv}{dt} + u = -\frac{P}{\rho f L U}\frac{\partial p}{\partial y} + E_H\left[\frac{\partial^2 v}{\partial x^2} + \frac{\partial^2 v}{\partial y^2}\right] + E_V\frac{\partial^2 v}{\partial z^2}, \tag{4.21b}$$

$$\delta^2\epsilon\frac{Dw}{dt} = -\frac{P}{\rho f L U}\frac{\partial p}{\partial z} + \delta^2 E_H(\frac{\partial^2 w}{\partial x^2} + \frac{\partial^2 w}{\partial y^2}) + \delta^2 E_V\frac{\partial^2 w}{\partial z^2}, \tag{4.21c}$$

$$\frac{\partial u}{\partial x} + \frac{\partial v}{\partial y} + \frac{\partial w}{\partial z} = 0, \tag{4.21d}$$

with

$$\frac{D}{dt} = \frac{\partial}{\partial t} + u\frac{\partial}{\partial x} + v\frac{\partial}{\partial y} + w\frac{\partial}{\partial z}. \tag{4.22}$$

In (4.21), we see the Rossby number ϵ, the aspect ratio δ and the horizontal and vertical Ekman numbers E_H and E_V. These are defined as

$$\delta = \frac{D}{L}; \epsilon = \frac{U}{fL}; E_H = \frac{A_H}{fL^2}; E_H = \frac{A_V}{fD^2}. \tag{4.23}$$

The large-scale ocean circulation is characterized by a huge difference in horizontal and vertical length scales, i.e., $L \gg D$ and hence $\delta \ll 1$. Typical values are $D = \mathcal{O}(10^3)$m and $L = \mathcal{O}(10^6)$m, which gives $\delta = \mathcal{O}(10^{-3})$.

Now consider the case when $E_H = E_V = 0$. The pressure gradient is either in balance with (i) the Coriolis acceleration or (ii) with the inertial acceleration. In case (i), the proper pressure scale is $P = \rho f U L$ and in case (ii) it is $P = \rho U^2$. It then follows from (4.21c) that

(i)

$$\delta^2\epsilon\frac{Dw}{dt} = -\frac{\partial p}{\partial z}, \tag{4.24}$$

(ii)

$$\delta^2\frac{Dw}{dt} = -\frac{\partial p}{\partial z}. \tag{4.25}$$

In case (i), the order of magnitude of ϵ is at most $\mathcal{O}(1)$, because otherwise the assumption of a balance between pressure gradient and Coriolis acceleration breaks down. In both cases, we conclude that (note that $Dw/dt = \mathcal{O}(1)$) the hydrostatic approximation

$$\frac{\partial p}{\partial z} = \mathcal{O}(\delta^2) \Leftrightarrow p_* = -\rho g z_* + \mathcal{O}(\delta^2), \tag{4.26}$$

is valid for flows with $(\delta \ll 1)$. One can show with similar arguments that (4.26) is still valid in a time-dependent problem with nonzero (but small) Ekman numbers E_H and E_V.

4.4.2. Inertial flows

The shallow-water equations follow from (4.17) with $A_H = A_V = 0$ and $\delta \to 0$, i.e.,

$$\rho(\frac{Du_*}{dt_*} - fv_*) = -\frac{\partial p_*}{\partial x_*}, \tag{4.27a}$$

$$\rho(\frac{Dv_*}{dt_*} + fu_*) = -\frac{\partial p_*}{\partial y_*}, \tag{4.27b}$$

$$\frac{\partial p_*}{\partial z_*} = -\rho g, \tag{4.27c}$$

$$\frac{\partial u_*}{\partial x_*} + \frac{\partial v_*}{\partial y_*} + \frac{\partial w_*}{\partial z_*} = 0. \tag{4.27d}$$

When friction is neglected the boundary conditions become

$$z_* = h_*(x_*, y_*, t_*) \quad : \quad \frac{D(z_* - h_*)}{dt_*} = 0;\ p_* = p_{a*} \tag{4.28a}$$

$$z_* = -D_0 + h_{b*}(x_*, y_*) \quad : \quad \frac{D(z_* + D_0 - h_{b*})}{dt_*} = 0, \tag{4.28b}$$

where p_{a*} is the atmospheric surface level pressure. From the second equation in (4.28a) and equation (4.27c) we find

$$p_*(x_*, y_*, z_*, t_*) = \rho g(h_*(x_*, y_*, t_*) - z_*) + p_{a*}, \tag{4.29}$$

from which it follows that horizontal pressure gradients are independent of z. The other equations (4.27) reduce to

$$\frac{Du_*}{dt_*} - fv_* = -g\frac{\partial h_*}{\partial x_*}, \tag{4.30a}$$

$$\frac{Dv_*}{dt_*} + fu_* = -g\frac{\partial h_*}{\partial y_*}, \tag{4.30b}$$

$$\frac{\partial u_*}{\partial x_*} + \frac{\partial v_*}{\partial y_*} + \frac{\partial w_*}{\partial z_*} = 0. \tag{4.30c}$$

From the kinematic conditions (4.28) it follows that

$$w_*(x_*, y_*, h_*, t_*) = \frac{\partial h_*}{\partial t_*} + u_*\frac{\partial h_*}{\partial x_*} + v_*\frac{\partial h_*}{\partial y_*}, \tag{4.31a}$$

$$w_*(x_*, y_*, h_{b*}, t_*) = u_*\frac{\partial h_{b*}}{\partial x_*} + v_*\frac{\partial h_{b*}}{\partial y_*}. \tag{4.31b}$$

The system (4.30)-(4.31) is the general form of the shallow-water equations.

Ex. 4.4

Now consider the special (but highly relevant) case where the velocity components u_* and v_* do not depend on z_*. In that case (4.30c) can be integrated over the layer and with (4.31) and $H_* = h_* + D_0 - h_{b*}$, we obtain

$$\frac{\partial H_*}{\partial t_*} + \frac{\partial}{\partial x_*}(H_* u_*) + \frac{\partial}{\partial y_*}(H_* v_*) =$$
$$= \frac{\partial H_*}{\partial t_*} + u_* \frac{\partial h_*}{\partial x_*} + v_* \frac{\partial h_*}{\partial y_*} + H_*(\frac{\partial u_*}{\partial x_*} + \frac{\partial v_*}{\partial y_*}) = 0. \tag{4.32}$$

The special form of the shallow-water equations are the equations (4.30a-b) and (4.32). We can write (4.32) as

$$\frac{DH_*}{dt_*} + H_*(\frac{\partial u_*}{\partial x_*} + \frac{\partial v_*}{\partial y_*}) = 0, \tag{4.33}$$

and consider a volume with layer thickness H_* and cross section A_*. The divergence of the horizontal velocity field is the relative change of the cross section area along a flow trajectory, hence

$$\frac{1}{A_*}\frac{DA_*}{dt_*} = \frac{\partial u_*}{\partial x_*} + \frac{\partial v_*}{\partial y_*}. \tag{4.34}$$

Elimination of the horizontal divergence in (4.32) gives

$$\frac{1}{A_*}\frac{DA_*}{dt_*} + \frac{1}{H_*}\frac{DH_*}{dt_*} = 0 \Rightarrow \frac{D}{dt_*}(A_* H_*) = 0. \tag{4.35}$$

The equation (4.32) is therefore just volume conservation. An increase in volume at a certain location (x_*, y_*) is compensated by changes in the height field h_*.

We now consider the interpretation of (4.32) and the transport of vorticity in a flow described by the special form of the shallow-water equations. For constant density flows, the vorticity equation (4.5) reduces to

$$\frac{D}{dt_*}(\boldsymbol{\omega_*} + 2\boldsymbol{\Omega}) - (\boldsymbol{\omega_*} + 2\boldsymbol{\Omega}) \cdot \nabla \mathbf{v}_* = 0, \tag{4.36}$$

with (in a Cartesian coordinate system) the relative and planetary vorticity given by

$$\boldsymbol{\omega_*} = \begin{pmatrix} \frac{\partial w_*}{\partial y_*} - \frac{\partial v_*}{\partial z_*} \\ \frac{\partial u_*}{\partial z_*} - \frac{\partial w_*}{\partial x_*} \\ \frac{\partial v_*}{\partial x_*} - \frac{\partial u_*}{\partial y_*} \end{pmatrix} \; ; \; \boldsymbol{\Omega} = \begin{pmatrix} 0 \\ 0 \\ \Omega \end{pmatrix}. \tag{4.37}$$

Because we have neglected friction, diffusion of vorticity is absent and baroclinic vorticity production is absent because of the constant density in the flow. With $\boldsymbol{\omega}_* = (\omega_{1*}, \omega_{2*}, \omega_{3*})$ we can write

$$(\boldsymbol{\omega_*} + 2\boldsymbol{\Omega}).\nabla \mathbf{v}_* = \begin{pmatrix} \omega_{1*}\frac{\partial u_*}{\partial x_*} + \omega_{2*}\frac{\partial u_*}{\partial y_*} + (\omega_{3*} + f)\frac{\partial u_*}{\partial z_*} \\ \omega_{1*}\frac{\partial v_*}{\partial x_*} + \omega_{2*}\frac{\partial v_*}{\partial y_*} + (\omega_{3*} + f)\frac{\partial v_*}{\partial z_*} \\ \omega_{1*}\frac{\partial w_*}{\partial x_*} + \omega_{2*}\frac{\partial w_*}{\partial y_*} + (\omega_{3*} + f)\frac{\partial w_*}{\partial z_*} \end{pmatrix}. \tag{4.38}$$

Making use of the scales (4.19), we observe that

$$\frac{D}{U}\omega_1 = \delta^2\frac{\partial w}{\partial y} - \frac{\partial v}{\partial z}, \tag{4.39a}$$

$$\frac{D}{U}\omega_2 = \frac{\partial u}{\partial z} - \delta^2\frac{\partial w}{\partial x}, \tag{4.39b}$$

$$\frac{L}{U}\omega_3 = \frac{\partial v}{\partial x} - \frac{\partial u}{\partial y}. \tag{4.39c}$$

Additional Material

B: The shallow-water equations form the cornerstone of many branches in geosciences, such as coastal dynamics and flows on outer planets. In chapter 5 of Gill (1982) the shallow-water equations are derived along with some illustrative flows problems.

D: For the numerical solution of the shallow-water equations in many different situations see Vreugdenhil (1994).

In the special case that u and v are independent of z, the horizontal components of the vorticity are negligible in the hydrostatic approximation. With the notation $\zeta_* = \omega_{3*}$ it follows from the z-component of (4.36) that

$$\frac{D(\zeta_* + f)}{dt_*} = -(\zeta_* + f)(\frac{\partial u_*}{\partial x_*} + \frac{\partial v_*}{\partial y_*}). \tag{4.40}$$

In addition to advection, vortex stretching can induce vorticity changes in these flows through divergences/convergencies in the horizontal velocity field. From (4.33-4.34) and (4.40) we find that

$$\frac{D(\zeta_* + f)}{dt_*} = \frac{\zeta_* + f}{H_*}\frac{DH_*}{dt} \Rightarrow \frac{D}{dt_*}\left(\frac{\zeta_* + f}{H_*}\right) = 0. \tag{4.41}$$

Ex. 4.5

This determines a scalar $(\zeta_* + f)/dt_*$ that is conserved with the motion of the liquid. Immediate applications of conservation of this shallow water potential vorticity are given in Fig. 4.6.

Can this quantity be written as a potential vorticity $\Pi_{\lambda *}$, such as generally defined through the Ertel theorem (cf. section 4.3)? To show this we need to find a quantity λ_* such that $\Pi_{\lambda *}$ in (4.12) is equal to $(\zeta_* + f)/H_*$. If the horizontal velocities u_* and v_* do not depend on height, the equation (4.30c) can be directly integrated in z. With (4.31b) this gives

$$w_* = (h_{b*} - D_0 - z_*)(\frac{\partial u_*}{\partial x_*} + \frac{\partial v_*}{\partial y_*}) + u_*\frac{\partial h_{b*}}{\partial x_*} + v_*\frac{\partial h_{b*}}{\partial y_*}, \tag{4.42}$$

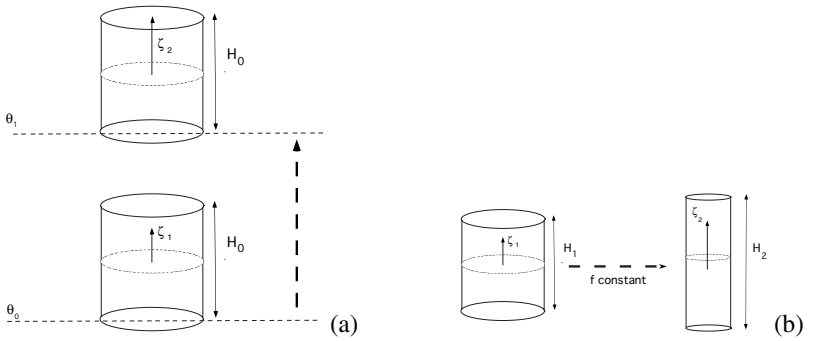

Figure 4.6. Applications of the conservation the shallow-water potential vorticity. (a) A column keep the same thickness but moves northward and hence its relative vorticity must decrease ($\zeta_2 < \zeta_1$). (b) A column moves eastward and its thickness H increases and hence the vorticity must increase ($\zeta_2 > \zeta_1$).

and with (4.31a)

$$w_* = \frac{z_* + D_0 - h_{b*}}{H_*} \frac{DH_*}{dt_*} + \frac{Dh_{b*}}{dt_*}. \tag{4.43}$$

Finally we find, with $w_* = Dz_*/dt_*$, that

$$\frac{D_*}{dt_*}\left[\frac{z_* + D_0 - h_{b*}}{H_*}\right] = 0, \tag{4.44}$$

and this provides the choice $\lambda_* = \rho(z_* + D_0 - h_{b*})/H_*$. This quantity is the relative position of a fluid parcel in the layer (Fig. 4.7). The potential vorticity

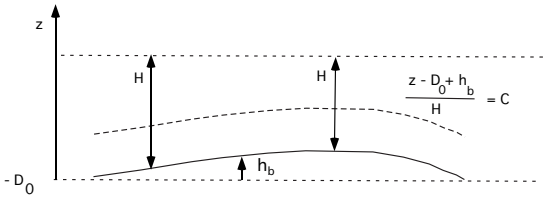

Figure 4.7. Illustration of the physical meaning of the quantity λ_*. The dashed curve is the relative position of a fluid element in the flow and this is constant.

$\Pi_{\lambda *}$, usually referred to as the shallow-water potential vorticity, is then

$$\Pi_{\lambda_*} = (\boldsymbol{\omega}_* + 2\boldsymbol{\Omega}) \cdot \nabla \left[\frac{z_* + D_0 - h_{b*}}{H_*}\right] = \frac{\zeta_* + f}{H_*}, \tag{4.45}$$

which is in accordance with the earlier result (4.41).

Summary

- There are basically four mechanisms of vorticity change in a rotating, stratified liquid, i.e., vortex stretching, vortex tilting, baroclinic vorticity production and vorticity diffusion.
- The concept of potential vorticity Π_λ refers to a family of possible scalar invariants in flows, usually parameterized by a conserved quantity λ, whose general form is

$$\Pi_\lambda = \frac{\boldsymbol{\omega} + 2\boldsymbol{\Omega}}{\rho} \cdot \nabla\lambda$$

  where $\boldsymbol{\omega}$ is the local vorticity vector.
- For the constant density shallow-water equations, the most commonly used invariant is the shallow-water potential vorticity

$$\Pi = \frac{\zeta + f}{H}$$

  where ζ is the vertical component of the vorticity vector, f the Coriolis parameter and H the total layer depth.

4.5. Exercises on chapter 4

(4.1) *Helmholtz theorem*

Let C_1 and C_2 be two curves on a closed vortex tube, S_i be the surfaces enclosed by the C_i, S be the total surface of the tube and V be the total volume enclosed by S (see Fig. 4.1). From the identity $\nabla \cdot \omega = 0$, show that

$$\Gamma_1 = \int_{C_1} \mathbf{v} \cdot \mathbf{ds} = \int_{C_2} \mathbf{v} \cdot \mathbf{ds} = \Gamma_2$$

(4.2) *Tornado*

A tornado consists of a thin vortex tube. Assume that the vorticity is constant over the cross section of the tube.

a. Show that locally the vorticity decreases when the thickness of the vortex tube increases.

b. About 10 m from the center of a tornado one measures wind speeds of 200 km/hr. Determine the pressure variations when the tornado passes by.

(4.3) *Taylor column*

Consider a flow with velocity field $\mathbf{v} = (u, v, w)$ in a horizontally unbounded layer of water. The water has a constant density ρ and rotates with an angular

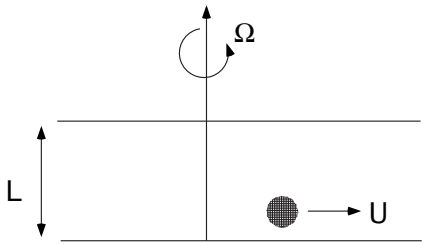

velocity Ω around the z-axis (see figure).

a. Give the vorticity equation of this flow.

We will focus now on variations in the flow on a time scale τ, a horizontal velocity scale U and a length scale L.

b. Estimate the order of magnitude of the terms in the vorticity equation.

Let $f = 2\Omega$. There is a special type of flow in case $\tau \gg 1/f$ and $\epsilon = U/(fL) \ll 1$.

c. Why is this case so special when considering the vorticity equation?

d. In an initially motionless layer, a sphere of radius R, with $R < L$, is moved over the bottom with a velocity U. After a while a steady flow results with $\epsilon \ll 1$. Make a sketch of this flow.

(4.4) *Topographic steering*

For large-scale flows in the deep ocean at locations for away from the equator, the relative vorticity can be neglected with respect to the planetary vorticity.

a. Argue why this holds and show that for a constant density flow, the shallow-water potential vorticity Π reduces to

$$\Pi = \frac{f}{H}$$

where H is the thickness of the layer and $f = f_0 + \beta_0 y$ is the Coriolis parameter on the β plane.

Consider now the east to west flow over a seamount as sketched in the figure below.

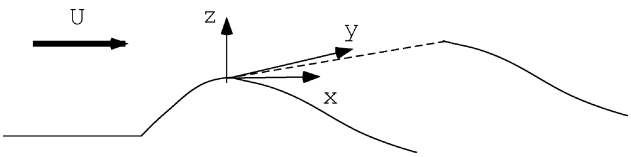

b. Describe the path of a watercolumn in this flow.

(4.5) *Altimetry*

Using a satellite, one can determine the height of the sea-surface η with respect to a reference surface (the geoid).

a. Describe how a seamount at the bottom of an ocean basin (through its influence on the local gravity field) affects the position of the sea surface.

b. How accurate can the geoid currently be determined (search the world wide web)?

c. Use the hydrostatic balance to show that

$$p = p_0 + \int_{-z}^{h} g\rho \, dz'$$

where z is the depth and p_0 is a constant pressure at the sea surface ($z = h$).

Take now a horizontal plane $z = -z_0$ below the sea surface and assume that the density ρ of the water is constant in the layer above this plane.

d. Assume that inertia is not important in the flow and that the flow is steady. Derive from the equations (4.30) that the surface velocities are given by

$$u = -\frac{g}{f}\frac{\partial h}{\partial y} \; ; \; v = \frac{g}{f}\frac{\partial h}{\partial x}$$

II

MIDLATITUDE DYNAMICS

Chapter 5

WIND-DRIVEN CIRCULATION

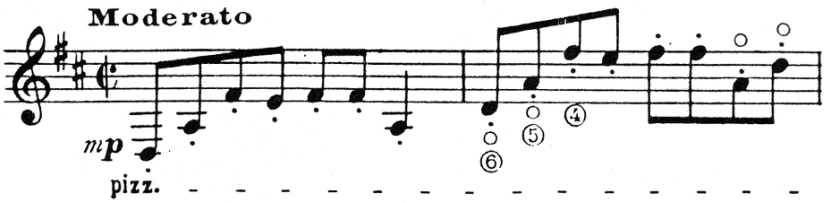

Berceuse (Canción de Cuna), L. Brouwer

In this chapter, we focus on the understanding of the wind-driven ocean circulation in the North Atlantic. After an introduction on this flow in section 5.1, an idealized model of a constant density flow (the barotropic midlatitude β-plane model) is derived in section 5.2. Local solutions of this model are constructed using asymptotic methods (inner- and outer expansions) which will naturally lead to the concepts of geostrophic equilibrium and the Ekman boundary layers (section 5.3) and the formulation of the barotropic quasi-geostrophic vorticity equation (section 5.4).

5.1. The North Atlantic surface circulation

A view of the surface circulation in the Atlantic basin can be obtained from an inspection of Fig. 2.4a. In the North Atlantic, the circulation is characterized by two cells, usually called 'gyres'. The smallest one, the subpolar gyre, is formed by currents south of Greenland and in the Labrador Sea such as the Irminger Current, the West Greenland Current and the Labrador Current. The largest one, the subtropical gyre, is formed by currents around the Sargasso Sea, such as the North Equatorial Current to the south. Near the western boundary, the latter current joins part of the South Equatorial current and part of the combined currents flows northward as the Antilles Current, while the other part flows into the Gulf of Mexico. The latter water eventually 'escapes' between Florida and Cuba as the Florida Current.

A merger of the Florida and Antilles current leaves the east coast of the US at Cape Hatteras and is then called the Gulf Stream. Snapshots of the circulation in the Gulf Stream region from a high resolution model are plotted in Fig. 5.1. The Gulf Stream flows northeastwards towards the Grand Banks of Newfoundland near (40°N, 50°W). The current that exists north-eastward of the Gulf Stream is called the North Atlantic Current. This current bifurcates into a part that contributes to the flows in the Norwegian Sea and a part that deflects southward as the Canary current.

Ex. 5.1

Characteristic of the flow in the North Atlantic as sketched in Fig. 5.1 are strong boundary currents (Florida Current and Gulf Stream) which exist at the western side of the basin. The Florida Current is situated above the continental slope, but the Gulf Stream is situated in the open ocean. The horizontal velocities in the Gulf Stream (up to 2.5 ms^{-1}) are among the largest measured in the ocean. Its mean velocity is about 1.5 ms^{-1} and its average width is about 115 km. The average volume transport of the Florida Current is 30 Sv (1 Sv = $10^6 \mathrm{m}^3\mathrm{s}^{-1}$). This transport increases towards Cape Hatteras up to 150 Sv near 65°W, but decreases again to 35 Sv near 40°W. In comparison, the average surface current velocity in the subtropical gyre is about 0.1 ms^{-1}.

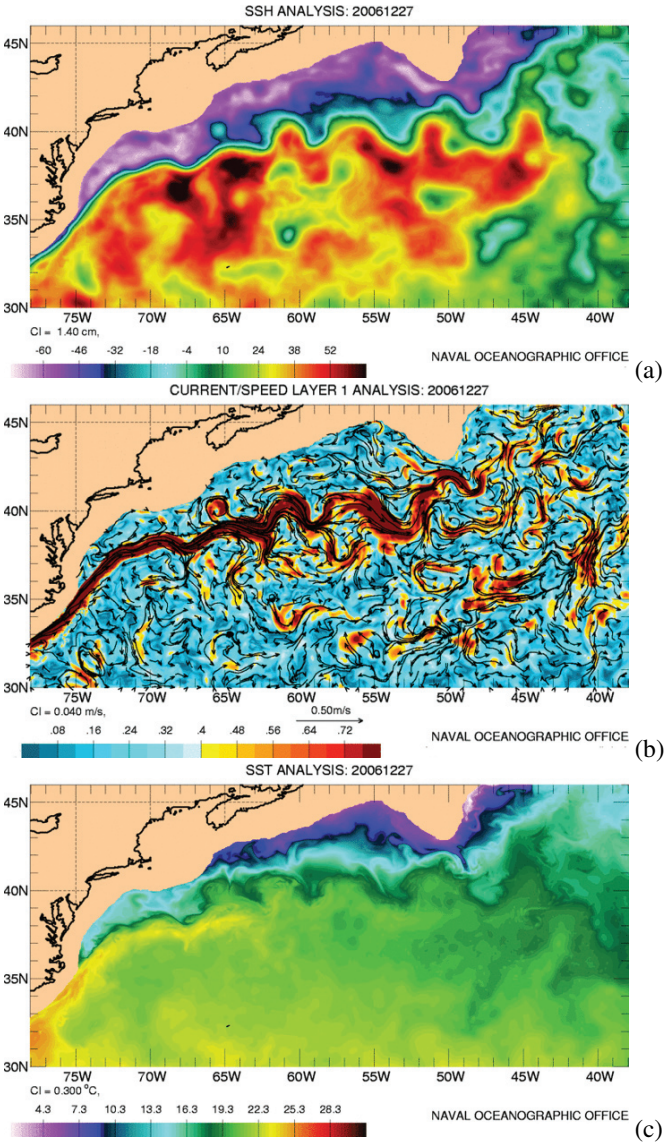

Figure 5.1. Snapshot of the surface circulation in the Gulf Stream region from a high resolution global ocean model (NLOM). (a) Sea surface height, (b) current speed, and (c) sea surface temperature.

The explanation of the surface circulation in the North Atlantic such as in Fig. 5.1, is one of classical problems in dynamical oceanography and forms the central problem of this chapter. The question can be formulated as *what processes control the 'gyres' and why is there a western amplification of the currents, in other words, why is there a Gulf Stream?*

Additional Material

B: The North Atlantic surface circulation is described in more detail in chapter 14 of Tomczak and Godfrey (1994) and chapter 7 of Knaus (1997). For bedtime reading, The Gulf Stream by Henry Stommel (Stommel, 1977) is recommended.

5.2. The barotropic circulation on the β-plane

The North Atlantic flow as described above is a typical mid-latitude phenomenon. This motivates the consideration of a model set up around a central latitude θ_0 (case (i) in section 3.3). As a first step, we investigate a situation in which the ocean water has constant density. In this case, only the pure wind-driven flow can be analyzed. Again, dimensional quantities will be indicated by a $*$ subscript.

For a flow with characteristic horizontal and vertical length scale L and D, horizontal and vertical velocity scale U and $W = UD/L$ and a time scale L/U, the magnitude of the Coriolis acceleration is $U2\Omega \sin\theta_0 = Uf_0$. From the analysis in section 3.3, we anticipate that the dominant horizontal momentum balance is between the Coriolis acceleration and the pressure force for small Rossby number $\epsilon = U/(f_0 L)$. Moreover, we anticipate a hydrostatic vertical momentum balance as $D \ll L$. This motivates us to scale the pressure as

$$p_* = -\rho_0 g D z + \rho_0 U f_0 L\, p. \tag{5.1}$$

We are now fully prepared to find proper reductions of the total equations of motion specifically targeted to explain the intensification of western boundary currents.

5.2.1. The β-plane approximation

As a first step in the reduction, local coordinates (x_*, y_*) (Fig. 5.2) are introduced with

$$x_* = xL = \phi\, r_0 \cos\theta_0, \tag{5.2a}$$
$$y_* = yL = (\theta - \theta_0) r_0, \tag{5.2b}$$
$$z_* = zD = r_* - r_0. \tag{5.2c}$$

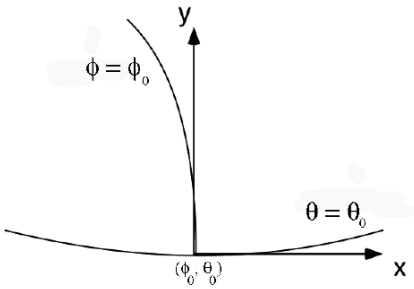

Figure 5.2. Local Cartesian coordinates as defined in (5.2).

After substitution of the scaled variables into (3.32) and use of the local coordinates (5.2), where derivatives are transformed as,

$$\frac{\partial u_*}{\partial \phi} = U \frac{\partial u}{\partial x_*} \frac{\partial x_*}{\partial \phi} = U \cos\theta_0 \frac{r_0}{L} \frac{\partial u}{\partial x}, \tag{5.3}$$

we find the dimensionless equations

$$\begin{aligned}
\epsilon \left[\frac{Du}{dt} + \frac{L}{r_*}(\delta uw - uv \tan\theta) \right] - v \frac{\sin\theta}{\sin\theta_0} + \delta w \frac{\cos\theta}{\sin\theta_0} &= \\
- \frac{\cos\theta_0}{\cos\theta} \frac{r_0}{r_*} \frac{\partial p}{\partial x} &+ \frac{\mathcal{F}_I^\phi}{U f_0}, \quad (5.4a) \\
\epsilon \left[\frac{Dv}{dt} + \frac{L}{r_*}(\delta vw + u^2 \tan\theta) \right] + u \frac{\sin\theta}{\sin\theta_0} &= \\
- \frac{r_0}{r_*} \frac{\partial p}{\partial y} &+ \frac{\mathcal{F}_I^\theta}{U f_0}, \quad (5.4b) \\
\epsilon\delta^2 \frac{Dw}{dt} - \epsilon\delta \frac{L}{r_*}(u^2 + v^2) - \delta u \frac{\cos\theta}{\sin\theta_0} &= \\
- \frac{\partial p}{\partial z} + \delta \frac{\mathcal{F}_I^r}{U f_0}, & \quad (5.4c) \\
\frac{\partial w}{\partial z} + 2\frac{D}{r_*} w - \frac{L}{r_*} v \tan\theta + + \frac{r_0}{r_*} \frac{\partial v}{\partial y} + \frac{r_0}{r_*} \frac{\cos\theta_0}{\cos\theta} \frac{\partial u}{\partial x} &= 0, \quad (5.4d)
\end{aligned}$$

with

$$\frac{D}{dt} = \frac{\partial}{\partial t} + u \frac{r_0}{r_*} \frac{\cos\theta_0}{\cos\theta} \frac{\partial}{\partial x} + \frac{r_0}{r_*} v \frac{\partial}{\partial y} + w \frac{\partial}{\partial z}.$$

We use the identity

$$\frac{r_*}{r_0} = 1 + \delta \frac{L}{r_0} z, \tag{5.5}$$

and locally around $\theta = \theta_0$ we use the expansions

$$\sin\theta = \sin\theta_0 + \frac{L}{r_0} y \cos\theta_0 + \mathcal{O}(\frac{L}{r_0})^2, \tag{5.6a}$$

$$\cos\theta = \cos\theta_0 - \frac{L}{r_0} y \sin\theta_0 + \mathcal{O}(\frac{L}{r_0})^2, \tag{5.6b}$$

$$\tan\theta = \tan\theta_0 + \frac{L}{r_0}\frac{y}{\cos^2\theta_0} + \mathcal{O}(\frac{L}{r_0}^2). \tag{5.6c}$$

In the equations above $\epsilon = U/(f_0 L)$ is the Rossby number and $\delta = D/L$ (cf. section 3.1.5).

In the β-plane approximation, the local variation of the Coriolis acceleration is taken into account while only terms $\mathcal{O}(L/r_0)$ are kept in (5.6). In the limit $\delta \to 0$, the equations then become (with $\beta = \beta_0 L^2/U$)

$$\epsilon\frac{Du}{dt} - v(1+\beta\epsilon y) = -\frac{\partial p}{\partial x} + \frac{\mathcal{F}_I^x}{U f_0}, \tag{5.7a}$$

$$\epsilon\frac{Dv}{dt} + u(1+\beta\epsilon y) = -\frac{\partial p}{\partial y} + \frac{\mathcal{F}_I^y}{U f_0}, \tag{5.7b}$$

$$\frac{\partial p}{\partial z} = 0, \tag{5.7c}$$

$$\frac{\partial w}{\partial z} + \frac{\partial v}{\partial y} + \frac{\partial u}{\partial x} = 0, \tag{5.7d}$$

with

$$\frac{D}{dt} = \frac{\partial}{\partial t} + u\frac{\partial}{\partial x} + v\frac{\partial}{\partial y} + w\frac{\partial}{\partial z}.$$

Note that for consistency of the asymptotic expansion, the $\beta\epsilon$ term should be smaller than unity.

In local coordinates, the mixing terms are represented as

$$\frac{\mathcal{F}_I^x}{U f_0} = \frac{A_H}{f_0 L^2}(\frac{\partial^2 u}{\partial x^2} + \frac{\partial^2 u}{\partial y^2}) + \frac{A_V}{f_0 D^2}\frac{\partial^2 u}{\partial z^2} = E_H\left[\frac{\partial^2 u}{\partial x^2} + \frac{\partial^2 u}{\partial y^2}\right] + E_V\frac{\partial^2 u}{\partial z^2}, \tag{5.8a}$$

$$\frac{\mathcal{F}_I^y}{U f_0} = \frac{A_H}{f_0 L^2}(\frac{\partial^2 v}{\partial x^2} + \frac{\partial^2 v}{\partial y^2}) + \frac{A_V}{f_0 D^2}\frac{\partial^2 v}{\partial z^2} = E_H\left[\frac{\partial^2 v}{\partial x^2} + \frac{\partial^2 v}{\partial y^2}\right] + E_V\frac{\partial^2 v}{\partial z^2}, \tag{5.8b}$$

where $E_H = A_H/(f_0 L^2)$ and $E_V = A_V/(f_0 D^2)$ are the horizontal and vertical Ekman numbers (cf. section 3.1.5).

5.2.2. Boundary conditions

The only boundary conditions which need further analysis are the conditions (3.37) at the ocean-atmosphere boundary. The mean interface position is at $z_* = 0$ and from (3.37d) and (5.1) it follows that at $z_* = h_*$ (or $z = h_*/D$):

$$-gh_*\rho_0 + \rho_0 U f_0 L\, p = 0, \tag{5.9}$$

where $p_{a*} = 0$ is chosen as reference level for the pressure.

To determine the scaling of the interface amplitude, we write $h_*/D = \mu\eta(\phi,\theta,t)$, where μ is, for the moment, still unknown. For small deviations h_*/D, it follows that at $z = 0$:

$$0 = -gD\rho_0\mu\eta + \rho_0 U f_0 L p_{|_{z=0}} + \cdots \rightarrow \mu\eta = \frac{U f_0 L}{gD} p, \tag{5.10}$$

This shows that $\mu = U f_0 L/(gD) = \epsilon F$, where $F = f_0^2 L^2/(gD)$ is the Froude number (cf. section 3.1.5). For midlatitude flows $F = \mathcal{O}(1)$, see Table 5.3 and hence $\epsilon F \ll 1$ justifying the expansion (5.10). As a consequence, we write $z = \epsilon F \eta(\phi,\theta,t)$ and the normal stress balance (3.37d) obtains the simple dimensionless form

$$p = \eta \tag{5.11}$$

With τ_0 as a characteristic value of the wind stress and hence $\boldsymbol{\tau_*} = \tau_0 \boldsymbol{\tau}$, the tangential stress boundary conditions become

$$\frac{\tau_0 D}{\rho_0 A_V U}\tau^\phi = \frac{\partial u}{\partial z} + \frac{A_H}{A_V}\frac{D}{r_*}\frac{\delta}{\cos\theta}\frac{\partial w}{\partial \phi}, \tag{5.12a}$$

$$\frac{\tau_0 D}{\rho_0 A_V U}\tau^\theta = \frac{\partial v}{\partial z} - \delta\frac{A_H}{A_V}\frac{D}{r_*}\frac{\partial w}{\partial \theta}. \tag{5.12b}$$

Although the values of the mixing coefficients A_H and A_V are not well known, the second terms in the right hand side are (with plausible estimates) much smaller than the first ones and they can be neglected in the limit $\delta \rightarrow 0$.

Finally, the kinematic condition in (3.37a) is written as

$$w = \epsilon F\left[\frac{\partial}{\partial t} + \frac{L}{r_*}\frac{u}{\cos\theta}\frac{\partial}{\partial\phi} + v\frac{\partial}{\partial\theta}\right]\eta, \tag{5.13}$$

and in local coordinates (5.2) with $L/r_0 \ll 1$ and $\delta \rightarrow 0$, this equation becomes

$$w = \epsilon F\left[\frac{\partial}{\partial t} + u\frac{\partial}{\partial x} + v\frac{\partial}{\partial y}\right]\eta, \tag{5.14}$$

with $\eta = \eta(x,y,t)$.

5.2.3. Model equations

To summarize the dimensionless equations: if we consider a basin with a bottom topography $z = -1 + h_b(x, y)$ and an ocean-atmosphere interface given by $z = \epsilon F \eta(x, y, t)$, the equations describing the constant density (barotropic) flow in the β-plane are (5.7-5.8), i.e.,

$$\epsilon \frac{Du}{dt} - v(1 + \beta\epsilon y) = -\frac{\partial p}{\partial x} + E_H \left[\frac{\partial^2 u}{\partial x^2} + \frac{\partial^2 u}{\partial y^2}\right] + E_V \frac{\partial^2 u}{\partial z^2}, \quad (5.15a)$$

$$\epsilon \frac{Dv}{dt} + u(1 + \beta\epsilon y) = -\frac{\partial p}{\partial y} + E_H \left[\frac{\partial^2 v}{\partial x^2} + \frac{\partial^2 v}{\partial y^2}\right] + E_V \frac{\partial^2 v}{\partial z^2}, \quad (5.15b)$$

$$0 = -\frac{\partial p}{\partial z} \quad (5.15c)$$

$$\frac{\partial w}{\partial z} + \frac{\partial v}{\partial y} + \frac{\partial u}{\partial x} = 0, \quad (5.15d)$$

with boundary conditions at the upper and layer boundaries given by

$$z = -1 + h_b(x, y) \quad : \quad \mathbf{n} \cdot \mathbf{u} = \mathbf{t}_1 \cdot \mathbf{u} = \mathbf{t}_2 \cdot \mathbf{u} = 0 \quad (5.16a)$$

$$z = \epsilon F \eta(x, y, t) \quad : \quad p = \eta \; ; \; w = \epsilon F \left(\frac{\partial \eta}{\partial t} + u\frac{\partial \eta}{\partial x} + v\frac{\partial \eta}{\partial y}\right),$$

$$: \quad \hat{\alpha}\tau^x = \frac{\partial u}{\partial z} \; ; \; \hat{\alpha}\tau^y = \frac{\partial v}{\partial z}, \quad (5.16b)$$

where (see Fig. 5.3)

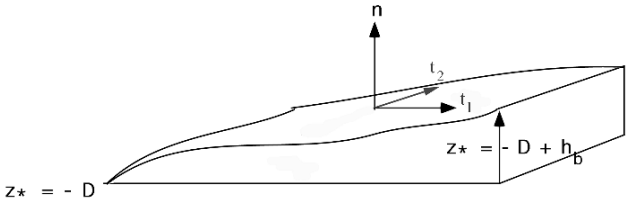

Figure 5.3. Sketch of the geometry of the bottom topography with normal $\mathbf{n}$ *and tangential vectors* t_1 *and* t_2.

$$\mathbf{t}_1 = \begin{pmatrix} 1 \\ 0 \\ \frac{\partial h_b}{\partial x} \end{pmatrix} \; ; \; \mathbf{t}_2 = \begin{pmatrix} 0 \\ 1 \\ \frac{\partial h_b}{\partial y} \end{pmatrix} \; ; \; \mathbf{n} = \begin{pmatrix} -\frac{\partial h_b}{\partial x} \\ -\frac{\partial h_b}{\partial y} \\ 1 \end{pmatrix}, \quad (5.17)$$

and the parameters are defined as

$$\epsilon = \frac{U}{f_0 L} \; ; \; \beta = \frac{\beta_0 L^2}{U} \; ; \; \hat{\alpha} = \frac{D\tau_0}{\rho_0 A_V U}$$

$$F = \frac{f_0^2 L^2}{gD} \; ; \; E_H = \frac{A_H}{f_0 L^2} \; ; \; E_V = \frac{A_V}{f_0 D^2}. \tag{5.18}$$

The barotropic midlatitude β-plane model

Under the shallow-water approximation $D/L \ll 1$, the β-plane approximation (linearized Coriolis parameter with $L/r_0 \ll 1$), the dimensional equations for a constant density flow (in a local Cartesian coordinate system) are

$$\begin{aligned}
\frac{Du_*}{dt_*} - v_*(f_0 + \beta_0 y_*) + \frac{1}{\rho_0}\frac{\partial p_*}{\partial x_*} &= A_H\left[\frac{\partial^2 u_*}{\partial x_*^2} + \frac{\partial^2 u_*}{\partial y_*^2}\right] + A_V \frac{\partial^2 u_*}{\partial z_*^2}, \\
\frac{Dv_*}{dt_*} + u_*(f_0 + \beta_0 y_*) + \frac{1}{\rho_0}\frac{\partial p_*}{\partial y_*} &= A_H\left[\frac{\partial^2 v_*}{\partial x_*^2} + \frac{\partial^2 v_*}{\partial y_*^2}\right] + A_V \frac{\partial^2 v_*}{\partial z_*^2}, \\
\frac{\partial p_*}{\partial z_*} &= -\rho_* g, \\
\frac{\partial u_*}{\partial x_*} + \frac{\partial v_*}{\partial y_*} + \frac{\partial w_*}{\partial z_*} &= 0,
\end{aligned}$$

with boundary conditions

$$\begin{aligned}
z_* = -D + h_{b*}(x_*, y_*) \quad &: \quad \mathbf{n}\cdot\mathbf{u}_* = \mathbf{t}_1\cdot\mathbf{u}_* = \mathbf{t}_2\cdot\mathbf{u}_* = 0, \\
z_* = h_* \quad &: \quad p_* = 0 \; ; \; w_* = \frac{\partial h_*}{\partial t} + u_*\frac{\partial h_*}{\partial x_*} + v_*\frac{\partial h_*}{\partial y_*} \\
&; \quad \frac{\tau_0}{\rho_0}\tau^x = A_V\frac{\partial u_*}{\partial z_*} \; ; \; \frac{\tau_0}{\rho_0}\tau^y = A_V\frac{\partial v_*}{\partial z_*}.
\end{aligned}$$

where $\mathbf{n}$ is the outward normal to the bottom and $\mathbf{t}_1$ and $\mathbf{t}_2$ are the two tangent vectors orthogonal to $\mathbf{n}$ (as defined in (5.17)).

For a typical basin at midlatitudes, typical values of the dimensionless parameters are given in Table 5.3. From this table, it can be seen that the product $\epsilon\beta$ is indeed small as is the product ϵF. In this case, the deviations of the ocean-atmosphere interface are small and we can take all boundary conditions at $z = 0$. In the remainder of this chapter, we will investigate stationary solutions of the equations (5.15-5.16).

5.3. Stationary solutions

From Table 5.3 it appears that the equations (5.15-5.16) contain a small parameter, the Rossby number ϵ. The solutions of the equations therefore look like those for $\epsilon = 0$, except maybe in relatively small areas in the flow field. To determine asymptotic solutions in ϵ, we have to determine the order of magnitude of the

Parameter	Value	Parameter	Value
L	1.0×10^6 m	τ_0	1.0×10^{-1} Pa
D	1.0×10^3 m	ρ_0	10^3 kgm^{-3}
f_0	1.0×10^{-4} s^{-1}	A_H	$10^2/10^4$ m^{2}s^{-1}
U	10^{-2} ms^{-1}	A_V	$10^{-4}/10^{-2}$ m^{2}s^{-1}
β_0	1.6×10^{-11} (ms)$^{-1}$	g	9.8 ms^{-2}
Parameter	Value	Parameter	Value
ϵ	1.0×10^{-4}	$\hat{\alpha}$	$10^3/10^5$
F	1.0	β	1.6×10^2
E_H	$10^{-6}/10^{-4}$	E_V	$10^{-6}/10^{-4}$

Table 5.1. Typical values of the dimensionless parameters in the barotropic midlatitude ocean model on the β-plane as given in (5.18).

other parameters with respect to ϵ. Table 5.3 indicates that $F = \mathcal{O}(1)$, $\beta = \mathcal{O}(1)$ and E_H and E_V are at most $\mathcal{O}(\epsilon)$.

We can already anticipate problems in the limit $\epsilon \to 0$, since higher order derivatives vanish in the equations (5.15-5.16) and we will not be able to satisfy all boundary conditions in this limit. In that case, we have to consider the boundary layers explicitly and a useful mathematical method for this is the method of 'inner' and 'outer' expansions. To illustrate this method, we first consider a relatively simple example.

▶

Example 5.1: Inner and outer expansions

Consider the following boundary value problem for $x \in [0, 1]$ and the function $y(x)$:

$$\epsilon y'' + y' = a, \tag{5.21a}$$

$$y(0) = 0; y(1) = 1, \tag{5.21b}$$

where $a \in R$, $\epsilon \ll 1$ and the primes indicate derivatives to x. This problem has an exact solution

$$y(x; \epsilon) = (1 - a)\frac{1 - e^{-x/\epsilon}}{1 - e^{-1/\epsilon}} + ax, \tag{5.22}$$

which is plotted for three different values of ϵ in Fig. 5.4. For small ϵ, a boundary layer appears near $x = 0$ that is needed to satisfy the boundary conditions.

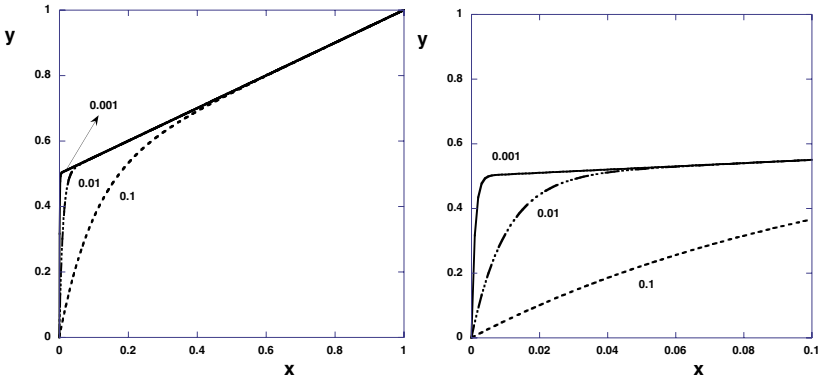

Figure 5.4. (a) Analytical solution $y(x;\epsilon)$ for three values of ϵ. (b) Magnification of the solution near $x = 0$.

The aim of the method of inner and outer expansions is to try to find an approximate solution for small values of ϵ in case we do not know the exact solution. First we expand

$$y(x;\epsilon) = y_0(x) + \epsilon y_1(x) + \epsilon^2 y_2(x) + \mathcal{O}(\epsilon^3), \tag{5.23}$$

where $\mathcal{O}$ indicates the higher order terms neglected. Substitution in (5.21) gives

$$\begin{aligned} \epsilon(y_0''(x) + \epsilon y_1''(x) + ...) + y_0'(x) + \epsilon y_1'(x) + \ldots &= a, && \text{(5.24a)} \\ y_0(0) + \epsilon y_1(0) + \ldots &= 0, && \text{(5.24b)} \\ y_0(1) + \epsilon y_1(1) + \ldots &= 1. && \text{(5.24c)} \end{aligned}$$

Now consider the $\mathcal{O}(1)$ system (the terms without ϵ); for arbitrary a, this provides the simple system

$$y_0'(x) = a, \tag{5.25a}$$

$$y_0(0) = 0, y_0(1) = 1. \tag{5.25b}$$

The general solution of (5.25), the outer solution $y_0(x) = ax + C_1$, can only satisfy one boundary condition; we choose $C_1 = 1 - a$ such that $y_0(1) = 1$. The resulting solution cannot satisfy the boundary condition at $x = 0$ and boundary layer behavior is expected.

Because the scaling of the thickness of the boundary layer with ϵ is a priori unknown we introduce a general boundary layer coordinate ζ through

$$\zeta = \frac{x}{\epsilon^p}. \tag{5.26}$$

Transformation of the problem (5.21) in the coordinate ζ for the function $\tilde{y}(\zeta;\epsilon)$ gives,

$$y'(x) = \frac{1}{\epsilon^p}\tilde{y}'(\zeta), \tag{5.27}$$

and the problem near $\zeta = x = 0$ becomes

$$\epsilon^{1-p}\tilde{y}'' + \tilde{y}' = \epsilon^p a, \tag{5.28a}$$

$$\tilde{y}(0) = 0, \tag{5.28b}$$

and the highest order derivative can only participate in a balance when $p = 1$.

We now proceed with the inner expansion

$$\tilde{y}(\zeta;\epsilon) = \tilde{y}_0(\zeta) + \epsilon\tilde{y}_1(\zeta) + \mathcal{O}(\epsilon^2), \tag{5.29}$$

from which the $\mathcal{O}(1)$ system becomes

$$\tilde{y}_0'' + \tilde{y}_0' = 0, \tag{5.30a}$$

$$\tilde{y}_0(0) = 0, \tag{5.30b}$$

with as a general solution (the inner solution)

$$\tilde{y}_0(\zeta) = C_2(e^{-\zeta} - 1). \tag{5.31}$$

The constant C_2 follows now from the fact that the inner solution must continuously connect to the outer solution $y_0(x)$ near $x = 0$. This results in the matching condition

$$\lim_{\zeta\to\infty} \tilde{y}_0(\zeta) = -C_2 = \lim_{x\to 0} y_0(x) = 1 - a, \tag{5.32}$$

with the result $C_2 = a - 1$. With the procedure, we find the $\mathcal{O}(1)$ asymptotic solution

$$y(x;\epsilon) = (1-a) + ax \quad \text{for } \epsilon \to 0, x > 0 \text{ fixed} \tag{5.33a}$$

$$y(\zeta;\epsilon) = (1-a)(1-e^{-\zeta}) \quad \text{for } \epsilon \to 0, \zeta = x/\epsilon > 0 \text{ fixed}. \tag{5.33b}$$

These solutions are plotted (together with the ones in Fig. 5.21b) in Fig. 5.5 and the boundary layer character of the solution is well represented by the asymptotic solutions.

◀

Additional Material

D: Asymptotic methods and their application to problems in Fluid Mechanics are well described in Kevorkian and Cole (1996). Another excellent reference on these methods is chapter 7 of Bender and Orszag (1999).

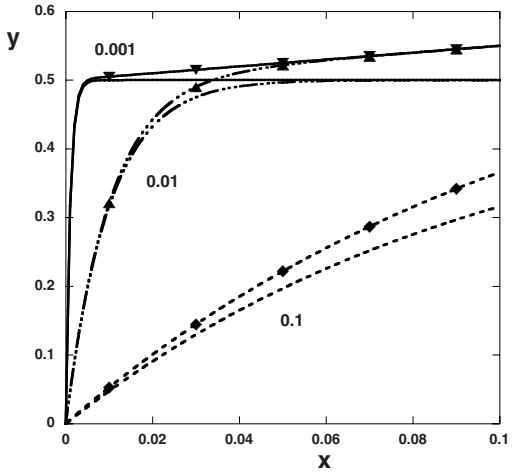

Figure 5.5. Asymptotic solutions (no label) and the analytic solutions (labelled), these are the same as in Fig. 5.4, for three different values of ϵ.

5.3.1. The geostrophic flow

We are now happy that we have the scaled dimensionless model equations (5.15-5.16) such that all dependent quantities are $\mathcal{O}(1)$ and the magnitude of the terms is measured by the dimensionless parameters in (5.18). To apply the method of inner and outer expansions to this model, we first formulate the outer expansion in ϵ as

$$\begin{pmatrix} \mathbf{v} \\ p \\ \eta \end{pmatrix} = \begin{pmatrix} \mathbf{v}^0 \\ p^0 \\ \eta^0 \end{pmatrix} + \epsilon \begin{pmatrix} \mathbf{v}^1 \\ p^1 \\ \eta^1 \end{pmatrix} + \dots \tag{5.34}$$

The outer flow (u^0, v^0, w^0, p^0) is determined by looking at the $\mathcal{O}(1)$ system of the equations (5.15). This system is

$$v^0 = \frac{\partial p^0}{\partial x}, \tag{5.35a}$$

$$u^0 = -\frac{\partial p^0}{\partial y}, \tag{5.35b}$$

$$0 = \frac{\partial p^0}{\partial z}, \tag{5.35c}$$

$$\frac{\partial w^0}{\partial z} + \frac{\partial v^0}{\partial y} + \frac{\partial u^0}{\partial x} = 0. \tag{5.35d}$$

Hence the flow outside boundary layers is in hydrostatic and geostrophic equilibrium.

Geostrophic and Hydrostatic balance

Under very small Rossby number ϵ, the dominant balances in the interior of a constant density flow are geostrophic (Coriolis and pressure gradient balance) and hydrostatic. The dimensional momentum equations are

$$\begin{aligned} f_0 v_* &= \frac{1}{\rho_0}\frac{\partial p_*}{\partial x_*}, \\ f_0 u_* &= -\frac{1}{\rho_0}\frac{\partial p_*}{\partial y_*}, \\ -\rho_0 g &= \frac{\partial p_*}{\partial z_*}. \end{aligned}$$

The velocities u_* and v_* are independent of z_* and the horizontal velocity field is divergence free, i.e., $\nabla_{H*} \cdot (u_*, v_*)^T = 0$. One can therefore introduce a streamfunction in the horizontal plane $\psi_* = p_*/(f_0\rho_0)$ ($\mathrm{m^2 s^{-1}}$) such that $\mathbf{u}_{H*} = \mathbf{e}_3 \wedge \nabla_* \psi_*$.

The dimensionless boundary conditions at $z = 0$ from (5.16b) become

$$p^0 = \eta^0 \; ; \; w^0 = 0, \tag{5.37a}$$

$$\hat{\alpha}\tau^x = \frac{\partial u^0}{\partial z} \; ; \; \hat{\alpha}\tau^y = \frac{\partial v^0}{\partial z} \; . \tag{5.37b}$$

From (5.35), it is easily derived that $\partial w^0/\partial z = 0$ and because of (5.37a), it follows that $w^0 \equiv 0$. According to (5.35c) both u^0 and v^0 must be independent of z. The geostrophic flow can therefore not satisfy the boundary conditions (5.37b) nor those at the bottom boundary.

The barotropic hydrostatic and geostrophic equations on the midlatitude β-plane are dynamically degenerate. If the pressure field is known, then the velocity field is determined. However, every pressure field provides such a consistent velocity field but the equations themselves provide no information to determine the pressure given the forcing and boundary conditions. The only information given is diagnostic: in time the pressure gradient field will balance the Coriolis acceleration. Hence, the ageostrophic effects (such as inertia, and mixing) and boundary conditions have to be considered to provide the evolution of the pressure field.

5.3.2. The bottom Ekman layer

For ease of understanding, we first consider the case of a flat bottom, with $h_b(x, y) \equiv 0$. The boundary layer variable ξ is introduced as

$$\xi = \frac{z+1}{\ell} \tag{5.38}$$

where ℓ is the scale of the (*a priori* unknown) thickness of the bottom boundary layer. The boundary layer (inner) solution is indicated by $(\tilde{\mathbf{v}}, \tilde{p})$ and it turns out to be convenient to use $\bar{E}_V = 2E_V$ and $\bar{E}_H = 2E_H$. The equations in the variables (x, y, ξ) become

$$\begin{aligned} \epsilon\frac{D\tilde{u}}{dt} - \tilde{v}(1+\beta\epsilon y) = \\ -\frac{\partial\tilde{p}}{\partial x} + \frac{\bar{E}_H}{2}\left[\frac{\partial^2\tilde{u}}{\partial x^2} + \frac{\partial^2\tilde{u}}{\partial y^2}\right] + \frac{\bar{E}_V}{2\ell^2}\frac{\partial^2\tilde{u}}{\partial\xi^2}, \end{aligned} \tag{5.39a}$$

$$\begin{aligned} \epsilon\frac{D\tilde{v}}{dt} + \tilde{u}(1+\beta\epsilon y) = \\ -\frac{\partial\tilde{p}}{\partial y} + \frac{\bar{E}_H}{2}\left[\frac{\partial^2\tilde{v}}{\partial x^2} + \frac{\partial^2\tilde{v}}{\partial y^2}\right] + \frac{\bar{E}_V}{2\ell^2}\frac{\partial^2\tilde{v}}{\partial\xi^2} \end{aligned} \tag{5.39b}$$

$$0 = \frac{\partial\tilde{p}}{\partial\xi}, \tag{5.39c}$$

$$\ell^{-1}\frac{\partial\tilde{w}}{\partial\xi} + \frac{\partial\tilde{v}}{\partial y} + \frac{\partial\tilde{u}}{\partial x} = 0, \tag{5.39d}$$

$$\frac{D}{dt} = \tilde{u}\frac{\partial}{\partial x} + \tilde{v}\frac{\partial}{\partial y} + \ell^{-1}\tilde{w}\frac{\partial}{\partial\xi}, \tag{5.39e}$$

and the boundary conditions become

$$\xi = 0: \ \tilde{u} = \tilde{v} = \tilde{w} = 0. \tag{5.40}$$

The condition that the vertical mixing of momentum should participate in the $\mathcal{O}$ balance leads to

$$\ell = \bar{E}_V^{1/2}. \tag{5.41}$$

From the continuity equation (5.39d) it follows that

$$\frac{\partial\tilde{w}}{\partial\xi} = -\bar{E}_V^{1/2}\left(\frac{\partial\tilde{v}}{\partial y} + \frac{\partial\tilde{u}}{\partial x}\right), \tag{5.42}$$

which indicates that $\tilde{w}$ must be rescaled. The relevant scale of the vertical velocity in the boundary layer is not UD/L but $\bar{E}_V^{1/2}UD/L = U\delta_E/L$, with

$\delta_E = \bar{E}_V^{1/2} D = \ell D$ the Ekman layer thickness. The inner expansion therefore becomes

$$(\tilde{u}, \tilde{v}, \tilde{w}, \tilde{p})^T = (\tilde{u}^0, \tilde{v}^0, \bar{E}_V^{1/2}\tilde{w}^0, \tilde{p}^0)^T + \epsilon(\tilde{u}^1, \tilde{v}^1, \bar{E}_V^{1/2}\tilde{w}^1, \tilde{p}^1)^T + \ldots \quad (5.43)$$

and the $\mathcal{O}(1)$ system of equations is

$$-\tilde{v}^0 = -\frac{\partial \tilde{p}^0}{\partial x} + \frac{1}{2}\frac{\partial^2 \tilde{u}^0}{\partial \xi^2}\,, \quad (5.44a)$$

$$\tilde{u}^0 = -\frac{\partial \tilde{p}^0}{\partial y} + \frac{1}{2}\frac{\partial^2 \tilde{v}^0}{\partial \xi^2}\,, \quad (5.44b)$$

$$0 = \frac{\partial \tilde{p}^0}{\partial \xi}\,, \quad (5.44c)$$

$$\frac{\partial \tilde{w}^0}{\partial \xi} = -\left[\frac{\partial \tilde{v}^0}{\partial y} + \frac{\partial \tilde{u}^0}{\partial x}\right]. \quad (5.44d)$$

From (5.44c) it follows that $\tilde{p}^0$ is independent of ξ and therefore also $\partial\tilde{p}^0/\partial x$ and $\partial\tilde{p}^0/\partial y$ in (5.44a-b). If (5.44b) is twice differentiated with respect to ξ and then (5.44a) is used, this leads to

$$\frac{\partial^4 \tilde{v}^0}{\partial \xi^4} + 4\,\tilde{v}^0 = 4\,\frac{\partial \tilde{p}^0}{\partial x}\,. \quad (5.45)$$

The characteristic polynomial of the homogeneous equation is $\lambda^4 + 4 = 0$, with solutions $\lambda = \pm(1 \pm i)$. Two of the roots $(1 + i)$ and $(1 - i)$ provide unbounded solutions for $\xi \to \infty$ and hence the general solution of (5.45) is

$$\tilde{v}^0(x, y, \xi) = A_1(x, y)e^{-\xi}(\cos\xi - i\sin\xi) + \\ +A_2(x, y)e^{-\xi}(\cos\xi + i\sin\xi) + \frac{\partial \tilde{p}^0}{\partial x}\,, \quad (5.46)$$

where the A_i are complex functions. From (5.44b) it follows that

$$\tilde{u}^0(x, y, \xi) = A_1(x, y)e^{-\xi}(i\cos\xi + \sin\xi) - \\ -A_2(x, y)e^{-\xi}(i\cos\xi - \sin\xi) - \frac{\partial \tilde{p}^0}{\partial y}\,. \quad (5.47)$$

The boundary conditions on $\xi = 0$ provide two conditions to solve for A_1 and A_2

$$A_1 = \frac{1}{2}\left[-i\frac{\partial \tilde{p}^0}{\partial y} - \frac{\partial \tilde{p}^0}{\partial x}\right]\;;\; A_2 = \frac{1}{2}\left[i\frac{\partial \tilde{p}^0}{\partial y} - \frac{\partial \tilde{p}^0}{\partial x}\right]. \quad (5.48)$$

Ex. 5.2

The outer and inner solution for the velocities are both expressed in the horizontal

pressure gradient, which is independent of the vertical coordinate since throughout the water column $\tilde{p}^0(x,y) = p^0(x,y)$. The matching principle for the pressure takes a simple form here.

The boundary layer (inner) solution becomes

$$\tilde{u}^0(x,y,\xi) = u^0(x,y)(1-e^{-\xi}\cos\xi) - v^0(x,y)e^{-\xi}\sin\xi, \quad (5.49a)$$
$$\tilde{v}^0(x,y,\xi) = v^0(x,y)(1-e^{-\xi}\cos\xi) + u^0(x,y)e^{-\xi}\sin\xi, \quad (5.49b)$$

and from (5.44d) we find for $\tilde{w}^0$

$$\tilde{w}^0(x,y,\xi) = \frac{\zeta^0}{2}(1-e^{-\xi}(\cos\xi+\sin\xi)), \quad (5.50)$$

where ζ^0 is the vertical component of the $\mathcal{O}(1)$ vorticity defined by

$$\zeta^0 = \frac{\partial v^0}{\partial x} - \frac{\partial u^0}{\partial y}. \quad (5.51)$$

▶

Example 5.2: Ekman bottom layer solution

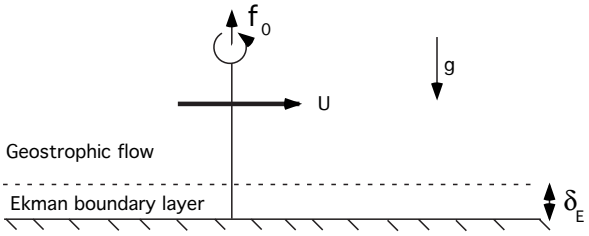

Figure 5.6. Sketch of the situation of the Ekman layer near a flat bottom below a parallel geostrophic flow with a constant zonal velocity U.

Consider as an example the situation in Fig. 5.6 where far from the bottom there is a geostrophic parallel flow with velocity field $\mathbf{v}_* = (U,0,0)^T$. From (5.49) with $u^0 = 1$ and $v^0 = 0$ it follows that

$$\tilde{u}^0(x,y,\xi) = 1 - e^{-\xi}\cos\xi, \quad (5.52a)$$
$$\tilde{v}^0(x,y,\xi) = e^{-\xi}\sin\xi, \quad (5.52b)$$
$$\tilde{w}^0 = 0. \quad (5.52c)$$

The velocity fields (5.52a-b) are plotted in Fig. 5.7a as a function of ξ. Both fields oscillate around the geostrophic field (which is obtained for $\xi \to \infty$) and

indeed satisfy the no-slip conditions at the bottom boundary ($\xi = 0$). In Fig. 5.7b, where v^0 is plotted versus u^0 with parameter ξ, part of the so-called Ekman spiral can be seen. As the momentum is transferred upwards from layer to layer in the liquid column, the velocity vector turns clockwise as a consequence of the Coriolis acceleration (see also Example 3.2). Near the bottom boundary, the flow is turned 45° counterclockwise with respect to the geostrophic flow, which also follows from

$$\lim_{\xi \to 0} \frac{\tilde{v}^0}{\tilde{u}^0} = 1. \tag{5.53}$$

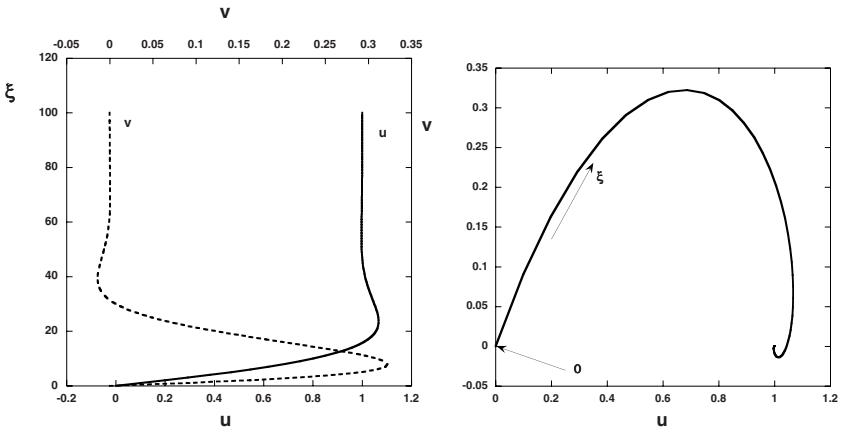

Figure 5.7. (a) Velocities $\tilde{u}^0$ and $\tilde{v}^0$ in (5.52) as a function of ξ. (b) Parameter plot of the velocity $\tilde{u}^0$ versus $\tilde{v}^0$ with ξ as parameter.

In dimensional quantities (note that $\xi = (z_*/D+1)/\bar{E}_V^{1/2}$ and $\delta_E = \bar{E}_V^{1/2} D = \sqrt{2A_V/f_0}$, i.e., $\xi = (z_* + D)/\delta_E$) we find

$$\tilde{u}_*^0(z_*) = U(1 - e^{-\frac{z_*+D}{\delta_E}} \cos \frac{z_* + D}{\delta_E}), \tag{5.54a}$$

$$\tilde{v}_*^0(z_*) = U e^{-\frac{z_*+D}{\delta_E}} \sin \frac{z_* + D}{\delta_E}, \tag{5.54b}$$

which shows that the boundary layer thickness is δ_E. With $\bar{E}_V$ in the range 10^{-7}-10^{-3} estimates of $\delta_E/D = 3 \times 10^{-4} - 3 \times 10^{-2}$ are obtained, and the Ekman layer thickness is in the range 1 – 100 m.

◀

Example 5.2 is also well suited to determining the transport of water in the Ekman layer. Consider a volume V with length L_x, width L_y and the height of the boundary layer (which is about δ_E) such as indicated in Fig. 5.8a. In the example, the boundary layer velocities are independent of x and y and the zonal ϕ_{x*} and meridional ϕ_{y*} volume transport (in $[m^3 s^{-1}]$) in the boundary layer are

$$\begin{pmatrix} \phi_{x*} \\ \phi_{y*} \end{pmatrix} = \begin{pmatrix} L_y \int_{-D}^{-D+\delta_E} (\tilde{u}_*^0 - U) dz_* \\ L_x \int_{-D}^{-D+\delta_E} \tilde{v}_*^0 dz_* \end{pmatrix}. \tag{5.55}$$

Evaluation of the integrals, with help of

$$\int_0^\infty e^{-\xi} \sin\xi \, d\xi = \int_0^\infty e^{-\xi} \cos\xi \, d\xi = \frac{1}{2}, \tag{5.56}$$

gives

$$\begin{pmatrix} \phi_{x*} \\ \phi_{y*} \end{pmatrix} = \frac{U\delta_E}{2} \begin{pmatrix} -L_y \\ L_x \end{pmatrix}. \tag{5.57}$$

The Ekman volume transport ($\mathbf{M}_{E*}$) per unit length perpendicular to the flow direction (in $\mathrm{m^2 s^{-1}}$) is

$$\mathbf{M}_{E*} = \begin{pmatrix} \frac{\phi_{x*}}{L_y} \\ \frac{\phi_{y*}}{L_x} \\ 0 \end{pmatrix} = \frac{\delta_E U}{2} \begin{pmatrix} -1 \\ 1 \\ 0 \end{pmatrix}. \tag{5.58}$$

There is a relation between this mass transport and the shear stress on the bottom boundary, $\mathbf{T}_{b*}$ ($\mathrm{Nm^{-2}}$) which is given (at $z_* = -D$) by

$$\mathbf{T}_{b*} = -\rho_0 A_V \begin{pmatrix} \frac{\partial \tilde{u}_*^0}{\partial z_*} \\ \frac{\partial \tilde{v}_*^0}{\partial z_*} \\ 0 \end{pmatrix} = \frac{\rho_0 A_V U}{\delta_E} \begin{pmatrix} -1 \\ -1 \\ 0 \end{pmatrix}, \tag{5.59}$$

and hence

$$\mathbf{M}_{E*} = \frac{\mathbf{T}_{b*} \wedge \mathbf{e}_3}{\rho_0 f_0}, \tag{5.60}$$

where $\mathbf{e}_3$ is the unit vector in vertical direction.

In the northern hemisphere, the total mass transport in the boundary layer is perpendicular and to the right of the bottom shear stress (Fig. 5.8b). The expression (5.60) shows that the result is independent of the representation of the vertical mixing of momentum. The result (5.60) is also general and can be deduced from the general form of the boundary layer solution (5.49).

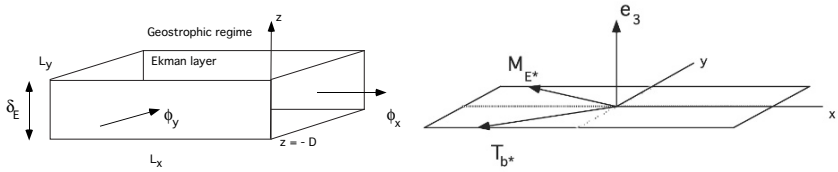

Figure 5.8. (a) Sketch to help determine the Ekman transport. (b) the bottom shear stress vector and the mass transport per unit length ($\mathbf{M}_{E*} in\ kgm^{-1}s^{-1}$).

5.3.3. The free surface Ekman layer

Similarly to the bottom Ekman layer formed due to the bottom friction, an Ekman layer forms at the surface through the wind-stress forcing. At the ocean-atmosphere interface, a boundary layer coordinate χ is introduced as

$$\chi \;=\; -\,\frac{z}{\ell}, \tag{5.61}$$

and similarly to the situation in the bottom boundary layer, it follows that $\ell \;=\; \bar{E}_V^{1/2}$. Hence, the vertical velocity is rescaled in the same way as in (5.43) and the equations for the $\mathcal{O}(1)$ boundary layer solution

$$(\hat{u},\hat{v},\hat{w},\hat{p})^T = (\hat{u}^0,\hat{v}^0,\bar{E}_V^{1/2}\hat{w}^0,\hat{p}^0)^T + \epsilon(\hat{u}^1,\hat{v}^1,\bar{E}_V^{1/2}\hat{w}^1,\hat{p}^1)^T + \cdots \tag{5.62}$$

become

$$-\hat{v}^0 \;=\; -\frac{\partial \hat{p}^{\,0}}{\partial x} + \frac{1}{2}\frac{\partial^2 \hat{u}^{\,0}}{\partial \chi^2}\,, \tag{5.63a}$$

$$\tilde{u}^0 \;=\; -\frac{\partial \hat{p}^{\,0}}{\partial y} + \frac{1}{2}\frac{\partial^2 \hat{v}^{\,0}}{\partial \chi^2}\,, \tag{5.63b}$$

$$0 \;=\; -\frac{\partial \hat{p}^{\,0}}{\partial \chi}\,, \tag{5.63c}$$

$$\frac{\partial \hat{w}^{\,0}}{\partial \chi} \;=\; \frac{\partial \hat{v}^{\,0}}{\partial y} + \frac{\partial \hat{u}^{\,0}}{\partial x}\,. \tag{5.63d}$$

In this case, the pressure is also homogeneous over the boundary layer and equal to that of the outer solution, $\hat{p}^0(x,y) = p^0(x,y)$.

The solution of (5.63) is again of the form of (5.46), but now the functions A_1 and A_2 are determined through the boundary conditions (5.16) at $z = 0$ (or $\chi = 0$), which become

$$\hat{\alpha}\tau^x \;=\; -\frac{\partial \hat{u}^{\,0}}{\partial \chi}\,\bar{E}_V^{-1/2}, \tag{5.64a}$$

$$\hat{\alpha}\tau^y = -\frac{\partial \hat{v}^0}{\partial \chi}\bar{E}_V^{-1/2}, \tag{5.64b}$$

where τ^x and τ^y are given functions of x and y. The final solution is

$$\hat{u}^0(x,y,\chi) - u^0(x,y) = \frac{\alpha e^{-\chi}}{2}([\tau^y - \tau^x]\sin\chi + (\tau^y + \tau^x)\cos\chi), \tag{5.65a}$$

$$\hat{v}^0(x,y,\chi) - v^0(x,y) = \frac{\alpha e^{-\chi}}{2}([\tau^y - \tau^x]\cos\chi - (\tau^y + \tau^x)\sin\chi), \tag{5.65b}$$

where $\alpha = \hat{\alpha}\bar{E}_V^{1/2} = 2\tau_0/(\rho_0 f_0 \delta_E U)$.

For the case $\tau^x = 1, \tau^y = 0$ and $\alpha = 1$, the difference velocity $\hat{\mathbf{u}}^0(x,y,\chi) - \mathbf{u}^0(x,y)$ is plotted in Fig. 5.9a. Both components of the difference velocity are the same at the ocean-atmosphere interface and approach zero for $\chi \to \infty$. In the parameter plot in Fig. 5.9b, we again observe the Ekman spiral; as momentum is transferred from the wind stress to the layers below, the velocity vector rotates clockwise.

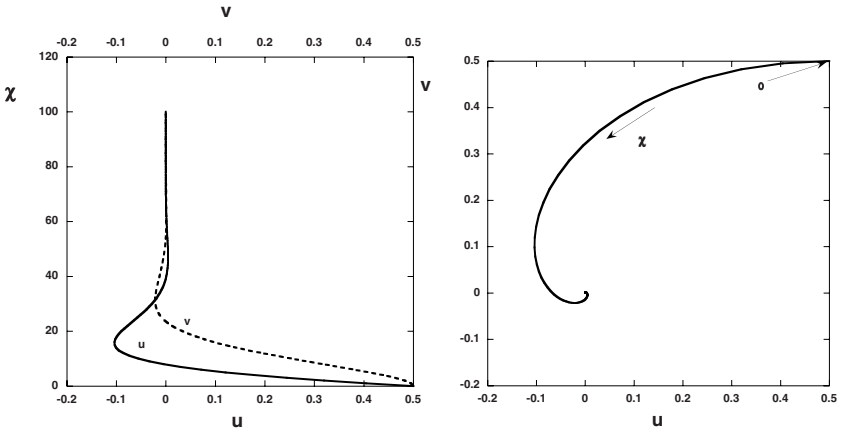

Figure 5.9. Ekman velocities as in (5.65) for the case $\tau^x = 1, \tau^y = 0$ and $\alpha = 1$. (a) Difference velocities $\hat{u}^0(x,y,\chi) - u^0(x,y)$ and $\hat{v}^0(x,y,\chi) - v^0(x,y)$ as a function of χ. (b) Parameterplot of the velocity $\hat{u}^0(x,y,\chi) - u^0(x,y)$ versus $\hat{v}^0(x,y,\chi) - v^0(x,y)$ with χ as parameter.

Ex. 5.3

If we indicate the dimensionless wind stress with the vector $\mathbf{T}$, then the velocity $\hat{\mathbf{u}}^0$ can be written as

$$\hat{\mathbf{u}}^0(x,y,\chi) = \mathbf{u}^0 + \frac{\alpha e^{-\chi}}{2}(\mathbf{T}(\cos\chi - \sin\chi) + (\mathbf{T} \wedge \mathbf{e}_3)(\cos\chi + \sin\chi)). \tag{5.66}$$

At the interface ($\chi = 0$) the relative velocity becomes

$$\hat{\mathbf{u}}^0 - \mathbf{u}^0 = \frac{\alpha}{2}(\mathbf{T} + \mathbf{T} \wedge \mathbf{e}_3), \tag{5.67}$$

and has rotated 45° with respect to $\mathbf{T}$. For the Ekman volume transport per unit length (in $\mathrm{m^2 s^{-1}}$), a similar expression can be derived as for the bottom Ekman layer. The result is

$$\mathbf{M}_{E*} = \frac{\mathbf{T}_* \wedge \mathbf{e}_3}{\rho_0 f_0}, \tag{5.68}$$

and hence the Ekman mass transport is always perpendicular and to the right of the wind stress (in the northern hemisphere).

▶

Example 5.3: Physics of the Ekman spiral

As we have seen in Fig. 5.7b and Fig. 5.9b, the velocity vector turns in the Ekman boundary layers. To explain this in more detail we again consider Example 5.2 where a simple case of the bottom boundary layer was presented. For the geostrophic flow far away from the boundary layer, we have from $\mathbf{a}_*^c = -2\boldsymbol{\Omega} \wedge \mathbf{v}_*$ and from geostrophic equilibrium

$$\mathbf{a}_*^c = \begin{pmatrix} f_0 v_* \\ -f_0 u_* \\ 0 \end{pmatrix} \; ; \; \frac{1}{\rho_0} \nabla_* p_* = \begin{pmatrix} f_0 v_* \\ -f_0 u_* \\ 0 \end{pmatrix},$$

where $f_0 = 2\Omega$ or in dimensionless form (with the flow in example 5.2)

$$\nabla p = \mathbf{a}^c = \begin{pmatrix} v^0 \\ -u^0 \\ 0 \end{pmatrix} = \begin{pmatrix} 0 \\ -1 \\ 0 \end{pmatrix}.$$

In Fig. 5.10a, $-\nabla p$ and the Coriolis acceleration $\mathbf{a}^c$ are sketched. The pressure decreases in the meridional direction; without the rotation of the Earth fluid would flow from high to low pressure. Through the Coriolis acceleration the flow is deflected to the right and in a final steady state, the pressure gradient exactly balances the Coriolis acceleration. In the boundary layer, the effect of friction becomes important and the velocity decreases, but the pressure gradient is the same as the one outside the boundary layer. Consider the situation in the boundary layer in Fig. 5.10b, where the velocity has decreased and hence the Coriolis acceleration also decreases. The velocity vector must turn counterclockwise such that the resulting frictional acceleration and the Coriolis acceleration are able to balance the pressure gradient.

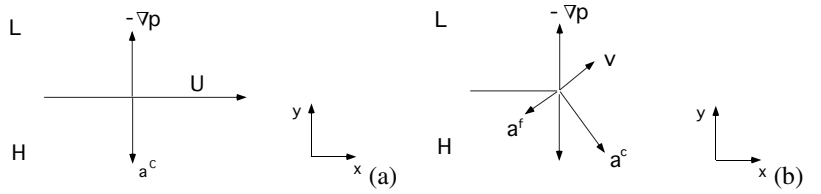

Figure 5.10. (a) Geostrophic balance outside the bottom Ekman boundary layer: the pressure gradient ∇p balances the Coriolis acceleration $\mathbf{a}^c$ (hence the sum of $\mathbf{a}^c$ and $-\nabla p$ is zero). (b) Balance in the Ekman boundary layer, where the sum of the Coriolis acceleration and the frictional acceleration $\mathbf{a}^f$ compensate the pressure gradient.

◄

5.3.4. Continuity of the vertical velocity

The results so far of the outer geostrophic flow and the inner Ekman boundary layer flows are sketched in Fig. 5.11. Through the Ekman boundary layers, the total flow satisfies the boundary conditions at the top and bottom, and the horizontal velocities and the pressure are continuous over the vertical. There is one variable that we need to consider: the vertical velocity. As deduced earlier, the

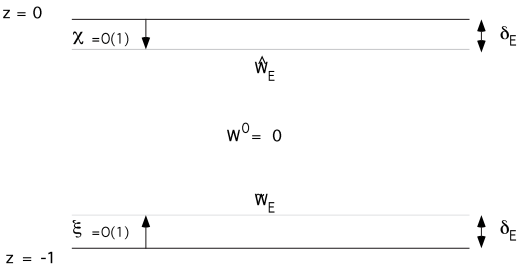

Figure 5.11. Sketch to clarify the matching of the vertical velocity over the top and bottom boundaries of the Ekman layer and the geostrophic domain.

outer vertical velocity $w^0 \equiv 0$. Equation (5.50) indicates that the $\mathcal{O}(1)$ vorticity (ζ^0) in the geostrophic domain generates, through the bottom friction (for a flat bottom) a vertical velocity at the top of the boundary layer ($\xi \to \infty$) according to

$$\lim_{\xi\to\infty} \tilde{w}(x,y,\xi) = \lim_{\xi\to\infty} \bar{E}_V^{1/2}\tilde{w}^0(x,y,\xi) = \frac{1}{2}\bar{E}_V^{1/2}\zeta^0. \tag{5.69}$$

We now consider the case of the presence of bottom topography. If $h_b(x,y) = \mathcal{O}(1)$ we see that the $\mathcal{O}(1)$ geostrophic problem no longer gives $w^0 \equiv 0$. The asymptotic methodology is no longer directly applicable and numerical methods need to be used. However, in the case $h_b(x,y) = \mathcal{O}(\epsilon)$ asymptotic methods can still be used. In this case, let

$$h_b(x,y) = \epsilon\eta_b(x,y). \tag{5.70}$$

The boundary conditions at $z = -1 + \epsilon\eta_b(x,y)$ are that both normal and tangential components of the velocity are zero. The tangent vectors and normal at a particular point is spanned by

$$\mathbf{t}_1 = \begin{pmatrix} 1 \\ 0 \\ \epsilon\eta_{b,x} \end{pmatrix} \; ; \; \mathbf{t}_2 = \begin{pmatrix} 0 \\ 1 \\ \epsilon\eta_{b,y} \end{pmatrix} \; ; \; \mathbf{n} = \begin{pmatrix} -\epsilon\eta_{b,x} \\ -\epsilon\eta_{b,y} \\ 1 \end{pmatrix}, \tag{5.71}$$

where $\eta_{b,x} = \partial\eta_b/\partial x$ (see Fig. 5.3). The conditions

$$\mathbf{v}\cdot\mathbf{t}_1 = \mathbf{v}\cdot\mathbf{t}_2 = \mathbf{v}\cdot\mathbf{n} = 0, \tag{5.72}$$

give

$$u + \epsilon\frac{\partial\eta_b}{\partial x}w = 0, \tag{5.73a}$$

$$v + \epsilon\frac{\partial\eta_b}{\partial y}w = 0, \tag{5.73b}$$

$$w - \epsilon(u\frac{\partial\eta_b}{\partial x} + v\frac{\partial\eta_b}{\partial y}) = 0. \tag{5.73c}$$

The vertical velocities w are now $\mathcal{O}(\epsilon)$ and

$$w - \epsilon(u^0\frac{\partial\eta_b}{\partial x} + v^0\frac{\partial\eta_b}{\partial y}) = 0. \tag{5.74}$$

If (5.44d) is integrated from $\xi = 0$ to $\xi = \infty$, we find that the correction due to the bottom topography leads to

$$\lim_{\xi\to\infty}\tilde{w}(x,y,\xi) = \epsilon\,\mathbf{u}^0\cdot\nabla\eta_b + \frac{1}{2}\bar{E}_V^{1/2}\zeta^0. \tag{5.75}$$

where $\mathbf{u}^0 = (u^0, v^0)$. This result can be seen as that for the flat bottom plus a part due to the kinematic boundary condition ($\mathbf{v}\cdot\mathbf{n} = 0$).

The vertical velocity at the lower boundary of the free surface Ekman layer follows from vertical integration of the continuity equation (5.63d) with the result

$$\lim_{\chi\to\infty}\hat{w}(x,y,\chi) = \bar{E}_V^{1/2}\hat{w}^0(x,y,0) + \frac{\alpha}{2}\bar{E}_V^{1/2}\nabla.(\mathbf{T}\wedge\mathbf{e}_3), \tag{5.76}$$

where $\hat{w}^0(x, y, 0)$ is the value of the vertical velocity at the free surface. We obtain this value from (5.16b) which in variables (x, y, z) (note that the boundary condition can be taken on $\chi = 0$) becomes

$$w = w^0 + \epsilon w^1 + \ldots = \epsilon F \left[\frac{D\eta}{dt}^0 + \epsilon \frac{D\eta}{dt}^1 + \ldots \right], \tag{5.77}$$

and (5.76) modifies as

$$\lim_{\chi \to \infty} \hat{w}(x, y, \chi) = \epsilon F \mathbf{u}^0 . \nabla \eta^0 + \frac{\alpha}{2} \bar{E}_V^{1/2} \nabla . (\mathbf{T} \wedge \mathbf{e}_3). \tag{5.78}$$

The relations (5.75) and (5.78) show an essential problem. It does not appear possible to match the $\mathcal{O}(1)$ boundary layer solution for the vertical velocity to the $\mathcal{O}(1)$ geostrophic solution. This can only be done when both the limit (5.75) and (5.78) become zero and as we have seen, one can then no longer satisfy the boundary conditions. The solution of this problem is to match the $\mathcal{O}(1)$ boundary layer solution with the $\mathcal{O}(\epsilon)$ geostrophic solution. This leads to the barotropic quasi-geostrophic theory in the next section.

To perform this matching, we need to fix the relative amplitude of ϵ and E_V; so far we have only mentioned that E_V was at most $\mathcal{O}(\epsilon)$. The equations (5.75) and (5.78) show that if $E_V^{1/2} \ll \epsilon$, only kinematic effects are included. Because the flow must be driven by the wind stress, we have to take the Ekman terms into account and hence we define the parameter r as

$$r = \frac{\bar{E}_V^{1/2}}{\epsilon}. \tag{5.79}$$

If $r = \mathcal{O}(1)$, then both terms in (5.75) and (5.78) are of the same order of magnitude. If we take the limit $r \to 0$, then there are only kinematic effects.

▶

Example 5.4: Ekman pumping and suction

Consider a situation where the dimensionless wind stress $\mathbf{T}$ is given by

$$\mathbf{T} = \begin{pmatrix} \gamma y \\ 0 \\ 0 \end{pmatrix}, \tag{5.80}$$

with $\gamma > 0$ and $y \in [-1, 1]$. It follows that $\nabla \cdot (\mathbf{e}_3 \wedge \mathbf{T}) = \gamma$ which is constant. The Ekman boundary layer velocity field follows from (5.65) as

$$u_E(x, y, \chi) \quad = \quad \hat{u}^0(x, y, \chi) - u^0(x, y) =$$

$$= \frac{\gamma y \alpha}{2} e^{-\chi}(-\sin\chi + \cos\chi), \tag{5.81a}$$

$$v_E(x,y,\chi) = \hat{v}^0(x,y,\chi) - v^0(x,y) =$$
$$= \frac{\gamma y \alpha}{2} e^{-\chi}(-\cos\chi + \sin\chi). \tag{5.81b}$$

At the surface $\chi = 0$, we have

$$\begin{pmatrix} u_E \\ v_E \end{pmatrix} = \frac{\gamma y \alpha}{2} \begin{pmatrix} 1 \\ -1 \end{pmatrix}, \tag{5.82}$$

while the total Ekman volume transport M_{E*} per unit length is

$$M_{E*} = \gamma \frac{U \delta_E \alpha}{2} \begin{pmatrix} 0 \\ -y \end{pmatrix} \tag{5.83}$$

The direction of M_{E*} and the surface velocities are plotted in Fig. 5.12a and the effect of vertical friction is to cause horizontal convergencies. This can explicitly be seen from

$$\nabla . \begin{pmatrix} u_E \\ v_E \end{pmatrix} = -\gamma \frac{\alpha}{2} e^{-\chi}(\cos\chi + \sin\chi), \tag{5.84}$$

which integrated over the boundary layer is equal to $-\alpha\gamma/2$. From (5.78), the vertical velocity is calculated as

$$w^1(x,y,0) = F\mathbf{u}^0.\nabla\eta^0 - \alpha r\gamma. \tag{5.85}$$

The second term on the right hand side is caused by the convergence of water. In the limit $F \to 0$, it follows that $w^1(x,y,0) < 0$ (in the northern hemisphere, it follows that $\alpha > 0$), and hence water is pumped from the boundary layer into the geostrophic flow domain. For $\gamma < 0$, the opposite happens: there is a divergence in the Ekman layer and mass is sucked into the Ekman boundary layer (Fig. 5.12b).

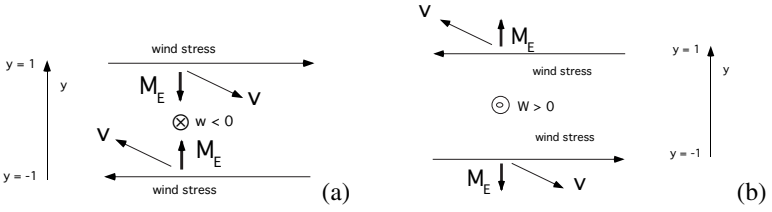

Figure 5.12. Example of Ekman (a) pumping ($\gamma > 0$) and (b) suction ($\gamma < 0$) caused by (a) a convergence and (b) a divergence of mass in the surface Ekman layer.

Surface Ekman layer

For a given wind stress $\mathbf{T}_* = (\tau_*^x, \tau_*^y, 0)^T$ there exists an Ekman boundary layer of thickness $\delta_E = D\sqrt{\bar{E}_V} = \sqrt{2A_V/f_0}$. At the ocean-atmosphere surface, the dimensional horizontal Ekman volume transport (in $\mathrm{m^3 s^{-1}}$) is

$$\phi_{x*} = \frac{\tau_*^y L_y}{\rho_0 f_0} \; ; \; \phi_{y*} = -\frac{\tau_*^x L_x}{\rho_0 f_0},$$

where L_x and L_y are the dimensions on the layer in x and y direction. The magnitude of the Ekman upwelling velocity is given by $w_* = \bar{E}_V^{1/2}\,(UD/L)\,(\alpha/2)\bar{E}_V^{1/2}\nabla\cdot(\mathbf{T}\wedge\mathbf{e}_3)$ and in dimensional quantities this becomes

$$w_* = \frac{1}{\rho_0 f_0}\left[\frac{\partial \tau_*^y}{\partial x_*} - \frac{\partial \tau_*^x}{\partial y_*}\right] = \frac{1}{\rho_0 f_0}\nabla\cdot(\mathbf{T}_*\wedge\mathbf{e_3})$$

The upwelling velocity thus scales with $\tau_0/(\rho_0 f_0 L)$ and is about 10^{-6} $\mathrm{ms^{-1}}$ (which is 10 cm/day) for a flow with $L = 1000$ km and $\tau_0 = 0.1$ Pa at 45°N.

In Fig. 5.13, the annual global wind-induced upwelling is plotted from data of the wind-stress field. There is downwelling in the midlatitude subtropical gyres and upwelling in the midlatitude subpolar gyres. There is also pronounced upwelling along the equator (we will explain this in chapter 11) and along some of the coastal boundaries.

◀

Additional Material

B: Having understood section 5.2 it is recommended to read chapter 4, sections 4.1 to 4.3, 4.5 to 4.8 and 4.10 to 4.11 in Pedlosky (1987). An alternative threatment of the Ekman layer can be found in chapter 5 of Cushman-Roisin (1994).

D: In section 4.9 of Pedlosky (1987) and section 5.5 of Cushman-Roisin (1994), the extension of the Ekman layer theory in the presence of a sloping boundary is described.

5.4. The barotropic vorticity equation

The analysis in the previous section shows that small deviations from geostrophic flow (in the flow outside the Ekman boundary layers) are necessary to solve the degeneracy problem of the geostrophic equations (cf. section 5.2.1). The $\mathcal{O}(\epsilon)$ equations (5.15) become

$$u^0\frac{\partial u^0}{\partial x}+v^0\frac{\partial u^0}{\partial y}-v^1-\beta y v^0 = -\frac{\partial p^1}{\partial x}+Re^{-1}\nabla_H^2 u^0, \quad (5.86a)$$

$$u^0\frac{\partial v^0}{\partial x}+v^0\frac{\partial v^0}{\partial y}+u^1+\beta y u^0 = -\frac{\partial p^1}{\partial y}+Re^{-1}\nabla_H^2 v^0, \quad (5.86b)$$

$$0 = \frac{\partial p^1}{\partial z}, \quad (5.86c)$$

$$\frac{\partial u^1}{\partial x}+\frac{\partial v^1}{\partial y}+\frac{\partial w^1}{\partial z} = 0, \quad (5.86d)$$

where $E_H = 2\epsilon Re^{-1}$ is assumed to be $\mathcal{O}(\epsilon)$ at most and $Re = UL/A_H$ is the Reynolds number. In general, Re^{-1} is a very small parameter but neglecting the term will lead to problems in satisfying lateral boundary conditions.

If the $\mathcal{O}(\epsilon)$ pressure p^1 is eliminated from (5.86a,b), we find

$$\frac{D\zeta^0}{dt}+\beta v^0 = u^0\frac{\partial\zeta^0}{\partial x}+v^0\frac{\partial\zeta^0}{\partial y}+\beta v^0 =$$
$$-(\frac{\partial u^1}{\partial x}+\frac{\partial v^1}{\partial y})+Re^{-1}\nabla^2\zeta^0 = \frac{\partial w^1}{\partial z}+Re^{-1}\nabla^2\zeta^0, \quad (5.87)$$

where $D/dt = u^0\partial/\partial x + v^0\partial/\partial y$. Because u^0 and v^0 and hence ζ^0 are independent of z we can integrate (5.87) over the layer thickness (from $z=-1$ to $z=0$) and find

$$u^0\frac{\partial\zeta^0}{\partial x}+v^0\frac{\partial\zeta^0}{\partial y}+\beta v^0 = w^1_{|_{z=0}}-w^1_{|_{z=-1}}+Re^{-1}\nabla^2\zeta^0. \quad (5.88)$$

Ex. 5.4

To close this equation for ζ^0, we need to express w^1 in terms of the boundary layer solutions. Using (5.75) and (5.78), i.e.,

$$w^1(x,y,-1) = \mathbf{u}^0\cdot\nabla\,\eta_b+\frac{r}{2}\zeta^0, \quad (5.89a)$$

$$w^1(x,y,0) = F\mathbf{u}^0\cdot\nabla\eta^0+\frac{\alpha r}{2}\nabla\cdot(\mathbf{T}\wedge\mathbf{e}_3), \quad (5.89b)$$

(5.88) becomes the barotropic potential vorticity equation given by

$$\frac{\partial\zeta^0-F\eta^0+\eta_b}{\partial t}+\beta v^0 = \frac{\alpha r}{2}\nabla.(\mathbf{T}\wedge\mathbf{e}_3)-\frac{r\zeta^0}{2}+\frac{1}{Re}\nabla^2\zeta^0, \quad (5.90a)$$

$$\zeta^0 = \frac{\partial v^0}{\partial x} - \frac{\partial u^0}{\partial y}, \tag{5.90b}$$

$$v^0 = \frac{\partial p^0}{\partial x} \quad ; \quad u^0 = -\frac{\partial p^0}{\partial y}, \tag{5.90c}$$

$$\eta^0 = p^0. \tag{5.90d}$$

Equation (5.90) is a scalar equation for the pressure $p^0(x, y)$. It is remarkable that the $\mathcal{O}(\epsilon)$ balance in the flow outside the Ekman boundary layers eventually determines the $\mathcal{O}(1)$ pressure field and hence the $\mathcal{O}(1)$ geostrophic flow field. The lateral boundary conditions for p^0 will be considered in later sections.

As p^0 is a streamfunction, often the dimensionless geostrophic streamfunction $\psi = p^0$ is used; the scalar equation for ψ then becomes

$$\begin{aligned}(\frac{\partial \psi}{\partial x}\frac{\partial}{\partial y} &- \frac{\partial \psi}{\partial y}\frac{\partial}{\partial x})(\nabla^2\psi - F\psi + \eta_b) + \beta\frac{\partial \psi}{\partial x} \\ &= \frac{\alpha r}{2}\nabla\cdot(\mathbf{T}\wedge\mathbf{e}_3) - \frac{r}{2}\nabla^2\psi + Re^{-1}\nabla^4\psi. \end{aligned} \tag{5.91}$$

The barotropic vorticity equation

This equation forms the basis for the description and explanation of the western intensification of boundary currents as we will see in the next chapter. It results from an asymptotic approximation of the solutions of the barotropic β-plane model for a constant density ocean in the limit of small Rossby number ϵ. The dominant balances in the flow interior are hydrostatic and geostrophic and the evolution of the pressure field is determined from a balance of the ageostrophic effects. Its steady dimensional form (with $\psi_* = p_*/(\rho_0 f_0)$ in $\mathrm{m^2 s^{-1}}$) is

$$\begin{aligned}(\frac{\partial \psi_*}{\partial x_*}\frac{\partial}{\partial y_*} &- \frac{\partial \psi_*}{\partial y_*}\frac{\partial}{\partial x_*})(\nabla_*^2\psi_* - \lambda_0\psi_* + \frac{f_0}{D}h_{b*}) + \beta_0\frac{\partial \psi_*}{\partial x} \\ &= \frac{1}{\rho_0 D}\nabla\cdot(\mathbf{T}_*\wedge\mathbf{e}_3) - \epsilon_0\nabla_*^2\psi_* + A_H\nabla_*^4\psi_*, \\ &= \frac{f_0}{D}w_{E*} - \epsilon_0\nabla_*^2\psi_* + A_H\nabla_*^4\psi_*, \end{aligned}$$

where $\epsilon_0 = f_0\delta_E/D$ ($\mathrm{s^{-1}}$) is a dimensional damping coefficient and $\lambda_0 = f_0^2/(gD) = 1/R_D^2$, where R_D is the external Rossby radius of deformation as defined in section 3.1.

The first two terms on the right hand side of (5.91) represent vorticity generation through the wind stress ($(\alpha r/2)\nabla.(\mathbf{T}\wedge\mathbf{e}_3)$) and the bottom friction ($-(r/2)\nabla^2\psi$ in (5.91)), both through Ekman pumping/suction and subsequent

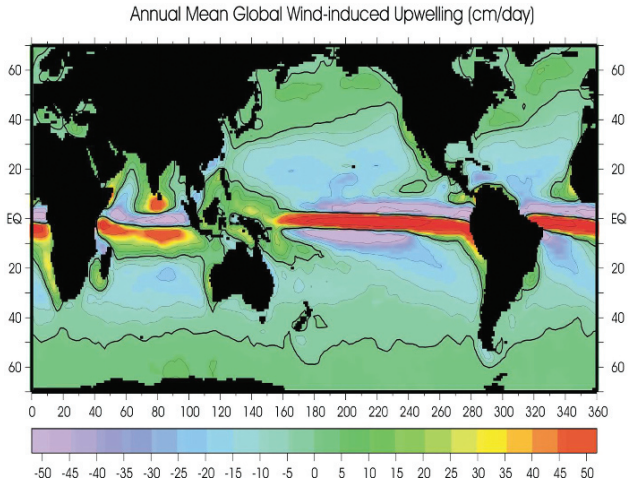

Figure 5.13. Annual mean wind-induced Ekman upwelling (in cm/day) over the global ocean (from http://www.ocgy.ubc.ca/projects/clim.pred/Upwell/index.html).

vortex stretching. The third term is the vorticity production due to lateral friction. To investigate the physical interpretation of the left hand side of (5.91), we write it, with $v^0 = Dy/dt$, as

$$\frac{D}{dt}\left[\zeta^0 - F\eta^0 + \eta_b + \beta y\right] = \frac{D\Pi}{dt}. \tag{5.92}$$

If $D\Pi/dt = 0$ then Π is constant along streamlines.

Now consider the dimensional potential vorticity Π_* on the β-plane defined by

$$\Pi_* = \frac{\zeta_* + f}{H_*}, \tag{5.93}$$

where H_* is the total thickness of the water column, $f = f_0 + \beta_0 y_*$ and ζ_* is the vertical component of the relative vorticity. For the case considered above with small amplitude topography, we have

$$H_* = h_* - (-D + h_{b*}) = D + h_* - h_{b*}. \tag{5.94}$$

In dimensionless quantities, this becomes

$$\frac{D}{f_0}\Pi_* = (1 + \epsilon F\eta - \epsilon\eta_b)^{-1}(\epsilon\zeta + 1 + \beta\epsilon y). \tag{5.95}$$

Expansion of the denominator in ϵ gives

$$(1 + \epsilon(F\eta - \eta_b))^{-1} = 1 - \epsilon(F\eta - \eta_b) + \mathcal{O}(\epsilon^2), \tag{5.96}$$

and eventually

$$\frac{D}{f_0}\Pi_* = 1 + \epsilon(\zeta + \beta y - F\eta + \eta_b) + \mathcal{O}(\epsilon^2) = 1 + \epsilon\Pi + \mathcal{O}(\epsilon^2). \tag{5.97}$$

The relation $D\Pi/dt = 0$ is thus a representation of conservation of potential vorticity and the dimensional potential vorticity

$$\Pi_* = \nabla_*^2\psi_* - \lambda_0\psi_* + \frac{f_0}{D}h_{b*} \tag{5.98}$$

is often referred to as the quasi-geostrophic potential vorticity.

Summary

- At the ocean-atmosphere surface, the wind-stress forcing leads to divergences or convergencies in the surface mass transport. This occurs in Ekman layers of thickness

$$\delta_E = \sqrt{\frac{2A_V}{f}}$$

  where A_V is the vertical viscosity.

- The dimensional horizontal Ekman volume transport (in $\mathrm{m^2 s^{-1}}$), i.e., per unit length perpendicular to the transport direction is

$$M^x_{E*} = \frac{\tau^y_*}{\rho_0 f_0} \; ; \; M^y_{E*} = -\frac{\tau^x_*}{\rho_0 f_0},$$

- This surface mass transport leads to Ekman pumping or suction with a vertical velocity given by

$$w_{E*} = \frac{1}{\rho_0 f_0}\left[\frac{\partial \tau^y_*}{\partial x_*} - \frac{\partial \tau^x_*}{\partial y_*}\right]$$

- Near the ocean bottom, similar features occur and the transports depend on the bottom stress (instead of on the surface wind stress).

- In both Ekman layers, the velocity vector undergoes a spiralling behavior because the pressure gradient vector is fixed (constant density case) and a balance between pressure gradient, friction and Coriolis acceleration has to be maintained.

- The quasi-geostrophic potential vorticity

$$\Pi_* = \nabla^2_* \psi_* - \lambda_0 \psi_* + \frac{f_0}{D} h_{b*}$$

  is a conserved quantity when (i) bottom friction is negligible, (ii) lateral friction is negligible and (iii) the Ekman pumping velocity $w_{E*} = 0$.

5.5. Exercises on chapter 5

(5.1) *Gulf Stream*

In this exercise, we consider the dominant balances in the horizontal momentum equations for the Gulf Stream. Characteristic length scales for the Gulf Stream are $L_x = 50$ km and $L_y = 500$ km. The characteristic velocity in east-west direction is about $U = 0.1$ m/s and that in north-south direction $V = 1.0$ m/s. Assume furthermore that the Gulf Stream is a steady current and take $A_H = 10^5$ m^{2}s^{-1} and $A_V = 0.1$ m^{2}s^{-1}.

a. Show that in the meridional direction the Gulf Stream is not quite in geostrophic balance. Which other terms contribute to this momentum balance?

b. Show that the zonal momentum equation is dominantly geostrophic.

(5.2) *An alternative approach to the bottom Ekman layer*

Consider an ocean with water of constant density ρ above a flat bottom (at $z_* = 0$). The horizontal velocities outside the Ekman layer (where the flow is hydrostatic and geostrophic) are indicated by (u_{g*}, v_{g*}). The total velocity can be written as

$$u_* = u_{g*} + u_{E*}; \qquad v_* = v_{g*} + v_{E*}$$

where u_{E*} en v_{E*} are the horizontal Ekman velocities.

a. Show that the Ekman velocities can be determined from

$$-f_0\, v_{E*} = A_V \frac{\partial^2 u_{E*}}{\partial z^2}$$

$$f_0\, u_{E*} = A_V \frac{\partial^2 v_{E*}}{\partial z^2}$$

b. Determine the Ekman transport $\boldsymbol{M}_{E*} = (M^x_{E*}, M^y_{E*})$ through vertical integration and show that the direction of this transport is perpendicular to the bottom shear stress.

c. Show that for $v_{g*} = 0$ and constant u_{g*}, the solution of the Ekman layer velocities is given by

$$u_{E*} = -u_{g*} e^{-z_*/\delta_E} \cos \frac{z_*}{\delta_E}$$

$$v_{E*} = u_{g*} e^{-z_*/\delta_E} \sin \frac{z_*}{\delta_E}$$

where $\delta_E = \sqrt{\frac{2A_V}{f_0}}$ is the bottom Ekman layer thickness.

d. Check that the total velocity field (u, v) satisfies the boundary conditions

$$\begin{aligned} (z = 0): \quad & u_* = v_* = 0 \\ (z \gg 1): \quad & u_* = u_{g*}; \quad v_* = 0 \end{aligned}$$

and make a sketch of the total velocity field in the Ekman layer.

(5.3) *Ekman layer at the ocean-atmosphere interface*

Suppose we have a basin of dimensions $1000 \times 1000 \times 1$ km at 45°N (domain $[0, 1] \times [-1, 1] \times [-1, 0]$) with the flow forced by the wind stress $\tau_*^x = \tau_0 y, \tau_*^y = 0$; take $\tau_0 = 10^{-1}\ Pa$ and choose $U = 10^{-2}$ ms^{-1}.

a. Write a computer program that calculates the dimensionless Ekman velocities for this wind stress field for different values of A_V. Make a plot of the velocitities $(\hat{u}^0, \hat{v}^0)$ versus $\chi \in [0, 10]$ for three different values of $A_V = 0.1, 0.01$ and 0.0001 m^{2}s^{-1}.

b. Calculate for each of the values of A_V the dimensional Ekman transport $\mathbf{M}_{E*}$.

(5.4) *Ekman layer at an eastern boundary*

Ekman layers can also occur near continental boundaries. Consider a flow near an east coast $x = x_E$ driven by wind stress $\tau^y = \tau_0$, $\tau^x = 0$, where τ_0 is constant. Bottom friction can be neglected.

a. Write down the zonal momentum equations in this case (integrated over depth) and determine the Ekman pumping at the surface.

b. Give a physical explanation of the upwelling velocity in the northern hemisphere, in case $\tau_0 < 0$.

c. Introduce a coordinate $\lambda = (x_E - x)/\delta$ and derive that the dominant zonal momentum balance is given by

$$u + (\frac{A_H}{f})^2 u_{xxxx} \approx 0$$

d. Determine the lateral Ekman boundary layer scale δ.

(5.5) *Steady geostrophic flow*

Consider a thin layer of water that rotates with a constant angular velocity Ω; the layer is bounded from below by a flat bottom. Initially, the water is motionless and the deviation h of the dimensionless sea surface from its equilibrium value is zero. At $t = 0$, the sea surface is deformed according to

$$h(x, y) = (-\mathcal{H}(x) + \mathcal{H}(-x))h_0$$

where h_0 is a constant and $\mathcal{H}$ is the Heaviside function. During the development of the flow, the Rossby number ϵ remains small.

a. Use quasi-geostrophic theory and formulate the equations which determine the geostrophic velocities u^0, v^0 and surface deformation h^0.

Assume now that the amplitudes of velocities are so small that products of these quantities can be neglected.

b. Determine the linear equation describing the evolution of h^0.

Consider now the special case that the steady state field h^0 does not depend on y.

c. Determine the steady state field h^0.

d. Determine and sketch the geostrophic velocities u^0 and v^0.

Chapter 6

WESTERN INTENSIFICATION

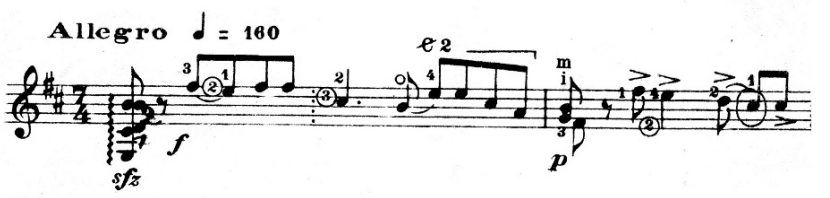

Pieza Sin Titulo, L. Brouwer

Through the analysis in the previous chapter, an enormous reduction of the mathematical problem of the wind-driven circulation has been accomplished. At the beginning of section 5.1, we needed to solve a system of four coupled partial differential equations in three space dimensions, which has now been reduced to the solution of one scalar partial differential equation (5.91) in two spatial dimensions. But the problem can be reduced even more! In section 6.1, inner and outer expansion techniques are used on the barotropic vorticity equation to obtain the famous Sverdrup balance outside continental boundary layers. The structure of the flow in the boundary layers is presented in section 6.2 for the frictional cases (the Munk and Stommel boundary layers) and in section 6.3 for the inertial case. From this theory, the mechanism of the western intensification of midlatitude ocean current such as the Gulf Stream is described. Finally, in section 6.4 some nonlinear aspects of the circulation are discussed.

6.1. The Sverdrup balance

As we have already seen, the values of $L = 1000$ km, $U = 10^{-2}$ ms^{-1} apply for the gyre-scale flow in the North Atlantic and with $\beta_0 = 2.0 \times 10^{-11}$ (ms)$^{-1}$ it follows that $\beta = \mathcal{O}(10^2)$. If we look at the terms in the equation (5.91), then the first term in the left hand side is $\mathcal{O}(1)$ and the last two terms in the right hand side are both at most $\mathcal{O}(1)$. Hence, only the wind stress term can balance the β term which leads to

$$\mathcal{O}(\frac{\alpha r}{2}) = \mathcal{O}(\beta) \rightarrow \mathcal{O}\left[\frac{\tau_0}{\rho f_0 \delta_E U}\frac{E_V^{1/2}}{\epsilon}\right] = \mathcal{O}\left[\frac{\tau_0}{\rho U D}\frac{L}{U}\right] = \mathcal{O}\left[\frac{\beta_0 L^2}{U}\right], \quad (6.1)$$

from which the horizontal velocity U (which was previously not related to the parameters, but based on observational values) follows as

$$U = \frac{\tau_0}{\rho D \beta_0 L}. \quad (6.2)$$

First of all, we need to check whether this gives consistent values of U. With $D = 10^3$ m, $\rho = 10^3$ kgm^3, $\tau_0 = 0.2$ Nm^{-2}, and $\beta_0 = 2.0 \times 10^{-11}$ (ms)$^{-1}$, we find $U \approx 10^{-2}$ ms^{-1} which is indeed consistent. As mentioned before, this velocity is a depth averaged velocity at the basin scale.

With the choice of U, the barotropic vorticity equation (5.91) becomes

$$\frac{1}{\beta}\left[\frac{\partial\psi}{\partial x}\frac{\partial}{\partial y} - \frac{\partial\psi}{\partial y}\frac{\partial}{\partial x}\right]\left[\nabla^2\psi - F\psi + \eta_b\right] + \frac{\partial\psi}{\partial x}$$

$$= \nabla \cdot (\mathbf{T} \wedge \mathbf{e}_3) - \frac{r}{2\beta}\nabla^2\psi - \frac{1}{\beta Re}\nabla^4\psi. \tag{6.3}$$

Because β is large, $F = \mathcal{O}(1)$, $r = \mathcal{O}(1)$ and $Re^{-1} \ll 1$, we can use $1/\beta$ as a small parameter and as this term occurs in the highest derivatives, we can again make use of the method of inner and outer expansions (cf. Example 5.1).

The outer expansion becomes

$$\psi(x, y) = \psi^0(x, y) + \beta^{-1}\psi^1(x, y) + \dots \tag{6.4}$$

and the $\mathcal{O}(1)$ system is simply

$$\frac{\partial \psi^0}{\partial x} = \nabla \cdot (\mathbf{T} \wedge \mathbf{e}_3), \tag{6.5}$$

which is called the Sverdrup balance.

The Sverdrup balance

The dimensional form of the Sverdrup balance (6.5) is

$$\beta_0 v_* = \frac{1}{\rho D}\left(\frac{\partial \tau_*^y}{\partial x_*} - \frac{\partial \tau_*^x}{\partial y_*}\right) = \frac{f_0}{D} w_{E*},$$

The right hand side of this equation is the vorticity input by the wind stress giving rise to the Ekman pumping velocity. The term $-\beta_0 v_*$ is the vorticity change of a fluid parcel when moving north-south on the sphere (cf. section 3.1). The $\beta-$ induced vorticity changes must compensate the vorticity input by the wind. For example, if the Ekman pumping velocity is negative fluid parcels must move southward such that their vorticity change is positive. The dimensional pressure field follows from $p_* = \rho_0 f_0 \psi_* = \rho_0 f_0 L U \psi$ and hence the flow follows isobars.

Ex. 6.1

For the Sverdrup flow (6.5) the streamfunction ψ^0 can be directly determined from (6.9) as

$$\psi^0(x, y) = \int_{x_0}^{x} \nabla \cdot (\mathbf{T} \wedge \mathbf{e}_3)(s, y) ds + \Psi^0(y), \tag{6.6}$$

where x_0 is still arbitrary and $\Psi^0(y)$ is an integration constant. The horizontal velocity u^0 is

$$u^0(x, y) = -\partial\psi^0/\partial y = -\int_{x_0}^{x} \frac{\partial}{\partial y}\left[\nabla \cdot (\mathbf{T} \wedge \mathbf{e}_3)(s, y)\right] ds + U(y), \tag{6.7}$$

where $U(y) = -\Psi^{0\prime}(y)$.

But can this solution satisfy the kinematic boundary conditions? Let the continental boundaries be described by $x_E = x_E(y)$ and $x_W = x_W(y)$, then the tangent $\mathbf{t}$ and the normal $\mathbf{n}$ are

$$\mathbf{t}_W = \begin{pmatrix} x'_W \\ 1 \end{pmatrix} \; ; \; \mathbf{n}_W = \begin{pmatrix} -1 \\ x'_W \end{pmatrix} \; ; \; \mathbf{t}_E = \begin{pmatrix} x'_E \\ 1 \end{pmatrix} \; ; \; \mathbf{n}_E = \begin{pmatrix} 1 \\ -x'_E \end{pmatrix}. \tag{6.8}$$

The kinematic boundary conditions ($\mathbf{v} \cdot \mathbf{n} = 0$) then become

$$x = x_W(y) : \; u = v x'_W \; ; \; x = x_E(y) : \; u = v x'_E, \tag{6.9}$$

and for later reference the no-slip conditions ($\mathbf{v} \cdot \mathbf{t} = 0$) are

$$x = x_W(y) : \; v = -u x'_W \; ; \; x = x_E(y) : \; v = -u x'_E. \tag{6.10}$$

If we try to satisfy (6.9b) with the solution (6.6) at $x_E(y)$ then

$$U(y) = \frac{\partial}{\partial y} \int_{x_0}^{x_E(y)} \nabla \cdot (\mathbf{T} \wedge \mathbf{e}_3)(s, y) ds, \tag{6.11}$$

and we cannot satisfy the boundary condition (6.9a) at x_W for an arbitrary wind-stress field. Similarly, if we determine $U(y)$ such that (6.9a) is satisfied at x_W, we cannot satisfy the kinematic boundary condition at x_E. Hence, the Sverdrup circulation cannot satisfy both kinematic boundary conditions.

For the total dimensionless Sverdrup transport Φ^y we find

$$\Phi^y(y) = \int_{x_W}^{x_E} v^0(x, y) dx = \int_{x_W}^{x_E} \nabla \cdot (\mathbf{T} \wedge \mathbf{e}_3)(x, y) dx, \tag{6.12}$$

which is independent of the boundary conditions. This transport has to be compensated in boundary layers, at the eastern or western (or both) boundaries. To obtain the dimensional transport in Sv, multiply by the factor ULD, i.e., $\Phi^y_* = UDL\Phi^y$.

▶

Example 6.1: Sverdrup flow

Consider, for a square ocean basin $x, y \in [0, 1] \times [0, 1]$, the Sverdrup flow caused by the wind stress

$$\tau^x(x, y) = -\frac{1}{2\pi} \cos 2\pi y, \tag{6.13a}$$

$$\tau^y(x, y) = 0, \tag{6.13b}$$

such that

$$\frac{\partial \psi^0}{\partial x} = v^0(x,y) = \nabla \cdot (\mathbf{T} \wedge \mathbf{e}_3) = -\sin 2\pi y. \tag{6.14}$$

The geostrophic streamfunction $\psi^0(x,y)$ is

$$\psi^0(x,y) = -x \sin 2\pi y + \Psi^0(y). \tag{6.15}$$

Note that ψ^0 is also the shape of the ocean-atmosphere boundary since $p^0 = \eta^0 = \psi^0$. The zonal geostrophic velocity is

$$u^0(x,y) = -\partial\psi^0/\partial y = -2\pi x \cos 2\pi y + U(y). \tag{6.16}$$

If we try to satisfy the boundary condition $u = 0$ at $x = 1$, then

$$U(y) = 2\pi \cos 2\pi y \rightarrow u^0(x,y) = -2\pi(1-x)\cos 2\pi y \tag{6.17a}$$

$$\psi^0(x,y) = (1-x)\sin 2\pi y + \psi_0, \tag{6.17b}$$

where ψ_0 is an arbitrary constant which can be taken as zero. The solution is plotted in Fig. 6.1a and it cannot satisfy the condition $u = 0$ at $x = 0$. To close the circulation, a boundary layer is needed near the western boundary.

If we try to satisfy the boundary condition $u = 0$ at $x = 0$, we find

$$\psi^0(x,y) = -x \sin 2\pi y + \psi_0. \tag{6.18}$$

Again, with $\psi_0 = 0$ the Sverdrup flow is plotted in Fig. 6.1b and this solution cannot satisfy the condition $u = 0$ at $x = 1$. To close the circulation, a boundary layer is needed near the eastern boundary.

Considering only Sverdrup dynamics, both solutions in Fig. 6.1 are equally possible and we have to resolve the boundary layer structure (as will be done in the next section) to determine which one is dynamically correct. For both solutions, the total meridional Sverdrup transport Φ^y is given by

$$\Phi^y(y) = \int_0^1 -\sin 2\pi y \, dx = -\sin 2\pi y. \tag{6.19}$$

With values of $\tau_0 = 0.1$ Pa, $L = 1000$ km and $D = 1000$ m, it follows from (6.2) that $U = 10^{-2}$ ms^{-1} and we find a maximum transport in each gyre of about 10 Sv. ◀

6.2. Continental boundary layers

To satisfy the boundary conditions (6.9) we have to investigate the flow behavior near the continents where the length scale L is not the characteristic length of

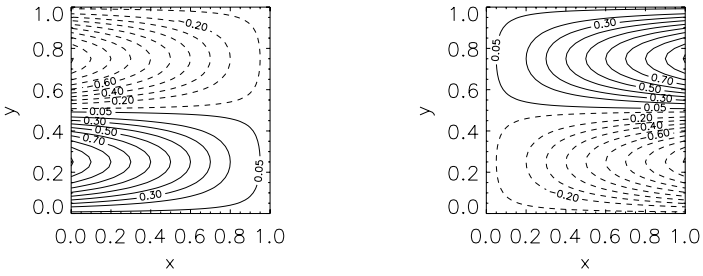

(a) (b)

Figure 6.1. Examples of Sverdrup flows for the wind stress field $\tau^x(x,y) = -1/(2\pi)\cos 2\pi y$, $\tau^y(x,y) = 0$. *(a) The flow satisfies* $u = 0$ *at* $x = 1$. *(b) The flow satisfies* $u = 0$ *at* $x = 0$.

the flow. From (5.91), there are three processes that can give a different balance in the boundary layer, i.e., inertia, bottom friction and lateral friction. The three associated length scales are

$$\delta_I = (\frac{U}{\beta_0})^{1/2}\ ,\ \delta_S = \frac{\delta_E f_0}{2D\beta_0}\ ,\ \delta_M = (\frac{A_H}{\beta_0})^{1/3}. \tag{6.20}$$

The scales are chosen such that

$$(\frac{\delta_I}{L})^2 = \frac{1}{\beta}, (\frac{\delta_M}{L})^3 = \frac{1}{\beta Re}, \frac{\delta_S}{L} = \frac{r}{2\beta}, \tag{6.21}$$

which are exactly the different terms in (5.91). If the scale of the flow is larger than $\max(\delta_I, \delta_M, \delta_S)$, then the Sverdrup balance holds, but if the scale of the flow is in the order of one of the δ's in (6.20), the equations need to be rescaled.

For the analysis of the boundary layer solutions, we consider the simple case where x_W and x_E are constant, the bottom is flat ($\eta_b = 0$) and the effect of the deformation of the ocean-atmosphere interface is neglected ($F \to 0$). In that case, (5.91) can be written as

$$\begin{aligned}(\frac{\delta_I}{L})^2 \left[\frac{\partial\psi}{\partial x}\frac{\partial}{\partial y} - \frac{\partial\psi}{\partial y}\frac{\partial}{\partial x}\right]\nabla^2\psi \quad &+ \quad \frac{\delta_S}{L}\nabla^2\psi - (\frac{\delta_M}{L})^3\nabla^4\psi = \\ -\frac{\partial\psi}{\partial x} \quad &+ \quad \nabla\cdot(\mathbf{T}\wedge\mathbf{e}_3).\end{aligned} \tag{6.22}$$

With a boundary layer coordinate λ given by

$$\lambda = \frac{x - x_W}{\ell}, \tag{6.23}$$

at the western boundary, (6.22) becomes

$$(\frac{\delta_I}{\ell_*})^2\left[\frac{\partial\psi}{\partial\lambda}\frac{\partial}{\partial y}-\frac{\partial\psi}{\partial y}\frac{\partial}{\partial\lambda}\right]\left[\frac{\partial^2\psi}{\partial\lambda^2}+\ell^2\frac{\partial^2\psi}{\partial y^2}\right] \quad + \quad \frac{\delta_S}{\ell_*}\left[\frac{\partial^2\psi}{\partial\lambda^2}+\ell^2\frac{\partial^2\psi}{\partial y^2}\right]- \\ -(\frac{\delta_M}{\ell_*})^3\left[\frac{\partial^2}{\partial\lambda^2}+\ell^2\frac{\partial^2}{\partial y^2}\right]^2\psi=-\frac{\partial\psi}{\partial\lambda} \quad + \quad \ell\nabla\cdot(\mathbf{T}\wedge\mathbf{e}_3), \tag{6.24}$$

where $\ell_*=L\ell$.

With a boundary layer coordinate μ given by

$$\mu=\frac{x_E-x}{\ell}, \tag{6.25}$$

at the eastern boundary, (6.22) becomes

$$-(\frac{\delta_I}{\ell_*})^2\left[\frac{\partial\psi}{\partial\mu}\frac{\partial}{\partial y}-\frac{\partial\psi}{\partial y}\frac{\partial}{\partial\mu}\right]\left[\frac{\partial^2\psi}{\partial\mu^2}+\ell^2\frac{\partial^2\psi}{\partial y^2}\right] \quad + \quad \frac{\delta_S}{\ell_*}\left[\frac{\partial^2\psi}{\partial\mu^2}+\ell^2\frac{\partial^2\psi}{\partial y^2}\right]- \\ -(\frac{\delta_M}{\ell_*})^3\left[\frac{\partial^2}{\partial\mu^2}+\ell^2\frac{\partial^2}{\partial y^2}\right]^2\psi=\frac{\partial\psi}{\partial\mu} \quad + \quad \ell\nabla\cdot(\mathbf{T}\wedge\mathbf{e}_3). \tag{6.26}$$

Each of the three terms on the left hand side will give higher derivatives but to satisfy no-slip conditions we have to take lateral friction into account. When only bottom friction and/or inertia is considered (with only second order derivatives), we can only satisfy kinematic boundary conditions. Hence, there are several possibilities:

(i) Effects of inertia and bottom friction can be neglected with respect to lateral friction, $\delta_M \gg \max(\delta_S,\delta_I)$. The boundary layer structure is relatively simple (Fig. 6.2a) and is called the Munk boundary layer.

(ii) Effects of inertia can be neglected with respect to those of bottom and lateral friction and the effect of bottom friction is much larger than that of lateral friction on a length scale ℓ_*^S. In this case $\delta_S \gg \max(\delta_M,\delta_I)$; on the scale ℓ_*^S only kinematic boundary conditions can be satisfied and the boundary layer is called the Stommel boundary layer. However, to satisfy no-slip conditions, there must be a sub-layer of scale $\ell_*^M < \ell_*^S$ within the Stommel boundary layer where lateral friction is important (Fig. 6.2b). On the scale ℓ_*^M it follows that

$$(\frac{\delta_M}{\ell_*^M})^3=\mathcal{O}(\frac{\delta_S}{\ell_*^M})\Rightarrow\ell_*^M=\mathcal{O}(\delta_S(\frac{\delta_M}{\delta_S})^{3/2}). \tag{6.27}$$

(iii) The effects of bottom friction are negligible everywhere, but the effect of inertia is larger than that of lateral friction on a scale ℓ_*^I. The boundary layer scale is called the inertial boundary layer and in that case there is the same situation

as in (ii) in that there must exist a sub-layer where lateral friction is important (Fig. 6.2c). With $\delta_I \gg \max(\delta_M, \delta_S)$, the sub-layer has the scale ℓ_*^M with

$$(\frac{\delta_M}{\ell_*^M})^3 = \mathcal{O}(\frac{\delta_I}{\ell_*^M})^2. \tag{6.28}$$

If all three effects have the same order of magnitude, the boundary layer structure is more complicated but the cases above cover all interesting and essentially different cases.

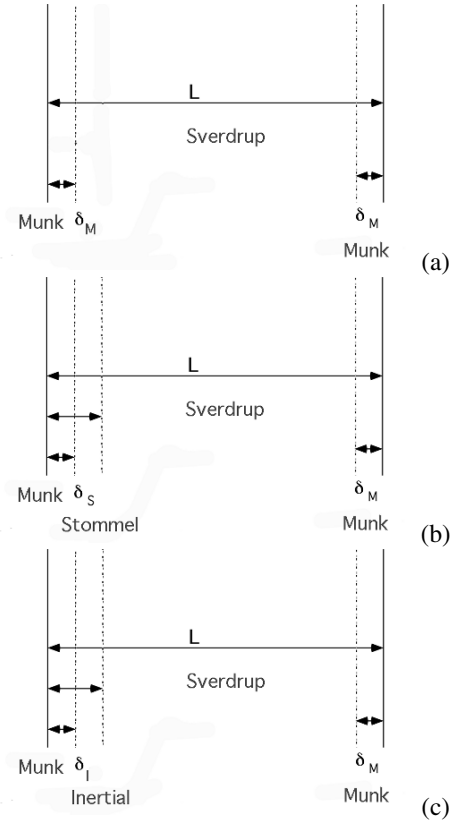

Figure 6.2. Boundary layer structure for three different cases. (a) Munk boundary layer, (b) Stommel boundary layer with viscous sublayer, and (c) inertial boundary layer with viscous sublayer.

6.2.1. The Munk boundary layer

Case (i) of the previous section is characterized by

$$\delta_M \gg \max(\delta_I, \delta_S), \tag{6.29}$$

and hence lateral friction dominates over inertia and bottom friction. We start from the Sverdrup solution ψ^0 in (6.6), with

$$\psi^0(x,y) = \int_{x_W}^{x} \nabla.(\mathbf{T} \wedge \mathbf{e}_3)(s,y)ds + \Psi^0(y), \tag{6.30}$$

where $\Psi^0(y)$ is still to be determined. For constant x_W and x_E, the kinematic (6.10) and no-slip (6.11) boundary conditions are

$$x = x_W, x_E : \psi = 0, \frac{\partial \psi}{\partial x} = 0. \tag{6.31}$$

Consider first the boundary layer at the eastern boundary. With $\ell_* = \delta_M$ and with (6.29), (6.26) becomes

$$\left[\frac{\partial^2}{\partial \mu^2} + \ell^2 \frac{\partial^2}{\partial y^2}\right]^2 \psi = \frac{\partial \psi}{\partial \mu} + \ell \nabla \cdot (\mathbf{T} \wedge \mathbf{e}_3). \tag{6.32}$$

It appears convenient to introduce the boundary layer correction ϕ_B by

$$\psi(\mu, y) = \psi^0(x,y) + \phi_B(\mu, y). \tag{6.33}$$

Substitution of (6.33) into (6.32) and use of

$$\frac{\partial \psi^0}{\partial \mu} = -\ell \frac{\partial \psi^0}{\partial x}, \tag{6.34}$$

gives, with $\ell = \delta_M / L \ll 1$, the dominant balance

$$\frac{\partial^4 \phi_B}{\partial \mu^4} + \frac{\partial \phi_B}{\partial \mu} = 0. \tag{6.35}$$

The characteristic polynomial is found through substitution of $e^{\mu z}$ into (6.35) which gives

$$z^4 + z = 0 \Rightarrow z = 0 \vee z = -1 \vee z = \frac{1}{2}(1 + i\sqrt{3}) \vee z = \frac{1}{2}(1 - i\sqrt{3}). \tag{6.36}$$

The general solution of (6.35) is

$$\phi_B(\mu, y) = C_1(y) + C_2(y)e^{-\mu} + C_3(y)e^{\frac{\mu}{2}} \cos\frac{\mu\sqrt{3}}{2} + C_4(y)e^{\frac{\mu}{2}} \sin\frac{\mu\sqrt{3}}{2}. \tag{6.37}$$

There are four integration constants (functions of y) and we need four boundary conditions to determine them. Two follow directly from the boundary conditions (6.31) at the eastern boundary $x = x_E$ ($\mu = 0$), i.e.,

$$\phi_B(0,y) = \psi(0,y) - \psi^0(x_E,y) = -\psi^0(x_E,y) \tag{6.38a}$$

$$\frac{\partial\psi}{\partial\mu} = -\ell\frac{\partial\psi^0}{\partial x} + \frac{\partial\phi_B}{\partial\mu} \approx \frac{\partial\phi_B}{\partial\mu} = 0. \tag{6.38b}$$

The other two follow from matching to the Sverdrup solution for $\mu \to \infty$, i.e.,

$$\lim_{\mu\to\infty}\phi_B = 0\,;\ \lim_{\mu\to\infty}\frac{\partial\phi_B}{\partial\mu} = 0. \tag{6.39}$$

For the solution (6.37), it follows from (6.39) directly that $C_1 = C_3 = C_4 = 0$ and from (6.38b) that $C_2 = 0$. The zeroth order boundary layer correction $\phi_B = 0$ and $\Psi^0(y)$ has to be fixed by requiring that $\psi = 0$ at the eastern boundary. In other words, the boundary analysis indicates that the Sverdrup solution has to satisfy the eastern boundary condition and hence (6.30) becomes

$$\psi^0(x,y) = \int_{x_E}^{x} \nabla.(\mathbf{T}\wedge\mathbf{e}_3)(s,y)ds. \tag{6.40}$$

At the western boundary, we follow the same approach with λ as boundary layer coordinate. With

$$\frac{\partial\psi^0}{\partial\lambda} = \frac{\partial\psi^0}{\partial x}\ell, \tag{6.41}$$

it follows in the same way (from (6.24)) that the zeroth order balance in the boundary layer is given by

$$\frac{\partial^4\phi_B}{\partial\lambda^4} - \frac{\partial\phi_B}{\partial\lambda} = 0. \tag{6.42}$$

The characteristic polynomial is

$$z^4 - z = 0 \Rightarrow z = 0 \vee z = 1 \vee z = -\frac{1}{2}(1+i\sqrt{3}) \vee z = -\frac{1}{2}(1-i\sqrt{3}), \tag{6.43}$$

and the general solution (6.42) is

$$\phi_B(\lambda,y) = C_1(y) + C_2(y)e^{\lambda} + C_3(y)e^{\frac{-\lambda}{2}}\cos\frac{\lambda\sqrt{3}}{2} + C_4(y)e^{\frac{-\lambda}{2}}\sin\frac{\lambda\sqrt{3}}{2}. \tag{6.44}$$

The boundary - and matching conditions become

$$\phi_B(0,y) = \psi(0,y) - \psi^0(x_W,y) = -\psi^0(x_W,y) \tag{6.45a}$$

$$\frac{\partial\psi}{\partial\lambda} = \ell\frac{\partial\psi^0}{\partial x} + \frac{\partial\phi_B}{\partial\lambda} \approx \frac{\partial\phi_B}{\partial\lambda} = 0 \tag{6.45b}$$

$$\lim_{\lambda\to\infty}\phi_B = 0\,;\ \lim_{\lambda\to\infty}\frac{\partial\phi_B}{\partial\lambda} = 0. \tag{6.45c}$$

From (6.45b) it follows that $C_1 = C_2 = 0$ and the conditions (6.45a) fix the zeroth order boundary layer correction through C_3 and C_4, with

$$C_3(y) = -\psi^0(x_W, y)\ ;\ C_4(y) = \frac{C_3}{\sqrt{3}}. \tag{6.46}$$

Finally, the boundary layer solution is given by

$$\psi(\lambda, y) = \psi^0(x_W, y)(1 - e^{\frac{-\lambda}{2}} \cos\frac{\lambda\sqrt{3}}{2} - \frac{1}{\sqrt{3}} e^{\frac{-\lambda}{2}} \sin\frac{\lambda\sqrt{3}}{2}), \tag{6.47}$$

and $\psi(\lambda, y)/\psi^0(x_W, y)$ is plotted as function of λ in Fig. 6.3. We see that indeed

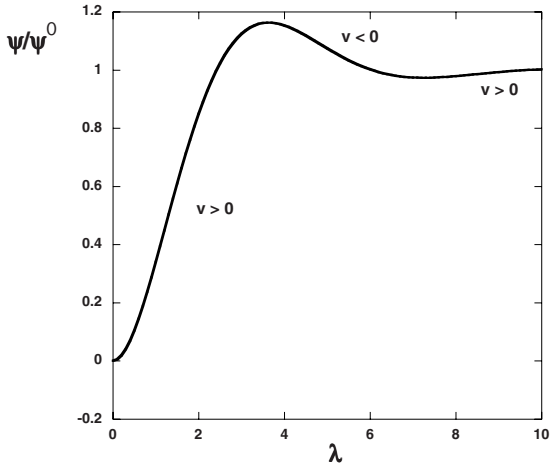

Figure 6.3. Plot of the boundary layer solution $\psi(\lambda, y)/\psi^0(x_W, y)$ from (6.47).

$\psi = 0$ and $\hat{v}(\lambda, y) = L/\delta_M \partial\hat{\psi}^0/\partial\lambda = 0$ at $\lambda = 0$. Note also that ψ oscillates and hence there are intervals where $\hat{v}$ is positive and negative.

6.2.2. The Stommel boundary layer

In case (ii), we consider the boundary layer structure due to bottom friction for which

$$\delta_S \gg \max\ (\delta_I,\ \delta_M). \tag{6.48}$$

The potential vorticity equation reduces to

$$\frac{\delta_S}{L}\nabla^2\psi = -\frac{\partial\psi}{\partial x} + \nabla\cdot(\mathbf{T}\wedge\mathbf{e}_3). \tag{6.49}$$

The Sverdrup solution is again

$$\psi^0(x,y) = \int_{x_W}^{x} \nabla \cdot (\mathbf{T} \wedge \mathbf{e}_3)(s,y)ds + \Psi^0(y), \tag{6.50}$$

where $\Psi^0(y)$ has to be determined. As the highest order derivative in (6.49) is of second order only kinematic conditions can be prescribed and for constant x_W and x_E, we have

$$x = x_W, x_E : \psi = 0. \tag{6.51}$$

We now consider the impact of bottom friction near $x = x_E$, take $\ell_* = \delta_S$ in (6.26) (note $\ell = \delta_S/L \ll 1$) and expand

$$\tilde{\psi}(\mu,y) = \tilde{\psi}^0(\mu,y) + \ell\tilde{\psi}^1(\mu,y) + \ldots \tag{6.52}$$

Equation (6.26) provides the $\mathcal{O}(1)$ system

$$\frac{\partial^2 \tilde{\psi}^0}{\partial \mu^2} - \frac{\partial \tilde{\psi}^0}{\partial \mu} = 0, \tag{6.53}$$

having the solution

$$\tilde{\psi}^0(\mu,y) = C_1(y)e^{\mu} + C_2(y). \tag{6.54}$$

Ex. 6.2

For $\mu \to \infty$, ψ^0 has to be bounded; this implies $C_1(y) = 0$ and because of (6.51) at $x = x_E$ also $C_2(y) = 0$. There can be no eastern boundary layer due to bottom friction and the Sverdrup solution has to satisfy the boundary condition at $X = x_E$. This gives

$$\Psi^0(y) = -\int_{x_W}^{x_E} \nabla \cdot (\mathbf{T} \wedge \mathbf{e}_3)(s,y)ds. \tag{6.55}$$

At the western boundary, we choose $\ell_* = \delta_S$ and expand

$$\hat{\psi}(\lambda,y) = \hat{\psi}^0(\lambda,y) + \ell\hat{\psi}^1(\lambda,y) + \ldots \tag{6.56}$$

From (6.24) the $\mathcal{O}(1)$ equations are

$$\frac{\partial^2 \hat{\psi}^0}{\partial \lambda^2} + \frac{\partial \hat{\psi}^0}{\partial \lambda} = 0. \tag{6.57}$$

The solution is

$$\hat{\psi}^0(\lambda,y) = C_1(y)e^{-\lambda} + C_2(y), \tag{6.58}$$

and this solution is bounded for $\lambda \to \infty$. The kinematic condition at $x = x_W$ ($\lambda = 0$) gives

$$C_1(y) = -C_2(y), \tag{6.59}$$

and the matching condition at $\lambda \to \infty$ leads to

$$\lim_{\lambda\to\infty} \hat{\psi}^0(\lambda, y) = C_2(y) = \lim_{x\downarrow x_W} \psi^0(x, y) = \Psi^0(y). \tag{6.60}$$

This gives the Stommel boundary layer flow solution as

$$\hat{\psi}^0(\lambda, y) = \Psi^0(y)(1 - e^{-\lambda}). \tag{6.61}$$

▶

Example 6.2: Stommel western boundary layer

Consider a square basin such as in Fig. 6.4 and take $x_W = 0$ and $x_E = 1$. As an example, the wind-stress field is given by

$$\tau^x(x, y) = -\frac{1}{2\pi}\cos 2\pi y, \tag{6.62a}$$

$$\tau^y(x, y) = 0, \tag{6.62b}$$

and the kinematic conditions on the boundaries are $\psi = 0$. The Sverdrup flow (Fig. 6.4a), that satisfies the kinematic boundary conditions at the eastern boundary, was already determined in Example 6.1 and is given by

$$\psi^0(x, y) = (1 - x)\sin 2\pi y. \tag{6.63}$$

According to the boundary analysis, the boundary layer flow is

$$\hat{\psi}^0(\lambda, y) = \sin 2\pi y(1 - e^{-\lambda}), \tag{6.64}$$

and the total solution for $\delta_S/L = 0.1$ is plotted in Fig. 6.4b. Bottom friction, as did lateral friction, can provide a boundary layer current at the western boundary of the continent to balance the Sverdrup transport. The dimensional boundary layer width is for this case 100 km and typical meridional horizontal velocities $V = UL/\delta_S$ in the boundary layer are about 10 cm/s.

The full solution to (6.49) can actually be analytically determined and with $\eta_1 = -L/(2\delta_S)$ and $\eta_2 = \sqrt{\eta_1^2 + 4\pi^2}$ it becomes

$$\psi(x, y) = \frac{L}{4\pi^2\delta_S}\left[1 - e^{\eta_1}\frac{e^{-\eta_1}\sinh\eta_2 x - \sinh\eta_2(x-1)}{\sinh\eta_2}\right]\sin(2\pi y). \tag{6.65}$$

Although this solution is useful to compare the validity of the asymptotic solutions, the boundary layer character of (6.65) is not so obvious. For $\delta_S/L = 0.1$

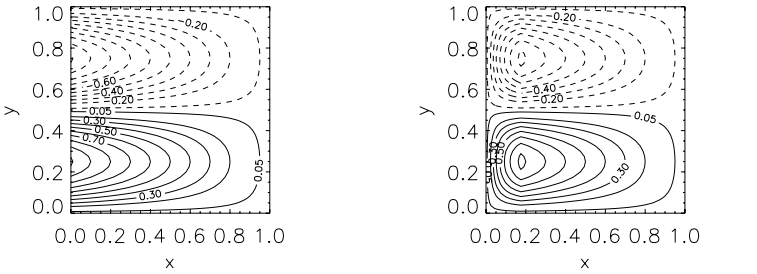

Figure 6.4. (a) Sverdrup flows for the wind stress field $\tau^x(x,y) = -1/(2\pi)\cos 2\pi y$, $\tau^y(x,y) = 0$. *(b) Total flow solution with Stommel western boundary current for* $\delta_S/L = 0.1$.

the asymptotic solution deviates substantially from the analytic one, but for $\delta_S/L = 0.01$ the difference is very small.

◀

To demonstrate the compensation of the Sverdrup transport by the western boundary current, we compute the dimensionless meridional velocity, $\hat{v}^0(\lambda, y)$ in the boundary layer and find

$$\hat{v}^0(\lambda, y) = \frac{1}{\ell}\frac{\partial \hat{\psi}^0}{\partial \lambda} = \frac{L}{\delta_S}\frac{\partial \hat{\psi}^0}{\partial \lambda} = \frac{L}{\delta_S}\Psi^0(y)e^{-\lambda}. \tag{6.66}$$

The total meridional transport in the boundary layer $\hat{\Phi}^y$ therefore is

$$\hat{\Phi}^y(y) = \ell \int_0^\infty \hat{v}^0(\lambda, y)d\lambda = \Psi_0(y) = -\Phi^y(y), \tag{6.67}$$

and from this it follows that

$$\hat{\Phi}^y + \Phi^y = 0, \tag{6.68}$$

which demonstrates the compensation.

Ex. 6.3

6.2.3. Physics of the western intensification

As shown by direct calculation, both bottom and lateral friction can provide provide western boundary currents which compensate for the complete Sverdrup transport. In this section, we focus on the physics of this result by looking at the vorticity balance for a subtropical gyre.

The wind stress induces negative vorticity into the flow (Fig. 6.5) and in the internal flows (outside boundary layers). This input of vorticity is compensated by southward movement of fluid parcels (the Sverdrup flow); through the β-effect the fluid parcels acquire positive vorticity. Both boundary layer currents should be northward to compensate for the (southward) Sverdrup transport. Through the β-effect there is negative vorticity production due to such a current which has to balance the vorticity produced by friction.

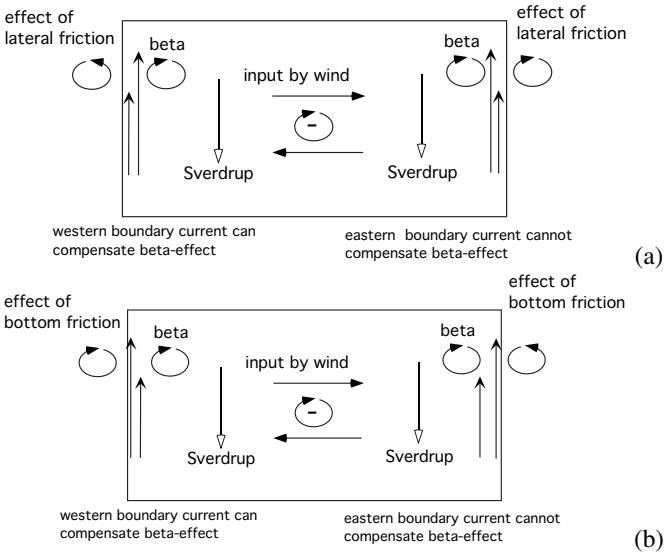

Figure 6.5. Vorticity balances in the Sverdrup regime and the western boundary layers. (a) Munk boundary layer and (b) Stommel boundary layer.

In the lateral friction (Munk) case (Fig. 6.5a), there are no-slip boundary conditions and the tangential velocity is zero at the boundary. The meridional velocity gradient is hence positive on the western boundary and positive vorticity is produced which is able to balance the negative vorticity due to the β-effect, according to (see (6.22))

$$0 = (\frac{\delta_M}{L})^3 \nabla^4 \psi - \frac{\partial \psi}{\partial x}.$$

At the eastern boundary, the friction generates negative vorticity which cannot achieve an appropriate balance.

In case of bottom friction (Stommel), the tangential velocity is maximal at the boundaries. The meridional velocity gradient $\partial v/\partial x$ is positive on the eastern boundary and negative on the western boundary. Hence, the vorticity in the flow

domain outside the Ekman layers (the term $\zeta^0 = \nabla^2\psi$) is negative in the west and positive in the east (Fig. 6.5b). The vorticity balance in the boundary layer is (in case of only bottom friction, see (6.22))

$$0 = -\frac{\delta_S}{L}\nabla^2\psi - \frac{\partial\psi}{\partial x}, \tag{6.69}$$

and hence bottom friction and β-effect have to compensate each other. This can only be accomplished in the western boundary and not in the eastern boundary.

In the Stommel boundary layer, the streamlines of the Sverdrup circulation are deflected, such that the normal velocity is zero on the boundary. To satisfy no-slip conditions, there must be a Munk sublayer within the Stommel boundary layer with a thickness $\mathcal{O}(\delta_S^{-1/2}\delta_M^{3/2})$. It can be shown that this Munk layer does not contribute much to the total meridional transport (Pedlosky, 1987).

6.3. The inertial boundary layer

Finally we consider the case

$$\delta_I \gg \max\,(\delta_S,\ \delta_M). \tag{6.70}$$

We take $\ell_* = \delta_I$ (with $\ell = \ell_*/L$) and if we write the western boundary layer solution as

$$\hat{\psi}(\lambda, y) = \hat{\psi}^0(\lambda, y) + \ell\hat{\psi}^1(\lambda, y) + \ldots \tag{6.71}$$

then the $\mathcal{O}(1)$ system in (6.26) becomes

$$\left[\frac{\partial\hat{\psi}^0}{\partial\lambda}\frac{\partial}{\partial y} - \frac{\partial\hat{\psi}^0}{\partial y}\frac{\partial}{\partial\lambda}\right]\frac{\partial^2\hat{\psi}^0}{\partial\lambda^2} + \frac{\partial\hat{\psi}^0}{\partial\lambda} = 0. \tag{6.72}$$

It is convenient to define the operator $\mathcal{J}$, also called the Jacobian operator, with respect to coordinates x, y as

$$\mathcal{J}_{x,y}(f, g) = \frac{\partial f}{\partial x}\frac{\partial g}{\partial y} - \frac{\partial g}{\partial x}\frac{\partial f}{\partial y}, \tag{6.73}$$

for two arbitrary scalar functions f and g. The Jacobian operator has the following properties

$$i)\ \mathcal{J}_{x,y}(f, f) = 0\ ;\ ii)\ \mathcal{J}_{x,y}(f, G(f)) = 0, \tag{6.74}$$

where G is an arbitrary operator. With (6.73), (6.72) can be written as

$$\mathcal{J}_{\lambda,y}(\hat{\psi}^0, \frac{\partial^2\hat{\psi}^0}{\partial\lambda^2} + y) = 0, \tag{6.75}$$

and solutions are determined from

$$\frac{\partial^2\hat{\psi}^0}{\partial\lambda^2} + y = G(\hat{\psi}^0). \tag{6.76}$$

Equation (6.76) expresses that the quasi-geostrophic potential vorticity (cf. section 5.3) is constant along streamlines.

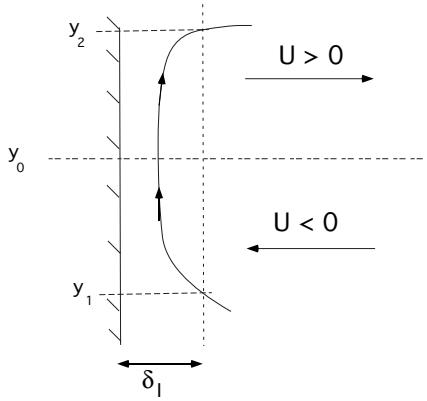

Figure 6.6. Sketch of a streamline in the inertial western boundary layer of thickness δ_I.

Ex. 6.4

Now consider a streamline that enters the western boundary layer at $y = y_1$ and leaves it at $y = y_2$, such as sketched in Fig. 6.6. For the Sverdrup solution, the relative vorticity is negligible and hence at y_1 we determine $G(\hat{\psi}^0) = y_1$. As potential vorticity is constant along the streamline, we find at y_2 that $\partial^2\hat{\psi}^0/\partial\lambda^2 = y_2 - y_1 > 0$. But at y_2, the solution has to match with the Sverdrup solution for which the relative vorticity is small and hence there is an inconsistency.

Equation (6.76) can therefore not hold everywhere along the streamline in Fig. 6.6. To analyze this, we use the boundary layer correction

$$\phi_B(\lambda, y) = \hat{\psi}^0(\lambda, y) - \psi^0(x_W, y), \tag{6.77}$$

where ψ^0 is the Sverdrup solution. According to the 'matching principle' with the Sverdrup solution, we find

$$\lim_{\lambda\to\infty} \phi_B(\lambda, y) = 0. \tag{6.78}$$

Consider the situation in Fig. 6.6 in the area $\lambda \gg 1$, such that $\mid \phi_B \mid \ll \mid \psi^0 \mid$. The linearized equation for ϕ_B in this area becomes (from (6.72)), neglecting terms of $\mathcal{O}(\delta_I/L)$,

$$u^0(x_W, y)\frac{\partial^2\phi_B}{\partial\lambda^2} + \phi_B = 0. \tag{6.79}$$

When u^0 is constant (for example, locally near y_0), the characteristic polynomial is $k^2 + 1/u^0 = 0$ for solutions $\phi_B \approx e^{k\lambda}$. The general solution of (6.76)

will show damped oscillatory behavior when $u^0(x_W, y) > 0$ and cannot satisfy the matching condition (6.78). Hence, a necessary condition for the existence of an inertial boundary layer is

$$u^0(x_W, y) < 0. \tag{6.80}$$

In Fig. 6.6, we see that south of y_0, where $u^0 < 0$, there can be an inertial boundary layer. For $y > y_0$, a pure inertial layer cannot occur and the excess of relative vorticity has to be dissipated through friction.

Additional Material

B: A less mathematical approach to the Sverdrup balance and western boundary layers can be found in chapter 8 of Cushman-Roisin (1994).

D: Having understood the material so far, extensions within reach are chapter 5 of Pedlosky (1987), where much more details are provided of the theory of the homogeneous wind-driven circulation, and chapter 14 (sections 14.1 to 14.6) of Vallis (2006) where for example topographic effects are discussed.

6.4. Highly nonlinear flows

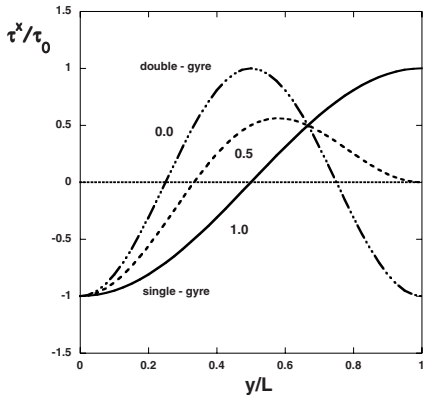

Figure 6.7. Plots of the zonal wind stress (6.81) for three different values of σ.

Steady solutions of the barotropic vorticity equation have been computed for values of Re far into the nonlinear regime. The dimensional wind-stress profile on a square basin $[0, L] \times [0, L]$ often considered is

$$\tau^x_*(x, y) = -\tau_0 \left(\sigma \cos \pi \frac{y_*}{L} + (1 - \sigma) \cos 2\pi \frac{y_*}{L}\right) ; \ \tau^y_*(x, y) = 0 \tag{6.81}$$

where the dimensionless parameter σ controls the shape of the wind stress and τ_0 is a typical amplitude. Since Veronis (1963), much attention has focussed on the subtropical (single) gyre system as obtained above with the choice $\sigma = 1$. The single-gyre wind-stress forcing consists of easterlies (westerlies) at the south (north) part of the basin. The so-called double-gyre case has more recently received much attention and is obtained with $\sigma = 0$ in (6.81). In this case, both the subtropical and subpolar gyres are forced and the wind stress is symmetric with respect to the mid-axis of the basin (Fig. 6.7).

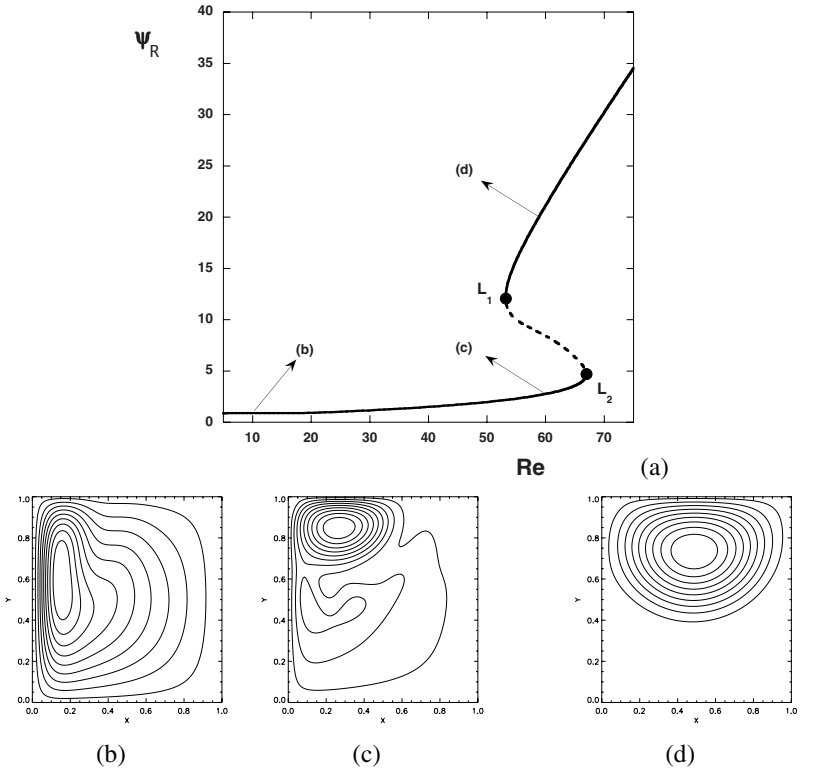

Figure 6.8. (a) Bifurcation diagram for the single-gyre ($\sigma = 1$) barotropic quasi geostrophic model for a square basin with $Re = UL/A_H$ as the control parameter. (b) Pattern of ψ near $Re = 10$ on the lower stable branch in (a). (c) Same for $Re = 60$ along lower branch and (d) for $Re = 60$ along the upper stable branch.

Ex. 6.5

Under a given steady wind-stress forcing, the linear steady quasi-geostrophic theory predicts a Sverdrup interior flow and a frictional western boundary layer. The linear theory provides a first order explanation of the existence of western

boundary currents, such as the Gulf Stream as we have seen above. The nonlinear theory is, however, far from complete. Although the strong effect of inertia on the flows was already shown by Veronis (1963), the work to determine systematically the solution structure of the barotropic vorticity equation (5.91) versus the lateral friction parameter A_H did not start until the mid 1990s (Cessi and Ierley, 1995; Jiang et al., 1995).

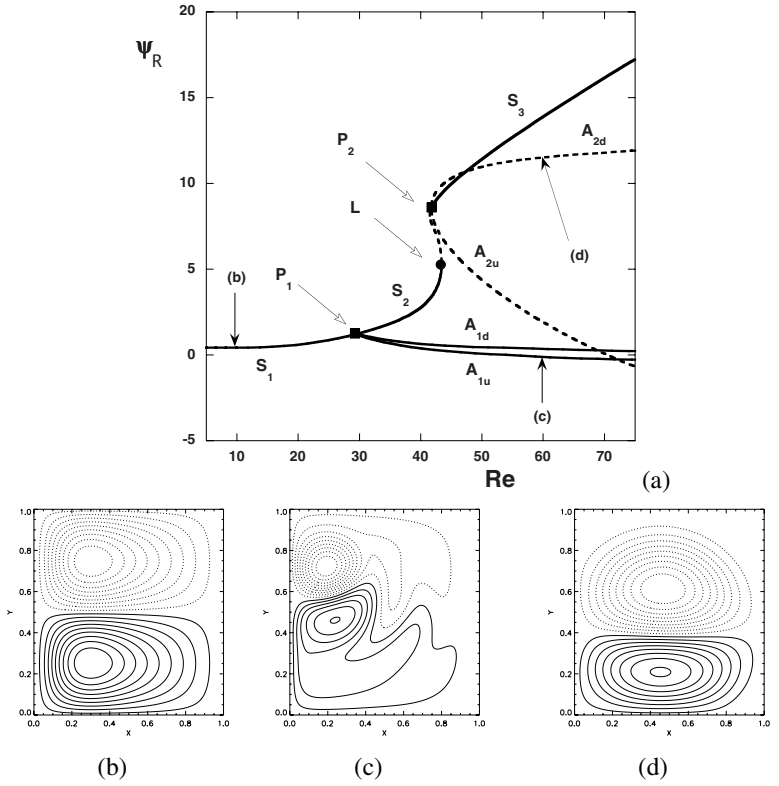

Figure 6.9. (a) Bifurcation diagram for the double-gyre ($\sigma = 0$) barotropic quasi geostrophic model for a square basin with $Re = UL/A_H$ as the control parameter. (b) Pattern of ψ near $Re = 10$ on the lower stable branch in (a). (c) Same for $Re = 60$ along the branch A_{1u}; the pattern on the branch A_{1d} at $Re = 60$ is the mirror image of (c) with respect to reflection through the midaxis of the basin. (d) The pattern at $Re = 60$ on the branch A_{2d}.

For large values of A_H, a unique and globally stable flow state for both single- and double-gyre cases is found. To investigate the solution structure of the equations when A_H is decreased, continuation methods (Dijkstra, 2005) have been used on discretized versions of the barotropic vorticity equation. In the results

Parameter	Value	Parameter	Value
L	1.0×10^6 m	τ_0	1.5×10^{-1} Pa
D	6.0×10^2 m	β_0	1.6×10^{-11} (ms)$^{-1}$
f_0	1.0×10^{-4} s^{-1}	g	9.8 ms^{-2}
ρ_0	10^3 kgm^{-3}	ϵ_0	0.0 s^{-1}

Table 6.1. Standard values of parameters used in the computations of Fig. 6.8 and Fig. 6.9.

below, a 128 x 128 equidistant grid is used to solve the barotropic vorticity equation

$$\begin{aligned}(\frac{\partial\psi_*}{\partial x_*}\frac{\partial}{\partial y_*} &- \frac{\partial\psi_*}{\partial y_*}\frac{\partial}{\partial x_*})(\nabla_*^2\psi_* - \lambda_0\psi_* + \frac{f_0}{D}h_{b*}) + \beta_0\frac{\partial\psi_*}{\partial x} \\ &= \frac{1}{\rho_0 D}\nabla.(\mathbf{T}_* \wedge \mathbf{e}_3) - \epsilon_0\nabla_*^2\psi_* + A_H\nabla_*^4\psi_*,\end{aligned}$$

with $h_{b*} = 0$ (no bottom topography), $\lambda_0 = 0.0$ (no effect of ocean-atmosphere surface deformations) and values of parameters as in Table 6.9. Steady states are determined versus A_H and in the results below a value of the dimensionless streamfunction ψ_R at a certain gridpoint is displayed versus the $Re = UL/A_H$. In other studies, also the ratio of boundary layer thicknesses δ_{I*}/δ_{M*}, where $\delta_{I*} = (U/\beta_0)^{1/2}$ and $\delta_{M*} = (A_H/\beta_0)^{1/3}$ is used as the control parameter. In the so-called bifurcation diagram (Fig. 6.8a) for the single-gyre flows ($\sigma = 1$), each point on the curve represents a steady state and its stability is indicated by the linestyle, with solid (dashed) curves indicating stable (unstable) solutions. At small and large values of Re, there is a unique steady solution, while between the two so-called saddle node bifurcations L_1 and L_2 there is a regime of multiple equilibria. Plots of the streamfunction ψ at labelled locations in Fig. 6.8a are shown in Fig. 6.8b-d. The pattern in Fig. 6.8b near $Re = 10$ deviates already from the symmetric linear Munk-Sverdrup solution. The effects of strong nonlinearities on the flow can be seen in the streamfunction for both solutions at $Re = 60$. A strong north-south asymmetric solution (Fig. 6.8c) appears on the lower branch and a gyre filling up the basin (Fig. 6.8d) develops on the upper branch.

Additional Material

D: Anyone who wants to know more on the bifurcation behavior of wind-driven ocean flows described by the barotropic vorticity equation, consult chapter 5 in Dijkstra (2005).

For the case $\sigma = 0$, the structure of the steady solutions is shown through the bifurcation diagram in Fig. 6.9a, where the value of the streamfunction at a point

in the southwest part of the domain (ψ_R) is plotted versus $Re = UL/A_H$. At large values of A_H (small Re), the anti-symmetric double-gyre flow (Fig. 6.9b) is a unique state. When lateral friction is decreased, this flow becomes unstable at a so-called pitchfork bifurcation P_1 and two branches of stable asymmetric states appear for smaller values of A_H (larger Re). The solutions on these branches have the jet displaced either southward or northward (Fig. 6.9c) and are exactly symmetrically related for the same value of Re. For even smaller friction, the anti-symmetric flow becomes inertially dominated and ψ_R increases rapidly. A pitchfork bifurcation P_2 occurs on the anti-symmetric branch where an additional pair of asymmetric solution branches appear (Fig. 6.9d); all these solutions are unstable. This brief analysis shows the enormous complexity in the flows when nonlinear effects become large.

Summary

- For a constant density ocean, the dominant (Sverdrup) balance in the interior of the domain is given by

$$\beta_0 v_* = \frac{1}{\rho D}\left(\frac{\partial \tau_*^y}{\partial x_*} - \frac{\partial \tau_*^x}{\partial y_*}\right) = \frac{f_0}{D} w_{E*},$$

  This is a vorticity balance where fluid parcels move north-south such that the β-induced vorticity change of this motion is compensating the wind-induced vorticity input.

- The continental boundary layers are only able to compensate the Sverdrup transport in the western part of the basin. The boundary layer thicknesses are either

$$\delta_I = \left(\frac{U}{\beta_0}\right)^{1/2}, \ \delta_S = \frac{\delta_E f_0}{2D\beta_0}, \ \delta_M = \left(\frac{A_H}{\beta_0}\right)^{1/3}.$$

  depending on the dominant vorticity balance in the western boundary layer. Here U is set by the Sverdrup velocity scale

$$U = \frac{\tau_0}{\rho D \beta_0 L}$$

  The boundary layer thicknesses δ_M and δ_S are set by lateral and bottom friction and are called the Munk and Stommel boundary layer thickness, respectively.

- The barotropic quasi-geostrophic theory of the wind-driven ocean circulation is a first step to understand the midlatitude gyres and the western intensification of boundary currents. It explains that the β-effect is responsible for the strong east-west symmetry of the midlatitude ocean currents and that inertial effects can induce north-south asymmetry in the flow.

6.5. Exercises on chapter 6

(6.1) *Sverdrup flow*

Given is the dimensionless wind-stress field

$$\boldsymbol{\tau} = \begin{pmatrix} \tau^x \\ \tau^y \end{pmatrix} = 0.1 \begin{pmatrix} \sin 6(y - \frac{\pi}{6}) \\ 0 \end{pmatrix}$$

over an ocean basin with $x \in [0, 1]$ and $y \in [0, \pi]$. The Sverdrup flow is assumed to satisfy the kinematic condition at the eastern boundary.

a. Determine the Sverdrup streamfunction $\psi^0(x, y)$.

b. Draw (or plot) the streamline pattern for $\frac{\pi}{12} < y < \frac{5\pi}{12}$ and interpret the result in terms of a vorticity balance.

(6.2) *Sverdrup flow and Stommel boundary layer*

Given is the same dimensionless wind-stress field as in exercise 6.1, over an ocean basin with $x \in [0, 1]$ and $y \in [0, \pi]$.

a. Determine the dimensionless Stommel boundary layer solution for this wind-stress field.

b. Determine now the dimensional pressure p_*, the sea surface elevation h_* and the meridional transport $\Phi_*(y_*)$ defined by

$$\Phi_*(y_*) = \int_0^L \psi_*(x_*, y_*)\, dx_*$$

where L is the basin length.

c. Sketch (or plot) these fields for typical values of the parameters as in Table 6.9. Is the flow in the Stommel boundary layer in geostrophic balance?

(6.3) *Integral balance*

Consider in the general situation of (6.22), i.e., with all physical processes taken into account, a closed streamline C that encloses an area A, as in the figure below. Show that for $Re \to \infty$, the velocity field $\mathbf{u} = (u, v)$ and the

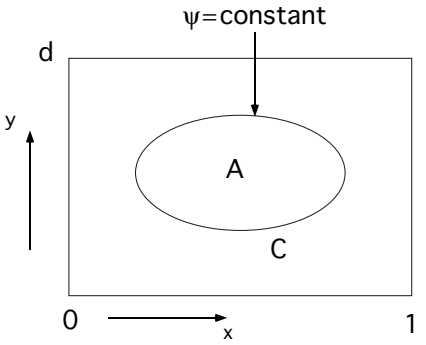

wind-stress vector $\tau = (\tau^x, \tau^y)$ satisfy the relation

$$\frac{\delta_S}{L} \int_C \mathbf{u} \cdot \mathbf{ds} = \int_C \tau \cdot \mathbf{ds}$$

and provide a physical explanation of the result.

(6.4) *Fofonoff inertial flow*

Consider a general pure inertial quasi-geostrophic flow in a homogeneous ocean. This flow satisfies the barotropic vorticity equation with zero wind stress ($\mathbf{T} = \mathbf{0}$) and without frictional effects ($\delta_S = \delta_M = 0$).

a. Show that the resulting equation is given by

$$\mathbf{u} \cdot \nabla \left(\left(\frac{\delta_I}{L} \right)^2 \nabla^2 \psi + y \right) = 0$$

where $\mathbf{u}$ is the horizontal velocity vector. Give a physical interpretation of this vorticity balance.

Consider now an inertial current and the situation that the ocean is bounded at $x = 0$ by a coast. The flow is purely zonal for $x \to \infty$ and it has a dimensionless horizontal velocity field given by $u = -1$ and $v = 0$.

b. Demonstrate that in this case, the absolute vorticity is a linear function of the streamfunction.

c. Consider the western boundary layer (with $\delta_I \ll L$) and show that the total solution is given by

$$\psi_W(x, y) = (y - y_0)(1 - e^{-xL/\delta_I})$$

where y_0 is an arbitrary north-south location for which $\psi = 0$ for all x. From now, take $y_0 = 0$.

Consider now the new situation in which there is also a continental boundary at $x = 1$. Between the continents, the flow is still purely zonal.

d. Show that the total solution (with western and eastern boundary layers) can be written as

$$\psi_{WE}(x, y) = y(1 - e^{-xL/\delta_I} - e^{-(1-x)L/\delta_I})$$

Finally, we consider a closed basin with a southern boundary at $y = -1$ and a northern boundary at $y = 1$ (where $\psi = 0$).

e. Why are there boundary layers at these northern and southern boundary? Show that the solution is given by

$$\psi_B(x, y) = \psi_{WE}(x, y) + c_1 e^{-(1-y)L/\delta_I} + c_2 e^{-(y+1)L/\delta_I}$$

and determine the constants c_1 and c_2.

f. Make a sketch (or plot) of the resulting flow under e. This is the Fofonoff inertial flow.

(6.5) *Weakly nonlinear Stommel model*

Consider the barotropic vorticity equation (6.22)

$$(\frac{\delta_I}{L})^2 \left[\frac{\partial \psi}{\partial x}\frac{\partial}{\partial y} - \frac{\partial \psi}{\partial y}\frac{\partial}{\partial x}\right] \nabla^2\psi + \frac{\delta_S}{L}\nabla^2\psi = -\frac{\partial \psi}{\partial x} - \frac{\partial \tau^x}{\partial y}$$

for the dimensionless wind-stress field

$$\tau^x = -\frac{1}{\pi}\cos \pi y$$

in an ocean basin $[0, 1] \times [0, 1]$. Let $\delta_S/L = \varepsilon$ (where $\varepsilon \ll 1$ is not the Rossby number but just a small parameter) and scale $\delta_I/L = R\,\varepsilon^p$ for certain p and $R = \mathcal{O}(1)$ with respect to ε.

For this case, the Sverdrup (ψ^0) and Stommel solution were determined in section 6.4. Introduce now a western boundary layer coordinate λ, with

$$\lambda = \frac{x}{\varepsilon^q}$$

with $q > 0$ and let $\phi = \psi - \psi^0$.

a. Show that the highest order balance at the western boundary reduces to

$$R\,\varepsilon^{p-2q}\left[\phi_\lambda \phi_{\lambda\lambda y} - \phi_{\lambda\lambda\lambda} - \psi^0_y\right] + \varepsilon^{1-q}\phi_{\lambda\lambda} + \phi_\lambda = 0$$

where $\phi_\lambda = \partial\phi/\partial\lambda$, etc.

b. Provide the correct boundary conditions for the function ϕ.

c. Determine all possible balances in the western boundary layer depending on (p, q) and sketch the different cases in the (p, q)-plane.

d. Argue why the nonlinear correction to the Stommel solution has no north-south symmetry.

Chapter 7

FREE WAVES

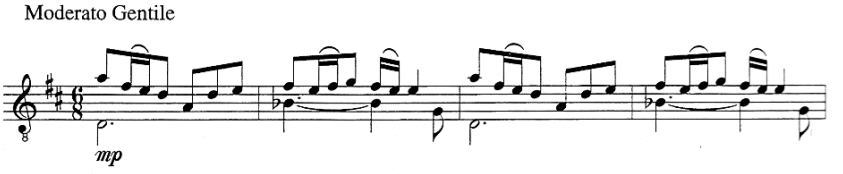

Etude No 4., G. Garcia

In the previous chapter, we only considered the steady circulation on large spatial scales. In this and the next three chapters, we will consider time-dependent problems. A prototype problem is how an ocean flow evolves when at a certain time t_0, the wind stress is changed. To solve this so-called adjustment problem (which is actually done in chapter 9), we focus in this chapter on the basic ingredients of the response: the free waves. We restrict ourselves here to the free waves that can be described by the constant density shallow-water equations (section 7.1). In section 7.2, gravity waves in a horizontally unbounded geometry and a zonal channel are presented (Poincaré and Kelvin waves) and mechanisms of propagation are presented. The impact of bottom topography and the β-effect is considered in the sections 7.3 and 7.4 leading to a description of Rossby waves.

Note: All equations in this chapter are dimensional and we will therefore omit the star subscript.

7.1. Small amplitude motions

Consider the situation of a motionless liquid layer with a constant depth $H_0(x, y)$ that rotates around the vertical axis with a constant angular velocity Ω. Suppose that the flow can be well-described by the special form of the shallow-water equations (4.30a-b) and (4.32), which we here restate for convenience

$$\frac{Du}{dt} - fv = -g\frac{\partial h}{\partial x}, \tag{7.1a}$$

$$\frac{Dv}{dt} + fu = -g\frac{\partial h}{\partial y}, \tag{7.1b}$$

$$\frac{\partial H}{\partial t} + \frac{\partial}{\partial x}(Hu) + \frac{\partial}{\partial y}(Hv) = 0. \tag{7.1c}$$

Here, $H = h + D_0 - h_b$ is the total depth of the layer, $f = 2\Omega$ is the Coriolis parameter and h is the surface elevation.

In this situation small amplitude perturbations (quantities with a tilde) are assumed to be superposed on the background state $\bar{H} = H_0, \bar{u} = \bar{v} = 0$, i.e.,

$$H(x, y, t) = H_0(x, y) + \varepsilon\tilde{h}(x, y, t), \tag{7.2a}$$

$$u(x, y, t) = \varepsilon\tilde{u}(x, y, t)\ ;\ v(x, y, t) = \varepsilon\tilde{v}(x, y, t), \tag{7.2b}$$

where ε (not the Rossby number ϵ here!) is the amplitude of the perturbations with $(\varepsilon \ll 1)$. The $\mathcal{O}(\varepsilon)$ balances in (4.30a-b) and (4.32) become

$$\frac{\partial\tilde{u}}{\partial t} - f\tilde{v} = -g\frac{\partial\tilde{h}}{\partial x}, \tag{7.3a}$$

$$\frac{\partial \tilde{v}}{\partial t} + f\tilde{u} = -g\frac{\partial \tilde{h}}{\partial y}, \tag{7.3b}$$

$$\frac{\partial \tilde{h}}{\partial t} + \frac{\partial}{\partial x}(H_0\tilde{u}) + \frac{\partial}{\partial y}(H_0\tilde{v}) = 0. \tag{7.3c}$$

With $U(x,y,t) = H_0(x,y)\tilde{u}(x,y,t), V(x,y,t) = H_0(x,y)\tilde{v}(x,y,t)$ and $\eta = \tilde{h}$, (7.3) can be written as

$$\frac{\partial U}{\partial t} - fV = -gH_0\frac{\partial \eta}{\partial x}, \tag{7.4a}$$

$$\frac{\partial V}{\partial t} + fU = -gH_0\frac{\partial \eta}{\partial y}, \tag{7.4b}$$

$$\frac{\partial \eta}{\partial t} + \frac{\partial U}{\partial x} + \frac{\partial V}{\partial y} = 0. \tag{7.4c}$$

This system of equations can be reduced to a single equation for η. First, we differentiate (7.4a) with respect to x and (7.4b) with respect to y and then we add the result. This gives

$$\frac{\partial}{\partial t}\left[\frac{\partial U}{\partial x} + \frac{\partial V}{\partial y}\right] - f\left[\frac{\partial V}{\partial x} - \frac{\partial U}{\partial y}\right] = -g\nabla\cdot(H_0\nabla\eta). \tag{7.5}$$

Next, we differentiate (7.4b) with respect to x and subtract (7.4a) differentiated with respect to y from the result. This gives

$$\frac{\partial}{\partial t}\left[\frac{\partial V}{\partial x} - \frac{\partial U}{\partial y}\right] + f\left[\frac{\partial V}{\partial y} + \frac{\partial U}{\partial x}\right] = -gJ(H_0,\eta), \tag{7.6}$$

where the Jacobian $J(f,g)$ is a short notation for (with f and g two arbitrary scalar functions)

$$J(f,g) = \frac{\partial f}{\partial x}\frac{\partial g}{\partial y} - \frac{\partial f}{\partial y}\frac{\partial g}{\partial x}. \tag{7.7}$$

as in (6.73 As a third step, we differentiate (7.5) with respect to t and use (7.6) with the result

$$\left[\frac{\partial^2}{\partial t^2} + f^2\right]\left[\frac{\partial U}{\partial x} + \frac{\partial V}{\partial y}\right] = -g\frac{\partial}{\partial t}\nabla\cdot(H_0\nabla\eta) - fg\,J(H_0,\eta). \tag{7.8}$$

As a final step, we use the relation (7.4c) in (7.8), and find the equation for η to be

$$\frac{\partial}{\partial t}\left[(\frac{\partial^2}{\partial t^2} + f^2)\eta - \nabla\cdot(gH_0\nabla\eta)\right] - fg\,J(H_0,\eta) = 0. \tag{7.9}$$

Ex. 7.1

If η is determined, then it follows that $\tilde{h} = \eta$ and the velocities $\tilde{u}$ and $\tilde{v}$ follow by differentiating (7.3a-b) with respect to t with the result

$$(\frac{\partial^2}{\partial t^2} + f^2)\tilde{u} = -g\frac{\partial^2 \tilde{h}}{\partial x \partial t} + f\frac{\partial \tilde{h}}{\partial y}, \tag{7.10a}$$

$$(\frac{\partial^2}{\partial t^2} + f^2)\tilde{v} = -g\frac{\partial^2 \tilde{h}}{\partial y \partial t} - f\frac{\partial \tilde{h}}{\partial x}. \tag{7.10b}$$

The equations above describe the evolution of small amplitude perturbations on the motionless solution. In the next sections, we will consider specific geometrical situations and determine the free wave solutions in these cases.

7.2. Free waves: H_0 constant

In the case where H_0 is constant, we introduce $C_0^2 = gH_0$ and (7.9) reduces to

$$\frac{\partial}{\partial t}\left[(\frac{\partial^2}{\partial t^2} + f^2)\eta - C_0^2 \nabla_H^2 \eta\right] = 0, \tag{7.11}$$

where $\nabla_H^2 = \partial^2/\partial x^2 + \partial^2/\partial y^2$ is the horizontal Laplace operator.

7.2.1. Unbounded domain

When the domain is horizontally unbounded, there exist free wave solutions of (7.11) with the representation

$$\eta(x, y, t) = \eta_0 \, e^{i(kx+ly-\sigma t)}, \tag{7.12}$$

with phase $\theta = kx + ly - \sigma t$ and wavevector $\mathbf{k} = \nabla\theta$ (see Fig. 7.1). Substitution

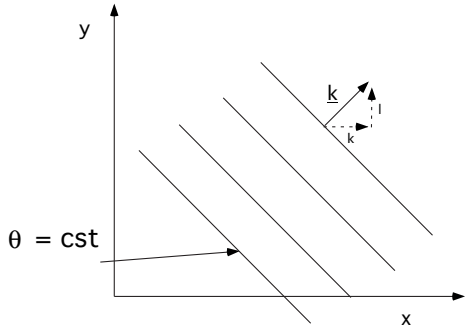

Figure 7.1. Lines of constant phase θ in the x-y plane and the wavevector $\mathbf{k}$.

of (7.12) into (7.11) gives

$$\sigma\eta_0(f^2 - \sigma^2 + C_0^2(k^2 + l^2)) = 0. \tag{7.13}$$

The interesting cases are when $\sigma \neq 0$ and from (7.13) we find the dispersion relation

$$\sigma = \pm\sqrt{f^2 + C_0^2(k^2 + l^2)}. \tag{7.14}$$

The dispersion relation shows that for every wavevector $\mathbf{k} = (k, l)^T$, there are two free waves with a phase speed $C = \sigma/|\mathbf{k}|$ in the (positive and negative) direction of the wavevector $\mathbf{k}$, with

$$C = \frac{\sigma}{\sqrt{k^2 + l^2}} = \pm\sqrt{C_0^2 + \frac{f^2}{(k^2 + l^2)}}. \tag{7.15}$$

For $f = 0$, the dispersion relation (7.14) reduces to that for 'normal' gravity waves with phase speed $C_0 = (gH_0)^{1/2}$. For $f \neq 0$, it follows from (7.14) that the frequency of these so-called Poincaré waves is always larger than f, in other words the period is always shorter than the inertial period f^{-1}. Ex. 7.2

The physical mechanism of propagation of a 'normal' gravity wave (with $f = 0$) is as follows. Consider a one-dimensional wave (with $\tilde{v} = 0$) as in Fig. 7.2a. At locations where $\partial\eta/\partial x < 0$, the corresponding pressure gradient causes a local acceleration $\partial\tilde{u}/\partial t > 0$. The resulting flow causes a local change in the position of the free surface according to

$$\frac{\partial\eta}{\partial t} = -H_0\frac{\partial\tilde{u}}{\partial x}.$$

and hence the wave propagates to the right. To determine the effect of plane-

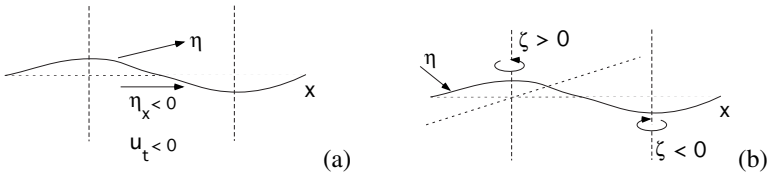

Figure 7.2. (a) Sketch to explain the propagation mechanism of a 'normal' gravity wave. (b) Sketch to explain the propagation mechanism of a Poincaré wave.

tary rotation on the propagation of the waves, we consider the change in relative vorticity, the latter has also the form

$$\zeta(x, y, t) = \zeta_0\, e^{i(kx+ly-\sigma t)}.$$

The amplitude ζ_0 follows through substitution (together with (7.12)) into (7.6) and we find

$$\sigma \left[\zeta_0 - \frac{f\eta_0}{H_0} \right] = 0,$$

which exactly represents the conservation of the linearized potential vorticity. With the help of (7.14), we see that the relative vorticity is proportional to the interface height through vortex stretching. If $\eta_0 > 0$ ($\eta_0 < 0$), then the change in relative vorticity (in the northern hemisphere) is also positive (negative); this is sketched in Fig. 7.2b. Because of the induced velocities through this vorticity distribution, the wave now propagates faster than the corresponding wave with $f = 0$.

7.2.2. Zonal channel

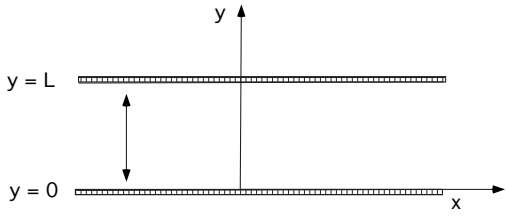

Figure 7.3. Sketch of the geometry of a zonal channel having a width L.

Now consider the free wave solutions in a zonal channel as sketched in Fig. 7.3, still using the assumption that H_0 is constant. The only new feature, compared to the previous case, is the existence of meridional boundaries at $y = 0, L$. Because lateral friction is neglected, the boundary conditions are only kinematic, e.g., $\tilde{v} = 0$. Free waves can again be described by (7.11) and (7.10b) with the latter only applied at $y = 0, L$:

$$\frac{\partial}{\partial t} \left[(\frac{\partial^2}{\partial t^2} + f^2)\eta - C_0^2 \nabla_H^2 \eta \right] = 0, \tag{7.16a}$$

$$y = 0, L: \qquad g\frac{\partial^2 \eta}{\partial y \partial t} + f\frac{\partial \eta}{\partial x} = 0. \tag{7.16b}$$

Because of the boundaries, solutions of the form of (7.12) no longer exist. The domain is, however, still unbounded in the x-direction and hence free wave solutions can be represented by

$$\eta(x, y, t) = \hat{\eta}(y) e^{i(kx - \sigma t)}, \tag{7.17}$$

where $\hat{\eta}(y)$ is the (still unknown) y-structure of the waves. Substitution of (7.17) into (7.16) gives

$$\hat{\eta}'' + \left[\frac{\sigma^2 - f^2}{C_0^2} - k^2\right]\eta = 0, \tag{7.18a}$$

$$g\hat{\eta}'(0) + f\frac{k}{\sigma}\hat{\eta}(0) = 0 \quad ; \quad g\hat{\eta}'(L) + f\frac{k}{\sigma}\hat{\eta}(L) = 0. \tag{7.18b}$$

where the primes indicate differentiation to y.

The solution of (7.18a) is

$$\hat{\eta}(y) = A\sin\alpha y + B\cos\alpha y \tag{7.19a}$$

$$\alpha^2 = \frac{\sigma^2 - f^2}{C_0^2} - k^2, \tag{7.19b}$$

and the two homogeneous boundary conditions (7.18b) lead to a system of two homogeneous equations for A and B, i.e.,

$$\alpha g A + \frac{fk}{\sigma}B = 0 \tag{7.20a}$$

$$A(\alpha g\cos\alpha L + \frac{fk}{\sigma}\sin\alpha L) + B(\frac{fk}{\sigma}\cos\alpha L - \alpha g\sin\alpha L) = 0 \tag{7.20b}$$

This system has only a nontrivial solution when the coefficient determinant is zero. This provides the eigenvalues σ as zeroes of

$$(\sigma^2 - f^2)(\sigma^2 - C_0^2k^2)\sin\alpha L = 0. \tag{7.21}$$

When σ is determined from (7.21), then α^2 follows immediately from (7.19b) and as the equations for A and B are a dependent system, the eigenfunction $\hat{\eta}(y)$ can be calculated from (7.19a).

From (7.21) several free wave types are obtained. These are summarized below:

(i) *Kelvin waves*

One of the solutions of (7.21) is

$$\sigma = \pm C_0 k, \tag{7.22}$$

and the phase speed of these so-called Kelvin waves is $\sigma/k = \pm C_0$; Kelvin waves are hence nondispersive waves. Consider a wave that moves in the positive x-direction, i.e. with $\sigma = C_0$k. With $\alpha^2 = -f^2/C_0^2$ it follows that $\alpha = if/C_0$ and with (7.19a) the eigenfunction $\hat{\eta}(y)$ is

$$\hat{\eta}(y) = -iA\, e^{-\frac{yf}{C_0}}. \tag{7.23}$$

As the amplitude A is arbitrary, we just make the choice $A = i$ such that (7.17) provides a real function η. The result is

Ex. 7.3

$$\eta(x, y, t) = e^{-\frac{yf}{C_0}} \cos k(x - C_0 t). \tag{7.24}$$

This is a 'normal' plane wave that propagates in the positive x-direction with a simple fixed y-profile. The characteristic meridional decay scale of η is the external Rossby deformation radius (cf. section 3.1)

$$R_D = \frac{C_0}{f} = \frac{\sqrt{gH_0}}{f}. \tag{7.25}$$

The velocities $\tilde{u}$ and $\tilde{v}$ of the Kelvin wave follow from (7.10) as

$$\tilde{u} = \frac{g}{C_0} e^{-\frac{yf}{C_0}} \cos k(x - C_0 t) = -\frac{g}{f}\frac{\partial \eta}{\partial y}, \tag{7.26a}$$

$$\tilde{v} = 0, \tag{7.26b}$$

such that the x-component of the velocity is in geostrophic balance, as sketched in Fig. 7.4. If the wave propagates westward, then $u > 0$ and the Coriolis acceleration (to the right of the motion for $f > 0$) is exactly compensated by the pressure gradient due to the deformation of the free surface. The external Rossby deformation radius is exactly that length scale such that the pressure differences due to deformation of the free surface are large enough to balance the Coriolis acceleration. The propagation mechanism in the x-direction is similar to that of gravity waves with $f = 0$.

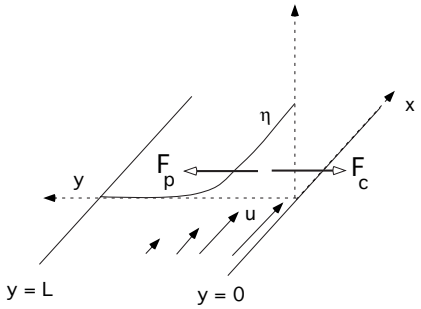

Figure 7.4. Momentum balances in the Kelvin wave (in the Northern Hemisphere), where F_p represents the pressure gradient force (- ∇p) and F_c the Coriolis force.

(ii) *Inertial oscillation* Another solution of the dispersion relation (7.21) is

$$\sigma = \pm f. \tag{7.27}$$

The case $k = f/C_0$ can be considered as a special case of a Kelvin wave and the amplitude of η is given by (for $\sigma = f$):

$$\eta(x, y, t) = e^{-ky} \cos(kx - ft). \tag{7.28}$$

(iii) *Poincaré waves*

The last solution of the dispersion relation is given by

$$\begin{aligned} \alpha^2 L^2 &= L^2\left(\frac{\sigma^2 - f^2}{C_0^2} - k^2\right) = n^2\pi^2, n = 1, 2, ... \Rightarrow \\ \sigma = \sigma_n &= \pm\sqrt{f^2 + C_0^2(k^2 + (\frac{n\pi}{L})^2)}, n = 1, 2, ... \end{aligned} \tag{7.29}$$

Comparing the dispersion relation (7.14) and (7.29), we see that the zonal channel has 'discretized' the spectrum of the Poincaré waves; the meridional wavenumber l is now given by $n\pi/L$. Note that the Poincaré wave for $n = 0$ does not provide a consistent solution since $\alpha = 0$ and hence $\hat{\eta}$ has no y dependence. This eigenfunction cannot satisfy the boundary conditions at the meridional walls. The Kelvin wave can be considered as this $n = 0$ wave in the limit $R_D \to \infty$.

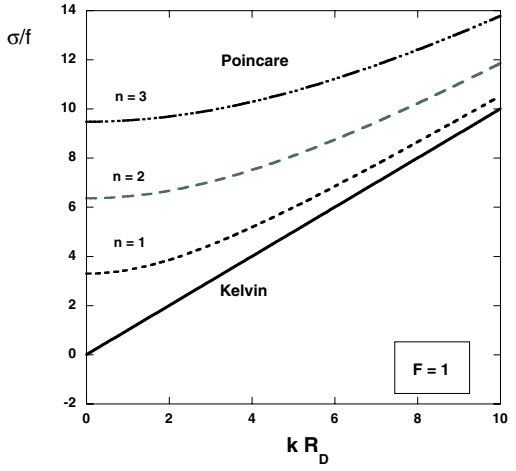

Figure 7.5. Dispersion relation (for $k > 0$) of (n=1, 2 and n=3) Poincaré waves and the Kelvin wave for $F = (L/R_D)^2 = 1$.

The total spectrum of free waves is summarized in Fig. 7.5 where the dispersion relation is plotted for the $n = 1, n = 2$ and $n = 3$ Poincaré waves and the

Kelvin wave. Note that the frequency approaches zero for the Kelvin wave but the Poincaré waves keep finite frequencies.

7.3. Free waves: $H_0 = H_0(y)$

In this section, we consider free waves in a zonal channel, but now in the presence of small variations in bottom topography. As a specific case, we choose

$$H_0(y) = D(1 - s\frac{y}{L}), \tag{7.30}$$

where L is the width of the channel (Fig. 7.3) and $s \ll 1$. Free waves are again of the form (7.17), e.g.,

$$\eta(x, y, t) = \hat{\eta}(y)\, e^{i(kx-\sigma t)}. \tag{7.31}$$

We substitute (7.31) into (7.9) and the boundary conditions (7.10b) at $y = 0, L$ ($\tilde{v} = 0$) with the result

$$(1 - s\frac{y}{L})\hat{\eta}'' - \frac{s}{L}\hat{\eta}' \quad + \quad \hat{\eta}(\frac{\sigma^2 - f^2}{C_0^2} - k^2(1 - s\frac{y}{L}) - \frac{fs}{L\sigma}) = 0, \tag{7.32a}$$

$$\hat{\eta}'(0) + f\frac{k}{\sigma}\hat{\eta}(0) \quad = \quad \hat{\eta}'(L) + f\frac{k}{\sigma}\hat{\eta}(L) = 0, \tag{7.32b}$$

where $C_0^2 = gD$. The general problem (7.32) can be solved numerically, but for $s \ll 1$, we can approximate $1 - sy/L \approx 1$. This is the only reduction, because we cannot *a priori* estimate the order of magnitude of the different terms in (7.32).

Solutions of (7.32) are given by

$$\hat{\eta}(y) = e^{\frac{sy}{2L}}(A \sin \alpha y + B \cos \alpha y), \tag{7.33a}$$

$$\alpha^2 = \frac{\sigma^2 - f^2}{C_0^2} - (k^2 + \frac{s^2}{4L^2}) - \frac{fks}{\sigma L}. \tag{7.33b}$$

The dispersion relation again follows through application of the boundary conditions and by requiring the coefficient determinant of the homogeneous system in A and B to be zero. One finds a similar expression as (7.21), i.e.,

$$(\sigma^2 - f^2)(\sigma^2 - C_0^2 k^2) \sin \alpha L = 0. \tag{7.34}$$

The Kelvin waves are therefore not influenced by small topographic features; this was expected based on the physical mechanism of their propagation. The solutions of the equation $\sin \alpha L = 0$ are

$$\alpha^2 L^2 = L^2 \left[\frac{\sigma^2 - f^2}{C_0^2} - (k^2 + \frac{s^2}{4L^2}) - \frac{fks}{\sigma L} \right] = (n\pi)^2, \tag{7.35}$$

or

$$\sigma^2 - \frac{fks}{\sigma L}C_0^2 - C_0^2(k^2 + \frac{n^2\pi^2}{L^2} + \frac{f^2}{C_0^2}) = 0. \tag{7.36}$$

Equation (7.36) is a third order polynomial and hence there are three roots. For $s = 0$ we again find the Poincaré waves and because now $|\sigma| > f$ these waves are slightly modified due to the topography. With $\sigma = \mathcal{O}(f)$, the second term in (7.36) is small when $s \to 0$. The only way in which this term can be of any importance is when $\sigma = \mathcal{O}(s)$; in that case, the terms with σ^2 can be neglected. The new class of waves, the so-called Rossby waves, therefore has a dispersion relation given by

$$\sigma = -\frac{skf}{L}\frac{1}{k^2 + \frac{n^2\pi^2}{L^2} + \frac{f^2}{C_0^2}}, n = 1, 2, 3, \ldots \tag{7.37}$$

and hence they are low-frequency waves (frequency much smaller than f).

In this situation, the existence of the waves depends on the variations of the topography. In addition, the waves occur only in a rotating fluid. In the physical mechanism of propagation of the waves, both these elements are crucial. The special character of the waves is that their phase speed in the x-direction ($C_x = \sigma/k$) is always negative. Because the fluid depth decreases with y, when $s > 0$, an observer moving with the wave always sees a deeper layer to the left. Ex. 7.4

For a Rossby wave, it follows that $|\sigma| \ll f$ which confirms that the period is much larger than $1/f$. Hence, these waves are prototypes for explaining low-frequency variability in the ocean and atmosphere. The corresponding eigenfunction $\hat{\eta}(y)$ is

$$\hat{\eta}(y) = \eta_0 \sin\frac{n\pi y}{L} + \mathcal{O}(s), \tag{7.38}$$

which follows from (7.32). The $n = 0$ case also gives a physically meaningful wave; it follows from (7.38) that $\tilde{v} = 0$ and boundary conditions can be satisfied.

For Rossby waves the time derivatives are an order of magnitude smaller than the spatial derivatives, for example $\partial^2/\partial t^2 = -\sigma^2 \ll f^2$), and the equations (7.3a-b) reduce to

$$f\tilde{u} = -g\frac{\partial\eta}{\partial y}, \tag{7.39a}$$

$$f\tilde{v} = g\frac{\partial\eta}{\partial x}. \tag{7.39b}$$

Hence, the horizontal velocity field is in geostrophic balance, while the propagation of the wave is controlled by ageostrophic processes.

To understand the propagation mechanism, we return to the general equation (7.9) which, for $H_0(y)$ and $|\sigma| \ll f$ reduces to

$$\frac{\partial}{\partial t}(f^2\eta - gH_0\nabla_H^2\eta - g\frac{\partial H_0}{\partial y}\frac{\partial\eta}{\partial y}) + fg\frac{\partial H_0}{\partial y}\frac{\partial\eta}{\partial x} = 0. \tag{7.40}$$

If $\partial H_0/\partial y$ is small, then the third term within the time-derivative can be neglected with respect to the other two terms. If we use (7.39) in the form

$$gH_0\nabla_H^2\eta = H_0 f(\frac{\partial \tilde{v}}{\partial x} - \frac{\partial \tilde{u}}{\partial y}) = H_0 f\tilde{\zeta}, \tag{7.41}$$

where $\tilde{\zeta}$ is the z-component of the vorticity vector, then it follows

$$\frac{\partial}{\partial t}\left[\tilde{\zeta} - \frac{f\eta}{H_0}\right] - \tilde{v}\frac{\partial H_0}{\partial y}\frac{f}{H_0} = 0. \tag{7.42}$$

This again suggests conservation of potential vorticity and this time in terms of small amplitude motions. Indeed, if we substitute $H = H_0(y) + \eta$, $u = \tilde{u}$, $v = \tilde{v}$ and $\zeta = \tilde{\zeta}$ into the potential vorticity $\Pi = (\zeta + f)/H$ with $D\Pi/dt = 0$ then we find (7.42) through linearization. The general equation (7.9) can thus be derived from a linearized form of conservation of potential vorticity. Hence, we can use

$$\frac{D}{dt}\left(\frac{\zeta + f}{H}\right) = 0, \tag{7.43}$$

to describe the physical mechanism of propagation of Rossby waves.

Three columns of water which are initially motionless at a latitude $y = y_0$ are sketched in Fig. 7.6. Assume that the topography is such that the layer thickness decreases northward and that the interface does not deform. Now at $t = 0$, column B is displaced northward as an initial perturbation. Because it moves to a location where H is smaller (note that f is constant), column B must get a negative relative vorticity because of conservation of potential vorticity. This anticyclonic movement of column B induces velocities in both columns A and C, such that A moves northward and C southward. Column C starts to rotate cyclonic (positive vorticity) because it moves into an area where the liquid depth increases, but column A get a negative vorticity, similar to column B. The velocities induced through the rotation of both columns A and C on column B drive column B back to the position $y = y_0$. As it passes through this latitude, it moves southward and hence the next half phase of the cycle can be described as above but with opposite signs of the motions. Through the description, we see the wave moving westward.

To summarize, we have seen that in a situation of constant f, there exist several types of gravity waves. The local acceleration is of central importance to the propagation of 'normal' gravity waves and Poincaré waves. These waves have relatively large phase speeds. In Kelvin waves the local acceleration is not important, but these waves only exist in the presence of a boundary (and at the equator, as we will see in chapter 11). Long Kelvin waves have a long period, but the only waves which are possibly relevant for long time scale variability in the oceans (with frequencies much smaller than f) are the Rossby waves.

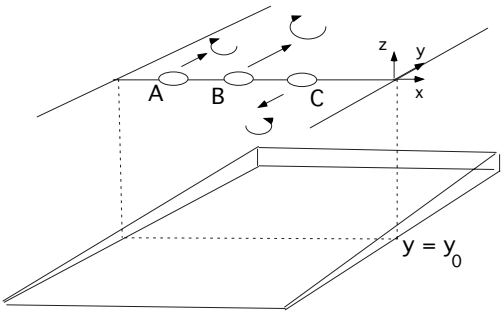

Figure 7.6. Propagation mechanism of Rossby waves in a layer of liquid on a sloping bottom.

Additional Material

B: Many books and articles deal with gravity waves in the atmosphere and ocean. A less mathematical approach can be found in chapter 6 of Cushman-Roisin (1994).

D: In the lectures 13 to 16 of Pedlosky (2003) and chapter 5 of Gill (1982) many issues on the energetics of waves and wave packets are discussed.

7.4. Free waves in the quasi-geostrophic model

We return to the barotropic quasi-geostrophic theory in section 5.3 where the evolution of the flow could be described by one scalar equation, the barotropic vorticity equation (5.91). In dimensional form (with the same scaling as in section 5.3), the unforced, nondissipative form of this equation is

$$\left[\frac{\partial}{\partial t} - \frac{\partial \psi}{\partial y}\frac{\partial}{\partial x} + \frac{\partial \psi}{\partial x}\frac{\partial}{\partial y}\right](\nabla^2\psi + \beta_0 y - \lambda_0\psi + \frac{f_0}{D}h_b) = 0, \tag{7.44}$$

where ψ is the geostrophic streamfunction and h_b the bottom topography and $\lambda_0 = f_0^2/(gD) = 1/R_D^2$. The evolution of small amplitude perturbations on the motionless flow for a bottom topography $h_b(y)$ can be described by

$$\frac{\partial}{\partial t}(\nabla^2\psi - \lambda_0\psi) + (\beta_0 + \frac{f_0}{D}\frac{\partial h_b}{\partial y})\frac{\partial \psi}{\partial x} = 0. \tag{7.45}$$

Consider the example $h_b = sDy/L$ equivalent to the case where the total layer thickness ($H = D - h_b$) of the situation $H_0 = D(1 - sy/L)$ in the previous section. Free wave solutions in the unbounded horizontal plane can be represented as

$$\psi(x, y, t) = \psi_0\, e^{i(kx+ly-\sigma t)}, \tag{7.46}$$

and substitution into (7.45) gives the dispersion relation as

$$\sigma = \frac{-k(\beta_0 + \frac{f_0}{sL})}{k^2 + l^2 + \lambda_0}. \tag{7.47}$$

With $\lambda_0 = f_0^2/C_0^2$ (section 5.3), we find

$$\sigma = -(\frac{sf_0}{L} + \beta_0)\frac{k}{k^2 + l^2 + f^2/C_0^2}, \tag{7.48}$$

Ex. 7.5

which is similar to the dispersion relation (7.37) for Rossby waves if $l = n\pi/L$ and $\beta_0 = 0$.

In the quasi-geostrophic theory, only the Rossby waves appear as free wave solutions and the other waves are 'filtered'. This is consistent with the results on the propagation mechanisms of the waves in the previous section: only for the Rossby waves the velocity field is in geostrophic equilibrium. In addition, it follows from (7.48) that in the homogeneous quasi-geostrophic case, there is a dynamic equivalence between the effect of small variations of bottom topography and latitudinal variations of the Coriolis acceleration. As a consequence, Rossby waves are expected to be fairly general in the ocean and will appear even without variations in topography.

Summary

- In a constant density rotating (with constant f_0) shallow-water layer of constant depth H_0 without horizontal boundaries there are only Poincaré waves with a dispersion relation

$$\sigma = \pm\sqrt{f_0^2 + C_0^2(k^2 + l^2)}$$

  where $C_0 = \sqrt{gH_0}$.

- When meridional boundaries are present with a distance L apart, Kelvin waves can occur. These waves have a typical length scale R_D and a frequency σ given by

$$R_D = \frac{C_0}{f_0}\ ;\ \sigma = \pm C_0 k$$

- When bottom topography and/or the β-effect is present, Rossby waves can occur. In case of a linear slope $H_0(y) = D(1 - sy/L)$, with $s \ll 1$ these Rossby waves have a dispersion relation on the β-plane given by

$$\sigma = -(\frac{sf_0}{L} + \beta_0)\,\frac{k}{k^2 + l^2 + f^2/C_0^2}$$

- In the quasi-geostrophic approximation, the Poincaré waves are filtered and only Rossby waves can be represented.

7.5. Exercises on chapter 7

(7.1) *Standing waves: closed basin*

Consider one-dimensional gravity waves with a sea surface amplitude $\eta(x,t)$ and velocity $u(x,t)$ in a basin with length L and in a water layer of depth H; assume rotation is absent.

a. Show that the equations (7.4) reduce to

$$\frac{\partial \eta}{\partial t} + H\frac{\partial u}{\partial x} = 0 \; ; \; \frac{\partial u}{\partial t} + g\frac{\partial \eta}{\partial x} = 0$$

b. Show that both u and η satisfy wave equations with wavespeed $C = \sqrt{gH}$.

c. What are the boundary conditions at $x = 0$ and $x = L$?

d. Show that the solutions of these equations can be written as

$$\eta(x,t) = \sum_{n=1}^{\infty} A_n \cos k_n x \cos \sigma_n t$$

$$u(x,t) = \frac{C}{H} \sum_{n=1}^{\infty} A_n \sin k_n x \sin \sigma_n t$$

where the A_n are constants and

$$k_n = \frac{n\pi}{L} \; ; \; \sigma_n = \frac{n\pi C}{L}$$

(7.2) *Standing waves: half open basin*

Consider the same situation as in the previous exercise, but now with an open boundary at $x = L$.

a. What is the boundary condition at $x = L$ in this case?

b. Show (again with separation of variables) that the solutions can be written as

$$\eta(x,t) = \sum_{n=1}^{\infty} \cos k_n x (A_n \sin \sigma_n t + B_n \cos \sigma_n t)$$

$$u(x,t) = \frac{C}{H} \sum_{n=1}^{\infty} \sin k_n x (-A_n \cos \sigma_n t + B_n \sin \sigma_n t)$$

where A_n and B_n are constants and determine the k_n and σ_n.

Suppose that the flow is forced at the open boundary by a tide with amplitude

$$\eta(L,t) = \eta_0 \cos \omega t$$

Assume that the sea-surface is at rest for $t = 0$.

c. Determine the total solution of this forced problem for $t > 0$.

(7.3) *Phase versus group velocity*

For Poincaré waves, the phase speed is given by (7.14). The group velocity is defined as:

$$\mathbf{C}_g = \begin{pmatrix} \frac{\partial \sigma}{\partial k} \\ \frac{\partial \sigma}{\partial l} \end{pmatrix}$$

a. Determine the group velocity for Poincaré waves.

b. Are these waves dispersive?

(7.4) *Kelvin wave*

At midlatitudes, Kelvin waves move along coasts.

a. In which direction (north or south) propagate these waves if they move along the European Atlantic coast?

Suppose that a Kelvin wave propagates in a layer of water with a thickness $H_0 = 10^3$ m.

b. Calculate the Rossby deformation radius of such a wave at 45°N.

c. Determine the time τ that is needed for a Kelvin wave to propagate over a distance of 1000 km.

(7.5) *Topography and Rossby waves*

A Rossby wave with wavenumbers $k = k_0$ and $l = 0$ propagates (at 45°N) over a seamount with a spatial distribution

$$\eta_b(x, y) = \eta_0 e^{-((x-x_0)^2+(y-y_0)^2)}$$

where (x_0, y_0) is a point in the middle of the basin.

a. Sketch the deviation of the lines of constant phase caused by the presence of the topography.

b. At which side of the seamount can stationary Rossby waves occur?

Chapter 8

STRATIFICATION

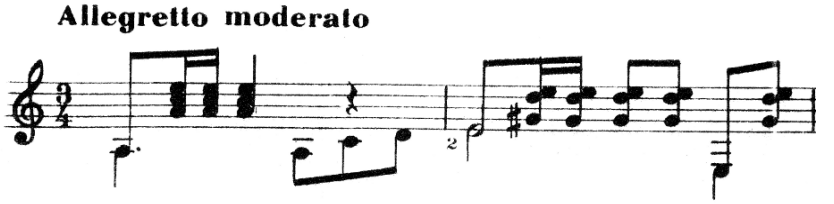

Bolero, B. Calatayud

In this chapter we will extend the theory so far to include stratification. In section 8.1 a heuristic introduction is given why the internal Rossby deformation radius L_D is such an important scale of motion. The formulation and use of potential vorticity in a stratified rotating liquid is presented in section 8.2. In section 8.3 we then proceed with the derivation of the continuously stratified quasi-geostrophic model. Finally, Rossby waves in a stratified, rotating liquid in a domain with bottom topography are discussed of section 8.4.

8.1. Rotation versus Stratification

Suppose we have flow with a stratification $\rho = \rho_0 + \bar{\rho}(z)$ where $\bar{\rho}(z)$ is called the background stratification and ρ_0 is a reference density. The effect of stratification on a flow with a horizontal length scale L is determined by the value of the buoyancy frequency N [s^{-1}], defined by

$$N^2 = -\frac{g}{\rho}\frac{d\rho}{dz} \approx -\frac{g}{\rho_0}\frac{d\bar{\rho}}{dz}, \tag{8.1}$$

as $\rho_0 + \bar{\rho}(z) \approx \rho_0$. We assume that this stratification is present over the length scale L.

The first issue to investigate is the horizontal length scale over which stratification effects will be important. Thereto we consider the situation of flow over topography as sketched in Fig. 8.1.

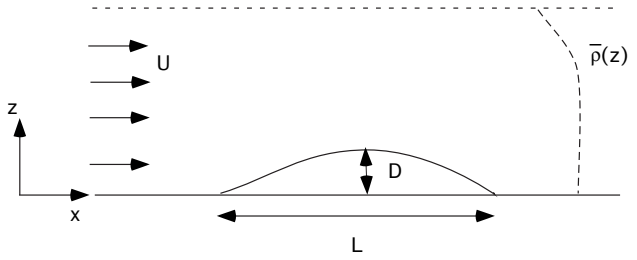

Figure 8.1. Flow over topography with a characteristic horizontal length scale L, vertical length scale D, horizontal velocity U and buoyancy frequency N, the latter determined by $d\bar{\rho}/dz$.

The time that a fluid element needs to cross the topography is the advective timescale $\tau_a = L/U$. Due to the presence of the topography, there will be vertical velocities with an, a priori unknown, characteristic velocity scale W. Due to the

vertical motion, there will be vertical displacements with an amplitude Δz with

$$\Delta z = W\tau_a. \tag{8.2}$$

With $d\bar{\rho}/dz < 0$, the density difference between a particular fluid element that has moved upwards with $\Delta z > 0$ and the background density field (on the same $z-$level) is equal to $\Delta\rho = -(d\bar{\rho}/dz)\Delta z > 0$. If $\Delta z < 0$, then the fluid element is lighter than its environment and $\Delta\rho = -(d\bar{\rho}/dz)\Delta z < 0$. With (8.1-8.2) it follows that

$$\Delta\rho = N^2\frac{\rho_0}{g}\Delta z = N^2\frac{\rho_0}{g}\frac{WL}{U}. \tag{8.3}$$

Differences in density $\Delta\rho$ cause pressure differences Δp and with the hydrostatic balance, we have the estimate

$$\Delta p \approx -gD\Delta\rho = -N^2\frac{\rho_0 WLD}{U}. \tag{8.4}$$

Whether these density induced pressure differences (with magnitude $P = N^2\rho_0 WLD/U$) will influence the flow now depends on other factors (such as the background rotation).

First consider the case in which there is no rotation and where inertia is the dominant term in the momentum balance, with a characteristic pressure scale $\rho_0 U^2$. With (8.4) it follows that

$$U^2 = \frac{P}{\rho_0} = N^2\frac{WLD}{U} \Rightarrow \frac{W/D}{U/L} = \frac{\Delta z}{D} = \frac{U^2}{N^2D^2} = Fr^2. \tag{8.5}$$

The stratified Froude number Fr is a measure of the relative influence of stratification versus inertia. When Fr is small then the stratification is strong and vertical motions will be very small. For large values of Fr, stratification is unimportant compared to inertia.

If we go back to chapter 5 and consider the constant density rotating case, then we know that for the vertical 'outer' velocity, we had the expansion

$$w = w^0 + \epsilon w^1 + \mathcal{O}(\epsilon^2), \tag{8.6}$$

where the first term $w^0 = 0$. The dimensional vertical velocity is scaled with DU/L, such that the actual scale of the vertical velocity is equal to $\epsilon DU/L$. It follows then that

$$W = \epsilon DU/L \Rightarrow \frac{W/D}{U/L} = \epsilon, \tag{8.7}$$

and it is exactly the Rossby number that determines the magnitude of the vertical motion. In a rotating flow with $\epsilon \ll 1$, vertical motions are very restricted and the motion is quasi two-dimensional.

Now assume that in a stratified flow, the Coriolis acceleration is the dominant term in the momentum balance with a characteristic geostrophic pressure $\rho_0 L f_0 U$. With the pressure differences P from (8.4) we derive

$$\frac{W/D}{U/L} = \frac{U^2}{N^2 D^2}\frac{f_0 L}{U} = \frac{Fr^2}{\epsilon}. \tag{8.8}$$

The parameter Fr^2/ϵ provides the scale of the vertical motions in a stratified rotating flow. When Fr increases, the influence of the stratification decreases and the vertical motions will be mainly determined by the rotation; we approximate the constant density case (Fig. 8.2). In the regime where $Fr^2/\epsilon \approx \epsilon$, i.e.

$$\frac{U^2}{N^2 D^2} \approx \frac{U^2}{f_0^2 L^2} \Rightarrow L \approx \frac{ND}{f_0} = L_D, \tag{8.9}$$

the effect of stratification is of the same magnitude as that of rotation. The length scale L_D is the internal Rossby deformation radius (cf. section 3.1).

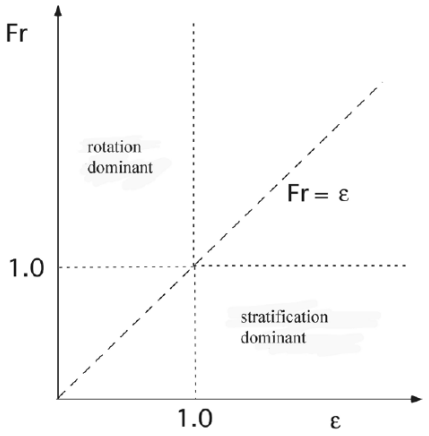

Figure 8.2. Overview of the different flow regimes in a stratified rotating flow.

Typical values of N^2 in the upper layers of the North Atlantic are $N^2 = 10^{-5}$ s^{-2}. With $D = 4 \times 10^3$ m and $f_0 = 10^{-4}$ s^{-1}, a typical value of L_D is about 100 km (see Table 8.1).

U	L	D	N	Fr	ϵ	Fr^2/ϵ
10^{-2}	10^6	10^3	10^{-2}	10^{-3}	10^{-4}	10^{-2}
10^{-1}	10^5	10^3	10^{-2}	10^{-2}	10^{-2}	10^{-2}
m/s	m	m	1/s	-	-	-

Table 8.1. Typical values of ϵ, Fr and Fr^2/ϵ for different values of L, D and N, with $f_0 = 10^{-4}$.

8.2. Potential vorticity (again ...)

In section 4.4 we introduced the general concept of potential vorticity through the Ertel theorem (4.12) as

$$\Pi_{\lambda *} = \frac{\boldsymbol{\omega}_* + 2\boldsymbol{\Omega}}{\rho_*} \cdot \nabla \lambda_*. \tag{8.10}$$

In case $\lambda_*(p_*, \rho_*)$ is a scalar which is constant along streamlines ($D\lambda_*/dt_* = 0$) and the flow is frictionless ($\mathcal{F}_{I*} = 0$), then the potential vorticity $\Pi_{\lambda *}$ is a conserved quantity ($D\Pi_{\lambda *}/dt_* = 0$).

In section 4.5, we saw one example of a constant density flow described by the shallow-water equations in a layer of total thickness H. Here the conserved quantity $\lambda_* = \rho_*(z_* + D - h_{b*})/H_*$ leads to the shallow-water potential vorticity $\Pi_* = (\zeta_* + f)/H_*$. Conservation of Π_* allowed to predict changes in rotation or northward/southward motion over topography, depending on the relative magnitude of ζ_* and f. In exercise (4.4) of chapter 4, for example, $|\zeta_*| \ll f$ and hence conservation of Π_* allows a prediction of poleward movement of a water column over bottom topography (here f/H has to remain constant along streamlines). We have also seen at the end of chapter 5 that in the quasi-geostrophic approximation, the shallow-water potential vorticity Π_* is approximated by

$$\Pi_* = \frac{1}{D}(\nabla^2 \psi_* - \lambda_0 \psi_* + \frac{f_0}{D} h_{b*} + \beta_0 y_*), \tag{8.11}$$

which resulted from an expansion of $\Pi_* = (\zeta_* + f)/H_*$ in the Rossby number ϵ.

If there is both rotation and stratification, one may ask what forms of potential vorticity are useful to predict again changes in rotation and/or latitudinal motion of a fluid column. Suppose that there is a stratification with a density distribution ρ. With a linear of state, the density equation (from 3.32e-f) can be written as

$$\frac{D\rho_*}{dt_*} = K_H \nabla_H^2 \rho_* + K_V \frac{\partial^2 \rho_*}{\partial {z_*}^2}, \tag{8.12}$$

where K_H and K_V are the vertical and horizontal diffusivities of heat and salt. When mixing is negligible, we then find $D\rho_*/dt_* = 0$. According to the Ertel

theorem, with $\lambda_* = \rho_*$ the potential vorticity

$$\Pi_{s*} = \frac{\boldsymbol{\omega}_* + 2\boldsymbol{\Omega}}{\rho_*} \cdot \nabla\rho_*, \tag{8.13}$$

is a conserved quantity. As in section 4.5, the dominant component is the last term (the product of the vertical components) in Π_s which gives

$$\Pi_{s*} \approx \frac{\zeta_* + f}{\rho} \frac{\partial \rho_*}{\partial z_*}, \tag{8.14}$$

where ζ is again the vertical component of the vorticity.

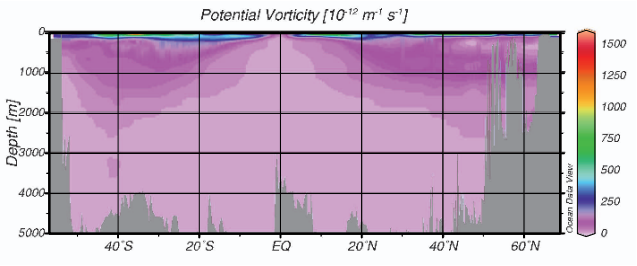

Figure 8.3. Potential vorticity Π_{s*} (8.15) distribution along the WOCE A16 section in units 10^{-12} (ms)$^{-1}$.

When the vertical vorticity can be neglected with respect to f, then Π_{s*} reduces to

$$\Pi_{s*} = -\frac{N^2 f}{g}. \tag{8.15}$$

This quantity can be directly calculated from hydrographic data. A plot of this potential vorticity (in units of 10^{-12} (ms)$^{-1}$) is shown in Fig. 8.3. The distribution of Π_s is fairly symmetrical about the equator (due to its f dependence) with low Π_s water in the equatorial region. The highest values of Π_s occur in the upper ocean where the stratification (and hence the values of N^2) are large.

When we approximate the stratification with layers of constant density differing by an amount $\Delta\rho$ and having a thickness h we can approximate (we will use these layer models in chapter 9)

$$\frac{d\rho_*}{dz_*} = \frac{\Delta\rho}{h_*}, \tag{8.16}$$

and in this case Π_{s*} becomes

$$\Pi_{s*} = \frac{\zeta_* + f}{h_*} \frac{\Delta\rho}{\rho_*}. \tag{8.17}$$

This has the same form as the shallow-water potential vorticity but h now indicates the thickness of a certain density layer instead of the total layer thickness.

With conservation of Π_s we can again predict changes in latitudinal motion or/and rotation when the stratification is changed. For example, when locally the stratification is reduced, then N^2 is reduced or equivalently a water mass of certain density gets a larger thickness with respect to its surroundings. On the large scale, where f is dominant over the relative vorticity, a decrease in stratification must lead to poleward motion as f has to increase. On a smaller scale, where f is nearly constant, a decrease in stratification locally must lead to an increase in local vorticity and hence in an increased counterclockwise motion.

Additional Material

B: See chapter 9 in Cushman-Roisin (1994) for additional details.

D: A more extensive discussion on the use of the potential vorticity concept can be found in section 4.7 of Vallis (2006) and the first sections of Müller (1995).

8.3. The stratified quasi-geostrophic model

From Table 8.1, it appears that on scales of $\mathcal{O}(100)$ km, adaptions to the homogeneous quasi-geostrophic theory as presented in chapter 5 are needed: this will lead to the stratified quasi-geostrophic theory.

We scale the horizontal and vertical velocities with U and $W = DU/L$, respectively and for the pressure scale we take

$$p_* = \bar{p}_* + \bar{\rho}_* U L f_0 p, \tag{8.18}$$

where $\bar{\rho}_*$ is the dimensional background density field and $\bar{p}_*$ the associated hydrostatic pressure field. Because the dynamic density field is also in hydrostatic equilibrium, it scales as

$$\rho_* = \bar{\rho}_* + \frac{\bar{\rho}_* U L f_0}{gD}\rho \Rightarrow \rho_* = \bar{\rho}_*(1 + \epsilon F \rho). \tag{8.19}$$

8.3.1. Model formulation

Use of local coordinates (x_*, y_*, z_*) which are again scaled with L and D, application of the β-plane approximation and taking the limit $\delta \to 0$ and $L/r_0 \ll 0$ gives (cf. section 5.1)

$$\epsilon\frac{Du}{dt} - v(1 + \beta\epsilon y) + \frac{\partial p}{\partial x}(1 + \epsilon F\rho)^{-1} \quad = \quad E_H\nabla_H^2 u + E_V\frac{\partial^2 u}{\partial z^2}, \tag{8.20a}$$

$$\epsilon\frac{Dv}{dt} + u(1+\beta\epsilon y) + \frac{\partial p}{\partial y}(1+\epsilon F\rho)^{-1} = E_H\nabla_H^2 v + E_V\frac{\partial^2 v}{\partial z^2}, \quad (8.20b)$$

$$0 = -\frac{\partial p}{\partial z} - \rho, \quad (8.20c)$$

$$\frac{\partial u}{\partial x} + \frac{\partial v}{\partial y} + \frac{\partial w}{\partial z} = 0, \quad (8.20d)$$

$$\epsilon F\frac{D\rho}{dt} + (1+\epsilon F\rho)\frac{w}{\bar{\rho}_*}\frac{d\bar{\rho}_*}{dz} = \mathcal{H}_\rho, \quad (8.20e)$$

$$\frac{D}{dt} = \frac{\partial}{\partial t} + u\frac{\partial}{\partial x} + v\frac{\partial}{\partial y} + w\frac{\partial}{\partial z}. \quad (8.20f)$$

Here ∇_H^2 is the horizontal Laplace operator and $\mathcal{H}_\rho$ contains all mixing terms of density. The dimensionless parameters in the equations are again the Rossby number $\epsilon = U/(f_0 L)$, the dimensionless planetary vorticity gradient $\beta = \beta_0 L^2/U$ and the rotational Froude number $F = f_0^2 L^2/gD$. The parameter F is small on length scales L = 100 km and anticipating an asymptotic expansion in ϵ, we assume $F = \mathcal{O}(\epsilon)$. For the mixing terms in the momentum equation we again assume that E_V and E_H are at most $\mathcal{O}(\epsilon)$.

Again we try to find solutions of the form

$$u(x,y,z) = u^0(x,y,z) + \epsilon u^1(x,y,z) + \ldots \quad (8.21)$$

with similar expansions for v, w, p and ρ. Using

$$\frac{N^2 D}{g} = -\frac{1}{\bar{\rho}_*}\frac{d\bar{\rho}_*}{dz} \approx \mathcal{O}(\epsilon), \quad (8.22)$$

the $\mathcal{O}(1)$ system in (8.20a-d) becomes

$$v^0 = \frac{\partial p^0}{\partial x}, \quad (8.23a)$$

$$u^0 = -\frac{\partial p^0}{\partial y}, \quad (8.23b)$$

$$0 = -\frac{\partial p^0}{\partial z} - \rho^0, \quad (8.23c)$$

$$0 = \frac{\partial u^0}{\partial x} + \frac{\partial v^0}{\partial y} + \frac{\partial w^0}{\partial z}. \quad (8.23d)$$

From (8.23) it follows that the $\mathcal{O}(1)$ geostrophic horizontal velocity field is divergence free and that w^0 is constant in z. Because $w^0 = 0$ at the bottom it again follows, as in the homogeneous case, that $w^0 \equiv 0$. The geostrophic, hydrostatic equations are again degenerate and at $\mathcal{O}(1)$, there is no evolution equation for the pressure.

When (8.23a-b) are both differentiated to z and (8.23c) is used, we find

$$\frac{\partial v^0}{\partial z} = -\frac{\partial \rho^0}{\partial x}, \tag{8.24a}$$

$$\frac{\partial u^0}{\partial z} = \frac{\partial \rho^0}{\partial y} \tag{8.24b}$$

The equations (8.24) are usually referred to as the thermal wind balance and they describe that in a stratified rotating flow horizontal density gradients are associated with vertical shear.

Ex. 8.1

Ex. 8.2

The thermal wind balance

The dimensional form of the thermal wind balance is given by

$$f_0 \frac{\partial v_*}{\partial z} = -\frac{g}{\rho_0}\frac{\partial \rho_*}{\partial x_*},$$

$$f_0 \frac{\partial u_*}{\partial z} = \frac{g}{\rho_0}\frac{\partial \rho_*}{\partial y_*},$$

Note that only the vertical shear is given by these equations and not the velocities itself (see Example 8.1).

▶

Example 8.1: Thermal wind balance

Consider first a situation where the density increases northward, i.e.,

$$\rho_* = \rho_0(1 + \alpha y_*),$$

with $\alpha > 0$. According to hydrostatic equilibrium, the vertical pressure increases faster with depth in the north than in the south, according to

$$p_* = -\rho_0 g z(1 + \alpha y) + p_0(y),$$

where p_0 is the surface pressure at $z = 0$. Relative to the mean pressure at particular levels $-z_1$ and $-z_2$, the pressure distribution has the high/low pattern as in Fig. 8.4. Pressure gradients are balanced by the Coriolis acceleration and hence at depth the zonal flow is eastward and near the surface the zonal flow is westward. The vertical shear in the zonal direction is according to the thermal wind balance given by

$$\frac{\partial u_*}{\partial z} = \frac{g}{f_0 \rho_0}\frac{\partial \rho_*}{\partial y_*} = \frac{g}{f_0}\alpha$$

which fits with the flow directions in Fig. 8.4. A similar picture can be drawn to illustrate the vertical shear in meridional direction due to a zonal density gradient.

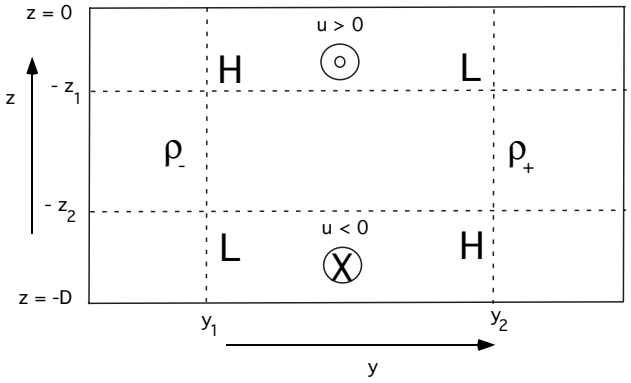

Figure 8.4. Sketch of the mechanism of the thermal wind balance relating the vertical shear in zonal direction to a meridional density gradient.

◄

The $\mathcal{O}(\epsilon)$ equations (8.20a-b/d) become

$$\frac{\partial u^0}{\partial t} + u^0\frac{\partial u^0}{\partial x} + v^0\frac{\partial u^0}{\partial y} - v^1 - \beta y v^0 = -\frac{\partial p^1}{\partial x}, \tag{8.26a}$$

$$\frac{\partial v^0}{\partial t} + u^0\frac{\partial v^0}{\partial x} + v^0\frac{\partial v^0}{\partial y} + u^1 + \beta y u^0 = -\frac{\partial p^1}{\partial y}, \tag{8.26b}$$

$$\frac{\partial w^1}{\partial z} + \frac{\partial u^1}{\partial x} + \frac{\partial v^1}{\partial y} = 0. \tag{8.26c}$$

The vorticity balance for the vertical component of the vorticity vector $\zeta^0 = \partial v^0/\partial x - \partial u^0/\partial y$ can be found by eliminating the pressure p^1 from (8.26a-b) and with (8.23a-d) and (8.26c) we find

$$(\frac{\partial}{\partial t} + u^0\frac{\partial}{\partial x} + v^0\frac{\partial}{\partial y})(\zeta^0 + \beta y) = \frac{\partial w^1}{\partial z}. \tag{8.27}$$

So far we have not used the density balance (8.20e). On the scale L_D, stratification must be an important ageostrophic effect. As the mixing of density (heat/

salt) is very small, we can neglect $\mathcal{H}_\rho$ and hence the dominant $\mathcal{O}(\epsilon)$ balance in (8.20e) becomes

$$\frac{D\rho^0}{dt} - w^1 S = 0, \tag{8.28}$$

where $S = FN^2D/g = N^2D^2/(f_0^2L^2)$ is the Burger number (cf. section 3.1). With the help of (8.28), we can express w^1 into terms of the pressure p^0 and finally, from (8.27), we find the quasi-geostrophic stratified potential vorticity equation (with $\psi = p^0$)

$$(\frac{\partial}{\partial t} + u^0\frac{\partial}{\partial x} + v^0\frac{\partial}{\partial y})(\nabla^2\psi + \frac{\partial}{\partial z}(\frac{1}{S}\frac{\partial\psi}{\partial z}) + \beta y) = 0. \tag{8.29}$$

The equation (8.29) can be written as $D\Pi_s/dt$ in the limit of small Rossby number, where Π_s is the potential vorticity defined in (8.13). Ex. 8.3

In the stratified case, the equations for motions on the scale of the Rossby deformation radius are closed by the density equation while in the constant density case they can only be closed by the Ekman layers. Note, however, that in the stratified case we cannot integrate over the layer because the horizontal velocities are z-dependent and hence we have to consider explicit boundary conditions.

8.3.2. Boundary conditions

How do the Ekman boundary layers change from the constant density formulation in chapter 5 to the stratified case discussed here? To analyze this, we first consider the flat bottom case at $z = -1$ as in chapter 5 and introduce a boundary layer coordinate $\xi = (z+1)/E_V^{1/2}$. Using the same expansions as in (5.43), but now also for $\tilde{\rho}$, the $\mathcal{O}(1)$ system of boundary layer equations is again (5.44a-d), but (5.44c) has changed to

$$\frac{\partial\tilde{p}^0}{\partial\xi} = -E_V^{1/2}\tilde{\rho}^0. \tag{8.30}$$

In addition, from (8.28) an estimate for $\tilde{\rho}^0$ follows as

$$\tilde{\rho}^0 = \mathcal{O}(\frac{\tilde{w}}{\epsilon}S) = \mathcal{O}(E_V^{1/2}\frac{S}{\epsilon}), \tag{8.31}$$

such that

$$\frac{\partial\tilde{p}^0}{\partial\xi} = \mathcal{O}(E_V\frac{S}{\epsilon}). \tag{8.32}$$

Hence, if $E_V \ll \epsilon/S$, then $\tilde{\rho}^0$ is approximately constant over the Ekman layer and we can use the results from the constant density theory. Because $S = \mathcal{O}(1)$ for motions with a horizontal scale L_D, this condition is satisfied when $E_V \ll \epsilon$.

If there is again an $\mathcal{O}(\epsilon)$ bottom topography, as in (5.70), with associated boundary conditions (5.71), then the boundary condition for ψ at $z = -1$ becomes

$$w^1 = \frac{1}{S}(\frac{\partial}{\partial t} + u^0\frac{\partial}{\partial x} + v^0\frac{\partial}{\partial y})\frac{\partial \psi}{\partial z} = \mathbf{u}^0.\nabla\eta_b - \frac{r}{2}\zeta^0. \tag{8.33}$$

At the ocean-atmosphere interface it can also be shown that if $E_V \ll \epsilon S$, the results of the homogeneous theory can also be used. The equation (5.77) (with $F = \mathcal{O}(\epsilon)$), with (8.28), then gives the boundary condition at $z = 0$

$$w^1 = -\frac{1}{S}(\frac{\partial}{\partial t} + u^0\frac{\partial}{\partial x} + v^0\frac{\partial}{\partial y})\frac{\partial \psi}{\partial z} = \frac{\alpha r}{2}\nabla.(\mathbf{T} \wedge \mathbf{e}_3), \tag{8.34}$$

where r is the parameter in (5.86), i.e. $r = \bar{E}_V^{1/2}/\epsilon$.

Because $F = \mathcal{O}(\epsilon)$ and $S = \mathcal{O}(1)$, the deformation of the ocean-atmosphere interface does not play any role in the stratified dynamics on the scale of the Rossby deformation radius. The isopycnals deform much easier than the ocean-atmosphere interface and those contribute most to the vorticity balance. For $F = \mathcal{O}(\epsilon)$, the ocean-atmosphere interface can be treated as a non-deformable surface; this is called the 'rigid lid' approximation.

The continuously stratified quasi-geostrophic model

Note that to convert back to dimensional quantities,

$$\alpha = \frac{2\tau_0}{\rho_0 U f_0 \delta_E}\ ;\ r = \frac{\delta_E f_0 L}{DU} \rightarrow \frac{\alpha r}{2} = \frac{\tau_0 L}{\rho_0 D U^2}$$

and

$$\psi_* = UL\psi\ :\ S = \frac{N^2 D^2}{L^2 f_0^2}\ ;\ \beta = \frac{\beta_0 L^2}{U}\ ;\ \epsilon_0 = \frac{f_0\delta_E}{D}$$

such that the dimensional equations become

$$(\frac{\partial}{\partial t_*} + u_*\frac{\partial}{\partial x_*} + v_*\frac{\partial}{\partial y_*})(\nabla_*^2\psi_* + \frac{\partial}{\partial z_*}(\frac{f_0^2}{N^2}\frac{\partial \psi_*}{\partial z_*}) + \beta_0 y_*) = 0,$$

with boundary conditions at $z = -D$:

$$-\frac{f_0^2}{N^2}(\frac{\partial}{\partial t_*} + u_*\frac{\partial}{\partial x_*} + v_*\frac{\partial}{\partial y_*})\frac{\partial \psi_*}{\partial z_*} = f_0\mathbf{u}_*.\nabla h_{b*} - D\epsilon_0\zeta_*,$$

and at $z = 0$:

$$-\frac{f_0^2}{N^2}(\frac{\partial}{\partial t_*} + u_*\frac{\partial}{\partial x_*} + v_*\frac{\partial}{\partial y_*})\frac{\partial \psi_*}{\partial z_*} = \frac{1}{\rho_0 D}(\frac{\partial \tau_*^y}{\partial x_*} - \frac{\partial \tau_*^x}{\partial y_*}).$$

8.4. Free waves

To determine the free waves of the stratified quasi-geostrophic model, we consider the unforced equation (8.29) with boundary conditions (8.33-8.34), i.e. with $r = \mathbf{T} = 0$. Furthermore, we will consider a horizontally unbounded ocean and boundary effects due to the presence of the continents are neglected. Free waves are again found by determining small amplitude motions with respect to the motionless state.

8.4.1. Vertical structure functions

The linearized equation (8.29) becomes

$$\frac{\partial}{\partial t}(\nabla^2\psi + \frac{\partial}{\partial z}(\frac{1}{S}\frac{\partial \psi}{\partial z}) + \beta\frac{\partial \psi}{\partial x}) = 0. \tag{8.35}$$

We search for separable solutions

$$\psi(x, y, z, t) = \Psi(x, y, t)\Phi(z), \tag{8.36}$$

for a vertical structure function $\Phi(z)$. It appears that solutions exist if Φ satisfies

$$(\frac{1}{S}\Phi')' = -\chi\Phi. \tag{8.37}$$

The boundary conditions for Φ follow from (8.33- 8.34). For a flat bottom these become

$$\Phi'(0) = \Phi'(-1) = 0. \tag{8.38}$$

The constant χ in (8.37) is a so-called separation constant which has to be determined such that the problem above has nontrivial solutions. Because S is positive and the problem (8.37) is self-adjoint, there exist a countable number of real eigenvalues. A special eigenvalue is $\chi = 0$ with associated eigenfunction $\Phi = 1$. Since the baroclinic vector $\nabla\rho \wedge \nabla p$ is zero for these waves, they are called barotropic waves. All other waves, with $\chi \neq 0$, are baroclinic waves and only exist because of the presence of the stratification.

In the special case where S is constant, the solutions of (8.37) are

$$\Phi(z) = A_1 \cos(z\sqrt{\chi S}) + A_2 \sin(z\sqrt{\chi S}). \tag{8.39}$$

The boundary conditions (8.38) imply that $A_2 \equiv 0$ and

$$\sin(\sqrt{\chi S}) = 0 \Rightarrow \chi = \chi_n = \frac{n^2\pi^2}{S}. \tag{8.40}$$

For $n = 0$, we find the barotropic mode and for $n > 0$ the baroclinic modes are given by (8.39). The vertical structure of the modes with $n = 0, 1, 2$ and $n = 3$

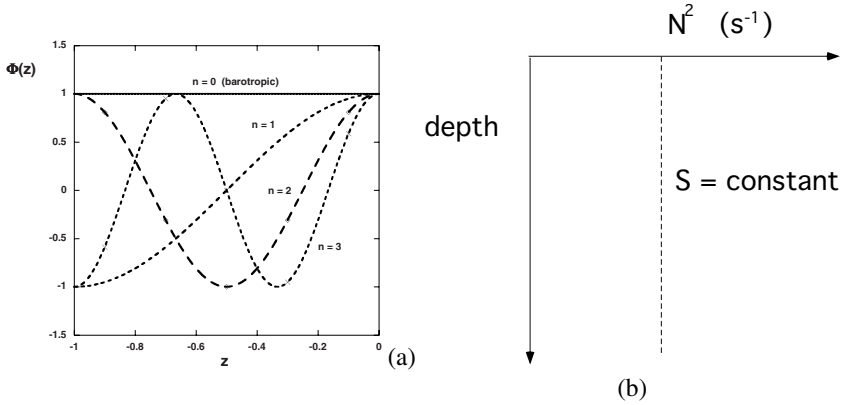

Figure 8.5. (a) Structure functions $\Phi_n(z)$ for the first four modes $n = 0, 1, 2$ and $n = 3$ for a N^2 profile such as in (b).

are plotted in Fig. 8.5b. The density profile $\bar{\rho}$ that corresponds to a constant S (Fig. 8.5a) is linear.

Through separation of variables, the function $\Psi(x, y, t)$ in (8.36) is determined from

$$\frac{\partial}{\partial t}(\nabla^2\Psi - \chi\Psi) + \beta\frac{\partial\Psi}{\partial x} = 0. \tag{8.41}$$

To determine free waves in a horizontally unbounded domain, we substitute traveling waves solutions of the form

$$\Psi(x, y, t) = \Psi_0 e^{i(kx+ly-\sigma t)}, \tag{8.42}$$

into (8.41), where k and l are the wavenumbers in the x- and y-direction, σ is the frequency of the wave and Ψ_0 is its amplitude. For a fixed value of χ_n, the dispersion relation follows as

$$\sigma_n = -\frac{\beta k}{\chi_n + k^2 + l^2}. \tag{8.43}$$

Hence, for each value of χ_n, there is an associated frequency σ_n and because χ_n is real, the corresponding σ_n are also real. For the barotropic mode we have $\chi_0 = 0$ and the frequency of these waves is

$$\sigma_0 = -\frac{\beta k}{k^2 + l^2}. \tag{8.44}$$

Rossby waves with a constant L_D.

In a flat bottom continuously stratified liquid layer characterized by a constant internal Rossby deformation radius L_D, the dimensional dispersion relation for Rossby waves is

$$\sigma_* = -\frac{\beta_0 k_*}{\frac{n^2\pi^2}{L_D^2} + k_*^2 + l_*^2}, n = 0, 1, \ldots$$

Here we have assumed that the external deformation radius R_D is much larger than L_D and furthermore the quasi-geostrophic approximation has been applied. The Rossby wave mode with $n = 0$ is the barotropic mode and it has no vertical structure; the modes with $n > 0$ are baroclinic Rossby modes.

8.4.2. Properties of Rossby waves

The phase speed $\mathbf{C}$ of the waves with dispersion relation (8.43) is

$$\mathbf{C} = \begin{pmatrix} C^x \\ C^y \end{pmatrix} = \begin{pmatrix} \frac{\sigma}{k} \\ \frac{\sigma}{l} \end{pmatrix} = \begin{pmatrix} -\frac{\beta}{\chi + k^2 + l^2} \\ -\frac{\beta}{\chi + k^2 + l^2}\frac{k}{l} \end{pmatrix}, \tag{8.45}$$

such that the phase speed in x direction is always negative. An observer moving with the waves always sees a larger planetary vorticity to the right.

The maximum frequency σ of Rossby waves is found for $k = (l^2 + \chi)^{1/2}$ with amplitude

$$\sigma_m = -\frac{\beta k}{2(l^2 + \chi)^{1/2}}. \tag{8.46}$$

The absolute maximum σ_M occurs for $l = 0$ with

$$\sigma_M = -\frac{\beta}{2\chi^{1/2}}. \tag{8.47}$$

For $l = 0$, the frequency σ is plotted as a function of $k/\sqrt{\chi}$ in Fig. 8.6a. The dimensional wavelength and frequency of this wave are

$$\lambda_* = \frac{2\pi L}{k} = \frac{2\pi L}{\sqrt{\chi}}, \tag{8.48a}$$

$$\sigma_{M*} = \frac{\sigma_M U}{L} = -\frac{\beta U}{2\sqrt{\chi} L}. \tag{8.48b}$$

For constant S, with eigenvalues χ given by (8.40), the Rossby waves with largest frequency have wavelengths

$$\lambda_{n*} = \frac{2\pi L}{n}\sqrt{S} = \frac{2}{n} L_D, \tag{8.49}$$

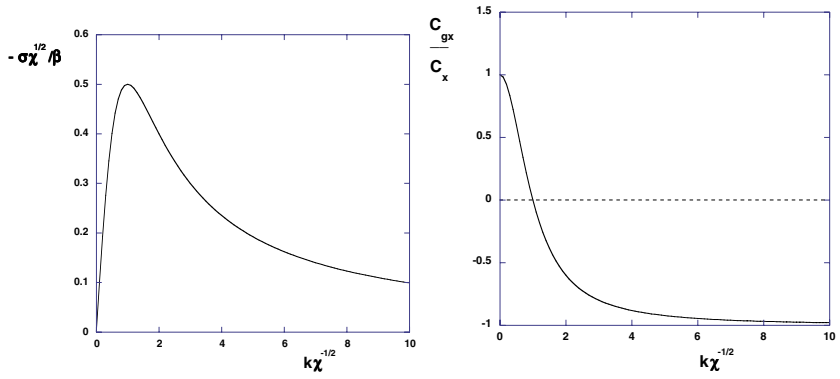

(a) (b)

Figure 8.6. (a) Dimensionless frequency and (b) ratio C_g^x/C^x for Rossby waves with $l = 0$ as a function of $k/\sqrt{\chi}$.

where L_D is the internal Rossby deformation radius, i.e. $L_D = ND/f_0$.

For typical values of N (N = 10^{-2} s^{-1}), we find $L_D \approx 100$ km and these waves move into the x-direction with phase speed

$$C_{n*}^x = \frac{\sigma_{M*}}{k_*} = -\frac{\beta_0 L_D^2}{2(n\pi)^2}. \tag{8.50}$$

Ex. 8.4

and as $\beta_0 L_D^2 = \mathcal{O}(10^{-1}$ ms$^{-1})$, typical travel times over 1000 km are in the order of years.

Waves can transport energy over large distances with respect to the characteristic displacement of the fluid elements when the wave passes. The plane wave is not suited to describing this energy transport; a more general form of the wavefield is needed. The most simple example is the wave packet

$$\Psi(x, y, t) = A(x, y, t)\cos(kx + ly - \sigma t), \tag{8.51}$$

where A is a slowly varying function of x, y, i.e.

$$A^{-1}\frac{\partial A}{\partial x} \ll (k^2 + l^2)^{1/2}\ ;\ A^{-1}\frac{\partial A}{\partial y} \ll (k^2 + l^2)^{1/2}\ ;\ A^{-1}\frac{\partial A}{\partial t} \ll \sigma. \tag{8.52}$$

This amplitude is a measure of the energy of the wave packet and hence we are interested in the evolution of A. When (8.51) is substituted into (8.35) we find, by equating the coefficients for both the sine and cosine to zero, the dispersion relation (8.43) and

$$\frac{\partial A}{\partial t} + \mathbf{C}_g \cdot \nabla A = 0, \tag{8.53}$$

where $\mathbf{C}_g$ is the group velocity, with

$$\mathbf{C}_g = \begin{pmatrix} \frac{\partial \sigma}{\partial k} \\ \frac{\partial \sigma}{\partial l} \end{pmatrix}. \tag{8.54}$$

For the Rossby waves (8.43), we find for the group velocity

$$\mathbf{C}_g = \begin{pmatrix} \beta \frac{k^2 - l^2 - \chi}{(k^2 + l^2 + \chi)^2} \\ \beta \frac{2kl}{(k^2 + l^2 + \chi)^2} \end{pmatrix}. \tag{8.55}$$

Waves for which $\mathbf{C}_g \neq \mathbf{C}$ are called dispersive waves and the Rossby wave is hence an example of these type of waves. From the expression for C_g^x, we can deduce that a wave packet that contains a wave with $k^2 > l^2 + \chi$ will move eastward while long Rossby waves with $k^2 < l^2 + \chi$ will move westward. For the absolute values of the group velocity, we find $\mid C_g^x \mid \leq \mid C^x \mid$, as can be seen in Fig. 8.6b for waves with $l = 0$.

Additional Material

D: Properties of Rossby waves are discussed in all textbooks on geophysical fluid dynamics, for example chapter 15 of Cushman-Roisin (1994) and chapter 4 of Mc Williams (2006).

D: Material for further study can be found in section 5.7 of Vallis (2006), sections 6.11, 6.12 and 6.15 of Pedlosky (1987) and lectures 14, 15 and 19 of Pedlosky (2003).

8.4.3. Topographic Rossby waves

Bottom topography can substantially affect the propagation of Rossby waves. We will study this using an example of a simple bottom profile given by

$$\eta_b(y) = \gamma y, \tag{8.56}$$

and assume that S is constant. The equation (8.29) with the boundary conditions (8.33-8.34) becomes

$$\frac{\partial}{\partial t}(\nabla^2 \psi + \frac{1}{S}\frac{\partial^2 \psi}{\partial z^2}) + \beta \frac{\partial \psi}{\partial x} = 0, \tag{8.57a}$$

$$z = -1 : \frac{\partial^2 \psi}{\partial t \partial z} = -\gamma S \frac{\partial \psi}{\partial x}, \tag{8.57b}$$

$$z = 0 : \frac{\partial^2 \psi}{\partial t \partial z} = 0. \tag{8.57c}$$

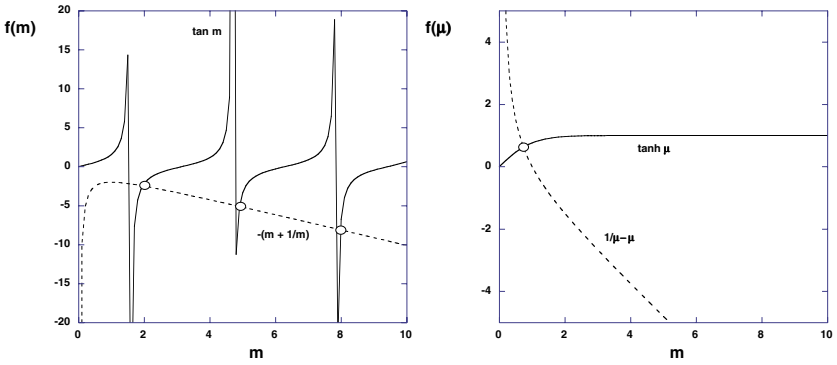

(a) (b)

Figure 8.7. (a) Plot of the functions $\tan m$ and $-(m + 1/m)$. (b) Plot of the functions $\tanh\mu$ and $1/\mu - \mu$.

Again, we look for plane wave solutions of the form

$$\psi(x, y, z, t) = \Phi(z)e^{i(kx+ly-\sigma t)}, \tag{8.58}$$

and through substitution in (8.57), we find the following eigenvalue problem for Φ (with eigenvalues σ)

$$\Phi'' + m^2\Phi = 0 \tag{8.59a}$$

$$\Phi'(0) = \Phi'(-1) - S\frac{\gamma k}{\sigma}\Phi(-1) = 0 \tag{8.59b}$$

$$m^2 = -S(\frac{\beta k}{\sigma} + k^2 + l^2). \tag{8.59c}$$

Ex. 8.5

The complication is now that for $\gamma \neq 0$, the eigenvalue σ is in the boundary condition. There are two types of solutions for $\beta \neq 0$, which depend on the sign of m^2, i.e. $m^2 > 0$ and $m^2 < 0$. When $m = 0$, then a constant Φ does not satisfy (8.59b) for $\gamma \neq 0$ unless $k = 0$ (but then also $l = 0$, due to (8.59c)) and we find only trivial solutions. Hence, bottom topography will strongly affect the barotropic mode.

For $m^2 > 0$, the solution Φ and the dispersion relation are

$$\Phi(z) = A\cos mz, \tag{8.60a}$$

$$m\tan m = \frac{\gamma k S}{\sigma} \quad \Rightarrow \quad \tan m = -\frac{\gamma}{\beta}(m + \frac{S(k^2 + l^2)}{m}). \tag{8.60b}$$

For fixed S and fixed wavevector $\mathbf{k}$, (8.60b) has a discrete set of roots m_i (Fig. 8.7a). Note that there is no intersection on the first branch of the function

$\tan m$, i.e. $m_1 \in (\pi/2, 3\pi/2)$. For $S \to 0$ and fixed wavevector $\mathbf{k}$, there is an intersection for $m = 0$. From (8.59c), we see that this is exactly the barotropic mode. For $S = \mathcal{O}(1)$ and $\gamma \to 0$, we find $m_i = i\pi$, i.e. the Rossby waves for a flat bottom, including the barotropic mode.

For $m^2 < 0$, we define $\mu^2 = -m^2 > 0$ and the solution for $\Phi(z)$ and the dispersion relation (directly from (8.60) through substitution $m = i\mu$) are

$$\Phi(z) = A \cosh \mu z, \tag{8.61a}$$

$$\mu \tanh \mu = -\frac{\gamma k S}{\sigma} \quad \Rightarrow \quad \tanh \mu = -\frac{\gamma}{\beta}(\mu - \frac{S(k^2 + l^2)}{\mu}). \tag{8.61b}$$

There is now only a single eigenvalue (Fig. 8.7b), which has special properties. The eigenfunction has a maximum amplitude at the bottom and decreases exponentially upwards; this type of mode is a so-called "bottom trapped" mode. For $S \to 0$ and fixed $\mathbf{k}$, the dispersion relation becomes

$$\sigma = -(\gamma + \beta)\frac{k}{k^2 + l^2}. \tag{8.62}$$

This is exactly the Rossby wave frequency for which bottom slope and β-effect are additive.

Summary

- In a rotating stratified flow, the effect of stratification and rotation on scale of vertical motions is of similar magnitude when

$$L \approx L_D = \frac{ND}{f}$$

- In stratified rotating flows, a useful potential vorticity is

$$\Pi_{s*} = -\frac{N^2}{g}(\zeta_* + f)$$

  where N is the buoyancy frequency and ζ is the vertical component of the vorticity vector.

- In the quasi-geostrophic approximation, this potential vorticity reduces to

$$\Pi_{s*} = \nabla^2\psi_* + \frac{\partial}{\partial z_*}\left(\frac{f_0^2}{N^2}\frac{\partial \psi_*}{\partial z_*}\right) + \beta_0 y_*$$

  where ψ is the geostrophic streamfunction. In the continuously stratified quasi-geostrophic model, this quantity is conserved.

- The dispersion relation of Rossby waves in this model is given by

$$\sigma = -\frac{\beta_0 k}{\frac{n^2\pi^2}{L_D^2} + k^2 + l^2}, n = 0, 1, \ldots$$

  For $L_D = 100$ km, barotropic ($n = 0$) waves cross an Atlantic size basin (5000 km) in a few days, while for baroclinic waves ($n > 0$) this takes several years.

- Bottom topography slightly modifies the baroclinic ($n > 0$) modes but strongly modifies the barotropic mode ($n = 0$) to become 'bottom trapped'.

8.5. Exercises on chapter 8

(8.1) *Thermal wind balance*

An ocean current has a velocity field given by

$$u_*(x_*, y_*, z_*) = 0 \; ; \; v_*(x_*, y_*, z_*) = V_0 \, e^{-\frac{(x_* - x_0)^2}{A}} e^{z_*/A}$$

a. Determine the density field $\rho_*(x_*, y_*, z_*)$ which is in thermal wind balance with this flow.

b. Sketch the velocity field and the density field of this flow.

(8.2) *Velocities from hydrographic data*

To determine geostrophic velocities from measurements of temperature T_* and salinity S_* one calculates (i) the slope of the isobars, or (ii) the pressure change along a surface of constant geopotential. Here, the geopotential Φ_* is defined by

$$\Phi_*(x_*, y_*, z_*) = \int_{-1}^{z_*} g \, dz'_*$$

a. Use the hydrostatic and geostrophic balances and derive that

$$\frac{\partial \Phi_*}{\partial x_*} = -f_0 v_* \; ; \; \frac{\partial \Phi_*}{\partial y_*} = f_0 u_*$$

where Φ_* is the value of the geopotential on an isobaric surface $p_* = p_0$ and f_0 is the local Coriolis parameter.

Consider now two isobaric surface (with pressures $p_{1*,A}$ and $p_{2*,A}$) at a station A as in the figure below.

b. Show that the geopotential difference between these two isobaric surfaces is given by

$$\Phi_*(p_{1*,A}) - \Phi_*(p_{2*,A}) = \int_{p_{1*,A}}^{p_{2*,A}} \alpha_*(S_*, T_*, p_*) \, dp_*$$

where $\alpha_* = 1/\rho_*$ is the specific volume.

As a next step, α_* is decomposed as

$$\alpha_*(S_*, T_*, p_*) = \alpha_*(35, 0, p_*) + \delta_*$$

where δ_* is the specific volume anomaly. It directly follows that

$$\Phi_*(p_{1*,A}) - \Phi_*(p_{2*,A}) = \int_{p_{1*,A}}^{p_{2*,A}} \alpha_*(35, 0, p_*)\, dp_* + \Delta\Phi_{A*}$$

where $\Delta\Phi_{A*}$ is the geopotential anomaly between the isobaric surfaces.

Consider now two isobaric surfaces (P_1 and P_2) that both intersect the stations A and B, at a distance L (see figure below).

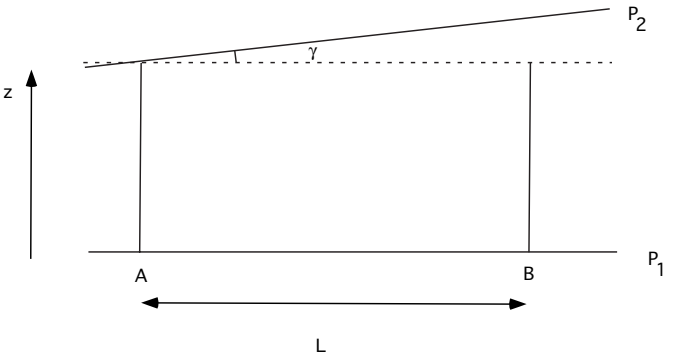

c. Show that the angle γ is determined through

$$\tan\gamma = \frac{\Delta\Phi_{B*} - \Delta\Phi_{A*}}{L}$$

d. Can one now determine the absolute meridional geostrophic velocity field? If not, what can one determine?

(8.3) *Coastal current*

Consider a steady, geostrophic and parallel flow on the western side of a coast at $x = 1$. The density field perpendicular to the coast is given by $\rho = \rho(x)$ with $\partial\rho/\partial x < 0$; this can occur for example due to the freshwater outflow of a river at the coast. The water is well mixed vertically and the height of the sea surface is given by $z = h(x)$ while the flat bottom is located at $z = -1$.

All quantities describing the flow are independent of the coordinate y. Assume that inertia and friction can be neglected, that $|h| \ll 1$ and that

$$\bar{v} \equiv \int_{-1}^{h} v \, dz = 0$$

a. Derive the equation determining the slope of the sea surface in terms in the density field.

b. Determine the velocity field of the flow and calculate the depth at which $v = 0$; this is the so-called 'level of no motion'.

c. Make a sketch of the sea surface height and the velocity field. Provide a physical interpretation of the result.

(8.4) *Rossby waves in the Pacific*

Rossby waves propagate westwards and can be observed at midlatitudes with altimeters. In the figure below (source http://topex-www.jpl.nasa.gov/), measurements of sea surface height anomalies (in cm) are plotted as a function of time along three latitudes in the Pacific (at 20°N, 32°N and 39°N, respectively).

a. Provide an estimate of the phase speed of the Rossby waves in these figures.

b. Calculate the dimensional phase speed of a Rossby wave with a zonal wavelength of 5000 km and with an infinite meridional wavelength in a constant density layer of water with a depth H_0 = 3 km at (i) 10°N and (ii) 60°N.

c. Are the waves in the figures barotropic or baroclinic Rossby waves?

(8.5) *Reflection of Rossby waves*

As we have seen in section 8.4, for a baroclinic Rossby wave with certain $\chi = \chi_n$ and with wavevector $\mathbf{k} = (k, 0)$, the dimensionless streamfunction ψ is given by

$$\psi(x, y, t) = \Psi_0 \exp\left[-i(kx - \sigma t)\right]$$

with Ψ_0 being a complex amplitude and with the dispersion relation

$$\sigma = \frac{-\beta k}{\chi + k^2}$$

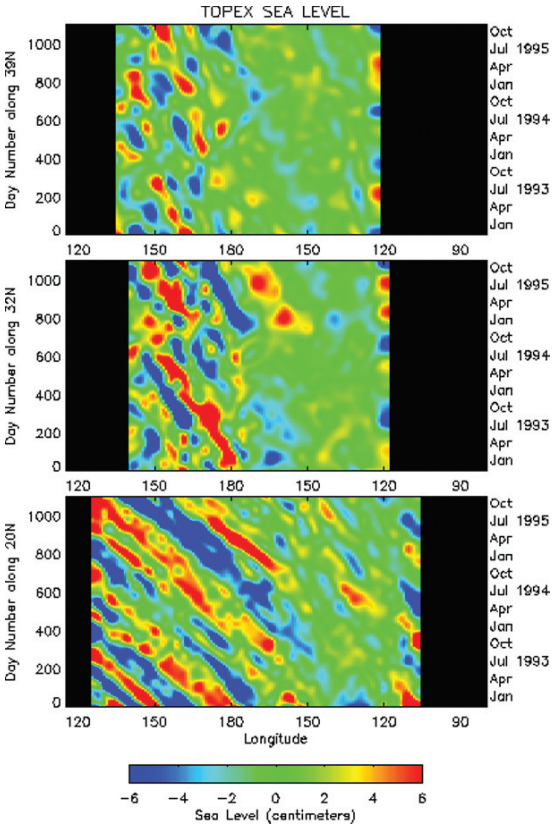

Consider now an incoming Rossby wave with wavenumber, angular frequency and streamfunction (k_i, σ_i, Ψ_i) which moves to the western boundary at $x = 0$.

a. Give the relation between k_i of the incoming wave and σ_i.

Consider now also the reflected wave; this wave can be represented by quantities (k_r, σ_r, Ψ_r).

b. What are the boundary conditions for ψ at $x = 0$.

c. Determine the streamfunction of the total flow consisting of the incoming and the reflected Rossby wave.

Chapter 9

ADJUSTMENT

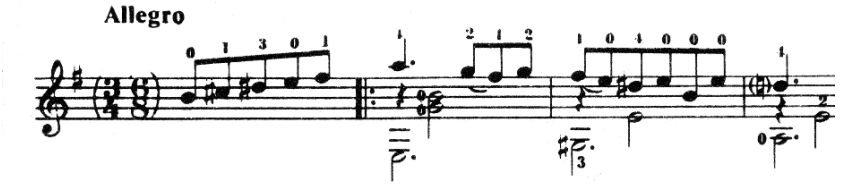

Vals Venezolano No. 2, A. Lauro

After the discussion on the free waves in the stratified and constant density case, we can now tackle the adjustment problem already mentioned in chapter 7. How does the time-dependent flow from a motionless state settle into a steady ocean circulation once a wind stress is forcing it? We therefore consider in this chapter a basin stratified motionless ocean that is suddenly forced by a wind-stress field. For the stratified case, we will restrict ourselves to the analysis of the two-layer model that will be derived in section 9.1; its free waves will be presented in section 9.2. In the constant density case we know that for $t \to \infty$, a Sverdrup balance with a western boundary current will appear. It will turn out that the adjustment can be studied simultaneously in the constant density and two-layer case (section 9.3)

9.1. The quasi-geostrophic two-layer model

As the ocean stratification can be imagined to be build up of layers which are advected without much mixing, layer models have been frequently used as a simplification of the continuous stratified model. In each layer, the density is assumed to be constant. In Fig. 9.1 a two-layer approximation is sketched with the upper layer having a density ρ_1, the lower with ρ_2 and $\rho_1 < \rho_2$. The layers are separated by a material surface, often called the thermocline, denoted by $z_* = -h_*(x, y, t)$.

Consider first the motionless flow where the thermocline is flat and given by

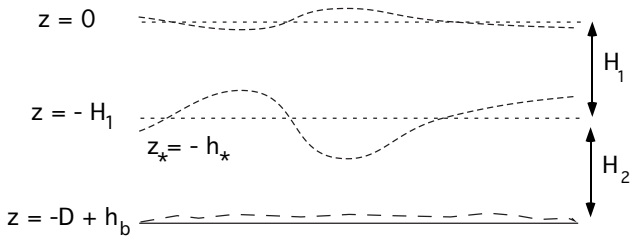

Figure 9.1. Sketch of a two-layer situation where layer i has a constant density ρ_i and an equilibrium thickness H_i.

$z_* = -H_1$ and the constant atmospheric pressure by p_0. The hydrostatic pressure, that is continuous over $z_* = -H_1$, is

$$p_{1*}(z_*) = -\rho_1 g(z_* + H_1) + p_I, \tag{9.1a}$$

$$p_{2*}(z_*) = -\rho_2 g(z_* + H_1) + p_I, \tag{9.1b}$$

where $p_I = \rho_1 g H_1 + p_0$ is the equilibrium pressure at the equilibrium thermocline. Ex. 9.1

In case of flow in both layers, the dimensional pressure also has to be continuous over the thermocline. To determine a scale μ for the amplitude of the thermocline we write

$$h_*(x,y,t) = H_1 + \mu\hat{h}(x,y,t) = Dh(x,y,t), \tag{9.2}$$

where $\hat{h} = \mathcal{O}(1)$. From the scaling (9.2) one can derive with $p_{1*} = p_{2*}$ at $z_* = -h_*$ that

$$g(\rho_1 - \rho_2)\mu\hat{h} = f_0 LU(\rho_2 p_2 - \rho_1 p_1). \tag{9.3}$$

With a reference density ρ_0, and if we choose

$$\mu = \frac{\rho_0 f_0 UL}{g(\rho_2 - \rho_1)} = \epsilon F D \frac{\rho_0}{\Delta\rho}, \tag{9.4}$$

then it follows from (9.3) that

$$-\hat{h} = \frac{\rho_2 p_2 - \rho_1 p_1}{\rho_0} \Rightarrow h = \frac{H_1}{D} + \epsilon F \frac{\rho_0}{\Delta\rho}\hat{h}. \tag{9.5}$$

Now we know that $\Delta\rho/\rho_0 \ll 1$ and that for $i = 1, 2$ $\rho_i/\rho_0 \approx 1$, such that from (9.5) we finally deduce

$$\hat{h} = p_1 - p_2. \tag{9.6}$$

Pressure differences between both layers cause deformations of the thermocline. Besides (9.6) the kinematic boundary condition at $z = -h$ is

$$w = -\frac{Dh}{dt} = -\epsilon F \frac{\rho_0}{\Delta\rho}\frac{D\hat{h}}{dt}. \tag{9.7}$$

Additional Material

B: Layers models are also discussed in section 6.16 of Pedlosky (1987), section 5.4 of Vallis (2006), chapter 12 of Cushman-Roisin (1994) and section 5.1 of Mc Williams (2006).

In both layers, the density is constant and we can apply the constant density theory from chapter 5. Expansions in ϵ and a procedure similar to that in section 5.3 leads to

$$\frac{D_i\zeta_i^0}{dt} + \beta v_i^0 = \frac{\partial w_i^1}{\partial z}, \tag{9.8}$$

for $i = 1, 2$, where

$$\frac{D_i}{dt} = \frac{\partial}{\partial t} + u_i^0 \frac{\partial}{\partial x} + v_i^0 \frac{\partial}{\partial y} \tag{9.9a}$$

$$u_i^0 = -\frac{\partial p_i^0}{\partial y} \quad ; \quad v_i^0 = \frac{\partial p_i^0}{\partial x} \tag{9.9b}$$

$$\zeta_i^0 = \nabla^2 p_i^0. \tag{9.9c}$$

At the bottom $z = -1$ we can use the Ekman theory in section 5.2 and we find from (5.75)

$$w_2 = \epsilon(\mathbf{u}_2^0 \cdot \nabla \eta_b + \frac{r}{2} \zeta_2^0), \tag{9.10}$$

and at the surface $z = 0$ from (5.78) we have

$$p_1^0 = \eta^0 \tag{9.11a}$$

$$w_1 = \epsilon(F \mathbf{u}_1 \cdot \nabla \eta^0 + \frac{\alpha r}{2} \nabla \cdot (\mathbf{T} \wedge \mathbf{e}_3)). \tag{9.11b}$$

Integration of (9.9) over the layers (-1 to $-h$ and $-h$ to 0) then gives, using (9.10-9.11),

$$\frac{D_1}{dt}(\zeta_1^0 + \beta y - \frac{DF}{H_1} p_1^0 + \frac{DF}{H_1} \frac{\rho_0}{\Delta \rho}(p_2^0 - p_1^0)) = \frac{D}{H_1} \frac{\alpha r}{2} \nabla \cdot (\mathbf{T} \wedge \mathbf{e}_3), \tag{9.12a}$$

$$\frac{D_2}{dt}(\zeta_2^0 + \beta y + \frac{D}{H_2} \eta_b - \frac{D}{H_2} F \frac{\rho_0}{\Delta \rho}(p_2^0 - p_1^0)) = -\frac{D}{H_2} \frac{r}{2} \zeta_2^0. \tag{9.12b}$$

We consider the case where $F \rho_0 / \Delta \rho = \mathcal{O}(1)$ (note that in the stratified case $F \ll 1$, see Table 8.1) where deformations of the ocean-atmosphere interface can be neglected. With

$$F_1 = \frac{f_0^2 L^2}{g' H_1} \quad ; \quad F_2 = \frac{f_0^2 L^2}{g' H_2}, \tag{9.13a}$$

$$r_1 = \frac{D}{H_1} \frac{\alpha r}{2} \quad ; \quad r_2 = \frac{D}{H_2} \frac{r}{2}, \tag{9.13b}$$

$$\tilde{\eta}_b = \frac{D}{H_2} \eta_b \quad ; \quad \beta = \frac{\beta_0 L^2}{U}, \tag{9.13c}$$

where the reduced gravity $g' = g \Delta \rho / \rho_0$. It follows with $\psi_i = p_i^0$, $i = 1, 2$, from (9.12) that

$$\frac{D_1}{dt} \left[\nabla^2 \psi_1 + \beta y + F_1 (\psi_2 - \psi_1) \right] = r_1 \nabla . (\mathbf{T} \wedge \mathbf{e}_3), \tag{9.14a}$$

$$\frac{D_2}{dt}\left[\nabla^2\psi_2 + \beta y + \tilde{\eta}_b - F_2(\psi_2 - \psi_1)\right] = -r_2\nabla^2\psi_2. \tag{9.14b}$$

We can write both parameters F_i as $F_i = L^2/L_{Di}^2$, where L_{Di} is the Rossby deformation radius, $L_{Di} = (g'H_i/f_0^2)^{1/2}$.

The two-layer quasi-geostrophic model

The dimensional form of the quasi-geostrophic two-layer model on a midlatitude β-plane with equilibrium thicknesses H_1 and H_2 and reduced gravity g' is

$$\begin{aligned}
\frac{D_1}{dt_*}\left[\nabla^2\psi_{1*} + \beta_0 y_* + \frac{f_0^2}{g'H_1}(\psi_{2*} - \psi_{1*})\right] - \frac{1}{\rho_1 H_1}\nabla.(\mathbf{T}_* \wedge \mathbf{e}_3) &= 0, \\
\frac{D_2}{dt_*}\left[\nabla^2\psi_{2*} + \beta_0 y_* + \frac{f_0}{H_2}h_{b*} - \frac{f_0^2}{g'H_2}(\psi_{2*} - \psi_{1*})\right] + \epsilon_0\nabla^2\psi_{2*} &= 0
\end{aligned}$$

where h_{b*} is the dimensional bottom topography and $\epsilon_0 = f_0\delta_E/H_2$ is the bottom friction coefficient.

9.2. Free waves

To consider free waves in the two-layer model, we consider the linearized equations (9.12) around the motionless flow without forcing and dissipation. These equations then become

$$\frac{\partial}{\partial t}(\nabla^2\psi_1 + F_1(\psi_2 - \psi_1)) + \beta\frac{\partial\psi_1}{\partial x} = 0, \tag{9.16a}$$

$$\frac{\partial}{\partial t}(\nabla^2\psi_2 - F_2(\psi_2 - \psi_1)) + \beta\frac{\partial\psi_2}{\partial x} = 0. \tag{9.16b}$$

If we multiply (9.16a) by F_2 and (9.16b) by F_1 and add both results, we find, with $\tilde{\Psi} = F_2\psi_1 + F_1\psi_2$

$$\frac{\partial}{\partial t}\nabla^2\tilde{\Psi} + \beta\frac{\partial\tilde{\Psi}}{\partial x} = 0. \tag{9.17}$$

In a similar way, by subtracting (9.16b) from (9.16a), with $\bar{\Psi} = \psi_1 - \psi_2$,

$$\frac{\partial}{\partial t}(\nabla^2\bar{\Psi} - (F_1 + F_2)\bar{\Psi}) + \beta\frac{\partial\bar{\Psi}}{\partial x} = 0. \tag{9.18}$$

In this way, we have obtained equations for the evolution of the barotropic mode $\tilde{\Psi}$ (9.17) and the first baroclinic mode $\bar{\Psi}$ (9.18). The dispersion relation of these waves is

$$\sigma = \frac{-\beta k}{\chi + k^2 + l^2}, \tag{9.19}$$

Ex. 9.2

where $\chi = 0$ for the barotropic wave and $\chi = F_1 + F_2$ for the baroclinic wave.

We know that the phase speed of these Rossby waves is westwards. Now the problem to be studied is what happens when these waves meet a continent. Consider an incoming Rossby wave (packet) with wavevector (k_i, l_i) and dispersion relation

$$\sigma_i = \frac{-\beta k_i}{\chi + k_i^2 + l_i^2}, \tag{9.20}$$

at the western boundary. The streamfunction of this incoming wave can be written as

$$\psi_i = A_i e^{i(k_i x + l_i y - \sigma_i t)}. \tag{9.21}$$

For the energy of the wave (packet) to reach the western boundary, the group velocity has to be negative In Fig. 9.2a, we see that the incoming wave has a

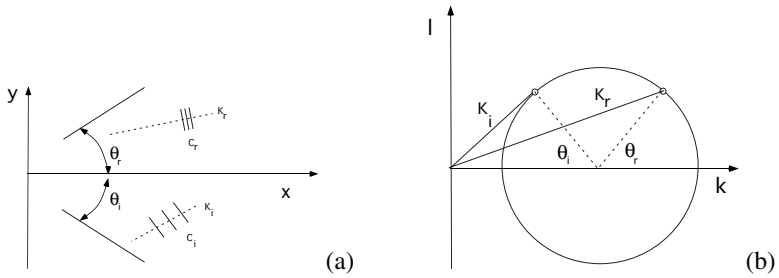

Figure 9.2. (a) Reflection of Rossby waves, where **k** *is the wavevector and* **c** *the group velocity. (b) Geometrical view of the change in wavelength during reflection.*

wavenumber which represents long Rossby waves. The wavenumber k_i is explicitly given by

$$k_i = -\frac{\beta}{2\sigma_i} - \sqrt{\frac{\beta^2}{4\sigma_i^2} - (\chi + l_i^2)}. \tag{9.22}$$

The reflected wave is represented by

$$\psi_r = A_r e^{i(k_r x + l_r y - \sigma_r t)}. \tag{9.23}$$

The total streamfunction is hence given by $\psi = \psi_i + \psi_r$. Because $u = -\partial\psi/\partial y = 0$ at the wall $(x = 0)$, the relations

$$l_i A_i e^{i(l_i y - \sigma_i t)} = -l_r A_r e^{i(l_r y - \sigma_r t)}, \tag{9.24}$$

must hold for every y and t which can only occur when

$$\sigma_i = \sigma_r \; ; \; l_i = l_r. \tag{9.25}$$

The angle of incidence is therefore equal to the angle of reflection ($\theta_i = \theta_r$) and the frequency is invariant under reflection. The wavenumber of the reflected wave must therefore lie in the same circle as the incoming wave (see Fig. 9.2b).

Because the energy of the reflected wave must propagate eastward, the reflected Rossby wave must have a short wavelength and hence the wavenumber is given by

$$k_r = -\frac{\beta}{2\sigma_i} + \sqrt{\frac{\beta^2}{4\sigma_i^2} - (\chi + l_i^2)}, \tag{9.26}$$

and $k_r > k_i$. The latter follows from (9.24); $A_i = -A_r$, such that the amplitude is the same but the phase is shifted by π. The conclusion is that long Rossby waves are reflected as short Rossby waves.

For long Rossby waves with $l = 0$ the dispersion relation in the limit $k \to 0$ becomes (see 9.19)

$$\sigma = -\frac{\beta k}{\chi}. \tag{9.27}$$

These waves satisfy the long-wave approximation

$$\beta \frac{\partial \psi}{\partial x} - \chi \frac{\partial \psi}{\partial t} = 0. \tag{9.28}$$

For short waves ($k \to \infty$ in (9.19)) the dispersion relation is

$$\sigma = \frac{-\beta}{k}, \tag{9.29}$$

and these waves satisfy the short -wave approximation

$$\frac{\partial}{\partial t}\frac{\partial^2 \psi}{\partial x^2} + \beta \frac{\partial \psi}{\partial x} = 0. \tag{9.30}$$

We will use the approximate equations (9.28) and (9.30) to solve for the adjustment problem in the next section.

9.3. Adjustment in a rectangular basin

Consider a rectangular basin as in Fig. 9.3 (with length L, width B, and aspect ratio $d = B/L$) having a flat bottom ($\eta_b = 0$). The dimensionless wind stress $\mathbf{T}$ is given by

$$\mathbf{T}(x, y, t) = f(t) \begin{pmatrix} -\cos(\pi y/d) \\ 0 \\ 0 \end{pmatrix}, \tag{9.31}$$

where $f(t)$ has not yet been specified.

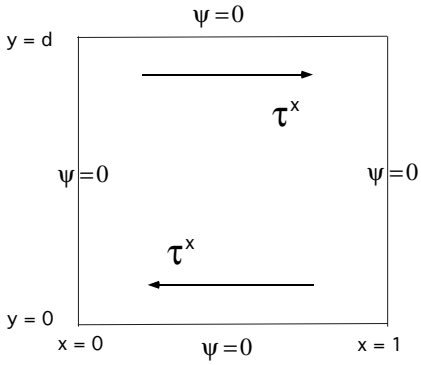

Figure 9.3. Sketch of the geometry in which the adjustment is studied.

9.3.1. Possible responses

Suppose that the function $f(t)$ has a characteristic time scale τ_p; note that this time scale can be independent of any wave propagation in the basin. We therefore rescale $t \rightarrow tL/(U\tau_p)$ and choose the velocity scale in (9.14) such that $\mathcal{O}(r_1) = \mathcal{O}(\beta)$, or

$$U = \frac{\tau_0}{\rho_1 H_1 \beta_0 L}. \tag{9.32}$$

With $H_1 = 10^3$ m and $L = 10^5$ m, this gives a value of $U = 10^{-1}$ ms^{-1}, which is of the order of the phase velocities of the first baroclinic Rossby wave. When inertia is neglected, this choice of U leads to the equations

$$\begin{aligned} \frac{L}{\beta U\tau_p}\frac{\partial}{\partial t}(\nabla^2\psi_1 + F_1(\psi_2 - \psi_1)) + \frac{\partial \psi_1}{\partial x} &= \nabla\cdot(\mathbf{T}\wedge\mathbf{e}_3), \\ \frac{L}{\beta U\tau_p}\frac{\partial}{\partial t}(\nabla^2\psi_2 - F_2(\psi_2 - \psi_1)) + \frac{\partial \psi_2}{\partial x} &= -\frac{r_2}{\beta}\nabla^2\psi_2. \end{aligned}$$

In case the bottom friction is negligible ($r_2 = 0$) then, as for the free waves, we can combine the two equations (9.33) above to get separate equations for the barotropic and baroclinic mode (as in section 9.2). As the resulting equations are uncoupled and have the same form, the adjustment problem can be formulated as

$$\frac{L}{\beta U\tau_p}\frac{\partial}{\partial t}(\nabla^2\Psi - \Lambda\Psi) + \frac{\partial \Psi}{\partial x} = -\upsilon f(t)\sin(\frac{\pi y}{d}), \tag{9.34}$$

where $\Lambda = F_1 + F_2$ for the baroclinic mode and $\Lambda = 0$ for the barotropic mode. Note that the amplitude υ is different for each of these cases. The problem is

closed by specifying kinematic boundary conditions at the basin boundaries and the initial conditions

$$t = 0 : \Psi = 0. \tag{9.35}$$

In dimensional quantities (note that time, streamfunction and horizontal coordinates were scaled with $1/(\beta_0 L)$, UL and L) the equation (9.35) becomes

$$\frac{\partial}{\partial t_*}(\nabla_*^2\psi_* - \lambda_0\psi_*) + \beta_0\frac{\partial \psi_*}{\partial x_*} = \frac{1}{\rho_0 H_1}\nabla.(\mathbf{T}_* \wedge \mathbf{e}_3), \tag{9.36}$$

where

$$\lambda_0 = \frac{f_0^2}{g\prime}(\frac{1}{H_1} + \frac{1}{H_2}) = \frac{1}{L_{D1}^2},$$

in the baroclinic response and $\lambda_0 = 0$ in the barotropic case. Note that from section 5.3, the adjustment problem for the constant density case satisfies also an equation of the form (9.34) but then with $\Lambda = F$ (and $\lambda_0 = f_0^2/(gD)$). Often a linear damping ($-\varepsilon_0\nabla_*^2\psi_*$) is added to the right hand side with a damping coefficient ε_0 (s^{-1}).

The equation (9.34) provides insight into the response of the flow to different frequencies in the wind forcing. Consider the baroclinic case with $H_2 \gg H_1$ and hence $F_2 \ll F_1$. We can write

$$\Lambda = F_1 = (\frac{L}{L_{D1}})^2 \tag{9.37a}$$

$$\frac{L}{\beta U \tau_p} = \frac{1}{\beta_0 L \tau_p} = \tau_\beta/\tau_p \tag{9.37b}$$

$$\frac{L}{\beta U \tau_p}\Lambda = \frac{L}{\beta_0 L_{D1}^2 \tau_p} = \frac{L}{c_r \tau_p}, \tag{9.37c}$$

where $c_r = \beta_0 L_D^2$ is the magnitude of the Rossby phase speed. The factor L/c_r is hence a wave time scale which is called the adjustment time scale τ_c. Ex. 9.3

With τ_p being the time scale of variation of the wind forcing, the following cases can be distinguished

(i) High frequency forcing, i.e., $\tau_\beta/\tau_p \gg 1$ and $\tau_c/\tau_p \gg 1$. In this case, fluctuations in the wind will not generate Rossby waves and the response is local.

(ii) Low frequency forcing, i.e., $\tau_\beta/\tau_p \ll 1$ and $\tau_c/\tau_p \ll 1$. In this case, the first term in (9.34) can be neglected and the ocean is always in Sverdrup balance with the changing wind stress.

(iii) On time scales τ_p on the order of τ_c or/and τ_β Rossby waves are an important component of the response.

Note that the adjustment time scale depends on the latitude through L_{Di} and β_0. At midlatitudes adjustment is relatively slow compared to more equatorial latitudes.

9.3.2. The spin-up problem

For convenience we choose $d = \pi$ and consider the spin-up to the stationary solution for the case $f(t) = \mathcal{H}(t)$. We choose $\tau_p = \tau_\beta = 1/(\beta_0 L), \upsilon = 1$ and can separate the equation (9.34) by

$$\Psi_n(x, y, t) = -\sin ny \; \Phi_n(x, t), \tag{9.38}$$

for certain n. Through this separation, the boundary conditions for Ψ at $y = 0, 1$ are satisfied and we write $\Phi = \Phi_n$. The equation for Φ becomes

$$\Phi_{xxt} - \tilde{\Lambda}\Phi_t + \Phi_x = \mathcal{H}(t), \tag{9.39}$$

Ex. 9.4

with $\tilde{\Lambda} = \Lambda + n^2$ and $\Phi = 0$ for $t = 0$. Boundary conditions at the western and eastern walls are kinematic and hence $\Phi = 0$.

We see that for $t \to \infty$, the Sverdrup solution $\Phi(x) = x - 1$ is reached. In addition, the homogeneous solutions of (9.39) are exactly the Rossby waves with dispersion relation (note that β is absorbed into the time scale)

$$\sigma = \frac{-k}{k^2 + \tilde{\Lambda}}. \tag{9.40}$$

If there were no zonal boundaries, then the solution would be $\Phi^I(t) = -t/\tilde{\Lambda}$. This is also the initial response, because then gradients of Φ in x are still small. However, Rossby waves will immediately be generated and these must eventually take care of the zero mass flux at the zonal boundaries. Moreover, they must collectively provide the Sverdrup flow in the limit $t \to \infty$.

The total solution of the problem (9.39) can be determined using Laplace transformation techniques but it turns out to be non transparent. Hence, we will present a more qualitative analysis of the response by writing the solution as

$$\Phi(x, t) = \Phi^I(t) + \Phi^L(x, t) + \Phi^S(x, t), \tag{9.41}$$

where Φ^I is the initial response, Φ^L the response due to long Rossby waves and Φ^S the response due to short Rossby waves.

At the east coast long Rossby waves are generated and transport energy (cf. section 9.2) westward. These waves satisfy the long-wave approximation (9.28), i.e.,

$$\frac{\partial \Phi^L}{\partial x} - \tilde{\Lambda}\frac{\partial \Phi^L}{\partial t} = 0. \tag{9.42}$$

The solution of this equation is

$$\Phi^L(x, t) = G(x + \tilde{\Lambda}^{-1}t), \tag{9.43}$$

where G is an arbitrary function. As short Rossby waves will only play a role near the western boundary (through reflection), the total solution outside the western boundary can be well approximated by

$$\Phi(x,t) = \Phi^I(t) + \Phi^L(x,t) = -\frac{t}{\tilde{\Lambda}} + G(x + \frac{t}{\tilde{\Lambda}}). \tag{9.44}$$

With this solution, we can only satisfy the eastern boundary condition, $\Phi = 0$ at $x = 1$, for all $t > 0$. This gives

$$-\frac{t}{\tilde{\Lambda}} + G(1 + \frac{t}{\tilde{\Lambda}}) = 0, \tag{9.45}$$

with $G(\eta) = (\eta - 1)H(\eta - 1)$ as a solution. From (9.44) the solution follows as

$$t < \tilde{\Lambda}(1-x) \quad : \quad \Phi(x,t) = -\frac{t}{\tilde{\Lambda}}, \tag{9.46a}$$

$$t > \tilde{\Lambda}(1-x) \quad : \quad \Phi(x,t) = x - 1. \tag{9.46b}$$

Plots of the time development of the solution for $\tilde{\Lambda} = 1$ are shown in Fig. 9.4.

The time $t_* = \tau_p \tilde{\Lambda}(1-x)$ is exactly the time a long Rossby waves takes to travel between the east coast and the location x. As according to (9.37) $\tilde{\Lambda} = L/(c_r \tau_p)$, the time needed to adjust to the Sverdrup flow at location x_* is hence approximately given by $(L - x_*)/(\beta_0 L_{D1}^2)$. For example, for Rossby wave speeds for the first baroclinic mode, about 5 cms^{-1}, the adjustment time is in the order of years. For the constant density case, it is $(L - x_*)/(\beta_0 R_D^2)$ and in the order of days.

To satisfy the boundary conditions at the western boundary, short Rossby waves are needed. These satisfy the short-wave approximation (9.30), i.e.,

$$\Phi^S_{xxt} + \Phi^S_x = 0, \tag{9.47}$$

with $\Phi = 0$ at $x = 0$ and a matching condition with the flow outside the boundary layer. We determine the solution through the Laplace transform technique; for $s > 0$, define

$$\phi(s,x) = \mathcal{L}(\Phi(x,t)) = \int_0^\infty \Phi(x,t) e^{-st}\, dt. \tag{9.48}$$

It then follows from (9.47), with $\Phi(s,0) = 0$, that

$$\phi(s,x) = \alpha_1(s)(e^{-x/s} - 1), \tag{9.49}$$

where $\alpha_1(s)$ is still undetermined. When the long Rossby waves have not reached the western boundary region, the matching condition becomes

$$\lim_{x\to\infty} \phi(s,x) = \mathcal{L}(\frac{-t}{\tilde{\Lambda}}) = -\frac{1}{\tilde{\Lambda} s^2} \Rightarrow \alpha_1(s) = \frac{1}{\tilde{\Lambda} s^2}. \tag{9.50}$$

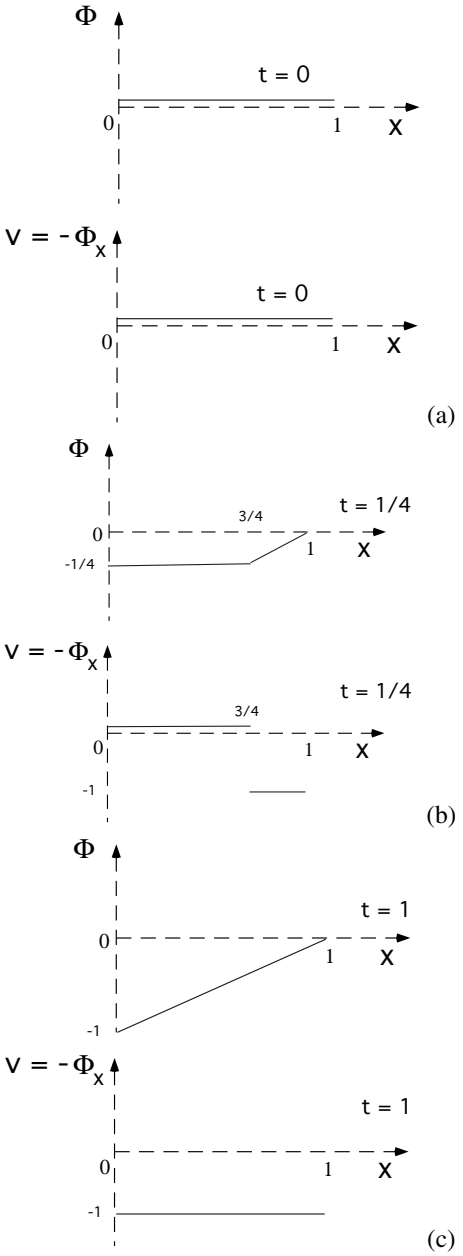

Figure 9.4. Time development of the solution Φ *in (9.46) for* $\tilde{\Lambda} = 1$. *(a) t =0, (b) t = 1/4 and (c) t = 1.*

For the inverse Laplace transformation, we use

$$\mathcal{L}^{-1}(s^{-n}e^{-a/s}) = (\frac{t}{a})^{(n-1)/2}J_{n-1}(2\sqrt{at}), \tag{9.51}$$

where J_{n-1} is the Bessel function of the first kind of order $n-1$.

►

Example 9.1: Bessel functions

The Bessel functions $J_n(x)$ are defined by

$$J_n(x) = \sum_{k=0}^{\infty} \frac{(-1)^k}{k!(n+k)!}(\frac{x}{2})^{n+2k}, \tag{9.52}$$

and satisfy the differential equation

$$x^2y'' + xy' + (x^2 - n^2)y = 0. \tag{9.53}$$

The functions J_0, J_1 and J_2 are plotted in Fig. 9.5. As can be seen, these func-

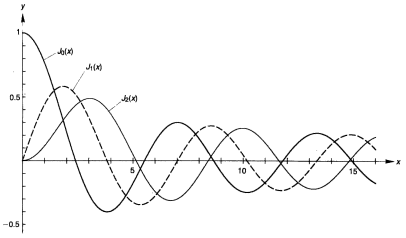

Figure 9.5. Bessel functions $J_0(x)$, $J_1(x)$ and $J_2(x)$ as a function of x.

tions oscillate for $x \to \infty$. The asymptotic behavior for $x \to 0$ and $x \to \infty$ is

$$\begin{aligned} J_n(x) &\to \sqrt{\frac{2}{\pi x}}\cos(x - \frac{\pi}{4} - \frac{n\pi}{2}) + \mathcal{O}(\frac{1}{x}), x \to \infty, \\ J_n(x) &\to \frac{1}{n!}(\frac{x}{2})^n, x \to 0, \end{aligned}$$

◄

For times $t < \tilde{\Lambda}$ the total solution is given by $(n = 2)$

$$\Phi(x,t) = \frac{1}{\tilde{\Lambda}}(-t + \sqrt{\frac{t}{x}} J_1(2\sqrt{xt})). \tag{9.55}$$

In Fig. 9.6a, the initial development of the western boundary layer is plotted for a value of $\tilde{\Lambda}$ such that the velocity of the long Rossby waves is relatively small and the solution (9.55) is visible. Note that for the baroclinic mode, the solution $\bar{\Psi}$ is equal to the dimensionless deformation of the thermocline ($\bar{\Psi} = \psi_1 - \psi_2 = \hat{h}$). The drawn line is the maximal distance, the short Rossby waves have travelled from the western boundary.

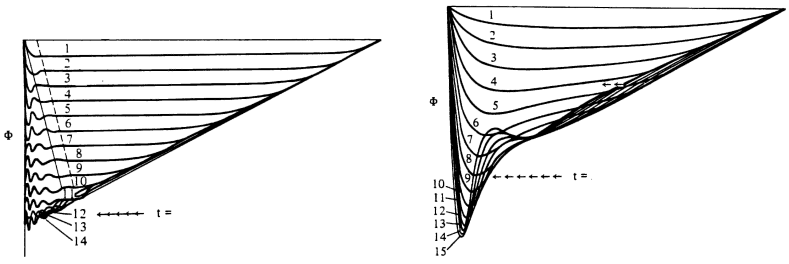

Figure 9.6. Adjustment for (a) $\tilde{\Lambda} = 600$ and (b) $\tilde{\Lambda} = 20$. The labels at the curves mark subsequent time steps (from Anderson and Gill (1975)).

Ex. 9.5

At this stage, there are three regimes in the ocean response: a western boundary current described by (9.55), an interior flow where only zonal flow is accelerated by the wind stress field (the solution Φ^I) and an eastern region where the westward expanding Sverdrup balance develops. After a dimensionless time $\tilde{\Lambda}$ (the time needed for Rossby waves to reach the western boundary, L/c_r dimensionally), the solution (9.55) is no longer valid and the western boundary layer has to match to the Sverdrup solution. We then have

$$\lim_{x\to\infty} \phi(s,x) = \mathcal{L}(-1) = -\frac{1}{s} \Rightarrow \alpha_1(s) = \frac{1}{s}, \tag{9.56}$$

and the total solution for $t > \tilde{\Lambda}$ becomes

$$\Phi(x,t) = J_0(2\sqrt{xt}) - 1 + x. \tag{9.57}$$

The flow development for $\tilde{\Lambda} = 20$ can be seen in Fig. 9.6b. Here the Rossby waves propagate so fast that the (9.57) solution appears nearly instantaneously.

Additional Material

B: It is useful at this point to read the original papers on the adjustment problem (Anderson and Gill, 1975; Anderson and Killworth, 1977; Anderson et al., 1979).

As can be seen from Fig. 9.5, both Bessel functions J_0 and J_1 oscillate and $J_0(0) = 1, J_1(0) = 0$. Both boundary layer corrections therefore display large oscillations; a measure of the thickness of the boundary layer (for $t < \tilde{\Lambda}$) is, for example, the position of the first zero of J_1. With increasing t this zero shifts to smaller values of x and the boundary layer thickness decreases. However, this thin boundary layer needs to compensate for the Sverdrup transport and hence the boundary layer velocities must increase. The larger zonal gradients in the streamfunction can be clearly seen in Fig. 9.6. Eventually, a singularity will develop in the boundary layer (the zero of J_0 moves to $x = 0$ for $t \to \infty$) and friction is needed (lateral or bottom) to regularize the solution.

Summary

- In a two-layer quasi-geostrophic model, only the barotropic and first ($n = 1$) baroclinic Rossby waves are represented.
- At a western boundary, long wavelength Rossby waves reflect into short wavelength Rossby waves.
- The response of an ocean basin to a step function in wind stress consists of an inertial response, a long wave response and a short wave response. The constant density and baroclinic spin-up time scale to the Sverdrup solution is determined by the propagation time scale ($L/(\beta_0 R_D^2)$ and $L/(\beta_0 L_D^2)$, respectively) of the longest Rossby wave in the basin. The western boundary layer flow is build up by the short Rossby waves.
- The adjustment time is proportional to f_0 and the adjustment is thus much faster in lower latitudes than at higher latitudes.

9.4. Exercises on chapter 9

(9.1) *Reduced gravity*

Consider an initially motionless two-layer system with equilibrium thicknesses H_1 and H_2 is. The density of the layers in ρ_1 and ρ_2, where $(\rho_2 - \rho_1) \ll \rho_1$. At t = 0, the surface is given an amplitude ϵ (positive upward) and as a consequence, the amplitude of the thermocline is δ(positive downward).

a. Show that

$$\delta = \epsilon \frac{\rho_1}{\rho_2 - \rho_1}$$

Assume that a wave in the sea surface has an amplitude of 1 cm.

b. Determine for typical values of $\rho_2 = 1026$ kg/m^3 and $\rho_1 = 1020$ kg/m^3 the amplitude of the thermocline.

(9.2) *Rossby waves in a two-layer model*

Small amplitude motions occur in an initially motionless two-layer system where layer i has a density ρ_i and equilibrium thickness H_i, $i = 1, 2$. Consider only waves with $l = 0$ and use $\rho_2 - \rho_1 = 1$ kgm^{-3} and $H_1 = 500\ m$, $H_2 = 4500\ m$.

a. Calculate the dimensional phase speed C_*^x of the baroclinic and barotropic Rossby waves with a wavelength $\lambda_* = 2\pi L/k$ of 100 km at a latitude $45°N$?

b. Sketch the velocity distributions as a function of depth for both types of Rossby waves.

(9.3) *Basin modes*

Resonance phenomena can occur in an ocean basin that is forced by a time-dependent wind stress through so-called basin modes. In this exercise, we investigate the frequencies and patterns of these modes. Consider the unforced problem (9.34) with $\tau_p = L/U$, i.e.,

$$\frac{\partial}{\partial t}(\nabla^2 \Psi - \Lambda \Psi) + \beta \frac{\partial \Psi}{\partial x} = 0$$

with $\Psi = 0$ at the boundaries $(x = 0, 1; y = 0, d)$. We look for solutions of the form

$$\Psi(x, y, t) = \hat{\Phi}(x, y) \exp(-i\sigma t)$$

a. Show that the equation for $\Phi(x, y)$ is given by

$$-i\sigma(\nabla^2\hat{\Phi} - \Lambda\hat{\Phi}) + \beta\frac{\partial\hat{\Phi}}{\partial x} = 0$$

With the transformation $\hat{\Phi}(x, y) = \Phi(x, y) \exp(-i\beta x/(2\sigma))$ this equation becomes the eigenvalue problem

$$\nabla^2\Phi + \mu^2\Phi = 0$$

with

$$\mu^2 = \frac{\beta^2}{4\sigma^2} - \Lambda$$

and homogeneous boundary conditions.

b. Show that the eigenvalues σ_{nm} are given by

$$\sigma_{nm}^2 = \frac{\beta^2}{4}\frac{1}{n^2\pi^2 + m^2\pi^2/d^2 + \Lambda}$$

and the eigenfunctions through

$$\psi_{nm}(x, y, t) = A_{nm} \sin(n\pi x) \sin(\frac{m\pi y}{d}) e^{-i(\sigma_{nm}t + \frac{x\beta}{2\sigma_{nm}})}$$

where A_{nm} is an arbitrary amplitude.

c. Sketch ψ_{11} for $\beta = 10^2, d = 1, \Lambda = 0$ and determine the dimensional frequency σ_{11}^*.

d. Describe briefly what happens when the flow in the basin is forced by a wind stress with a time dependence $f(t) = \cos\sigma_{11}t$.

(9.4) *Sverdrup balance in a two-layer model*

Consider a quasi-geostrophic two-layer model for the wind-driven ocean circulation in a square basin of length L on the midlatitude β plane. Both layers have the same equilibrium thickness and their density difference is small compared to the mean density.

a. Show that in the part of the basin where the Sverdrup balance holds, the bottom layer is motionless.

b. If one can measure the slope of the thermocline with an accuracy of 10%, show that one cannot measure the sea surface height with a better accuracy.

(9.5) *Adjustment: a numerical simulation*

To study the adjustment of a motionless liquid layer to the Sverdrup-Stommel steady solution, consider the adjustment problem defined by

$$\frac{\partial}{\partial t}(\nabla^2\psi - \Lambda\psi) + \frac{\partial\psi}{\partial x} = -\mathcal{H}(t)\sin y - r\nabla^2\psi$$

on the domain $[0,1]\times[0,\pi]$, with the wind-stress field $\tau^x(y) = -\mathcal{H}(t)\cos y$ and $\tau^y = 0$. Here, $\mathcal{H}(t)$ is the Heaviside function and linear friction is added (with coefficient r) for reasons which will become clear below. Kinematic boundary conditions $\psi = 0$ hold on each lateral boundary. Furthermore, $\Lambda = 0$ for the barotropic case $\psi = \tilde{\Psi}$ and $\Lambda = F_1 + F_2$ for the baroclinic case ($\psi = \bar{\Psi}$).

The equation above has solutions of the form

$$\psi(x,y,t) = -\Phi(x,t)\sin y$$

and the equation for Φ becomes

$$\Phi_{xxt} - (\Lambda+1)\Phi_t + \Phi_x + r(\Phi_{xx} - \Phi) = H(t)$$

with boundary conditions $\Phi(0,t) = \Phi(1,t) = 0$ and initial condition $\Phi(x,0) = 0$.

The aim of this exercise is to solve this equation numerically for given values of the parameters r and Λ. Define the grid $x_i, i = 0,\cdots,m$, with $x_0 = 0$ and $x_m = 1$, such that $\Delta x = 1/m$. Use central discretization in space and an implicit Crank-Nicholson in time, i.e.,

$$\begin{aligned}
\Phi_{xx} &\approx \frac{\Phi_{i+1} + \Phi_{i-1} - 2\Phi_i}{\Delta x^2} \\
\Phi_x &\approx \frac{\Phi_{i+1} - \Phi_{i-1}}{2\Delta x} \\
\Phi_t &\approx \frac{\Phi^{n+1} - \Phi^n}{\Delta t}
\end{aligned}$$

where $\Delta t = t^{n+1} - t^n$ is the time step.

We can write the resulting equations as

$$C_W \Phi_{i-1}^{n+1} + C_C \Phi_i^{n+1} + C_E \Phi_{i+1}^{n+1} = g(\Phi_{i-1}^n, \Phi_i^n, \Phi_{i+1}^n)$$

During each time step, we have to solve a system of equations $Ax = b$ with a tridiagional matrix A.

a. Determine the coefficients C_W, C_C, C_E and the function g in the expression above.

b. Write a program in your favorable language to solve the system of equations.

c. Take $r = 0.1$ and determine how long we have to integrate for different values of Λ. Take $\Lambda = 1$ and $\Lambda = 100$ and determine a suitable integration time. What are optimal time steps in both cases?

d. Consider now the convergence of solutions with m en Δt for $r = 0.1$. Choose the same two values of Λ as under b). Justify the use of specific m and Δt in connection with the accuracy of the solutions.

e. Choose an optimal value of m and Δt for $\Lambda = 0$. Perform a set of simulations with different $r \in [0.001, 0.1]$ and describe the different phenomena (wave propagation, boundary layers) you see in the solutions.

f. Do the same for $\Lambda = 100$ and provide an overview of the different adjustment phenomena in the parameter plane (r, Λ). Give a physical explanation for these phenomena.

Chapter 10

STABILITY OF ZONAL FLOWS

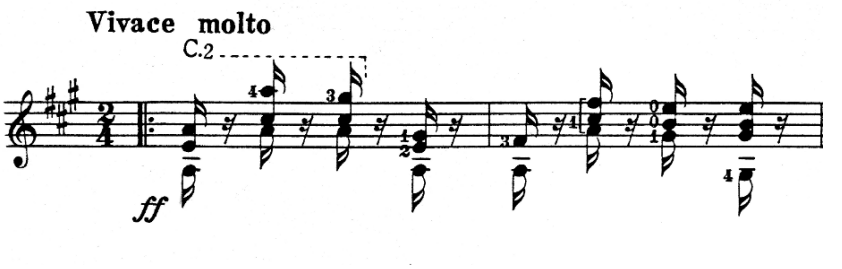

Valses Poeticos No. 1, E. Granados

In chapter 6, we used the Sverdrup-Stommel-Munk theory to explain the existence of a strong western boundary current, such as the Gulf Stream. From observations, it is clear that the Gulf Stream is a strong meandering current and that vortices, such as rings and eddies, are continuously being shed. An example is shown in Fig. 10.1, where a snapshot of the sea surface temperature of the North Atlantic Ocean is plotted. The behavior of these vortices is complex; they grow on the background flow and interact with it and with each other. A typical length scale of these features is 100 km, and the time scale of development is about 60-90 days. In this chapter, we focus on the understanding of the physical mechanisms of the instabilities of zonal ocean currents. The question is: under what circumstances are small perturbations amplified by drawing energy from the mean flow? In section 10.1, we consider the general problem in the quasi-geostrophic continuously stratified model and in the following sections, both the mechanisms of barotropic (section 10.2) and baroclinic (sections 10.3-10.5) instability are presented.

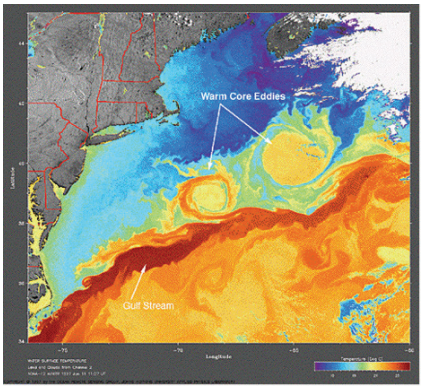

Figure 10.1. Multipass satellite image of the sea-surface temperature in the Gulf Stream region in May 1996 (image from http://fermi.jhuapl.edu/avhrr/).

10.1. Quasi-geostrophic theory

The quasi-geostrophic continuously stratified model for flow in a midlatitude ocean basin was formulated in section 8.1. The governing equations are (8.29)

with boundary conditions (8.33- 8.34), i.e.,

$$
\begin{aligned}
(\frac{\partial}{\partial t}+u\frac{\partial}{\partial x}+v\frac{\partial}{\partial y})(\nabla^2\psi+\frac{\partial}{\partial z}(\frac{1}{S}\frac{\partial\psi}{\partial z}) &+ \beta y)=0, && \text{(10.1a)}\\
z=-1:-\frac{1}{S}(\frac{\partial}{\partial t}+u\frac{\partial}{\partial x}+v\frac{\partial}{\partial y})\frac{\partial\psi}{\partial z} &= \mathbf{u}.\nabla\eta_b-\frac{r}{2}\nabla^2\psi, && \text{(10.1b)}\\
z=0:-\frac{1}{S}(\frac{\partial}{\partial t}+u\frac{\partial}{\partial x}+v\frac{\partial}{\partial y})\frac{\partial\psi}{\partial z} &= \frac{\alpha r}{2}\nabla\cdot(\mathbf{T}\wedge\mathbf{e}_3), && \text{(10.1c)}\\
u=-\frac{\partial\psi}{\partial y} &; \quad v=\frac{\partial\psi}{\partial x}. && \text{(10.1d)}
\end{aligned}
$$

If we consider a zonal channel bounded by lateral walls at $y\pm 1$ then the boundary conditions (the horizontal mixing of momentum is neglected) are

$$y=\pm 1:\mathbf{u}\cdot\mathbf{n}=0, \tag{10.2}$$

where $\mathbf{u}=(u,v)^T$ is the horizontal geostrophic velocity vector and $\mathbf{n}$ the outward normal on each lateral wall.

Suppose there is a steady solution $\bar{\psi}(x,y,z)$ of the equations above. To investigate the stability of this solution, we look at small perturbations $\phi(x,y,z,t)$ on the steady state. With

$$\psi(x,y,z,t)=\bar{\psi}(x,y,z)+\phi(x,y,z,t), \tag{10.3}$$

the equations for ϕ become

$$
\begin{aligned}
(\frac{\partial}{\partial t}+\bar{u}\frac{\partial}{\partial x}+\bar{v}\frac{\partial}{\partial y})\left[\nabla^2\phi+\frac{\partial}{\partial z}(\frac{1}{S}\frac{\partial\phi}{\partial z})\right]+\\
(-\frac{\partial\phi}{\partial y}\frac{\partial}{\partial x}+\frac{\partial\phi}{\partial x}\frac{\partial}{\partial y})\left[\nabla^2\bar{\psi}+\frac{\partial}{\partial z}(\frac{1}{S}\frac{\partial\bar{\psi}}{\partial z})+\beta y\right]+\\
(-\frac{\partial\phi}{\partial y}\frac{\partial}{\partial x}+\frac{\partial\phi}{\partial x}\frac{\partial}{\partial y})\left[\nabla^2\phi+\frac{\partial}{\partial z}(\frac{1}{S}\frac{\partial\phi}{\partial z})\right]=0.
\end{aligned}
\tag{10.4}
$$

The boundary condition at $z=-1$ becomes

$$
\begin{aligned}
-(\frac{\partial}{\partial t}+\bar{u}\frac{\partial}{\partial x}+\bar{v}\frac{\partial}{\partial y})\frac{\partial\phi}{\partial z} &- (-\frac{\partial\phi}{\partial y}\frac{\partial}{\partial x}+\frac{\partial\phi}{\partial x}\frac{\partial}{\partial y})\frac{\partial\bar{\psi}}{\partial z}-\\
(-\frac{\partial\phi}{\partial y}\frac{\partial}{\partial x}+\frac{\partial\phi}{\partial x}\frac{\partial}{\partial y})\frac{\partial\phi}{\partial z} &= S\begin{pmatrix}-\frac{\partial\phi}{\partial y}\\ \frac{\partial\phi}{\partial x}\end{pmatrix}\cdot\nabla\eta_b-\frac{r}{2}\nabla^2\phi,
\end{aligned}
\tag{10.5}
$$

and at $z=0$:

$$
\begin{aligned}
-(\frac{\partial}{\partial t}+\bar{u}\frac{\partial}{\partial x}+\bar{v}\frac{\partial}{\partial y})\frac{\partial\phi}{\partial z} &- (-\frac{\partial\phi}{\partial y}\frac{\partial}{\partial x}+\frac{\partial\phi}{\partial x}\frac{\partial}{\partial y})\frac{\partial\bar{\psi}}{\partial z}-\\
&- (-\frac{\partial\phi}{\partial y}\frac{\partial}{\partial x}+\frac{\partial\phi}{\partial x}\frac{\partial}{\partial y})\frac{\partial\phi}{\partial z}=0,
\end{aligned}
\tag{10.6}
$$

and the boundary conditions on the lateral walls are

$$\begin{pmatrix} -\frac{\partial \phi}{\partial y} \\ \frac{\partial \phi}{\partial x} \end{pmatrix} \cdot \mathbf{n} = 0. \tag{10.7}$$

With the notation

$$\bar{\Pi} = \nabla^2 \bar{\psi} + \frac{\partial}{\partial z}\left(\frac{1}{S}\frac{\partial \bar{\psi}}{\partial z}\right) + \beta y, \tag{10.8a}$$

$$q = \nabla^2 \phi + \frac{\partial}{\partial z}\left(\frac{1}{S}\frac{\partial \phi}{\partial z}\right), \tag{10.8b}$$

we can write (10.4) as

$$\frac{\partial q}{\partial t} + \bar{u}\frac{\partial q}{\partial x} + \bar{v}\frac{\partial q}{\partial y} - \frac{\partial \phi}{\partial y}\frac{\partial \bar{\Pi}}{\partial x} + \frac{\partial \phi}{\partial x}\frac{\partial \bar{\Pi}}{\partial y} - \frac{\partial \phi}{\partial y}\frac{\partial q}{\partial x} + \frac{\partial \phi}{\partial x}\frac{\partial q}{\partial y} = 0. \tag{10.9}$$

With the Jacobian

$$\mathcal{J}(f, g) = \frac{\partial f}{\partial x}\frac{\partial g}{\partial y} - \frac{\partial f}{\partial y}\frac{\partial g}{\partial x}, \tag{10.10}$$

we can write it as

$$\frac{\partial q}{\partial t} + \mathcal{J}(\bar{\psi}, q) + \mathcal{J}(\phi, \bar{\Pi}) + \mathcal{J}(\phi, q) = 0. \tag{10.11}$$

In the sections below, we will consider specific simple basic state flows for which the stability problem can be reduced to ordinary differential equations. In general, one has to use numerical techniques to solve these problems.

Additional Material

B: For a general introduction into hydrodynamic stability theory, consult Drazin and Reid (2004).

10.2. Barotropic instability

Consider a zonal flow for which $\bar{\psi} = \bar{\psi}(y)$, i.e. $\bar{v} = 0$ and $U(y) = \bar{u}(y) = -\bar{\psi}'(y)$ in a zonal channel that is bounded by walls at $y = \pm 1$. We will restrict the analysis to the most simple case of the model where bottom topography ($\eta_b = 0$) and bottom friction ($r \to 0$) are neglected.

The zonal flow $\bar{\psi}$ is a solution of the unforced equations (10.1). Sufficient conditions for instability can be determined by looking at the evolution of infinitesimally small perturbations on the zonal flow. In that case, we can linearize the equations (10.4) around this flow and hence the linear stability problem becomes

$$\left(\frac{\partial}{\partial t} - \bar{\psi}'\frac{\partial}{\partial x}\right)\left[\nabla^2 \phi + \frac{\partial}{\partial z}\left(\frac{1}{S}\frac{\partial \phi}{\partial z}\right)\right] + (\bar{\psi}''' + \beta)\frac{\partial \phi}{\partial x} = 0, \tag{10.12}$$

where the prime indicates differentiation to y. The boundary conditions are

$$z = -1, 0 \quad : \quad (\frac{\partial}{\partial t} - \bar{\psi}' \frac{\partial}{\partial x}) \frac{\partial \phi}{\partial z} = 0, \tag{10.13a}$$

$$y = -1, 1 \quad : \quad \frac{\partial \phi}{\partial x} = 0. \tag{10.13b}$$

This system of equations has solutions of the form

$$\phi(x, y, z, t) = \hat{\phi}(y, z) e^{ik(x-ct)}, \tag{10.14}$$

where $c = c_r + ic_i$ is the complex growth factor. If $c_i > 0$, then perturbations will grow and the zonal flow will be unstable. The problem for $\hat{\phi}(y, z)$ becomes

$$-(\bar{\psi}' + c) \left[\frac{\partial^2 \hat{\phi}}{\partial y^2} - k^2 \hat{\phi} + \frac{\partial}{\partial z} (\frac{1}{S} \frac{\partial \hat{\phi}}{\partial z}) \right] + (\bar{\psi}''' + \beta) \hat{\phi} = 0, \tag{10.15}$$

with boundary conditions

$$z = -1, 0 \quad : \quad \frac{\partial \hat{\phi}}{\partial z} = 0, \tag{10.16a}$$

$$y = -1, 1 \quad : \quad \hat{\phi} = 0. \tag{10.16b}$$

If (10.18a) is satisfied then (10.13a) will certainly be satisfied; we will restrict ourselves here to perturbations that satisfy (10.16a).

Just as with the structure of the stratified Rossby waves in chapter 7, there again exist separable solutions

$$\hat{\phi}(y, z) = \Phi(z) A(y), \tag{10.17}$$

if Φ satisfies the equation

$$(S^{-1} \Phi')' = -\chi \Phi, \tag{10.18a}$$

$$\Phi'(0) = \Phi'(-1) = 0. \tag{10.18b}$$

With this splitting, the eigenvalue problem (10.15) (with eigenvalue c) becomes

$$A'' - (\chi + k^2) A - A \frac{U'' - \beta}{U - c} = 0 \tag{10.19a}$$

$$A(-1) = A(1) = 0. \tag{10.19b}$$

The growth of the barotropic ($\chi = 0$) as well as of the baroclinic ($\chi > 0$) modes is described by a similar eigenvalue problem as in section 8.3.1.

If we multiply (10.19a) by A^*, the complex conjugate of A, we find

$$A^* A'' - (\chi + k^2) |A|^2 - \mid A \mid^2 \frac{U'' - \beta}{U - c} = 0, \tag{10.20}$$

where $\mid A \mid$ is the norm of the complex number A. Integration over the interval $[-1, 1]$ and use of the boundary conditions (10.19b), which also must be satisfied by A^*, gives

$$\int_{-1}^{1} \left[|A'|^2 - (\lambda + k^2)|A|^2 \right] \, dy - \int_{-1}^{1} |A|^2 \frac{U'' - \beta}{U - c} \, dy = 0. \tag{10.21}$$

By multiplying the numerator and denominator of the integrand in the second

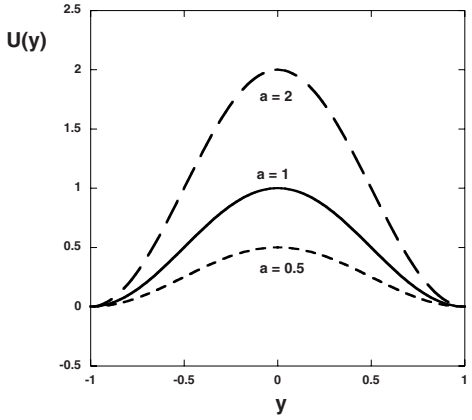

Figure 10.2. Plot of the zonal velocity $U(y) = \frac{a}{2}(1 + \cos \pi y)$ *for* $a = 0.5, 1.0$ *and* $a = 2.0$.

integral of (10.21) by $U - (c_r - ic_i)$, the integral can be written as

$$\int_{-1}^{1} \mid A \mid^2 \frac{(U'' - \beta)(U - (c_r - ic_i))}{\mid U - c \mid^2} \, dy. \tag{10.22}$$

The equality (10.21) must hold for both real and imaginary part. The first integral is a real number and for the second (10.22) gives

$$c_i \int_{-1}^{1} |A|^2 \frac{U'' - \beta}{\mid U - c \mid^2} \, dy = 0. \tag{10.23}$$

Ex. 10.1

For instability, the inequality $c_i > 0$ must hold and hence a necessary condition for instability is that the function $U'' - \beta$ must change sign on the interval $[-1, 1]$. If this does not occur, then $c_i = 0$ must hold and the flow $U(y)$ cannot be unstable. For $\beta > 0$, this condition is called the Kuo criterium; for $\beta = 0$ it is called the Rayleigh criterium. Be careful with this criterium, because it does not provide a sufficient condition for instability; a flow which satisfies this condition can still

be stable. Note that the dimensional form of the Kuo criterium is based on the quantity $U_*'' - \beta_0$.

▶

Example 10.1: Barotropic instability

As an example we consider $U(y) = \frac{a}{2}(1+\cos \pi y)$ with $a > 0$ (Fig. 10.2) where the parameter a is a measure of the horizontal shear in the flow. The zonal velocity is maximal in the center of the channel and zero on the boundaries $y = \pm 1$. In this case,

$$U'' - \beta = -\frac{1}{2}\pi^2 a \cos \pi y - \beta. \tag{10.24}$$

If $2\beta/(\pi^2 a) > 1$ then $U'' - \beta$ does not change sign and hence the zonal flow is stable. We can take $b = \beta/(a\pi^2)$ as a control parameter for the stability problem. Growth factors kc_i as a function of k and b are plotted in Fig. 10.3 for the barotropic mode ($\lambda = 0$); the curve for which $c_i = 0$ is called the neutral curve. The barotropic mode is the most unstable mode; i.e. all modes with $\lambda > 0$ have larger growth factors than the barotropic mode. There is a strong asymmetry

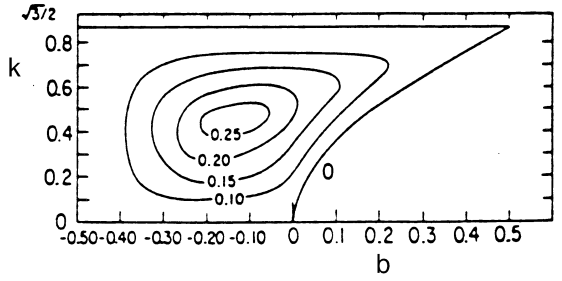

Figure 10.3. Contour plot (from Kuo (1951)) of the growth factor kc_i of the problem (10.19) for the zonal velocity field $U(y) = \frac{a}{2}(1 + \cos \pi y)$, where $b = \beta/(a\pi^2)$, k the wavenumber and $\chi = 0$ (barotropic mode). .

in the results as an eastward jet is more stable ($b > 0$) than a westward jet. There is also a clear short wave boundary in the waves with wavenumbers $k > \sqrt{3}/2$ will damp exponentially. For $b > 0.5$, the zonal flow is stable consistent with the Kuo criterium. The spatial scale of the fastest growing perturbation is determined by $k_m = 0.5$ for $b \cong -0.2$.

◄

To describe the mechanism of barotropic instability, we again consider the motion of three water columns on the β-plane (Fig. 10.4) similar to the description used of the propagation of the Rossby wave in section 7.3. Assume that column B initially moves northward then, through conservation of potential vorticity, it acquires a negative rotation. For an eastward flow, the horizontal shear induces a positive rotation (Fig. 10.4a) that will counteract the rotation of B. For a westward flow, the horizontal shear amplifies the negative rotation of B (Fig. 10.4b), which explains the asymmetry of the growth of perturbations. The growth of the perturbation itself is identical to that of plane shear instabilities where the Reynolds' stress induces the energy transfer between the mean state and the perturbations.

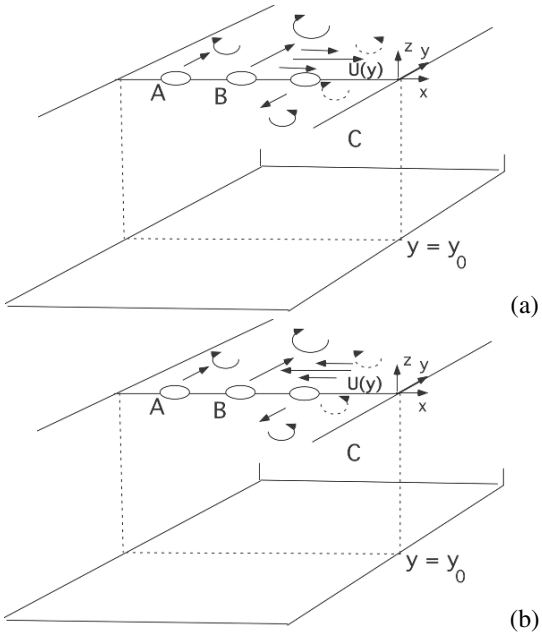

Figure 10.4. Sketch to understand the mechanism of barotropic instability for (a) an eastward flow and (b) a westward flow.

10.3. The Eady model

One of the simple situations in which baroclinic instability occurs is the flow in a zonal channel with lateral walls at $y = \pm 1$. Bottom friction is neglected,

($r = 0$), there is no bottom topography ($\eta_b = 0$), S is constant and we put $\beta = 0$ (f-plane approximation). Consider the steady state $\bar{\psi}(y, z) = -y(z+1)$, such that the velocity field is given by $U(z) = \bar{u}(z) = z + 1, V = \bar{v} = 0$. Hence there is only vertical shear in the basic flow and from the geostrophic and hydrostatic balances

$$\frac{\partial \psi}{\partial x} = v\ ;\ -\frac{\partial \psi}{\partial y} = u\ ;\ \frac{\partial \psi}{\partial z} = -\rho, \tag{10.25}$$

the thermal wind balance is (section 8.3)

$$\frac{\partial u}{\partial z} = \frac{\partial \rho}{\partial y}\ ;\ \frac{\partial v}{\partial z} = -\frac{\partial \rho}{\partial x}, \tag{10.26}$$

The density field of the zonal flow is hence given by

$$\bar{\rho}(y, z) = y. \tag{10.27}$$

The equations which describe the evolution of small perturbations on this steady flow are (with $q = \nabla^2\phi + S^{-1}\phi_{zz}$)

$$\frac{\partial q}{\partial t} + (z+1)\frac{\partial q}{\partial x} = 0, \tag{10.28a}$$

$$z = 0 : -(\frac{\partial}{\partial t} + \frac{\partial}{\partial x})\frac{\partial \phi}{\partial z} + \frac{\partial \phi}{\partial x} = 0, \tag{10.28b}$$

$$z = -1 : -\frac{\partial}{\partial t}\frac{\partial \phi}{\partial z} + \frac{\partial \phi}{\partial x} = 0, \tag{10.28c}$$

$$y = \pm 1 : \frac{\partial \phi}{\partial x} = 0. \tag{10.28d}$$

These contain solutions

$$\phi(x, y, z, t) = \Phi(y, z)e^{ik(x-ct)}, \tag{10.29}$$

and substitution gives

$$(z + 1 - c)(\frac{1}{S}\frac{\partial^2 \Phi}{\partial z^2} + \frac{\partial^2 \Phi}{\partial y^2} - k^2\Phi) = 0, \tag{10.30a}$$

$$z = -1 : c\frac{\partial \Phi}{\partial z} + \Phi = 0, \tag{10.30b}$$

$$z = 0 : (1 - c)\frac{\partial \Phi}{\partial z} - \Phi = 0, \tag{10.30c}$$

$$y = \pm 1 : \Phi = 0. \tag{10.30d}$$

For $z + 1 - c \neq 0$ we find solutions of (10.30a) of the form

$$\Phi(y, z) = A(z)\cos(n + \frac{1}{2})\pi y, \tag{10.31}$$

and the eigenvalue problem for the eigenvalue c becomes

$$A'' - \mu^2 A = 0, \tag{10.32a}$$
$$(1-c)A'(0) - A(0) = 0, \tag{10.32b}$$
$$cA'(-1) + A(-1) = 0, \tag{10.32c}$$

with $\mu^2 = (k^2 + [(n+\frac{1}{2})\pi]^2)S$. The solution of (10.32a) is

$$A(z) = C_1 e^{\mu z} + C_2 e^{-\mu z}. \tag{10.33}$$

Substitution of this solution into the homogeneous equations (10.32b-c) and setting the coefficient determinant to zero provides the eigenvalues c. We find

$$c = \frac{1}{2} \pm \frac{1}{\mu}\left[(\frac{\mu}{2} - \frac{1}{\tanh\frac{\mu}{2}})(\frac{\mu}{2} - \tanh\frac{\mu}{2})\right]^{1/2}. \tag{10.34}$$

In Fig. 10.5, the three functions x, $\tanh(x)$ and $1/\tanh(x)$ are plotted. We see that $x - \tanh(x) > 0$ for all x and that for $x > x_0 \cong 1.2$ it follows that $x > 1/\tanh(x)$. If $\mu > \mu_c = 2x_0 \cong 2.4$, then both values of $c \in \mathbb{R}$ and hence $c_i = 0$. These are neutral waves that will stabilize if friction is added. For $\mu < \mu_c$,

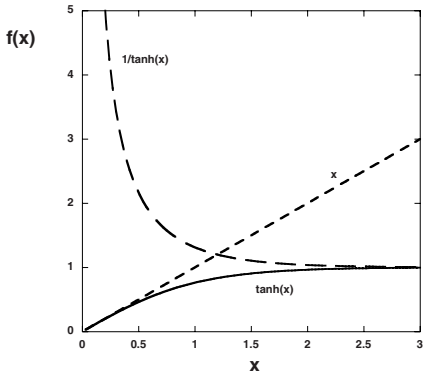

Figure 10.5. Plot of the functions $1/tanh(x)$, $tanh(x)$ and x.

Ex. 10.2

the values of c are complex conjugated and there is at least one perturbation for which $c_i > 0$ with growth factor

$$kc_i = \frac{k}{\mu}\left[(-\frac{\mu}{2} + \frac{1}{\tanh\frac{\mu}{2}})(\frac{\mu}{2} - \tanh\frac{\mu}{2}).\right]^{1/2} \tag{10.35}$$

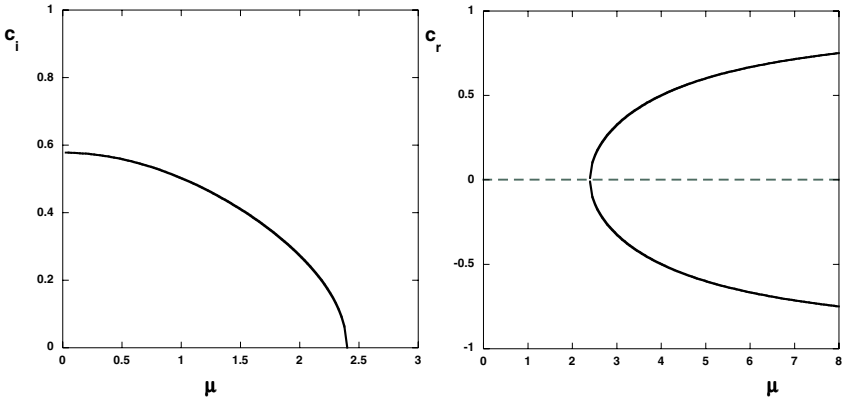

(a) (b)

Figure 10.6. (a) Plot of the positive growth factor c_i over the interval $\mu \in [0, \mu_c]$ for the $n = 0$ mode. For this case, the complex growth factors are given by $c = 1/2 \pm ic_i$. (b) The phase speed $c_r - 1/2$ as a function of μ over the interval $\mu \in [\mu_c, \infty]$, where both branches are plotted; for these branches of eigenvalues the growth factor $c_i = 0$.

The eigenvalues c for the $n = 0$ mode (the fastest growing mode) are plotted as a function of μ in Fig. 10.6. Ex. 10.3

The growth factor kc_i for the $n = 0$ mode is plotted versus μ in Fig. 10.7 for four values of S. Dimensional growth factors $k_* c_{i*}$ can be obtained from $k_* c_{i*} = kc_i/\tau_a$, where τ_a is the advective time scale. The largest growth factor at $S = 0.25$ appears at $k_m = 3.128$ and hence the dimensional wavelength of this fastest growing mode is given by (note $S = (L_D/L)^2$)

$$\lambda_* = \frac{2\pi}{k_m} L = \frac{4\pi}{k_m} L_D \approx 4L_D. \tag{10.36}$$

Ex. 10.4

For the ocean, a typical value of L_D = 100 km which corresponds to a quarter wavelength according to (10.36). This is in qualitative agreement with the scale of the observed baroclinic eddies in western boundary currents such as the Gulf Stream. Stratification is essential for this type of instability, because μ is proportional to S. The physical mechanism of baroclinic instability must therefore be different from that of barotropic instability.

10.4. Mechanism of baroclinic instability

The instability depends crucially on the fact that isopycnals of the steady flow do not coincide with isobars. The dimensional density of the zonal flow is given by

$$\rho_* = \rho_{b*}(1 + \epsilon F \bar{\rho}), \tag{10.37}$$

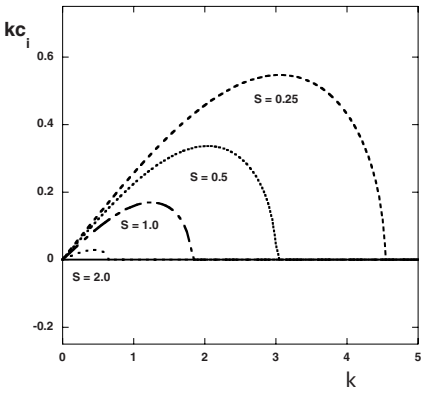

Figure 10.7. Plot of the growth factor kc_i as a function of the wavenumber k for four values of the Burger number S.

where ρ_b is the density distribution associated with the background stratification and $\bar{\rho}$ is the dimensionless dynamically induced density distribution.

According to the thermal wind balance for a zonal flow that only depends on z, i.e. $U = U(z)$, $V = 0$, the density $\bar{\rho}$ only depends on y (cf. (10.27), i.e.,

$$\frac{\partial \bar{u}}{\partial z} = \frac{\partial \bar{\rho}}{\partial y} \Rightarrow \bar{\rho} \text{ linear in } y. \tag{10.38}$$

If we assume that S is constant (as in the Eady model) then from the definition of $S = N^2 D^2/(f_0^2 L^2)$ and it follows that ρ_b is approximately linear in z. Hence, for this particular zonal flow, the density field can be approximated by

$$\rho_* = \rho_0 - \delta z_* + \gamma y_*, \tag{10.39}$$

where ρ_0 is a reference density, $\delta = \partial \rho_*/\partial z_*$ and $\gamma = \partial \rho_*/\partial y_*$.

For a zonal flow, the streamlines (and isobars) at $y_* = 0$ are given by the lines $z_* = C_1$ (constant) whereas lines of constant density in the $y_* - z_*$ plane are given by

$$z_* = \frac{\gamma}{\delta} y_* + C_2, \tag{10.40}$$

Ex. 10.5

where C_2 is a constant. The isopycnals hence make an angle α (with $\tan \alpha = \gamma/\delta$) with the horizontal plane (Fig. 10.8).

Consider a fluid element with volume V that moves adiabatically, and without salinity change, from A to B along a vector $\mathbf{P}$ due to a particular perturbation

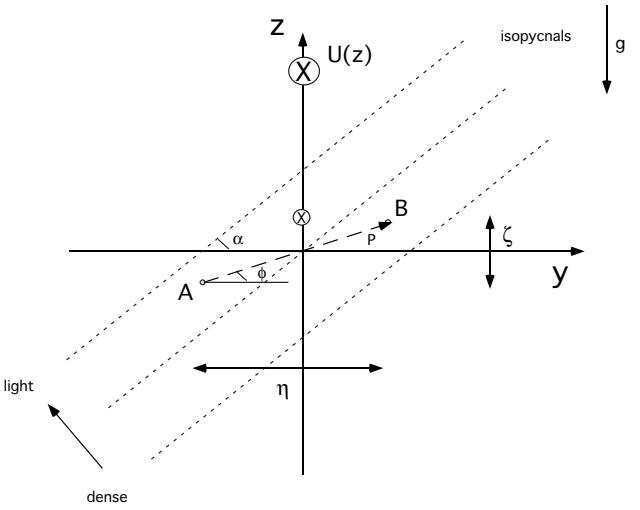

Figure 10.8. Sketch to help explain the mechanism of baroclinic instability.

(Fig. 10.8). The density of the fluid element is unchanged but the density of the surrounding liquid at B is equal to

$$\rho_{*B} = \rho_{*A} + \frac{\partial \rho_*}{\partial y_*}(y_{*B} - y_{*A}) + \frac{\partial \rho_*}{\partial z_*}(z_{*B} - z_{*A}), \tag{10.41}$$

where all derivatives are taken at point A. The volume force, and hence the acceleration on the fluid element, due to the density difference is

$$\mathbf{f}_* = \mathbf{g}(\rho_{*A} - \rho_{*B}) = -\mathbf{g}(\frac{\partial \rho_*}{\partial y_*}\eta_* + \frac{\partial \rho_*}{\partial z_*}\zeta_*), \tag{10.42}$$

with $\zeta_* = (z_{*B} - z_{*A})$ and $\eta_* = (y_{*B} - y_{*A})$. The acceleration a_* into the direction of $\mathbf{P}$ is

$$a_* = \frac{\mathbf{f}_* \cdot \mathbf{P}}{\rho_{A*}}. \tag{10.43}$$

From (10.42- 10.43) it follows (the subscript A is now omitted)

$$a_* = -\frac{\mathbf{g} \cdot \mathbf{P}}{\rho_*} \frac{\partial \rho_*}{\partial z_*} \zeta_* (\frac{\frac{\partial \rho_*}{\partial y_*}}{\frac{\partial \rho_*}{\partial z_*}} \frac{\eta_*}{\zeta_*} + 1) = -\frac{\mathbf{g} \cdot \mathbf{P}}{\rho_*} \frac{\partial \rho_*}{\partial z_*} \zeta_* (1 - \frac{\gamma}{\delta} \frac{\eta_*}{\zeta_*}). \tag{10.44}$$

Because $\mathbf{g} \cdot \mathbf{P} < 0$ and $\partial \rho_* / \partial z_* < 0$ it follows that the acceleration in the direction of $\mathbf{P}$ is positive when the slope of the trajectory $(\tan \phi)$ is smaller than the

slope of the isopycnals ($\tan\alpha$), i.e., $\tan\phi/\tan\alpha < 1$. In this case, the original perturbation is amplified and lighter fluid from location A will move upwards due to buoyancy. This is characteristic of baroclinic instability: in this way, the potential energy associated with the basic state density field is transferred to kinetic energy of the perturbations.

Additional Material

B: Barotropic and baroclinic instability theory are discussed in many textbooks, such as chapter 7 and 16 of Cushman-Roisin (1994) and section 5.2 of Mc Williams (2006).

D: In chapter 6 of Vallis (2006) the energetics of the instability mechanisms are discussed. A comprehensive treatment can be found in chapter 7 of Pedlosky (1987), where also aspects of nonlinear development of the perturbations are presented.

10.5. The Phillips model

In the Eady model of the previous section only the f-plane case was considered as $\beta = 0$ was assumed. To study the effect of the background planetary vorticity gradient we consider the two-layer model as derived in chapter 9. To simplify the analysis, we will assume that the flow is bounded is confined to a zonal channel. The unforced equations (9.14) of the model are then given by

$$\frac{D_1}{dt}(\nabla^2\psi_1 + \beta y + F_1(\psi_2 - \psi_1)) = 0, \tag{10.45a}$$

$$\frac{D_2}{dt}(\nabla^2\psi_2 + \beta y - F_2(\psi_2 - \psi_1)) = 0, \tag{10.45b}$$

where the meaning of the parameters is explained in section 9.1. With the walls of the zonal channel at $y = \pm 1$, the boundary condition is again that the meridional velocity has to be zero.

Again, looking at perturbations (for both layers $n = 1, 2$) on the steady basic zonal flow ($\bar{\psi}_1(y)$, $\bar{\psi}_2(y)$), i.e.

$$\psi_n(x, y, t) = \bar{\psi}_n(y) + \phi_n(x, y, t), \tag{10.46}$$

we obtain equations for the evolution of these perturbations

$$\begin{aligned}(\frac{\partial}{\partial t} - \bar{\psi}'\frac{\partial}{\partial x})q_n + \frac{\partial\phi_n}{\partial x}\frac{\partial\bar{\Pi}_n}{\partial y} \quad + \\ \frac{\partial\phi_n}{\partial x}\frac{\partial q_n}{\partial y} - \frac{\partial\phi_n}{\partial y}\frac{\partial q_n}{\partial x} = 0,\end{aligned} \tag{10.47}$$

where

$$q_n = \nabla^2\phi_n - F_n(-1)^n(\phi_2 - \phi_1), \tag{10.48a}$$
$$\bar{\Pi}_n(y) = \beta y + \bar{\psi}''(y) - F_n(-1)^n(\bar{\psi}_2'(y) - \bar{\psi}_1'(y)), \tag{10.48b}$$

with boundary conditions

$$y = \pm 1 : \frac{\partial \phi_n}{\partial x} = 0. \tag{10.49}$$

We consider the special case that

$$\bar{\psi}_n(y) = -U_n y. \tag{10.50}$$

Here, the U_n are the constant zonal velocities in both layers and this flow is a solution of (10.45) and satisfies the boundary conditions (Fig. 10.9).

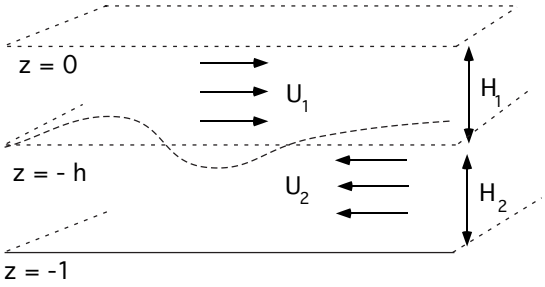

Figure 10.9. Sketch of the steady flow and perturbations in the Phillips model.

We search for separable solutions of (10.47) of the form

$$\phi_n(x, y, t) = \Phi_n(y) e^{ik(x-ct)}. \tag{10.51}$$

This gives two coupled equations for the Φ_n as

$$\begin{aligned}(U_1 - c)(\Phi_1'' &- k^2\Phi_1 - F_1(\Phi_1 - \Phi_2)) \\ &+ \Phi_1(\beta + F_1(U_1 - U_2)) = 0,\end{aligned} \tag{10.52a}$$
$$\begin{aligned}(U_2 - c)(\Phi_2'' &- k^2\Phi_2 - F_2(\Phi_2 - \Phi_1)) \\ &+ \Phi_2(\beta + F_2(U_2 - U_1)) = 0,\end{aligned} \tag{10.52b}$$

with

$$\Phi_1(-1) = \Phi_1(1) = \Phi_2(-1) = \Phi_2(1) = 0. \tag{10.53}$$

The eigenfunctions are

$$\Phi_n(y) = A_n \cos l_j y, l_j = (j + \frac{1}{2})\pi, \tag{10.54}$$

and substitution of these solutions into (10.52) leads to a set of homogeneous equations for the A_n. Setting the coefficient determinant to zero provides the eigenvalues c as

$$c = U_2 + \frac{U_s K^2(K^2 + 2F_2) - \beta(2K^2 + F_1 + F_2)}{2K^2(K^2 + F_1 + F_2)} \pm \frac{[\beta^2(F_1 + F_2)^2 + 2\beta U_s K^4(F_1 - F_2) - K^4 U_s^2(4F_1F_2 - K^4)]^{\frac{1}{2}}}{K^2(K^2 + F_1 + F_2)}, \tag{10.55}$$

with $K^2 = k^2 + l_j^2$. In the case $U_1 = U_2 = U$, we find two real eigenvalues

$$c_1 = U - \frac{\beta}{K^2}, \tag{10.56a}$$

$$c_2 = U - \frac{\beta}{K^2 + F_1 + F_2}, \tag{10.56b}$$

and, apart from an additive constant, we find the phase speeds of the Rossby waves of the first baroclinic mode (c_2) and the barotropic mode (c_1) (cf. section 9.2).

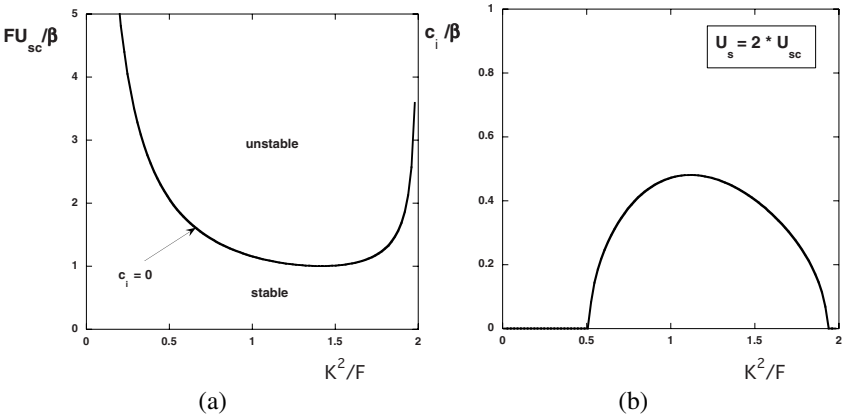

Figure 10.10. (a) Plot of the critical value of U_{sc} from (10.62). Note that with $y = U_{sc}F/\beta$ and $x = K^2/F$, here the function $y = 2/(x\sqrt{4 - x^2})$ is plotted. (b) The growth factor c_i from (10.61) for $U_s = 2\beta/F$; with $y = c_i/\beta$ and $x = K^2/F$ here the function $y = \sqrt{x^2(4 - x^2) - 1}/(x^2+2)$ is plotted.

In the case $\beta = 0$, the eigenvalues become

$$c = U_2 + \frac{U_s K^2(K^2 + 2F_2)}{2K^2(K^2 + F_2 + F_1)} \pm \frac{[U_s^2(K^4 - 4F_1F_2)]^{\frac{1}{2}}}{(K^2 + F_2 + F_1)}, \tag{10.57}$$

and hence there is instability ($c_i > 0$) when

$$K^2 = k^2 + (j + \frac{1}{2})^2\pi^2 < 2(F_1F_2)^{1/2}. \tag{10.58}$$

If $(j + \frac{1}{2})^2\pi^2 < 2(F_1F_2)^{1/2}$, then there is an interval of wavenumbers $[0, k_0]$ for which the basic flow is unstable. For a given F_1 and F_2 the largest wavenumber k_{0m} (for $j = 0$) perturbation that can grow is given by

$$k_{0m}^2 = 2(F_1F_2)^{1/2} - \frac{\pi^2}{4}. \tag{10.59}$$

This condition is an approximation (i.e., in the two-layer model) of the condition $\mu < \mu_c$ in the Eady model. Wavenumbers larger than $(4F_1F_2)^{1/4}$ and hence perturbations with wavelength λ_* with

$$\lambda_* > \frac{2\pi L}{k_{0m}} = 2\pi L(4F_1F_2)^{-1/4}, \tag{10.60}$$

will be damped.

In the case where $F_1 = F_2 = F$, the eigenvalues are given by

$$c = \frac{1}{2}(U_1 + U_2) - \frac{\beta(K^2 + F)}{K^2(K^2 + 2F)} \pm \frac{[4\beta^2F^2 - K^4U_s^2(4F^2 - K^4)]^{1/2}}{2K^2(K^2 + 2F)}, \tag{10.61}$$

and hence if $K^2 > 2F$, then the basic state is stable. For $K^2 < 2F$, the flow only becomes unstable if U_s is large enough, i.e.

$$U_s^2 > U_{sc}^2 = \frac{4\beta^2F^2}{K^4(4F^2 - K^4)}. \tag{10.62}$$

This critical value of the shear stress depends on β but is independent of the sign of U_s. The β-effect is hence stabilizing in the baroclinic instability mechanism. In Fig. 10.10a, $U_{sc} > 0$ is plotted as a function of K. The minimum of the curve ($\partial U_s/\partial K = 0$) is given by $U_{sm} = \beta$/F. For $U_s > U_{sm}$, there exists an interval of perturbations (characterized by K) that will grow exponentially. For $U_s = 2U_{sm}$, the growth factors c_i are plotted in Fig. 10.10b.

Summary

- Necessary conditions for instability of a zonal flow can be determined through a linear stability analysis. If the flow is unstable, then there will be an interval of wavenumbers that will grow exponentially. After some time, the amplitudes of the perturbations become so large that they will influence the flow and nonlinear interactions of the different modes can no longer be neglected. Only a nonlinear theory can then provide an answer to how the perturbations develop and how they will modify the basic state.
- A necessary condition for barotropic instability of a zonal flow with velocity $U_*(y_*)$ is that there is sign change in the quantity $U_*'' - \beta_0$. Note that this is not a sufficient condition: when $U_*'' - \beta_0$ changes sign, the flow may still be stable.
- The barotropic instability mechanism can be considered as an amplification of Rossby waves through the background horizontal shear.
- Whenever there is vertical shear in a rotating stratified flow, baroclinic instability will occur and perturbations over a band of wavenumbers are amplified. During the instability process, potential energy from the background density field is converted into kinetic energy of the disturbances.
- The β-effect is a stabilizing effect in baroclinic instability as it modifies the potential vorticity of the background state.

10.6. Exercises on chapter 10

(10.1) *Barotropic instability*

As we have seen in section 10.2 a necessary, but not sufficient, condition for barotropic instability of zonal flows is the Kuo criterium. This criterium implies that there can be no growth of perturbations on a background flow $U = U(y)$ if $U'' - \beta$ does not change sign with the flow domain. Consider now the dimensionless zonal flow

$$U(y) = \bar{U}(3y - 2y^3)$$

on the domain $-1 \leq y \leq 1$ on a β plane, where $\bar{U}$ is a constant amplitude.

a. Show that this flow is stable when $|\bar{U}|$ is smaller than $\beta/12$.

b. Is this flow unstable on an f-plane?

(10.2) *Baroclinic instability*

Consider a dimensionless background flow with horizontal velocity field $u = u(z) = a(z + 1)$, $v = 0$, with $a > 0$.

a. Determine the density field that is compatible with this velocity field; use quasi-geostrophic theory.

b. Calculate the angle between the isopycnals and the horizontal when it is assumed that the Burger number is constant.

(10.3) *Eddy scales*

A typical value of the buoyancy frequency N in the Gulf Stream region is $N = 10^{-3}$ s^{-1}.

a. Determine the wavelength of the perturbation with the largest growth factor in the Eady model for the Gulf Stream.

b. Why do we see (in general) eddies with a larger diameter?

(10.4) *Barotropic and baroclinic instability*

Consider a zonal channel with $y \in [-1, 1]$ and a background stratification $\rho_b = \rho_b(z)$. Assess the stability (and the type of instability mechanism responsible) of the following (dimensionless) flows:

a. $U(y) = 6 \sin \pi y,\ V = W = 0.$

b. $\psi(y, z) = -y^4(z + 1).$

c.

$$U = \begin{cases} -\frac{\bar{U}}{2} & : \quad -1 < y < -\frac{1}{2} \\ \bar{U}y & : \quad -\frac{1}{2} < y < \frac{1}{2} \\ \frac{\bar{U}}{2} & : \quad \frac{1}{2} < y < 1 \end{cases}$$

where $\bar{U}$ is constant.

(10.5) *Baroclinic instability in the Eady model*

The relation between the condition of the motion of fluid particles with respect to isopycnals and the instability condition in the Eady model ($\mu < \mu_c$) is not immediately transparent.

a. Show that

$$\frac{\frac{\partial \rho_*}{\partial y_*}}{\frac{\partial \rho_*}{\partial z_*}} = -\frac{D\epsilon}{SL}\frac{\partial \bar{\rho}}{\partial y} + \mathcal{O}(\frac{D}{L}\epsilon F)$$

b. Derive for this case that the acceleration a_* is

$$a_* = -\mathbf{g}.\mathbf{P}\frac{\zeta_*}{\rho_*}\frac{\partial \rho_*}{\partial z_*}(1 - \frac{D\epsilon}{SL}\frac{\partial \bar{\rho}}{\partial y}\frac{\eta_*}{\zeta_*})$$

c. Subsequently show that η_* and ζ_* are related to the perturbation velocities through

$$\frac{\eta_*}{\zeta_*} = \frac{\tilde{v}_*}{\tilde{w}_*} = \frac{L}{D\epsilon}\frac{\tilde{v}^0}{\tilde{w}^1}$$

where $\tilde{v}^0$ and $\tilde{w}^1$ are the dimensionless velocities of the perturbations; these are determined from the eigensolutions with positive growth factor.

d. Show that the background flow is unstable when

$$\frac{\partial \bar{\rho}}{\partial y} > S \tan \phi$$

where S is the Burger number.

e. Explain now why there is instability only when $\mu < \mu_c$, where $\mu^2 = (k^2 + [(n + 1/2)\pi]^2)S$ (section 10.3).

III

EQUATORIAL DYNAMICS

Chapter 11

EQUATORIAL OCEAN CIRCULATION

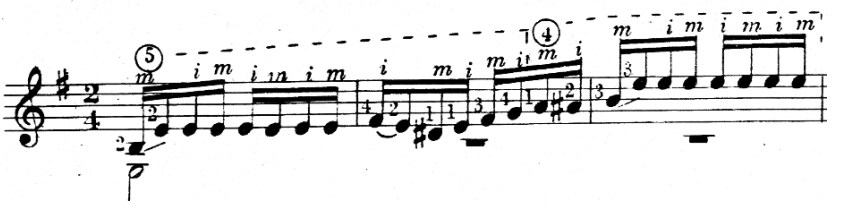

El Colibri, J. Sagreras

The tropical zone of the ocean basins has a special place within dynamical oceanography. Through the existence of the trade winds, there is a large transfer of momentum from the atmosphere to the ocean. In section 11.1 a few characteristics of the velocity, temperature and salinity fields are presented together with the main issues which motivate this chapter. The constant density and reduced gravity models on the equatorial β-plane are formulated in section 11.2. With these models the physics of the Equatorial Counter Current is explained in section 11.3 and the zonal slope in the equatorial thermocline in section 11.6. Equatorial waves are described in section 11.4 and this material is needed in section 11.5 to describe the wind-driven ocean circulation in an equatorial basin.

11.1. Characteristics

The annual mean wind stress over the Tropical Pacific is shown in Fig. 11.1. Clearly, the trade winds are mainly zonal and directed from east to west. The maximum amplitude of the zonal wind stress is about 0.1 Pa (note: 1 dyn/cm^2 = 0.1 Pa). At the equator, there is a small component of the meridional wind stress with an amplitude of about 0.025 Pa. The structure of the winds is not symmetric with respect to the equator since the convergence of the South Pacific trade winds and North Pacific trade winds is located slightly north of the equator. This is associated with the fact that the Intertropical Convergence Zone (ITCZ) is, on average, located north of the equator.

As we saw in Fig. 5.13, there is a strong upwelling along the equator with a maximum amplitude of about 2 m/day. The existence of this upwelling is directly related to the Ekman transport associated with the trade winds. This transport is 90° to the right of the winds (and hence northward) in the northern hemisphere and 90° to the left of the wind (and hence southward) in the southern hemisphere. The resulting horizontal divergence of the mass transport has to be compensated and hence upwelling results.

The equatorial surface flows have a rather complex structure as is illustrated by the circulation by the snapshots of surface speed in the Pacific from the a high resolution ocean (the NLOM) model (Fig. 11.2). Equatorial currents are highly variable and intense in each of the three ocean basins with surface speeds up to 1 ms^{-1}. In the Pacific, the westward South Equatorial Current has a maximum north of the equator, which seems related to the asymmetry in the wind stress (Fig. 11.1), while the North Equatorial Current has a maximum just north of 10°N.

A meridional section of the zonal geostrophic velocity at 155°W in the Pacific (Fig. 11.3) shows the North and South Equatorial Current as strong westward flows. The eastward Equatorial Counter Current is situated between these two

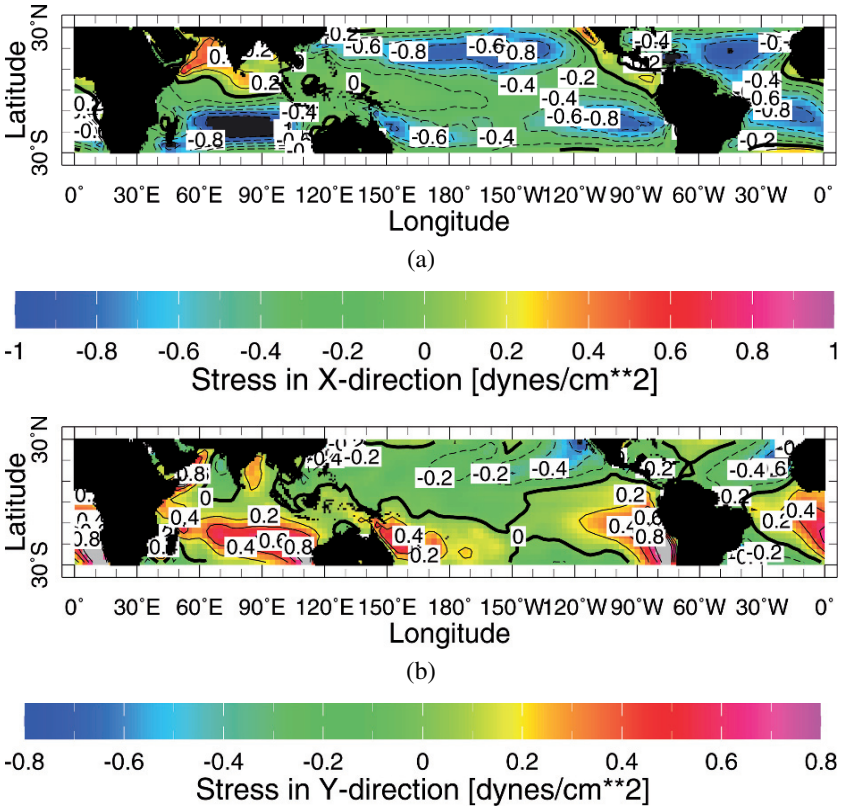

Figure 11.1. Annual mean (a) zonal and (b) meridional wind stress over the Tropical Oceans from Trenberth et al. (1989) in units of dyn/cm^2 (1 dyn/cm^2 = 0.1 Pa).

currents with maximum positive zonal velocities of 40 cm s^{-1} at about 5°N. At about 100 m depth between the latitudes 2°N and 2°S, there is a strong eastward current, the Equatorial Under Current, with maximum velocities of about 1 ms^{-1}. The physics of the Equatorial Counter Current is the first motivating problem of this chapter. Ex. 11.1

The annual mean sea surface temperature (SST) in the Pacific (Fig. 11.4) indicates that there is a strong asymmetry between the relatively warm western part of the basin (the so-called Warm Pool) and the cooler eastern basin (the so-called Cold Tongue). The Cold Tongue has a mean temperature of about 24°C while the Warm Pool temperature is about 29°C giving a zonal temperature difference over

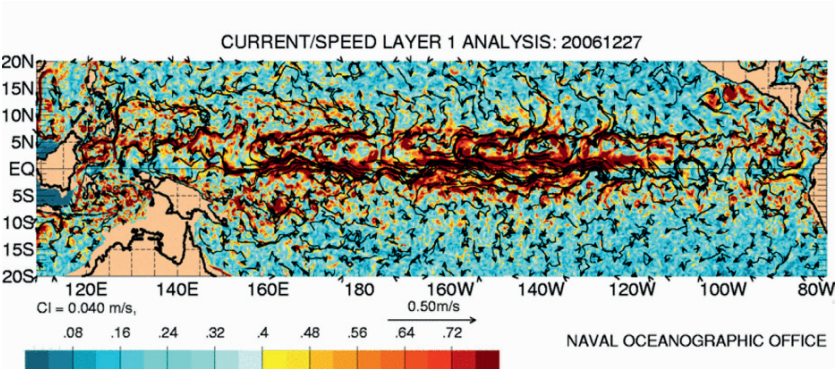

Figure 11.2. Snapshot of the surface speed from a high resolution ocean model (the NLOM, see http://www7320.nrlssc.navy.mil/global_nlom32/skill.html) in the equatorial Pacific.

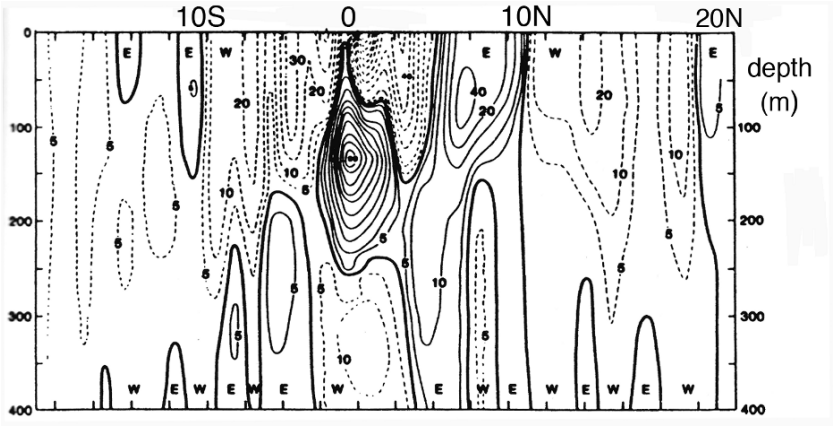

Figure 11.3. Meridional cross section of the zonal geostrophic velocity (in cm s^{-1}) at 155°W between Hawaii and Tahiti (from Wyrtki and Koblinksy (1984)).

the basin of about 5°C . There is also a north-south asymmetry about the equator, with more warm water situated north of the equator.

Physical processes up to a few hundred meters depth in the ocean play an important role in the Pacific climate system. During the Tropical Ocean Global Atmosphere (TOGA) program (1985-1995), a whole array of measurement devices has been set-up in the Tropical Pacific (McPhaden and coauthors, 1998). Hence,

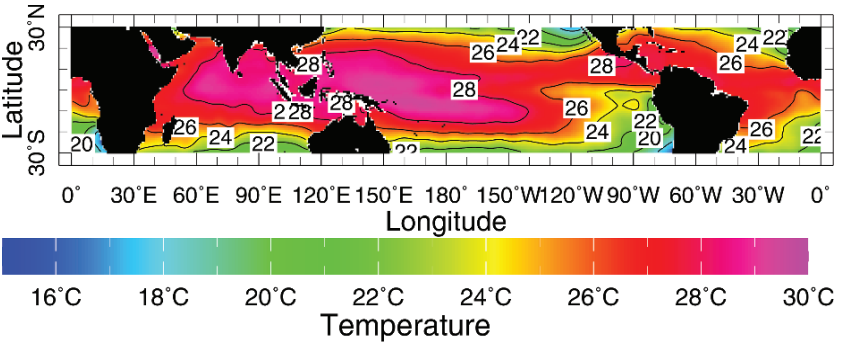

Figure 11.4. Annual mean SST in the Tropical Oceans (Levitus and Boyer, 1994).

only over the last decade, the temperature at these depths have been measured routinely through the TAO-buoy network (see http://www.pmel.noaa.gov/toga-tao). In Fig. 11.5, a longitude-depth section of the equatorial temperature (from 2°S to 2°N) is shown for November 1996; this situation is close to annual-mean conditions for the Tropical Pacific. At each longitude, there is a strong vertical gradient

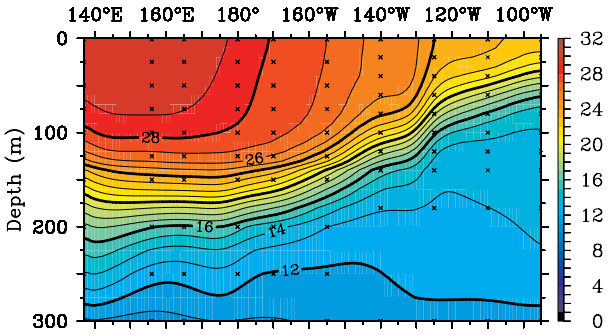

Figure 11.5. Depth-longitude section of the near-equatorial Pacific temperature in the monthly averaged over November 1996. The crosses in the figure indicate the measurement positions of the TAO-buoys (from http://www.pmel.noaa.gov/toga-tao).

in the temperature distribution; this transition region is the equatorial thermocline. The depth of the 20°C isotherm is a reasonable measure of the location of the thermocline. This depth changes from about 200 m at the western part of the basin to about 50 m at the eastern boundary. Hence, in the annual-mean state, the colder water is much closer to the surface in the east than in the west. This slope in the

equatorial thermocline is the second motivating problem of the material in this chapter.

Temperature and salinity are plotted in Fig. 11.6 along the same meridional section in the Pacific as in Fig. 11.3 (at 155°W). The north-south structure of the 20° isotherm indicates a shallowing of the thermocline near the equator. Slightly north of the equator there is a region where the thermocline depth has a large meridional gradient. The salinity distribution is fairly north-south asymmetric with slightly higher salinities south of the equator. The Equatorial Under Current is contained between the 15°C and 25°C isotherms and appears associated with large meridional salinity gradients.

Additional Material

B: An elementary introduction on equatorial currents (with nice illustrations) is given in chapter 5 of OU-staff (1989).

D: An extensive description of the tropical ocean circulation is given in chapter 4.3 (Godfrey et al.) of WOCE (2001) and in section 6.1 of Pedlosky (1996).

11.2. Equatorial ocean models

From the description of the phenomena in the previous section, it appears that the characteristic zonal flow scale is the basin length, but the meridional scale is much smaller. Furthermore, the vertical scale is only a few hundred meters. In fact, most phenomena of interest are present only in a relatively small zone around the equator. This motivates the use of the equatorial β-plane models; again, the constant density case is considered first and then later extended to a layer-type model.

11.2.1. Constant density equatorial β-plane model

For the case of constant density ρ, the starting equations are the dimensional equations in chapter 4. The only thing to change for the equatorial case is the value of the Coriolis parameter at the central latitude, which is the equator, hence $f_0 = 0$. In this way, the dimensional equations become

$$\begin{aligned} \frac{Du_*}{dt_*} - \beta_0 y_* v_* &= -\frac{1}{\rho}\frac{\partial p_*}{\partial x_*} + \\ +A_H\left[\frac{\partial^2 u_*}{\partial x_*^2} + \frac{\partial^2 u_*}{\partial y_*^2}\right] &+ A_V \frac{\partial^2 u_*}{\partial z_*^2}, \qquad (11.1a) \\ \frac{Dv_*}{dt_*} + \beta_0 y_* u_* &= -\frac{1}{\rho}\frac{\partial p_*}{\partial y_*} + \end{aligned}$$

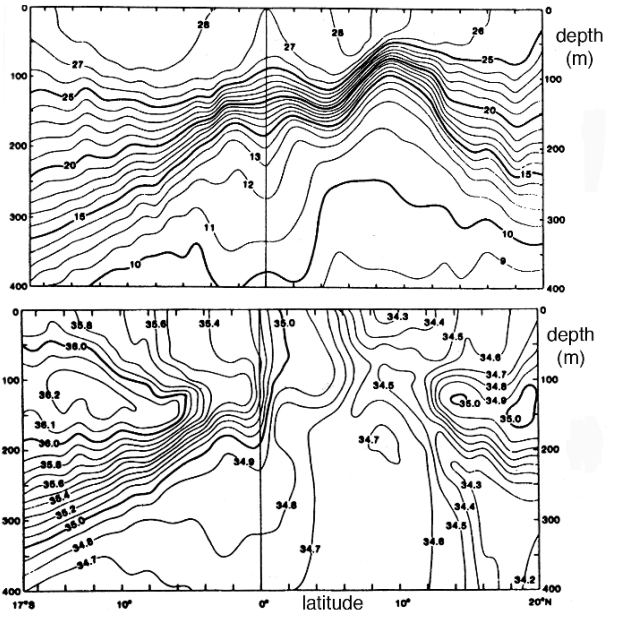

Figure 11.6. Temperature in C° (a) and salinity in psu (b) along a meridional section at 155°W in the Pacific (from Wyrtki and Koblinksky (1984)).

$$+A_H\left[\frac{\partial^2 v_*}{\partial x_*^2}+\frac{\partial^2 v_*}{\partial y_*^2}\right] \quad + \quad A_V\frac{\partial^2 v_*}{\partial z_*^2}, \tag{11.1b}$$

$$\frac{\partial p_*}{\partial z_*} \quad = \quad -\rho g, \tag{11.1c}$$

$$\frac{\partial w_*}{\partial z_*}+\frac{\partial v_*}{\partial y_*}+\frac{\partial u_*}{\partial x_*} \quad = \quad 0, \tag{11.1d}$$

with

$$\frac{D}{dt_*}=\frac{\partial}{\partial t_*}+u_*\frac{\partial}{\partial x_*}+v_*\frac{\partial}{\partial y_*}+w_*\frac{\partial}{\partial z_*}.$$

The dimensional boundary conditions at the ocean-atmosphere interface, described by $z_* = \eta_*$, are of the form

$$p_* = p_{a*}, \tag{11.2a}$$

$$\rho A_V\frac{\partial u_*}{\partial z_*}=\tau_*^x, \tag{11.2b}$$

$$\rho A_V \frac{\partial v_*}{\partial z_*} = \tau_*^y, \tag{11.2c}$$

$$\frac{D}{dt_*}(z_* - \eta_*) = 0. \tag{11.2d}$$

In these equations, u_* and v_* are the horizontal velocities, w_* is the vertical velocity and p_* is the pressure. The quantities g, A_H, and A_V are the acceleration due to gravity and the horizontal and vertical mixing coefficients of momentum. The quantity p_{a*} is the background atmospheric sea level pressure and (τ_*^x, τ_*^y) is the wind-stress forcing. Other boundary conditions for the flow, for example at the continental boundaries, will be specified later.

11.2.2. The reduced gravity model

A slight extension of the previous model is the flow in a two-layer ocean in which the bottom layer is assumed to be motionless (Fig. 11.7). In this case, the equations (11.1- 11.2) hold for the top layer (with density ρ and equilibrium depth H) and also for the second layer (with slightly larger density $\rho + \Delta\rho$). The horizontal pressure gradient is zero in the second layer and hence only the hydrostatic pressure equation applies, i.e.

$$\frac{\partial p_{2*}}{\partial z_*} = -(\rho + \Delta\rho)g. \tag{11.3}$$

Let the interface between the layers be prescribed through $z_* = -H + \zeta_*$, as seen in Fig. 11.7, then at this interface the continuity of pressure and the kinematic

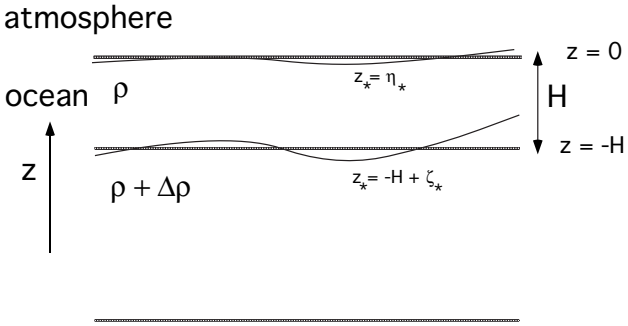

Figure 11.7. Sketch of the reduced gravity ocean model. The upper active layer has a density ρ and equilibrium depth H. The bottom layer is infinitely deep, has a density $\rho + \Delta\rho$ and is motionless.

condition become

$$p_{1*} = p_{2*}, \tag{11.4a}$$

$$\frac{D}{dt_*}(z_* + H - \zeta_*) \;=\; 0, \tag{11.4b}$$

where the material derivative can be taken in both layers, since the vertical velocity is continuous. The equatorial reduced gravity ocean model is obtained by integrating over the upper layer, with total thickness $h_* = \eta_* + H - \zeta_*$. The equations become

$$\begin{aligned}
\frac{\partial u_*}{\partial t_*} + u_*\frac{\partial u_*}{\partial x_*} + v_*\frac{\partial u_*}{\partial y_*} - \beta_0 y_* v_* \;&=\; \\
= -g'\frac{\partial h_*}{\partial x_*} + \frac{\tau^x_*}{h_*\rho} \;&+\; A_H\left[\frac{\partial^2 u_*}{\partial x_*^2} + \frac{\partial^2 u_*}{\partial y_*^2}\right], \qquad (11.5a)\\
\frac{\partial v_*}{\partial t_*} + u_*\frac{\partial v_*}{\partial x_*} + v_*\frac{\partial v_*}{\partial y_*} + \beta_0 y_* u_* \;&=\; \\
= -g'\frac{\partial h_*}{\partial y_*} + \frac{\tau^y_*}{h_*\rho} \;&+\; A_H\left[\frac{\partial^2 v_*}{\partial x_*^2} + \frac{\partial^2 v_*}{\partial y_*^2}\right], \qquad (11.5b)\\
\frac{\partial h_*}{\partial t} + \frac{\partial (u_* h_*)}{\partial x_*} + \frac{\partial (v_* h_*)}{\partial y_*} \;&=\; 0. \qquad (11.5c)
\end{aligned}$$

where $g' = g\Delta\rho/\rho$ is the reduced gravity. This reduced gravity shallow water type model is a first cornerstone of the theory explaining the equatorial current structure.

11.3. The Equatorial Counter Current

The first problem we address is whether we can explain the Equatorial Counter Current (ECC) with the homogeneous (constant density) theory. After introduction of a typical horizontal velocity scale U, a horizontal length scale L and a vertical length scale D, we scale the other variables as

$$t_* = \frac{t}{\beta_0 L}\;;\; u_* = Uu\;; v_* = Uv\;;\; w_* = U\frac{D}{L}w\;;\; p_* = \rho\beta_0 L^2 U p. \tag{11.6}$$

With this scaling, the equations (11.1) become

$$\begin{aligned}
\beta^{-1}\frac{Du}{dt} - yv \;&=\; -\frac{\partial p}{\partial x} + \frac{\bar{E}_V}{2}\frac{\partial^2 u}{\partial z^2}, \qquad (11.7a)\\
\beta^{-1}\frac{Dv}{dt} + yu \;&=\; -\frac{\partial p}{\partial y} + \frac{\bar{E}_V}{2}\frac{\partial^2 v}{\partial z^2}, \qquad (11.7b)\\
0 \;&=\; -\frac{\partial p}{\partial z}, \qquad (11.7c)\\
\frac{\partial w}{\partial z} + \frac{\partial v}{\partial y} + \frac{\partial u}{\partial x} \;&=\; 0, \qquad (11.7d)
\end{aligned}$$

where $\bar{E}_V = 2A_V/(\beta_0 L^3) = 2E_V$, where E_V is the equatorial vertical Ekman number; horizontal mixing is neglected.

The ECC is located north of the equator and so we consider a zone $\mid y \mid > y_0 > 0$ away from the equator. We take $1/\beta$ as our expansion parameter and assume that E_V is at most $\mathcal{O}(\beta^{-1})$. The $\mathcal{O}(1)$ system of equations in this zone then becomes (see section 5.2 for details on the asymptotic techniques),

$$yv^0 = \frac{\partial p^0}{\partial x}, \tag{11.8a}$$

$$yu^0 = -\frac{\partial p^0}{\partial y}, \tag{11.8b}$$

$$\frac{\partial p^0}{\partial z} = 0, \tag{11.8c}$$

$$\frac{\partial u^0}{\partial x} + \frac{\partial v^0}{\partial y} + \frac{\partial w^0}{\partial z} = 0, \tag{11.8d}$$

and hence u^0 and v^0 are z-independent. The vorticity equation follows from (11.8) as

$$y\frac{\partial w^0}{\partial z} = v^0, \tag{11.9}$$

and as the horizontal flow is not divergence free (because the variation of the Coriolis parameter enters the geostrophic balance), the $\mathcal{O}(1)$ problem is not dynamically degenerate.

For the Ekman layer at the surface and at the bottom, we determine boundary layer solutions in the same way as in section 5.2.4. In fact, if we use the transformation $\lambda = \sqrt{|y|}$ and boundary layer coordinates $\bar{\xi} = \lambda\xi$ and $\bar{\chi} = \lambda\chi$ in the Ekman layers, the solutions (5.49) and (5.65) from the midlatitude β-plane can be copied with ξ and χ substituted by $\bar{\xi}$ and $\bar{\chi}$, respectively. The results for the Ekman pumping velocities and Ekman mass transport are for the surface layer,

$$\hat{w}_E = \frac{\alpha}{2}\bar{E}_V^{1/2}\nabla\cdot\left(\frac{\mathbf{T}\wedge\mathbf{e}_3}{y}\right) \rightarrow \hat{w}_{E*} = \frac{1}{\rho\beta_0}\nabla\cdot\left(\frac{\mathbf{T}_*\wedge\mathbf{e}_3}{y_*}\right), \tag{11.10a}$$

$$\mathbf{M}_E = \frac{\alpha}{2}\bar{E}_V^{1/2}\frac{\mathbf{T}_*\wedge\mathbf{e}_3}{y} \rightarrow \mathbf{M}_{E*} = \frac{1}{\rho\beta_0}\frac{\mathbf{T}\wedge\mathbf{e}_3}{y_*}, \tag{11.10b}$$

as $\alpha = 2\tau_0/(\rho\beta_0 L\delta_E U)$ and $\delta_E = \bar{E}_V^{1/2}D$; $\mathbf{e}_3$ is the unit vector in z-direction. The dimensionless Ekman pump velocity and mass transport near the flat bottom are

$$\tilde{w}_E = \frac{1}{2}\bar{E}_V^{1/2}\left[\nabla\cdot\left(\frac{\mathbf{u}^0}{\lambda}\right) + \nabla\cdot\left(\frac{\mathbf{u}^0}{\lambda}\wedge\mathbf{e}_3\right)\right], \tag{11.11a}$$

$$\mathbf{M}_E = \frac{1}{2\lambda}\bar{E}_V^{1/2}(\mathbf{u}^0 + \mathbf{u}^0\wedge\mathbf{e}_3). \tag{11.11b}$$

The vorticity equation follows directly from (11.9) through integration over the layer as

$$\frac{y}{2}E_V^{1/2}\left[\alpha\nabla\cdot(y^{-1}\mathbf{T}\wedge\mathbf{e}_3)-\nabla\cdot(\frac{\mathbf{u}^0}{\lambda})-\nabla\cdot(\frac{\mathbf{u}^0}{\lambda}\wedge\mathbf{e}_3)\right]=v^0. \qquad (11.12)$$

If we choose U such that $\alpha\bar{E}_V^{1/2}=2$, i.e., $U=\tau_0/(\rho\beta_0 LD)$ then the Sverdrup balance becomes

$$v^0=y\nabla\cdot(y^{-1}\mathbf{T}\wedge\mathbf{e}_3)=\frac{\partial\tau^y}{\partial x}-\frac{\partial\tau^x}{\partial y}+\frac{\tau^x}{y}. \qquad (11.13)$$

With $L=10^6$ and $D=10^3$ we find $U\approx 10^{-2}$ ms^{-1} if $\tau_0=10^{-1}$ Nm^{-2}; this velocity should again be seen as a depth averaged velocity.

▶

Example 11.1: Idealized model of the ECC

As an example we consider an idealization of the equatorial wind-stress field as

$$\tau^x(y)=-\frac{1}{2}(1+\cos 2\pi(y-y_0)), \qquad (11.14)$$

where $y>y_0>0$ and $\tau^y=0$ (Fig. 11.8a). This mimics the strong south equatorial trade winds (negative τ^x), a weakening more northward followed by the strong north equatorial trade winds.

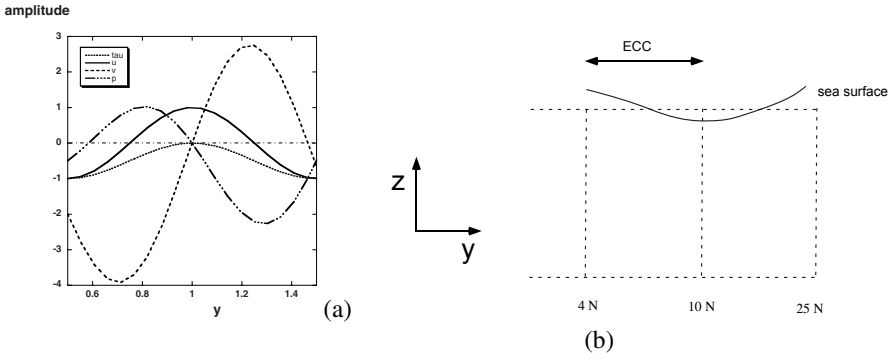

Figure 11.8. (a) Plot of the zonal wind stress field (11.14) versus y, the zonal velocity u^0/π^2, the meridional velocity v^0 and the pressure p^0 at $x=1/2$ with $x_E=1$; here $y_0=0.5$. (b) Sketch to help explain the existence of the ECC.

The geostrophic velocities (u^0, v^0) can easily be determined from (11.13a) and with $u^0(x_E, y) = 0$, where x_E is the eastern boundary, they become

$$u^0(x,y) = 2\pi^2(x - x_E)\cos 2\pi(y - y_0) \quad (11.15a)$$

$$v^0(x,y) = -\frac{1}{2y}(1 + \cos 2\pi(y - y_0)) - \pi \sin 2\pi(y - y_0) \quad (11.15b)$$

$$p^0(x,y) = y(x_E - x)\pi \sin 2\pi(y - y_0) + x\tau^x(y) \quad (11.15c)$$

The profiles of τ^x, u^0, v^0 and p^0 are plotted in Fig. 11.8a for $x = 1/2$, $x_E = 1$ and $y_0 = 0.5$. Indeed, over an interval in y, the zonal velocity is positive and in opposite direction to the zonal wind stress. From the meridional velocity, we see that there is a convergence of mass at $y = y_0$ and a divergence at $y = y_0 + 1/2$. The pressure p^0 (which is also the sea surface height) profile indicates that there the sea surface height decreases over the region where the zonal velocity is positive in agreement with geostrophic equilibrium.

◀

The example above serves to explain the physics of the ECC. The wind stress pushes water up to the western continent and hence induces an east-west slope in the sea surface height. Because the zonal winds vary in meridional direction the sea level height also changes (Fig. 11.8b). This can be seen from the solution of the geostrophic pressure (11.15c) which is also the sea surface height (Fig. 11.8a). Imagine y_0 to be located at about 4° where the trade winds are still strong. With the weakening of the trade winds more northward the meridional slope in the sea level is negative inducing a positive zonal geostrophic velocity. Because of the variation in the Coriolis parameter, there is a slight shift in the sea level height variations with the wind stress variations.

Ex. 11.2

We have assumed here that the value of the Coriolis parameter f_0 was so small that strict (constant $f_0 \neq 0$) geostrophic equilibrium on the f-plane was not possible. At latitudes of the ECC, however, Coriolis effect are not zero and one could do with a midlatitude β-plane model to compute velocities and sea surface height with latitude. It appears that this does not change anything in the explanation of the ECC as given above.

11.4. Equatorial waves

In the reduced gravity model of section 11.2.2, consider the motionless ($\bar{u}_* = \bar{v}_* = 0$) reference state with $\bar{h}_* = H$. This is a stationary solution of the unforced, nondissipative equations (11.5). The equations governing small amplitude motions are obtained by linearizing the equations (11.5) around this reference state and become

$$\frac{\partial u_*}{\partial t_*} - \beta_0 y_* v_* = -g' \frac{\partial h_*}{\partial x_*}, \quad (11.16a)$$

$$\frac{\partial v_*}{\partial t_*} + \beta_0 y_* u_* = -g' \frac{\partial h_*}{\partial y_*}, \tag{11.16b}$$

$$\frac{\partial h_*}{\partial t_*} + H(\frac{\partial u_*}{\partial x_*} + \frac{\partial v_*}{\partial y_*}) = 0. \tag{11.16c}$$

It is convenient to introduce nondimensional quantities by

$$t_* = \frac{L}{c_o} t \; ; \; x_* = Lx \; ; \; y_* = \lambda_o y, \tag{11.17a}$$

$$h_* = Hh \; ; \; u_* = c_o u \; ; \; v_* = \frac{\lambda_o}{L} c_o v. \tag{11.17b}$$

Here, L is the zonal basin length, c_o is a shallow water gravity wave speed and λ_o is a characteristic meridional length scale, the equatorial Rossby radius of deformation, given by

$$c_o = \sqrt{g'H} \; ; \; \lambda_o = \sqrt{\frac{c_o}{\beta_0}}. \tag{11.18}$$

Using these scales, the dimensionless equations become

$$\frac{\partial u}{\partial t} - yv + \frac{\partial h}{\partial x} = 0, \tag{11.19a}$$

$$\zeta_o^2 \frac{\partial v}{\partial t} + yu + \frac{\partial h}{\partial y} = 0, \tag{11.19b}$$

$$\frac{\partial h}{\partial t} + \frac{\partial u}{\partial x} + \frac{\partial v}{\partial y} = 0, \tag{11.19c}$$

with $\zeta_o = \lambda_0 / L$.

Travelling wave solutions of the form

$$u(x,y,t) = \hat{u}(y) e^{i(kx - \sigma t)}, \tag{11.20a}$$

$$v(x,y,t) = \hat{v}(y) e^{i(kx - \sigma t)}, \tag{11.20b}$$

$$h(x,y,t) = \hat{h}(y) e^{i(kx - \sigma t)}, \tag{11.20c}$$

are sought with k being the nondimensional wavenumber and σ the angular frequency. The boundary conditions are

$$y \to \pm\infty : \hat{u}, \hat{v}, \hat{h} \to 0. \tag{11.21}$$

The solutions with $\hat{v} \equiv 0$ have a dispersion relation

$$\sigma^2 = k^2, \tag{11.22}$$

and the meridional structure of the wave is

$$\hat{u}(y) = \hat{u}(0) e^{\frac{-ky^2}{2\sigma}}, \tag{11.23a}$$

$$\hat{h}(y) = \frac{\sigma}{k} \hat{u}(y), \tag{11.23b}$$

with $\hat{u}(0)$ being an arbitrary amplitude. The solutions which are bounded for $y \to \pm\infty$ exist only when $\sigma = +k$. Hence, the phase velocity of these waves is positive and the waves only move eastward. These are the well-known Kelvin waves with a dimensional wavelength and phase speed (σ/k) given by

$$\lambda_* = \frac{2\pi L}{k}\ ;\ c_* = c_o. \tag{11.24}$$

Patterns of the thermocline field h of a Kelvin wave are plotted in Fig. 11.9 for four stages during the propagation. The dimensionless wavenumber is chosen to be $k = \pi$, corresponding to a wavelength of exactly twice the basin $\lambda_* = 2L$. For the Kelvin wave, the dimensionless period $\mathcal{P}$ is $2\pi/\sigma = 2$ and the pictures in Fig. 11.9 are at times $t = 0, t = 1/8, t = 1/4, t = 3/8$, which covers a quarter of a period. The maximum amplitude of the thermocline field for the Kelvin wave is located just at the equator.

Ex. 11.3

Free wave solutions with $\hat{v} \neq 0$ also exist. In (11.19), $\hat{u}$ and $\hat{p}$ can be eliminated to give a scalar equation for $\hat{v}$, i.e.

$$\hat{v}'' + \hat{v}\left[\zeta_0^2(\sigma^2 - k^2) - \frac{k}{\sigma} - y^2\right] = 0, \tag{11.25}$$

where the $'$ indicates differentiation with respect to y. Equation (11.25) only has bounded solutions when

$$\zeta_0^2(\sigma^2 - k^2) - \frac{k}{\sigma} = 2j + 1, \tag{11.26}$$

for $j = 0, 1, \cdots$. These solutions of (11.26) are of the form

$$\hat{v}_j(\eta) = \psi_j(y) = \frac{e^{\frac{-y^2}{2}} H_j(y)}{(2^j j! \pi^{1/2})^{1/2}}, \tag{11.27}$$

with H_j being the Hermite polynomials. The ψ_j are called the Hermite functions (see Example 11.2).

▶

Example 11.2: Hermite polynomials and Hermite functions

The Hermite polynomials $H_n(x)$ are solutions of the differential equation

$$y'' - 2xy' + 2ny = 0. \tag{11.28}$$

for a function $y_n(x)$. The first Hermite polynomials are

$$H_0(x) = 1; H_1(x) = 2x; H_2(x) = 4x^2 - 2; H_3(x) = 8x^3 - 12x, \tag{11.29}$$

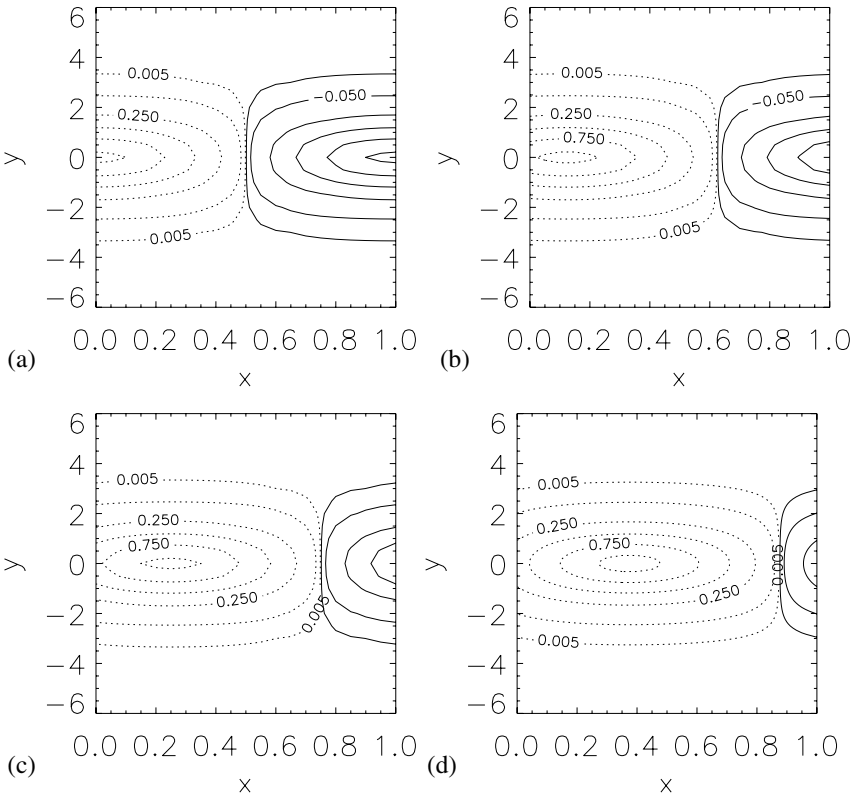

Figure 11.9. Patterns of the dimensionless thermocline field for the Kelvin wave at four different times during one period $\mathcal{P} = 2$ of evolution (a) $t = 0$ (b) $t = \mathcal{P}/8$, (c) $t = \mathcal{P}/4$ and $t = 3\mathcal{P}/8$. The wavenumber $k = \pi$ and plotted is $\psi_0(y)cos(\pi(x-t))/\sqrt{2}$, where ψ_0 is the Hermite function in (11.27). Note that x and y are scaled according to (11.17).

and the following relations can be derived

$$H_{n+1}(x) = 2xH_n(x) - 2nH_{n-1}(x) \tag{11.30a}$$

$$H_n'(x) = 2nH_{n-1}(x). \tag{11.30b}$$

The Hermite polynomials form a complete orthogonal system on the interval $[-\infty, \infty]$ with a weight function $w(x) = \exp(-x^2/2)$ and inner product

$$\int_{-\infty}^{\infty} H_k(x)H_n(x)e^{-x^2}dx = n!2^n\pi^{1/2}\delta_{kn}. \tag{11.31}$$

where $\delta_{kn} = 1$ when $k = n$ and zero otherwise (the Kronecker symbol). The Hermite functions $\psi_n(x)$, with

$$\psi_n(x) = (n!2^n\pi^{1/2})^{-1/2}\exp(-x^2/2)H_n(x), \tag{11.32}$$

are solutions of the differential equation

$$y'' + (2n + 1 - x^2)y = 0, \tag{11.33}$$

From (11.31) it follows that

$$\int_{-\infty}^{\infty} \psi_k(x)\psi_n(x)dx = \delta_{kn}. \tag{11.34}$$

For the Hermite functions, the following relations apply

$$x\psi_n(x) = \sqrt{\frac{n}{2}}\psi_{n-1}(x) - \sqrt{\frac{n+1}{2}}\psi_{n+1}(x), \tag{11.35a}$$

$$\psi(x) = \sqrt{\frac{n}{2}}\psi_{n-1}(x) + \sqrt{\frac{n+1}{2}}\psi_{n+1}(x). \tag{11.35b}$$

◀

First, we consider the full spectrum of these waves by putting $\zeta_o = 1$, which is equivalent to using L as a meridional length scale. The dispersion relation (11.26) can be written as

$$k = -\frac{1}{2\sigma} \pm \frac{1}{2}\left[(\frac{1}{\sigma} - 2\sigma)^2 - 8j\right]^{1/2}. \tag{11.36}$$

For $j > 0$, two real roots exist provided $(1/\sigma - 2\sigma)^2 \geq 8j$ in which case σ satisfies

$$0 < \sigma < \frac{1}{\sqrt{2}}((j+1)^{1/2} - j^{1/2})$$

or

$$\sigma > \frac{1}{\sqrt{2}}(j^{1/2} + (j+1)^{1/2}).$$

The first interval of σ is in the low frequency range and the waves are called equatorial Rossby waves. The second interval represents the high frequency so-called 'inertia-gravity' waves.

For the case $j = 0$, two roots are found from (11.36), the first one being $\sigma = -k$ which leads to a westward travelling Kelvin wave which becomes unbounded far from the equator. The second root is

$$k = -\frac{1}{\sigma} + \sigma, \tag{11.37}$$

which gives a bounded wave called the Yanai wave. For large σ, the character of the wave becomes Kelvin like, whereas for small σ it becomes Rossby like. A classical picture of the dispersion relation for the Kelvin wave, the Yanai wave and $j = 1$ Rossby and inertia-gravity waves is plotted in Fig. 11.10. The Yanai and

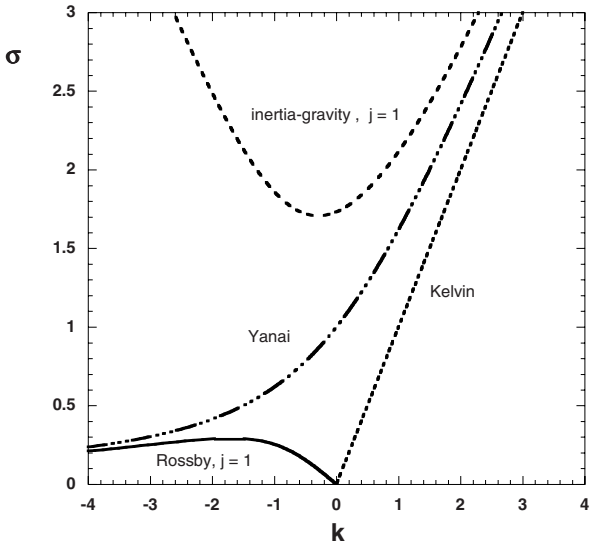

Figure 11.10. Dispersion relation of equatorial free waves. Shown are the Kelvin wave, the Yanai wave and the $j = 1$ Rossby wave.

Kelvin waves have a positive group velocity and for inertia-gravity and Rossby waves, the group velocity c_g becomes

$$c_g = \frac{\partial \sigma}{\partial k} = \frac{1 + 2\sigma k}{2\sigma^2 + \frac{k}{\sigma}}. \tag{11.38}$$

For low frequency Rossby waves (Fig. 11.10), the group velocity is negative and the approximate dispersion relation is (note that both $k^2 << 1$ and $\sigma^2 << 1$)

$$\sigma = -\frac{k}{2j+1}. \tag{11.39}$$

Their dimensional phase velocity is given by

$$c_* = -\frac{c_o}{2j+1},$$

and depends on the meridional wavenumber j. In the limit $\zeta_o \to 0$, only these long waves remain which can be immediately concluded from (11.26). This limit

is therefore called the long wave limit. The first long Rossby wave ($j = 1$) travels westward with a phase velocity which is $1/3$ of that of the Kelvin wave. From the expressions of the Hermite functions in (11.27), one can see that the amplitude is restricted to a relatively small meridional interval around the equator; these waves are therefore called 'equatorially trapped'.

Patterns of the thermocline field for the $j = 1$ Rossby wave, with again a dimensionless wavenumber $k = \pi$ ($k_* = \pi/L$), are plotted in Fig. 11.11 for four stages during the propagation. The dimensionless period of the $j = 1$ Rossby wave is $\mathcal{P} = 2\pi/\sigma = 6$, and the pictures are shown at $t = 0, t = 3/8, t = 3/4, t = 9/8$. The maximum amplitude of the $j = 1$ Rossby wave is located off-

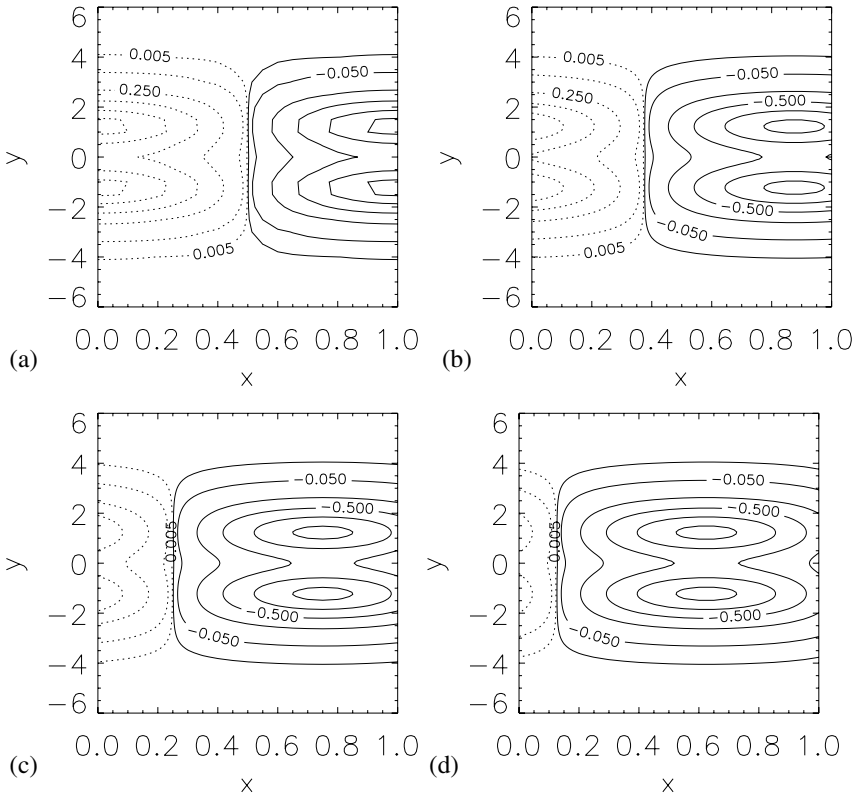

Figure 11.11. Patterns of the thermocline field h of the $j = 1$ Rossby wave for four different times during one period $\mathcal{P} = 6$ of evolution (a) $t = 0$ (b) $t = 3/8$, (c) $t = 3/4$ and (d) $t = 9/8$. The wavenumber k is equal to π and plotted is $(\psi_0(y) + \psi_2(y)/\sqrt{2})cos(\pi(x-t)))/(2\sqrt{2})$, where ψ_0 and ψ_2 are Hermite functions as in (11.27).

equatorial at about $1.33\lambda_o$ from the equator. This distance increases (Fig. 11.12) for higher Rossby waves, i.e., larger j. For c_o = 2 ms^{-1}, the dimensional values of

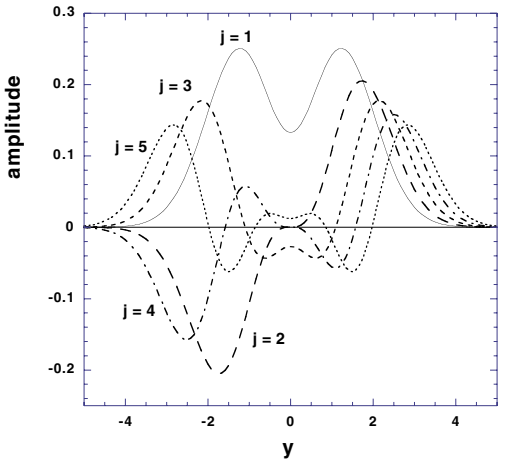

Figure 11.12. Meridional structure of the dimensionless thermocline field $\hat{h}_j$ (see e.g., (11.46c) below) associated with the first 5 (long) free Rossby waves ($j = 1, ..., 5$).

the meridional locations at which Rossby wave thermocline amplitudes have their maximum are shown in Table 11.1 for the long waves with $j = 1, ..., 5$ together with dimensional crossing times for a basin of 15,000 km.

Wave type	y_{max}	θ_{max}	τ_d (days)
Kelvin	0.0	0.0	87
Rossby, $j = 1$	1.22	$\pm$3.31	260
Rossby, $j = 2$	1.75	$\pm$4.75	434
Rossby, $j = 3$	2.17	$\pm$5.88	608
Rossby, $j = 4$	2.50	$\pm$6.77	781
Rossby, $j = 5$	2.83	$\pm$7.67	955

Table 11.1. Typical quantities of free equatorial waves for $c_o = 2\ m/s$, and $\beta_0 = 2.2 \times 10^{-11}(ms)^{-1}$, such that $\lambda_o = 301.5\ km$. The dimensionless quantity y_{max} is the position of the maximum amplitude of the thermocline depth as seen in Fig. 11.12; θ_{max} is the latitude of this position. The travel time τ_d is based on the time it takes for the wave to cross a basin of 15,000 km. The Kelvin wave travels from west to east whereas all Rossby waves travel from east to west.

Additional Material

B: Equatorial waves are discussed at length in section 8.5 of Pedlosky (1987), the chapters 3 and 4 of Philander (1990) and lecture 18 of Pedlosky (2003).

11.5. Forced response in a basin

Using the reduced model derived in section 11.2, we next consider the changes in the ocean circulation in a finite basin due to the presence of a prescribed wind stress. Under limitations of small amplitude forced motion, the shallow water model can be linearized around a motionless reference state with constant thermocline depth H. Small amplitude zonal winds are assumed to be present, while the meridional component of the wind is neglected. A further simplification arises by idealizing the horizontal friction to be linear rather than harmonic. This can be justified by recognizing that for equatorially trapped motions in which the zonal length scale L is much larger than the meridional scale λ_o,

$$A_H \left[\frac{\partial^2 u_*}{\partial x_*^2} + \frac{\partial^2 u_*}{\partial y_*^2} \right] \approx -\frac{2A_H}{\lambda_o^2} u_* = -a_m u_* \tag{11.40}$$

which can, for example, be derived using central differences around the equator. With the scaling (11.17), the dimensionless problem to determine the small amplitude response to the wind stress is obtained from (11.5) and given by

$$\frac{\partial u}{\partial t} - yv + \frac{\partial h}{\partial x} + \epsilon_o u = F_0 \tau^x, \tag{11.41a}$$

$$\zeta_o^2 \frac{\partial v}{\partial t} + yu + \frac{\partial h}{\partial y} + \epsilon_o \zeta_o v = 0, \tag{11.41b}$$

$$\frac{\partial h}{\partial t} + \frac{\partial u}{\partial x} + \frac{\partial v}{\partial y} + \epsilon_o h = 0, \tag{11.41c}$$

where $F_0 = \tau_0 L/(c_o^2 \rho H)$ is the dimensionless amplitude of the zonal wind stress and $\epsilon_o = a_m L/c_o$ is the dimensionless linear damping coefficient. In a finite basin on the equatorial β-plane, the boundary conditions are

$$x = 0, 1 \quad : \quad u = 0, \tag{11.42a}$$

$$y \to \pm\infty \quad : \quad u, v, h \to 0. \tag{11.42b}$$

With $\mathbf{F} = (\tau^x, 0, 0)$ and $\mathbf{u} = (u, v, h)$, this system of equations can be written as

$$\mathcal{M} \frac{\partial \mathbf{u}}{\partial t} + \mathcal{L}\mathbf{u} = \mathbf{F}, \tag{11.43a}$$

$$\mathcal{L} = \begin{pmatrix} \epsilon_o & -y & \frac{\partial}{\partial x} \\ y & \zeta_o \epsilon_o & \frac{\partial}{\partial y} \\ \frac{\partial}{\partial x} & \frac{\partial}{\partial y} & \epsilon_o \end{pmatrix} \quad ; \quad \mathcal{M} = \begin{pmatrix} 1 & 0 & 0 \\ 0 & \zeta_o^2 & 0 \\ 0 & 0 & 1 \end{pmatrix}. \tag{11.43b}$$

Applying a Fourier transformation in x, according to

$$\hat{\mathbf{u}}(k,y,t) = \int_{-\infty}^{\infty} \mathbf{u}(x,y,t) e^{-ikx}\, dx, \tag{11.44a}$$

$$\hat{\mathbf{F}}(k,y,t) = \int_{-\infty}^{\infty} \mathbf{F}(x,y,t) e^{-ikx}\, dx, \tag{11.44b}$$

all x-derivatives in $\mathcal{L}$ transform to ik in $\hat{\mathcal{L}}$ and $\hat{\mathcal{M}} = \mathcal{M}$. All free wave solutions of the previous section, written say as $\hat{\mathbf{U}}$, are solutions of the eigenvalue problem (for $\epsilon_o = 0$)

$$\hat{\mathcal{L}}\hat{\mathbf{U}} = i\sigma \hat{\mathcal{M}}\hat{\mathbf{U}}, \tag{11.45}$$

Ex. 11.4

where σ is given through the dispersion relation (11.26).

In the limit $\zeta_o \to 0$, only the long (small k), low frequency modes (small σ) Rossby waves remain, having a dispersion relation and eigenfunctions for $j = 1, 2, \ldots$

$$\sigma_j = \frac{-k}{2j+1} \tag{11.46a}$$

$$\hat{u}_j(y) = \frac{1}{2\sqrt{2}}\left(\frac{\psi_{j+1}(y)}{\sqrt{j+1}} - \frac{\psi_{j-1}(y)}{\sqrt{j}}\right), \tag{11.46b}$$

$$\hat{h}_j(y) = \frac{1}{2\sqrt{2}}\left(\frac{\psi_{j+1}(y)}{\sqrt{j+1}} + \frac{\psi_{j-1}(y)}{\sqrt{j}}\right), \tag{11.46c}$$

$$\hat{v}_j(y) = \psi_j(y), \tag{11.46d}$$

The Kelvin waves with dispersion relation and eigenfunction

$$\sigma_0 = k, \tag{11.47a}$$

$$\hat{u}_0(y) = \frac{1}{\sqrt{2}}\psi_0(y), \tag{11.47b}$$

$$\hat{h}_0(y) = \frac{1}{\sqrt{2}}\psi_0(y), \tag{11.47c}$$

$$\hat{v}_0(y) = 0, \tag{11.47d}$$

have to be included to get a complete system of basis functions for the meridional structure of the solutions of the problem (11.19). The vector eigenfunctions (11.46) and (11.47) will be indicated below by $\mathbf{\Phi}_j$ and $\mathbf{\Phi}_0$, respectively. A consequence of the elimination of the small waves in the limit $\zeta_o \to 0$ is that one can

no longer satisfy the kinematic boundary condition ($u = 0$) at the western boundary of the basin. A consistent boundary condition is to balance the incoming and outgoing zonal mass flux, which gives

$$x = 0 \; : \; \int_{-\infty}^{\infty} u \, dy = 0. \tag{11.48}$$

As a next step, the zonal wind stress is assumed to have the particular form

$$\tau^x(x, y, t) = \delta(x - x_0) g(y) e^{i\omega t}, \tag{11.49}$$

where δ is the Dirac delta distribution, x_0 a point in the basin and $g(y)$ a prescribed function. The time dependence is assumed to be periodic with frequency ω. Since the system of equations (11.19) is separable in time, the solutions $\mathbf{u}$ also have the same time dependence, i.e., $\mathbf{u}(x, y, t) = e^{i\omega t}\tilde{\mathbf{u}}(x, y)$. If the solution $\tilde{\mathbf{u}}(x, y)$ for the wind-stress shape (11.49) is determined and is indicated by $\mathbf{G}(x, y; x_0)$ then the solution for every wind stress with spatial dependence $\tau^x(x, y, t) = f(x)g(y)e^{i\omega t}$, is given by

$$\mathbf{u}(x, y, t) = e^{i\omega t} \int_0^1 \mathbf{G}(x, y; x_0) g(x_0) \, dx_0, \tag{11.50}$$

which is easily verified by substitution of (11.50) into (11.43). Hence the solution $\mathbf{G}$ acts as a Green's function (see Example 11.3) and it is worthwhile determining it explicitly.

▶

Example 11.3: Green's functions

Inhomogeneous boundary value problems can be efficiently solved using a Green's function. As an example, consider the one-dimensional boundary value problem for the function $y(x)$ on the interval $x \in [0, 1]$, defined by

$$(1 + x)y'' + y' = h(x), \tag{11.51a}$$

$$y'(0) = y(1) = 0, \tag{11.51b}$$

for an arbitrary function $h(x)$. The Green's function $G(x, \xi)$ is defined on the square $0 \leq x, \xi \leq 1$ as the solution of

$$(1 + x)G'' + G' = \delta(x - \xi), \tag{11.52a}$$

$$G'(0) = G(1) = 0, \tag{11.52b}$$

where the primes indicate differentiation to x and δ is the Dirac distribution. Once G has been determined, then the general solution to (11.51) follows immediately

as

$$y(x) = \int_0^1 G(x,\xi)h(\xi)\,d\xi. \tag{11.53}$$

This is easily verified by substitution since

$$\begin{aligned}(1+x)y'' + y' &= \int_0^1 ((1+x)G''(x,\xi) + G'(x,\xi))h(\xi)\,d\xi = \\ &= \int_0^1 \delta(x-\xi)h(\xi)\,d\xi = h(x).\end{aligned} \tag{11.54}$$

In our example, we can determine G analytically from

$$(1+x)G''+G' = ((1+x)G')' = \delta(x-\xi) \rightarrow (1+x)G' = \mathcal{H}(x-\xi)+C_1, \tag{11.55}$$

where $\mathcal{H}$ is the Heaviside function. When we use $G'(0) = 0$, it follows that $C_1 = 0$ (the Heaviside function has an argument $-\xi < 0$). We can then solve

$$G' = \frac{\mathcal{H}(x-\xi)}{1+x} \rightarrow G(x,\xi) = (\ln(1+x) - \ln(1+\xi))\mathcal{H}(x-\xi) + C_2 \tag{11.56}$$

and the constant C_2 follows from $G(1) = 0$ as $C_2 = \ln(1+\xi) - \ln\ 2$. The solution finally is

$$G(x,\xi) = \mathcal{H}(x-\xi)\,\ln\frac{1+x}{1+\xi} + \ln\frac{1+\xi}{2} \tag{11.57}$$

The example illustrates why often Heaviside functions appear in Green's functions.

◄

First the (particular) solution $\mathbf{G}_f$ to the inhomogeneous problem is derived followed by the total solution $\mathbf{G}$ which satisfies the boundary conditions. After the Fourier transformation of the equations (11.43) for $\mathbf{u} = \tilde{\mathbf{u}}e^{i\omega t}$, the following system of equations results

$$\phi\hat{u} - y\hat{v} + ik\hat{h} = e^{-ikx_0}g(y), \tag{11.58a}$$

$$y\hat{u} + \frac{\partial\hat{h}}{\partial y} = 0, \tag{11.58b}$$

$$\phi\hat{h} + ik\hat{u} + \frac{\partial\hat{v}}{\partial y} = 0, \tag{11.58c}$$

with $\phi = \epsilon_o + i\omega$.

The forcing function $g(y)$ and the dependent quantities $\hat{u}, \hat{v}, \hat{h}$ are expanded into the free wave solutions as follows

$$g(y) = r_0 \hat{u}_0(y) + \sum_{j=1}^{\infty} r_j \hat{u}_j(y), \tag{11.59a}$$

$$\hat{\mathbf{u}} = a_0 \mathbf{\Phi}_0(y) + \sum_{j=1}^{\infty} a_j \mathbf{\Phi}_j(y), \tag{11.59b}$$

where the $\mathbf{\Phi}_j$ satisfy (11.45). Equating term by term, the coefficients a_j are solved in terms of the r_j as

$$a_j = \frac{r_j e^{-ikx_0}}{\phi + i\sigma_j}, \tag{11.60}$$

where σ_j is the frequency of eigenmode j. The inverse Fourier transform now gives the formal solution as

$$\mathbf{G}_f(x, y, \phi; x_0) = \frac{1}{2\pi i} \int_{-\infty}^{\infty} e^{ik(x-x_0)} \times$$
$$\times \left[\frac{r_0}{k - i\phi} \mathbf{\Phi}_0(y) - \sum_{j=1}^{\infty} \frac{r_j (2j+1)}{k + i\phi(2j+1)} \mathbf{\Phi}_j(y) \right] dk. \tag{11.61}$$

The integrals can be evaluated through the residue theorem (see any text on complex function theory) and one gets

$$\mathbf{G}_f(x, y, \phi; x_0) = r_0 \mathbf{\Phi}_0(y) e^{-\phi(x-x_0)} \mathcal{H}(x - x_0) +$$
$$+ \sum_{j=1}^{\infty} (2j+1)\, r_j\, e^{\phi(2j+1)(x-x_0)} \mathbf{\Phi}_j(y) \mathcal{H}(x_0 - x), \tag{11.62}$$

where $\mathcal{H}$ is the Heaviside function. The physics of this forced response is easy to understand. If a wind-stress forcing is applied at $x = x_0$, then to the west ($x < x_0$) only a Rossby wave response ($\mathbf{\Phi}_j$) is found whereas to the east ($x > x_0$), a Kelvin wave response ($\mathbf{\Phi}_0$) is found.

This solution does not satisfy the boundary conditions at the eastern and western boundaries and solutions of the homogeneous problem have to be added to accomplish this. These solutions are the actual eigenfunctions $\mathbf{\Phi}_j$, the free wave solutions, with up to now undetermined amplitudes b_j. One obtains for $x > x_0$,

$$\mathbf{G}(x, y, \phi; x_0) = (r_0 + b_0) \mathbf{\Phi}_0(y) e^{-\phi(x-x_0)} +$$
$$+ \sum_{j=1}^{\infty} b_j e^{\phi(2j+1)(x-x_0)} \mathbf{\Phi}_j(y), \tag{11.63}$$

while for $x < x_0$, one obtains

$$\mathbf{G}(x, y, \phi; x_0) = b_0 \mathbf{\Phi}_0(y) e^{-\phi(x-x_0)} + \tag{11.64}$$

$$+ \sum_{j=1}^{\infty} ((2j+1) r_j + b_j) e^{\phi(2j+1)(x-x_0)} \mathbf{\Phi}_j(y). \tag{11.65}$$

From the condition at the eastern boundary ($u = 0$), it follows from (11.41b) that

$$\frac{\partial h(1, y, \phi; x_0)}{\partial y} = 0 \Rightarrow h_E^G(\phi; x_0) = h(1, y, \phi; x_0), \tag{11.66}$$

where the superscript G refers to the Green's function. To determine the coefficients b_j, the identities

$$0 = \lim_{M \to \infty} \left[\hat{u}_0 + 2 \sum_{j=0}^{M} \alpha_{2j+1} \hat{u}_{2j+1} \right], \tag{11.67a}$$

$$\pi^{-\frac{1}{4}} = \lim_{M \to \infty} \left[\hat{h}_0 + 2 \sum_{j=0}^{M} \alpha_{2j+1} \hat{h}_{2j+1} \right], \tag{11.67b}$$

$$\alpha_{2j+1} = \frac{\sqrt{(2j+1)!}}{2^j j!}, \tag{11.67c}$$

are used. Note that the convergence with M in these identities is very poor for the zonal velocity component and for both zonal velocity and thermocline off the equator. Convergence is best for the thermocline deviation on the equator. Application of the eastern boundary condition and comparing term by term gives

$$\begin{aligned} (r_0 + b_0) e^{-\phi(1-x_0)} &= \pi^{\frac{1}{4}} h_E^G, \\ b_{2j+1} e^{\phi(4j+3)(1-x_0)} &= 2\alpha_{2j+1}\, \pi^{\frac{1}{4}} h_E^G, \\ b_{2j} &= 0, \end{aligned}$$

from which the coefficients b_j can be solved. Eventually, the complete solution to the pulse forcing at $x = x_0$, i.e., the Green's function for the problem, is found as

$$\mathbf{G}(x, y, \phi; x_0) = \pi^{\frac{1}{4}} h_E^G \mathbf{K}(\phi(1-x), y) - \mathbf{L}(\phi(x_0 - x), y) \mathcal{H}(x_0 - x), \tag{11.69}$$

where vector functions $\mathbf{K}$ and $\mathbf{L}$ are defined as

$$\mathbf{K}(\eta, y) = e^{\eta} \mathbf{\Phi}_0(y) + 2 \sum_{j=0}^{\infty} \alpha_{2j+1} e^{-\eta(4j+3)} \mathbf{\Phi}_{2j+1}(y), \tag{11.70a}$$

$$\mathbf{L}(\eta, y) = r_0 e^{\eta} \mathbf{\Phi}_0(y) - \sum_{j=0}^{\infty} (2j+1) r_j e^{-\eta(2j+1)} \mathbf{\Phi}_j(y). \tag{11.70b}$$

Up to this point, only the eastern boundary amplitude of the thermocline h_E^G is still unknown, but it can be determined from the western boundary condition (11.48) and becomes

$$\pi^{\frac{1}{4}} h_E^G(\phi; x_0) = \frac{\int_{-\infty}^{\infty} L_u(\phi x_0, y) dy}{\int_{-\infty}^{\infty} K_u(\phi, y) dy}, \tag{11.71}$$

where K_u and L_u are the first components of $\mathbf{K}$ and $\mathbf{L}$, respectively. This completes the basic machinery needed in the next section to understand the response of the ocean to varying wind stress forcing.

11.6. The equatorial thermocline

To understand the spatial structure of the thermocline (as in Fig. 11.5), we first consider the forced ocean response to a zonal forcing $\tau^x = f(x)e^{i\omega t}$ which can be explicitly determined using the Green's function. The basic identity used is the explicit summation

$$\begin{aligned} e^{-iz} \begin{pmatrix} \hat{u}_0 \\ \hat{h}_0 \end{pmatrix} + 2 \sum_{j=0}^{\infty} \alpha_{2j+1} e^{iz(4j+3)} \begin{pmatrix} \hat{u}_{2j+1} \\ \hat{h}_{2j+1} \end{pmatrix} = \\ = \pi^{-\frac{1}{4}} \, e^{\frac{i}{2} y^2 \tan 2z} \frac{1}{\sqrt{\cos 2z}} \begin{pmatrix} -i \sin 2z \\ \cos 2z \end{pmatrix}, \end{aligned} \tag{11.72}$$

for complex z with $Im(z) \geq 0$. Note that for $z = 0$, the identities reduce to (11.67).

Computation of the values of r_j in (11.59a) gives (for $g(y) = 1$)

$$\begin{aligned} r_0 = \frac{1}{\sqrt{2}} \int_{-\infty}^{\infty} \psi_0(y) \, dy &= \pi^{\frac{1}{4}}, \\ r_{2j+1} = \frac{1}{2\sqrt{2}} \int_{-\infty}^{\infty} \left(\frac{\psi_{2j+2}}{\sqrt{2j+2}} - \frac{\psi_{2j}}{\sqrt{2j+1}} \right) dy &= -\pi^{\frac{1}{4}} \frac{2\alpha_{2j+1}}{4j+3}, \\ r_{2j} &= 0, \end{aligned}$$

and hence one finds from (11.70b) that

$$\mathbf{L}(\eta, y) = \pi^{\frac{1}{4}} \mathbf{K}(\eta, y). \tag{11.74}$$

Using the integral

$$\int_{-\infty}^{\infty} e^{i \frac{y^2}{2} \tan(2z)} \, dy = \sqrt{\frac{2\pi}{i \tan 2z}},$$

one obtains as a solution for h_E^G in (11.71), using the identity (11.72) for $z = -i\phi$, as

$$h_E^G(\tilde{\phi}; x_0) = \sqrt{\frac{\sin(2\tilde{\phi} x_0)}{\sin(2\tilde{\phi})}},$$

where $\tilde{\phi} = -i\phi = \omega - i\epsilon_o$. The Green's function $\mathbf{G}$ is then completely known and the total response to a wind stress with zonal dependence $f(x)$ can be computed from (11.50) as

$$u(x,y;\tilde{\phi}) = h_E(\tilde{\phi})\frac{\sin 2\tilde{\phi}(x-1)}{\sqrt{\cos 2\tilde{\phi}(x-1)}}e^{i\frac{y^2}{2}\tan(2\tilde{\phi}(x-1))} - \\ - \int_x^1 f(x_0)\frac{\sin 2\tilde{\phi}(x-x_0)}{\sqrt{\cos 2\tilde{\phi}(x-x_0)}}\, e^{i\frac{y^2}{2}\tan 2\tilde{\phi}(x-x_0)}\, dx_0, \tag{11.75a}$$

$$h(x,y;\tilde{\phi}) = h_E(\tilde{\phi})\sqrt{\cos 2\tilde{\phi}(x-1)}e^{i\frac{y^2}{2}\tan(2\tilde{\phi}(x-1))} - \\ - \int_x^1 f(x_0)e^{i\frac{y^2}{2}\tan(2\tilde{\phi}(x-x_0))}\sqrt{\cos 2\tilde{\phi}(x-x_0)}\, dx_0, \tag{11.75b}$$

where

$$h_E(\tilde{\phi}) = \int_0^1 \sqrt{\frac{\sin(2\tilde{\phi}x_0)}{\sin(2\tilde{\phi})}} f(x_0)\, dx_0, \tag{11.76}$$

is the thermocline amplitude at the east coast.

The thermocline response to a periodic wind stress with a spatial structure mimicking the zonal wind stress due to the trade winds, i.e.,

$$\tau^x = 0.6\,(0.12 - \cos^2\frac{\pi(x-0.57)}{1.14})\cos\frac{2\pi t}{\mathcal{P}}, \tag{11.77}$$

is shown in Fig. 11.13 with a period $\mathcal{P}$ corresponding to 3 years. In the panels, time $t = 0$ the indicates the phase of maximum westerly winds and no winds are present at $t = -\mathcal{P}/4$. At times when the wind stress is present, the thermocline response is nearly in steady balance with the wind stress. However, the ocean does not only react to the instantaneous wind stress but also to previous winds through propagation of waves. The structures off the equator to the west of the wind are partly free Rossby waves which are still adjusting to the wind but part of this response is just a forced response in steady balance with the wind stress. It is the departure of this steady balance which is crucial to further evolution of the flow and provides the ocean with a memory.

Ex. 11.5

As a special case, we consider $\omega = 0$ and $\epsilon_o = 0$ in the solution (11.75) and are therefore looking at the stationary response to the wind stress field $\tau^x(x,y) = f(x)$ and $\tau^y = 0$. The equatorial thermocline distribution is found from (with $\tilde{\phi} = 0$, and the proper limit in (11.76))

$$h_e(x) = \int_0^1 s^{1/2} f(s)ds - \int_x^1 f(s)ds. \tag{11.78}$$

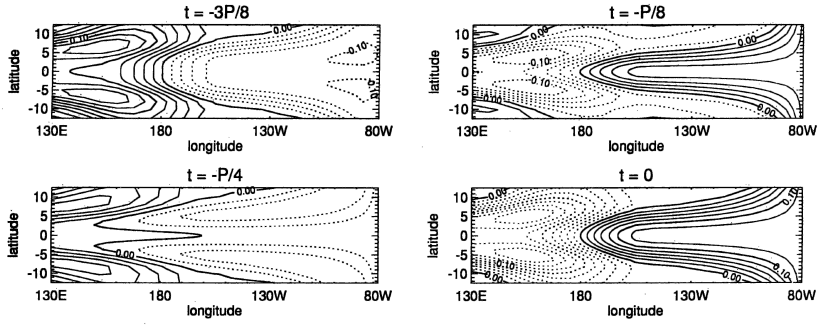

Figure 11.13. Response of the thermocline (amplitudes relative to the equilibrium layer depth H) to a periodic wind fluctuation having a spatial structure (11.77). Plotted are the spatial patterns of the oscillation for several phases of the oscillation (from Neelin et al. (1998)).

Using (11.78), we see that at the equator the balance $\tau^x = h_x = f(x)$ holds and hence from (11.78) it follows that the first term in the right hand side determines the value of the thermocline at the eastern boundary. The dimensional form of (11.78) is

$$h_{e*}(x_*) = \frac{\tau_0 L}{\rho H g'}\left(\int_0^1 x^{1/2} f(s)ds - \int_x^1 f(s)ds\right). \tag{11.79}$$

For a pure zonal wind field $f(x) = -1$, the thermocline solution becomes

$$h_e(x) = \frac{1}{3} - x \rightarrow h_{e*}(x_*) = \frac{\tau_0}{\rho H L g'}\left(\frac{1}{3} - \frac{x_*}{L}\right) \tag{11.80}$$

The fact that the thermocline is deeper in the west than in the east can be completely explained from the wind-stress field. Because the sea surface is higher in the west than in the east, the resulting pressure difference has an immediate impact on the slope of the thermocline. With $\tau_0 = 0.1$ Pa, H = 200 m, L = 10,000 km, $g' = 0.05$ ms^{-2} and $\rho = 10^3$ kgs^{-3}, we find that the factor $\tau_0 L/(\rho H g')$ = 100 m which provides a realistic amplitude of the thermocline deviation.

Summary

- Interesting features of the equatorial ocean circulation are the Equatorial Counter Currents (ECCs) and Equatorial Under Currents (EUCs).
- A reduced gravity model is a two-layer model in which the lower layer is motionless.
- Equatorial Counter Currents exist because of the weakening of the trade winds slightly north of the equator leading to a negative meridional gradient in the sea surface height.
- Long baroclinic waves in the equatorial wave guide consist of Kelvin waves (with phase speed $c_0 = \sqrt{g'H}$) and Rossby waves with phase speeds
$$c_{j*} = -\frac{c_0}{2j+1}$$
where j is associated with the meridional structure of the wave. The travel time of the Kelvin wave over the Pacific is about 3 months (with $c_0 = 2$ ms^{-1}) and this is 9 months for the $j = 1$ Rossby wave.
- The response of an equatorial ocean basin to a wind-stress field can be determined using Green's function theory. The thermocline deviation due to a zonal wind stress of 0.1 Pa is about 100 m.

11.7. Exercises on chapter 11

(11.1) *The Equatorial Under Current*

Consider a column of water with a thickness h_0 below the Ekman layer. Water moves from a location $y_0 > 0$ to the equator as a compensation of water which flows northward in the upper layer. Assume that at y_0, the relative vorticity is small with respect to the planetary vorticity.

a. Show that from conservation of potential vorticity, it follows that

$$\frac{\beta_0 y - u'}{h} = \frac{f_0}{h_0}$$

where $h(y)$ is the thickness of the water column at location y and $u(y)$ the steady zonal velocity at the equator.

b. Determine the solution $u(y)$ as a model for the Equatorial Under Current and provide an estimate of the amplitude of the zonal velocity of this current.

c. Is this a good model to explain the existence of the Equatorial Under Current?

(11.2) *Equatorial Counter Current*

The model in section 11.2 does qualitatively indicate the existence of the Equatorial Counter Current (ECC). We have assumed that $f_0 = 0$ and computed the flow on the equatorial β-plane. At latitudes between 4°N and 10°N, the Coriolis parameter f_0 is not strictly zero and one could compute the flow using a midlatitude β-plane model such as presented in the chapters 5 and 6.

a. Use the dimensionless Sverdrup balance (6.5) to compute the zonal velocity, meridional velocity and sea surface height for the same wind stress as in Example 11.1.

b. Show that an ECC occurs at latitudes where the meridional gradient in the sea surface height is negative.

c. Determine from observations a reasonable amplitude of the wind stress north of the equator in the Pacific and estimate the amplitude of the corresponding velocities with the model in section 11.2. Does this agree with observations?

(11.3) *Properties of equatorial waves*

a. Determine the dimensional vertical velocity field associated with the equatorial Kelvin wave and the $j = 1$ Rossby wave.

b. Determine the ratio of the sea surface height amplitude and the thermocline depth amplitude for both waves as in a.

c. During an El Niño the eastern Pacific thermocline can deepen by 50 m. Compute the amplitude of the sea surface height anomaly during such an event.

(11.4) *Reflection of equatorial waves at a western boundary*

Consider the reflection of the $j = M$ equatorial Rossby wave at a western boundary located at $x = 0$. The incoming wave has a wavenumber

$$k_I = -\frac{1}{2\sigma_I} + (\sigma^2 + \frac{1}{4\sigma^2} - (2M+1))^{\frac{1}{2}}$$

and hence its group velocity is westward.

a. Show that the incoming velocity field of the wave is given by

$$v_I(x,y,t) = e^{i(k_I x - \sigma t)}\psi_M(y)$$

$$u_I(x,y,t) = \frac{i}{2}e^{i(k_I x-\sigma t)}(\frac{\sqrt{(2(M+1))}}{\sigma - k_I}\psi_{M+1}(y) + \frac{\sqrt{(2M)}}{\sigma + k_I}\psi_{M-1}(y))$$

$$h_I(x,y,t) = \frac{i}{2}e^{i(k_I x-\sigma t)}(\frac{\sqrt{(2(M+1))}}{\sigma - k_I}\psi_{M+1}(y) + \frac{\sqrt{(2M)}}{\sigma - k_I}\psi_{M-1}(y))$$

The reflected wave is a superposition of Rossby waves (with amplitude $B_m, m = 1, ..., M$) and a Kelvin wave (with amplitude B_K).

b. Provide an expression for the zonal velocity field $u_R(x,y,t)$ of this superposition.

c. Determine the coefficients B_m and B_K.

d. Show that the $j = 1$ Rossby waves reflects into a Kelvin wave.

(11.5) *Equatorial thermocline*

To get familiar with the solutions (11.75) we consider the limit $\omega = 0$ (steady forcing, hence $\tau^x = f(x)$) but keep $\epsilon_0 \neq 0$.

a. Determine the thermocline solution at the equator explicitly for this case.

b. Now take the limit $\epsilon_0 \to 0$ in the result of a. and derive (11.78).

c. Describe which physical processes determine the zonal slope in the thermocline and which processes set the thermocline depth at the western boundary of the domain.

Chapter 12

DYNAMICS OF ENSO

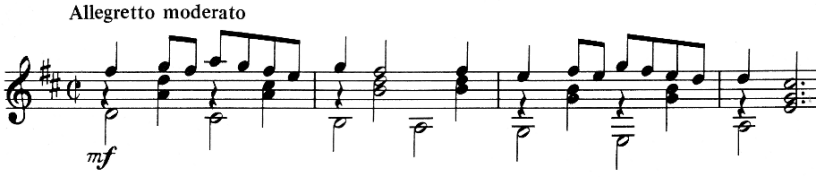

Suite Polulaire Brésilienne, No 4. (Gavotta-Chôro), H. Villa-Lobos

The spatial patterns of the annual mean state of the surface winds and sea surface temperature (SST) in the Pacific were shown in chapter 11 (Fig. 11.1 and Fig. 11.2). In this chapter, anomalies of this mean state are considered. About once every four years the sea surface temperature in the eastern Pacific is much higher than average; this phenomenon is called El Niño. Sea surface temperature anomalies of up to a few degrees can occur and are accompanied by a weakening/strengthening of the trade winds, the latter called the Southern Oscillation. In this chapter, the focus is on a dynamical understanding of the El Niño/ Southern Oscillation (ENSO) phenomenon. After the presentation of a few basic characteristics of ENSO in section 12.1, we discuss coupled processes and feedbacks between the equatorial ocean circulation and atmosphere in section 12.2. Sections 12.3 and 12.4 introduce modern conceptual models of ENSO viewed as a delayed oscillator phenomenon.

12.1. Basic Phenomena

The El Niño/Southern Oscillation (ENSO) is the most prominent example of interannual variability in the climate system. Because it develops on relatively short time scales, it is one of the best studied climate phenomena, both observationally and theoretically. ENSO is caused by processes in both the tropical ocean and atmosphere with a central role for the sea surface temperature.

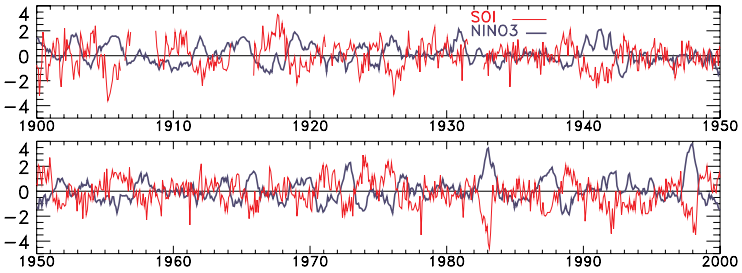

Figure 12.1. Time series of NINO3 and SOI over the period 1900-2000 (from http://ingrid.ldgo.columbia.edu).

Two important indices that are frequently used to monitor the state of the Tropical Pacific system are the SOI and the NINO3. In Fig. 12.1 the NINO3 index (the SST anomaly averaged over the box [150°W-90°W] $\times$ [5°S-5°N]) is

plotted. It appears that the occurrence of El Niño's (positive NINO3) and La Niña's (negative NINO3) is quite irregular. Strong El Niño's such as in 1982-1983 and 1997-1998 are rare as are strong La Niña's and actually long intervals exist with either weak warm or weak cold conditions. An index that captures the amplitude of the sea level pressure anomaly pattern is the Southern Oscillation Index (SOI), which is the normalized difference of the pressure anomalies between Tahiti (18°S, 150°W) and Darwin (12°S, 131°E). When this index is positive, the trade winds are stronger and when it is negative the trade winds are weaker than normal. Generally, periods with a high NINO3 index have a low SOI and vice versa (Fig. 12.1). The correlation between 12-month means of the monthly NINO3 index and the SOI is close to -0.9 over the last 50 years.

An accurate data set of Tropical Pacific SST fields is now available for long enough, such that dominant patterns of variability at interannual time scales can be extracted. When the seasonal signal is filtered out, the equatorial SST anomalies over the years 1990-2000 show an irregularly oscillating signal (Fig. 12.2, left panel) with maximum amplitudes east of the dateline. The maximum temperature anomaly during the 1997-1998 El Niño is about 5°C. As a measure of thermocline

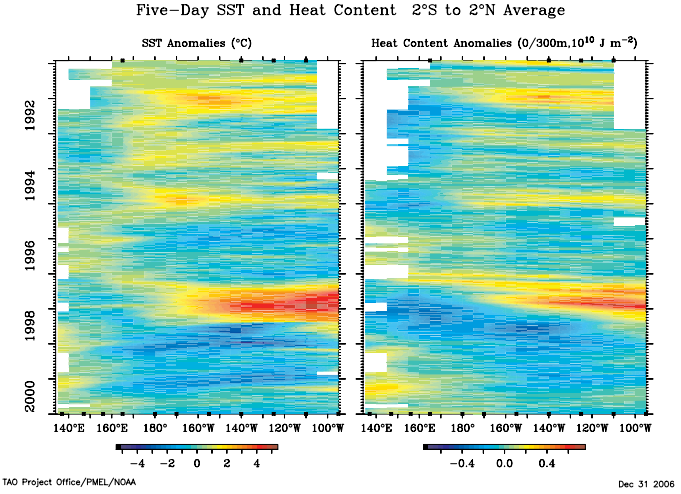

Figure 12.2. Plot of the equatorial SST anomalies (left panel) and the heat content anomalies (with respect to the seasonal mean) over the years 1990-2000. The plots were made using data and software at http://www.pmel.noaa.gov/toga-tao/realtime.html.

anomalies, the upper ocean heat content H_c in $10^{10}\ J/m^2$ is defined as

$$H_c = \rho_0 C_p \int_{-H_f}^{0} T\, dz, \tag{12.1}$$

where H_f is a fixed depth usually chosen as 300 m. If the thermocline (e.g. the depth of the 20°C isotherm) is depressed (elevated), then the upper layer is warmer (colder) leading to a larger (smaller) heat content. In the right panel of Fig. 12.2, the equatorial heat content anomaly is plotted over the years 1990-2000. The upper layer (300 m) was in 1997 about 4°C warmer than average leading to a positive heat content anomaly of $H_c = 0.5 \times 10^{10}$ Jm^{-2} at 120°W. The anomalies in heat content show a clear propagation eastward with west leading east. Note that there are time intervals where the zonally averaged heat content is positive (at the end of 1996) or negative (at the beginning of 1995). Positive easterly SST anomalies occur simultaneously with an anomalously low western Pacific heat content.

Together with the variations of the SOI and NINO3 indices, Fig. 12.2 suggests that ENSO is an oscillatory signal which can be characterized by several patterns at different phases of the oscillation. The patterns for the zonal wind, SST and

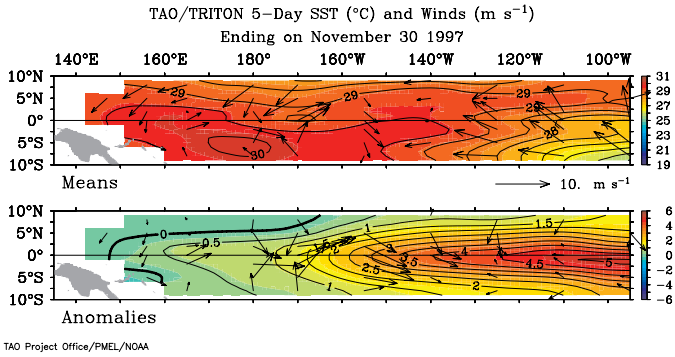

Figure 12.3. Plot of the zonal wind and SST and their anomalies with respect to the seasonal mean at November 30, 1997. The plots were made using data and software at http://www.pmel.noaa.gov/toga-tao/realtime.html.

their anomalies are plotted in Fig. 12.3 for the warm (El Niño) phase of the oscillation (November 1997). The SST anomaly is positive over nearly the whole basin with maxima in the eastern equatorial region and a fairly equatorial symmetrical pattern in the Pacific cold tongue. The positive SST anomaly is accompanied by a westerly wind-stress anomaly (arrows in the lower panel of Fig. 12.3) with a maximum west of the maximum SST anomaly.

In this oscillatory view, the cold phase of the 1997-1997 ENSO (the La Niña-phase) occurred at the end of 1995. Between the cold and warm phase of the oscillation is a transition phase which occurred at the beginning of 1997 (Fig. 12.2a). During this 'transition phase', SST anomalies are nearly zero over the basin as are the wind-stress anomalies. However, the heat content anomaly in the western and central Pacific is positive, since the thermocline is deepened. The latter is consistent with the equatorial anomalies in heat content in Fig. 12.2b.

Additional Material

B: In Glantz (1996), a broad overview of the weather phenomena associated with El Niño is given with a description of their impact on society. Other bedtime reading is Philander (2004).

12.2. A coupled ocean-atmosphere system

The equatorial ocean-atmosphere system is a strongly coupled system and an impression of the whole system is given in Fig. 12.4. In this picture the mean state is shown with its Cold Tongue in the east and its Warm Pool in the west. The trade winds form part of a larger tropical circulation system consisting of the Walker circulation and the Hadley circulation. The nature of the coupling between

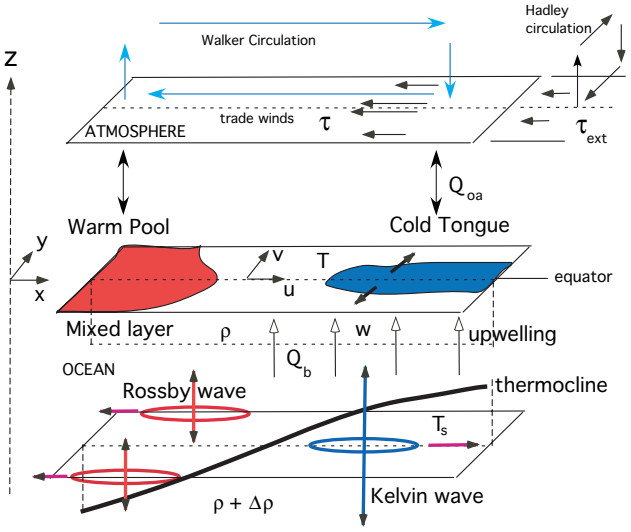

Figure 12.4. Overview of the oceanic and atmospheric processes of the equatorial coupled ocean-atmosphere system.

ocean and atmosphere is the following. A sea surface temperature anomaly will

give, through local heating, a lower-level wind anomaly. The resulting wind-stress anomaly on the ocean-atmosphere surface will (i) change the thermocline slope through horizontal pressure differences in the upper ocean, will (ii) change the strength of the upwelling through the Ekman divergences in the upper layer and will (iii) affect the upper ocean currents (u, v) in the mixed layer. The change in velocity field and thermocline field will affect the sea surface temperature.

From observations, the wind stress response associated with a NINO3 anomaly is indeed closely related to the sea-level pressure anomaly pattern of the Southern Oscillation. The wind response is concentrated around the equator in an area around the date line west of the NINO3 area, as shown in Fig. 12.5. The westward response of the wind means that the trade winds are weakened (or even reversed) during El Niño's.

In section 12.2.1 below we consider the processes which determine the temperature in the ocean mixed layer. Section 12.2.2 discusses the effect of wind-stress anomalies on the upper ocean circulation. The last subsection (section 12.2.3) presents two important feedbacks which play a role in El Niño .

12.2.1. Processes determining the SST

The upper layers of the ocean are generally well mixed up to a depth of 50 m and the temperature is vertically fairly homogeneous within this layer. Consider

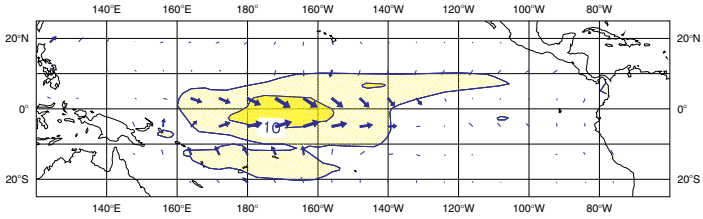

Figure 12.5. Response of pseudo wind stress (pseudo wind stress is a vector in the direction of the surface wind and a magnitude that is the square of the wind speed) to NINO3 anomalies, from a regression of observed FSU pseudo wind stress fields to the NCEP NINO3 index over the period 1968–1999. Contours at 5 and 10 $m^2 s^{-2} K^{-1}$ denote the magnitude of the response.

such a mixed layer in Fig. 12.6 with a constant depth H_m. The temperature in the mixed layer changes due to air-sea interaction, processes at the bottom of the mixed layer and advection. The net heat flux from the atmosphere into the ocean is denoted by Q_{oa} (positive when heat is transferred from atmosphere into the mixed layer) and the heat flux at the bottom of the mixed layer by Q_b (positive when heat leaves the mixed layer). The general temperature equation is given by

$$\frac{\partial T_*}{\partial t_*} + \mathbf{u}_* \cdot \nabla T_* = K_H \nabla_H^2 T_* + K_V \frac{\partial^2 T_*}{\partial {z_*}^2}, \tag{12.2}$$

where ∇_H^2 is the horizontal Laplace operator. The horizontal and vertical diffusivities are indicated by K_H and K_V (both $\mathrm{m^2 s^{-1}}$), respectively. The boundary conditions are

$$z_* = 0 \quad : \quad \rho C_p K_V \frac{\partial T_*}{\partial z_*} = Q_{oa}, \tag{12.3a}$$

$$z_* = -H_m \quad : \quad \rho C_p K_V \frac{\partial T_*}{\partial z_*} = Q_b. \tag{12.3b}$$

where ρ is the constant density in the mixed layer and C_p the constant heat capacity. Using the approximation that the temperature is vertically homogeneous over the layer, one can integrate (12.2) over the layer which results in

$$\frac{\partial T_*}{\partial t} + u_* \frac{\partial T_*}{\partial x_*} + v_* \frac{\partial T_*}{\partial y_*} = K_H \nabla_H^2 T_* + \frac{Q_{oa} - Q_b}{\rho C_p H_m}. \tag{12.4}$$

The net heat flux Q_{oa} can be parameterized into a simple form as, for example, given by

$$Q_{oa} = -a_1 (T_* - T_{r*}), \tag{12.5}$$

where T_{r*} is a reference atmospheric equilibrium temperature. At the lower boundary, the heat flux is composed of diffusive and advective contributions, with the latter dominating. An approximation of this heat flux is

$$\frac{Q_b}{\rho C_p} = w_* \frac{T_* - T_{s*}}{H_u}, \tag{12.6}$$

where w_* is a typical vertical velocity at the bottom of the mixed layer, H_u a vertical distance such that the temperature gradient between the mixed layer and the subsurface temperature T_{s*} is well approximated. The subsurface temperature will depend on the vertical temperature distribution and hence on the position of the thermocline. For example, if the thermocline depth increases then the colder water is further from the surface and T_{s*} will increase.

12.2.2. Wind induced ocean flow anomalies

Ex. 12.1

As can be deduced from Fig. 12.4, SST anomalies lead to surface wind-stress anomalies. From the theory on the equatorial ocean circulation in chapter 11, we know that wind-stress anomalies lead to (i) changes in the Ekman flow, (ii) changes in the thermocline slope and (iii) the generation of a spectrum of free waves, in particular of Kelvin and Rossby waves.

The surface Ekman layer theory was discussed in section 11.3 using a Laplacian form of momentum friction. In the reduced gravity model in section 11.2, however, linear friction was used. If the frictional processes in the equatorial Ekman layer are idealized to be linear, with damping coefficient a_s, then a vertically

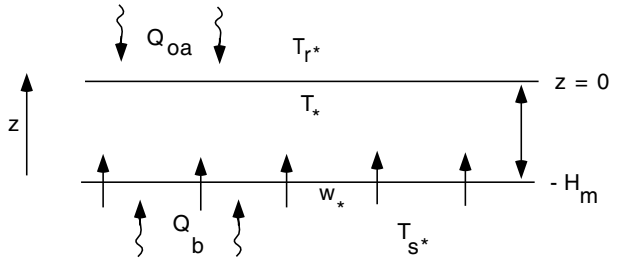

Figure 12.6. Sketch of the mixed layer ocean model. The heat flux Q_{oa} is taken positive when heat is transferred from the atmosphere to the ocean and the heat flux Q_b is taken positive when heat leaves the mixed layer.

integrated balance of the frictional processes, the Coriolis acceleration and wind stress leads to

$$a_s u_{E*} - \beta_0 y_* v_{E*} = \frac{\tau_*^x}{\rho H_E} \tag{12.7a}$$

$$a_s v_{E*} + \beta_0 y_* u_{E*} = \frac{\tau_*^y}{\rho H_E} \tag{12.7b}$$

where u_{E*} and v_{E*} are the vertically averaged horizontal Ekman layer velocities, H_E is the Ekman layer depth and β_0 is the variation of the Coriolis acceleration on the equator. The vertical velocity w_{E*} at the lower boundary of the Ekman layer is given by

$$w_{E*} = H_E\left(\frac{\partial u_{E*}}{\partial x} + \frac{\partial v_{E*}}{\partial y}\right) \tag{12.8}$$

Ex. 12.2

For a constant zonal wind stress $\tau_*^x = -\tau_0$, the equatorial dimensional upwelling w_{E*} is given by

$$w_{E*} = \frac{\tau_0 \beta_0}{\rho a_s^2} \tag{12.9}$$

which for $a_s = 5.0 \times 10^{-6}$ s^{-1} and $\tau_0 = 0.1$Pa leads to a few m/day. Wind-stress anomalies lead hence to changes in the Ekman upwelling velocity at the equator: when the trade winds increase in strength the upwelling increases and vice versa.

From the theory in the sections 11.5 and 11.6, the effect of wind-anomalies on the ocean velocities below the Ekman layer can be deduced. The ocean zonal current velocity was given by (11.75) and stronger trade winds leads to a stronger westward equatorial zonal velocity and vice versa. For a constant zonal wind-stress $\tau_* = -\tau_0$, (11.80) provided the explicit expression for the thermocline as

$$h_{e*}(x_*) = \frac{\tau_0}{\rho H L g'}\left(\frac{1}{3} - \frac{x_*}{L}\right) \tag{12.10}$$

Stronger trade winds lead to a deeper thermocline in the west and a shallower one in the east and vice versa.

12.2.3. Feedbacks

In the previous sections, the elementary physical processes have been discussed and there is enough background now to discuss feedbacks in the coupled system. There are three important feedbacks, which are called the thermocline, the upwelling and the zonal advection feedback. The first two are associated with changes in the vertical heat transport modelled by (12.6), and the third is associated with horizontal heat transport. The first two feedbacks are described in this section in their most elementary form and the zonal advection feedback will be the topic of an exercise at the end of this chapter.

Ex. 12.3

This thermocline feedback is best explained by looking at a sloping thermocline in a constant upwelling ocean (with constant $w_* = \bar{w}_*$) as sketched in Fig. 12.7. Assume that a positive SST perturbation $\tilde{T}$ is present in the eastern part of the basin (Fig. 12.7). This leads to a perturbation in the low level zonal wind which is westerly with a maximum located west of the maximum of the SST anomaly according to the response shown in Fig. 12.4. Since the background trade winds are weakened locally, the slope of the thermocline decreases and it becomes more flat. In this case, the colder water will be closer to the surface in the west but it will be farther down in the east. In other words, in the east the thermocline is deeper and hence the subsurface temperature is higher. Hence, the subsurface temperature effectively increases at the level of upwelling, giving a positive heat flux perturbation at the bottom of the mixed layer according to (12.4) and (12.6), i.e.,

$$\frac{\partial \tilde{T}_*}{\partial t_*} \approx -\bar{w}_* \frac{\tilde{T}_* - \tilde{T}_{s*}}{H_u}. \tag{12.11}$$

As $\bar{w}_*$ is positive, the first term in the right hand side represent the local damping of SST anomalies. However, when $\tilde{T}_{s*} > 0$ then the second term on the right hand side is positive and the original disturbance may be amplified.

As another prototype situation, consider that the thermocline (and hence the subsurface temperature $\bar{T}_{s*}$) is fixed with a certain slope related to the background winds, the latter similar to the previous case. Again a positive SST anomaly is present in the east which generates the same changes in the wind as before (Fig. 12.7). However, now the changes only influence the upwelling ($\tilde{w}_*$), mainly through the Ekman layer dynamics. Weaker easterly winds imply less upwelling and hence less colder water enters the mixed layer. This can also be seen from (12.6), i.e.,

$$\frac{\partial \tilde{T}_*}{\partial t_*} \approx -\tilde{w}_* \frac{\bar{T}_* - \bar{T}_{s*}}{H_u}. \tag{12.12}$$

If $\tilde{w} < 0$ and the background vertical temperature gradient is stably stratified ($\bar{T}_* > \bar{T}_{s*}$), then the surface temperature perturbation is amplified.

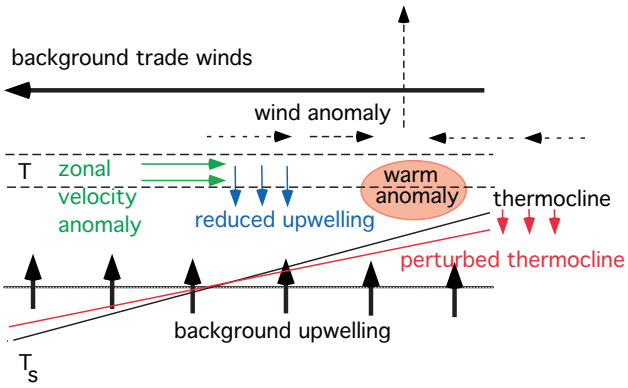

Figure 12.7. Sketch to illustrate the thermocline feedback, the upwelling feedback and the zonal advection feedback as indicated. In each case, a warm SST anomaly induces wind-stress anomalies. (i) Thermocline feedback: the wind anomaly leads to changes in the thermocline slope, which in turn induces — with constant background upwelling — an amplification of the SST anomaly. (ii) Upwelling feedback: the wind anomaly leads to changes in the upwelling which in turn induces — in a background stably stratified temperature field — an amplification of the SST anomaly. (iii) Zonal advection feedback: the wind anomaly induces stronger zonal advection which, if the annual-mean zonal SST gradient is negative, leads to amplification of the SST anomaly.

Additional Material

B: Chapter 11 (sections 11.11 to 11.15) of Gill (1982) is a nice introduction into the tropical atmospheric circulation. There are several review papers on coupled processes (Cane, 1986; Neelin et al., 1994, 1998; Dijkstra and Burgers, 2002) and ENSO and see also Philander (1990).

12.3. The delayed oscillator view of ENSO

From the material presented in the previous section it can be anticipated how an El Niño grows once an SST anomaly is present in the eastern Pacific. A warm anomaly will lead to a weakening of the trade winds which will give a smaller Ekman upwelling and a smaller thermocline slope. The two feedbacks above then may lead to amplification of the SST anomaly. The question is now what eventually stops this growth. Here the transient nature of the response (adjustment due to waves) comes into play and although the full responses were given in section 11.5, there are more conceptual models providing insight into these issues.

The first step in obtaining a reduced model is the simplification of the shallow water response. For convenience, the dimensionless shallow water equations using the long wave approximation ($\zeta_0 \to 0$) in (11.41) are again given below with the dimensionless zonal wind stress forcing indicated by τ, i.e.

$$\frac{\partial u}{\partial t} - yv + \frac{\partial h}{\partial x} + \epsilon_o u = \tau, \tag{12.13a}$$

$$yu + \frac{\partial h}{\partial y} = 0, \tag{12.13b}$$

$$\frac{\partial h}{\partial t} + \frac{\partial u}{\partial x} + \frac{\partial v}{\partial y} + \epsilon_o h = 0. \tag{12.13c}$$

To obtain a single equation for h, (12.13a) is differentiated with respect to y and the result is then multiplied by y. When (12.13a) is subtracted from this result one obtains

$$(yu_y - u)_t - y^2 v_y + y h_{xy} + \epsilon_o y u_y - h_x - \epsilon_o u = y\,\tau_y - \tau, \tag{12.14}$$

where the subscripts now indicate differentiation. Next, (12.13b) is differentiated with respect to x and the result multiplied by y. When also (12.13b) is differentiated with respect to y, the two relations

$$y^2 u_x + y h_{xy} = 0, \tag{12.15a}$$

$$y u_y + u + h_{yy} = 0, \tag{12.15b}$$

are obtained. The terms yu_y and yh_{xy} are now eliminated from (12.14) using (12.15). When the relation $u = -h_y/y$ is used and the term with $u_x + v_y$ is eliminated using (12.13c), the final equation obtained is

$$y^2\left(\frac{\partial h}{\partial t} + \epsilon_o h\right) + \left(\frac{2}{y}\frac{\partial}{\partial y} - \frac{\partial^2}{\partial y^2}\right)\left(\frac{\partial h}{\partial t} + \epsilon_o h\right) - \frac{\partial h}{\partial x} = y\frac{\partial \tau}{\partial y} - \tau. \tag{12.16}$$

The boundary conditions then become

$$x = 0 \quad : \quad \int_{-\infty}^{\infty} \frac{1}{y}\frac{\partial h}{\partial y}\, dy = 0, \tag{12.17a}$$

$$x = 1 \quad : \quad \frac{\partial h}{\partial y} = 0. \tag{12.17b}$$

It can be assumed that h has a near parabolic dependence near the equator, a property which does not seem unreasonable, when looking at the thermocline structures of the free equatorial Rossby waves. Hence,

$$h(x, y, t) = h_e(x, t) + y^2 \Delta h(x, t). \tag{12.18}$$

If one takes $(h_n + h_e)/2 = h(x, 1, t)$, the right hand side being the thermocline deviation at a distance λ_o from the equator, then it follows that $\Delta h = (h_n - h_e)/2$. Note that the zonal velocity is given by $u = -h_y/y = h_e - h_n$. Now (12.18) is substituted into (12.16) and considered at $y = 0$ giving one equation relating h_e and h_n. A second equation is obtained by realizing that the second term in the left hand side of (12.16) is much smaller than the first at $y = y_n$ where $h \approx h_n$. This leads to the so-called two-strip model

$$(\frac{\partial}{\partial t} + \epsilon_o)(h_e - h_n) + \frac{\partial h_e}{\partial x} = \tau_{|y=0}, \tag{12.19a}$$

$$(\frac{\partial}{\partial t} + \epsilon_o)h_n - \frac{1}{y_n^2}\frac{\partial h_n}{\partial x} = \frac{\partial}{\partial y}(\frac{\tau}{y})_{|y=y_n}. \tag{12.19b}$$

Note that the free wave solutions of (12.19b) with wavenumber k (in a zonally unbounded domain) have a frequency $-k/y_n^2$, and hence represent Rossby waves. For $y_n = 2$, these have a phase velocity $1/4$ of the free Kelvin wave signal (of the wave with the same wavenumber k) which is contained in (12.19a). The boundary conditions can be approximated by

$$h_n(1, t) = r_E h_e(1, t)\ ;\ h_e(0, t) = r_W h_n(0, t), \tag{12.20}$$

where r_E and r_W are a measure of the degree of zonal mass flux allowed at each boundary. For example, at the eastern boundary, the zonal velocity is given by $u_E(1, t) = h_e(1, t) - h_n(1, t) = (1 - r_E)h_e(1, t)$. Hence, if $r_E = 1$ the zonal mass flux is zero but for $r_E < 1$ a nonzero mass flux is allowed. In general, $r_W < 1$, since energy leaks through the western boundary under condition (12.17b) and a choice $r_W = 3/5$ is the appropriate value under the two-strip approximation with $h = 0$ at $y = 2y_n$ and beyond. Both r_W and r_E therefore monitor the degree of exchange of mass between the equatorial strip and off-equatorial regions.

We now turn to the SST equation. When advection and horizontal diffusion are neglected in (12.4), we find the equation

$$\frac{\partial T_*}{\partial t} = \epsilon_w(T_{r*} - T_*) - w_* \frac{T_* - T_{s*}}{H_u} \tag{12.21}$$

where ϵ_w is a damping coefficient and T_{r*} was the radiation equilibrium temperature. As the thermocline deepens, the subsurface temperature increases and hence we can represent this effect as a dependence $T_{s*} = T_{s*}(h_*)$, where h_* is the thermocline thickness. If we linearize the equation (12.21) around a given background state, scale the equations using (11.17), then the equation governing the equatorial SST-anomalies is given by

$$\frac{\partial T_e}{\partial t} + C_T\, T_e - C_h\, h_e = 0, \tag{12.22}$$

with C_T representing local damping and C_h the effect of thermocline variations on the temperature perturbations. As the SST perturbations change mostly in the eastern part of the basin, one can average (12.22) over the eastern half of the basin, say from $x = 1/2$ to $x = 1$, to give

$$\frac{dT_{eE}}{dt} + C_{TE}T_{eE} - C_{hE}h_{eE} = 0. \tag{12.23}$$

A westerly wind response west of positive T_{eE} can be represented by

$$\tau_{|y=0} = \mu\ A_0\ T_{eE}\ f(x), \tag{12.24}$$

with a fixed pattern $f(x)$ and amplitude A_0. The proportionality factor μ serves as coupling coefficient with $\mu = 1$ being a 'realistic' strength. The function $f(x)$ mimics the spatial pattern of the wind response and can be taken piecewise constant, for example

$$f(x) = \frac{1}{x_2 - x_1} \text{ for } x_1 < x < x_2, \tag{12.25}$$

and zero elsewhere. In this way, the forcing in (12.19b) can be approximated as

$$\frac{\partial}{\partial y}(\frac{\tau}{y})_{|y=y_n} \approx -\mu\ A_0\ T_{eE}\ f(x)\frac{\theta}{y_n^2}, \tag{12.26a}$$

Ex. 12.4

where θ is an $\mathcal{O}(1)$ coefficient.

A nice element in the coupled model developed in this way is that the two-strip equations can be integrated along the (Kelvin and Rossby) wave characteristics, which are given by

$$x - x_0 = t - t_0, \tag{12.27a}$$

$$x - x_0 = \frac{t_0 - t}{y_n^2}, \tag{12.27b}$$

respectively, where (x_0, t_0) is any point in the domain. When damping is neglected, the solutions h_e and h_n can be obtained by first integrating (12.19b) along a Rossby wave characteristic starting at the eastern boundary and reaching the western boundary. Next, (12.19b) is integrated along a characteristic starting at the western boundary over the Kelvin crossing time, in which the wave has reached the eastern boundary. Using mean value approximations and the fact that $1 + y_n^2 >> 1$, this leads to delay equations of the form

$$\begin{aligned} h_{eW}(t) &= r_W r_E h_{eW}(t - 1 - y_n^2) + \\ +\mu A_0 r_W(r_E T_{eE}(t - 1 - x_P) &- \theta T_{eE}(t - y_n^2 x_P)), \end{aligned} \tag{12.28a}$$

$$\begin{aligned} h_{eE}(t) &= r_W r_E h_{eE}(t - 1 - y_n^2) - \\ -\mu A_0(\theta r_W T_{eE}(t - 1 - y_n^2 x_P) &- T_{eE}(t - 1 + x_P)), \end{aligned} \tag{12.28b}$$

$$\frac{dT_{eE}}{dt} + C_{TE}T_{eE} - C_{hE}h_{eE} = 0, \tag{12.28c}$$

where x_P is a chosen fixed point within the area of wind response $[x_1, x_2]$.

When the effect of the eastern boundary reflection is neglected ($r_E = 0$), then (12.28b) and (12.28c) give

$$\begin{aligned} \frac{dT_{eE}}{dt} &= -C_{TE}T_{eE} + \mu A_0 C_{hE} \\ (T_{eE}(t-1+x_P) &- \theta r_W T_{eE}(t-1-y_n^2 x_P)), \end{aligned} \tag{12.29}$$

which shows that the average eastern basin temperature is influenced by local damping and a remote signal due to propagation of Kelvin and Rossby waves. The delay time $1 - x_P$ is the effect due to the Kelvin wave and as this is relatively fast, it can be neglected on long time scales. It provides the local amplification of temperature perturbations by thermocline feedback through a forced Kelvin wave response. The delay $1 + y_n^2 x_P$ is the time taken for the Rossby wave to travel from the center of wind patch near x_P to the western boundary plus the time it takes the reflected Kelvin wave to cross the basin. When returned in the eastern part of the basin, it provides a delayed negative feedback to the temperature perturbation (since $r_W > 0$).

Additional Material

B: The articles Cane and Zebiak (1985), Battisti and Hirst (1989), Schopf and Suarez (1988) provide an overview on the early modeling and understanding of El Niño .

D: The papers Jin (1997a) and Jin (1997b) provide a complete overview on the different delayed oscillator models as the delayed oscillator equations are derived from shallow-water dynamics.

Equation (12.29) forms the basis of the delayed oscillator theory of the late 1980's where a differential delay equation with local feedback was proposed as a model of ENSO. The equations are

$$\frac{dT_*(t_*)}{dt_*} = aT_*(t_*) - bT_*(t_* - d) - cT_*^3(t_*). \tag{12.30}$$

Ex. 12.5

Here a represents the growth rate of the temperature disturbance T in the eastern Pacific and would correspond to $\mu A_0 C_{hE} - C_{TE}$ in (12.29). The quantity d is the delay time due to the propagation of equatorial waves, corresponding to $1 + y_n^2 x_P$ in (12.29), and b measures its influence with respect to the local feedbacks. The nonlinear term in (12.30) is needed for equilibration of the temperature to finite amplitude.

This delayed oscillator model represents the central elements of the ENSO cycle in terms of local growth due to instability and subsequent adjustment through

(individual) Kelvin and Rossby waves. In the eastern part of the basin, strong feedback takes place which leads to amplification of disturbances: positive SST anomalies cause wind-stress anomalies, which weaken the background trade winds, with maximum weakening west of the SST anomaly. This is turn creates a different slope in the thermocline which leads through the thermocline feedback to a larger SST anomaly.

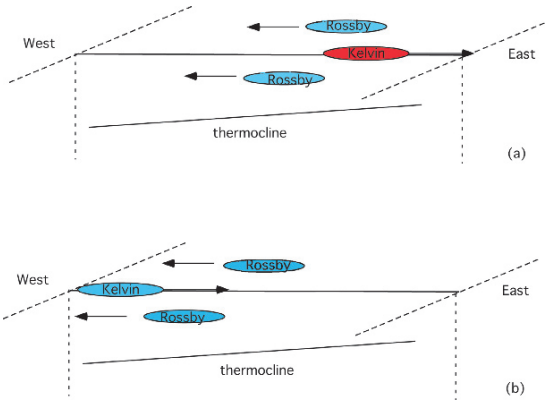

Figure 12.8. Sketch to illustrate the negative delayed feedback. Stage (a) is just after the maximum of El Nino where the Kelvin wave (deepening the thermocline) propagates to the eastern boundary and Rossby waves appear which shallow the thermocline in the central Pacific. Stage (b) is just before the start of the La Nina phase where the Rossby waves have reflected into a Kelvin wave which shallows the thermocline. Although the largest amplitude of the waves is in the thermocline, the waves are drawn at the surface and their color (blue: cold and red: warm) indicates their temperature signal in the mixed layer.

However, the ocean does not react instantaneously to the changing winds, but has a memory component which partly determines its long term evolution. The wind anomaly also generates westward travelling Rossby waves that make the thermocline shallower in off-equatorial regions in the western part of the basin (Fig. 12.8a). The Rossby waves reach the western boundary and cause a Kelvin wave reflection which causes a shallower thermocline (Fig. 12.8b). This Kelvin wave signal provides the delayed negative feedback, through which the SST anomaly reduces to zero and becomes slightly negative. Then the feedback start to operate with a different sign to amplify the negative temperature anomaly leading to a La Niña state. Hence, the period of the oscillation is basically determined by the wave transit time associated with the delayed feedback. Slightly different (and important) details have been added to this mechanism, but the basic mechanism of the delayed oscillator at work is that sketched above.

Summary

- The El Niño phenomenon is associated with an interannual sea surface temperature anomaly in the eastern to central Pacific. There are connected changes in the sea level pressure and surface winds which are called the Southern Oscillation.
- A positive SST anomaly in the eastern Pacific leads to low-level heating of the tropical atmosphere and to a westerly wind anomaly located west of the SST anomaly and hence a weakening of the trade winds.
- A weakening of the trade winds leads to a reduction of upwelling and a reduction in the slope of the thermocline.
- There exist three positive feedbacks in the coupled system: the thermocline feedback, the upwelling feedback and the zonal advection feedback.
- El Niño is brought about through coupled interactions between the equatorial ocean and the global atmosphere. Anomalies in sea surface temperature induce wind-stress anomalies which cause changes in thermocline depth and upwelling and the three feedbacks can amplify these anomalies. The ocean adjusts to the changes in wind stress through the propagation of equatorial waves. The ocean basin adjustment provides a negative feedback which damps the anomalies and which induces a transition to the opposite phase (La Niña). This is the essence of the delayed oscillator view of ENSO.

12.4. Exercises on chapter 12

(12.1) *Ocean-atmosphere interaction*

Assume that the temperature in the eastern Pacific (in the NINO3 region) increases by 1°C.

a. Use Fig. 12.4 and information in section 2.1 such as (2.1) to determine the amplitude response of the zonal wind stress τ_*^x caused by a SST (NINO3) anomaly.

Assume that the wind-stress anomaly is purely zonal, i.e., $\tau^y = 0$.

b. Calculate the amplitude of the equatorial upwelling anomaly w_{E*} caused by the zonal wind-stress anomaly.

c. Calculate the amplitude of the thermocline anomaly h_{e*} in the west Pacific caused by the zonal wind-stress anomaly.

(12.2) *Equatorial upwelling*

In section 12.2.2 the Ekman layer equations (12.7) were given in case of linear friction with damping coefficient a_s. Assume that $\tau^y = 0$.

a. Determine the horizontal Ekman velocities u_{E*} and v_{E*} in terms of the wind stress τ_*^x.

b. Explain why $v_{E*} = 0$ at the equator.

c. Determine the upwelling velocity w_{E*} at the equator for a constant zonal wind stress $\tau^x = -\tau_0$.

d. With a wind stress amplitude $\tau_0 = 0.1\ Pa$ and a damping coefficient $a_s = 5.0 \times 10^{-6}$ s^{-1}, determine w_E in m/day.

(12.3) *The zonal advection feedback*

Apart form the thermocline and the upwelling feedback, there is a third feedback: the zonal advection feedback. Assume that there is a region with a strong zonal background temperature gradient with $\partial \bar{T}_*/\partial x_* < 0$. Such a region, for

example, exists at the eastern side of the warm pool.

a. Assume that there is a positive temperature anomaly that causes westely wind anomalies. Describe the effect on the zonal currents in the ocean.

b. Consider in the SST-equation, the balance

$$\partial \tilde{T}_*/\partial t_* \approx -\tilde{u}_* \, \partial \bar{T}_*/\partial x_*$$

that describes the evolution of temperature anomalies $\tilde{T}_*$ due to anomalies in the zonal current $\tilde{u}_*$. Describe the mechanism of the zonal advection feedback.

(12.4) *The two-strip model*

From the two-strip model in section 12.3, the delayed oscillator equations can be derived explicitly from the shallow-water model and the SST equation. Central in this derivation is the integration over characteristics defined by Kelvin and Rossby waves.

a. Determine the characteristics of a free Kelvin wave along the equator and sketch these in the $x - t$ plane.

b. Determine the characteristics of a free $j = 1$ Rossby wave along the y_{max} value in Table 11.1 and also sketch these in the $x - t$ plane.

c. Why can y_n in the two-strip model be identified with y_{max} as given in Table 11.1?

d. Carry out the integration of the equations (12.19) along both characteristics under a. and b. and derive the equations (12.28a-b).

(12.5) *The delayed oscillator*

Equation (12.30) forms the basic model for the delayed oscillator.

a. Scale time with $1/a$ and temperature by $\sqrt{a/c}$, derive the dimensionless equation

$$\frac{dT}{dt} = T(t) - \alpha T(t - \delta_T) - T^3(t),$$

and determine α and δ_T.

b. Show that for $\alpha < 1$, the equation has three different steady states.

c. Using linear stability theory (as in chapter 10, see also chapter 16), determine the stability of the nontrivial steady states for $\alpha < 1$. What are the periods of oscillation of the unstable modes?

IV

PLANETARY DYNAMICS

Chapter 13

THERMOCLINE PROBLEM

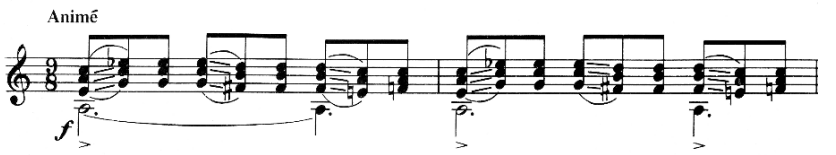

Etude No 12., H. Villa-Lobos

In the chapters 5-10, basic theory of the midlatitude ocean circulation was presented. The constant density case was considered in chapter 5 followed by the case where the stratification was uniformly characterized by a typical profile of the buoyancy frequency N (chapter 7). In this chapter, we relax the restriction of fixed N over the basin by allowing the density to vary over the whole flow domain. Although these density differences arise through gradients in temperature and salinity, here we will only consider the density field itself. The effect of both quantities on the density and its consequences for the stability of the large-scale flow will be discussed in chapter 16. In section 13.1 some characteristics of the thermocline are presented and the mathematical thermocline problem in section 13.2. The planetary extension of the constant density theory in chapter 5 is subject of section 13.3 and the planetary extension of two-layer model follows in section 13.4. In the last section 13.5, the ventilation theory and the internal boundary layer theory of the thermocline are presented.

13.1. Characteristics of the thermocline

Profiles of potential temperature ϑ, salinity S and potential density σ_0 (cf. chapter 1) at a station (along the WOCE A16 section) in the North Atlantic near (21°W, 26.5°N) are plotted in the Figs. 13.1a-c. The potential density increases at depths between 500 and 1500 meter and then quickly approaches its deep sea value. The region where the largest gradients occur is called the pycnocline (Fig. 13.1c) and because there are also strong temperature gradients in this region (Fig. 13.1a), it is also called the thermocline; we will use this terminology below. The depth of the thermocline is large at midlatitudes and decreases towards the equator and the poles. This can be seen in a plot of the potential density σ_0 along the WOCE A16 section (Fig. 13.1d). For this section, potential temperature and salinity profiles were plotted in Fig. 1.6 (chapter 1).

Horizontal density gradients influence the ocean circulation e.g., through the thermal wind balance. These partly density driven flows, however, in turn determine the density distribution through advection of heat and salt. The existence of the thermocline is the net result of the interaction between flow field and the density field in the ocean and it is therefore a complicated nonlinear problem. It maybe no surprise that this problem has not been satisfactorily solved up till now. The central issue discussed in this chapter is the theory attempting to explain the presence of the thermocline.

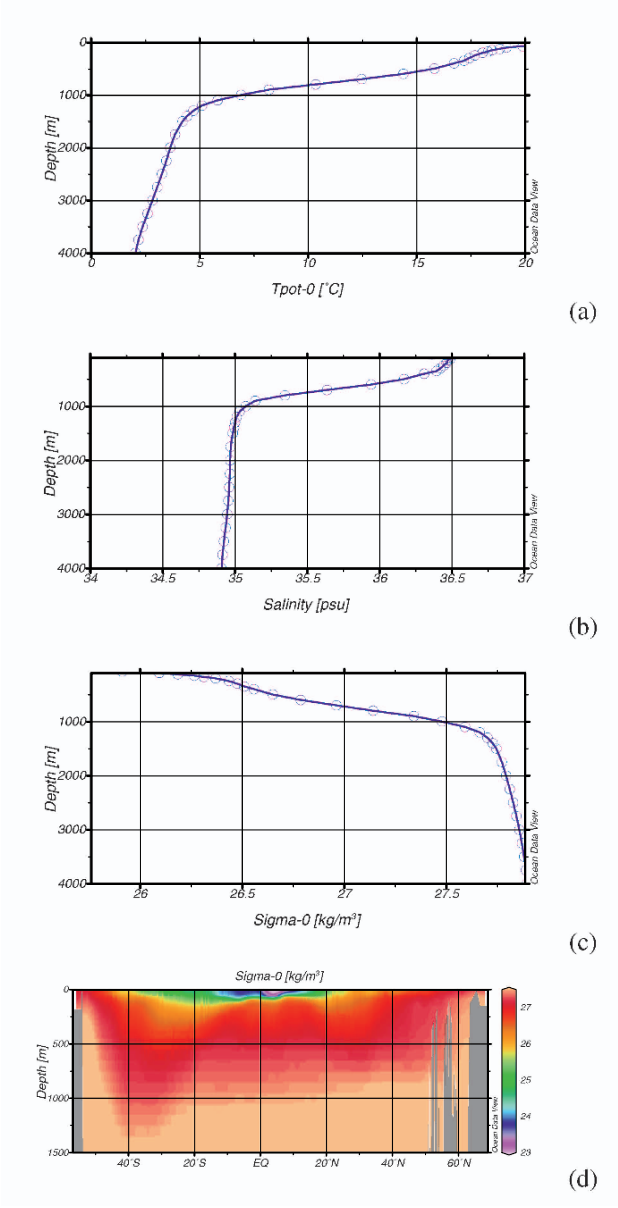

Figure 13.1. Profiles of (a) the potential temperature, (b) the salinity and (c) the potential density (σ_0) in the eastern part of the Atlantic Ocean near (58°W, 37°N). (d) Plot of the potential density σ_0 along the WOCE A16 section.

13.2. Formulation of the problem

We consider an ocean basin that is bounded in the zonal direction by continents at $\phi = \phi_W(\theta)$ and $\phi = \phi_E(\theta)$ and which has a meridional extent $[\theta_S, \theta_N]$. In the vertical direction, the ocean water is bounded by an ocean bottom with average depth D and by the ocean-atmosphere interface with a mean position at $z = 0$.

On the planetary scale, the characteristic length scale of the flow is $L = r_0$ and because the density variations are large, the static stability parameter (the buoyancy frequency N) will vary strongly. Hence we can no longer use a reference density $\bar{\rho}_*(z)$ and the only reasonable choice for such a reference is a constant $\bar{\rho}_* = \rho_0$. With these choices, the appropriate scales for pressure and density follow as (cf. section 3.3)

$$p_* = -gD\rho_0 z + 2\rho_0 U\Omega r_0 p, \tag{13.1a}$$

$$\rho_* = \rho_0(1 + \frac{2\Omega U r_0}{gD}\rho) = \rho_0(1 + \epsilon_p F_p \rho), \tag{13.1b}$$

where $z_* = Dz$. Here $\epsilon_p = U/(2\Omega r_0)$ and $F_p = 4\Omega^2 r_0^2/(gD)$ are the planetary Rossby and rotational Froude numbers.

To simplify matters, we will take a linear equation of state

$$\rho_* = \rho_0(1 - \alpha_T(T_* - T_0) + \alpha_S(S_* - S_0)), \tag{13.2}$$

with constant α_T and α_S. Because we will focus on the understanding of the vertical structure of the wind- and density driven flow, we neglect horizontal mixing of momentum, heat and salt. The vertical mixing of heat and salt is represented by the vertical diffusivity K_V.

With a linear equation of state the equations for temperature and salinity (3.32e-f) can be combined into one equation for the density ρ, which becomes (in spherical coordinates)

$$\frac{D\rho}{dt} = \frac{u}{\cos\theta}\frac{\partial\rho}{\partial\phi} + v\frac{\partial\rho}{\partial\theta} + w\frac{\partial\rho}{\partial z} = \lambda_V \frac{\partial^2\rho}{\partial z^2}. \tag{13.3}$$

with $\lambda_V = K_V r_0/(UD^2)$. The parameter λ_V represents the small scale vertical mixing of density. With an estimate of $K_V = 5 \times 10^{-5}$ m^{2}s^{-1} and $U = 10^{-3}$ ms^{-1} it follows that $\lambda_V \approx \mathcal{O}(1)$, but this value is very uncertain. Likely, the value of λ_V is much smaller.

From chapter 3, the scaled momentum balance and the continuity equation can (in the limit $\delta = D/r_0 \to 0$) be written as

$$\epsilon_p\left[\frac{Du}{dt} - uv\tan\theta\right] - v\sin\theta = -\frac{1}{\cos\theta}\frac{\partial p}{\partial\phi} + \frac{1}{2}\bar{E}_V\frac{\partial^2 u}{\partial z^2}, \tag{13.4a}$$

$$\epsilon_p\left[\frac{Dv}{dt} + u^2\tan\theta\right] + u\sin\theta = -\frac{\partial p}{\partial\theta} + \frac{1}{2}\bar{E}_V\frac{\partial^2 v}{\partial z^2}, \tag{13.4b}$$

$$\rho = -\frac{\partial p}{\partial z}, \tag{13.4c}$$

$$\frac{\partial u}{\partial \phi} + \frac{\partial (v \cos\theta)}{\partial \theta} + \cos\theta \frac{\partial w}{\partial z} = 0, \tag{13.4d}$$

where $\bar{E}_V = A_H/(\Omega r_0^2)$ is the vertical planetary Ekman number. If we consider the case with a flat bottom and neglect the effect of free surface deformations, then the boundary conditions become

$$z = -1 \quad : \quad u = v = w = 0, \frac{\partial \rho}{\partial z} = 0, \tag{13.5a}$$

$$z = 0 \quad : \quad \hat{\alpha}\tau^{\phi} = \frac{\partial u}{\partial z} \; ; \; \hat{\alpha}\tau^{\theta} = \frac{\partial v}{\partial z} \; ; \; w = 0 \; ; \; \rho = \rho_s, \tag{13.5b}$$

where $\hat{\alpha} = \tau_0 D/(\rho_0 A_V U)$ and ρ_s is the prescribed surface density distribution. The bottom boundary condition for ρ (13.5a) implies that there are no fluxes of heat and salt at the bottom of the ocean. The equations (13.4) and boundary conditions (13.5) are the dimensionless mathematical model associated with the the thermocline problem.

13.3. The constant density planetary circulation

It is again helpful to discuss the homogeneous (constant density) theory for the planetary case first and then look at the modifications needed to incorporate the effects of stratification. For the planetary homogeneous case, there are again small parameters, i.e. $\epsilon_p = 10^{-4}$, $\bar{E}_V \leq 10^{-4}$ and $F_p = 10^2$, such that $\epsilon_p F_p \ll 1$. Again, asymptotic solutions can be determined by using the parameter ϵ_p and we write the solution as

$$u(\phi, \theta, z) = u^0(\phi, \theta, z) + \epsilon_p \, u^1(\phi, \theta, z) + \ldots, \tag{13.6}$$

with similar expansions for v, w and p. The $\mathcal{O}(1)$ system of equations describes the geostrophic flow

$$v^0 \sin\theta = \frac{1}{\cos\theta}\frac{\partial p^0}{\partial \phi}, \tag{13.7a}$$

$$u^0 \sin\theta = -\frac{\partial p^0}{\partial \theta}, \tag{13.7b}$$

$$0 = -\frac{\partial p^0}{\partial z}, \tag{13.7c}$$

$$\frac{\partial u^0}{\partial \phi} + \frac{\partial (v^0 \cos\theta)}{\partial \theta} + \cos\theta \frac{\partial w^0}{\partial z} = 0. \tag{13.7d}$$

The planetary geostrophic balance

On the planetary scale where the full variation of the Coriolis parameter is taken into account, the geostrophic balances are given by

$$\begin{aligned} 2\Omega\, v_* \,\sin\theta &= \frac{1}{\rho_0 r_0 \cos\theta}\frac{\partial p_*}{\partial \phi}, \\ 2\Omega\, u_* \,\sin\theta &= -\frac{1}{\rho_0 r_0}\frac{\partial p_*}{\partial \theta}. \end{aligned}$$

From (13.7c), it follows with (13.7a-b) that u^0 and v^0 cannot depend on z and hence the boundary conditions (13.5) cannot be satisfied. Again, an analysis of the Ekman boundary layers is needed, but contrary to the β-plane case, the planetary geostrophic equations are not dynamically degenerate. When the pressure is eliminated from (13.7a-b) using (13.7d) the vorticity equation follows as

$$\sin\theta \frac{\partial w^0}{\partial z} - v^0 \cos\theta = 0. \tag{13.9}$$

In dimensional quantities, (13.9) is written as

$$\frac{2\Omega}{r_0}\, v_* \,\cos\theta = 2\Omega\, \frac{\partial w_*}{\partial z_*}\, \sin\theta, \tag{13.10}$$

where the 2Ω is added for comparison to the midlatitude case. Because of the $\mathcal{O}(1)$ variation of the Coriolis parameter in the planetary case, the $\mathcal{O}(1)$ horizontal geostrophic velocity field is no longer divergence free. The equation (13.10) expresses that the vorticity due to north-south movement of a fluid column on the rotating sphere can balance the vortex stretching of the column.

13.3.1. The bottom Ekman layer

At the bottom, we introduce a boundary layer coordinate $\xi = (z+1)/\bar{E}_V^{1/2}$ and write the solution in the boundary layer as

$$\tilde{u}(\phi,\theta,\xi) = \tilde{u}^0(\phi,\theta,\xi) + \epsilon_p\, \tilde{u}^1(\phi,\theta,\xi) + \ldots \tag{13.11}$$

with similar expansions for v and p. For the vertical velocity the expansion becomes

$$\tilde{w}(\phi,\theta,\xi) = w^0(\phi,\theta,z) + \bar{E}_V^{1/2}(\tilde{w}^0(\phi,\theta,\xi) + \epsilon_p \tilde{w}^1(\phi,\theta,\xi) + \ldots \tag{13.12}$$

The first term in the right hand side is needed because the $\mathcal{O}(1)$ geostrophic solution w^0 is nonzero. The rescaling with the factor $\bar{E}_V^{1/2}$ is needed to balance terms of the continuity equation in the boundary layer.

The $\mathcal{O}(1)$ system of equations in the boundary layer becomes

$$-\tilde{v}^0 \sin\theta = -\frac{1}{\cos\theta}\frac{\partial \tilde{p}^0}{\partial \phi} + \frac{1}{2}\frac{\partial^2 \tilde{u}^0}{\partial \xi^2}, \tag{13.13a}$$

$$\tilde{u}^0 \sin\theta = -\frac{\partial \tilde{p}^0}{\partial \theta} + \frac{1}{2}\frac{\partial^2 \tilde{v}^0}{\partial \xi^2}, \tag{13.13b}$$

$$0 = -\frac{\partial \tilde{p}^0}{\partial \xi}, \tag{13.13c}$$

$$\frac{\partial \tilde{u}^0}{\partial \phi} + \frac{\partial (\tilde{v}^0 \cos\theta)}{\partial \theta} + \cos\theta \left[\frac{\partial w^0}{\partial z} + \frac{\partial \tilde{w}^0}{\partial \xi}\right] = 0, \tag{13.13d}$$

from which it follows that the pressure is again constant over the boundary layer, i.e. $\tilde{p}^0 = p^0$.

Let $\lambda = \sqrt{|\sin\theta|}$ and define $\bar{\xi} = \lambda\xi$. The equations (13.13a-b) are then transformed into

$$-\tilde{v}^0 = -v^0 + \frac{1}{2}\frac{\partial^2 \tilde{u}^0}{\partial \bar{\xi}^2}, \tag{13.14a}$$

$$\tilde{u}^0 = u^0 + \frac{1}{2}\frac{\partial^2 \tilde{v}^0}{\partial \bar{\xi}^2}, \tag{13.14b}$$

where also (13.7) has been used. This is the same system of equations as for the Ekman boundary layer on the β-plane. Hence, the solutions (5.49) can be copied with ξ substituted by $\bar{\xi}$.

Substitution of these solutions into (13.13) and use of (13.7d) gives

$$\begin{aligned}\cos\theta \frac{\partial \tilde{w}^0}{\partial \xi} &= \left[\frac{\partial u^0}{\partial \phi}\cos\lambda\xi + \frac{\partial v^0}{\partial \phi}\sin\lambda\xi\right] e^{-\lambda\xi} \\ &+ \frac{\partial}{\partial \theta}\left[(v^0 \cos\lambda\xi - u^0 \sin\lambda\xi) e^{-\lambda\xi}\cos\theta\right].\end{aligned} \tag{13.15}$$

Through integration over the boundary layer and making use of the definite integrals

$$\int_0^\infty e^{-\lambda\xi}\begin{pmatrix}\sin\lambda\xi \\ \cos\lambda\xi\end{pmatrix} d\xi = \frac{1}{2\lambda}\begin{pmatrix}1 \\ 1\end{pmatrix}, \tag{13.16a}$$

$$\int_0^\infty \xi e^{-\lambda\xi}\begin{pmatrix}\sin\lambda\xi \\ \cos\lambda\xi\end{pmatrix} d\xi = \frac{1}{2\lambda^2}\begin{pmatrix}1 \\ 0\end{pmatrix}, \tag{13.16b}$$

we find

$$\lim_{\xi\to\infty} \tilde{w}^0(\phi,\theta,\xi) = \tilde{w}^0(\phi,\theta,0) + \frac{1}{2\lambda}\left(\frac{1}{\cos\theta}\left(\frac{\partial u^0}{\partial \phi} + \frac{\partial (v^0\cos\theta)}{\partial \theta}\right) +\right.$$

$$\frac{1}{\cos\theta}\left(\frac{\partial v^0}{\partial\phi} - \frac{\partial(u^0\cos\theta)}{\partial\theta}\right) + \frac{1}{4\lambda\tan\theta}(u^0 - v^0),$$

$$= \tilde{w}^0(\phi,\theta,0) + \frac{1}{2\lambda}\left(\nabla\cdot\mathbf{u}^0 + \nabla\cdot(\mathbf{u}^0\wedge\mathbf{e}_3) + \frac{1}{2\tan\theta}(u^0 - v^0)\right) =$$

$$= \tilde{w}^0(\phi,\theta,0) + \frac{1}{2}\left(\nabla\cdot\left(\frac{\mathbf{u}^0}{\lambda}\right) + \nabla\cdot\left(\frac{\mathbf{u}^0}{\lambda}\wedge\mathbf{e}_3\right)\right), \tag{13.17}$$

where $\mathbf{u}^0 = (u^0, v^0, 0)^T$.

From the boundary conditions $w = 0$ at $z = -1$, it follows

$$\bar{E}_V^{1/2}\tilde{w}^0(\phi,\theta,0) + w^0(\phi,\theta,-1) = 0, \tag{13.18}$$

and hence we finally find from (13.17) and (13.18) that

$$\begin{aligned}\tilde{w}_E(\phi,\theta) &= \lim_{\xi\to\infty}\bar{E}_V^{1/2}\tilde{w}^0(\phi,\theta,\xi) + \lim_{z\to-1} w^0(\phi,\theta,z)\\ &= \frac{1}{2}\bar{E}_V^{1/2}\left(\nabla\cdot\left(\frac{\mathbf{u}^0}{\lambda}\right) + \nabla\cdot\left(\frac{\mathbf{u}^0}{\lambda}\wedge\mathbf{e}_3\right)\right).\end{aligned} \tag{13.19}$$

The dimensionless Ekman transport $\mathbf{M}_E$ is determined through integration of $\tilde{\mathbf{u}}^0 - \mathbf{u}^0$ over the boundary layer and becomes

$$\mathbf{M}_E = \frac{\bar{E}_V^{1/2}}{2\lambda}(\mathbf{u}^0 + \mathbf{u}^0\wedge\mathbf{e}_3), \tag{13.20}$$

Note that this expression is very similar to that on the equatorial β-plane (section 11.2) where $\lambda = \sqrt{|y|}$.

Bottom Ekman layer

On the planetary scale the dimensional vertical Ekman pumping velocity (ms^{-1}) and the Ekman volume transport ($\mathrm{m}^2\mathrm{s}^{-1}$) at the ocean (flat) bottom are

$$\begin{aligned}\tilde{w}_{E*} &= \frac{1}{2r_0}\sqrt{\frac{A_V}{\Omega}}\left(\nabla\cdot\left(\frac{\mathbf{u}_*}{\sqrt{|\sin\theta|}}\right) + \nabla\cdot\left(\frac{\mathbf{u}_*}{\sqrt{|\sin\theta|}}\wedge\mathbf{e}_3\right)\right),\\ \mathbf{M}_{E*} &= \frac{1}{2}\sqrt{\frac{A_V}{\Omega}}\frac{1}{\sin\theta}(\mathbf{u}_* + \mathbf{u}_*\wedge\mathbf{e}_3).\end{aligned}$$

13.3.2. The free surface Ekman layer

In the boundary layer at the free surface, we introduce the boundary layer coordinate $\chi = -z/\bar{E}_V^{1/2}$ and the expansions (for u, v and p) become

$$\begin{aligned}\hat{u}(\phi,\theta,\chi) &= \hat{u}^0(\phi,\theta,\chi) + \epsilon_p\hat{u}^1(\phi,\theta,\chi) + \ldots\\ \hat{w}(\phi,\theta,\chi) = -w^0(\phi,\theta,z) &+ \bar{E}_V^{1/2}(\hat{w}^0(\phi,\theta,\chi) + \epsilon_p\tilde{w}^1(\phi,\theta,\chi) + \ldots\end{aligned}$$

The $\mathcal{O}(1)$ system becomes

$$
\begin{aligned}
-\hat{v}^0 \sin\theta &= -\frac{1}{\cos\theta}\frac{\partial \hat{p}^0}{\partial \phi} + \frac{1}{2}\frac{\partial^2 \hat{u}^0}{\partial \chi^2}, && \text{(13.23a)}\\
\hat{u}^0 \sin\theta &= -\frac{\partial \hat{p}^0}{\partial \theta} + \frac{1}{2}\frac{\partial^2 \hat{v}^0}{\partial \chi^2}, && \text{(13.23b)}\\
0 &= -\frac{\partial \hat{p}^0}{\partial \chi}, && \text{(13.23c)}\\
\frac{\partial \hat{u}^0}{\partial \phi} + \frac{\partial (\hat{v}^0 \cos\theta)}{\partial \theta} &- \cos\theta\left(\frac{\partial w^0}{\partial z} + \frac{\partial \hat{w}^0}{\partial \chi}\right) = 0. && \text{(13.23d)}
\end{aligned}
$$

We transform $\bar{\chi} = \chi\lambda$ and the boundary conditions at $\chi = 0$ become

$$
\begin{aligned}
\hat{\alpha}\bar{E}_V^{1/2}\tau^{\phi} &= \lambda\frac{\partial \hat{u}^0}{\partial \chi}, && \text{(13.24a)}\\
\hat{\alpha}\bar{E}_V^{1/2}\tau^{\theta} &= \lambda\frac{\partial \hat{v}^0}{\partial \chi}. && \text{(13.24b)}
\end{aligned}
$$

Ex. 13.1

The solutions are therefore given by (5.75) with χ substituted by $\lambda\chi$ and $\alpha = \bar{E}_V^{1/2}\hat{\alpha}$ substituted by α/λ. Integration of the continuity equation (13.23d) over the boundary layer and making use of the boundary conditions at $z = 0$, i.e.

$$
\bar{E}_V^{1/2}\hat{w}^0(\phi,\theta,0) - w^0(\phi,\theta,0) = 0, \tag{13.25}
$$

eventually provides the vertical Ekman velocity $\hat{w}_E$ as

$$
\begin{aligned}
\hat{w}_E(\phi,\theta) &= \lim_{\chi\to\infty}\bar{E}_V^{1/2}\hat{w}^0(\phi,\theta,\chi) - \lim_{z\to 0} w^0(\phi,\theta,z) = \\
&= \frac{\alpha}{2}\bar{E}_V^{1/2}\nabla\cdot\left(\frac{\mathbf{T}}{\sin\theta}\wedge\mathbf{e}_3\right), && \text{(13.26)}
\end{aligned}
$$

where $\mathbf{T} = (\tau^{\phi}, \tau^{\theta}, 0)$. For the dimensionless Ekman transport we then find

$$
\mathbf{M}_E = \frac{\alpha\bar{E}_V^{1/2}}{2\sin\theta}\mathbf{T}\wedge\mathbf{e}_3, \tag{13.27}
$$

Again note that this expression is again very similar to that on the equatorial β-plane (section 11.2) where $\sin\theta \sim y$.

Surface Ekman layer

On the planetary scale the dimensional vertical Ekman pumping velocity (ms^{-1}) and the Ekman volume transport (($\mathrm{m}^2\mathrm{s}^{-1}$)) at the ocean surface are

$$\begin{aligned} \hat{w}_{E*} &= \frac{1}{2\Omega\rho_0}\nabla\cdot(\frac{\mathbf{T}_*}{\sin\theta}\wedge\mathbf{e}_3), \\ \mathbf{M}_{E*} &= \frac{1}{2\Omega\rho_0}\frac{1}{\sin\theta}\mathbf{T}_*\wedge\mathbf{e}_3. \end{aligned}$$

13.3.3. The planetary Sverdrup-Stommel theory

Integration of (13.9) over the geostrophic flow domain gives

$$\sin\theta\,(\hat{w}_E-\tilde{w}_E)=v^0\cos\theta. \tag{13.29}$$

Using the expressions for the vertical Ekman velocities of the previous section, the potential vorticity equation becomes

$$\frac{\sin\theta}{2}\bar{E}_V^{1/2}\left[\alpha\,\nabla\cdot(\frac{\mathbf{T}}{\sin\theta}\wedge\mathbf{e}_3)-\nabla\cdot(\frac{\mathbf{u}^0}{\lambda})-\nabla\cdot(\frac{\mathbf{u}^0}{\lambda}\wedge\mathbf{e}_3)\right]=v^0\cos\theta, \tag{13.30}$$

with $\lambda=\sqrt{|\sin\theta|}$.

The vorticity change due to north-south motion is represented by the right hand side. It is balanced by vorticity changes due to the wind stress and the bottom friction. Because both u^0 and v^0 can be expressed in terms of the pressure p^0, (13.30) is a scalar equation for p^0. Note that the horizontal velocity field is not divergence free and hence there is no streamfunction ψ such that $\mathbf{u}^0=\nabla\wedge(\mathbf{e}_3\psi)$. We can, however, write $p^0=\psi$ and then (13.30) becomes a scalar equation for ψ. In this case, curves of constant ψ are in general not streamlines.

From (13.30) it follows that there is only a nontrivial balance in the interior of the basin (far from the continental boundaries), if the characteristic velocity U is chosen such that

$$\frac{\alpha\bar{E}_V^{1/2}}{2}=1\Rightarrow U=\frac{\tau_0}{2\rho_0\Omega D}. \tag{13.31}$$

We then find that $U\approx 10^{-3}\ \mathrm{ms}^{-1}$ and subsequently $\epsilon_p=\mathcal{O}(10^{-5})$. The choice of U is therefore consistent with the approximation $\epsilon_p\ll 1$. In (13.30) there is only one small parameter, i.e., $\bar{E}_V^{1/2}$.

If we denote $\epsilon=\bar{E}_V^{1/2}$ and expand the solution of (13.30) as

$$\psi(\phi,\theta)=\psi^0(\phi,\theta)+\epsilon\,\psi^1(\phi,\theta)+\ldots \tag{13.32}$$

and we find the $\mathcal{O}(1)$ balance in (13.30) to be

$$\frac{\partial \psi^0}{\partial \phi} = \sin^2\theta \, \nabla \cdot (\frac{\mathbf{T}}{\sin\theta} \wedge \mathbf{e}_3) \equiv \mathcal{T}(\phi, \theta). \tag{13.33}$$

Ex. 13.2

This is the planetary Sverdrup balance and just as on the β-plane, in general we cannot satisfy both kinematic conditions $\mathbf{u}\cdot\mathbf{n} = 0$ on the continental boundaries.

The planetary Sverdrup balance

On the planetary scale the dimensional Sverdrup balance is given by

$$\frac{2\Omega}{r_0} v_* \cos\theta = \frac{\sin\theta}{\rho_0 D} \nabla \cdot (\frac{\mathbf{T}_*}{\sin\theta} \wedge \mathbf{e}_3),$$

The solution of (13.33) follows immediately through integration in zonal direction as

$$\psi^0(\phi, \theta) = \int_{\phi_0}^{\phi} \mathcal{T}(s, \theta) ds + \Psi^0(\theta), \tag{13.34}$$

where $\Psi^0(\theta)$ is still an arbitrary function.

To study the flow in the continental boundary layers we consider the case where ϕ_W and ϕ_E are constant. At the western boundary, we introduce a boundary layer coordinate ζ with $\zeta = (\phi - \phi_W)/\epsilon^q$, where q is to be determined. The highest order terms in ϵ will come from the second order derivatives of ϕ in the expression $\nabla \cdot (\mathbf{u}^0/\lambda) + \nabla \cdot ((\mathbf{u}^0/\lambda) \wedge \mathbf{e}_3)$. The coefficient of $\partial^2\psi/\partial\phi^2$ in this expression is $1/(\lambda^3 \cos^2\theta)$. The equation (13.30) therefore becomes

$$\epsilon^{-q} \frac{\partial \psi}{\partial \zeta} = \mathcal{T}(\phi, \theta) - \epsilon^{q-2} \frac{\lambda}{2\cos^2\theta} \frac{\partial^2 \psi}{\partial \zeta^2} + \mathcal{O}(\epsilon^{q-1}), \tag{13.35}$$

and bottom friction can only play a role when $q = 1$.

The boundary layer expansion becomes

$$\hat{\psi}(\zeta, \theta) = \hat{\psi}^0(\zeta, \theta) + \epsilon \hat{\psi}^1(\zeta, \theta) + \ldots, \tag{13.36}$$

and the $\mathcal{O}(1)$ balance in (13.35) gives, with $\delta(\theta) = \lambda/(2\cos^2\theta)$

$$\frac{\partial \hat{\psi}^0}{\partial \zeta} = -\delta(\theta) \frac{\partial^2 \hat{\psi}}{\partial \zeta^2}. \tag{13.37}$$

The solution is

$$\hat{\psi}^0(\zeta, \theta) = C_1(\theta) + C_2(\theta) e^{-\frac{\zeta}{\delta(\theta)}}, \tag{13.38}$$

and the functions $C_i(\theta)$ are determined from

$$\hat{u}^0(0,\theta) = -\frac{1}{\sin\theta}\frac{\partial\hat{\psi}^0}{\partial\theta}(0,\theta) = 0 \tag{13.39a}$$

$$\lim_{\zeta\to\infty}\hat{\psi}^0(\zeta,\theta) = C_1(\theta) = \lim_{\phi\to\phi_W}\psi^0(\phi,\theta). \tag{13.39b}$$

At the eastern boundary the minus sign in (13.37) changes into a plus sign and, as in the β-plane case, it follows that there is no boundary layer due to bottom friction. The function $\Psi^0(\theta)$ in (13.34) has to be chosen such that the zonal velocity is zero at $\phi = \phi_E$ and this fixes also C_1 and C_2.

The boundary layer thickness $\delta(\theta)$ is relatively small near the equator and increases monotonically with θ. The dimensional boundary layer thickness $\delta_*(\theta)$ follows from (13.37), the definition of ζ and the horizontal length scale $L = r_0$ and becomes

$$\delta_*(\theta) = \bar{E}_V^{1/2} r_0 \delta(\theta) = \frac{r_0}{D\cos^2\theta}\left(\frac{A_V\sin\theta}{\Omega}\right)^{1/2}. \tag{13.40}$$

At $\theta = 45°$N we find that $\delta_* \approx 40$ km for $A_V = 10^{-3}$ m^{2}s^{-1}.

13.4. The planetary two-layer model

The governing equations in the stratified case are given by (13.4). When we neglect mixing and inertia in these equations, we find again the planetary geostrophic and hydrostatic balances. Just as in the stratified quasi-geostrophic case in chapter 7, horizontal density differences will cause a vertical shear according to the dimensionless thermal wind relations

$$\sin\theta\frac{\partial v}{\partial z} = -\frac{1}{\cos\theta}\frac{\partial\rho}{\partial\phi}, \tag{13.41a}$$

$$\sin\theta\frac{\partial u}{\partial z} = \frac{\partial\rho}{\partial\theta}. \tag{13.41b}$$

Planetary thermal wind balance

On the planetary scale the thermal wind balance is

$$2\Omega\sin\theta\frac{\partial v_*}{\partial z_*} = -\frac{g}{\rho_0 r_0\cos\theta}\frac{\partial\rho_*}{\partial\phi},$$

$$2\Omega\sin\theta\frac{\partial u_*}{\partial z_*} = \frac{g}{\rho_0 r_0}\frac{\partial\rho_*}{\partial\theta}.$$

To help understand the existence of the thermocline one can idealize it as a boundary between two layers of constant density. The upper layer (which is

bounded above by the ocean-atmosphere interface) has a constant density ρ_1 and the lower layer (bounded below by a flat bottom) has a constant density $\rho_2 > \rho_1$. The layers are separated by a deformable interface at $z = -h(\phi, \theta)$.

In each layer, the results of the homogeneous theory from the previous section can be used; we denote the velocity vector in layer *i* with $(u_i, v_i, w_i)^T$. In each layer outside the Ekman layers, (13.7) applies and hence

$$v_i \sin\theta = \frac{1}{\cos\theta}\frac{\partial p_i}{\partial \phi}, \tag{13.43a}$$

$$u_i \sin\theta = -\frac{\partial p_i}{\partial \theta}, \tag{13.43b}$$

$$\frac{\partial p_i}{\partial z} = 0, \tag{13.43c}$$

$$\frac{1}{\cos\theta}\left(\frac{\partial u_i}{\partial \phi} + \frac{\partial (v_i \cos\theta)}{\partial \theta}\right) + \frac{\partial w_i}{\partial z} = 0. \tag{13.43d}$$

The boundary conditions at the thermocline (that is made dimensionless with the depth D, i.e. $h_* = Dh$, but there is no *a priori* scaling) $z = -h(\phi, \theta)$ become

$$p_{1*} = p_{2*}, \tag{13.44a}$$

$$\frac{D}{dt}(z + h(\phi, \theta)) = 0 \quad \Rightarrow \quad u\frac{\partial h}{\partial \phi} + v\cos\theta\frac{\partial h}{\partial \theta} + w\cos\theta = 0, \tag{13.44b}$$

which represents the continuity of normal stress and the nonexistence of mass transfer over the interface.

From (13.1a) and (13.44a) it follows that

$$\gamma h = p_1 - p_2, \tag{13.45}$$

with $\gamma = (\rho_2 - \rho_1)/(\epsilon_p F_p \rho_0) = g'D/(2\Omega r_0 U)$, i.e. this parameter now contains the reduced gravity $g' = g(\rho_2 - \rho_1)/_r h o_0$. From (13.45) it follows that small pressure differences between layer 1 and 2 can cause substantial amplitudes in the thermocline. Although the pressure is continuous over $z = -h$, this does not hold for the horizontal velocities (that are independent of z in each layer). It is not difficult to show that the vertical velocity is continuous.

Ex. 13.3

The final equations of the planetary two-layer model are obtained by integration of (13.43) over each layer. The vorticity equations then become (with $h_1 = h, h_2 = 1 - h$),

$$v_1 h_1 \cos\theta = (\hat{w}_E - w_{|z=-h})\sin\theta, \tag{13.46a}$$

$$v_2 h_2 \cos\theta = (w_{|z=-h} - \tilde{w}_E)\sin\theta, \tag{13.46b}$$

where $\hat{w}_E$ and $\tilde{w}_E$ are the vertical Ekman velocities at top and bottom of the Ekman layer. Because of the continuity of w over the thermocline, the Sverdrup

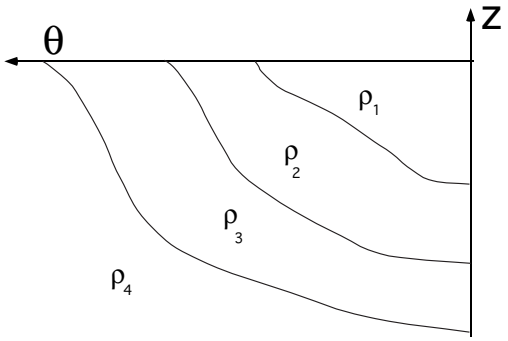

Figure 13.2. Sketch of a layer model needed to satisfy a prescribed surface density distribution $\rho = \rho_s$.

balance in the two-layer model becomes

$$(v_1 h_1 + v_2 h_2)\cos\theta = \sin\theta(\hat{w}_E - \tilde{w}_E). \tag{13.47}$$

With the choice of U as in (13.31) it follows that $\hat{w}_E = \mathcal{O}(1)$ and $\tilde{w}_E = \mathcal{O}(\bar{E}_V^{1/2})$. In many cases, the effect of the bottom boundary layer can be neglected.

The planetary two-layer model

On the planetary scale the two-layer model, where the interface is located at $z_* = -h_*$, is given by

$$\begin{aligned} \frac{2\Omega\cos\theta}{r_0} v_{1*} h_{1*} &= 2\Omega\sin\theta(\hat{w}_{E*} - w_{I*}) \\ \frac{2\Omega\cos\theta}{r_0} v_{2*} h_{2*} &= 2\Omega\sin\theta(w_{I*} - \tilde{w}_{E*}), \end{aligned}$$

where $h_{1*} = h_*$ and $h_{2*} = 1 - h_*$. In addition, $\hat{w}_{E*}$ and $\tilde{w}_{E*}$ are presented in section 13.3 and

$$w_{I*} = \frac{Dh_*}{dt_*}.$$

Ex. 13.4

With the two-layer model, we have reduced the mathematical problem of section 13.1 substantially. But how do we satisfy conditions of a prescribed surface density field with this type of model? Well, the two-layer model can easily be generalized to an n-layer model. If the layers outcrop to the surface, as sketched

in Fig. 13.2, then a surface density distribution can be mimicked. In this way, the vertical density difference is also coupled to the horizontal density difference.

13.5. Thermocline theory

There are two different theories of the physics of the thermocline: the ventilation theory and the internal boundary layer theory. Both can considered as limits of a final theory, which unfortunately has not been developed yet. The ventilation theory has the attractive property that it is purely advective. However, it can only provide a good description in cases where the surface Ekman pumping velocity $\hat{w}_E < 0$. The internal boundary layer theory includes a dependency on the magnitude of λ_V in (13.3). To give realistic thermocline depths the value of λ_V has to be larger than indicated by observations.

13.5.1. Ventilation theory

The central idea of the ventilation theory is that properties of the surface ocean are transported through advection to deeper regions of the ocean. In other words, these properties are ventilated from the surface to the deeper ocean. In this way, water of relatively high density in polar areas can be advected equatorward (southward in the northern hemisphere) below surface water which has a smaller density. The net result is the formation of a thermocline. The ventilation theory is purely advective as with $\lambda_V = 0$ in (13.3) we find

$$\frac{D\rho}{dt} = 0. \tag{13.49}$$

and the density is constant along streamlines. As one can anticipate problems will arise to satisfy surface boundary conditions for the density when the Ekman vertical velocity is negative.

We consider the ventilation process in more detail using a simple three-layer ocean model, as sketched in Fig. 13.3. The flow domain is bounded by a flat bottom and coastlines at $\phi = \phi_W$ and $\phi = \phi_E$. The layers have a constant density ρ_j and the third layer is assumed to be motionless. The location of the interfaces between the layers are indicated by the dimensionless z-coordinates z_j, with $z_1 = 0$, $z_4 = -1$, and

$$z_2 = -h_1, \tag{13.50a}$$
$$z_3 = -(h_1 + h_2). \tag{13.50b}$$

The effect of ocean-atmosphere deformation can be neglected on the large scale, and the layer thicknesses are given by

$$h_1 = -z_2, \tag{13.51a}$$
$$h_2 = z_2 - z_3, \tag{13.51b}$$
$$h_3 = z_3 + 1. \tag{13.51c}$$

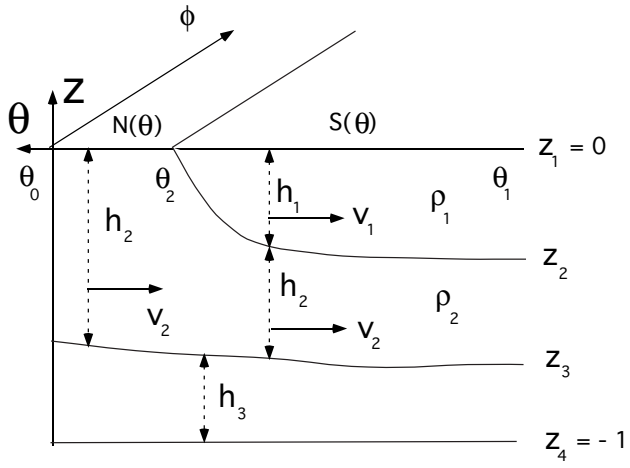

Figure 13.3. Sketch of the three-layer ocean model, where the thickness of the layer with density ρ_1 becomes zero at $\theta = \theta_2$; note that $\theta_2 < \theta_0$.

The vertical velocity $\hat{w}_E$ due to Ekman pumping is assumed negative on the whole interval $\theta_1 < \theta < \theta_0$ and $\hat{w}_E(\theta = \theta_0) = 0$. In the domain $S(\theta)$, for which $\theta_1 < \theta < \theta_2$, layer 1 is exposed to the wind forcing. In the domain $N(\theta)$ for which $\theta_2 < \theta < \theta_0$, layer 2 surfaces.

We first consider the domain $N(\theta)$ where $h_1 = 0$. In each layer j the governing equations of the flow outside the Ekman layer are

$$v_j \sin\theta = \frac{1}{\cos\theta}\frac{\partial p_j}{\partial \phi}, \tag{13.52a}$$

$$u_j \sin\theta = -\frac{\partial p_j}{\partial \theta}, \tag{13.52b}$$

$$\frac{\partial p_j}{\partial z} = 0, \tag{13.52c}$$

$$\frac{\partial u_j}{\partial \phi} + \frac{\partial (v_j \cos\theta)}{\partial \theta} + \cos\theta \frac{\partial w_j}{\partial z} = 0. \tag{13.52d}$$

Just as in the two-layer model in the previous section, the pressure and vertical velocity are continuous over the interfaces and hence

$$p_2 - p_3 = \gamma_2 h_2 = -\gamma_2 z_3, \tag{13.53a}$$

$$z = z_3 = -h_2 : \frac{D}{dt}(z + h_2) = 0, \tag{13.53b}$$

with $\gamma_2 = (\rho_3 - \rho_2)/(\rho_0 \epsilon_p F_p)$, $\epsilon_p = U/(2\Omega r_0)$ and $F_p = 4\Omega^2 r_0^2/(gD)$. In the motionless third layer we have $u_3 = v_3 = 0$ and hence $p_3 = \bar{p}_3$ is constant and consequently $p_2 = \bar{p}_3 - \gamma_2 z_3$.

In the domain $N(\theta)$ there are two active layers and the Sverdrup balance (13.47) over layer 2 and 3 becomes (use $v_3 = \tilde{w}_E = 0$)

$$v_2 h_2 \cos\theta = \hat{w}_E \sin\theta. \tag{13.54}$$

From (13.52a) it follows for $j = 2$,

$$v_2 \cos\theta = \frac{1}{\sin\theta} \frac{\partial p_2}{\partial \phi}, \tag{13.55}$$

such that with $p_2 = \bar{p}_3 - \gamma_2 z_3$ we have

$$v_2 h_2 \cos\theta = \frac{h_2}{\sin\theta} \frac{\partial p_2}{\partial \phi} = z_3 \frac{\gamma_2}{\sin\theta} \frac{\partial z_3}{\partial \phi} = \sin\theta \, \hat{w}_E. \tag{13.56}$$

Through integration over ϕ, the Sverdrup balance (13.54) can be written as

$$\gamma_2 \int_\phi^{\phi_E} z_3 \frac{\partial z_3}{\partial \phi} d\phi = \frac{1}{2} \gamma_2 (z_3^2(\phi_E, \theta) - z_3^2(\phi, \theta)) = \sin^2\theta \int_\phi^{\phi_E} \hat{w}_E(\phi, \theta) d\phi, \tag{13.57}$$

and with $h_2 = -z_3$ we find

$$\gamma_2 h_2^2(\phi, \theta) = -2 \sin^2\theta \int_\phi^{\phi_E} \hat{w}_E(\phi, \theta) d\phi + \gamma_2 h_2^2(\phi_E, \theta). \tag{13.58}$$

The geostrophic velocities are calculated from

$$u_2 = -\frac{1}{\sin\theta} \frac{\partial p_2}{\partial \theta} = -\frac{\gamma_2}{\sin\theta} \frac{\partial h_2}{\partial \theta}, \tag{13.59a}$$

$$v_2 = \frac{1}{\sin\theta \cos\theta} \frac{\partial p_2}{\partial \phi} = \frac{\gamma_2}{\sin\theta \cos\theta} \frac{\partial h_2}{\partial \phi}. \tag{13.59b}$$

Because of the kinematic boundary condition $u_2 = 0$ at the eastern continental boundary ($\phi = \phi_E$) it follows from (13.59a) that

$$\frac{\partial h_2}{\partial \theta}(\phi_E, \theta) = 0. \tag{13.60}$$

The layer thickness at the eastern boundary is therefore fixed if given at $\theta = \theta_0$. The layer thickness of the second layer is also determined from (13.58) once $\hat{w}_E$ is prescribed.

▶

Example 13.1: Outcropping

Consider the situation for which

$$\hat{w}_E(\phi,\theta) = \frac{\alpha}{2}\frac{\theta-\theta_0}{\sin^2\theta}, \tag{13.61}$$

for a constant $\alpha \neq 0$ on the domain $N(\theta)$, such that $\hat{w}_E(\phi,\theta_0) = 0$ and choose $h_2(\phi_E,\theta_0) = H_2$ with H_2 constant. From (13.58) we then find that

$$\gamma_2(h_2^2(\phi,\theta) - H_2^2) = \alpha(\theta_0-\theta)(\phi_E-\phi). \tag{13.62}$$

Because $\phi_E - \phi > 0$, h_2 increases westward (see Fig. 13.4) when $\alpha > 0$. Because $\partial h_2/\partial\phi < 0$, the meridional velocity $v_2 < 0$ (see (13.59b)) such that the geostrophic transport is directed southward advecting water with a density ρ_2.

In the case where $\alpha < 0$, and hence $\hat{w}_E > 0$, then h_2 decreases westwards. If for a certain latitude θ_s

$$\frac{\mid \alpha \mid}{\gamma_2}(\theta_0-\theta_s)(\phi_E-\phi_W) > H_2^2, \tag{13.63}$$

then h_2 becomes zero for a certain longitude ϕ_s. This surfacing of a layer is called 'outcropping'. This simple example illustrates the problems that arise in the ventilation theory when $\hat{w}_E > 0$. In Fig. 13.4, the solution h_2 is plotted as a function of ϕ for different values of θ and for $\alpha > 0$. The slope $\partial h_2/\partial\phi$ increases with southward and has a maximum at the southern boundary of the domain $\theta = \theta_2$ which is the 'outcropping' curve of layer 1.

Ex. 13.5

◀

As a next step, we consider the solution in the domain $S(\theta)$ where there are three layers. The domain $S(\theta)$ is special in that layer 2 is no longer exposed to the wind forcing. The conditions at the interfaces now become

$$p_1 - p_2 = \gamma_1 h_1 \tag{13.64a}$$

$$p_2 - p_3 = \gamma_2 h_2, \tag{13.64b}$$

$$z = z_2 = -h_1 \quad : \quad \frac{D}{dt}(z+h_1) = 0, \tag{13.64c}$$

$$z = -z_3 = -(h_1+h_2) \quad : \quad \frac{D}{dt}(z+h_1+h_2) = 0, \tag{13.64d}$$

with

$$\gamma_1 = \frac{\rho_2-\rho_1}{\rho_0\epsilon_p F_p}\ ;\ \gamma_2 = \frac{\rho_3-\rho_2}{\rho_0\epsilon_p F_p}. \tag{13.65}$$

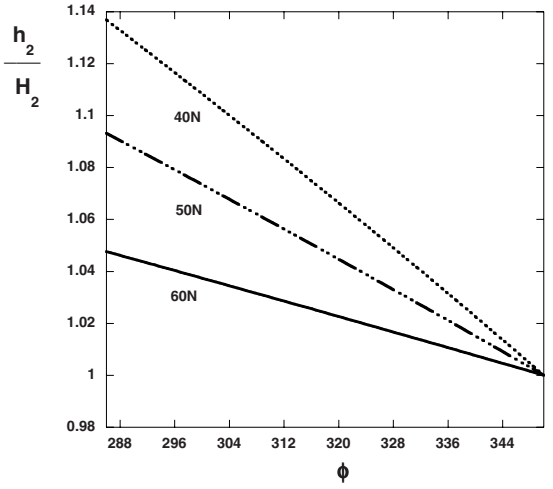

Figure 13.4. Plot of the solution $h_2(\phi,\theta)$ as in (13.62) versus ϕ for different values of θ. The value of $\alpha/(\gamma H_2^2) = 0.5$ and the domain is $[\phi_W,\phi_E] = [286,350]$ and $[\theta_1,\theta_0] = [40,70]$.

Now consider the changes in the potential vorticity of layer 2, i.e.,

$$q_2 = \frac{\sin\theta}{h_2}, \tag{13.66}$$

along curves of constant pressure p_2. These curves coincide with streamlines because (with (13.52a-b)),

$$\mathbf{u}_2 \cdot \nabla p_2 = \begin{pmatrix} u_2 \\ v_2 \end{pmatrix} . \begin{pmatrix} \frac{1}{\cos\theta}\frac{\partial p_2}{\partial \phi} \\ \frac{\partial p_2}{\partial \theta} \end{pmatrix} = 0, \tag{13.67}$$

and hence the velocity vector is tangent to curves of constant pressure. Elimination of the pressure in (13.52a-b) gives the vorticity equation

$$v_2 \cos\theta = \sin\theta \frac{\partial w_2}{\partial z}. \tag{13.68}$$

Integration over the layer (with thickness h_2) gives, with (13.64c),

$$\int_{z_2}^{z_3} v_2 \cos\theta \, dz = h_2 v_2 \cos\theta = \sin\theta \left(\frac{Dz_2}{dt} - \frac{Dz_3}{dt}\right) = \sin\theta \frac{Dh_2}{dt}, \tag{13.69}$$

and hence with $D(\sin\theta)/dt = v_2 \cos\theta$, it is found that

$$\frac{Dq_2}{dt} = \frac{1}{h_2}\frac{D(\sin\theta)}{dt} - \frac{\sin\theta}{h_2^2}\frac{Dh_2}{dt} = 0. \tag{13.70}$$

The potential vorticity q_2 is therefore conserved along streamlines.

At $\theta = \theta_2$, we know the value of q_2 from the solution in the domain $N(\theta)$ and we indicate it with q_2^N, i.e.,

$$q_2^N = \frac{\sin\theta_2}{h_2} = -\frac{\sin\theta_2}{z_3}. \tag{13.71}$$

For $\theta < \theta_2$, the potential vorticity q_2 is given by

$$q_2 = \frac{\sin\theta}{h_2} = \frac{\sin\theta}{z_2 - z_3}. \tag{13.72}$$

From (13.71-13.72) it follows that along a streamline in the second layer in the domain $S(\theta)$, we have

$$q_2 = q_2^N \Rightarrow z_2 = (1 - \frac{\sin\theta}{\sin\theta_2})z_3. \tag{13.73}$$

The Sverdrup balance (13.52) with $\tilde{w}_E = 0$, now becomes

$$(v_1 h_1 + v_2 h_2)\cos\theta = \sin\theta\ \hat{w}_E. \tag{13.74}$$

If the layer thicknesses are expressed in terms of z_j, and the geostrophic velocities and the relations (13.64a) are used with (13.74) we find

$$\gamma_1 z_2 \frac{\partial z_2}{\partial\phi} + \gamma_2 z_3 \frac{\partial z_3}{\partial\phi} = \sin^2\theta\ \hat{w}_E(\phi,\theta), \tag{13.75}$$

which, after integration in the zonal direction, can be written as

$$\begin{aligned} \gamma_1(z_2^2(\phi_E,\theta) - z_2^2(\phi,\theta)) \quad &+ \quad \gamma_2(z_3^2(\phi_E,\theta) - z_3^2(\phi,\theta)) = \\ &= \quad 2\sin^2\theta \int_{\phi_E}^{\phi} \hat{w}_E(\phi,\theta)d\phi. \end{aligned} \tag{13.76}$$

Because $z_2 = -h_1, h_1(\phi,\theta_2) = 0$ and $u_1(\phi_E,\theta) = 0$ it follows from (13.52b) that $z_2(\phi_E,\theta) = 0$. The thickness of the upper layer remains zero at the eastern boundary. If we write $f = \sin\theta$ and $f_2 = \sin\theta_2$ and introduce h through

$$h_2 = h\frac{f}{f_2}, \tag{13.77}$$

then it follows from (13.73) that

$$h_2 = z_2 - z_3 = -\frac{f}{f_2}z_3 \rightarrow h = -z_3; z_2 = -(1 - \frac{f}{f_2})h, \tag{13.78}$$

such that (13.76) becomes

$$(\gamma_1(1-\frac{f}{f_2})^2 + \gamma_2)h^2(\phi,\theta) = \gamma_2 z_3^2(\phi_E,\theta) - 2\sin^2\theta \int_{\phi}^{\phi_E} \hat{w}_E(\phi,\theta)d\phi. \tag{13.79}$$

Because $z_2(\phi_E, \theta) = 0$ and $z_3(\phi_E, \theta)$ has to be constant in the meridional direction (since $u_2 = 0$ at $\phi = \phi_E$) it follows that $z_3(\phi_E, \theta) = H_2$. This determines the thickness h through the Ekman vertical velocity $\hat{w}_E$ and hence $h_1(\phi, \theta)$ and $h_2(\phi, \theta)$ as well.

▶

Example 13.2: The shadow zone

Just as in Example 13.1, let the Ekman vertical velocity be given by

$$\hat{w}_E(\phi, \theta) = \frac{\alpha}{2} \frac{\theta - \theta_0}{\sin^2 \theta}, \tag{13.80}$$

with $\alpha > 0$. The solution (13.79) in the domain $S(\theta)$ then becomes

$$h^2(\phi, \theta) = \frac{\alpha(\theta_0 - \theta)(\phi_E - \phi) + \gamma_2 H_2^2}{\gamma_1 (1 - \frac{f}{f_2})^2 + \gamma_2}, \tag{13.81}$$

and the layer thicknesses are

$$h_1 = h(1 - \frac{\sin\theta}{\sin\theta_2}), \tag{13.82a}$$

$$h_2 = h \frac{\sin\theta}{\sin\theta_2}. \tag{13.82b}$$

The solution matches the solution in the domain $N(\theta)$ at $\theta = \theta_2$, for which (see Example 13.1)

$$h_1 = 0, \tag{13.83a}$$

$$\gamma_2(h_2^2(\phi, \theta) - H_2^2) = \alpha(\theta_0 - \theta_2)(\phi_E - \phi). \tag{13.83b}$$

Now consider the streamlines that, in layer 2, intersect the curves $\theta = \theta_2$ at a certain longitude $\tilde{\phi}$ (Fig. 13.5). Because $z_3 = -h$, curves of constant pressure h are also streamlines in layer 2 (note $p_2 - p_3 = \gamma_2 h$). For the streamline through $\phi = \tilde{\phi}$ we find

$$\begin{aligned} h^2(\phi, \theta) &= \frac{\alpha(\theta_0 - \theta)(\phi_E - \phi) + \gamma_2 H_2^2}{\gamma_1 (1 - \frac{f}{f_2})^2 + \gamma_2} = \\ = h^2(\tilde{\phi}, \theta_2) &= \frac{\alpha(\theta_0 - \theta_2)(\phi_E - \tilde{\phi}) + \gamma_2 H_2^2}{\gamma_2}. \end{aligned} \tag{13.84}$$

The streamline that connects to the eastern boundary in layer 2 ($\tilde{\phi} = \phi_E$) is determined in the domain $S(\theta)$ through the relation

$$\alpha(\theta_0 - \theta)(\phi_E - \phi) = H_2^2 \gamma_1 (1 - \frac{f}{f_2})^2. \tag{13.85}$$

We can write the streamline as a function $\phi_c(\theta)$ with

$$\phi_c(\theta) = \phi_E - \frac{H_2^2 \gamma_1}{\alpha} \frac{(1 - \frac{f}{f_2})^2}{\theta_0 - \theta}. \tag{13.86}$$

For $\theta = \theta_2$ the second term in the right hand side becomes zero and hence

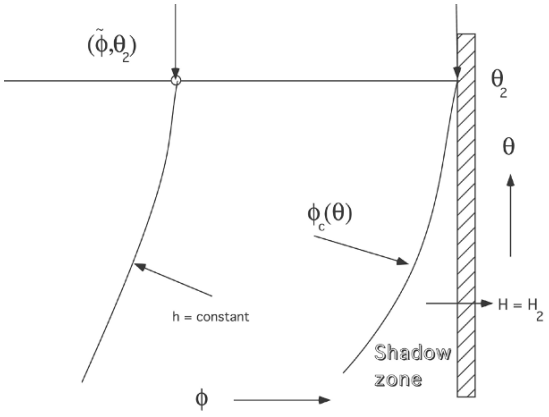

Figure 13.5. Sketch to understand the existence of the shadowzone.

$\phi = \phi_E$. However, when $\theta < \theta_2$, then $\phi < \phi_E$ and the streamline deflects to the west (Fig. 13.5). The area east of the streamline cannot be reached by water in layer 2 that was originally north of the 'outcrop' line $\theta = \theta_2$.

In general, the solution (13.79) cannot be valid up to the eastern boundary which also follows from the fact that h is not constant for $\phi = \phi_E$. The conditions that $h(\phi_E, \theta)$ must be constant and potential vorticity is conserved in layer 2 cannot both be satisfied. This causes a shadowzone in which the flow is zero (and the layer thickness constant) to satisfy the boundary conditions. In the shadow zone, the total Sverdrup transport is carried by layer 1. From (13.79) it follows with $z_3 = -H_2$ and $z_2 = -h_1$ that

$$h_1^2(\phi, \theta) = \frac{\alpha}{\gamma_1}(\phi_E - \phi)(\theta_0 - \theta), \tag{13.87}$$

and hence the thickness of the first layer increases in southward and westward direction.

◀

Additional Material

D: The material in the previous sections should (hopefully) make one prepared for the more comprehensive texts on the ventilation theory of the thermocline problem such as in sections 6.21 to 6.23 in Pedlosky (1987), chapter 4 in Pedlosky (1996) and chapter 16 (sections 16.1 to 16.4) in Vallis (2006).

13.5.2. The internal boundary layer model

The second theory of the physics of the thermocline is the internal boundary layer theory. The central idea of the internal boundary layer idea is that the thermocline arises through an advection/diffusion balance at mid-depth. The existence of such a balance can be studied by using the continuous equations (13.3-13.4) with the boundary conditions (13.5).

First we investigate whether we can extract a characteristic length scale for the depth of the thermocline that depends both on the dynamics and the thermodynamics of the flow. Let W_E be a (dimensional) characteristic vertical velocity due to Ekman pumping at the surface, $U = W_E r_0/D$ and $\hat{w}_E(\phi,\theta)$ the horizontal (dimensionless) distribution of the Ekman vertical velocity. Now consider typical horizontal density variations $\Delta\rho$ in the surface density field $\rho_s(\phi,\theta)$. The total density $\rho_*(\phi,\theta,0)$ is then given by

$$\rho_*(\phi,\theta,0) = \rho_0 + \Delta\rho\,\rho_s(\phi,\theta), \tag{13.88}$$

and with (13.1b) it follows that

$$\begin{aligned} \rho(\phi,\theta,0) &= \frac{\Delta\rho}{\rho_0}\frac{gD}{2\Omega U r_0}\rho_s(\phi,\theta) = \\ = \frac{\Delta\rho}{\rho_0}\frac{gD^2}{2\Omega W_E r_0^2}\,\rho_s(\phi,\theta) &= (\frac{D}{\delta_a})^2\rho_s(\phi,\theta), \end{aligned} \tag{13.89}$$

where

$$\delta_a = (\frac{2\Omega\, W_E\, \rho_0}{g\Delta\rho})^{1/2}\, r_0 \tag{13.90}$$

is called the advective thermocline scale. With $W_E = 10^{-6}\,\mathrm{ms}^{-1}$, $\Delta\rho/\rho_0 = 10^{-3}$ we find $\delta_a \approx 700$ m which is a reasonable scale for the thermocline. The vertical length scale δ_a is the scale at which dynamically induced density differences are balanced by changes in the surface density field. Another vertical length scale is the diffusive scale δ_D, that is defined by a balance between vertical advection ($w_*\partial\rho_*/\partial z_* \sim W_E\Delta\rho/\delta_D$) and vertical mixing ($K_V\partial^2\rho_*/\partial z_*^2 \sim K_V\Delta\rho/\delta_D^2$), i.e.,

$$\delta_D = \frac{K_V}{W_E}. \tag{13.91}$$

Having identified these two different length scales, we know that the ratio δ_D/δ_a provides a guideline for investigating the different balances that can occur in the flow. The possible cases are systematically discussed below; we will indicate the scale D of the thermocline below (don't confuse this with the total layer thickness as used in earlier chapters).

(A) First we consider the case where $\delta_D/\delta_a \gg 1$, which corresponds to small W_E according to (Fig. 13.6a)

$$\frac{\delta_D}{\delta_a} \approx W_E^{-3/2}. \tag{13.92}$$

and hence the Ekman pumping is relatively weak.

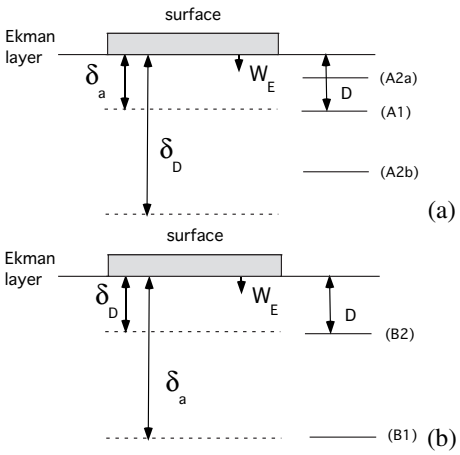

Figure 13.6. Sketch to help understand the different cases in the scales of the thermocline depth. (a) Case A with $\delta_D/\delta_a \gg 1$. (b) Case B with $\delta_D/\delta_a \ll 1$.

There are now several choices that can be made for the characteristic vertical length scale of the flow D:

(A1) If we choose $D = \delta_a$ then it follows that

$$\lambda_V = \frac{K_V r_0}{UD^2} = \frac{K_V}{W_E D} = \frac{\delta_D}{D} = \frac{\delta_D}{\delta_a} \gg 1, \tag{13.93}$$

and because $\rho = \rho_s$ according to (13.89), the surface density extends (because of large vertical mixing) to the deep sea which is not what is observed.

(A2) If (D/δ_a) is not $\mathcal{O}(1)$, then it follows from (13.88) that $\rho = (D/\delta_a)^2\rho_s$ and hence ρ has to be rescaled to be able to satisfy the surface boundary condition. We therefore rescale

$$\rho = (\frac{D}{\delta_a})^2\tilde{\rho}, \tag{13.94}$$

and from (13.4) it appears that u, v and w also need to be rescaled, with $u = (D/\delta_a)^2\tilde{u}$, $v = (D/\delta_a)^2\tilde{v}$ and $w = (D/\delta_a)^2\tilde{w}$. For the balance (13.3) this gives

$$(\frac{D}{\delta_a})^2\left[\frac{\tilde{u}}{\cos\theta}\frac{\partial\tilde{\rho}}{\partial\phi} + \tilde{v}\frac{\partial\tilde{\rho}}{\partial\theta} + \tilde{w}\frac{\partial\tilde{\rho}}{\partial z}\right] = \frac{\delta_D}{D}\frac{\partial^2\rho}{\partial z^2}, \tag{13.95}$$

while the boundary conditions at the surface become $\tilde{\rho} = \rho_s$ and $\tilde{w} = (\delta_a/D)\hat{w}_E$.

Within this case (note that we still require $\delta_D/\delta_a \gg 1$) there are two options

(A2a) If $D \ll \delta_a$ then $D \ll \delta_D$ and hence $\lambda_V \gg 1$) and (13.95) reduces to $\partial^2\rho/\partial z^2 = 0$. Again the surface density extends (because of large vertical mixing) to the deep sea which is not realistic.

(A2b) An advection-diffusive balance is possible when

$$D = (\delta_a^2\delta_D)^{1/3} = (\frac{2\Omega r_0^2 K_V}{g\Delta\rho/\rho_0})^{1/3}, \tag{13.96}$$

In this case we have $\lambda = \delta_D/D = (\delta_D/\delta_a)^{2/3} \gg 1$,

$$\frac{D}{\delta_a} = (\frac{\delta_D}{\delta_a})^{1/3} \gg 1. \tag{13.97}$$

and hence $D \gg \delta_a$. In this diffusive limit, since $w = (D/\delta_a)^2\tilde{w}$ the boundary condition at the surface reduces to $\tilde{w} = 0$ which shows again that the problem is independent of the Ekman pumping. The downward mixing of density is so strong that the internal density gradients induce vertical velocities that are much larger than the Ekman velocity.

In summary, the $\delta_D/\delta_a \gg 1$ is not realistic because it either provides solutions without a vertical structure or a thermocline scale independent of the Ekman pumping velocity.

(B) We now consider the second case $\delta_D/\delta_a \ll 1$; again there are several possible choices for D (Fig. 13.6b). We discuss only two interesting ones:

(B1) There can be a balance in (13.3) for $D = \delta_a$, i.e., $\lambda_V = \delta_D/D = \delta_D/\delta_a \ll 1$ and we find $D\rho/dt = 0$. In this case, the density is constant along streamlines and hence the name of advective length scale for δ_a. In this advective limit, again (13.89) reduces to $\rho = \rho_s$; the solutions of $D\rho/dt = 0$, however, in general cannot satisfy this boundary condition unless the Ekman pumping is negative.

(B2) Another balance is possible when $D = \delta_D \ll \delta_a$ such that $\lambda_V = 1$. In this case ρ has to be rescaled as $\rho = (\delta_D/\delta_a)^2\hat{\rho}$ and consequently u and v have to be rescaled as well according to the thermal wind balance. Because $\delta_D/\delta_a \ll 1$, (13.3) now becomes

$$w\frac{\partial\hat{\rho}}{\partial z} = \frac{\partial^2\hat{\rho}}{\partial z^2}, \tag{13.98a}$$

$$\frac{\partial w}{\partial z} = 0. \tag{13.98b}$$

In the region with length scale δ_D, the vertical velocity is constant in z and equal to w_E. Moreover, (13.98) only has bounded solutions for $w_E > 0$ as is illustrated by Example 13.3.

▶

Example 13.3: Flow in a circumglobal channel

Consider the flow in a circumglobal channel (Fig. 13.7) that is bounded by the latitudes $\theta = \theta_0$ and $\theta = \theta_2$. At the surface, the flow is forced by a density distribution $\rho = \rho_s(\theta)$ and a wind-stress field $\tau^\phi = \tau^\phi(\theta)$ and $\tau^\theta = 0$. We assume that the layer is infinitely deep and are searching for solutions that are independent of the zonal coordinate, i.e., $u(\theta, z)$, $v(\theta, z)$, $w(\theta, z)$, $p(\theta, z)$ and $\rho(\theta, z)$.

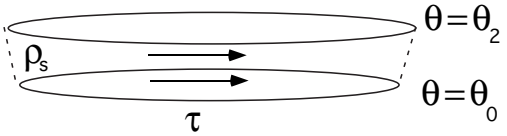

Figure 13.7. Sketch of a circumglobal channel on the sphere (drawn here in the Southern Hemisphere).

Outside the Ekman layers the equations (13.3) become

$$v = 0, \tag{13.99a}$$

$$u\sin\theta = -\frac{\partial p}{\partial \theta}, \tag{13.99b}$$

$$\frac{\partial w}{\partial z} = 0, \tag{13.99c}$$

$$\rho = -\frac{\partial p}{\partial z}, \tag{13.99d}$$

$$w\frac{\partial \rho}{\partial z} = \lambda\frac{\partial^2 \rho}{\partial z^2}, \tag{13.99e}$$

and it follows immediately that $w = w(\theta)$. The advection-diffusion balance for the density can be integrated with the result

$$\rho(\theta, z) = C_1(\theta)e^{\frac{w(\theta)z}{\lambda_V}} + C_2(\theta). \tag{13.100}$$

When $w(\theta) < 0$ then $C_1 = 0$, because otherwise the density becomes unbounded, and hence $\rho = \rho_s(\theta)$. When $w(\theta) > 0$ the solution becomes

$$\rho(\theta, z) = (\rho_s(\theta) - \rho_\infty(\theta))e^{\frac{zw(\theta)}{\lambda_V}} + \rho_\infty(\theta), \tag{13.101}$$

where $\rho_\infty(\theta)$ is the density at $z \to \infty$. Hence the characteristic vertical scale of the density anomalies is $\lambda/w(\theta)$ and we can take $h(\theta) = \lambda_V/w(\theta)$ as a measure of the depth of the thermocline. The corresponding dimensional vertical scale of the thermocline is δ_D.

◀

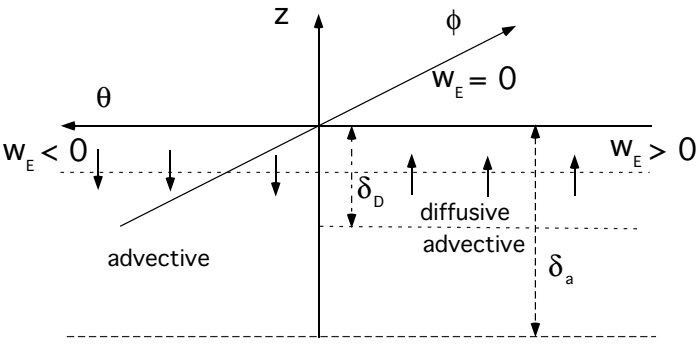

Figure 13.8. Sketch to help explain the internal boundary layer idea. Region I is the domain where $w_E < 0$ and region II where $w_E > 0$.

Case (B) is therefore the most realistic case with different balances depending on whether $w_E > 0$ or $w_E < 0$. This is summarized in Fig. 13.8 which gives a

sketch of the Ekman pumping in a basin where the flow is forced by a prescribed wind stress. In the region where $w_E < 0$, liquid with surface density values is pumped into the geostrophic region and then advected through this region. Here, the vertical scale can be set pure by advection, we have case (B1) above. In the region where $w_E > 0$, liquid with a certain density enters the Ekman layer and hence in general cannot match to a prescribed surface density distribution. Here a balance according to case (B2) above is set between advection and mixing on a small scale δ_D above the advectively controlled flow below (under the conditions that mixing is still small).

Summary

- The thermocline is a vertical interval with relatively large gradients in the temperature and the density field. The thermocline arises through the nonlinear coupling of the velocity field with the density field.
- The constant density midlatitude Sverdrup-Stommel theory can be easily generalized to the planetary case. The Stommel boundary layer thickness is given by

$$\delta_*(\theta) = \frac{r_0}{D\cos^2\theta}\left(\frac{A_V \sin\theta}{\Omega}\right)^{1/2}.$$

- Two characteristic scales for the thermocline depth are the advective scale δ_a and the diffusive scale δ_D given by

$$\delta_a = \left(\frac{2\Omega\, W_E\, \rho_0}{g\Delta\rho}\right)^{1/2} r_0\ ;\ \delta_D = \frac{K_V}{W_E}.$$

  where W_E is the characteristic Ekman pump velocity, $\Delta\rho$ a characteristic horizontal density difference and K_V the vertical diffusivity.
- Two theories describe different aspects of the thermocline problem. The internal boundary layer model is able to provide a reasonable representation in regions where $\hat{w}_E > 0$ but is based on a relatively large vertical mixing coefficient. This is complementary to the ventilation theory which is purely advective, but it is only applicable when $\hat{w}_E < 0$. The final solution of the thermocline problem will likely contain elements from both theories.

13.6. Exercises on chapter 13

(13.1) *Planetary Ekman layers*

Consider the flow in the spherical sector $[\phi, \theta] \in [286, 350] \times [10, 70]$ as a model of the ocean circulation in the North Atlantic Ocean. The density of the water is constant and the flow is driven by the wind-stress field

$$\tau_*^{\phi}(\phi, \theta) = -\frac{\tau_0}{2\pi} \cos 2\pi(\frac{\theta - 10}{60}) \; ; \; \tau^{\theta} = 0 \tag{13.102}$$

where $\tau_0 = 0.1$ Pa. The depth of the basin D = 4000 m and the bottom is flat. Assume that the mixing coefficients of momentum are constant with $A_V = 10^{-3}$ m^{2}s^{-1} and $A_H = 10^5$ m^{2}s^{-1}.

a. Determine the thickness (in m) of the Ekman layers at the ocean-atmosphere interface and near the bottom.

b. Determine the pattern and amplitude of the upwelling over the basin.

c. Determine the difference in sea surface height between the subtropical gyre and the subpolar gyre (in m).

d. Determine the pattern and amplitude (in ms^{-1}) of the geostrophic meridional velocity in the basin.

(13.2) *Homogeneous planetary circulation*

Consider a circumglobal zonal channel for $\theta \in [\theta_0, \theta_1] \subset (-\pi/2, 0)$ bounded between the latitudes θ_0 en θ_1. The wind stress at the ocean-atmosphere surface is of the form

$$\tau^{\phi} = \sin(\pi \frac{\theta - \theta_1}{\theta_0 - \theta_1}) \; ; \; \tau^{\theta} = 0$$

The bottom of the channel is flat and the surface deformation of the ocean-atmosphere surface is negligible. The density of the ocean water is constant, the flow caused by the wind stress is steady and horizontal mixing of momentum can be neglected. In this exercise we try to find flows which are independent of the zonal coordinate, i.e., solutions of the form $(u(\theta, z), v(\theta, z) w(\theta, z), p(\theta, z))$.

a. Determine the equations that describe the flow outside the boundary layers at the bottom and at the surface.

b. Derive solutions of the velocity field in the Ekman layer at the bottom and at the ocean-atmosphere surface.

c. Show by matching of the vertical velocity that the geostrophic zonal velocity field is given by

$$u^0(\theta) = C_1 \tau^{\phi}(\theta) + C_2 \frac{\sqrt{|\sin\theta|}}{\cos\theta}$$

and argue that $C_2 = 0$.

d. Choose two simple latitudes θ_0 and θ_1 and sketch the velocity field, including the flow in the Ekman layers.

(13.3) *Continuity of the vertical velocity*

In this exercise we consider the continuity of the vertical velocity in the two-layer planetary model over the thermocline.

a. Show that

$$w_{2|_{z=-h}} - w_{1|_{z=-h}} = (\mathbf{u}_1 - \mathbf{u}_2) \cdot \nabla h$$

where

$$\nabla h = \begin{pmatrix} \frac{1}{\cos\theta} \frac{\partial h}{\partial \phi} \\ \frac{\partial h}{\partial \theta} \end{pmatrix}.$$

b. Next, use the geostrophic balance to show that

$$\mathbf{u}_2 \sin\theta = \mathbf{e}_3 \wedge \nabla(p_1 - \gamma h),$$

c. Prove that w is continuous at $z = -h$.

(13.4) *Two-layer planetary model*

Consider the situation as in exercise (13.1), but now for a two-layer ocean with $g' = 0.01$ ms^{-2} and equilibrium layer thicknesses $H_1 = 500$ m and $H_2 = 3500$ m.

a. Prove that with a time-independent wind forcing, the lower layer is motionless.

b. Determine the pattern and amplitude of the thermocline field (in m).

(13.5) *Ventilation*

Consider the situation as in Example 13.1 with the same spatial pattern of the Ekman pumping $\hat{w}_E$ in a spherical sector $[\phi, \theta] \in [286, 350] \times [10, 45]$. Take $\alpha = -1$ and assume that the maximum magnitude of the upwelling is equal to 0.1 m day^{-1}. The layer thicknesses in the three-layer model are $H_1 = 500$ m, $H_2 = 1000$ m and $H_3 = 2000$ m. The density difference between the layers are such that $g(\rho_3 - \rho_2)/\rho_2 = 0.02$ en $g(\rho_2 - \rho_1)/\rho_2 = 0.01$ ms^{-2}.

a. Calculate the profile of the layer thickness h_2.

b. Determine the latitude ϕ_s where outcropping occurs.

Chapter 14

ANTARCTIC CIRCUMPOLAR CURRENT

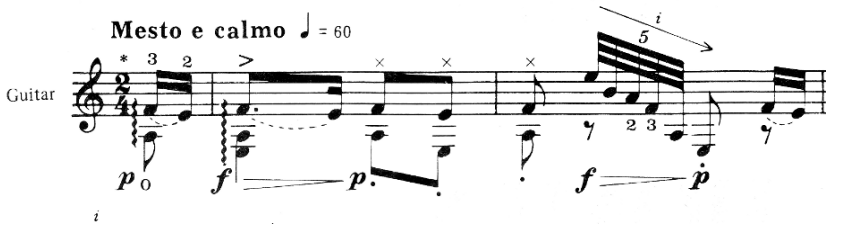

Homenaja, M. de Falla

The absence of a continental barrier near the latitude of Drake Passage has a large influence on the ocean circulation in the Southern Ocean. Between 45°S and 65°S there is a strong zonal current, known as the Antarctic Circumpolar Current (ACC), which connects the three ocean basins. The ACC plays an important role in the transport of heat, salt and other quantities between the ocean basins and hence has an important role in the climate system. In this chapter some characteristics of the ACC, as determined from the (limited) observations, are presented in section 14.1. One of the central motivations of the material in this chapter is the physical processes which control the volume transport through Drake Passage. In section 14.2 we consider barotropic wind-driven flows in a zonal channel discuss the role of bottom topography (and the so-called 'form stress') in these flows. The theory of stratified flows is presented in section 14.3 where we discuss the JEBAR effect. At the end of this section we touch on the role of instabilities and the resulting eddies.

Note: All equations in this chapter are dimensional and we will therefore omit the star subscript.

14.1. Observations

The annual average wind-stress forcing (τ^ϕ, τ^θ) from Trenberth et al. (1989) over the globe was plotted in Fig. 2.1. The zonally averaged profile of the zonal wind stress τ^ϕ over the Southern Hemisphere is shown in Fig. 14.1. The zonally averaged value of τ^ϕ is positive between 65°S and 30°S and negative elsewhere. As a consequence, the meridional Ekman transport M_E^θ, determined in section 13.2 as

$$M_E^\theta = -\frac{\tau^\phi}{2\Omega\rho_0 \sin\theta}, \tag{14.1}$$

is northward between 65°S and 30°S (note that $\sin\theta < 0$ in the Southern Hemisphere) and southward south of 65°S and north of 30°S.

A sketch of the flow patterns in the Southern Ocean is given in Fig. 14.2a together with the annual mean temperature and salinity in Fig. 14.2b and c, respectively. The ACC is the dominant flow around Antarctica, with gyres – the Weddell Gyre and the Ross Gyre – near the boundaries of this continent. The ACC is composed of different zonal jets, each associated with a strong gradient in density, a so-called front. Two of these fronts are indicated in Fig. 14.2, e.g., the Polar Front and the Subantarctic Front. Signatures of the fronts are visible in the plots of sea surface temperature and sea surface salinity (Fig. 14.2b,c).

The fronts are also visible in the profiles of temperature and salinity (Fig. 14.3a,b), as measured along the WOCE 140°E meridional section (between

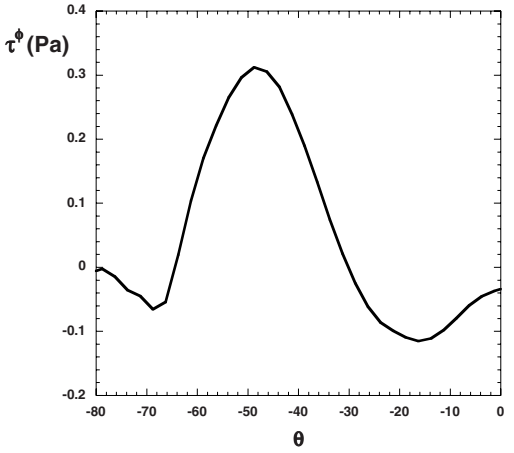

Figure 14.1. Profile of the zonally averaged zonal wind stress (τ^{ϕ}) (as deduced from Trenberth et al. (1989)) over the Southern Hemisphere.

Australia and Antarctica). The contours of potential density σ_0 (Fig. 14.3c) slope upward to the south ($\partial\rho/\partial\theta < 0$), consistent with an eastward zonal surface current through the thermal wind balance

$$2\Omega \sin\theta \frac{\partial u}{\partial z} = \frac{g}{\rho_0 r_0} \frac{\partial \rho}{\partial \theta}. \tag{14.2}$$

The deep water, the Antarctic Bottom water (AABW), is characterized by a relatively low potential temperature (-0.2°C), a salinity of 34.68 psu and a potential density $\sigma_0 = 28.3$. Another water mass is the Antarctic Intermediate Water (AAIW) with a salinity of 34.4 psu and a potential temperature of 5-6°C. The associated circulation is sketched in Fig. 14.3d. North of 65°S, the Ekman transport is divergent and there is upwelling in the upper ocean. South of this latitude, there is downwelling and formation of deepwater (in the Weddell Sea). The NADW (the North Atlantic Deepwater) also surfaces in the southern ocean and mixes with water masses in the Southern Ocean.

The zonal flow along the WOCE 140°E section has a relatively complicated spatial structure and it is difficult to determine the total transport. The transport of the zonal jet near the Subantarctic Front is estimated to be about 105 Sv and that near the Polar Front is about 22 Sv. It are these types of observations that have resulted in the estimate of 134 ± 13 Sv for the transport through Drake Passage. In the remainder of this chapter, we will address the problem of the processes controlling this Drake Passage transport.

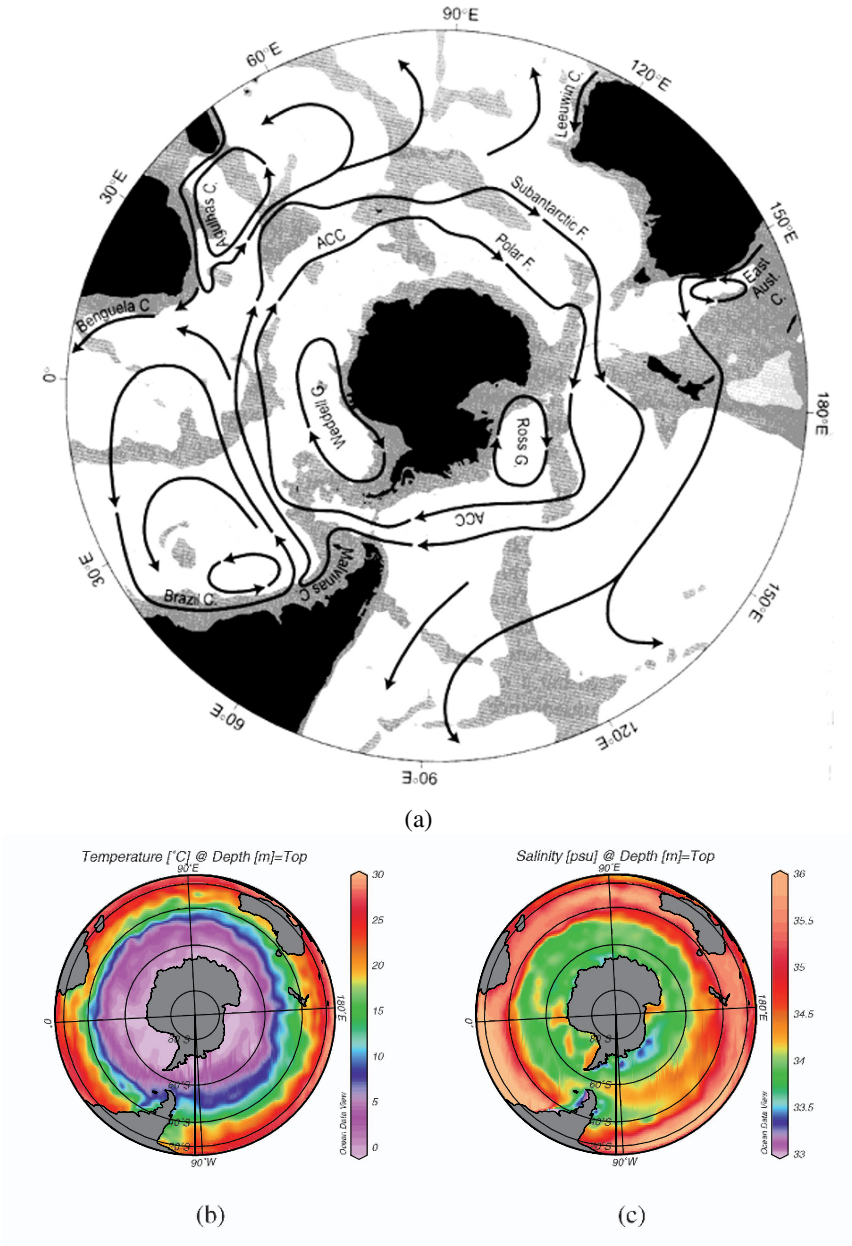

Figure 14.2. (a) Overview of the surface current system in the Southern Ocean; two of the fronts are indicated (from WOCE (2001)). (b) Annual mean sea surface temperature, and (c) annual mean sea surface salinity.

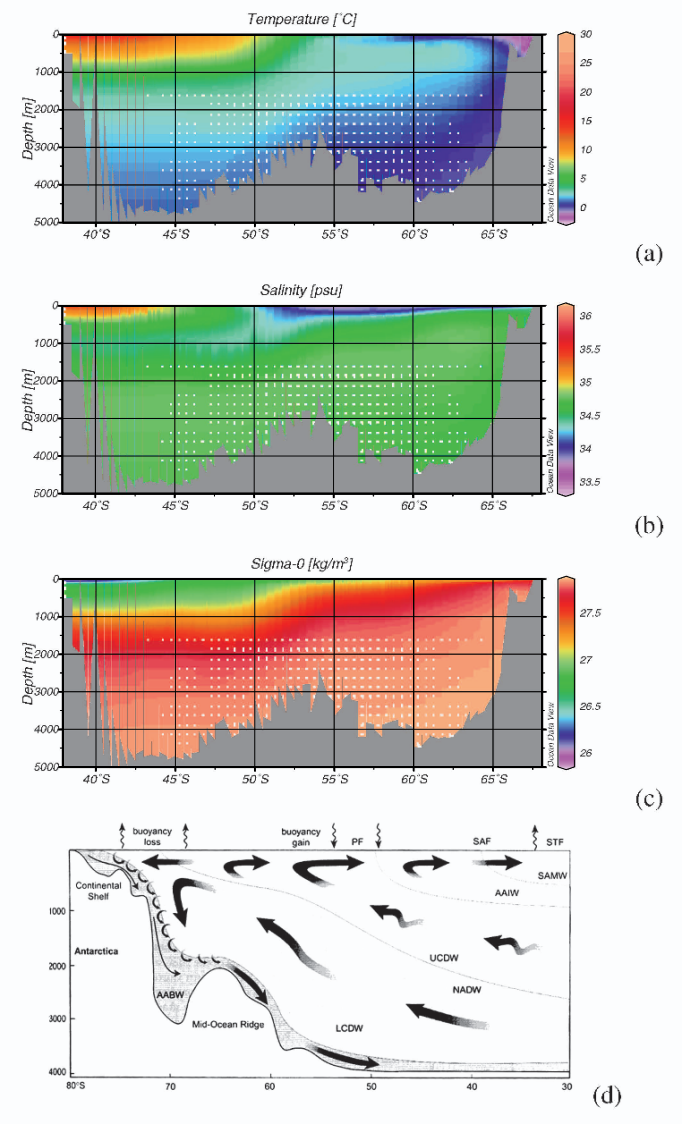

Figure 14.3. Profiles of temperature (a), salinity (b) and (c) potential density σ_0 along the WOCE 140° E meridional section; note that in all panels south is to the right. (d) Sketch of the zonally averaged circulation in the Southern Ocean; note that south is to the left (from WOCE (2001)).

Additional Material

B: A description of Antarctic Oceanography can be found in chapter 6 of Tomczak and Godfrey (1994). A more extensive discussion on the flow in the Southern Ocean is given in section 4.6 of WOCE (2001).

14.2. The barotropic channel model

An idealized model of the ACC is that of a barotropic flow in a zonal channel with a geometry as in Fig. 13.7. This channel is located in the Southern Hemisphere and it is bounded by latitudes $\theta = \theta_1$ and $\theta = \theta_2$. The flow is forced at the ocean-atmosphere interface by an idealized wind stress (τ^ϕ, τ^θ). The bottom topography is represented by a function $h_b(\phi, \theta)$.

The equations governing the constant density flow were presented in section 13.2. Neglecting inertial terms, the dimensional equations are

$$-2\Omega v \sin\theta + \frac{1}{\rho_0 r_0 \cos\theta}\frac{\partial p}{\partial \phi} = A_V \frac{\partial^2 u}{\partial z^2} + \mathcal{F}^\phi, \tag{14.3a}$$

$$2\Omega u \sin\theta + \frac{1}{r_0 \rho_0}\frac{\partial p}{\partial \theta} = A_V \frac{\partial^2 v}{\partial z^2} + \mathcal{F}^\theta, \tag{14.3b}$$

$$0 = \frac{\partial p}{\partial z}, \tag{14.3c}$$

$$\frac{1}{r_0}\left(\frac{\partial u}{\partial \phi} + \frac{\partial (v\cos\theta)}{\partial \theta}\right) + \cos\theta \frac{\partial w}{\partial z} = 0, \tag{14.3d}$$

where A_V is the vertical mixing coefficient of momentum. The terms $\mathcal{F}^\phi$ and $\mathcal{F}^\theta$ are added as a representation of the lateral friction. If we assume that deformations of the ocean-atmosphere interface are unimportant then the boundary conditions become

$$z = -D + h_b : \frac{D(z-h_b)}{dt} = 0;\ \mathbf{t}_1 \cdot \mathbf{u} = 0;\ \mathbf{t}_2 \cdot \mathbf{u} = 0, \tag{14.4a}$$

$$z = 0 : \tau^\phi = \rho_0 A_V \frac{\partial u}{\partial z};\ \tau^\theta = \rho_0 A_V \frac{\partial v}{\partial z};\ w = 0, \tag{14.4b}$$

where

$$\mathbf{t}_1 = \begin{pmatrix} 1 \\ 0 \\ \frac{1}{\cos\theta}\frac{\partial h_b}{\partial \phi} \end{pmatrix};\ \mathbf{t}_2 = \begin{pmatrix} 0 \\ 1 \\ \frac{\partial h_b}{\partial \theta} \end{pmatrix},$$

are the tangent vectors at the bottom. In the zonal direction, periodic boundary conditions are chosen and no-slip conditions apply at the meridional channel boundaries.

14.2.1. Flat bottom case

In the flat bottom case, we find from (14.4a) that the vertical velocity $w = 0$ at $z = -D$. Integration of the equations (14.3) over depth (from $-D$ to 0) gives

$$-2\Omega\bar{v}\sin\theta = -\frac{1}{r_0\rho_0\cos\theta}\frac{\partial\bar{p}}{\partial\phi} + \frac{\tau^\phi}{\rho_0} - \frac{\tau_b^\phi}{\rho_0} + \bar{\mathcal{F}}^\phi, \tag{14.5a}$$

$$2\Omega\bar{u}\sin\theta = -\frac{1}{r_0\rho_0}\frac{\partial\bar{p}}{\partial\theta} + \frac{\tau^\theta}{\rho_0} - \frac{\tau_b^\theta}{\rho_0} + \bar{\mathcal{F}}^\theta, \tag{14.5b}$$

$$0 = \frac{\partial\bar{u}}{\partial\phi} + \frac{\partial(\bar{v}\cos\theta)}{\partial\theta}, \tag{14.5c}$$

where the barred quantities indicate vertically integrated quantities, i.e.,

$$\bar{u} = \int_{-D}^{0} u\,dz$$

and $\boldsymbol{\tau}_b$ is the bottom shear stress.

In a zonally periodic channel with $\tau^\phi = \tau^\phi(\theta)$ and $\tau^\theta = 0$, we have seen in Example 13.3 that there exists solutions which are independent of ϕ with $\bar{v} = 0$. For these solutions, the zonal momentum balance (14.5a), provides two possibilities: (i) the wind-stress forcing is compensated for by bottom friction or (ii) it is compensated by lateral friction. In case (ii) (case (i) will be subject exercise 14.1) assume that the lateral friction is proportional to the lateral viscosity A_H and is of the form $A_H\nabla^2\mathbf{u}$. If U indicates a characteristic zonal velocity, then it follows from a balance between the wind-stress term (τ^ϕ/ρ_0) and the lateral friction term ($\bar{\mathcal{F}}^\phi$) that

Ex. 14.1

$$\frac{\tau_0}{\rho_0} \approx \frac{A_H U D}{r_0^2} \rightarrow U = \frac{\tau_0 r_0^2}{\rho_0 D A_H}, \tag{14.6}$$

and hence the transport Φ scales as

$$\Phi = \int_{\theta_1}^{\theta_2} r_0\bar{u}\,d\theta \rightarrow r_0 D U = \frac{\tau_0 r_0^3}{\rho_0 A_H}. \tag{14.7}$$

▶

Example 14.1: Channel transport: flat bottom

Consider a channel with $\theta_1 = 65°$S and $\theta_2 = 55°$S, for which the flow is forced by the wind stress

$$\tau^\phi(\theta) = \tau_0 \sin\frac{(\theta-\theta_1)}{(\theta-\theta_1)}\ ;\ \tau^\theta = 0.$$

For parameters $A_V = 10^{-3}$ m^{2}s^{-1}, $D = 4000$m and $\rho_0 = 1000$ kgm^{-3}, steady solutions were determined of the full equations (14.3) using the fully implicit THCM model De Niet et al. (2007). In the drawn curve labeled 0.0 in Fig. 14.4, the transport Φ (in Sv) is plotted versus $1/A_H$. As can be seen, the transport indeed increases with $1/A_H$ according to a straight line as predicted by the simple scaling argument above. An already large value of $A_H = 2.5\times10^4$ m^{2}s^{-1} leads to quite unrealistic transports of a thousand Sv and hence the barotropic flat bottom channel model is not a good model for the ACC.

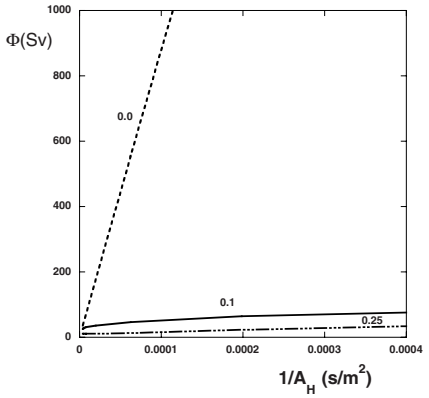

Figure 14.4. Transport Φ through a zonal channel (in Sv) versus the lateral viscosity $1/A_H$ as computed with the full model (14.3) over the domain $[280, 360] \times [-65, -55]$. The curves are labeled by the factor h_0/D where h_0 is the height of the Gaussian Hump and $D = 4000$ m is the total depth of the layer. The curve labelled $h_0/D = 0.0$ is for a flat bottom.

◀

Ex. 14.2

14.2.2. The role of bottom topography

The presence of bottom topography changes the character of the constant density flow rather dramatically. To derive the depth averaged equations in this case, frequent use is made of Leibnitz's rule

$$\frac{d}{dx}\int_{f(x)}^{g(x)} F(x,t)\,dt = F(x,g(x))\frac{dg}{dx} - F(x,f(x))\frac{df}{dx} + \int_{f(x)}^{g(x)} \frac{\partial F}{\partial x}(x,t)\,dt \tag{14.8}$$

for general scalar functions f, g and F. Define the total layer depth $H = D - h_b$ then the vertical integration (from $z = -D + h_b$ to $z = 0$) of (14.3), neglecting

lateral friction, gives

$$-2\Omega\bar{v}\sin\theta = -\frac{1}{r_0\rho_0\cos\theta}\left[\frac{\partial\bar{p}}{\partial\phi} - p_b\frac{\partial H}{\partial\phi}\right] + \frac{\tau^\phi}{\rho_0} - \frac{\tau_b^\phi}{\rho_0}, \quad (14.9a)$$

$$2\Omega\bar{u}\sin\theta = -\frac{1}{r_0\rho_0}\left[\frac{\partial\bar{p}}{\partial\theta} - p_b\frac{\partial H}{\partial\theta}\right] + \frac{\tau^\theta}{\rho_0} - \frac{\tau_b^\theta}{\rho_0} \quad (14.9b)$$

$$0 = \frac{\partial\bar{u}}{\partial\phi} + \frac{\partial(\bar{v}\cos\theta)}{\partial\theta}, \quad (14.9c)$$

and hence compared to (14.5) extra terms $-p_b\nabla H$ involving the bottom pressure $p_b = p(\phi,\theta,-H(\phi,\theta))$ enter the right hand side. The presence of the bottom topography has an important effect on the volume transport through the zonal channel.

►

Example 14.2: Channel transport: Gaussian Hump

We consider the same geometry and wind forcing as in Example 14.1 but now there is a Gaussian Hump present in the middle of the channel. The bottom topography is described is

$$h_b(\phi,\theta) = h_0\, e^{-(\frac{(\phi-\phi_m)}{\delta})^2},$$

where h_0 is the maximum topography height at $\phi = \phi_m$ and δ is a measure of its width. Again for parameters $A_V = 10^{-3}$ m^{2}s^{-1}, $D = 4000$m and $\rho_0 = 1000$ kgm^{-3}, steady solutions were determined of the full equations (14.3) using the fully implicit THCM model De Niet et al. (2007) using a $80\times20\times20$ equidistant grid. In the curves labeled 0.1 and 0.25 in Fig. 14.4, the transport Φ (in Sv) is plotted versus $1/A_H$ for two values of h_0/D showing that the transport is much decreased when bottom topography is present. The explicit dependence of Φ on h_0/D is plotted in Fig. 14.5.

◄

To understand the effect of bottom topography on the flow in this channel configuration, we turn to a slightly simpler configuration in local Cartesian coordinates on the β-plane. Consider a zonal channel $x \in [0,L], y \in [y_0,y_1]$ with bottom topography of the form

$$h_b(x,y) = h_0\, e^{-(\frac{(x-x_m)}{\delta})^2}, \quad (14.10)$$

which represents again a Gaussian Hump with width δ. The total thickness of the water layer is given by $H(x,y) = D - h_b(x,y)$ and hence its minimum value is

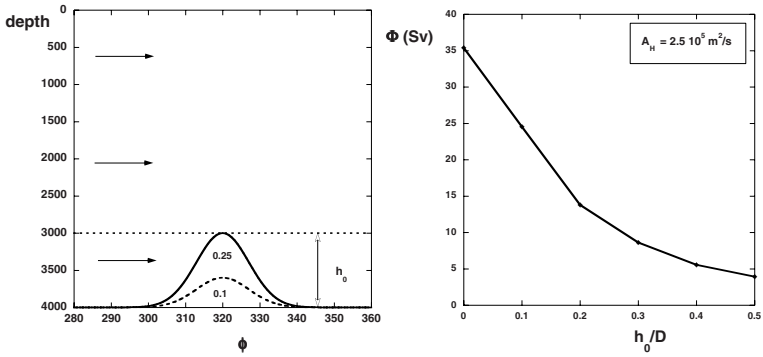

(a) (b)

Figure 14.5. (a) Plot of the bottom topography versus the parameter h_0/D for $\delta = 10°$. (b) Plot of the channel transport Φ versus h_0/D for $A_H = 2.5 \times 10^5\ m^2 s^{-1}$.

$H_0 = D - h_0$. Let $z = -H_0$ be the z-coordinate of the top of the highest point of the bottom topography in the channel and let δ_E be a measure of the Ekman layer thickness near the ocean-atmosphere interface, with $\delta_E \ll H_0$.

The momentum balances and continuity equation, neglecting lateral friction, become

$$-fv = -\frac{1}{\rho_0}\frac{\partial p}{\partial x} + A_V \frac{\partial^2 u}{\partial z^2}, \tag{14.11a}$$

$$fu = -\frac{1}{\rho_0}\frac{\partial p}{\partial y} + A_V \frac{\partial^2 v}{\partial z^2}, \tag{14.11b}$$

$$\frac{\partial u}{\partial x} + \frac{\partial v}{\partial y} + \frac{\partial w}{\partial z} = 0. \tag{14.11c}$$

where $f = f_0 + \beta_0 y$. From (14.4) the boundary conditions become

$$\begin{aligned} z = 0 \quad &: \quad \rho_0 A_V \frac{\partial u}{\partial z} = \tau^x, \rho_0 A_V \frac{\partial v}{\partial z} = \tau^y, w = 0 \\ z = -H(x,y) \quad &: \quad \frac{D(z + H(x,y))}{dt} = 0, u - w\frac{\partial H}{\partial x} = 0, v - w\frac{\partial H}{\partial y} = 0 \end{aligned} \tag{14.12}$$

The depth-integrated continuity equation (14.11c) is

$$\frac{\partial \bar{u}}{\partial x} + \frac{\partial \bar{v}}{\partial y} = 0, \tag{14.13}$$

as all terms due to Leibnitz's rule cancel through the boundary conditions (14.12). If we integrate (14.13) over the zonal direction and use the periodic boundary

conditions, we find at every 'longitude' y

$$< v >= \int_0^L \bar{v}\, dx = \int_0^L \left[\int_{-H}^0 v\, dz \right] dx = 0 \tag{14.14}$$

Using an integration of the momentum equation (14.11a) over different intervals in the vertical, we can determine the different contributions to $< v >$. Integration of (14.11a) over the depth of the Ekman layer (on a contour $y = y_c$) gives

$$-f < v >_E = \int_0^L \left[\int_{-\delta_E}^0 (-fv)\, dz \right] dx = \int_0^L \frac{\tau^x}{\rho_0}\, dx. \tag{14.15}$$

The pressure gradient vanishes due to the periodic boundary conditions and the stress term at $z = -\delta_E$ can be neglected outside the Ekman layer. The equation (14.15) is the integrated meridional Ekman transport along the contour $y = y_c$. In the southern hemisphere, with $f < 0$ and a zonal wind $\tau^x > 0$ it follows that $< v >_E > 0$ and hence the transport is northward.

Integration of (14.11) over $[-H_0, -\delta_E]$ and over a contour $y = y_c$ gives

$$-f < v >_I = \int_0^L \left[\int_{-H_0}^{-\delta_E} (-fv) dz \right] dx = 0. \tag{14.16}$$

as there are no contributions from the stress in this region and the pressure gradient again vanishes due to the periodic boundary conditions. In this internal region there cannot be a geostrophic flow and hence $< v >_I = 0$.

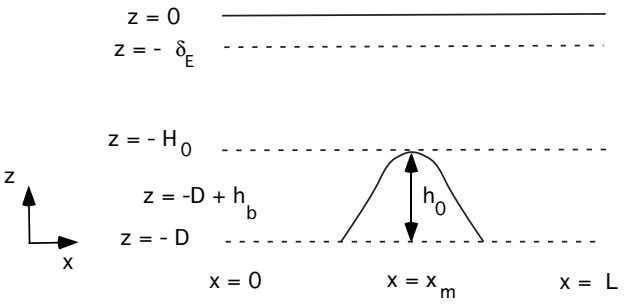

Figure 14.6. Sketch of the topography (14.10) with the vertical structure of the flow domain.

Integration of (14.11) over $[-H(x,y), -H_0]$ and a contour $y = y_c$ gives

$$-f < v >_G = \int_0^L \left[\int_{-H}^{-H_0} (-fv) dz \right] dx =$$

$$= -\frac{1}{\rho_0}\int_0^L \left[\int_{-H}^{-H_0} \frac{\partial p}{\partial x}\right] dx - \int_0^L \frac{\tau_b^x}{\rho_0}\, dx, \tag{14.17}$$

where τ_b^x is again the zonal component of the bottom shear stress. Using Leibnitz's rule we find

$$\int_{-H}^{-H_0} \frac{\partial p}{\partial x}\, dz = \frac{\partial}{\partial x}\left(\int_{-H}^{-H_0} p\, dz\right) - p(x,y,-H)\frac{\partial H}{\partial x}, \tag{14.18}$$

and the integral balance (14.17) becomes

$$-f < v >_G = \frac{1}{\rho_0}\int_0^L \left[p(x,y,-H)\frac{\partial H}{\partial x} - \tau_b^x\right] dx. \tag{14.19}$$

In the region of the flow where there is bottom topography, a geostrophic flow can occur. The net effect along the contour is given by the first term in the right hand side of (14.19). When pressure gradients develop in the presence of bottom topography, these establish a net 'stress'; this is the so-called 'bottom form stress'.

▶

Example 14.3: Form stress

We consider the same geometry and wind forcing as in Example 14.2 for the Gaussian Hump present in the middle of the zonal channel. The patterns of the barotropic streamfunction ψ_B with

$$\bar{u} = -\frac{1}{r_0}\frac{\partial \psi_B}{\partial \theta}\ ;\ \bar{v} = \frac{1}{r_0 \cos\theta}\frac{\partial \psi_B}{\partial \phi},$$

for three different solutions $h_0/D = 0.0$, $h_0/D = 0.1$ and $h_0/D = 0.25$ are plotted in Fig. 14.7a-c; in these computations $A_H = 2.5 \times 10^5$ m^{2}s^{-1}. For the flat bottom case (Fig. 14.7, upper left panel) the streamlines are lines of constant y. A weak amplitude bottom topography $h_0/D = 0.25$ causes a deviation of the streamlines over the topography (Fig. 14.7, upper right panel). As the surface pressure field has qualitative the same pattern as the barotropic streamfunction (Fig. 14.7, lower left panel), it can be seen that the flow left of the hump is northward (as $\partial p/\partial\phi < 0$ and $v \sin\theta \sim \partial p/\partial\phi$). Right of the hump where the pressure anomaly is negative whereas left of the hump the pressure anomaly (with respect to the flat bottom case) is positive. The meridional overturning streamfunction ψ_M defined by

$$\overline{w} = -\frac{1}{r_0}\frac{\partial \psi_M}{\partial \theta}\ ;\ \overline{v} = \frac{1}{r_0 \cos\theta}\frac{\partial \psi_M}{\partial z},$$

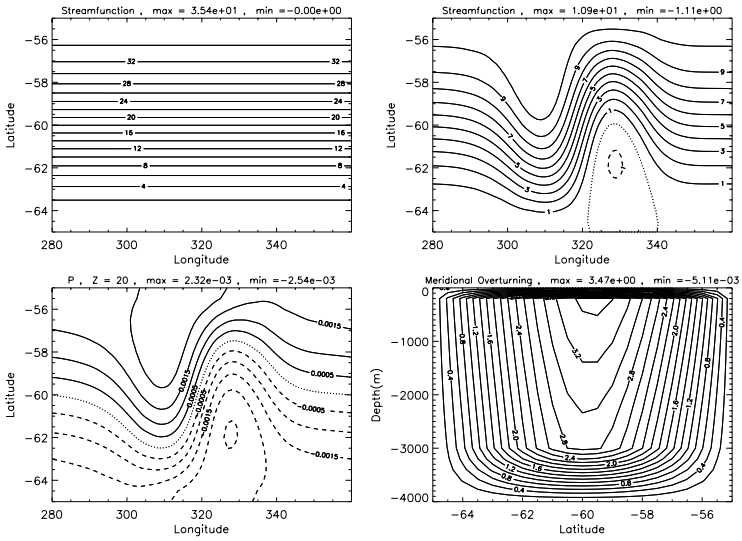

Figure 14.7. Solutions of the full problem for the Gaussian Hump with $A_H = 2.5 \times 10^5\ m^2 s^{-1}$. *Upper left panel: barotropic streamfunction (in Sv) for* $h_0/D = 0.0$. *Upper right panel: barotropic streamfunction for* $h_0/D = 0.25$. *Lower left panel: surface pressure field for* $h_0/D = 0.25$. *Lower right panel: meridional overturning streamfunction (in Sv) for* $h_0/D = 0.25$.

(where $\overline{v}$ is the zonal average of v) is plotted in (Fig. 14.7, lower right panel) and shows that below the topography indeed a southward flow is present compensating for the northward Ekman flow at the surface.

◀

To understand the physics of the bottom form stress in more detail, we recall that the pressure is that part of the stress tensor describing the normal flux of momentum. Consider two coordinate planes in the flow defined by $z = -h(x)$ and $z = -d(x)$ as in Fig. 14.8. Let x_w and x_e be located west and east of the topography, then

$$\begin{aligned}\int_{x_w}^{x_e}\int_{-d(x)}^{-h(x)} \frac{\partial p}{\partial x}\, dz\, dx &= \bar{p}_e - \bar{p}_w + \\ + \int_{x_w}^{x_e} (p(x,-h(x))\frac{\partial h}{\partial x} &- p(x,-d(x))\frac{\partial d}{\partial x})\, dx \end{aligned} \tag{14.20}$$

with

$$\bar{p} = \int_{-d(x)}^{-h(x)} p\, dz. \tag{14.21}$$

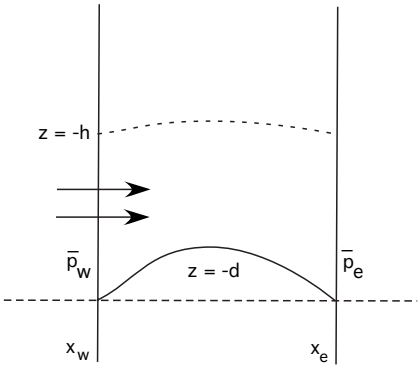

Figure 14.8. Sketch to illustrate the physics of the 'bottom form stress'.

The term $\bar{p}_e - \bar{p}_w$ on the right hand side is the net horizontal flux of momentum in the area bounded by x_w and x_e. The integral term on the right hand side is sum of the flux of horizontal momentum through $z = -h(x)$ and that through the bottom at $z = -d(x)$. In an ocean basin bounded by continents at x_w and x_e, and a flat bottom, the first term provides a balance with the wind-stress forcing. In a zonally unbounded basin (with periodic boundary conditions), the first term on the right hand side is zero, and a balance is established between the two integral terms and the wind stress forcing. When the sea surface height gradient can be neglected, the second term in the integral (the 'bottom form stress') provides the balance with the wind stress.

Going back to the analysis in the zonal channel we can see this dominant balance by realizing that $< v >=< v >_E + < v >_I + < v >_G = 0$ and hence

$$< v >_G + < v >_E = 0 \rightarrow \int_0^L \left[\frac{\tau^x - \tau_b^x}{\rho_0} + p_b \frac{\partial H}{\partial x} \right] dx = 0, \qquad (14.22)$$

where $p_b = p(x, y, -H(x, y)$ is the bottom pressure. When the bottom stress is small compared to the surface stress, the Ekman transport is compensated by the geostrophic flow. In the flows in Example 14.3, where the first term in (14.22) is positive, this implies that the second term must be negative. The bottom pressure anomalies have the same sign as the surface pressure anomalies in this example. Indeed $p_b > 0$ in areas where the layer thickness decreases (left of the hump) and $p_b < 0$ in areas where the layer thickness increases which provide a negative value of the integral involving the form stress.

We can now explain the decrease in transport due to bottom topography. Since the pressure distribution is not in phase with the topography there is momentum transfer from the ocean water to the bottom topography. The total force of the

topography on the water is given by

$$\mathbf{F}_s = \int p \nabla H \, d^2x$$

and points in the example in the negative x-direction providing a effective drag (the 'form drag', although it is not a real drag). This drag induces a reduction in the volume transport as in Fig. 14.5.

Additional Material

B: There are several interesting papers on the concept of 'form stress' which clarify many more aspects of it (Warren et al., 1997; Olbers, 1998). Further discussion on the role of the 'bottom form stress' in relation to the Antarctic Circumpolar Current can be found in section 4.6 of WOCE (2001).

14.3. Stratification

There are two basic effects caused by the presence of stratification:

(i) through baroclinic pressure gradients a flow is generated according to the thermal wind balance.

(ii) the zonal currents are susceptible to baroclinic instability, which leads to eddies whose dominant size is the scale of the internal Rossby deformation radius $L = ND/f$, where N is the buoyancy frequency.

We will consider these two special cases in the next subsections.

14.3.1. Stationary baroclinic flows

Near the Antarctic continent the water is strongly cooled by the atmosphere increasing its density. Sea-ice formation can also contribute to a density increase of the ocean water. So, apart from an increase in density with depth, there is also a meridional density gradient; the density increase poleward (Fig. 14.3c).

To study the effect of the presence of stratification on the flow in the zonal channel, we consider a situation in which the bottom topography is piecewise linear (Fig. 14.9). The channel has a zonal extent $[x_w, x_e]$ and a meridional extent $[y_0, y_1]$ and in the region without topography, the layer depth is equal to D. Over the interval $[x_0, (x_0 + x_1)/2]$ the height of the topography increases linearly up to a height h_0 and over the interval $[(x_0 + x_1)/2, x_1]$ it decreases to zero. The total depth of the layer H is

$$H(x,y) = \begin{cases} D & : \quad x \in [x_w, x_0] \wedge x \in [x_1, x_e] \\ D - \alpha_b(x - x_0) & : \quad x \in [x_0, \frac{x_0+x_1}{2}] \\ D + \alpha_b(x - x_1) & : \quad x \in [\frac{x_0+x_1}{2}, x_1] \end{cases}$$

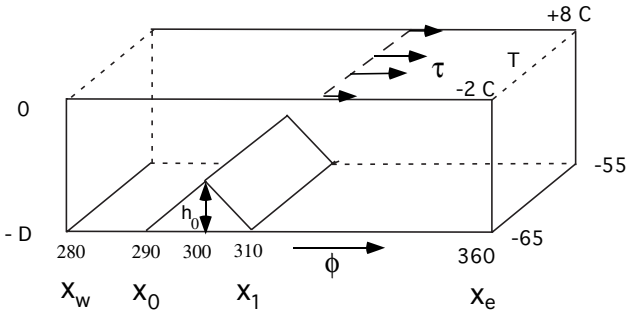

Figure 14.9. Sketch of the flow configuration in a zonal channel with bottom topography, wind- and buoyancy forcing.

where $\alpha_b = 2(D - h_0)/(x_1 - x_0) > 0$. The flow in the channel is forced by a zonal wind stress field τ^x and a meridional surface temperature distribution $T_s(y)$ as shown in Fig. 14.9. The latter causes a meridional density gradient $\rho(y)$ through a linear equation of state, $\rho = \rho_0(1 - \alpha_T(T - T_0))$.

The momentum balances in the channel, neglecting inertia and horizontal mixing, are

$$-fv = -\frac{1}{\rho_0}\frac{\partial p}{\partial x} + A_V\frac{\partial^2 u}{\partial z^2}, \tag{14.23a}$$

$$fu = -\frac{1}{\rho_0}\frac{\partial p}{\partial y} + A_V\frac{\partial^2 v}{\partial z^2}, \tag{14.23b}$$

$$g\frac{\rho - \rho_0}{\rho_0} = -\frac{1}{\rho_0}\frac{\partial p}{\partial z}, \tag{14.23c}$$

where the background hydrostatic pressure has been subtracted. To investigate the impact of stratification (in combination with bottom topography), we want again to integrate the equations over depth and introduce

$$\bar{u} = \int_{-H}^{0} u\,dz\ ;\ \bar{v} = \int_{-H}^{0} v\,dz\ ;\ \bar{p} = \int_{-H}^{0} p\,dz\ ;\ \chi = \frac{g}{\rho_0}\int_{-H}^{0} z(\rho - \rho_0)dz,$$

where $\rho_0\chi$ m^{3}s^{-2} is the vertically integrated potential energy. Again using Leibnitz's rule and the surface boundary conditions (we neglect bottom friction), vertical integration of the horizontal momentum equations gives

$$-f\bar{v} = -\frac{1}{\rho_0}(\frac{\partial \bar{p}}{\partial x} - p_b\frac{\partial H}{\partial x}) + \frac{\tau^x}{\rho_0}, \tag{14.24a}$$

$$f\bar{u} = -\frac{1}{\rho_0}(\frac{\partial \bar{p}}{\partial y} - p_b\frac{\partial H}{\partial y}) + \frac{\tau^y}{\rho_0}. \tag{14.24b}$$

Ex. 14.3

When we multiply (14.23c) by z and then integrate over depth, we find

$$\chi = -\int_{-H}^{0} \frac{z}{\rho_0}\frac{\partial p}{\partial z} dz. \tag{14.25}$$

Through partial integration, we can write

$$\chi = \frac{1}{\rho_0}(Hp_b - \bar{p}) \rightarrow -\frac{1}{\rho_0}\bar{p} = \chi - \frac{H}{\rho_0}p_b. \tag{14.26}$$

When we take the x-derivative of (14.24b) and the y-derivative of (14.24a) and eliminate the bottom pressure p_b, this gives

$$\nabla \cdot (\frac{f}{H}\bar{\mathbf{u}}) = J(\chi, \frac{1}{H}) + \nabla \cdot (\frac{f}{H}\mathbf{M}_E), \tag{14.27}$$

where $J(f, g)$ is again the Jacobian

$$\mathcal{J}(f, g) = \frac{\partial f}{\partial x}\frac{\partial g}{\partial y} - \frac{\partial g}{\partial x}\frac{\partial f}{\partial y},$$

and

$$M_E^x = \frac{\tau^y}{\rho_0 f}\ ;\ M_E^y = -\frac{\tau^x}{\rho_0 f}$$

are the Ekman transports. In (14.27), we recognize the term f/H as the shallow-water potential vorticity (note that we have neglected inertia and hence the relative vorticity term does not appear).

The curves of constant f/H are called geostrophic contours and two of these contours for the channel configuration are sketched in Fig. 14.10. Outside of the interval where bottom topography is present, these are the lines $y = c$, where c is a constant. In the interval between x_0 and $(x_0 + x_1)/2$ these geostrophic contours are determined by

$$f_0 + \beta_0 y = c(D - \alpha_b(x - x_0)). \tag{14.28}$$

For example, the geostrophic contour through $x = x_0, y = 0$ is given by

$$y = -\frac{f_0}{\beta_0 D}\alpha_b(x - x_0),$$

and as $f_0 < 0$ and $\alpha_b > 0$, this contour has a positive slope and it is deflected northward when the layer thickness decreases. This is in correspondence with what is deduced from the conservation of potential vorticity: without forcing, friction and stratification, a water column will get deflected northward when moving over this part of the bottom topography.

Integration of the depth integrated continuity equation ($\nabla \cdot \bar{\mathbf{u}} = 0$), the vector identity $\nabla \cdot (\phi\mathbf{u}) = \phi\nabla \cdot \mathbf{u} + \nabla\phi \cdot \mathbf{u}$ for an arbitrary vector $\mathbf{u}$ and scalar ϕ, it follows from (14.27) can be rewritten as

$$\nabla(\frac{f}{H}) \cdot \bar{\mathbf{u}} = J(\chi, \frac{1}{H}) + \nabla \cdot (\frac{f}{H}\mathbf{M}_E). \tag{14.29}$$

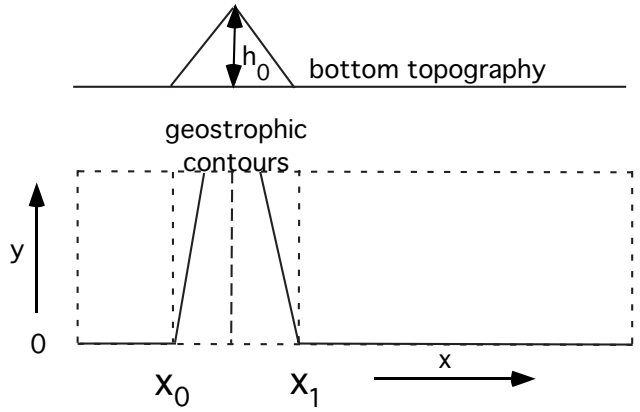

Figure 14.10. Sketch of the geostrophic contours for the flow configuration as in Fig. 14.9.

Ex. 14.4

In the absence of wind forcing and stratification, the equation above indicates that $\bar{\mathbf{u}}$ is perpendicular to the gradient of the geostrophic contours. In other words, the transport is tangent to the geostrophic contours. The wind-driven Ekman transports are able to induce deviations from this behavior. In addition, the first term on the right hand side of (14.29) can induce deviations from transport along geostrophic contours; this term is usually referred to as the J(oint) E(ffect) of B(aroclinicity) and R(elief), or JEBAR.

We illustrate the JEBAR effect, by writing

$$J(\chi, \frac{1}{H}) = \frac{1}{H^2}(\frac{\partial \chi}{\partial y}\frac{\partial H}{\partial x} - \frac{\partial \chi}{\partial x}\frac{\partial H}{\partial y}) = \frac{1}{H^2}\begin{pmatrix} \frac{\partial \chi}{\partial x} \\ \frac{\partial \chi}{\partial y} \end{pmatrix} \cdot \begin{pmatrix} -\frac{\partial H}{\partial y} \\ \frac{\partial H}{\partial x} \end{pmatrix},$$

For fixed x, χ decreases as a function of y because the density decreases northward. Left of the topographic maximum we have $\partial H/\partial x < 0$ and $\partial \chi/\partial y < 0$ and hence $J(\chi, 1/H) > 0$. As $\nabla(f/H)\cdot\bar{\mathbf{u}} \approx \cos\gamma$, where γ is the angle between the normal to the geostrophic contours and the velocity vector; without JEBAR $\gamma = 90°$. With JEBAR with $J(\chi, 1/H) > 0$, we have $0 < \gamma < \pi/2$ and hence the zonal character of the flow over the topography is strengthened. To the right of the topographic maximum (Fig. 14.11), we have $\partial H/\partial x < 0$ and hence we find $-\pi/2 < \gamma < 0$ which also increases the zonality of the flow (because the slope of the geostrophic contours has changed). To illustrate the effect, we also plot in Fig. 14.11a-b two solutions (one with only wind forcing, the other with wind + temperature forcing) of the full equations for the configuration as in Fig. 14.9. The JEBAR effect indeed causes an increase in the zonal transport by making the flow more zonal.

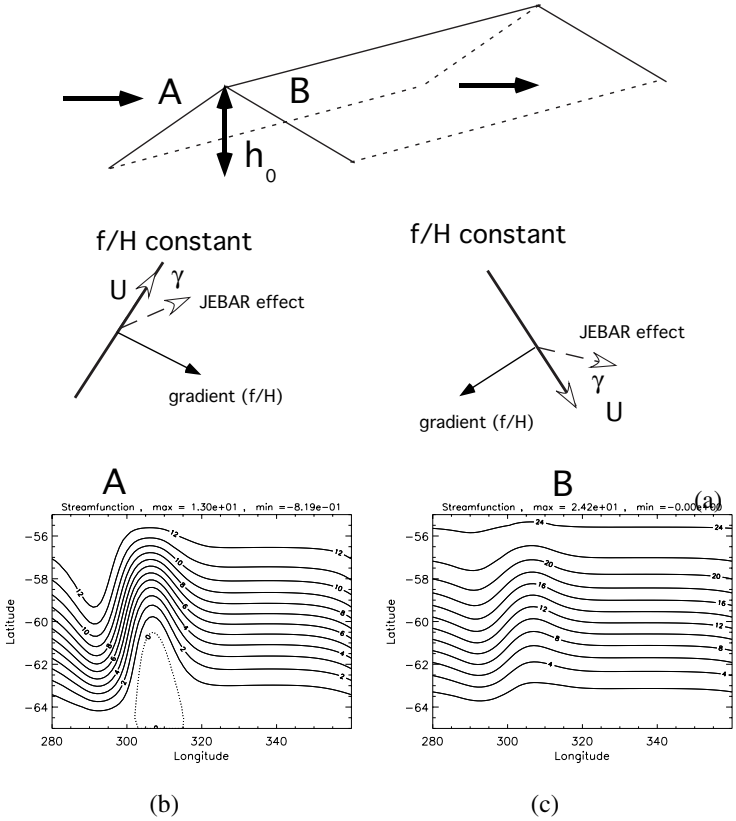

Figure 14.11. (a) Sketch of the JEBAR effect on the flow over the topography as in Fig. 14.9. The layer is cooled in the south and heated in the north such that the meridional density gradient is negative. (b) Barotropic streamfunction of the steady solution of the full model in the configuration with only wind forcing. (c) Same for the case of both wind- and temperature forcing.

14.3.2. Time dependent phenomena

We have seen that the input of momentum through the wind stress is balanced by the 'bottom form stress' and we now focus on the processes which transport the momentum through the flow. From chapter 10, we know that zonal currents can become unstable through barotropic and baroclinic instability. Small perturbations develop to finite amplitude and eddies are formed with a length scale of the internal Rossby deformation radius. Eventually, a geostrophic turbulent flow appears through interaction of these eddies. A plot of the instantaneous global

sea level height (in a high-resolution ocean model) as in Fig. 14.12 shows the signatures of these eddies, in particular in the ACC region.

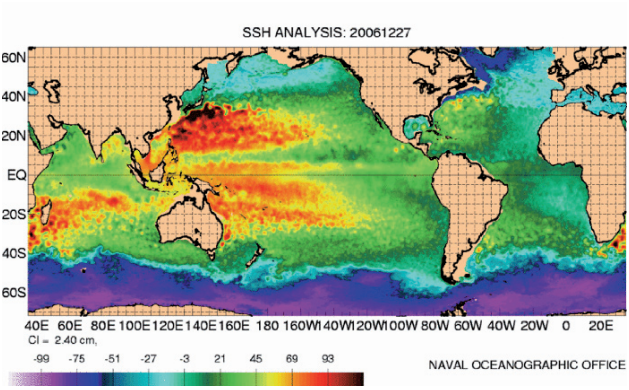

Figure 14.12. Snapshot of the global sea-level height field from a high-resolution ocean model (NLOM, 1/32°, see http://www7320.nrlssc.navy.mil/html/7320-home.html).

These type of flows are complex and the flow field is usually decomposed into a time mean ($\overline{\mathbf{u}}$) and a deviation ($\tilde{\mathbf{u}}$) from this time mean as follows,

$$\mathbf{u} = \overline{\mathbf{u}} + \tilde{\mathbf{u}} \rightarrow \overline{\tilde{\mathbf{u}}} = 0. \tag{14.30}$$

As an example, consider the zonal momentum balance in local Cartesian coordinates, i.e.,

$$\frac{\partial u}{\partial t} + \frac{\partial (uu)}{\partial x} + \frac{\partial (vu)}{\partial y} + \frac{\partial (wu)}{\partial z} - fv = -\frac{1}{\rho_0}\frac{\partial p}{\partial x} + A_H \nabla^2 u + A_V \frac{\partial^2 u}{\partial z^2}. \tag{14.31}$$

We cannot neglect inertia in these flows as it determines the interaction between the eddies. Substitution of (14.30) for all fields, and then taking an average gives

$$\frac{\partial (\overline{uu} + \overline{\tilde{u}\tilde{u}})}{\partial x} + \frac{\partial (\overline{vu} + \overline{\tilde{v}\tilde{u}})}{\partial y} + \frac{\partial (\overline{wu} + \overline{\tilde{w}\tilde{u}})}{\partial z} - f\overline{v} = -\frac{1}{\rho_0}\frac{\partial \overline{p}}{\partial x} + A_H \nabla^2 \overline{u} + A_V \frac{\partial^2 \overline{u}}{\partial z^2}. \tag{14.32}$$

Additional Material

B: The JEBAR concept is worked out in more detail in Mertz and Wright (1992). Further discussion on the effects of eddies on the Southern Ocean flow can be found in section 4.6 of WOCE (2001).

The first two terms on the left hand side represent a horizontal flux of momentum through the divergence of the Reynolds' stress terms associated with the 'standing eddies' (the terms with $\overline{uu}$, etc.) and with the 'transient eddies' (the terms with $\overline{\tilde{u}\tilde{u}}$, etc.). Vertical transport of horizontal momentum is represented by the third term on the left hand side. The remainder of the terms are the Coriolis acceleration, the pressure gradient, and the lateral and vertical friction in the same way as in the stationary equations. When the different terms are calculated from

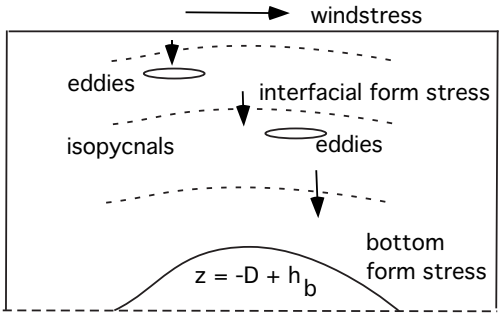

Figure 14.13. Sketch to illustrate the vertical momentum transfer through eddy driven 'interfacial form stress'.

a high-resolution simulation of an ocean model one finds that in the zonally and vertically integrated equations, there is a balance between the wind stress and the bottom form stress over the whole ACC region. The other terms are relatively small compared to these dominant terms and so 'eddies' don't effect the vertically averaged momentum balance.

The momentum transport from top to bottom is caused by a so-called 'interfacial form stress' which is similar to the bottom form stress but now between layers of different density in the flow (Fig. 14.13). When the upper layer flow is unstable, a time-dependent perturbation will appear which causes a time-mean pressure difference on both sides of the interface separating the layers. In this case, we have the same situation as for the bottom form stress but the boundary is now the interface. An eddy-induced net stress, the 'interfacial form stress', can be imagined as occurring on the interface to accomplish the downward transfer of zonal momentum. Eventually this is transferred to the bottom topography through the bottom form stress.

Summary

- In a barotropic channel model without topography and with only lateral friction, the zonal transport scales with $1/A_H$ where A_H is the lateral viscosity.
- The presence of bottom topography substantially decreases the zonal transport because the topography exerts a force ('bottom form stress') on the overlying water. This force $\mathbf{F}_s$ is given by

$$\mathbf{F}_s = -\int p \nabla h_b \, d^2x$$

  where p is the pressure and h_b is the bottom shape.
- Stratification and bottom topography can act together to cause flows to deviate from being along geostrophic contours; this combined effect is the JEBAR effect.
- Eddies are important in the region of the Antarctic Circumpolar Current to transfer momentum downward in the water column through an interfacial form stress.

14.4. Exercises on chapter 14

(14.1) *Scaling of the ACC transport*

In section 14.2, we derived that in the case of lateral friction, the zonal transport through the zonal channel scales as $1/A_H$. Consider now the case where only bottom friction is the dissipation mechanism.

a. Determine an expression for the bottom shear stress with help of the (planetary) bottom Ekman solution in chapter 13.

b. Determine the scaling of the ACC transport versus A_V, in case the bottom friction balances the wind stress.

(14.2) *Depth averaged vorticity balance*

Consider a constant density flow in a zonal channel as in section 14.2 and neglect the bottom stress term.

a. Use the depth-averaged equations (14.9) to derive the vorticity equation for this flow, i.e.,

$$2\Omega\bar{v}\cos^2\theta = \frac{1}{\rho_0 r_0} J(H, p_b) + \frac{1}{\rho_0}\left(\frac{\partial \tau^\theta}{\partial \phi} - \frac{\partial(\tau^\phi \cos\theta)}{\partial \theta}\right),$$

where J is the Jacobian.

b. Compare the result above for the flat bottom case with the Sverdrup balance (13.33) derived in section 13.2. Why are the results different?

(14.3) *Geostrophic contours*

a. Determine the geostrophic contours for the bottom topography given by

$$h_b(x, y) = h_0 e^{-(\frac{x}{L})^2},$$

where $h_0 > 0$, $x \in [-L, L]$ and $y \in [y_0, y_1]$.

Assume that the flow is driven by a constant wind stress $\tau^x = \tau_0$, $\tau^y = 0$, that the density is constant and neglect bottom friction.

b. Sketch the deviation of the flow compared to that along geostrophic contours.

(14.4) *JEBAR*

Consider a channel flow on the domain $x \in [0, L], y \in [-L, L], z \in [-H, 0]$ where $H = D - h_b$ as in section 14.3 and assume that

$$\rho(y, z) = \alpha y(1 - e^{\gamma z})$$

and

$$h_b(x, y) = h_0 \sin \pi \frac{x}{L} \sin \pi \frac{y}{L}$$

where $\alpha > 0$, $h_0 > 0$ and $\gamma > 0$ are constants.

a. Determine the vertically integrated potential energy $\rho_0 \chi$.

b. Determine the expresssion for the JEBAR term $J(\chi, 1/H)$.

c. Describe how pressure gradients are generated by the JEBAR effect and sketch the deviations of the flow due to these effects.

(14.5) *Interfacial form stress*

In section 14.3.2 it was stated that the effect of eddies introduces an interfacial form stress by which momentum can be transported downward.

a. Use (14.32) and the analysis of section 14.2.2 and determine the meridional transport $< v >_I$ is case eddies are present.

b. Give a description of the interfacial form stress in terms of vertical momentum transfer as was done for the bottom form stress in section 14.2.2.

Chapter 15

ARCTIC OCEAN CIRCULATION

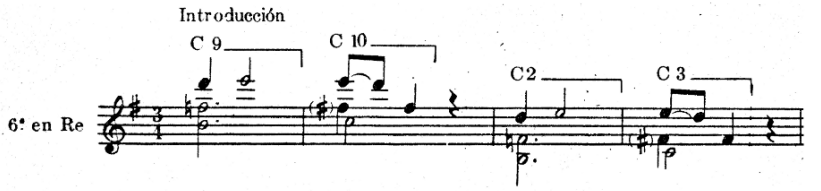

Vals (Opus 8, No. 4), A. Barrios

The continental geometry of the Arctic basin is substantially different from that in the Southern Ocean. Whereas the Southern Ocean is unblocked over a range of latitudes, the Arctic basin is quite isolated having only a few connections with the other ocean basins. Together with the fact that a large part of the Arctic is ice covered during most of the year, this gives rise to a peculiar Arctic Ocean circulation. In this chapter, several characteristics of the Arctic circulation will be mentioned in section 15.1. Next we will focus on two questions: (i) why are the surface velocities closely following bottom topographic features and (ii) why are the deep velocities relatively large? To answer these questions, the occurrence of closed geostrophic contours is important and introductory dynamical theory is presented in section 15.2. An idealized model that is used to tackle both questions above is presented in section 15.3 and its application to the Arctic Ocean and Nordic Seas appears in section 15.4.

Note: All equations in this chapter are dimensional and we will therefore omit the star subscript.

15.1. Characteristics

As bottom topography is one of the foremost important factors for the circulation in the Arctic Ocean, we start by showing a map of the bathymetry in Fig. 15.1. The Arctic basin north of Svalbard is comprised of several subbasins (Canada basin, Makarov basin, Amundsen basin, Nansen basin) of about 3000-4000 m depth which are separated by ridges (e.g., Alpha-Mendeleyev ridge and Lomonosov ridge) with depths of only 1000-1500m. The major connection between the Arctic and the surrounding oceans is through Fram Strait (to the Atlantic) and the Bering Strait (to the Pacific). The Bering Strait is only 45 m deep and 85 km wide. There are some small connections to the Atlantic through the Canadian Archipelago (e.g., Lancaster Sound) but these are of minor importance compared to Fram Strait (between Greenland and Svalbard). South of Svalbard, the area is usually referred to as the Nordic Seas including the Greenland basin and Norwegian basin.

A large part of the Arctic is ice covered during most of the year. The sea ice concentration (this quantity is 1 in a particular grid box if the area is totally covered and 0 if there is no sea ice) over the Arctic basin in Winter and Summer (both averaged over the years 1985-1995) is plotted in Fig. 15.2. What can be seen directly from Fig. 15.2a is that the sea ice extends much more southward in the Canadian area than in the Nordic Seas. Harbours in northern Norway are ice free during most of the winter. This is due to the inflow of warm water through the Norwegian Current (an extension of the Gulf Stream) which has a mean

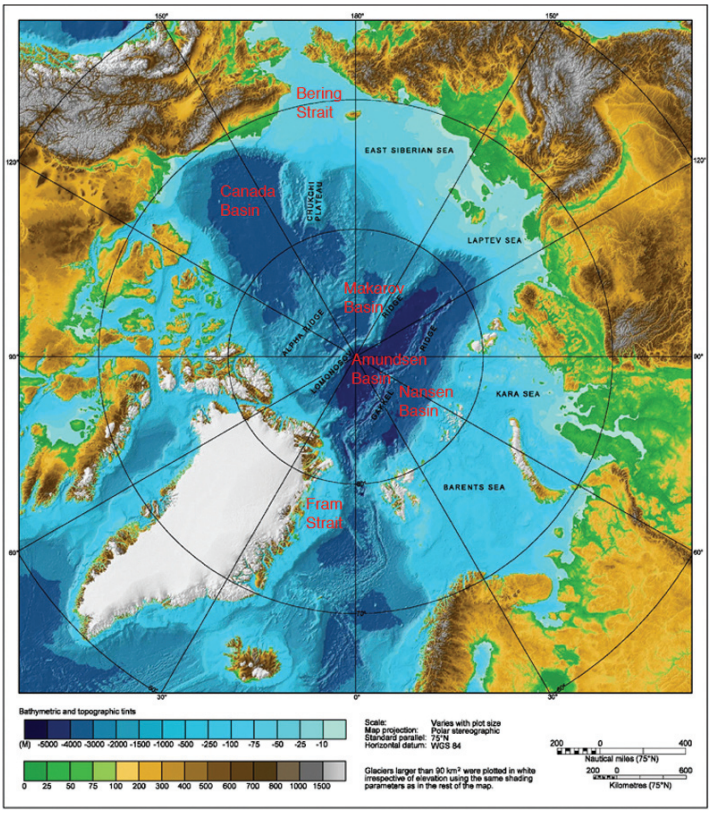

Figure 15.1. Bottom topography of the Arctic Basin and Nordic Seas with the names of geographic features indicated (slightly modified from http://www.ngdc.noaa.gov/mgg/image/IBCAO_betamap.jpg).

temperature of about 6-8 °C. In Summer (Fig. 15.2b), most of the Canadian Archipelago becomes ice free as well as parts of the boundaries of the Arctic basin.

The wind- and buoyancy forcing over the global ocean was presented in chapter 3; over the Arctic measurements are relatively sparse. As in this chapter, we are only concerned with wind-driven flows and to get an impression of the wind stress field, the sea level pressure distribution over the Arctic is plotted in Fig. 15.3. We will not consider the heat flux and freshwater flux over the region. A relatively high pressure area in the vicinity of the North Pole (in particular in Winter) de-

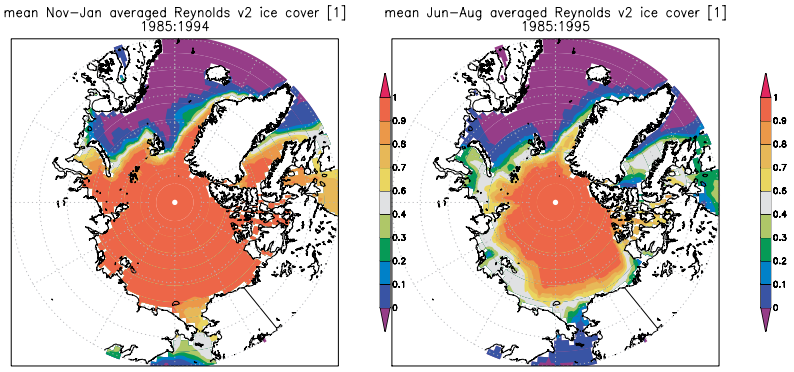

Figure 15.2. The 1985-1995 average Winter (a) and Summer (b) ice concentration in the Arctic and Nordic Seas (made by software and data available through http://climexp.knmi.nl/). The sea ice concentration is 1, when a grid box is totally filled with sea ice; it is 0 when there is no sea ice.

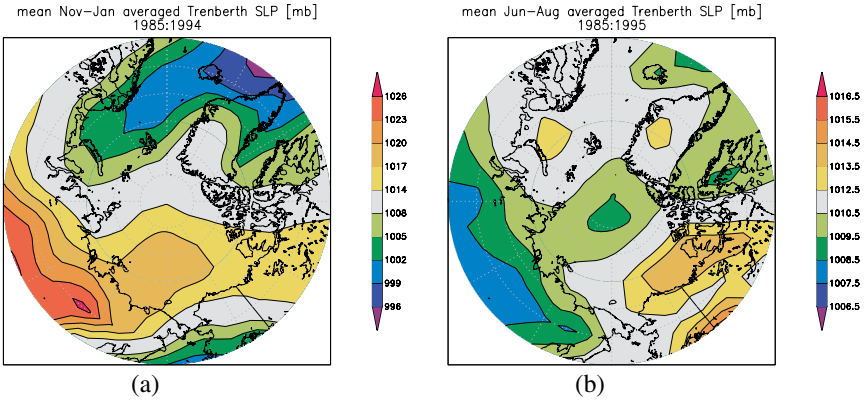

Figure 15.3. The 1985-1995 averaged Winter (a) and Summer (b) sea level pressure (in mb) over the Arctic (made by software and data available through http://climexp.knmi.nl/).

termines the annual average wind-stress distribution over the Arctic basin. Most of the Arctic seas are therefore subjected to polar easterlies with a corresponding anti-cyclonic (westward) surface wind stress. Over Greenland and the Norwegian Seas, the wind-stress field is determined by the Icelandic low which generates cyclonic (anti-clockwise) surface winds.

With the use of Lagrangian surface drifters in the Nordic seas, reliable surface flow estimates are now available. The time-mean field over the period 1991-1995 is shown in Fig. 15.4a. Note that the coverage of drifters is large in the southern

and eastern part of the domain and sparse in the northern and westerns parts. The Atlantic inflow branches in two currents at the northern coast of Norway: one branch continues northward into the Barents Sea and the other branch (the West Spitsbergen Current) continues towards Fram Strait. Both branches finally enter the Arctic basin. A sketch of the circulation over the Arctic basin is plotted in Fig. 15.4b. A major feature of the circulation is the Arctic Ocean Boundary Current (AOBC) with a transport of about 3-5 Sv together with cyclonic gyres in the different basins. There are boundary undercurrents along all of the major topography and these flows are the strongest persistent features in the Arctic Ocean. These boundary currents are a few tens of kilometers wide and they are trapped over the margins of each of the major basins.

Additional Material

B: The description of all characteristics of Arctic Oceanography, in particular the different water masses, is far beyond the scope of this book and other sources should be consulted. Many details can be found in Chapter 7 of Tomczak and Godfrey (1994). On the role of the Arctic in the global climate system, see for example Bobylev et al. (2003).

15.2. Quasi-geostrophic flows with topography

In this section, we will present basic theory to understand the effects of bathymetry, such as in the Arctic, on the bottom current structure. We will start with explaining in more detail the concept of geostrophic contours (section 15.2.1) and then proceed with quasi-geostrophic theory of flows in the presence of closed geostrophic contours (section 15.2.2).

15.2.1. Geostrophic contours

In section 4.4, the concept of potential vorticity was introduced and its usefulness was shown in many following chapters. If we consider the shallow-water potential vorticity Π under conditions of small Rossby number (such that the relative vorticity is much smaller than the planetary vorticity), it reduces to

$$\Pi = \frac{f}{H}, \tag{15.1}$$

where f is the local Coriolis parameter ($f = 2\Omega \sin\theta$) and H is the total depth of the ocean. When Π is conserved and the assuming a steady flow, it follows that

$$\frac{D\Pi}{dt} = \mathbf{u} \cdot \nabla\Pi = \mathbf{u} \cdot \nabla(\frac{f}{H}) = 0, \tag{15.2}$$

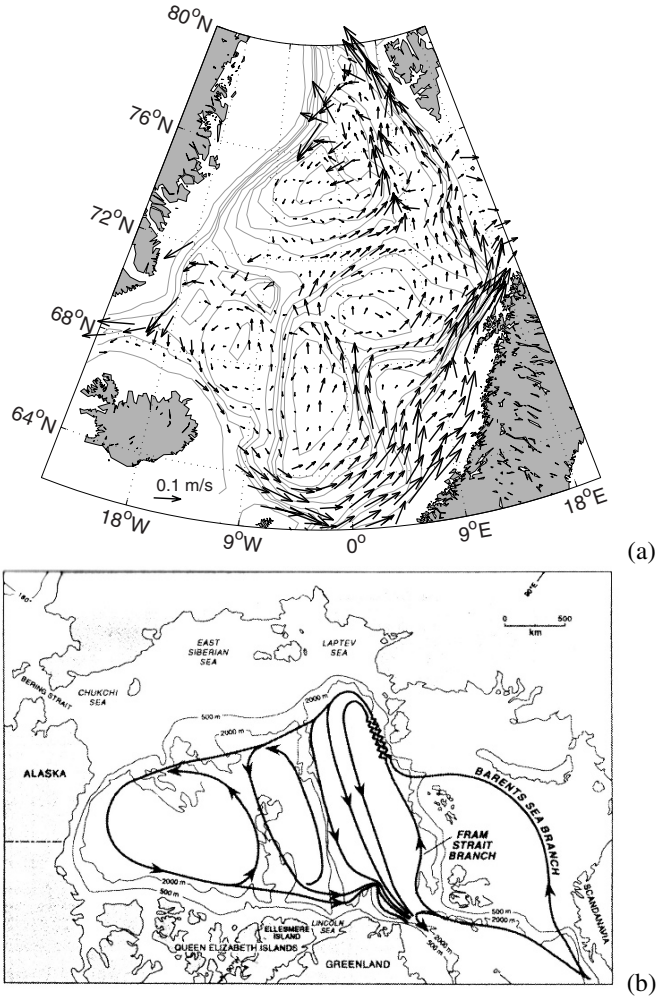

Figure 15.4. (a) Mean surface flow (arrows) in the Nordic Seas from Lagrangian drifters; the bathymetry is shown as the grey curves (from Nøst and Isachsen (2003)). (b) Mean circulation of upper layer waters (more specifically, the water between 200 and 1700 m) in the Arctic (from Rudels et al. (1999)).

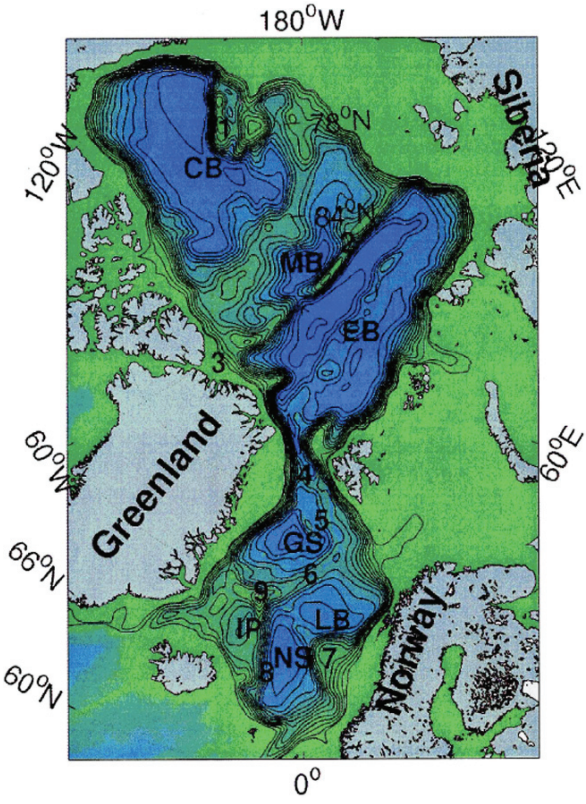

Figure 15.5. Contour plot of f/H for the Arctic Ocean and the Nordic Seas (from Nøst and Isachsen (2003)).

and hence the velocity field is tangent to the contours of the f/H field (note that the vector $\nabla f/H$ is orthogonal to curves of constant f/H).

The f/H field can be determined from bottom topography data and is plotted in Fig. 15.5. What is striking here is that many geostrophic contours are closed due to the presence of the bottom topography. Contrary to the Canada basin and Makarov basin, the Eurasian basin is split into two large areas (Nansen + Amundsen basins) with closed contours. Hence, already from this picture and the theory in section 14.2, one expects the depth-averaged flow along bottom topographic features.

15.2.2. Steady flows with closed geostrophic contours

To look at the effect of closed geostrophic contours on the bottom flow, we use the two-layer quasi-geostrophic model on the midlatitude β-plane derived in section 9.1. In particular, we start from the dimensional equations (9.14), here repeated for convenience

$$\begin{aligned}\frac{D_1}{dt}\left[\nabla^2\psi_1+\beta_0 y+\frac{f_0^2}{g'H_1}(\psi_2-\psi_1)\right]-\frac{1}{\rho_1 H_1}\nabla\cdot(\mathbf{T}\wedge\mathbf{e}_3) &= 0,\\ \frac{D_2}{dt}\left[\nabla^2\psi_2+\beta_0 y+\frac{f_0}{H_2}h_b-\frac{f_0^2}{g'H_2}(\psi_2-\psi_1)\right]+\epsilon_0\nabla^2\psi_2 &= 0,\end{aligned}$$

where

$$\frac{D_i\phi}{dt}=J(\psi_i,\phi)=\frac{\partial\phi}{\partial x}\frac{\partial\psi_i}{\partial y}-\frac{\partial\psi_i}{\partial x}\frac{\partial\phi}{\partial y}$$

is the Jacobian for every scalar quantity ϕ. Furthermore, the quantities ψ_1 and ψ_2 are the geostrophic streamfunctions in both layers, with constant densities ρ_1 and ρ_2 and with equilibrium layer thicknesses H_1 and H_2; $g'=(\rho_2-\rho_1)/\rho_0$ is the reduced gravity. The quantity f_0 is the local Coriolis parameter, β_0 is its local gradient and ϵ_0 is the bottom friction parameter. From section 5.2, we can write

$$\frac{1}{\rho_1 H_1}\nabla\cdot(\mathbf{T}\wedge\mathbf{e}_3)=\frac{f_0}{H_1}w_E, \tag{15.4}$$

where w_E is the Ekman pump velocity. In the equations, we have neglected lateral friction (for example Laplacian friction terms $A_H\nabla^4\psi_i$) and also a frictional coupling between the layers, but we will do this later when needed.

The ratio of the relative vorticity term and the term associated with the variation in the layer thickness in (15.3) is proportional to the parameter $F_i=L^2/L_{Di}^2$ where L_{Di} is in the internal Rossby deformation in each layer. When we assume that both the F_i are large, the relative vorticity can be neglected and when use is made of $J(\psi_i,\psi_i)=0$ (where J is the Jacobian), we find from (9.14) the equations

$$\frac{f_0^2}{g'H_1}J(\psi_1,\psi_2)+\beta_0\frac{\partial\psi_1}{\partial x} = \frac{f_0}{H_1}w_E, \tag{15.5a}$$

$$\frac{f_0^2}{g'H_2}J(\psi_2,\psi_1)+\beta_0\frac{\partial\psi_2}{\partial x}+\epsilon_0\nabla^2\psi_2 = -J(\psi_2,\frac{f_0}{H_2}h_b). \tag{15.5b}$$

We now first determine the depth-averaged flow by multiplying (15.5a) by H_1 and (15.5b) by H_2 and adding the result. Using also the identity $J(\psi_1,\psi_2)=-J(\psi_2,\psi_1)$, we find

$$\beta_0\frac{\partial}{\partial x}(H_1\psi_1+H_2\psi_2)+J(\psi_2,\frac{f_0}{H_2}h_b)=f_0w_E-H_2\epsilon_0\nabla^2\psi_2. \tag{15.6}$$

Under conditions that friction is negligible and bottom topography is absent, we introduce the depth-averaged streamfunction ψ_B as

$$\psi_B = \frac{H_1\psi_1 + H_2\psi_2}{D}, \tag{15.7}$$

where $D = H_1 + H_2$ is the total equilibrium depth. The relation (15.6) then reduces to the Sverdrup balance

$$\beta_0 \frac{\partial \psi_B}{\partial x} = \frac{f_0}{D} w_E, \tag{15.8}$$

and the solution for ψ_B satisfying a no-flow eastern boundary conditions at $x = x_e$ is given by

$$\psi_B(x,y) = -\frac{f_0}{\beta_0 D}\int_x^{x_e} w_E(x',y)dx', \tag{15.9}$$

and hence ψ_B is known when w_E is prescribed. The streamfunction in each layer is related to ψ_B through

$$\psi_1 = \frac{D\psi_B - H_2\psi_2}{H_1}\ ;\ \psi_2 = \frac{D\psi_B - H_1\psi_1}{H_2}. \tag{15.10}$$

We now proceed first with the case without bottom topography (which is easier) and then come back to this issue at the end of this section. In the flat bottom case, using (15.10) in the vorticity equations (15.5) gives

$$J(\psi_1, \beta_0 y + \hat{F}\psi_B) = \frac{f_0}{H_1} w_E, \tag{15.11a}$$

$$J(\psi_2, \beta_0 y + \hat{F}\psi_B) = -\epsilon_0 \nabla^2 \psi_2, \tag{15.11b}$$

where $\hat{F} = f_0^2 D/(g' H_1 H_2)$. These are linear equations in ψ_1 and ψ_2 which can be easily solved.

In the interior of the second layer, bottom friction is small and (15.11b) gives

$$J(\psi_2, \hat{q}_2) = 0\ ;\ \hat{q}_2 = \beta_0 y + \hat{F}\psi_B, \tag{15.12}$$

and hence $\psi_2 = \Psi(\hat{q}_2)$ for some function Ψ. Streamlines in the lower layer are hence identical to isolines of the known function $\hat{q}_2$. These are also isolines of the potential vorticity of the lower layer q_2 (the geostrophic contours), since

$$q_2 = \beta_0 y - \frac{f_0^2}{g' H_2}(\psi_2 - \psi_1) = \hat{q}_2 - \hat{F}\Psi(\hat{q}_2). \tag{15.13}$$

The interesting case is now whether closed geostrophic contours will exist in the lower layer. When the wind forcing is zero, ψ_B is zero and the geostrophic

contours are lines of constant y. Such contours will always intersect the eastern boundary where $\psi_2 = 0$ and hence ψ_2 is zero everywhere. When the wind forcing is so small that the geostrophic contours (curves of constant q_2) still intersect the eastern boundary, then there is flow in the upper layer, but the lower layer is still motionless. To see how the geostrophic contours are deformed by the upper-layer flow, we first consider an example.

▶

Example 15.1: Localized Ekman pumping: specification

Consider a situation of localized Ekman pumping in a disk with radius R around $(0, 0)$, such that $R < x_e$, where x_e is the eastern boundary. On the disk, the Ekman pumping (Fig. 15.6a) is given by

$$w_E = -\gamma x, \tag{15.14}$$

where $\gamma > 0$ is a positive constant; $w_E = 0$ outside the disk.

The Sverdrup streamfunction ψ_B is immediately found from (15.9). It is zero for points (x, y) outside the disk (when $x > R$, this follows from $w_E = 0$ and when $x < -R$, it follows from the anti-symmetry of w_E with respect to $x = 0$) and for values (x, y) within the disk it becomes

$$\psi_B(x, y) = \frac{\gamma f_0}{\beta_0 D} \int_x^{X(y)} x' dx' = \frac{\gamma f_0 \hat{F}}{2\beta_0 D}(R^2 - x^2 - y^2), \tag{15.15}$$

where $X(y) = \sqrt{R^2 - y^2}$. The geostrophic contours are now given by curves of constant $\hat{q}_2 = \beta_0 y$ for points outside the disk and by curves of constant $\hat{q}_2 = \beta_0 y + (\hat{F}\gamma f_0)/(2\beta_0 D)(R^2 - x^2 - y^2)$ for points inside the disk.

When we write $y_0 = \beta_0^2 D/(\gamma f_0 \hat{F})$, the expression for $\hat{q}_2$ within the disk can be written as

$$\hat{q}_2 = \frac{\beta_0}{2y_0}(R^2 + y_0^2 - x^2 - (y - y_0)^2). \tag{15.16}$$

Hence the geostrophic contours are only deformed within the disk and two examples ($y_0/R = 2$ and $y_0/R = 1/4$) are shown in Fig. 15.6b and Fig. 15.6c, respectively. When the center of the circular arc y_0 lies outside of the disk ($y_0 > R$), the curves remain open circular arcs and connect to the constant latitude lines outside the disk. However, when $y_0 < R$ the center lies within the disk and hence there are isolines which are closed and which are not connected to the constant latitude lines.

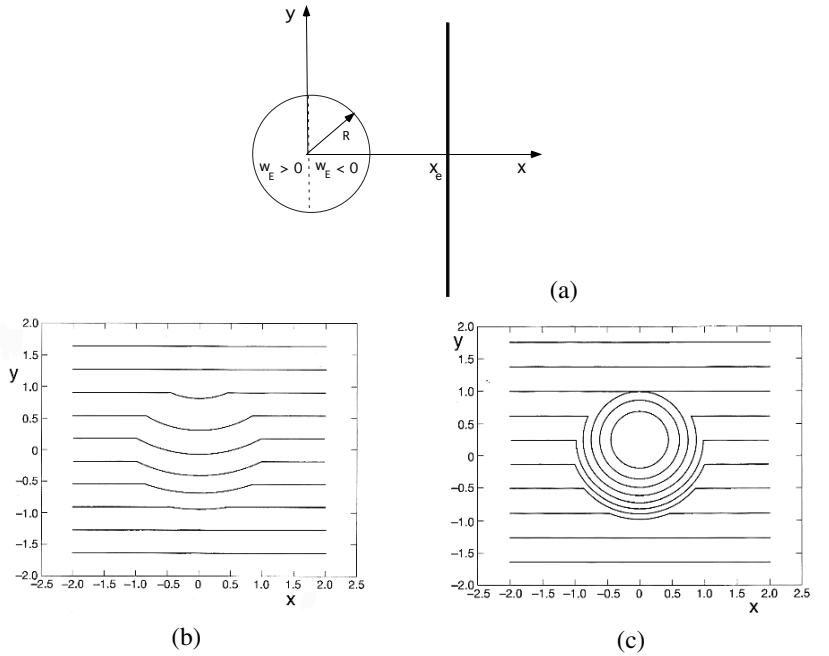

Figure 15.6. (a) Sketch of the situation of localized Ekman pumping within a disk of radius R. (b) Isolines of $\hat{q}_2$ for the case $y_0 = 2$, $R = 1$. (c) Same for $y_0 = 0.25$ and $R = 1$ (from Pedlosky (1996)).

The critical value of the forcing which is required to have closed contours is determined by the condition $y_0 \leq R$, which is equivalent to

$$\frac{\beta_0^2 D}{\gamma f_0 \hat{F}} \leq R \rightarrow \gamma \geq \frac{\beta_0^2 D}{f_0 \hat{F} R}. \tag{15.17}$$

When $\gamma = W_0/R$, where W_0 is a typical amplitude of the Ekman pump velocity, then by defining a mean Rossby deformation radius L_d using $\hat{F} = 1/L_d^2$, we find

$$W_0 \geq \frac{\beta_0^2 L_d^2 D}{f_0}. \tag{15.18}$$

With typical values $f_0 = 10^{-4}$ s^{-1}, $\beta_0 = 10^{-11}$ (ms)$^{-1}$, $D = 1000$ m and $L_d = 50$ km, we find as critical value $W_0 \approx 2.5 \times 10^{-6}$ m s^{-1} = 0.2 m/day, which is well within the realistic range of high latitude Ekman pump velocities (Fig. 5.13) observed.

◄

The example clearly shows that the upper-layer flow caused by the Ekman pumping can deform the lower-layer geostrophic contours such that they can become closed. When closed, these contours are disconnected from the eastern boundary and hence, in principle, flow is possible within such regions. But how is it determined?

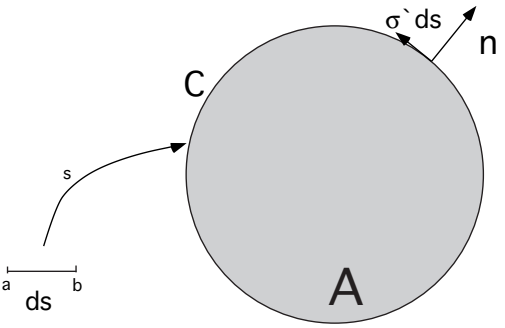

Figure 15.7. (a) Sketch of a closed geostrophic contour C parametrized by the curve $\boldsymbol{\sigma}$ and enclosing an area A.

It turns out that friction between the layers is crucial to set the flow in the lower layer. Such type of friction may be established by time-dependent processes associated with eddies (as briefly discussed in section 14.3), but it is usually represented in the right hand side of the momentum equation of the lower layer by a term $-A_f(\mathbf{u}_2 - \mathbf{u}_1)$. As the vorticity equation results from taking the curl of the momentum equations, we then obtain by adding the interfacial friction term to (15.11b),

$$J(\psi_2, \hat{q}_2) = -\epsilon_0 \nabla^2 \psi_2 - A_f \nabla \wedge (\mathbf{u}_2 - \mathbf{u}_1). \tag{15.19}$$

Now consider a region A in the lower layer enclosed by a closed geostrophic contour C (Fig. 15.7). Integration of (15.19) over this region gives

$$\int_A J(\psi_2, \hat{q}_2)\, dxdy = \int_A \mathbf{u}_2 \cdot \hat{q}_2\, dxdy = \int_A \nabla \cdot (\mathbf{u}_2 \hat{q}_2)\, dxdy = \oint_C , \hat{q}_2 \mathbf{u}_2 \cdot \mathbf{n} ds \tag{15.20}$$

where $\mathbf{n}$ is the outward normal and $ds = |\mathbf{ds}|$ the scalar element along the curve C. As $\hat{q}_2$ is constant along the geostrophic contour C it can be taken out of the integral. As was discussed above, the geostrophic contour is also a streamline as $\psi_2 = \Psi(\hat{q}_2)$ and parameterizing the curve C by a mapping $\boldsymbol{\sigma}(s) : \mathbb{R} \rightarrow \mathbb{R}^2$, we

have $\psi_2(\boldsymbol{\sigma}(s)) =$ constant. By taking the derivative to s we find

$$\nabla\psi_2 \cdot \boldsymbol{\sigma}' = 0. \tag{15.21}$$

Now because $\mathbf{n}$ is orthogonal to the tangent to the curve ($\boldsymbol{\sigma}'$) and for the geostrophic streamfunction, we have $\mathbf{u}_2 = \mathbf{e}_3 \wedge \nabla\psi_2$, it is found that

$$\oint \hat{q}_2 \mathbf{u}_2 \cdot \mathbf{n}\, ds = \hat{q}_2 \oint \mathbf{u}_2 \cdot \mathbf{n}\, ds = \hat{q}_2 \oint \frac{d}{ds}\psi_2(\boldsymbol{\sigma}(s))ds = 0, \tag{15.22}$$

the latter step because the contour is closed and ψ_2 is single valued.

Integration of (15.19) therefore gives

$$\int_A \left[\epsilon_0 \nabla^2\psi_2 + A_f \nabla \wedge (\mathbf{u}_2 - \mathbf{u}_1)\right]\, dxdy = 0, \tag{15.23}$$

and applying Gauss' and Stokes' theorems to the integrals above we obtain

$$A_f \oint \mathbf{u}_1 \cdot \mathbf{ds} = (\epsilon_0 + A_f) \oint \mathbf{u}_2 \cdot \mathbf{ds}. \tag{15.24}$$

To obtain another relation between $\mathbf{u}_1$ and $\mathbf{u}_2$ we use (15.10) to give

$$\mathbf{u}_1 = \frac{D}{H_1}\mathbf{u}_B - \frac{H_2}{H_1}\mathbf{u}_2, \tag{15.25}$$

where $\mathbf{u}_B$ is the Sverdrup velocity field. Substituting this expression into (15.24) gives

$$\oint \mathbf{u}_2 \cdot \mathbf{ds} = \frac{DA_f}{H_1\epsilon_0 + DA_f} \oint \mathbf{u}_B \cdot \mathbf{ds}. \tag{15.26}$$

On the other hand, when friction is negligible we have $\psi_2 = \Psi(\hat{q}_2)$ (because of conservation of potential vorticity in the lower layer) and hence

$$\oint \mathbf{u}_2 \cdot \mathbf{ds} = \oint \mathbf{e}_3 \wedge \nabla\psi_2 \cdot \mathbf{ds} = \oint \mathbf{e}_3 \wedge \frac{\partial\Psi}{\partial\hat{q}_2}\nabla\hat{q}_2 \cdot \mathbf{ds}. \tag{15.27}$$

Again, $\partial\Psi/\partial\hat{q}_2$ is only a function of $\hat{q}_2$ and hence constant along C. With $\hat{q}_2 = \hat{F}\psi_B + \beta_0 y$, we then find

$$\oint \mathbf{u}_2 \cdot \mathbf{ds} = \frac{\partial\Psi}{\partial\hat{q}_2} \oint \mathbf{e}_3 \wedge \nabla(\hat{F}\psi_B + \beta_0 y) \cdot \mathbf{ds} = \frac{\partial\Psi}{\partial\hat{q}_2} \oint \hat{F}\mathbf{u}_B \cdot \mathbf{ds}, \tag{15.28}$$

since $\mathbf{e}_3 \wedge \nabla y = -\mathbf{e}_1$ and its contour integral is zero. Combining (15.26) and (15.28), one can solve

$$\psi_2(x,y) = \Psi(\hat{q}_2) = \frac{DA_f}{\hat{F}(\epsilon_0 H_1 + DA_f)}(\hat{q}_2(x,y) - \hat{q}_{20}) \tag{15.29}$$

where $\hat{q}_{20}$ is an integration constant which is determined by the value of $\hat{q}_2$ on the outermost closed geostrophic contour where $\psi_2 = 0$. The conclusion of this analysis is that weak dissipation (interfacial friction) sets the flow in the lower layer in the region of closed geostrophic contours.

Ex. 15.1

Example 15.2: Localized Ekman pumping: solution

We now continue the analysis of the situation of localized Ekman pumping as in Example 15.1. Assume that $y_0 < R$ such that closed streamlines exist; the outermost closed geostrophic contour touches the boundary of the disk at $(0, R)$ and hence the value of $\hat{q}_{20} = \beta_0 R$. The outermost geostrophic contour in the lower layer (where $\psi_2 = 0$) is therefore given by (from (15.16)) by

$$\beta_0 R = \frac{\beta_0}{2y_0}(R^2 + y_0^2 - x^2 - (y - y_0)^2) \rightarrow x^2 + (y - y_0)^2 = (R - y_0)^2. \quad (15.30)$$

The streamfunctions in both layers follow from (15.29) and (15.10)

$$\psi_2(x, y) = \frac{DA_f}{\epsilon_0 H_1 + DA_f}(\psi_B + \beta_0 \frac{y - R}{\hat{F}}), \quad (15.31a)$$

$$\psi_1(x, y) = \frac{D\psi_B(x, y) - H_2\psi_2(x, y)}{H_1}. \quad (15.31b)$$

For $\epsilon_0 = 0$ (no bottom friction) and $y_0 = 1/4, R = 1$, both streamfunctions ψ_1 and ψ_2 are plotted in Fig. 15.8. In layer 2 (Fig. 15.8b), one observes that the circulation is limited to the region of closed geostrophic contours. The explicit solution for ψ_2 within the disk for this case is given by

$$\psi_2(x, y) = \frac{\beta_0}{\hat{F}}\left[\frac{1}{2y_0}(R^2 - x^2 - y^2) + y - R)\right], \quad (15.32)$$

and the streamlines are circles with center $(0, y_0)$. The solution for ψ_1 in Fig. 15.8a is more complicated as it is composed of part of the Sverdrup solution (which is nonzero over the forcing disk) and part of the solution ψ_2. Outside of the regions of closed contours (the dark contour in Fig. 15.8a), the solution is just the Sverdrup solution weighted by a factor D/H_1. At the intersection of the forcing region and that of the outermost closed contour, jumps occur in the upper layer streamfunction.

Ex. 15.2

Ex. 15.3

While we have totally neglected bottom topography in this section, it is clear that the addition of bottom topography in the quasi-geostrophic case easily leads to closed contours as it is part of the potential vorticity q_2. The material in this section has illustrated that subtle effects may control bottom layer currents once geostrophic contours become closed. To investigate the bottom currents in the Arctic, the quasi-geostrophic approximation is questionable because the

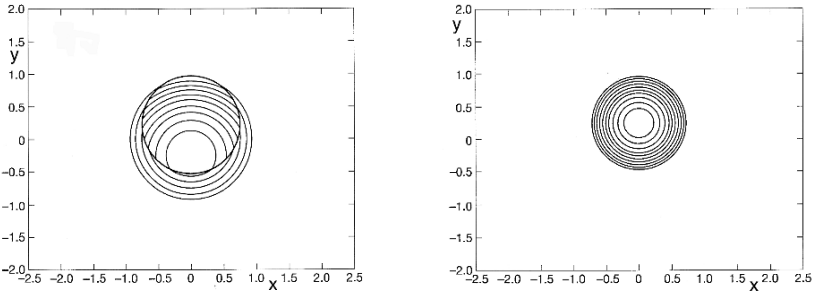

(a) (b)

Figure 15.8. (a) Plot of the streamfunction ψ_1 for the case $y_0 = 0.25, R = 1$. (b) Plot of the streamfunction ψ_2 for the case $y_0 = 0.25, R = 1$ (from Pedlosky (1996)).

amplitude of the bottom topography is no longer in the order of the Rossby number. Hence, in the next section we turn to a slightly more complicated model.

Additional Material

B: For a more extensive discussion see sections 3.5 to 3.8 in Pedlosky (1996). An alternative approach to this problem can be found in section 14.7 of Vallis (2006).

D: The Arctic Ocean flow has motivated much work on the representation of eddy-topography interactions, see e.g., Holloway (1992). For the quasi-geostrophic case incorporating bottom topography, see Dewar (1998).

15.3. An idealized model of the Arctic circulation

The starting point (Nøst and Isachsen, 2003) are the horizontal momentum equations for an ocean layer bounded by $z = 0$ at the surface and by $z = -H$ at the bottom. The steady horizontal momentum equations are written as

$$\mathbf{v} \cdot \nabla \mathbf{v} + \mathbf{e}_3 \wedge f\mathbf{v} = -\frac{1}{\rho_0}\nabla p + A_V \frac{\partial^2 \mathbf{v}}{\partial z^2}, \tag{15.33}$$

where $\mathbf{v} = (u, v)$ is the horizontal velocity vector, $\mathbf{e}_3$ is the unit vector in vertical direction and only vertical mixing processes are considered. The boundary conditions are as in (14.4).

As a first step, the flow is split into a geostrophic and an ageostrophic part according to $\mathbf{v} = \mathbf{v}_g + \mathbf{v}_a$, with

$$\mathbf{v}_g = \frac{1}{f\rho_0}\mathbf{e}_3 \wedge \nabla p \tag{15.34a}$$

$$\mathbf{e}_3 \wedge f\mathbf{v}_a = A_V \frac{\partial^2 \mathbf{v}}{\partial z^2} - \mathbf{v} \cdot \nabla \mathbf{v} \tag{15.34b}$$

The horizontal momentum equation (15.33) can then be written as

$$\mathbf{e}_3 \wedge f\mathbf{v} = -\frac{1}{\rho_0} \nabla p + \mathbf{e}_3 \wedge f\mathbf{v}_a \tag{15.35}$$

As a next step, we define the depth-integrated horizontal velocity as

$$\mathbf{V} = \int_{-H}^{0} \mathbf{v}\, dz \tag{15.36}$$

and split the total horizontal transport into

$$\mathbf{V} = \mathbf{V}_a + \mathbf{V}_s + H\mathbf{v}_b, \tag{15.37a}$$

$$\mathbf{V}_s = \int_{-H}^{0} (\mathbf{v}_g - \mathbf{v}_b)\, dz, \tag{15.37b}$$

$$\mathbf{V}_a = \int_{-H}^{0} \mathbf{v}_a\, dz. \tag{15.37c}$$

Here $\mathbf{v}_b$ is the bottom horizontal velocity, i.e., $\mathbf{v}_b = \mathbf{v}|_{z=-H}$, which is independent of z.

To arrive at the depth averaged vorticity equation, we use the fact that the horizontal divergence of $\mathbf{V}$ (through vertical integration of the continuity equation) is zero to give

$$\nabla \cdot (\mathbf{V}_s + \mathbf{V}_a + H\mathbf{v}_b) = 0. \tag{15.38}$$

We use Leibnitz's rule for writing

$$\begin{aligned} \nabla \cdot \mathbf{V}_s &= \nabla \cdot \int_{-H}^{0} (\mathbf{v}_g - \mathbf{v}_b)\, dz = \\ &= \int_{-H}^{0} \nabla \cdot (\mathbf{v}_g - \mathbf{v}_b)\, dz + \nabla H \cdot (\mathbf{v}_g - \mathbf{v}_b)|_{z=-H}, \end{aligned} \tag{15.39}$$

and the last term in the right hand side can be neglected if the ageostrophic velocities near the bottom are assumed small.

Using the vector identities (for arbitrary vectors $\mathbf{a}$ and $\mathbf{b}$ and scalar ϕ)

$$\nabla \cdot (\mathbf{a} \wedge \mathbf{b}) = \mathbf{b} \cdot \nabla \wedge \mathbf{a} - \mathbf{a} \cdot \nabla \wedge \mathbf{b},$$

and

$$\nabla \wedge (\phi \mathbf{a}) = \phi \nabla \wedge \mathbf{a} + \nabla \phi \wedge \mathbf{a},$$

we evaluate

$$\nabla \cdot \mathbf{v}_g = \mathbf{e}_3 \wedge \nabla p \cdot \nabla(\frac{1}{f}) = -\frac{1}{f}\mathbf{v}_g \cdot \nabla f, \tag{15.40a}$$

$$\nabla \cdot \mathbf{v}_b = \mathbf{e}_3 \wedge \nabla p \cdot \nabla(\frac{1}{f}) = -\frac{1}{f}\mathbf{v}_b \cdot \nabla f, \tag{15.40b}$$

and

$$\nabla \cdot (H\mathbf{v}_b) = \nabla \cdot (\frac{H}{\rho_0 f}\mathbf{e}_3 \wedge \nabla p_b) = f\mathbf{v}_b \cdot \nabla(\frac{H}{f}) = -\frac{H^2}{f}\mathbf{v}_b \cdot \nabla(\frac{f}{H}). \tag{15.41}$$

Ex. 15.4

Eventually one then finds from (15.38) the vorticity equation

$$\frac{H^2}{f}\mathbf{v}_b \cdot \nabla(\frac{f}{H}) = -\frac{1}{f}\mathbf{V}_s \cdot \nabla f + \nabla \cdot \mathbf{V}_a. \tag{15.42}$$

If we assume that inertia can be neglected, then vertical integration of (15.34), and taking the divergence of the result gives

$$\nabla \cdot \mathbf{V}_a = \mathbf{e}_3 \cdot \left[\nabla \wedge \frac{\boldsymbol{\tau}_s}{\rho_0 f} - \nabla \wedge \frac{\boldsymbol{\tau}_b}{\rho_0 f}\right], \tag{15.43}$$

where $\boldsymbol{\tau}_s$ and $\boldsymbol{\tau}_b$ are the surface wind stress and the bottom stress vectors, respectively. In this case, the vorticity equation becomes

$$\frac{H^2}{f}\mathbf{v}_b \cdot \nabla(\frac{f}{H}) + \mathbf{e}_3 \cdot \nabla \wedge \frac{\boldsymbol{\tau}_b}{\rho_0 f} = \mathbf{e}_3 \cdot \nabla \wedge \frac{\boldsymbol{\tau}_s}{\rho_0 f} - \frac{1}{f}\mathbf{V}_s \cdot \nabla f. \tag{15.44}$$

When the wind-stress field and the transport due to the shear velocities $\mathbf{V}_s$ are given, this equation is a single scalar equation for the streamfunction ψ_b associated with the bottom velocities, i.e.,

$$\mathbf{v}_b = \frac{1}{f\rho_0}\mathbf{e}_3 \wedge \nabla \psi_b. \tag{15.45}$$

Note that when the bottom velocities and bottom stress are zero, the balance (15.44) reduces to the Sverdrup balance as f only varies in the meridional direction.

►

Example 15.3: Idealized basin

Let the layer depth of an idealized basin in Cartesian coordinates be given by

$$H(x,y) = H_0 e^{-\frac{r^2}{L^2}} + H_1, \tag{15.46}$$

where $r^2 = (x - x_0)^2 + (y - y_0)^2$ and H_1 and H_0 are constants. Hence, at $r = 0$, we have $H = (H_0 + H_1)$ m and for $r \gg L$, we have $H \approx H_1$ m. We assume that the right hand side, say F, of (15.44) is known as

$$F(x, y) = F_0(\frac{x}{x_0})^2, \tag{15.47}$$

which is constant in y and increasing quadratically in x. Let us assume that the Coriolis parameter f is constant. Certainly, the geostrophic contours f/H are closed. Let furthermore the bottom stress be parameterized as

$$\boldsymbol{\tau}_b = \rho_0 R \, \mathbf{v}_b, \tag{15.48}$$

with R being constant, then (15.44) becomes

$$-\mathbf{v}_b \cdot \nabla H + \frac{R}{f} \nabla \wedge \mathbf{v}_b = F \rightarrow -\frac{1}{\rho_0 f} J(\psi_b, H) + \frac{R}{\rho_0 f^2} \nabla^2 \psi_b = F, \tag{15.49}$$

Ex. 15.5

where J is again the Jacobian. For given H and F this is a linear equation for the streamfunction ψ_b which can be solved numerically.

A plot of the velocity field $\mathbf{v}_b$ for values $R = 10^{-4}$ ms^{-1}, $H_1 = 300$ m, $H_0 = 3700$ m, $L = 6 \times 10^5$ m, $F_0 = 5 \times 10^{-7}$ ms^{-1} in a domain of 5000×5000 km is shown in Fig. 15.9b, while the H field is plotted in Fig. 15.9a. It indicates the close alignment of the velocity vectors with the f/H contours.

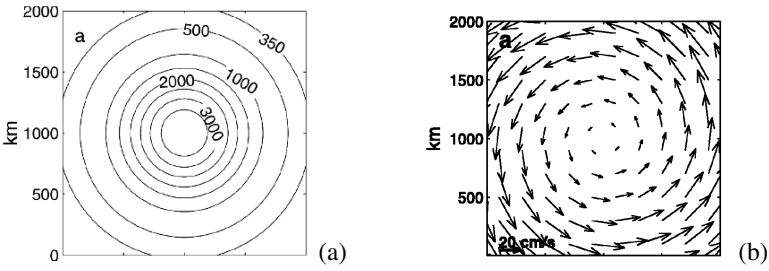

Figure 15.9. (a) Contours of H for the problem as defined by (15.46) in Example 15.3. (b) Bottom velocity vector plot as the solution of (15.49) where the bottom velocity $\mathbf{v}_b = \mathbf{e}_3 \wedge \psi_b/(\rho_0 f)$ *(from Nøst and Isachsen (2003)).*

◄

15.4. Application to the Arctic basin

Estimates for the terms in the right hand side of (15.44) from observations have been made in Nøst and Isachsen (2003). The wind-stress term was calculated

from the NCEP/NCAR reanalysis project and averaged over the years 1950-2000 whereas the term involving $\mathbf{V}_s$ was calculated from several ocean atlases. Over most of the Nordic seas (with the exception of regions near Svalbard and Iceland), there is upwelling (Fig. 15.10a) while there is downwelling over the remainder of the Arctic basin. The spatial pattern of the hydrographic term in Fig. 15.10b is quite different from that of the wind-stress term with large positive values south of Fram Strait in the East Greenland Current and relatively small values of the Arctic basin. It can be immediately seen that the spatial patterns of both fields do not cancel which indicates that a Sverdrup balance is not likely in the Arctic Ocean and Nordic Seas. The vertical velocities associated with the right hand side of (15.44) have an absolute maximum of about 2×10^{-6} ms^{-1}.

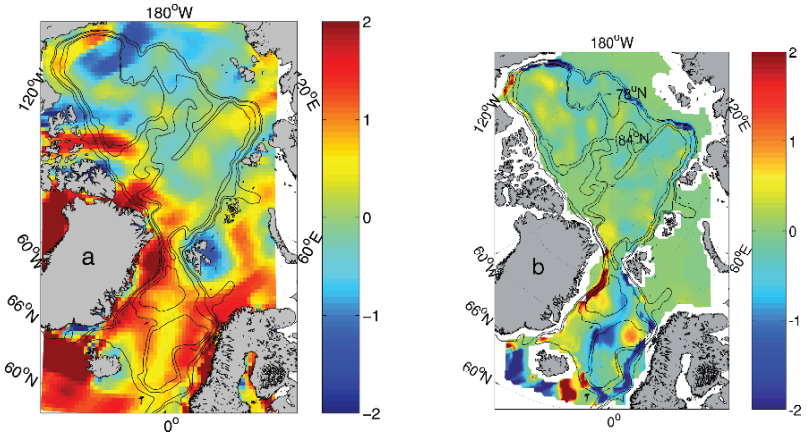

Figure 15.10. (a) Surface Ekman pumping velocities (the term $\mathbf{e}_3 \cdot \nabla \wedge \boldsymbol{\tau}_s/(\rho_0 f)$ in (15.44)) calculated from NCEP wind stress data and (b) hydrographic forcing (the term $-(\mathbf{V}_s/f) \cdot \nabla f$ in (15.44)) calculated from EWG Arctic Atlas and World Ocean Atlas 98. The units are in 10^{-6} ms^{-1} (from Nøst and Isachsen (2003)).

Once the right hand of (15.44) is known, the bottom streamfunction can be determined once the bottom friction law is specified. In Nøst and Isachsen (2003), the quadratic bottom friction law

$$\boldsymbol{\tau}_b = \rho_0 C_D \sqrt{u_b^2 + v_b^2}\, \mathbf{v}_b, \tag{15.50}$$

is used with a drag coefficient $C_D = 10^{-3}$. Using the full bathymetry of the Arctic Ocean and Nordic Seas, the equation (15.44) was solved. In Fig. 15.11, the bottom velocity fields for the Arctic Ocean (Fig. 15.11a) and the Nordic Seas (Fig. 15.11b) are shown. The red arrows indicate current measurements from moored instruments.

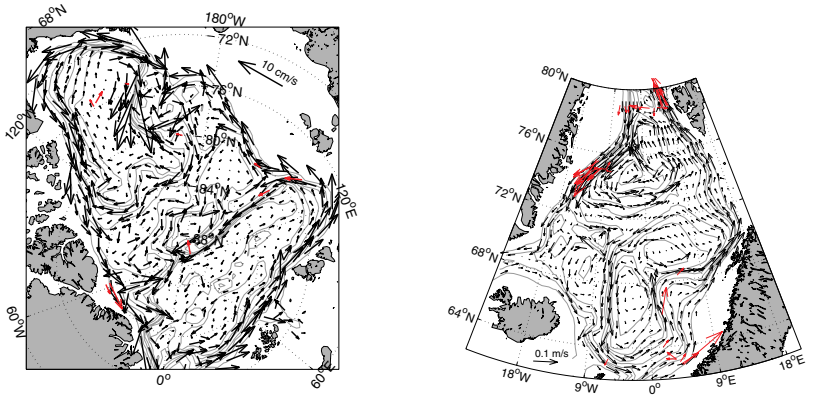

(a) (b)

Figure 15.11. (a) Modeled bottom geostrophic velocities (black arrows) and those observed (red arrows) at specific locations for the Arctic Ocean. (b) Modeled bottom geostrophic velocities (black arrows) and observed near-bottom currents (red arrows) for the Nordic Seas (from Nøst and Isachsen (2003)).

The most pronounced feature of the model circulation in the Arctic basin is the counter-clockwise Arctic Circumpolar Boundary Current along the perimeter of the entire region, in agreement with the available current meter data. Near (80°W, 150°E) this current splits and part flows along the Lomonosov Ridge towards the North Pole. Near the North Pole there is a gap in the Lomonosov Ridge and the model predicts a bottom flow into the Makarov basin following the f/H contours. In the Canada basin, the circulation is clockwise and much weaker. The bottom velocities in the Nordic Seas show also strong currents in and out of Fram Strait, with the East Greenland current being most pronounced. Much more on the description of the model currents and the comparison with observations can be found in Nøst and Isachsen (2003).

Summary

- The Arctic Ocean circulation is characterized by a cyclonic Arctic Ocean Boundary Current and cyclonic gyres in the different sub basins.
- Surface winds, and the associated Ekman pumping, is already able to close geostrophic contours in the deep ocean as the potential vorticity in the deep ocean is influenced by the depth averaged (Sverdrup) flow. Bottom topography also contributes to the closure of geostrophic contours.
- Once closed contours exist in the lower layer, flow is possible in this layer through frictional coupling with the upper layer.
- The flow in the Arctic Ocean and Nordic Seas is strongly controlled by bottom topography as geostrophic contours are closed over much of the flow domain.

15.5. Exercises on chapter 15

(15.1) *Limits*

There are two interesting limits in the problem discussed in Example 15.2.

a. First consider the limit $\epsilon_0 H_1/DA_f \rightarrow \infty$. Determine the resulting streamfunction solutions and provide a physical interpretation for the result.

b. Second, consider the limit $\epsilon_0 \rightarrow 0$ as was used in the Figs. 15.8. Again, determine the resulting solutions and provide a physical interpretation of the result.

(15.2) *Homogenization of PV*

The solution of the problem in Example 15.3 has an interesting potential vorticity distribution.

a. Determine the potential vorticity q_2 (of the bottom layer) and in particular consider the limit $\epsilon_0 \rightarrow 0$.

Assume more generally that the dissipation term in the lower layer vorticity equation can be written as $\nabla \cdot (\kappa \nabla q_2)$ instead of using the interfacial friction term. Instead of (15.19) we then obtain with $\epsilon_0 = 0$,

$$J(\psi_2, \hat{q}_2) = \nabla \cdot (\kappa \nabla q_2)$$

b. Show that

$$\oint_C \kappa \nabla q_2 \cdot \mathbf{n}\, ds = 0$$

where the integral is taken over a closed streamline in the lower layer.

We can also use the constraint of potential vorticity conservation in the frictionless limit, i.e., $q_2 = \Psi(\psi_2)$.

c. Show that for all closed streamlines

$$\frac{d\Psi}{d\psi_2} = 0$$

and provide a physical interpretation of the result.

(15.3) *Topography in the quasi-geostrophic case*

In this exercise the quasi-geostrophic two-layer model with bottom topography is considered. Starting equations are again given by (15.3) on a domain $[x_w, x_e] \times [-L, L]$ which contains the point $(0, 0)$. We will neglect bottom friction and hence put $\epsilon_0 = 0$. The bottom topography is given by

$$h_b(x, y) = h_{b0} \left[1 - \frac{x^2 + y^2}{R^2} \right]$$

when $x^2 + y^2 < R^2$ and it is zero over the rest of the domain. The Ekman pumping is chosen as

$$w_E(x, y) = \begin{cases} \alpha(y - L) & : \quad y_0 < y < L \\ \alpha(y_0 - L) & : \quad -y_0 < y < y_0 \\ -\alpha(y + L) & : \quad -L < y < -y_0 \end{cases}$$

and hence w_E is everywhere negative over the domain.

a. Assume that $R < x_e$ and $h_{b0} = 0$. Show that near the eastern boundary the lower layer is at rest and determine the streamfunction in the upper layer.

b. Determine the conditions under which closed geostrophic contours appear.

Now assume that the conditions under b. are such that no closed geostrophic contours appear due to the wind-stress forcing and consider the case $h_{b0} > 0$.

c. Determine the condition on h_{b0} such that closed geostrophic contours appear in the lower layer.

(15.4) *Bottom velocities on closed f/H contours*

It is possible to derive an approximate formula for the bottom velocities on closed f/H contours for the model in section 15.4. To do this, we start from (15.45) here rewritten for convenience as

$$\mathbf{v}_b = \frac{1}{f\rho_0} \mathbf{e}_3 \wedge \nabla \psi_b$$

a. Introduce $q = f/H$ as one coordinate and p as a coordinate perpendicular to q (hence along $\nabla(f/H)$). Show that when velocities perpendicular to f/H are much larger than those perpendicular to it, the bottom velocities can be determined from

$$\mathbf{v}_b \approx \frac{1}{f\rho_0} \frac{\partial \psi_b}{\partial q} \mathbf{e}_3 \wedge \nabla q$$

Assume now that ψ_b is a function only of q.

b. Consider the linear friction law $\boldsymbol{\tau}_b = RC_D\mathbf{v}_b$ and integrate the vorticity equation (15.44) along a closed contour C of constant f/H. Show that the result can be written as

$$\oint \frac{RC_D}{\rho_0 f}\mathbf{v}_b \cdot \mathbf{ds} = \int_A (\mathbf{e}_3 \cdot \nabla \wedge \frac{\boldsymbol{\tau}_s}{\rho_0 f} - \frac{1}{f}\mathbf{V}_s \cdot \nabla f)\, dxdy$$

where A is the area enclosed by C.

c. Now use the results under a. in that of b. to derive an expression for $\partial\psi_b/\partial q$.

d. Show that

$$\mathbf{v}_b = \alpha_b \left[\int_A (\mathbf{e}_3 \cdot \nabla \wedge \frac{\boldsymbol{\tau}_s}{\rho_0 f} - \frac{1}{f}\mathbf{V}_s \cdot \nabla f)\, dxdy\right] \mathbf{t}$$

where $\mathbf{t}$ is the tangent vector to C and determine α_b.

(15.5) *Explicit bottom velocities in Example 15.3*

As an application of the results in exercise (15.4), it is possible to determine explicit expressions for the bottom velocities in the case of Example 15.3.

a. Show that for this case the expression for $\mathbf{v}_b$ in exercise 15.4 (part d.) reduces to

$$\mathbf{v}_b = |\nabla H| \frac{f}{R} \frac{\int F dxdy}{\oint |\nabla H| f^2 ds}\, \mathbf{t}$$

b. Use the expression for F in Example 15.3 to derive

$$\mathbf{v}_b = \frac{fF_0}{8Rx_0^2}(r^3 + 4x_0^2 r)\, \mathbf{t}$$

where $r = \sqrt{x^2 + y^2}$ and interpret the result.

Chapter 16

THERMOHALINE CIRCULATION

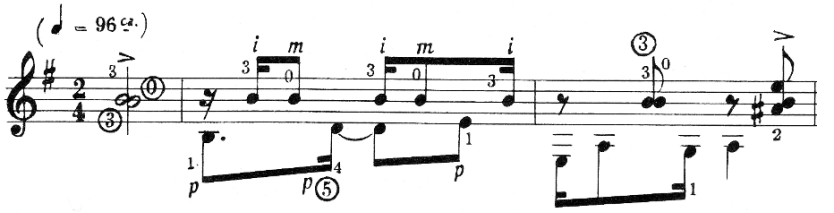

Preludios Americanos No. 5, A. Carlevaro

In this chapter the focus will be on the different roles of the transport of heat and salt in the component of the ocean circulation associated with density differences, the thermohaline circulation. It will appear that the stability properties of the large-scale ocean circulation are highly sensitive to the representation of these transports. Note that we have totally neglected these aspects in chapter 13, where only the density field was considered and not the separate effects of heat and salt. The motivation to study the thermohaline circulation in isolation is that variability in this flow may have been responsible for rapid climate change in the past (section 16.1). In section 16.2 we present an idealized model to investigate the stability of the thermohaline circulation, the Stommel two-box model. In the following sections (16.3 and 16.4) we analyze the equilibrium solutions of this model and the feedbacks affecting the stability of the thermohaline circulation (section 16.5).

16.1. Past climate variability

Much information on past climates has been obtained through measurement of isotope content, such as oxygen and carbon isotopes in material derived from ocean sediments and from ice cores, combined with accurate dating techniques. For example, the carbonate in shells of marine organisms (e.g. foraminifera) and water in ice caps contain two isotopes of oxygen, ^{18}O and ^{16}O. The normalized isotope ratio $\delta^{18}O$ is calculated as a deviation from a reference sample as

$$\delta^{18}O = \frac{(\frac{^{18}O}{^{16}O})_{sample} - (\frac{^{18}O}{^{16}O})_{reference}}{(\frac{^{18}O}{^{16}O})_{reference}}, \tag{16.1}$$

where the reference sample is different for ice cores (i.e. standard mean ocean water) than for carbonate shells (i.e. a specific fossil Cretaceous species). The isotope ^{16}O is lighter than ^{18}O so that water containing ^{16}O is preferentially evaporated and a temperature-dependent fractionation occurs. Under cold conditions, less water containing ^{18}O is able to evaporate into the atmosphere.

Changes in $\delta^{18}O$ reflect the combined effect of changes in global ice volume and temperature at the time of deposition of the sampled material. During very cold conditions, global ice volume is relatively large and hence sea level is low, which enriches water in the ocean with ^{18}O. Also because of the colder temperatures, more ^{18}O remains in the ocean and less ^{18}O becomes locked in the ice. Hence, in ocean sediments the ratio $\delta^{18}O$ will increase under cold conditions, whereas in ice cores it will decrease.

When corrections for global ice volume (with respect to the reference sample) are made, $\delta^{18}O$ can be used as an indicator for the temperature at the time of

deposition. The $\delta^{18}O$ record from the last 2.5 My, as obtained from deep sea sediments (ODP site 677 in the equatorial Pacific at 1°N, 84°W), is plotted in Fig. 16.1. One observes the variations in climate superposed on a gradual cooling

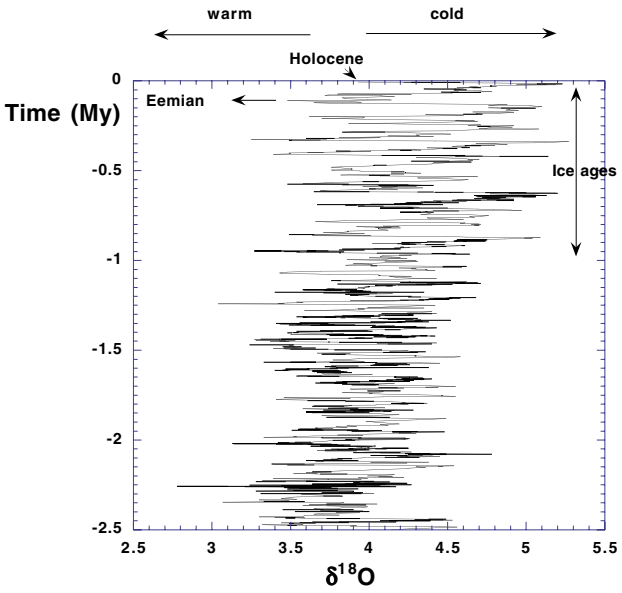

Figure 16.1. Isotope ratio $\delta^{18}O$ for benthic foraminifera at Ocean Drilling Program site 677 located in the eastern equatorial Pacific at 1°N, 84°W. A change in $\delta^{18}O$ of 0.23 units can be translated into a temperature change of about 1°C. All this data (and many more) is available through NOAA's Paleoclimatology site (http://www.ngdc.noaa.gov/paleo/paleo.html).

trend, with a change in pace about 0.7 My ago. From then on, a dominant period of about 100,000 years is found, reflecting the frequency of major glaciations which occurred in the northern hemisphere. Termination of these glaciations seems to be rather abrupt and leads to warmer periods, called interglacials; at the moment, we live in the Holocene interglacial. The transitions between glacials and interglacials are global in extent, since their signatures are found in available data from all over the globe.

The oxygen isotope record of the last 110,000 years within the GRIP ice core from Greenland is plotted in Fig. 16.2. Note that, contrary to the values of ocean sediments, values of $\delta^{18}O$ are now negative and cool periods have smaller (larger negative) values. From the last interglacial (the Eemian), the transition to the last glacial period has been in several stages, with again warmer periods alternating with cold intervals. The Last Glacial Maximum (LGM) occurred at about 20,000 years ago, and the temperature difference between LGM and Eemian is about

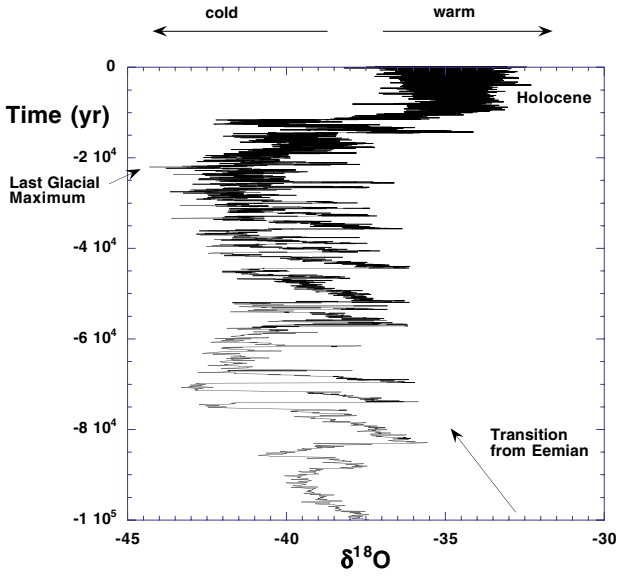

Figure 16.2. Oxygen isotope record of the last interglacial and the most recent glacial episode. A change in $\delta^{18}O$ of one unit corresponds to about a temperature change of about 2°C.

10°C. Spectral analysis reveals that the periodicities of the cold/warm fluctuations are about 40,000 and 20,000 years. The signatures of these changes are also visible globally, but the spatial extent of the signal reveals that these fluctuations are somehow forced in the northern hemisphere.

When the transition from the Last Glacial Maximum to the Holocene is considered in more detail, rapid transitions are observed. Sudden warm periods (interstadials), which last for 500 - 2,000 years, appear with temperature changes of about 5°C. These transitions between cold and warm episodes are also confirmed in $\delta^{18}O$ records from ocean sediments and are called Dansgaard-Oeschger events (cf. section 2.4). A magnification of the $\delta^{18}O$ record from the GRIP ice core is plotted in Fig. 16.3. Of particular interest is that the warming of the earth from 20,000 years ago onward has been in several relatively distinct stages. First, relatively fast transitions to the Bølling and Allerød interstadials occur, where the temperatures are relatively high. This is followed by a period of significant cooling between 12,500 and 11,500 years ago. The resulting stadial is referred to as the Younger Dryas, during which the apparent warming trend was delayed for approximately 1,000 years. The period ends with a rapid shift to warmer temperatures into the beginning of the Holocene, with indications of a temperature rise of 1°C per decade!

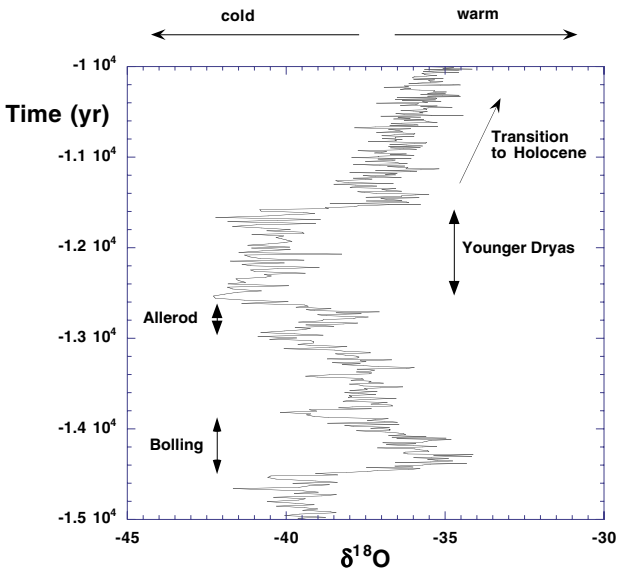

Figure 16.3. Oxygen isotope record from the GRIP ice core (shown in Fig. 16.2) over a smaller window of time, showing the Bølling and Allerød interstadials and the Younger Dryas stadial.

What processes caused these rapid transitions? As the ocean circulation is responsible for a substantial part of the meridional heat transport, fluctuations in the ocean currents can lead to climate changes. In the next section the possibility of relatively rapid transitions in the ocean circulation is explored using conceptual models.

Additional Material

B: For an introduction on the role of ocean circulation in paleoclimate, see Ruddiman (2001). An overview of the Younger Dryas and its possible causes is given in Berger and Jansen (1994).

16.2. The Stommel two-box model

Global ocean models with a coarse resolution (about 4° horizontally) are quite capable of simulating the main features of the global ocean circulation. One problem is the buoyancy flux forcing; when the models are forced with prescribed

heat flux, freshwater flux and wind stress, the resulting circulation has a very weak meridional overturning in the Atlantic. Hence, ocean modelers have used the observed surface salinity field to force the ocean models. Once equilibrium solutions are obtained, the freshwater flux is derived by computation and used in further investigations on sensitivity.

In typical studies of the stability of the thermohaline circulation, the freshwater forcing is changed by adding slowly varying perturbations at different locations. In this way the sensitivity of the overturning flow to the freshwater forcing can be determined. When the perturbation is added in the northern North Atlantic (with an inflow of typically 0.05 Sv per 1,000 years) a response as shown in Fig. 16.4 is obtained. On the vertical axis, for example, the amount of North Atlantic Deep Water is plotted (or the strength of the zonally integrated flow, the meridional overturning circulation) while the horizontal axis shows the strength of the anomalous freshwater forcing. With increasing freshwater forcing, the strength of the over-

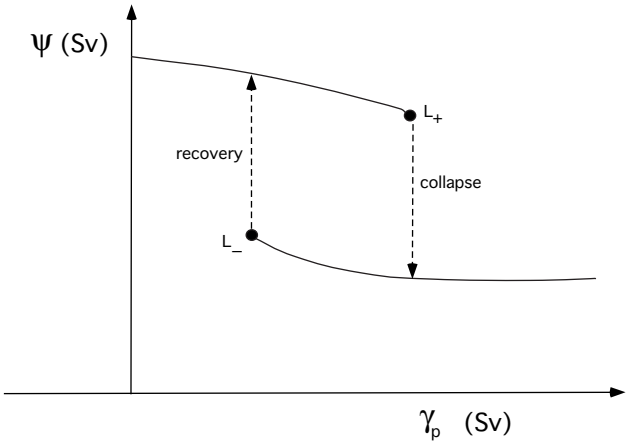

Figure 16.4. Typical hysteresis behavior associated with the changes in the strength of the Atlantic meridional overturning when the strength of the freshwater flux γ_p is changed slowly in time (first an increase followed by a decrease).

turning circulation decreases; at some point L_+ the overturning collapses. When the freshwater input is reversed, hysteresis occurs as the transition to the original state occurs at a smaller value of γ_p (at L_-) than the reverse transition.

This result indicates that there is more than one equilibrium circulation pattern for a given set of forcing conditions and that rapid transitions between them may occur on relatively short time scales. This is an alarming result when we consider the anticipated changes in the buoyancy forcing of the ocean due to the increase in greenhouse gases. In most climate models, precipitation increases over higher

latitudes and hence this would weaken the meridional overturning in the Atlantic. However, different models display a mosaic of different responses to the same greenhouse forcing conditions. In some of the models, the meridional overturning decreases substantially whereas in others it is hardly affected. We will focus only on the basic mechanisms which cause the occurrence of the multiple equilibria and which are responsible for the sensitivity of the ocean circulation to the freshwater and heat flux forcing.

In a model proposed by Stommel in 1961, this problem was first studied in its most essential form, using two vessels (boxes) having volumes V_p and V_e. These boxes contain well-mixed water of temperature and salinity (T_{e*}, S_{e*}) and (T_{p*}, S_{p*}), with the subscripts 'e' and 'p' indicating the equatorial and polar box, respectively. The boxes are connected at the surface by an overflow region and at the bottom by a capillary tube, to keep the volume in each box constant.

The flow rate Ψ_* is directed from high to low pressure (or from high to low density) and is assumed to be linearly related to the density difference between the liquid in the two boxes, i.e.

$$\Psi_* = \gamma \, \frac{\rho_{p*} - \rho_{e*}}{\rho_0}, \tag{16.2}$$

where ρ_0 is a reference density and γ a hydraulic constant. Hence the flow rate is taken to be positive if the liquid in the polar box is denser. The exchange of properties does not depend on the sign of Ψ_* because it only matters that properties from one box are transported to the other box. The pathway (either through the overflow, or through the capillary) is unimportant, because mass is conserved. A linear equation of state of the form

$$\rho_* = \rho_0(1 - \alpha_T(T_* - T_0) + \alpha_S(S_* - S_0)), \tag{16.3}$$

is assumed, where the subscript '0' refers to reference values.

Exchange of heat and salt in each box due to the surface forcing is modelled through relaxation to a prescribed surface temperature and salinity (T^a, S^a) with relaxation coefficients C^T and C^S. These coefficients are different for each box and for each quantity considered (heat or salt). In this way, the balances of heat and salt in each box are given by

$$V_p \frac{dT_{p*}}{dt_*} = C_p^T(T_p^a - T_{p*}) + \mid \Psi_* \mid (T_{e*} - T_{p*}), \tag{16.4a}$$

$$V_e \frac{dT_{e*}}{dt_*} = C_e^T(T_e^a - T_{e*}) + \mid \Psi_* \mid (T_{p*} - T_{e*}), \tag{16.4b}$$

$$V_p \frac{dS_{p*}}{dt_*} = C_p^S(S_p^a - S_{p*}) + \mid \Psi_* \mid (S_{e*} - S_{p*}), \tag{16.4c}$$

$$V_e \frac{dS_{e*}}{dt_*} = C_e^S(S_e^a - S_{e*}) + \mid \Psi_* \mid (S_{p*} - S_{e*}). \tag{16.4d}$$

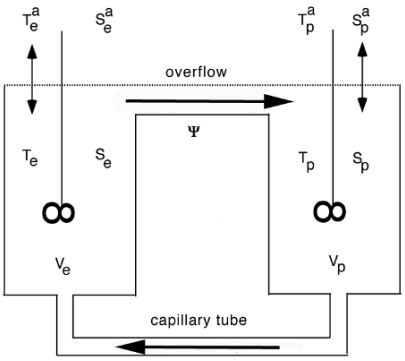

Figure 16.5. Sketch of the two-box model set-up. Two reservoirs contain well-mixed water and are connected through an overflow and a capillary tube. The circulation is driven by density gradients between the boxes which are set-up by the exchange at the surface.

In the following analysis, we will restrict ourselves to the case of realistic forcing, for which $T_e^a - T_p^a > 0$ and $S_e^a - S_p^a > 0$. For simplicity it is assumed that the relaxation times for temperature in both boxes is proportional to their volume and hence $C_p^T/V_p = C_e^T/V_e \equiv R_T$ is constant. The same simplification is made for salinity with $R_S = C_p^S/V_p = C_e^S/V_e$. When time, temperature, salinity and flow rate are scaled with $1/R_T$, $V_eV_pR_T/(\gamma\alpha_T(V_e+V_p))$, $V_eV_pR_T/(\gamma\alpha_S(V_e+V_p))$ and $V_eV_pR_T/((V_e+V_p)$, respectively the dimensionless equations become

$$\frac{dT}{dt} = \eta_1 - T(1+ \mid T - S \mid), \tag{16.5a}$$

$$\frac{dS}{dt} = \eta_2 - S(\eta_3 + \mid T - S \mid), \tag{16.5b}$$

where $T = T_e - T_p,\ S = S_e - S_p$ and $\Psi = T - S$ is the dimensionless flow rate. The three parameters that appear in the equations (16.5) are given by

$$\begin{aligned} \eta_1 &= \frac{(T_e^a - T_p^a)\,\gamma\alpha_T(V_e+V_p)}{V_eV_pR_T}, \\ \eta_2 &= \frac{R_S}{R_T}\frac{(S_e^a - S_p^a)\,\gamma\alpha_S(V_e+V_p)}{V_eV_pR_T}, \\ \eta_3 &= \frac{R_S}{R_T}. \end{aligned} \tag{16.6}$$

The model is thus a two-dimensional system of ordinary differential equations containing three independent parameters $\eta_i,\ i = 1, 2, 3$ and describing the evolution of the temperature and salinity differences between the boxes. Clearly,

the equations (16.5) form a relatively simple mathematical model which immediately suggests proceeding with analytical methods. However, imagine that we had many more, say ten or more, of these boxes all coupled through exchanges of heat and salt, which models the horizontal and vertical structure of the exchanges of these properties in more and more detail. Then, a typical way to proceed would be to choose parameter values as 'realistic' as possible and compute the time evolution of the temperature and salinity in the boxes, starting from some initial state. Such a time series is called a trajectory. Starting from the initial state (0,0) ($T = 0, S = 0$), such a trajectory is shown in Fig. 16.6a for the case $\eta_1 = 3.0$, $\eta_2 = 0.5$ and $\eta_3 = 0.3$. In this case, the freshwater forcing is relatively small and the flow evolves to a steady state with sinking in the north, since $\Psi = T - S > 0$. It turns out, that whatever initial condition one takes for these parameter values, this same steady state is always reached.

However, one usually likes to know the sensitivity of the system to changes in parameters and so three trajectories are plotted in Fig. 16.6b for the case $\eta_2 = 1.0$. The trajectories starting at the initial conditions $(0, 0)$ and $(2.5, 2.5)$ approach a steady state with sinking in the north similar to the case $\eta_2 = 0.5$. However, the evolution from the initial condition $(3.0, 3.0)$ approaches a steady state with sinking in the south, since $\Psi = T - S < 0$. Apparently, there are multiple steady states under the same forcing conditions in this model, provided that η_2 is large enough. But what is the limiting value of η_2 (somewhere between 0.5 and 1.0), where these multiple equilibria just appear? This question motivates us to look at the steady equations directly and solve these states as functions of parameters.

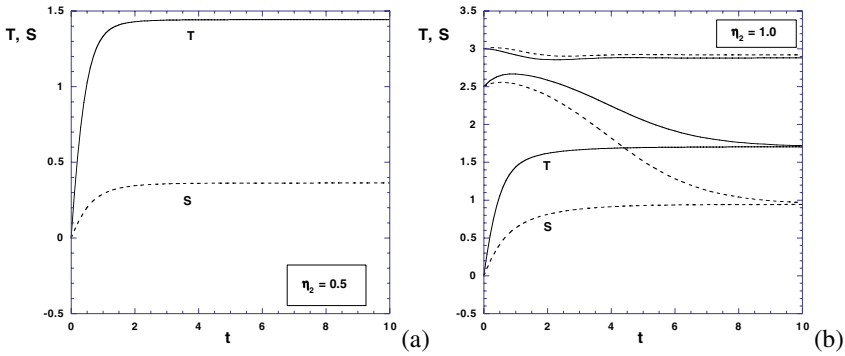

Figure 16.6. (a) Trajectory starting from the zero solution ($T = S = 0$) for the model (16.4) with $\eta_3 = 0.3$, $\eta_1 = 3.0$ and $\eta_2 = 0.5$. (b) Three different initial conditions lead to the approach of two different steady states for $\eta_3 = 0.3$, $\eta_1 = 3.0$ and $\eta_2 = 1.0$.

16.3. Equilibrium solutions

For steady states, the time derivatives in (16.5) are zero which gives the solutions

$$T = \frac{\eta_1}{1+ \mid \Psi \mid} \; ; \; S = \frac{\eta_2}{\eta_3 + \mid \Psi \mid},$$

and Ψ has to be solved using the implicit equation

$$\Psi = \frac{\eta_1}{1+ \mid \Psi \mid} - \frac{\eta_2}{\eta_3 + \mid \Psi \mid}.$$

When $\eta_2 = 0$, then $S = 0$ and hence $\Psi = T > 0$. The solution for Ψ follows from a quadratic equation and its positive root gives the solution

$$T = -\frac{1}{2} + \sqrt{\frac{1}{4} + \eta_1} \; ; \; S = 0,$$

which is referred to as the TH-solution. The flow, with sinking in the northern box is driven by the temperature difference between equator and pole with warm water flowing poleward through the overflow and cold water going equatorward through the tube (Fig. 16.5).

When $\eta_1 = 0$, there is no heat forcing and hence $T = 0$. It follows that $\Psi = -S < 0$ and hence a flow driven by the high salinity at the equator is obtained, giving the solution

$$T = 0 \; ; \; S = \frac{1}{2}\eta_3 - \sqrt{\frac{1}{4}\eta_3^2 + \eta_2},$$

which is referred to as the SA-solution.

Although the structure of the equilibrium solutions can be explicitly solved, it is more illustrative to show some typical results. With fixed $\eta_3 = 0.3$, a plot of steady solutions T and S versus η_2 are shown in Fig. 16.7a for $\eta_1 = 0.25$. Such a diagram will later be called a bifurcation diagram. There is a unique solution which is temperature driven for small η_2 (in this case, $\Psi = T - S > 0$), it is motionless at $\eta_2 = 0.1$ (at the intersection of the T and S curves) and becomes salinity driven at larger η_2. Hence, with increasing η_2 the solution changes from TH-type to SA-type.

The same diagram is shown for $\eta_1 = 3.0$ in Fig. 16.7b. As the time-dependent results also indicated, for $\eta_1 = 3.0$ there are multiple stationary solutions of the equations over a certain interval in η_2. Up to the point L_1 in Fig. 16.7b, the solution is unique of TH-type. Between the points L_1 and L_2, both TH and SA solutions exist and for values of η_2 beyond L_2 only the SA solution exists. The points L_1 and L_2 exactly bound the region of multiple equilibria. When the position of these points is determined for other values of η_1, the area in the (η_1, η_2) parameter plane where both TH and SA solutions occur is bounded by

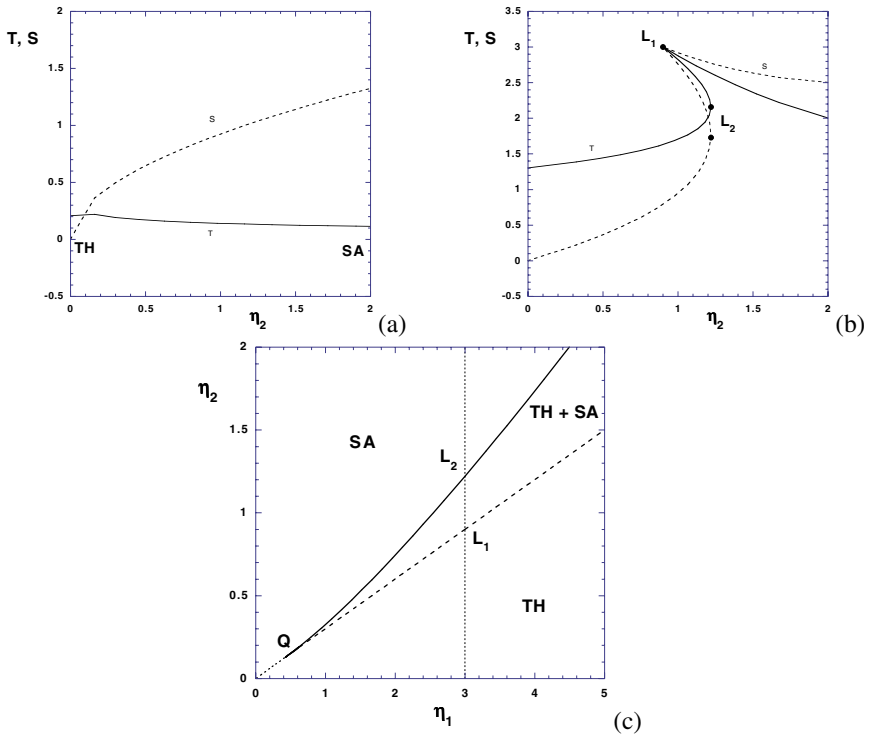

Figure 16.7. (a) Plot of steady values of temperature (T) and salinity (S) for the model (16.4) for different η_2 with fixed $\eta_1 = 0.25$ and $\eta_3 = 0.3$. (b) Same as in (a) but for $\eta_1 = 3.0$. (c) Path of the points L_1 and L_2 in (b) in the (η_1, η_2) parameter plane. These paths intersect at the point Q and connect to the curve $\eta_2 = \eta_1\eta_3$ which defined the motionless flow $\Psi = 0$ and extends from Q to the origin.

two curves (Fig. 16.7c). To the right of the curve of points L_1, there is unique northern sinking (TH) solution, whereas to the left of the curve of points L_2, there is a unique southern sinking (SA) solution. At the point Q, which is given by $Q = (\eta_3/(1-\eta_3), \eta_3^2/(1-\eta_3))$, both curves intersect. This point is located on the line for which there is no motion ($\Psi = 0$), described by $\eta_2 = \eta_1\eta_3$ (shown as the dotted curve in Fig. 16.7c). A diagram as in Fig. 16.7c, will later be referred to as a regime diagram.

In summary, the most important result is that for some of the parameter values, multiple steady states exist. Under the same forcing conditions, different steady (T, S) states exist in combination with opposite circulation directions. Two points

on the solution branches, indicated by L_1 and L_2, play a central role in the origin of these equilibria. The regime diagram in Fig. 16.7c provides a complete overview of where in the parameter plane these multiple equilibria occur.

16.4. Stability of equilibrium solutions

If a particular steady state from the previous section is indicated by $(\overline{T}, \overline{S})$, the next step is to consider the evolution of perturbations $(\tilde{T}, \tilde{S})$ on this steady state,

$$T = \overline{T} + \tilde{T}, \tag{16.7a}$$

$$S = \overline{S} + \tilde{S}. \tag{16.7b}$$

For the box model the notation $\mathcal{M}$ is used for a smoothed version of the modulus function, i.e.

$$\mathcal{M}(\Psi) = [\mathcal{H}(\Psi) - \mathcal{H}(-\Psi)]\,\Psi,$$

where $\mathcal{H}$ is a smoothed version of the Heaviside function, for example

$$\mathcal{H}(\Psi) = \frac{1}{2}(1 + \tanh\,\frac{\Psi}{\epsilon})\;;\; \epsilon \ll 1, \tag{16.8}$$

such that derivatives of $\mathcal{M}$ exist. For the linear stability boundary, quadratic interactions in the perturbations are neglected and using

$$\mathcal{M}(\overline{\Psi} + \tilde{\Psi}) = \mathcal{M}(\overline{\Psi}) + \mathcal{M}'(\overline{\Psi})\tilde{\Psi} + \cdots,$$

leads to the evolution equations

$$\frac{d\tilde{T}}{dt} = -\left[(1 + \mathcal{M}(\overline{\Psi}))\,\tilde{T} + \mathcal{M}'(\overline{\Psi})\overline{T}\,(\tilde{T} - \tilde{S})\right], \tag{16.9a}$$

$$\frac{d\tilde{S}}{dt} = -\left[(\eta_3 + \mathcal{M}(\overline{\Psi}))\,\tilde{S} + \mathcal{M}'(\overline{\Psi})\overline{S}\,(\tilde{T} - \tilde{S})\right], \tag{16.9b}$$

with $\tilde{\Psi} = \tilde{T} - \tilde{S}$. These equations admit solutions of the form

$$\tilde{T} = \hat{T}\,e^{\sigma t}\;;\; \tilde{S} = \hat{S}\,e^{\sigma t}, \tag{16.10}$$

where $\sigma = \sigma_r + i\sigma_i$ is the complex growth factor. The real part σ_r monitors the exponential growth rate of the perturbations. Hence, when $\sigma_r < 0$ for a particular perturbation $(\hat{T}, \hat{S})$ this perturbation is damped and when $\sigma_r > 0$ it will grow, leading to instability of the steady state. Substituting these expressions into the equations (16.9) gives an eigenvalue problem

$$\begin{pmatrix} -(1 + \mathcal{M}(\overline{\Psi}) + \mathcal{M}'(\overline{\Psi}))\overline{T} & \mathcal{M}'(\overline{\Psi})\overline{T} \\ -\mathcal{M}'(\overline{\Psi})\overline{S} & -(\eta_3 + \mathcal{M}(\overline{\Psi}) - \mathcal{M}'(\overline{\Psi}))\overline{S} \end{pmatrix} \hat{\mathbf{x}} = \sigma\hat{\mathbf{x}}. \tag{16.11}$$

where $\hat{\mathbf{x}} = (\hat{T}, \hat{S})$ The matrix on the left hand side is called the Jacobian matrix and will in most cases be indicated by J.

In Fig. 16.8a, the solutions in Fig. 16.7b are replotted with $\overline{\Psi}$ on the vertical axis. Along the branches, the sign ($\pm$) of both real eigenvalues σ is shown. For values of η_2 up to the point L_1, the TH-solution is stable and similarly for values beyond L_2, the SA-solution is stable. On the branch of solutions connecting the solutions at L_1 and L_2, one of the eigenvalues is positive. According to (16.10), small perturbations will grow on this steady state and hence it is unstable. This is demonstrated by computing the time evolution of the temperature and salinity fields starting exactly at this steady state (point A, $T = 2.80, S = 2.74$) for $\eta_2 = 1.0$ as plotted in Fig. 16.8b. The time-dependent state diverges away from the unstable steady state and eventually the steady TH-state at point B is reached. With the analysis of the steady states and their linear stability in parameter space

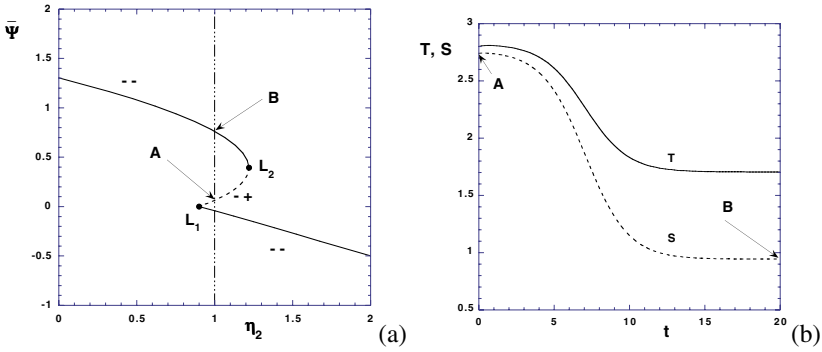

Figure 16.8. (a) Plot of steady values of the flow Ψ for the model (16.4) for different η_2 with fixed $\eta_1 = 3.0$ and $\eta_3 = 0.3$. (b) Evolution of the temperature and salinity fields for $\eta_1 = 3.0$, $\eta_2 = 1.0$ and $\eta_3 = 0.3$ starting at the steady state at point A ($T = 2.80, S = 2.74$). The $\pm$-signs indicate the sign of the (real) eigenvalue of the Jacobian matrix of the solution.

the trajectories computed for $\eta_2 = 1.0$ in Fig. 16.6 can also be understood. For $\eta_2 = 0.5$, the system is in the unique stable TH-regime according to Fig.16.7c. For $\eta_2 = 1.0$, the system in the regime of overlapping stable TH-states and SA-states and hence trajectories with two different initial conditions may approach different steady states.

Additional Material

D: For results of bifurcation studies on a hierarchy of models of the thermohaline circulation, see Dijkstra (2005) or the review paper on the application of dynamical systems theory to the large-scale ocean circulation (Dijkstra and Ghil, 2005).

16.5. Physical mechanisms

In this section, we will look at the two mechanisms which may cause multiple equilibria in more detail: the salt-advection feedback and the convective feedback.

16.5.1. Advective feedback

A nonlinear feedback between the flow and the density structure, called the (salt) advection feedback, is responsible for the non-uniqueness of equilibrium solutions in the Stommel model. Consider a zonally averaged (meridional overturning) circulation from the equator towards northern latitudes in Fig. 16.9. The surface forcing saltens/warms the low latitude region and freshens/cools the high latitude region and the circulation is driven by the meridional density gradient. Since there is northern sinking, the circulation is thermally driven. If the circulation strengthens, then more salt is transported northward. This enhanced salt transport will increase the density in the north and consequently amplify the original perturbation in the circulation. The strengthening of the circulation also transports more heat northward, which will weaken the flow by lowering the density. Heat transport therefore provides a negative feedback on the circulation.

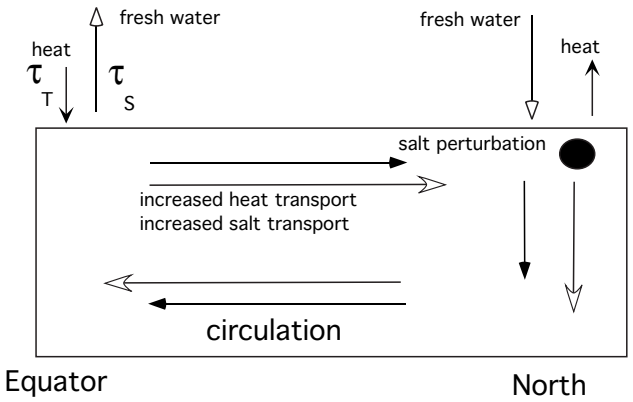

Figure 16.9. Sketch of the physics of the salt advection feedback. The mean circulation is indicated by the closed arrows. The upper ocean temperature and salinity fields can be inferred from the surface forcing of heat and freshwater. A salt perturbation which strengthens the circulation leads to a northward salt transport, which leads to amplification (open arrows) of the circulation (positive feedback). The perturbation in the circulation also leads to increased heat transport which opposes the original density perturbation. However, this perturbation is more damped by the atmosphere than the salinity perturbation.

In addition to the advection feedback, a central ingredient to the existence of multiple steady states are the different damping times of salinity and temperature

anomalies. The atmosphere exerts quite a strong control on the sea surface temperature anomalies, but salinity in the ocean does not affect the freshwater flux at all. In the two-box model in section 15.3, these different response time scales of salinity and temperature, with $\tau_S = 1/R_S$ and $\tau_T = 1/R_T$, were taken into account by the coefficient $\eta_3 = R_S/R_T = \tau_T/\tau_S$, which was smaller than unity. In general, the different surface boundary conditions for temperature and salinity are referred to as mixed boundary conditions. The extreme case is a prescribed surface temperature ($\tau_T << 1$) and prescribed surface freshwater flux ($\tau_S >> 1$) for which surface temperature perturbations are essentially zero.

Together, the advective feedback and the different response time scales provide a potential mechanism of change of the thermohaline circulation. Consider the thermally driven circulation as in Fig. 16.9 and imagine that a surface freshwater anomaly is suddenly present in the north part of the domain. Because the density is lowered in the north, the meridional buoyancy gradient decreases and hence the strength of the circulation decreases. The effect is that both the northward salt and heat transport decrease. Now, the negative heat anomaly is rapidly damped at the sea surface, but the freshwater anomaly is not damped at all and hence amplifies the original freshwater perturbation. This positive feedback is able to rapidly weaken the thermally driven overturning circulation.

16.5.2. Convective feedback

A convective feedback may also be responsible for multiple equilibria. In Fig. 16.10 we consider a box model with time-varying temperature T_* and salinity S_* due to a surface heat flux $F_T = \alpha(T_a - T_*)$ and surface salinity flux F_S in the surface box, coupled to a box with constant temperature T_i and S_i and constant prescribed flow rate q. Convective exchange with time constant τ^{-1} occurs if the surface water becomes denser than the deep water, which has constant temperature T_b and salinity S_b.

The equations for the evolution of the temperature T_* and salinity S_* are

$$\frac{dT_*}{dt_*} = \alpha(T_a - T_*) + q(T_i - T_*) + \tau_c \mathcal{H}(\rho_* - \rho_b)(T_b - T_*), \quad (16.12a)$$

$$\frac{dS_*}{dt_*} = F_S + q(S_i - S_*) + \tau_c \mathcal{H}(\rho_* - \rho_b)(S_b - S_*), \quad (16.12b)$$

with $\mathcal{H}$ being the Heaviside function. With the equation of state

$$\rho_*(T_*, S_*) = \rho_0 - \alpha_T T_* + \alpha_S S_*, \quad (16.13)$$

the steady states can be easily solved and become

$$T_* = \frac{qT_i + \alpha T_a + \tau_c \mathcal{H}(\rho_* - \rho_b) T_b}{q + \alpha + \tau_c \mathcal{H}(\rho_* - \rho_b)}, \quad (16.14a)$$

$$S_* = \frac{qS_i + F_S + \tau_c \mathcal{H}(\rho_* - \rho_b) S_b}{q + \tau \mathcal{H}(\rho_* - \rho_b)}. \quad (16.14b)$$

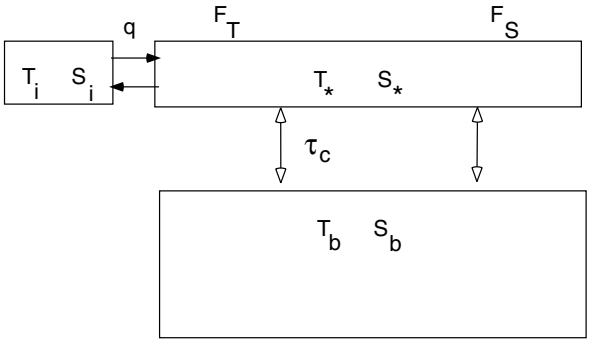

Figure 16.10. Sketch of the box model set-up to illustrate the convective feedback. An active box of temperature T_*, S_* is coupled to boxes of constant temperature T_i, S_i and T_b, S_b. Advective exchange takes place with flow rate q and vertical (convective) exchange occurs, on a time scale τ_c, if the surface water is denser than the bottom water.

Two types of equilibria can be distinguished. Those for which the argument of the Heaviside function is positive are called convective equilibria, and those for which it is negative are called non-convective equilibria. With the new parameters

$$\Phi_T = -\alpha_T(\alpha(T_a - T_b) + q(T_i - T_b)), \tag{16.15a}$$

$$\Phi_S = \alpha_S(F_S + q(S_i - S_b)), \tag{16.15b}$$

$$\kappa(\tau) = \frac{q+\tau}{q+\tau+\alpha}, \tag{16.15c}$$

three different solution regimes exist (Fig. 16.11).

The condition that a convective equilibrium exists can be written as $\Phi_S > -\kappa(\tau)\Phi_T$ (indicated as the line $a - b$ in Fig. 16.11) which defines regime **1** in Fig. 16.11. Similarly, the condition for a non-convective equilibrium to exists can be written as $\Phi_S < -\kappa(0)\Phi_T$ (indicated as the line $c - d$ in Fig. 16.11) which defines regime **2**. In regime **3**, both convective and non-convective equilibria exist and transitions between these solutions can occur under the same forcing conditions. Consider a non-convective state with cold/freshwater above warm/salty water which is only marginally stable and an atmospheric forcing which is cooling and freshening the upper box. A finite amplitude positive density perturbation is able to induce convection and if this occurs, warmer and saltier water is mixed to the surface. The heat in the surface layer is quickly lost to the atmosphere but the surface salinity is increased and hence convection is maintained, leading to a convective state.

For the particular case $\Phi_T = 1.0$, $q/\alpha = 0.5$ and $\tau/\alpha = 2.0$, the bifurcation diagram of the model (16.12) is plotted. In this diagram, both the dimensionless

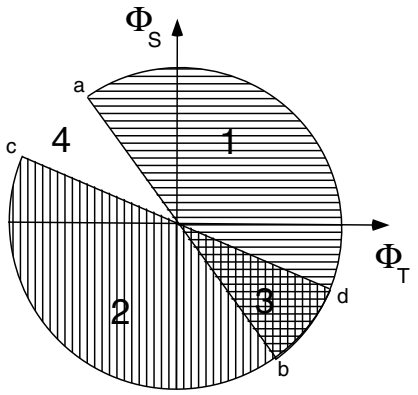

Figure 16.11. Sketch of the regimes of convective and non-convective equilibria in the box model in the (Φ_T, Φ_S) *parameter plane. In regime* **1***, there are convective states, in regime* **2** *there are non-convective states, whereas in regime* **3** *both states are present. In regime* **4** *no steady states exist.*

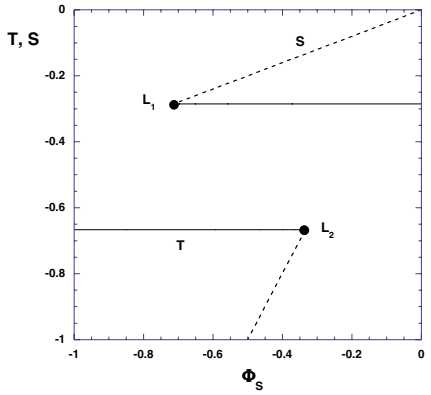

Figure 16.12. Diagram showing the equilibria for the box model (16.12) with $\Phi_T = 1.0$*,* $q/\alpha = 0.5$ *and* $\tau/\alpha = 2.0$ *and* Φ_S *as control parameter.*

temperature $T = \alpha_T(T_* - T_b)$ and salinity $S = \alpha_S(S_* - S_b)$ are plotted versus the control parameter Φ_S. Two saddle node bifurcations (L_1 and L_2) occur at $\Phi_S = -5/7$ and $\Phi_S = -1/3$. These are exactly the values $-\kappa(\tau)$ and $-\kappa(0)$ bounding the regions of convective and non-convective regimes, respectively. Hence, the high temperature and salinity states are convective and exist for $\Phi_S > -5/7$

(regime **1**) whereas the low salinity and temperature states are non-convective and exist for $\Phi_S < -1/3$ (regime **2**). Regime **3** is exactly located in the interval $-5/7 < \Phi_S < -1/3$ and in this regime, multiple equilibria exist. Note that regime **4** is not reached here, because $\Phi_T > 0$.

Summary

- The thermohaline circulation is the circulation associated with the transport of the heat and salt in the world oceans. The meridional overturning circulation is the zonally averaged flow in each ocean basin.
- Variations in the Atlantic meridional overturning circulation may have been important in relatively rapid climate variations in the past, such as the Younger Dryas.
- The meridional overturning circulation may be destabilized by two mechanisms: (i) the salt advection feedback, and (ii) a convective feedback. Box models such as the Stommel two-box model are important to understand these feedbacks.

16.6. Exercises on chapter 16

(16.1) *Transports in the Stommel model*

a. Reformulate the Stommel model in dimensional form in case (i) there is a prescribed freshwater flux H at the polar box and one with opposite sign (-H) at the equatorial box, and (ii) the volume of the boxes are different.

b. Provide an estimate of the volume of both boxes by dividing the North Atlantic in two sectors.

A reasonable value of the restoring time of heat at the ocean-atmosphere surface is about 1 month.

c. Based on the temperature and salinity plots in chapter 2, provide an estimate of the north-south density difference and estimate the value of the hydraulic constant in the Stommel model (γ) such that the meridional overturning is about 15 Sv.

d. Does the thermally driven circulation provides a good estimate of the meridional heat transport under reasonable values of the freshwater flux?

(16.2) *The Rooth model*

One of the shortcomings of the Stommel two-box model is that it only describes flow in the northern hemisphere. In a box model designed by Rooth (1982), the flow is driven by a north-south density difference, caused by freshwater fluxes H_S and H_N only.

Assume that the temperature is constant and only salinity varies in the boxes. It follows then that

$$q_* = k(S_{3*} - S_{1*})$$

where k is a transport coefficient.

a. Formulate the equations describing the evolution of the salinity in the boxes.

b. Determine the steady states of the model.

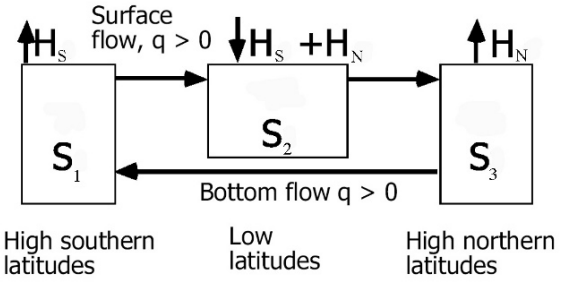

c. Show that the strength of the overturning circulation only depends on the freshwater flux H_N. Provide a physical explanation of this result.

(16.3) *Convective adjustment*

A problem in hydrostatic ocean models is the representation of convection which occurs when the water column becomes statically unstable. Assume a situation where, for example through advective transport, a layer of cold water with a temperature $T_* = T_1$ is situated above a layer of warmer water with a temperature $T_* = T_2$; the density is fully determined by the temperature.

a. Why can the resulting convection not be represented by the hydrostatic equations?

In an unstable situation, heat is mixed vertically to guarantee static stability of the water column.

b. What is the resulting temperature in case layer 1 has a thickness H_1 and layer 2 a thickness H_2?

c. Describe how this adjustment influences the large-scale flow?

(16.4) *Mechanism of meridional overturning*

It is nontrivial that a meridional density gradient $\Delta\rho$ is responsible for a meridional overturning.

a. The density gradient causes a meridional pressure difference Δp_M. Show that

$$\Delta p_M = gD\Delta\,\rho,$$

and argue that D depends on K_V (the vertical diffusivity).

b. This pressure gradient sets up a zonal flow through geostrophy with a characteristic velocity U. Explain why this flow causes a zonal pressure gradient Δp_Z.

c. Explain why $\Delta p_Z \approx \Delta p_M$.

d. Describe how the meridional flow can be driven by a meridional density difference.

(16.5) *Scaling*

As a sequel to exercise (16.4), we try to find a scaling relation between the strength of the meridional overturning circulation ψ_M and the meridional density difference $\Delta\rho$.

a. Scale U according to the geostrophic balance and use the scale of Δp_M from exercise (16.4) to show that

$$U = \frac{Dg\Delta\rho}{fL},$$

where f is the average Coriolis parameter over the flow domain.

b. Use the advection diffusion balance for the thermocline, i.e.,

$$w_* \frac{\partial \rho_*}{\partial z_*} = K_V \frac{\partial^2 \rho_*}{\partial {z_*}^2},$$

to show that

$$U = \frac{K_V L}{D^2}.$$

c. Show that $\psi_M \approx (\Delta\rho)^{\frac{1}{3}}$.

Bibliography

Anderson, D. L. T., K. Bryan, A. E. Gill, and R. C. Pacanowski, 1979: The transient response of the North Atlantic: Some model studies. *J. Geophys. Res.*, **84**, 4795–4815.

Anderson, D. L. T. and A. E. Gill, 1975: Spin-up of a stratified oceaan, with applications to upwellings. *Deep-Sea Research*, **22**, 583–596.

Anderson, D. L. T. and P. D. Killworth, 1977: Spin-up of a stratified ocean, with topography. *Deep-Sea Research*, **24**, 709–733.

Batchelor, G., 2000: *Introduction to Fluid Dynamics*. Cambridge University Press, First Cambridge Mathematical Library Edition, Cambridge, UK.

Battisti, D. and A. Hirst, 1989: Interannual variability in a tropical atmosphere-ocean model: Influence of the basic state, ocean geometry and nonlinearity. *J. Atmos. Sci.*, **46**, 1687–1712.

Bender, C. M. and S. A. Orszag, 1999: *Advanced Mathematical Methods for Scientists and Engineers*. Springer Verlag, New York, USA.

Berger, W. H. and E. Jansen, 1994: *Younger Dryas episode: ice collapse and super-fjord heat pump*. North Holland, Amsterdam, The Netherlands, 61-105.

Bigg, G. R., 2003: *The Oceans and Climate*. Cambridge University Press, Cambridge UK.

Bobylev, L. P., K. Y. Kondratyev, and O. M. Johannessen, 2003: *Arctic Environment Variability in the Context of Global Change*. Springer, New York.

Broecker, W. S., 1991: The great ocean conveyor. *Oceanography*, **4**, 79–89.

Cane, M. A., 1986: El Niño. *Anual Rev. Earth Plane. Sci*, **14**, 43–70.

Cane, M. A. and S. E. Zebiak, 1985: A theory for El Nino and the Southern Oscillation. *Science*, **228**, 1084–1087.

Cessi, P. and G. R. Ierley, 1995: Symmetry-breaking multiple equilibria in quasi-geostrophic, wind-driven flows. *J. Phys. Oceanogr.*, **25**, 1196–1205.

Cushman-Roisin, B., 1994: *Introduction to geophysical fluid dynamics*. Prentice Hall.

De Niet, A., F. W. Wubs, A. D. Terwisscha van Scheltinga, and H. A. Dijkstra, 2007: A tailored solver for bifurcation analysis of ocean-climate models. *J. Comp. Physics*, **doi:10.1016/j.jcp.2007.08.006**, 242–254.

Dewar, W. K., 1998: Topography and barotropic transport control by bottom friction. *J. Mar. Res.*, **56**, 295–328.

Dijkstra, H. A., 2005: *Nonlinear Physical Oceanography: A Dynamical Systems Approach to the Large Scale Ocean Circulation and El Niño, 2nd Revised and Enlarged edition.* Springer, New York, 532 pp.

Dijkstra, H. A. and G. Burgers, 2002: Fluid Dynamics of El Nino Variability. *Annual Review of Fluid Mechanics*, **34**, 531–558.

Dijkstra, H. A. and M. Ghil, 2005: Low-frequency variability of the large-scale ocean circulation. *Rev. Geophysics*, **43**, RG3002, doi:10.1029/2002RG000122.

Drazin, P. G. and W. H. Reid, 2004: *Hydrodynamic Stability 2nd Edition*. Cambridge Univ. Press.

Duxbury, A. C., A. B. Duxbury, and K. A. Sverdrup, 2000: *An introductin to the World's Oceans, sixth edition*. Addison-Wesley, Reading, MA, U.S.A.

Emery, W. J. and R. E. Thomson, 2004: *Data an]alysis methods in Physical Oceanography*. Elsevier, Amsterdam, Netherlands.

Fofonoff, N. P. and R. C. Millard, 1983: Algorithms for computation of fundamental properties of seawater. Technical Report 44, UNESCO technical papers in Marine Science.

Ganachaud, A. and C. Wunsch, 2000: Improved estimates of global ocean circulation, heat transport and mixing from hydrographic data. *Nature*, **408**, 453–457.

Gill, A. E., 1982: *Atmosphere-Ocean Dynamics*. Academic Press, New York, U.S.A.

Glantz, M. H., 1996: *Currents of Change*. Cambridge University Press, Cambridge UK.

Gordon, A. L., 1986: Interocean exchange of thermocline water. *J. Geophys. Res.*, **91**, 5037–5046.

Gouretski, V. V. and K. P. Koltermann, 2004: Berichte des Bundesambtes für Seeschifffahrt und Hydrographie. Technical Report 35, .

Griffies, S. M., 2004: *Fundamentals of ocean-climate models*. Princeton University Press, Princeton, USA.

Holloway, G., 1992: Representing topography stress for large-scale ocean models. *J. Phys. Oceanogr.*, **22**, 1033–1046.

Imbrie, J. and K. P. Imbrie, 1986: *Ice Ages: Solving the Mystery*. 2nd Edn., Harvard Univ. Press, Cambridge, Mass., 224 pp.

Jackett, D. R., T. J. McDougall, R. Feistel, D. G. Wright, and S. M. Griffies, 2006: Algorithms for Density, Potential Temperature, Conservative Temperature, and the Freezing Temperature of Seawater. *J. Atmos. Ocean. Technol.*, **12**, 17091728.

Jiang, S., F.-F. Jin, and M. Ghil, 1995: Multiple equilibria and aperiodic solutions in a wind-driven double-gyre, shallow-water model. *J. Phys. Oceanogr.*, **25**, 764–786.

Jin, F.-F., 1997a: An equatorial recharge paradigm for ENSO. I: Conceptual Model. *J. Atmos. Sci.*, **54**, 811–829.

Jin, F.-F., 1997b: An equatorial recharge paradigm for ENSO. II: A stripped-down coupled model. *J. Atmos. Sci.*, **54**, 830–8847.

Jochum, M. and R. Murtugudde, 2006: *Physical Oceanography: Developments Since 1950*. Springer, Heidelberg, Germany.

Kevorkian, J. K. and J. D. Cole, 1996: *Multiple Scale and Singular Perturbation Methods*. Springer, New York, USA.

Knaus, J. A., 1997: *Introduction to Physical Oceanography, 2e edition*. Prentice Hall, Upper Saddle River, NJ, USA.

Kuo, H. L., 1951: The general circulation and the stability of zonal flow. *Tellus*, **3**, 268–284.

Levitus, S. and T. Boyer, 1994: World Ocean Atlas 1994, Volume 4: Temperature. *NOAA Atlas NESDIS, US Department of Commerce, Washington DC*, **4**, 0–117.

Levitus, S., R. Burgett, and T. Boyer, 1994: World Ocean Atlas 1994, Volume 3: Salinity. *NOAA Atlas NESDIS, US Department of Commerce, Washington DC*, **3**, 0–99.

Mc Williams, J. C., 2006: *Fundamentals of Geophysical Fluid Dynamics*. Cambridge University Press, Cambridge, U.K.

McDougall, T. J., D. R. Jackett, D. G. Wright, and R. Feistel, 2003: Accurate and computationally efficient algorithms for potential temperature and density of seawater. *J. Atmos. Ocean. Technol.*, **5**, 730–741.

McPhaden, M. and coauthors, 1998: The Tropical Ocean-Global Atmosphere observing system: a decade of progress. *J. Geophys. Res.*, **103**, 14,169–14,240.

Mertz, G. and D. G. Wright, 1992: Interpretation of the jebar term. *J. Phys. Oceanogr.*, **22**, 301–305.

Müller, P., 1995: Ertels potential vorticity theorem in physical oceanography. *Review of Geophysics*, **33**, 67–98.

Neelin, J. D., D. S. Battisti, A. C. Hirst, F.-F. Jin, Y. Wakata, T. Yamagata, and S. E. Zebiak, 1998: ENSO Theory. *J. Geophys. Res.*, **103**, 14,261–14,290.

Neelin, J. D., M. Latif, and F.-F. Jin, 1994: Dynamics of coupled ocean-atmosphere models: The tropical problem. *Ann. Rev. Fluid Mech.*, **26**, 617–659.

Nøst, O. A. and P. E. Isachsen, 2003: The large-scale time-mean ocean circulation in the Nordic Seas and Arctic Ocean estimated from simplified dynamics. *J. Mar. Res.*, **61**, 175–210.

Oberhuber, J. M., 1988: *The Budget of Heat, Buoyancy and Turbulent Kinetic Energy at the Surface of the Global Ocean*. Max Planck Institute für Meteorologie Hamburg report nr. 15, Hamburg, Germany.

Olbers, D., 1998: Comments on "On the obscurantist physics of form drag in theorizing about the Circumpolar Current". *J. Phys. Oceanogr.*, **28**, 1647–1654.

OU-staff, 1989: *Ocean Circulation*. Pergamom Press.

OU-staff, 2004a: *Seawater: Its Composition, Properties and Behaviour*. Pergamom Press.

OU-staff, 2004b: *The Ocean Basins: Their Structure and Evolution*. Pergamom Press.

Pedlosky, J., 1987: *Geophysical Fluid Dynamics. 2nd Edn*. Springer-Verlag, New York.

Pedlosky, J., 1996: *Ocean Circulation Theory*. Springer, New York.

Pedlosky, J., 2003: *Waves in the Ocean and Atmosphere*. Springer, New York.

Peixoto, J. P. and A. H. Oort, 1992: *Physics of Climate*. AIP Press, New York.

Philander, S. G. H., 1990: *El Niño and the Southern Oscillation.* Academic Press, New York.

Philander, S. G. H., 2004: *Our Affair with El Niño*. Princeton University Press, Princeton, USA.

Pickard, G. L. and W. J. Emery, 1990: *Descriptive Physical Oceanography, 5th edition*. Pergamom Press, Oxford, UK.

Pond, E. and G. L. Pickard, 1983: *Introduction to Dynamical Oceanography, 5th edition*. Pergamom Press, Oxford, UK.

Rooth, C., 1982: Hydrology and ocean circulation. *Progress in Oceanography*, **11**, 131–149.

Ruddiman, W. F., 2001: *Earth's Climate: Past and Future*. W.H. Freeman and Company, New York, U.S.A.

Rudels, B., H. J. Friedrich, and D. Quadfasel, 1999: The Arctic Circumpolar Boundary Current. *Deep-Sea Research*, **46**, 1023–1062.

Salmon, R., 1998: *Lectures on Geophysical Fluid Dynamics*. Oxford Univ. Press, 400pp.

Schmitz, W. J., 1995: On the interbasin-scale thermohaline circulation. *Rev. Geophys.*, **33**, 151–173.

Schopf, P. and M. Suarez, 1988: Vacillations in a coupled ocean-atmosphere model. *J. Atmos. Sci.*, **45**, 549–566.

Stommel, H., 1977: *The Gulf Stream*. Univ. California Press, Los Angeles, USA.

Stommel, H. and D. W. Moore, 1989: *An introduction to the Coriolis force*. Columbia University Press, New York, USA.

Thorpe, S. A., 2005: *The Turbulent Ocean*. Cambridge University Press, UK, 437 pp.

Tomczak, M. and J. S. Godfrey, 1994: *Regional Oceanography: an introduction. First Edition*. Pergamon Press, Cambridge, U.K.

Trenberth, K. E., J. G. Olson, and W. G. Large, 1989: A global ocean wind stress climatology based on ECMWF analyses. Technical report, National Center for Atmospheric Research, Boulder, CO, U.S.A.

Vallis, G. K., 2006: *Atmospheric and Oceanic Fluid Dynamics: Fundamentals and Large-Scale Circulation*. Cambridge University Press, Cambridge, U.K.

Veronis, G., 1963: An analysis of the wind-driven ocean circulation with a limited number of Fourier components. *J. Atmos. Sci.*, **20**, 577–593.

Vreugdenhil, C. B., 1994: *Numerical Methods for Shallow-Water Flow*. Springer, New York, USA.

Warren, B. A., J. H. LaCasce, and P. E. Robbins, 1997: On the obscurantist physics of form drag in theorizing about the Circumpolar Current. *J. Phys. Oceanogr.*, **26**, 2297–2301.

Wijffels, S. E., R. W. Schmitt, H. L. Bryden, and A. Stigebrandt, 1992: Transport of fresh water by the ocean. *J. Phys. Oceanogr.*, **22**, 155–163.

WOCE, 2001: *Ocean Circulation and Climate: Observing and Modeling the Global Ocean Ocean [Siedler, G. and Church, J. and Gould, J. (eds)]*. Academic Press, San Diego, USA, 715.

Wright, D. G., 1997: An equation of state for use in ocean models: Eckart's formula revisited. *Journal of Atm. Ocenic Techn.*, **14**, 735–741.

Wunsch, C., 2002: What is the thermohaline circulation? *Science*, **298**, 1179–1180.

Wyrtki, K. and B. Koblinksky, 1984: Mean water and current structure during the Hawaii to Tahiti shuttle experiments. *J. Phys. Oceanogr.*, **14**, 242–254.

Copyright Acknowledgements

I gratefully acknowledge the following copyright holders who have kindly provided permission to reproduce the figures indicated. Sources of all figures are also referenced in each figure caption.

Chapter 1: Opening; Composer: F. Sor; Title: Estudio No. 1 Copyright and Publisher: Edward B. Marks Music Company, USA, 1945. Permission by Albersen Muziek, the Hague, The Netherlands. ♯ ■ Chapter 2: Opening; Composer: F. Tarrega; Title: Preludio (Lagrima); Copyright and Publisher: Daniel Forea, Madrid, 1930. Permission by Albersen Muziek, the Hague, The Netherlands. ♭ Fig. 2.4a by Springer-Verlag (Peixoto and Oort, 1992). ♯ Fig. 2.5 by Nature (Ganachaud and Wunsch, 2000), copyright (2000) Macmillan Magazines Ltd. ♭ Fig. 2.6 by Nature (Ganachaud and Wunsch, 2000), copyright (2000) Macmillan Magazines Ltd. ♯ Fig. 2.7, by AMS (Wijffels et al., 1992). ♭ Fig. 2.8, by AGU (Dijkstra and Ghil, 2005). ♯ ■ Chapter 3: Opening; Composer E. Pujol; Title: El Abejorro; Copyright and Publisher: Ricordi Americana S.A.E.C. Buenos Aires, 1955. Permission by Albersen Muziek, the Hague, The Netherlands. ♭ ■ Chapter 4: Opening; Composer M. Ponce; Title: Prelude IX; Copyright and Publisher: B. Schott's Söhne, Mainz, 1930. Permission by Albersen Muziek, the Hague, The Netherlands. ♯ ■ Chapter 5: Opening; Composer L. Brouwer; Title: Berceuse; Copyright and Publisher: Editions Max Eschig, 1978. Permission by Albersen Muziek, the Hague, The Netherlands. ♭ ■ Chapter 6: Opening; Composer L. Brouwer; Title: Pieza Sin Titulo; Copyright and Publisher: Editions Max Eschig, 1972. Permission by Albersen Muziek, the Hague, The Netherlands. ♯ ■ Chapter 7: Opening; Composer G. Garcia; Title: Etude No. 4; Copyright and Publisher: Mel Bay Publications, Inc. USA, 1995. Permission by Albersen Muziek, the Hague, The Netherlands. ♭ ■ Chapter 8: Opening; Composer B. Calatayud; Title: Bolero; Copyright and Publisher: Union Musical Espanola, Madrid, 1962. Permission by Albersen Muziek, the Hague, The Netherlands. ♯ ■ Chapter 9: Opening; Composer A. Lauro; Title: Valse Venezolano No. 2; Copyright and Publisher: Ricordi Americana S.A.E.C. Buenos Aires, 1964. Permission by Albersen Muziek, the Hague, The Netherlands. ♭ ■ Chapter 10: Opening; Composer E. Granados; Title: Valses Poeticos No. 1; Copyright and Publisher: Union Musical Espaniola, Madrid, 1926. Permission by Albersen Muziek, the Hague, The Netherlands. ♯ ■ Chapter 11: Opening; Composer J. Sagrerias; Title: El Colibri; Copyright and Publisher: Ricordi Americana S.A.E.C. Buenos Aires, 1954. Permission by Albersen Muziek, the Hague, The Netherlands. ♭ Fig. 11.3 by AMS (Wyrtki and Koblinksky, 1984). ♯ Fig. 11.5 by AMS (Wyrtki and Koblinksky, 1984). ♭ Fig. 11.13 by AGU (Neelin et al., 1998). ♯ ■ Chapter 12: Opening; Composer: H. Villa-Lobos; Title: Suite Polulaire Brésilienne, No. 4; Copyright and Publisher: Editions Max Eschig, 1990; Permission by Albersen Muziek, the

Hague, The Netherlands. ♭ ■ Chapter 13: Opening; Composer: H. Villa-Lobos; Title: Etude nr. 12; Copyright and Publisher: Editions Max Eschig, 1990; Permission by Albersen Muziek, the Hague, The Netherlands. ♯ ■ Chapter 14: Opening; Composer M. de Falla; Title: Homenaja; Copyright and Publisher: Chester Music Limited, UK, 1994. Permission by Albersen Muziek, the Hague, The Netherlands. ♭ Fig. 14.2a by Academic Press (now Elsevier) (WOCE, 2001). ♯ Fig. 14.3d by Academic Press (now Elsevier) (WOCE, 2001). ♭ ■ Chapter 15: Opening; Composer A. Barrios; Title: Vals; Copyright and Publisher: Permission by Albersen Muziek, the Hague, The Netherlands. ♭ Fig. 15.4a by Journal of Marine Research (Nøst and Isachsen, 2003). ♯ Fig. 15.4b by Elsevier (Rudels et al., 1999). ♭ Fig. 15.5 by Journal of Marine Research (Nøst and Isachsen, 2003). ♯ Fig. 15.6 by Springer (Pedlosky, 1996). ♭ Fig. 15.8 by Springer (Pedlosky, 1996). ♯ Fig. 15.9, 15.10 and 15.11 by Journal of Marine Research (Nøst and Isachsen, 2003). ♭ ■ Chapter 16: Opening; Composer A. Carlevaro; Title: Preludios Americanos No.5: Tamboriles; Copyright and Publisher: D.A.C.I.S.A. Montivideo, Uruguay, 1975 Permission by Albersen Muziek, the Hague, The Netherlands. ♯ ■

Index